Experiments in Thermal Ignition: Influence of Natural Convection on Properties of Gaseous Explosions

Thesis by
Conor Daniel Martin

In Partial Fulfillment of the Requirements for the
Degree of
Doctor of Philosophy

CALIFORNIA INSTITUTE OF TECHNOLOGY
Pasadena, California

2023
Defended May 24, 2023

Conor Daniel Martin
ORCID: 0000-0003-2332-7383

ACKNOWLEDGEMENTS

This work was made possible through the steady guidance and support of my excellent advisor Joseph Shepherd. His wealth of experience was seemingly endless and enabled timely guidance and insights throughout the course of our many projects together. I am truly fortunate to have been able to learn from his experience and mentorship and am grateful to have had his countless hours of guidance and encouragement to continuously push me to be a better researcher and engineer.

I also want to thank my committee members, Joanna Austin, Tim Colonius, and Hans Hornung for their time spent on careful evaluation and reading of this work and for insightful discussions over the years. I would also like to thank Beverley McKeon for her insights as a member of my candidacy committee and for facilitating the Base 11 AMP program which was a joy to run, even entirely over Zoom.

This work was chiefly supported by The Boeing Company (CT-BA-GTA-1). Our collaborators at Boeing were instrumental in providing not only funding but impetus to do good and interesting work. I would like to thank our close collaborators Phil Boettcher, Jason Damazo, Eddie Kwon, Dominic Martinez, and Brad Moravec for this and their insights during our many meetings.

I am also grateful to have been supported by the Department of Defense (DoD) through the National Defense Science & Engineering Graduate Fellowship (NDSEG) Program and for the networking, travel, and career opportunities enabled by this program

I had the good fortune of learning from many wonderful graduate student mentors when I first joined Caltech and the Explosion Dynamics Lab; J.C. Veilleux, Matt Leibowitz, Nelson Yanes, and Silken Jones were all welcoming and helped me learn my way around the lab and fiddle with their experiments early on.

I would further like to thank all other current and former members of EDL whom I had the chance to work with and have many insightful discussions with over the years: Donner Schoeffler, Branson Davis, Charline Fouchier, Ken Matsuoka, Yunliang Qi, Bohoon Kim, and Sveinung Sund. Of course our group administrators, Barbara McKinzie-Slater and Liza Bradulina, also deserve thanks for their help with many bureaucratic and logistical details in addition to their always uplifting attitudes.

Thanks also to the many friendships that were forged from the 2017 GALCIT G1 cohort and beyond. Eric, Wesley, Jean, Emile, Mike, Ben, Kai, Hiro, Uba, Harsha, Alex, Akshay, Kira, Avinash, Greg, Cai, Ziyun, and Michelle. I look forward to seeing the great things you all accomplish. To Emile, Uba, Cai, and Nelly I couldn't have asked for a better COVID bubble to keep me sane and entertained the past few years.

I am grateful to my parents, Janet and Doug, and my brothers, Sean and Aaron, for all of their love and encouragement throughout my life and for frequently crossing the country to visit me. I would not be here today without them, especially if not for Sean's role model in pursuing engineering.

Lastly a loving thank you to my warmhearted Fianceé Keree for her unwavering support and encouragement over the years. You always know when I need your strength and I am grateful to have you by my side. Thank you for embarking on this cross country journey with me and I can't wait for the next chapter of our lives.

— Go Bills.

ABSTRACT

Explosion hazards exist in many industrial sectors including chemical processing, mining, nuclear power, and aviation. Thermal ignition is the name given to the particular case where the initiation energy is supplied via thermal heating of a gas. The critical conditions leading to thermal ignition are in general highly configuration dependent and require a broad set of experimentation to investigate the influence of wide ranging physical processes on ignition. To aid this effort the present work comprises three main experiments covering a range of thermal ignition hazards. First, a heated atmosphere test with fuel injection (ASTM-E659) was implemented to enable the study of heavy hydrocarbon fuels such as Jet A and multicomponent surrogates. This approach showed the existence of cool flame ignition modes near the ignition thresholds for most fuels. The autoignition temperature (AIT) of commodity Jet A was found to be reasonably reproducible by most alkane fuels including n-hexane. Multicomponent surrogates were also able to match the cool flame ignition regimes reasonably well.

Next, ignition using a vertical heated surface in a cold reactive atmosphere was studied in the laminar flow regime. The effects of dilution with nitrogen and reduced pressure were explored for n-hexane/oxygen/nitrogen mixtures. Results found a modest dependence of minimum ignition temperatures on pressure and nitrogen fraction however, with a significant reduction in explosion severity as measured by the maximum overpressure and transient duration. At sufficiently reduced oxygen concentrations, localized weakly propagating flames were found to form in the thermal layer near the surface and produce sustained puffing flame instabilities. One-dimensional flame simulations with detailed kinetics were conducted to supplement and aid in interpretation of the experimental measurements for diluted mixtures. Correlation of ignition thresholds were found to be possible using simplified flame properties and laminar natural convection boundary layer theory.

Finally, a novel experiment was designed to explore the effects of turbulent transition and confinement of large heated surfaces on ignition thresholds. Modeling of the energy balance for resistive heating showed that cylinders up to 36 in. long could be heated using modest power supplies. Six cylinder sizes of varying length were chosen based on this analysis to explore laminar, transitional, and turbulent flow regimes. A large scale flow visualization system was created to study these flow regimes and found that turbulent transition occurred for cylinders as small as 10 in. long for wall temperatures of 1000 K. A study of the transitional dependence on temperatures for large temperature difference (T_w = 555–1140 K), highly non-Boussinesq conditions found that the transitional Ra_H decreased by two orders of magnitude in this regime. The thermal layer thickness at the transition height, $\delta_{T,trans}$, was estimated in order to obtain a relevant length scale to the boundary layer transition problem. Using this a more consistent transition criteria, $Ra_{\delta_{T,trans}}$, was obtained

and found to vary by only a factor of two in the high temperature cases studied.

The implementation of these cylinders in ignition testing revealed that there was a strong influence of heating rate due to confinement. The use of absorption spectroscopy showed that for low heating rates the fuel was mostly consumed in low temperature reactions prior to or in place of rapid ignition. This resulted in larger ignition temperatures and weak flames which propagate only in the thermal boundary layer. This effect was explained as a consequence of reduced flow recirculation times due to confinement. A strong influence of turbulence was also found for ignition thresholds when compared with other data for ignition by vertical hot surfaces in the laminar regime. Turbulence was also found to strongly influence the explosion properties due to turbulent flame acceleration. This resulted in larger explosion pressures, shorter transients, and faster flames.

PUBLISHED CONTENT AND CONTRIBUTIONS

Martin, C. D., & Shepherd, J. E. (2022). Thermal ignition: Effects of fuel, ambient pressure and nitrogen dilution. *Proceedings of the 14th International Symposium on Hazards, Prevention and Mitigation of Industrial Explosions (ISHPMIE 2022)*, 675–689. https://doi.org/10.7795/810.20221124.

C.D.M participated in the conception of the project, constructed and conducted the experiments, implemented software for data processing, led analysis of results, and was the lead author in writing of the manuscript

Martin, C. D., & Shepherd, J. E. (2021). Low temperature autoignition of jet a and surrogate jet fuel. *Journal of Loss Prevention in the Process Industries*, *71*, 104454. https://doi.org/10.1016/j.jlp.2021.104454.

C.D.M participated in the conception of the project, designed, constructed, and conducted the experiments, designed and implemented software for data processing, led analysis of results, and was the lead author in writing of the manuscript

Martin, C. D., & Shepherd, J. E. (2020). Low temperature autoignition of jet a and surrogate jet fuels. *Proceedings of the 13th International Symposium on Hazards, Prevention and Mitigation of Industrial Explosions (ISHPMIE 2020)*, 891–907. https://doi.org/10.7795/810.20200724.

C.D.M participated in the conception of the project, designed, constructed, and conducted the experiments, designed and implemented software for data processing, led analysis of results, and was the lead author in writing of the manuscript

TABLE OF CONTENTS

LIST OF ILLUSTRATIONS

LIST OF TABLES

Chapter 1

INTRODUCTION

1.1 Motivation

Fire and explosion hazards exist in many industrial sectors including chemical processing, mining, nuclear power, and aviation. These events can lead to severe structural damage, economic loss, and loss of human life. There are a wide range of applications such as fuel storage facilities, aircraft fuel tanks, chemical processing industry, and power generation where components can either deliberately contain flammable mixtures, or fuels that will form flammable mixtures if accidentally released into the atmosphere. Eliminating or mitigating the risk posed by accidental ignition hazards is key to the safe operation of such systems and components. Ignition hazards can come in many forms such as open flames, hot particles, sparks, hot gas jets, and hot surfaces. The investigations described in this dissertation focus on the particular hazard of thermal ignition of a flammable atmosphere by a hot surface with application to aircraft design and certification.

Thermal ignition is the name given to any kind of ignition for which the energy is supplied via thermal heating of a gas. This heating can occur by exposure of hot surfaces, particles, or gas jets to a reactive atmosphere or fuel spray impinging on a hot surface or into a heated volume of gas. In such cases sufficient thermal energy is added to the system to initiate fuel pyrolysis and oxidation which are generally exothermic processes. The energy release from these gas phase reactions competes with heat loss to surrounding surfaces and surrounding cold gas. At sufficiently high temperatures, the energy supplied by reaction overcomes losses to the surroundings and the excess energy further increases the temperature of the gas. This process is referred to as self-heating.

In flammable or combustible materials the chemical reaction rates are generally strongly increasing functions of temperature. The self-heating process increases the reaction rate causing further excess energy generation and further self-heating. This uncontrolled positive feedback loop can lead to thermal runaway: the rapid increase in gas temperature. If this occurs in a flammable gas then an ignition kernel of extremely hot gas and combustion products is formed which supplies heat to further accelerate reactions in surrounding gas and produce an explosion. The critical surface temperature where thermal runaway begins is referred to as the ignition temperature or ignition threshold. Determination of this quantity is therefore of primary interest in mitigating the risk of such explosion hazards. Ignition by thermal runaway is also referred to as *autoignition* or *self-ignition* to distinguish these cases from ignition initiated by some deliberately introduced energy source such as a spark or hot particle.

Explosion is a generic term referring to the outcome of an ignition event which results in a substantial temperature rise and for high-speed or confined events, a substantial pressure increase. The explosive events investigated in the present study are subsonic combustion waves that propagate away from the ignition location with speeds of 0.5 to 10 m/s, transforming the reactants (fuel and oxidizer) in thin (less than 1 mm) flames to products (mostly water and carbon dioxide for hydrocarbon fuels) with peak temperatures on the order of 2000 K and peak pressure up to 8 times the initial pressure for confined explosions. In some situations flames can accelerate to high speeds, in the most extreme cases transitioning to a supersonic combustion wave or detonation. All of the explosion processes examined in the present study are low-speed events and detonations are not considered.

The focus of the present study is on the conditions resulting in thermal ignition and the nature of the explosion event as a function of key parameters of the hot surfaces, surrounding volume, and the nature of the flammable mixture.

1.2 Background

The study of thermal ignition and self-heating has been of interest to scientists for several hundred years. The motivation for the earliest studies was the study of chemical reactions and the atomic nature of compounds. The motivation for continued and more contemporary studies arises from areas like process safety where the use, storage and shipment of combustible liquids and gases is important and commonplace in many areas of the global economy. Early on the safety hazards associated with the handling of such substances motivated attempts to understand their ignition characteristics. Particular interest was focused on attempts at determining a threshold ignition criterion in terms of temperature differences with surroundings. Early on in these efforts it became clear that precise determination of such a simple sounding quantity was monstrously difficult in practice. The challenges are well put by (Bone & Townend, 1927) in their review of early explosion research

> *Although the temperature at which autogeneous or self-propellant reaction begins in a given gaseous mixture is usually termed its 'ignition temperature' or 'ignition point', it is not ordinarily a well-defined physical constant, being dependent on the way in which heat is conveyed to the medium and other circumstances. It is clear also that it does not necessarily correspond with the actual appearance of flame in the mixture; indeed, there is often a definite 'pre-flame period', during which the reaction is self-propellant.*
> - Bone and Townend (1927)

This statement illustrates the ongoing issue that the minimum ignition temperature of a substance

is not an immutable physical constant but rather is a product of the method employed in its determination. Furthermore the processes of fuel decomposition and oxidation which produce the aforementioned self-heating need not necessarily result in explosive reaction and/or appearance of a flame.

1.2.1 Historical Background

Some of the earliest studies[1] on ignition were those of Davy on the experimental ignition of "firedamp" (flammable gas released in coal mining) using various ignition sources like hot metal sparks, electrical sparks, candles, hot platinum wires, and hot iron rods (Davy, 1816; Davy, 1817). Davy's motivation was to understand and mitigate the cause of accidental explosions in mine shafts. One outcome of Davy's work was his design of a "Miners' Safe-Lamp" which could be carried into mines for illumination without posing an ignition hazard if exposed to coal gas. Thus the practical benefit of understanding ignition hazards was demonstrated immediately.

More precise scientific investigations examining ignition with other flammable mixtures were conducted in the later part of the 19th century, particularly by Mallard and Le Chatelier (1880, 1883) who used an evacuated and heated porcelain vessel to study ignition upon filling with flammable mixtures of hydrogen, carbon monoxide, and methane with pure oxygen and nitrogen mixtures. They observed that a delay or "time-lag" of up to 10 s was possible prior to ignition of methane-air mixtures. This was early indication of the interplay of chemical reaction, temperature, and heat transfer in thermal ignition problems. This lag was later attributed to "pre-flame" combustion, or the self-heating process previously described (Bone & Townend, 1927).

Freyer and Meyer (1893) employed two methods for ignition temperature determination: (1) a slow flowing reactor consisting of a tube immersed in a bath of hot liquid or vapor maintained at constant temperature and (2) a sealed glass bulb pre-filled at atmospheric pressure and plunged suddenly into the same bath. Freyer and Meyer used sulphur oil baths and the boiling points of various pure chemical compounds to achieve these stable high temperature baths up to 730 °C. In all cases the closed bulb experiment yielded much lower ignition temperatures than those determined by the free flowing reactor. Dixon and Coward (1909) employed a method wherein the fuel and oxidizer were separately heated in concentric porcelain tubes to a set temperature before being allowed to mix via an exit nozzle in an enclosure at the same temperature. By separately heating the gases, effects of low temperature oxidation of the fuel were avoided however pyrolysis, especially for larger fuel molecules, was still possible and likely.

Mason and Wheeler (1924) focused on the importance of Mallard and Le Chatelier's "time-lag"

[1] A comprehensive outline of the early history of ignition and combustion studies can be found in Bone and Townend (1927). The material presented in this section of the dissertation focuses on a few, select studies relevant to thermal ignition in particular.

for higher paraffins (up to pentane) using a heated quartz cylinder and found delays up to 144 s were possible. Effects of flow velocity, pressure, and oxygen concentration were also explored at that time (Bone & Townend, 1927). Ignition by adiabatic compression using a piston and cylinder was also thoroughly studied, most notably by (Tizard & Pye, 1922). While important for the development of future work conducted in rapid compression machines (RCM), the temperature rise in this case is accompanied by a pressure increase and the ignition occurs within the gas rather that originating at a hot surface.

Setchkin (1954) classified early thermal ignition experiments into two general types: (1) the rising temperature methods and (2) the constant temperature methods. In the rising temperature case, the reactive mixture is introduced to the apparatus prior to heating such that the mixture vessel/surface are heated together until ignition occurs. In the constant temperature methods, the vessel/surface is preheated to a set temperature before the mixture is introduced. Repeated testing at a range of initial temperatures then determines the minimum ignition temperature. In either case there is some unavoidable transient and there exists no practical method to fully eliminate all of these these transient effects in ignition temperature determination.

In any test method there exists some transient processes such as heat transfer from surfaces, between gases, fluid motion, fluid mixing, or chemical reaction which obfuscate the system state at the time of ignition. This is at the root of the observation by Bone and Townend (1927) that minimum ignition temperature is not a fundamental "physical constant". Because ignition temperature depends on many factors like the particular fuel, mixture composition, hot surface geometry, fluid motion, and heating rate, a wide range of testing apparatus are needed to fully understand the influence of these parameters. Many tests have been developed and used to characterize hazards. Some of these have become "industry standards" and widely used to characterize the potential for hazards. An example is the ASTM-E659 test that is the subject of Chapter 2 of this dissertation.

1.2.1.1 Hot Surface Ignition

A particular problem of interest and the focus of the present study is ignition of a cold, premixed flammable atmosphere by a heated surface. This situation is more representative of industrial thermal ignition hazards than many laboratory scale investigations. Several cases can be distinguished depending on the temperature history of the surface, the size of the surface, the nature of the flow over the surface, and volume of any surrounding vessel. Examples of studies on problems of this type are discussed in this section.

Impulsive Heating Adomeit (1965) studied ignition by small (3.8 cm^2) impulsively heated vertical cylinders using hydrogen, propane, and pentane air mixtures. Cutler (1974), Cutler (1978),

and Laurendeau and Caron (1982) are similar examples using small impulsively heated plates with methane, propane and ethylene air mixtures.

Natural Convection Ono et al. (1976) used vertical plates of varying height and modest surface areas (1.5 to 9 cm^2) with lower heating rates to study propane, ethanol, and diethyl ether-air mixtures. Cairnie et al. (1981) used a much larger plate (130 cm^2) than these previous studies for diethyl ether-air mixtures and observed ignition at the top of the plate which was preceded by the development of a cool flame near the ignition threshold. Harrison and Cairnie (1988) extended this work with an even larger surfaces (270 cm^2) and successfully captured the cool flame development and ignition behavior using a highly reduced chemical model for acetaldehyde-air mixtures. In both cases the mixture is flowed in at a rate which balances the induced natural convection flow which creates a stagnant boundary layer along the plate.

Ignition by small vertical hot surfaces (diesel engine glow plugs) and heated cylinders (0.01 - 1.6 cm^2) have been extensively investigated at Caltech in experiments (Boettcher, 2012; Boeck et al., 2017) and by numerical simulation (Melguizo-Gavilanes et al., 2016; Melguizo-Gavilanes et al., 2017) using hydrogen, ethylene, and n-hexane-air mixtures. These studies found that ignition kernel formation occurs in the stagnation region above the tip or on the sides of the hot cylinder near the top of the surface. Menon et al. (2016) studied this geometry numerically using an n-heptane kinetic model and observed a two-stage ignition process where the fuel is first broken down into smaller hydrocarbons and hydrogen peroxide (H_2O_2) is formed which thermally decomposes into OH radicals leading to the main ignition event. In these studies it was observed that ignition kernels form in the stagnation region on top of the glowplug, where the thermal layer is thickest.

Kuchta et al. (1965) conducted experiments on heated wires and cylinders of sizes ranging from 0.65 - 40.5 cm^2. He proposed a decrease in ignition temperature with heated surface size, with a dramatic drop at a critical size. Jones (2020) critically examined Kuchta's findings, conducting a parametric study of various vertical cylinder geometries at large scales (up to 200 cm^2) for n-hexane and heavier fuels like Jet A and surrogates. Jones demonstrated the correlation of the ignition temperature with hot surface size was erroneous and actually a consequence of attempting to equate data from two highly different types of tests, as discussed further below. In particular there is not a dramatic drop in ignition threshold with increasing surface size, and when the correct scaling parameter (height) for vertical cylinders is used, there is only a modest decrease in ignition temperature with increasing size.

Tests with short vertical cylinders showed a preferential location of the ignition kernel formation at the top of the cylinder where the thermal layer is thickest. The location of the ignition kernel at the top of the heated cylinders or glow plugs is not surprising. The cold flammable gas is being heated

as it is entrained in the natural convection boundary layer and travels upward as it is heated. The hot gas molecules at the top of the boundary layer, have had on average the longest time to react and are further from the surface, minimizing the heat loss to the surface. Tests with taller cylinders by Jones (2020) revealed that the ignition location depends on the heating rate and does not have to occur near the top of the cylinder.

Forced convection over heated surfaces was studied by Mullen et al. (1948), who used flow rates of 50 - 500 ft/s (15 - 150 m/s) over small heated cylinders (2 cm^2 <) for wide range of fuel-air mixtures and found that the ignition temperatures increased with increasing flow velocity. Smyth (1990) and Smyth and Bryner (1997) also investigated forced convection over a 25 cm^2 flat plate inclined at a 45°angle with a variety of surface materials and hydrocarbon fuels. They observed a narrow range of ignition temperatures for linear and branched alkanes and suggested that this is the result of the short boundary layer residence times due to the imposed flow velocity.

Hot particles Early work by Silver (1937) used spheres of 10 - 50 mm in diameter injected into a flammable mixture with velocities up to 5 m/s. Paterson (1939) and Paterson (1940) studied ignition by spheres of similar size but with a fixed flow velocity of 1.2 m/s. These studies found that ignition temperatures increased with decreasing sphere size and with increasing flow velocity and were found to be independent of the surface material. More contemporary work has been conducted for even smaller spheres (0.3 - 0.8 mm diameter) in a stationary configuration (Roth et al., 2014; Roth et al., 2017). The results showed a similar positive correlation between ignition temperatures and sphere diameter and found that the results were relatively independent of stoichiometry except near the flammability limits. Häber et al. (2017) numerically studied the stationary sub-millimeter particle ignition problem and the influence of many parameters including stoichiometry and particle size. Their ignition temperatures were again found to depend strongly on fuel type and particle size and results agreed well with experimental work.

Coronel et al. studied ignition by spheres of similar sizes for n-hexane air mixtures both experimentally (Coronel, 2016) and numerically (Coronel et al., 2018). This work illustrated that the ignition kernel formation occurred in the flow separation region around the sphere. The numerical work found that prior to ignition, the gas in this region was composed primarily of ethylene indicating that significant pyrolysis had occurred prior to ignition.

1.2.2 Models and Theories of Thermal Ignition

Various theories and models have been proposed to explain the thermal ignition process and predict thermal ignition thresholds. An early and greatly influential step was the proposal by van't Hoff (1896) who based ignition on purely thermal considerations based on heat transfer processes near the hot surface used for ignition. The "van't Hoff ignition criterion" is based on the notion that

the critical condition for ignition occurs when the energy released by combustion is just balanced by heat transfer at the igniting surface. van't Hoff illustrated this graphically and subsequent researchers interpreted this mathematically as the vanishing of the temperature gradient at the wall

$$\left.\frac{dT}{dy}\right|_{wall} = 0. \tag{1.1}$$

The fundamental idea of a critical balance between energy release and heat transfer defining ignition remains an essential component of simplified analyses of thermal ignition to this day. The condition in Equation (1.1) has also been a staple of approximate analyses of thermal ignition by hot surface although subsequent work has shown this is incorrect (Cairnie et al., 1981; Song et al., 1991). The gradient at the wall is actually slightly positive at the critical condition as thermal runaway occurs some distance offset from the hot surface.

One of most significant and influential analyses of thermal ignition was carried out by Semenov (1928) who considered the competition between chemical energy release and heat transfer to define the critical conditions for ignition. Semenov did not consider thermal gradients but assumed that all the heat transfer took place due to the temperature difference with the surroundings at the boundary of a homogeneous, uniform temperature self-heating material. The *Semenov* model has become one of the two classical approaches to thermal explosion analysis.

Semenov considered a highly simplified approach to modeling chemical reaction and thermal energy that has been widely adopted for simplified analyses of self-heating and combustion. This model assumes that the chemical reaction proceeds by a single reaction with energy release and chemical reaction occurring simultaneously.

$$\mathcal{R} \rightarrow \mathcal{P} \tag{1.2}$$

The feedback between chemical energy release and reaction rates is due to a reaction rate that increases rapidly with increasing temperature through an Arrhenius form for the reaction rate constant

$$K = Ae^{-E_a/\tilde{R}T}\,. \tag{1.3}$$

The frequency factor A and activation energy E_a are empirical constants determined through thermo-chemical analyses. For a homogeneous explosive mass with no motion, no gradients in properties, and heat transfer occurring only at the boundaries, the balance equation for energy is

$$\frac{\partial T}{\partial t} = \frac{QA}{\rho c_P}\left(1-Y\right)e^{-E_a/\tilde{R}T} - \frac{S}{V}\frac{h}{\rho c_P}(T-T_0)\,, \tag{1.4}$$

where h is the heat transfer coefficient, T_0 is the temperature of the surroundings, V is the volume, S is the surface area of the volume, Q is the energy release per unit volume of explosive reacted, ρ

is the density, and c_P is the specific heat capacity of the explosive. The balance equation for the product species $\mathcal{P}$ can be written in terms of mass fraction Y

$$\frac{\partial Y}{\partial t} = K(1-Y) = A\,(1-Y)\,e^{-E_a/\tilde{R}T}\,, \tag{1.5}$$

assuming a first-order dependence of reaction rate on concentration. In this model, the mass fraction of the reactants $\mathcal{R}$ is $1-Y$ and the reaction is considered irreversible so that $Y = 0$ in the unreacted material and $Y = 1$ for complete reaction.

Semenov proposed that the critical condition for self-heating ignition is defined by finding the largest temperature that enables a balance between heat transfer and chemical energy release at steady-state conditions. He further proposed key simplifications at the critical condition: (1) the extent of reaction, i.e., depletion of the reactants is considered to be negligible ($Y \approx 0$); (2) the energy balance in Equation (1.4) can be approximated as in steady state, $\partial T/\partial t \approx 0$. With these approximations, Semenov found an exact solution for the critical temperature

$$T_C = \frac{E_a}{2\tilde{R}}\left(1 - \sqrt{1 - 4\frac{\tilde{R}T_0}{E_a}}\right). \tag{1.6}$$

The Semenov model defines an ignition temperature that depends only on a single chemical property of the explosive, the activation energy E_a, and the temperature T_0 of the surroundings. Curiously, the critical temperature is independent of all other parameters which gives misleading support to the notion of a well-defined and universal ignition temperature for a given substance. The Semenov model and elaborations have been widely used to explain thermal runaway and critical conditions in self-heating situations. However, is it not a useful starting point for hot-surface ignition within a thermal boundary layer with significant temperature gradients.

In 1939, Frank-Kamenetskii (1955) recognized the drawbacks of the Semenov approach and refined the model by including energy transport within the self-heating material by including diffusion of thermal energy via temperature gradients in the self-heating material. The *Frank-Kamenetskii* model adopts many of the simplifications used by Semenov and extends the energy balance equation by using Fourier's model of heat transfer and a nonuniform distribution of temperature within the material. For a one-dimensional slab of material, the energy balance is a partial differential equation

$$\frac{\partial T}{\partial t} = \frac{k}{\rho c_P}\frac{\partial^2 T}{\partial x^2} + \frac{QA}{\rho c_P}\,(1-Y)\,e^{-E_a/\tilde{R}T}\,, \tag{1.7}$$

The temperature of the surroundings and heat transfer rate will enter in through the conditions on temperature and spatial gradient of temperature that model the thermal processes at the boundary. To determine critical conditions for ignition, Frank-Kamentskii adopted Semenov's idea of considering

the possible steady-state solutions to define the limiting temperature distribution prior thermal runaway. Neglecting reactant depletion, the energy balance equation is

$$\frac{\partial^2 T}{\partial x^2} = -\frac{QA}{k} e^{-E_a/\tilde{R}T} \,. \tag{1.8}$$

Depending on the boundary conditions, solutions to this equation only exist for combinations of the physical and chemical parameters less than a critical value. The Frank-Kamenetskii model has also been widely used to evaluate critical conditions for thermal runaway due to self-heating. Inclusion of temperature (and species) gradients has enabled extensions for realistic analyses of hot surface ignition and most importantly, enables the consideration of ignition within thermal boundary layers. An important simplification that is often used in applying the ideas of Semenov and Frank-Kameneskii is the notion that for many chemical reactions relevant to self-heating, the activation energy E_a is much larger than $\tilde{R}T_0$. This leads to significant simplification in the equation through approximations using expansions based on the small parameter, $\tilde{R}T_0/E_a$. Modern analytical analyses are based on the basic model of Frank-Kamenetskii with the refinement of using matched-asymptotic expansions to explore the details of the spatial and temporal evolution of the self-heating and thermal runaway event.

Law and Law (1979) extended the approach of Frank-Kamenetskii to analyze thermal runaway within a thermal boundary layer. Law considers a two-dimensional forced-convection, laminar flow over a hot vertical isothermal plate and used matched asymptotic analysis to develop a solution using one-step chemistry. The analysis is based on using the boundary layer approximation and examines the reaction process exceedingly close to the surface so that convection is unimportant and it is only necessary to consider the variation of temperature and concentration in the direction normal to the plate. For the purposes of analysis, the flow was divided into two distinct regions, an inner reactive region near the surface and a chemically-frozen outer region defined by the gradient in temperature within the boundary layer. Law's analysis showed that the critical state is determined by a one-dimensional equation (in the wall-normal coordinate) of the type proposed by Frank-Kamenetskii and leads to a relationship between the temperature gradient in the outer region and the thermochemical properties of the mixture at the critical condition. Law (1979) analyzed the related problem of transient, one-dimensional heating using a similar approach. There have also been a number of analyses of ignition in thermal layers adjacent to hot surfaces based on the van't Hoff criterion. Notable examples include Ono et al. (1976) and Laurendeau (1982).

It has long been recognized that self-heating and thermal runaway in flammable gases with hydrocarbon fuels is a coupled thermal-chemical explosion with reaction mechanisms involving hundreds of species and reactions with transport of species by molecular diffusion equally important as thermal diffusion. Treating this quantitatively requires numerical solution of the balance and reaction

equations using computational fluid dynamics to model fluid motion and energy transport to the chemical reactions. One notable example is Maas and Warnatz (1988), who examined several aspects of self-heating and explosion of hydrogen-air mixtures using detailed chemistry considering radial motion in spherical geometries. The role of intermediate and radical species for ignition within stagnation-point flow on hot surfaces was analyzed using detailed chemical models for hydrogen and methane by Vlachos et al. (1993, 1994). The importance of low-temperature reactions ($< 500°C$) of acetaldehyde (CH_3CHO) involving species such as methyl hydroperoxide (CH_3OOH) was highlighted by the study of Harrison and Cairnie (1988), who examined the "cool-flame" regime of ignition relevant to the ASTM-E659 autoignition test.

Despite these substantial analytical and numerical efforts on hot surface ignition modeling, the quantitative prediction of hot surface ignition conditions from first principles remains an elusive goal. Experimentation is therefore necessary for appropriately studying these problems and exploring the influence of ,among other things, buoyant fluid motion.

1.2.3 Natural Convection Boundary Layers

One of the critical aspects of hot surface ignition in the thermal environment is the motion of flammable gas adjacent to the hot surface. A key parameter identified in analyses is the temperature gradient which exists between the heated surface and the surrounding gas. This thermal gradient controls the rate of heat transfer to or from the gas and therefore plays a critical role in the conditions at which thermal runaway and ignition kernel formation occur. The heating produces a density gradient in the gas which results in a buoyancy force and is the primary source of fluid motion. This density gradient (and the gradients in temperature, velocity, and species) is localized close to the heated surface in a thin layer. The thin nature of this layer motivates analysis using the boundary layer approach of Prandtl. The gradients within the boundary layer are responsible for thermal energy exchange from the heated surface to the gas and entrainment of the distant cold gas. The velocity gradients within the layer generate vorticity and shear flows that may cause instability of the flow and transition from laminar to turbulent flow.

The properties of the flow can be characterized by several nondimensional groups that arise naturally from analysis of the governing equations. These are the Grashof number

$$Gr = \frac{g\beta(T - T_\infty)L^3}{\nu^2}, \tag{1.9}$$

Prandtl number

$$Pr = \frac{\nu}{\alpha}, \tag{1.10}$$

Rayleigh number

$$Ra = GrPr = \frac{g\beta(T - T_\infty)L^3}{\nu\alpha}, \tag{1.11}$$

and Nusselt number

$$Nu = \frac{hL}{k_f}\,. \tag{1.12}$$

These groups represent the competition between the important processes in natural convection and are useful in characterizing the flow regime and heat transfer rate. In forced convection flows, the Reynolds number $Re = \rho UL/\mu$ can be interpreted as the ratio of inertial to viscous forces and is used to characterize the flow regime as laminar, transitional or turbulent. The analog of Re in natural convection problems is Gr or Ra which can be interpreted as the ratio of buoyancy to viscous forces and is typically used for flow regime determination. Pr is the ratio of viscous to thermal diffusion of the working fluid. For gases Pr is approximately constant and a value of 0.7 is often used. Ra represents the combined effects of Gr and Pr and has the same interpretation as Gr being the competition between buoyancy and viscous forces. Nu is used to determine the heat transfer rate through a heat transfer coefficient h that is correlated with either Ra or Gr in natural convection flows.

The following discussion illustrates features of a non-reacting natural convection flow along a vertical heated surface, which is the case relevant to the experiments to be discussed in Chapter 3, Chapter 6, and Chapter 7. Those experiments consist of vertical cylinders, but there are no simple solutions for the cylindrical case so instead we examine a vertical flat plate in Cartesian coordinates (Gebhart et al., 1988). The flat plate solution closely approximates the cylinder solution as long as the boundary layer is thin compared to the radius of the cylinder, which is the case for the shorter cylinders considered in the present study (Jones, 2020). A sketch of the thermal layers on an isothermal vertical surface is shown in Figure 1.1. The associated vertical velocity flow has a pronounced maximum within the boundary layer and goes to zero at the surface and in the distant gas.

The conventional boundary layer analysis considers initially the following equations for mass, momentum and energy.

$$\frac{\partial \rho}{\partial t} + \nabla \cdot (\rho \boldsymbol{u}) = 0 \tag{1.13}$$

$$\rho \frac{\partial \boldsymbol{u}}{\partial t} + \rho(\boldsymbol{u} \cdot \nabla)\boldsymbol{u} = -\nabla p + \boldsymbol{F_b} + \nabla \cdot \boldsymbol{\tau} \tag{1.14}$$

$$\frac{\partial(\rho e)}{\partial t} + \nabla \cdot (\rho \boldsymbol{u} e) = -\nabla \cdot \boldsymbol{q} - p\nabla \cdot \boldsymbol{u} + \boldsymbol{\tau} : \nabla \boldsymbol{u} \tag{1.15}$$

Applying the boundary layer approximations (Gebhart et al., 1988), we obtain the following simpler set of equations.

$$\frac{(\partial \rho u)}{\partial x} + \frac{(\partial \rho v)}{\partial y} = 0 \tag{1.16}$$

$$\rho\left(u\frac{\partial u}{\partial x} + v\frac{\partial v}{\partial y}\right) = \frac{\partial}{\partial y}\left(\mu\frac{\partial u}{\partial y}\right) - g(\rho - \rho_\infty) \tag{1.17}$$

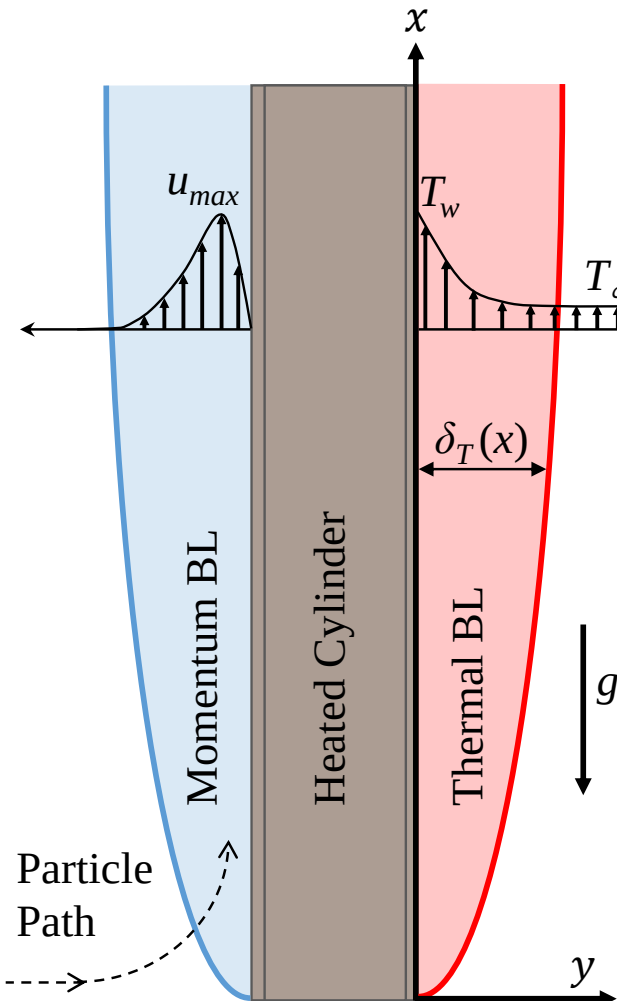

Figure 1.1: Natural convection flow developed around an isothermal vertical cylinder. The fully laminar case is illustrated here but at sufficient axial distances x, the boundary layer (BL) becomes turbulent.

$$\rho c_P \left(u \frac{\partial T}{\partial x} + v \frac{\partial T}{\partial y} \right) = \frac{\partial}{\partial y} \left(\lambda \frac{\partial T}{\partial y} \right) \tag{1.18}$$

In this formulation the fluid properties are still assumed to be variable which is important to consider for large temperature differences. Commonly the Boussinesq approximation (Tritton, 1988) is used to further simplify the equations by assuming that fluid properties are constant, density gradients are small, and that the density variations are linear with temperature,

$$\Delta\rho = -\beta\rho_0\Delta T \quad and \quad \beta = -\frac{1}{\rho}\left(\frac{\partial\rho}{\partial T}\right)_P . \tag{1.19}$$

An often-used similarity solution assuming constant properties and Equation (1.19) was developed by Ostrach (1953) and presented in Gebhart et al. (1988). However for thermal ignition problems

these assumptions are not valid since the temperature gradients are large. Sparrow and Gregg (1958) developed a similarity solution to the variable fluid property case without invoking the Boussinesq approximation. The following is a summary of their solution approach.

A modified stream function ψ is defined to account for the variable density and the velocities are computed from the continuity equation

$$\rho u = -\rho_w \frac{d\psi}{\partial y} \quad \text{and} \quad \rho v = -\rho_w \frac{d\psi}{\partial x} \,. \tag{1.20}$$

The co-ordinates are transformed using a similarity variable

$$\eta = c x^{-1/4} \int_0^y \frac{\rho}{\rho_\infty} \, dy \quad \text{with} \quad c = \left(\frac{g(\rho_\infty - \rho_w)/\rho_w}{4 {\nu_w}^2} \right)^{1/4} \,. \tag{1.21}$$

We also define a scaled stream function

$$F(\eta) = \left(\frac{\psi}{x^{3/4}} \right) \left(\frac{1}{4\nu_w c} \right) \,. \tag{1.22}$$

and a nondimensional temperature

$$\theta = \frac{T - T_\infty}{T_w - T_\infty} \,. \tag{1.23}$$

The velocities can be obtained using Equation (1.24) and Equation (1.25)

$$u = 4\nu_w c^2 x^{1/2} F' \tag{1.24}$$

$$v = \left(\frac{\rho}{\rho_w} \right) \left(\frac{\nu_w c}{x^{1/4}} \right) (\eta F' - 3F) \,. \tag{1.25}$$

Under these transformations, Equation (1.17) and Equation (1.18) are transformed into the following set of ordinary differential equations:

$$\frac{d}{d\eta} \left(\frac{\rho\mu}{\rho_w \mu_w} F'' \right) + 3FF'' - 2(F')^2 + \frac{\rho_\infty/\rho - 1}{\rho_\infty/\rho_w - 1} = 0 \tag{1.26}$$

$$\frac{d}{d\eta} \left(\frac{\rho k}{\rho_w k_w} \theta' \right) + 3Pr_w \frac{c_P}{c_P, w} F\theta' = 0 \,. \tag{1.27}$$

The transformed boundary conditions are

$$\begin{aligned} &F(0) = F'(0) = 0 \\ &\theta(0) = 1 \\ &F'(\infty) = \theta(\infty) = 0 \,. \end{aligned} \tag{1.28}$$

Using the ideal gas law equation of state ($P = \rho RT$) enables further simplification of these equations. If pressure is constant then the density differences can be transformed into temperature differences without need for the Boussinesq approximation. From the ideal gas law it follows that

$$\frac{\rho_\infty/\rho - 1}{\rho_\infty/\rho_w - 1} = \frac{T - T_\infty}{T_w - T_\infty} = \theta \,. \tag{1.29}$$

This simplifies Equation (1.26) by replacing the last term with θ. These equations can now be solved numerically using functional forms of fluid property variation with temperature or tabulated values.

Cairnie and Harrison (1982) provide a numerical solution methodology and validated the approach using experimental data obtained for air on a 0.144 m vertical flat plate at wall temperatures up to 698 K. Using this similarity variable, an explicit expression for the boundary layer thickness cannot be obtained directly since the similarity variable dependence on the wall normal coordinate is in the upper integration limit in Equation (1.21). However, far from the surface the similarity variables of Ostrach (1953) and that given by Equation (1.21) should approach the same value since the temperature gradient and property variation become insignificant. Therefore the boundary layer thickness can be reasonably estimated using the constant property formulation using Ostrach's variable.

$$\eta_o = \frac{y}{x}\left(\frac{Gr_x}{4}\right)^{-1/4} = \frac{y}{x}\left(\frac{g\Delta T x^3}{4T_\infty \nu_\infty^2}\right)^{1/4}, \tag{1.30}$$

where $\Delta T = T_w - T_\infty$. From Fig. 3 of Cairnie and Harrison (1982), a value of $\eta_o = 4.42$ can be used to define the thermal boundary thickness δ_T for the purposes of computing the temperature gradient at the wall

$$\left.\frac{dT}{dy}\right|_{wall} = -\frac{T_w - T_\infty}{\delta_T}. \tag{1.31}$$

From Equation (1.30), we obtain

$$\delta_T = 4.24\left(\frac{4T_\infty \nu_\infty^2 x}{g\Delta T}\right)^{1/4}. \tag{1.32}$$

The boundary layer thickness is a slowly increasing function of vertical height, $\delta_T \sim x^{1/4}$ and is typically on the order of ten mm at the top of the shorter cylinders used in the present study. From Fig. 5 of Cairnie and Harrison (1982) and Equation (1.24) the maximum vertical velocity in the boundary layer is approximately

$$u_{max} = 0.28\left(\frac{4g\Delta T x}{T_\infty}\right)^{1/2}. \tag{1.33}$$

1.2.4 Autoignition vs. Hot Surface Ignition

The early scientific ignition investigations eventually informed the development of standardized laboratory methods for determining minimum autoignition temperature (AIT) or self-ignition temperature (SIT) criteria. These investigations examined the ignition of liquid or gaseous fuel injected into a heated vessel filled with oxidizer or a fuel-oxidizer mixture injected into a hot, evacuated vessel. The early studies showed that the lowest ignition temperatures typically occurred in experiments with heated vessels held at constant temperature prior to fuel injection.

Several diverse test methods were proposed for studying ignition in hot atmospheres before a standardized test was developed. These test methods are sometimes referred to as hot surface ignition tests but combine both hot surfaces and hot atmospheres in most cases. These differ from tests consisting of a hot surface in a cold atmosphere since the entire combustion chamber is at sufficiently high temperatures for reaction rates to produce self-heating. In cold-atmosphere, hot-surface tests, self-heating is confined to the thin boundary layer region close to the hot surface. In the hot-atmosphere, hot-surface tests, thermal energy transferred from the hot atmosphere augments the heat transfer from the hot surface, typically resulting in the much lower ignition temperatures as illustrated by Figure 1.2. This effect is more pronounced at larger scales because losses to the vessel walls become much less significant than in smaller volumes. A comprehensive summary of these early experiments and these considerations was given by Setchkin (1954). His studies led him to develop what would become the forerunner to the modern day ASTM-E659 standardization for determination of the AIT (International, 2005). In this test, a small quantity of liquid fuel (0.05 to 0.5 mL) is injected into a preheated 500 mL flask containing hot air with ignition determination made by visual observations and temperature measurements.

Setchkin's original approach is quite similar to the contemporary ASTM E659 specification with a few key differences being his use of a larger (1 L) flask, arrangement of heating elements, and the use of a stopper placed in the flask opening (Setchkin, 1954). A similar test was also proposed by Zabetakis et al. (1954) in the same year, the major difference was the use of a 200 mL Erlenmeyer flask in place of the larger spherical flask. This apparatus seems to have been the forerunner of a separate AIT standardization, ASTM-D2155, which was discontinued in 1978 in favor of the E659 standard (International, 1976), as well as the current international standard (ISO/IEC, 2017). Setchkin's study found that the minimum AIT is typically decreased as combustion chamber size is increased. Depending on the substance, this can have a large effect (50 - 100°C) on the measured AIT. This effect was attributed to the decrease in the surface area to volume ratio as chamber volume is increased which reduces the rate of heat loss to the surroundings as noted by the previous discussion of Figure 1.2. From this and other details uncovered in these early studies it became clear that the AIT is not a fundamental property of a substance alone but is rather highly dependent on the method and apparatus used in its determination. More recent work at PTB has further illustrated this fact through studies on the influence of increased pressure, alternative oxidizers, oxygen enrichment, and combustion vessel volume on AIT (Hirsch & Brandes, 2005; Brandes et al., 2017b, 2017a; Brandes & Hirsch, 2017). This makes it crucial to fully understand the methodology used in obtaining an AIT value if it is to be of any use in practical analysis and engineering design applications.

As made abundantly clear by the historical thermal ignition work, there is no singular approach to

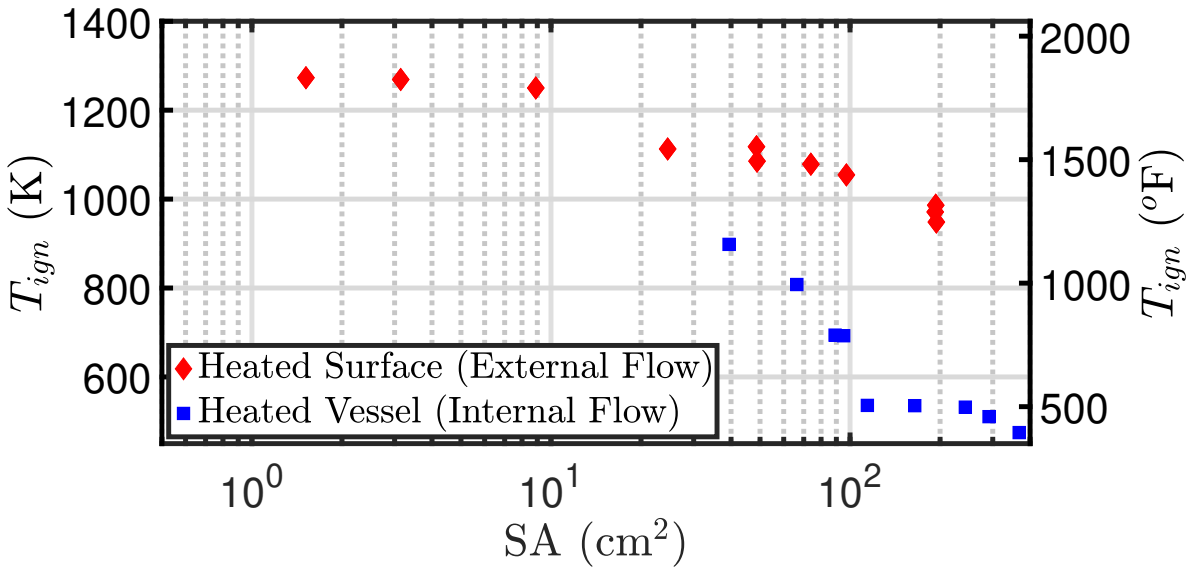

Figure 1.2: Ignition temperature plotted vs surface area of heated surface or vessel. Data adapted from range of groups and fuel sources.

determination of the ignition temperature since results are often highly configuration dependent. The influence of factors like the type of fuel, mixture composition, hot surface geometry, fluid motion, and heating rate can be significant and change how ignition thresholds are defined across different experimental configurations. These factors can also influence the severity of the explosion as measured by flame temperature, peak pressure, and duration of pressure transient. One crucial distinction in ignition testing can be made between heated vessel and heated surface experiments.

At typical test vessel sizes with surface area $SA \geq 100$ cm^2, heated vessel experiments produce far lower ignition thresholds than equivalently sized heated surfaces. This is illustrated in Figure 1.2 which is a collection of experimental ignition data from many studies of ignition by heated vessels and surfaces with various fuels (Kuchta et al., 1965; White, 1967; Ono et al., 1976; Boettcher, 2012; Melguizo-Gavilanes et al., 2016; Boeck et al., 2017; Jones, 2020; Martin & Shepherd, 2021). This distinction is quite important since most practical thermal ignition hazards are analogous to heated surface experiments while the only well established and widely used thermal ignition criterion, the AIT is one derived from a heated vessel experiment, typically the ASTM-E659 (International, 2005).

Although the ASTM-E659 test is simple to implement and widely used, the processes responsible for determining AIT for a given fuel are complex and some are poorly understood. These processes include fuel injection, droplet formation, impact and breakup on the vessel surfaces, atomization, vaporization and diffusion of the fuel into the air, convective motion, low temperature chemical kinetics, self- heating, thermal runaway, ignition and flame propagation. This makes for a very

challenging situation to interpret and model. Further effects of the potential droplet impingement and pooling of low vapor pressure fuels on the hot flask surface can further complicate the matter. For many applications, the AIT determined from this test is used in design to define limiting (highest) temperatures of hot surfaces in regions where flammable vapor may be present. Using the AIT as the only number for design of potential thermal ignition hazards is an extremely conservative approach in almost all situations and ignores the results of other thermal ignition experiments that may be more relevant for the intended application.

Furthermore, the use of “autoignition” to describe the result of the ASTM test can be confusing. Precise distinctions should be made between this use and other common usages in the combustion community. Autoignition is a term that is widely used in the combustion community for a variety of ignition situations such as testing by rapid compression machines (RCM), shock tubes, and flow reactors. RCMs and shock tubes produce ignition by the use of adiabatic compression of a premixed reactive gas mixture to rapidly and uniformly increase the gas temperature. This process is related to the "knock" effect which occurs in spark ignition engines when portions of the combustion chamber gas are ignited by the compression rather than the spark (Turns, 1996). The mechanisms leading to ignition in these cases is distinct from the previously discussed processes of thermal ignition by hot surfaces and hot vessel autoignition used for AIT testing. The pressure at which the combustion takes place in these tests is usually much higher than atmospheric due to the adiabatic compression processes used to raise the gas temperature. This pressure change can influence reaction kinetics and result in different chain branching pathways than those in atmospheric and low pressure thermal ignition experiments. Heat losses to the surroundings also tend to be lower since volumetric gas temperatures achieved in such autoignition testing are typically far in excess of those in thermal ignition testing. These approaches are valuable for studying chemical reaction rates and other properties such as homogeneous ignition delay times at high temperatures and short duration but are not suitable for studies of typical thermal ignition hazards.

There have in fact been many recent studies of autoignition behavior of commodity fuels using heated shock tubes and RCMs to measure ignition delay times. These studies have well-controlled conditions and instrumentation that enables validation of chemical reaction models however these efforts are mostly focused on in engine combustion regimes where pressures and temperatures are elevated. In comparison to ASTM-E659 testing, the test gas temperatures (625 - 1381 K) and pressures (8 - 51 atm) are significantly higher than conditions that are characteristic of thermal ignition hazards in aircraft and industrial hazards associated with accidental explosions (Vasu et al., 2008; Wang & Oehlschlaeger, 2012; Liang et al., 2012; Zhukov et al., 2014; De Toni et al., 2017; Valco et al., 2017). One notable study by Tang et al. (2012) was conducted at only moderately increased pressures (2 - 4 atm) but still at much higher temperatures (1100 - 1500 K). The disparity

between these studies and the regimes of interest for the present work is illustrated conceptually in Figure 1.3 for real Jet A and some surrogate fuel studies.

1.2.5 Aviation Safety

One of the main motivations of the present study is the application of thermal ignition testing to aviation safety. In the aviation industry, the areas of concern for ignition hazards are fuel tanks and flammable leakage zones adjacent to fuel tanks, engine compartments, and anywhere there exists potential for fuel to form a flammable mixture with air. The Federal Aviation Administration (FAA) sets regulations (AC 25.981; FAA, 2018) that specify the maximum allowable surface temperature for any surface to be at least 50 °F less than the AIT of Jet A, which is given as 435 - 450°F (223.9 - 232.2°C). This number was obtained from a similar heated vessel standard to those previously mentioned, the ASTM-D286, withdrawn in 1966. The original source of data for this regulation however is not traceable to its original source, as is often the case with AIT values reported in chemical databases, material properties book, and safety data sheets for most substances. Additionally there is no indication of the mixture composition, number of repeated tests, and temperature or pressure transients resulting from those ignition tests. Knowledge of these thermal ignition characteristics of simple fuels as well as real fuels like aviation kerosene (Jet A) is critical to enabling the safe design of aircraft in addition to the safe storage and handling of these substances in industrial refining processes. It is this particular application towards aircraft safety

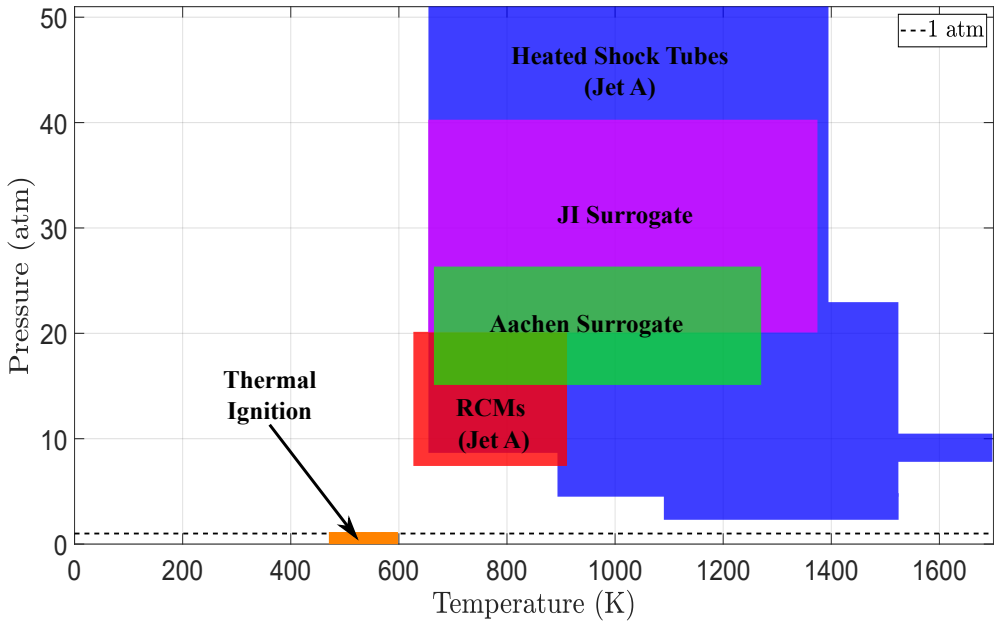

Figure 1.3: Relevant design space for thermal ignition as compared to validated regime of existing literature surrogates and Jet A ignition data.

that is the focus of this work due to the lack of literature discussing the low temperature and low pressure thermal ignition regime with regard to Jet A.

With this in mind, the goals of this investigation were to study the thermal ignition process and factors affecting ignition thresholds in both the traditional ASTM-E659 AIT test apparatus and in vastly different situations in order to better inform regulations and certification of aircraft components and industrial processes involving flammable substances. The use of realistic commodity fuels and surrogates, variations in mixture properties, effects of turbulent transition, and influence of flow confinement and recirculation are all explored in this study.

1.3 Project Scope and Outline

Chapter 1 provided an introduction to thermal ignition, natural convection and autoignition processes including their history and various experimental and modeling approaches. That background provides a motivation for this investigation in the study of thermal ignition hazards related to aircraft design. The rest of the thesis presents a series of experiments and data analysis which contribute to these lacking areas of thermal explosion research in a variety of ways. Chapter 2 discusses some additional background of the adopted ASTM-E659 standard for autoignition temperature (AIT) determination and presents some of the only detailed published data produced using this method. The importance of appropriate fuel selection for ignition testing is discussed and data are presented for simple fuels as well as multicomponent Jet A surrogates and standardized batches of Jet A. Chapter 3 presents a different class of thermal ignition testing: ignition in a laminar boundary layer over a hot surface. The experiments were conducted using a well characterized facility and ignition source in an effort to study effects of lighter gaseous fuels, low pressure, and nitrogen dilution on the thermal ignition and flame propagation processes. This experiment is considered to have minimal recirculation effects due to the use of short test times relative to recirculation times in the combustion vessel. Chapter 4 introduces a one-dimensional flame model that was used to calculate flame speeds and thickness for mixtures that are relevant to those in Chapter 3. This was done in an effort to better understand the measured explosion properties and in attempts to correlate fluid and flame properties to experimental thermal ignition data. Chapter 5 introduces a novel experimental configuration referred to as the Confined Autoignition Test (CAT). This facility enables the extension of experimental efforts to engineering scale large hot surfaces and the study of turbulent thermal ignition in highly confined environments. The much larger aspect ratios of the vessels employed for this study also significantly reduce vessel recirculation times and enable exploration of this effect on ignition thresholds. Chapter 6 provides an approach to study the flow field developed by these engineering scale surfaces. Visualization of the flow features and analysis of the images were performed to quantitatively estimate turbulent transition for these non-Boussinesq natural convection flows. Implications for the ignition testing and relevance of the Rayleigh number

for such problems are also discussed. Chapter 7 introduces the experimental procedure and measurement techniques employed in the CAT facility. Ignition data for a range of heating rates and steady state conditions are presented for n-hexane/air mixtures. Significant effects of turbulence on the ignition thresholds and explosion properties in the large scale configurations are also observed and discussed. Chapter 8 summarizes the results of these three distinct experimental approaches and the effects on the ignition process. The influence of experimental configuration on resulting ignition thresholds and areas left for future work are also discussed.

References

Adomeit, G. (1965). Ignition of gases at hot surfaces under nonsteady-state conditions. *Symposium (International) on Combustion, volume 10* (pp. 237–243). (Cit. on p. 4).

Boeck, L., Meijers, M., Kink, A., Mével, R., & Shepherd, J. (2017). Ignition of fuel–air mixtures from a hot circular cylinder. *Combustion and Flame*, *185*, 265–277. https://doi.org/10.1016/j.combustflame.2017.07.007 (Cit. on pp. 5, 16)

Boettcher, P. A. (2012). *Thermal Ignition* (Doctoral dissertation) [Electronic version available at]. California Institute of Technology. Pasadena, California. (Cit. on pp. 5, 16).

Bone, W. A., & Townend, D. T. A. (1927). *Flame and Combustion in Gases* (1st ed.). Longman's Green & Co. (Cit. on pp. 2–4).

Brandes, E., & Hirsch, W. (2017). *Zündtemperaturen in großen Behältern* [EN: Ignition Temperatures In large containers]. PTB Braunschweig. (Cit. on p. 15).

Brandes, E., Hirsch, W., & Stolz, T. (2017a). *Zündtemperaturen in anderen Oxidationsmitteln als luft; Projekt – Zündtemperaturen brennbarer Flüssigkeiten bei erhöhtem Sauerstoffanteil im O2+N2-Gemisch* [EN: Ignition Temperatures In oxidants other than air; Project - Ignition temperatures of flammable liquids with increased oxygen content in the O2+N2 mixture]. PTB Braunschweig. (Cit. on p. 15).

Brandes, E., Hirsch, W., & Stolz, T. (2017b). *Zündtemperaturen in anderen Oxidationsmitteln als luft; Projekt – Zündtemperaturen brennbarer Flüssigkeiten in Luft+N2O-Gemisch* [EN: Ignition Temperatures In oxidants other than air; Project - Ignition temperatures of flammable liquids in air+N2O mixture]. PTB Braunschweig. (Cit. on p. 15).

Cairnie, L., & Harrison, A. (1982). Natural convection adjacent to a vertical isothermal hot plate with a high surface-to-ambient temperature difference. *International Journal of Heat and Mass Transfer*, *25*(7), 925–934. https://doi.org/10.1016/0017-9310(82)90068-0 (Cit. on p. 14)

Cairnie, L., Harrison, A., & Morgan, P. (1981). Autoignition in a free convection boundary layer. *Symposium (International) on Combustion*, *18*(1), 1799–1806. https://doi.org/10.1016/S0082-0784(81)80185-3 (Cit. on pp. 5, 7)

Coronel, S., Lapointe, S., & Shepherd, J. (2019). Boundary layer ignition modeling, 10 (Cit. on p. 6).

Coronel, S., Melguizo-Gavilanes, J., Mével, R., & Shepherd, J. (2018). Experimental and numerical study on moving hot particle ignition. *Combustion and Flame*, *192*, 495–506. https://doi.org/10.1016/j.combustflame.2018.02.027 (Cit. on p. 6)

Coronel, S. A. (2016). *Thermal Ignition Using Moving Hot Particles*. California Institute of Technology. (Cit. on p. 6).

Cutler, D. (1974). The ignition of gases by rapidly heated surfaces. *Combustion and Flame*, *22*(1), 105–109. https://doi.org/10.1016/0010-2180(74)90015-7 (Cit. on p. 4)

Cutler, D. (1978). Further studies of the ignition of gases by transiently heated surfaces. *Combustion and Flame*, *33*, 85–91. https://doi.org/10.1016/0010-2180(78)90048-2 (Cit. on p. 4)

Davy, H. (1816). On the fire-damp of coal mines, and on methods of lighting the mines so as to prevent its explosin. *Philosophical Transactions of the Royal Society of London*, *106*, 1–22. https://doi.org/10.1098/rstl.1816.0001 (Cit. on p. 3)

Davy, H. (1817). Some new experiments and observations on the combustion of gaseous mixtures, with an account of a method of preserving a continued light in mixtures of in ammable gases and air without ame. *Philosophical Transactions of the Royal Society of London*, *107*, 77–85. https://doi.org/10.1098/rstl.1817.0009 (Cit. on p. 3)

De Toni, A., Werler, M., Hartmann, R., Cancino, L., Schießl, R., Fikri, M., Schulz, C., Oliveira, A., Oliveira, E., & Rocha, M. (2017). Ignition delay times of Jet A-1 fuel: Measurements in a high-pressure shock tube and a rapid compression machine. *Proceedings of the Combustion Institute*, *36*(3), 3695–3703. https://doi.org/10.1016/j.proci.2016.07.024 (Cit. on p. 17)

Dixon, H. B., & Coward, H. (1909). The ignition-temperatures of gases. *Journal of the Chemical Society, Transactions*, *95* (Cit. on p. 3).

FAA. (2018, September 24). FAA AC 25.981-1D: Fuel tank ignition source prevention guidelines. (Cit. on p. 18).

Frank-Kamenetskii, D. (1955). *Diffusion and Heat Exchange in Chemical Kinetics* (N. Thon, Trans.). Princeton University Press. (Cit. on p. 8).

Freyer, F., & Meyer, V. (1893). Über die Entzündungstemperaturen explosiver Gasgemische [EN: On the ignition temperatures of explosive gas mixtures]. *Zeitschrift für Physikalische Chemie*, *11U*(1), 28–37. https://doi.org/10.1515/zpch-1893-1104 (Cit. on p. 3)

Gebhart, B., Jaluria, Y., Mahajan, R. L., & Sammakia, B. (1988). *Buoyancy induced flows and transport: Reference edition*. Hemisphere Publ. Corp. (Cit. on pp. 11, 12).

Häber, T., Zirwes, T., Roth, D., Zhang, F., Bockhorn, H., & Maas, U. (2017). Numerical Simulation of the Ignition of Fuel/Air Gas Mixtures Around Small Hot Particles. *Zeitschrift für Physikalische Chemie*, *231*(10), 1625–1654. https://doi.org/10.1515/zpch-2016-0933 (Cit. on p. 6)

Harrison, A., & Cairnie, L. (1988). The development and experimental validation of a mathematical model for predicting hot-surface autoignition hazards using complex chemistry. *Combustion and Flame*, *71*(1), 1–21. https://doi.org/10.1016/0010-2180(88)90101-0 (Cit. on pp. 5, 10)

Hirsch, W., & Brandes, E. (2005). *Zündtemperaturen binärer Gemische bei erhöhten Ausgangsdrücken* [EN: Ignition temperatures of binary mixtures at increased outlet pressures]. PTB Braunschweig and Berlin. (Cit. on p. 15).

International, A. (1976). ASTM-D2155: Standard test method for determination of fire resistance of aircraft hydraulic fluids by autoignition temperature. https://doi.org/10.1520/D2155-18. (Cit. on p. 15)

International, A. (2005). ASTM-E659: Standard test method for autoignition temperature of liquid chemicals. (Cit. on pp. 15, 16).

ISO/IEC. (2017). ISO/IEC 80079-20-1: Explosive atmospheres – Part 20-1: Material characteristics for gas and vapour classification – Test methods and data. (Cit. on p. 15).

Jones, S. M. (2020). *Thermal ignition by vertical cylinders*. California Institute of Technology. (Cit. on pp. 5, 6, 11, 16).

Kuchta, J. M., Bartkowiak, A., & Zabetakis, M. G. (1965). Hot surface ignition temperatures of hydrocarbon fuel vapor-air mixtures. *Journal of Chemical and Engineering Data*, *10*(3), 282–288 (Cit. on pp. 5, 16).

Laurendeau, N. M. (1982). Thermal ignition of methane-air mixtures by hot surfaces: A critical examination. *Combustion and Flame*, *46*, 29–49 (Cit. on p. 9).

Laurendeau, N. M., & Caron, R. N. (1982). Influence of hot surface size on methane-air ignition temperature. *Combustion and Flame*, *46*, 213–218 (Cit. on p. 5).

Law, C. K. (1979). Transient ignition of a combustible by stationary isothermal bodies. *Combustion Science and Technology*, *19*(5-6), 237–242 (Cit. on p. 9).

Law, C. K., & Law, H. K. (1979). Thermal-ignition analysis in boundary-layer flows. *Journal of Fluid Mechanics*, *92*, 01 (Cit. on p. 9).

Liang, J., Wang, S., Hu, H., Zhang, S., Fan, B., & Cui, J. (2012). Shock tube study of kerosene ignition delay at high pressures. *Science China Physics, Mechanics and Astronomy*, *55*(6), 947–954. https://doi.org/10.1007/s11433-012-4723-8 (Cit. on p. 17)

Maas, U., & Warnatz, J. (1988). Ignition processes in hydrogen-oxygen mixtures. *Combustion and Flame*, *74*(1), 53–69. https://doi.org/10.1016/0010-2180(88)90086-7 (Cit. on p. 10)

Mallard, F., & Le Chatelier, H. (1880). Sur les températures d'inflammation des mélanges gazeux [EN: On the ignition temperatures of gas mixtures]. *Comptes rendus hebdomadaires des séances de l'Académie des sciences*, *91*, 825–828 (Cit. on p. 3).

Mallard, F., & Le Chatelier, H. (1883). *Recherches expérimentales et théoriques sur la combustion des mélanges gazeux explosifs* [EN: Experimental and theoretical research on the combustion of explosive gas mixtures]. Dunod. (Cit. on p. 3).

Martin, C., & Shepherd, J. (2021). Low temperature autoignition of Jet A and surrogate jet fuel. *Journal of Loss Prevention in the Process Industries*, *71*, 104454. https://doi.org/10.1016/j.jlp.2021.104454 (Cit. on p. 16)

Mason, W., & Wheeler, R. V. (1924). CCXXXV.—The ignition of gases. Part IV. Ignition by a heated surface. Mixtures of the paraffins with air. *Journal of the Chemical Society, Transactions*, *125*, 1869–1875 (Cit. on p. 3).

Melguizo-Gavilanes, J., Boeck, S., Mevel, R., & Shepherd, J. (2017). Hot surface ignition of stoichiometric hydrogen-air mixtures. *J. Hydrogen Energ.*, *42*(11), 7393–7403. https://doi.org/10.1016/j.ijhydene.2016.05.095. (Cit. on p. 5)

Melguizo-Gavilanes, J., Nové-Josserand, A., Coronel, S., Mével, R., & Shepherd, J. (2016). Hot surface ignition of n-hexane mixtures using simplified kinetics. *Combustion Science and Technology*, *188*(11-12), 2060–2076 (Cit. on pp. 5, 16).

Menon, S. K., Boettcher, P. A., Ventura, B., & Blanquart, G. (2016). Hot surface ignition of n - hexane in air. *Combustion and Flame*, *163*, 42–53. https://doi.org/10.1016/j.combustflame.2015.08.011 (Cit. on p. 5)

Mullen, J. W., Fenn, J. B., & Irby, M. R. (1948). The ignition of high velocity streams of combustible gases by heated cylindrical rods. *Symposium on Combustion and Flame, and Explosion Phenomena, Volume 3*, 317–329 (Cit. on p. 6).

Ono, S., Kawano, H., Niho, H., & Fukuyama, G. (1976). Ignition in a Free Convection from Vertical Hot Plate. *Bulletin of JSME*, *19*(132), 676–683 (Cit. on pp. 5, 9, 16).

Ostrach, S. (1953, January 1). *An Analysis of Laminar Free-Convection Flow and Heat Transfer About a Flat Plate Parallel to of the Generating Body Force* (Technical Report No. 1111). NACA. (Cit. on pp. 12, 14).

Paterson, S. (1939). I. the ignition of inflammable gases by hot moving particles. *The London, Edinburgh, and Dublin Philosophical Magazine and Journal of Science*, *28*(186), 1–23 (Cit. on p. 6).

Paterson, S. (1940). XLII. The ignition of inflammable gases by hot moving particles: II. *The London, Edinburgh, and Dublin Philosophical Magazine and Journal of Science*, *30*(203), 437–457. https://doi.org/10.1080/14786444008520734 (Cit. on p. 6)

Roth, D., Häber, T., & Bockhorn, H. (2017). Experimental and numerical study on the ignition of fuel/air mixtures at laser heated silicon nitride particles. *Proceedings of the Combustion Institute*, *36*(1), 1475–1484. https://doi.org/10.1016/j.proci.2016.05.054 (Cit. on p. 6)

Roth, D., Sharma, P., Haeber, T., Schiessl, R., Bockhorn, H., & Maas, U. (2014). Ignition by Mechanical Sparks: Ignition of Hydrogen/Air Mixtures by Submillimeter-Sized Hot Particles. *Combustion Science and Technology*, *186*(10-11), 1606–1617. https://doi.org/10.1080/00102202.2014.935606 (Cit. on p. 6)

Semenov, N. N. (1928). Zur Theorie des Verbrennungsprozesses [EN: On the theory of the combustion process]. *Zeitschrift für Physik*, *48*, 571–582 (Cit. on p. 7).

Setchkin, N. (1954). Self-ignition temperatures of combustible liquids. *Journal of Research of the National Bureau of Standards*, *53*(1), 49. https://doi.org/10.6028/jres.053.007 (Cit. on pp. 4, 15)

Silver, R. S. (1937). The ignition of gaseous mixtures by hot particles. *The London, Edinburgh, and Dublin Philosophical Magazine and Journal of Science*, *23*(156), 633–657. https://doi.org/10.1080/14786443708561839 (Cit. on p. 6)

Smyth, K. C., & Bryner, N. P. (1997). Short-duration autoignition temperature measurements for hydrocarbon fuels near heated metal surfaces. *Combustion Science and Technology*, *126*(1-6), 225–253 (Cit. on p. 6).

Smyth, K. C. (1990). *Short-duration autoignition temperature measurements for hydrocarbon fuels* (NIST IR 4469). National Institute of Standards and Technology. Gaithersburg, MD. https://doi.org/10.6028/NIST.IR.4469. (Cit. on p. 6)

Song, X., Schmidt, L., & Aris, R. (1991). The Ignition Criteria for Stagnation-Point Flow: SemenovFrank-Kamenetski or van't Hoff. *Combustion Science and Technology*, *75*(4-6), 311–331. https://doi.org/10.1080/00102209108924094 (Cit. on p. 7)

Sparrow, E. M., & Gregg, J. (1958). The Variable Fluid-Property Problem in Free Convection. *Transactions of the ASME*, *80*, 879–886 (Cit. on p. 13).

Tang, H.-C., Zhang, C.-H., Li, P., Wang, L.-D., Ye, B., & Li, X.-Y. (2012). Experimental study of autoignition characteristics of kerosene. *Acta Physico-Chimica Sinica*, *28*(4), 787–791 (Cit. on p. 17).

Tizard, H., & Pye, D. (1922). VIII. *Experiments on the ignition of gases by sudden compression*. *The London, Edinburgh, and Dublin Philosophical Magazine and Journal of Science*, *44*(259), 79–121. https://doi.org/10.1080/14786440708633981 (Cit. on p. 4)

Tritton, D. J. (1988). *Physical fluid dynamics* (2nd ed, pp. 163–196). Clarendon Press ; Oxford University Press. (Cit. on p. 12).

Turns, S. R. (1996). *An introduction to combustion: Concepts and applications*. McGraw-Hill. (Cit. on p. 17).

Valco, D. J., Min, K., Oldani, A., Edwards, T., & Lee, T. (2017). Low temperature autoignition of conventional jet fuels and surrogate jet fuels with targeted properties in a rapid compression machine. *Proceedings of the Combustion Institute*, *36*(3), 3687–3694. https://doi.org/10.1016/j.proci.2016.05.032 (Cit. on p. 17)

van't Hoff, J. H. (1896). The Influence of Temperature on Chemical Change. *Studies in Chemical Dynamics* (pp. 136–142). Frederick Muller & Co. (Cit. on pp. 6, 7).

Vasu, S. S., Davidson, D. F., & Hanson, R. K. (2008). Jet fuel ignition delay times: Shock tube experiments over wide conditions and surrogate model predictions. *Combustion and Flame*, *152*(1-2), 125–143. https://doi.org/10.1016/j.combustflame.2007.06.019 (Cit. on p. 17)

Vlachos, D. G., Schmidt, L. D., & Aris, R. (1994). Ignition and extinction of flames near surfaces: Combustion of CH4 in air. *AIChE Journal*, *40*(6), 1005–1017. https://doi.org/10.1002/aic.690400611 (Cit. on p. 10)

Vlachos, D., Schmidt, L., & Aris, R. (1993). Ignition and extinction of flames near surfaces: Combustion of H2 in air. *Combustion and Flame*, *95*(3), 313–335. https://doi.org/10.1016/0010-2180(93)90135-P (Cit. on p. 10)

Wang, H., & Oehlschlaeger, M. A. (2012). Autoignition studies of conventional and Fischer–Tropsch jet fuels. *Fuel*, *98*, 249–258. https://doi.org/10.1016/j.fuel.2012.03.041 (Cit. on p. 17)

White, R. (1967). *Spontaneous ignition of kerosene - AVTUR - vapour: The effect of the ratio, vessel surface area to volume. Spontaneous ignition of kerosene (AVTUR) vapour : The effect of the ratio vessel surface area to volume.* (Technical Report No. 67107). Royal Aircraft Establishment Farnborough. England. (Cit. on p. 16).

Zabetakis, M. G., Furno, A. L., & Jones, G. W. (1954). Minimum spontaneous ignition temperatures of combustibles in air. *Industrial & Engineering Chemistry*, *46*(10), 2173–2178. https://doi.org/10.1021/ie50538a047 (Cit. on p. 15)

Zhukov, V. P., Sechenov, V. A., & Starikovskiy, A. Y. (2014). Autoignition of kerosene (Jet-A)/air mixtures behind reflected shock waves. *Fuel*, *126*, 169–176. https://doi.org/10.1016/j.fuel.2014.02.036 (Cit. on p. 17)

Chapter 2

AUTOIGNITION TESTING USING THE ASTM-E659 APPARATUS

2.1 Introduction

2.1.1 Motivation

In this chapter the standardized experimental apparatus for autoignition temperature determination is explored and detailed data presented for a variety of fuels including those relevant to aviation like Jet A and simplified surrogates. Autoignition in this context is the phenomenon wherein a substance "spontaneously" ignites due to self heating and thermal runaway which originates only from heating of the reactive mixture following injection into a pre heated volume of air. As discussed in the introduction, the ASTM-E659 (International, 2005) is the standardized test method that has been adopted for this purpose. In this test, a small quantity of liquid fuel (0.05 to 0.5 mL) is injected into a preheated flask containing hot air with ignition determination made by visual observations and temperature measurements.

Although the ASTM-E659 is now the widely accepted standard in North America for AIT determination, literature sources rarely specify this as the method used in obtaining their reported AITs. Many safety data sheets (SDS) and chemical databases cite the origin of reported AIT numbers, but in almost all cases these sources are simply other chemical databases or property handbooks which do not claim to have performed any testing themselves or have cited a different test method for AIT determination, e.g. Sax (1957), Zabetakis (1965), CRC (1983), NFPA (1991), USCG (1999), and Zakel et al. (2019). As a consequence, it is challenging to determine the origin of reported AIT numbers or the details of the testing method. Even when the sources are well documented, the test methods described for determining the AIT are not always cited as the ASTM-E659 and in fact most often the sources cite the outdated ASTM-D2155 standard or the use of entirely different classes of test methods (Zabetakis, 1965; Robinson & Smith, 1984; CRC, 1983). These discrepancies can be quite significant since the AIT is known to depend strongly on the method and apparatus as demonstrated by Setchkin (1954). This lack of consistency in the literature complicates the comparison of AIT values of different fuels or the same fuels tested by different research groups.

2.1.2 AIT Data Correlation and Modeling Attempts

A significant issue in interpreting and modeling the ASTM-E659 test is the lack of characterization or control of the mixing processes between the fuel and hot air. The formation of droplets, vaporization and diffusion of the fuel into the air, convective motion and the potential impingement of the fuel on the hot flask surface make this a challenging situation to measure and model.

The fuel-air mixture is likely to be highly nonuniform as is the temperature distribution due to the cooling effects of fuel vaporization. Despite the widespread use of ASTM-E659 and related test methods, the inherent variability and complexity has inhibited scientific investigations and modeling efforts. A brief summary and discussion of some of these issues related to modeling and theoretical treatment of AIT is presented in Hattwig and Steen (2004). Additional attempts to correlate ignition data for a wide variety of fuel types and development of predictive models have also been attempted. Hilado and Clark (1972) attempted to develop a correlation to explain differences in AIT across different test methods by using reported ignition delay times to normalize existing data and facilitate comparison between different apparatuses. They proposed an equation of the form

$$\log \tau_{ign} = \frac{A}{T_{ign}} + B\,, \tag{2.1}$$

where τ_{ign} is the ignition delay time, T_{ign} is the corresponding ignition temperature at which the delay time was recorded, A and B are constants determined from test data. This approach was motivated by empirical observations and simple models of explosion for one-step reactions governed by an Arrhenius rate law. However this correlation is limited since it does not specify or account for composition changes and, more importantly, it does not predict the restrictions on physically allowable ignition delay times for a given fuel. For instance in the present work, the maximum ignition delay time found for n-Dodecane was measured to be around 170 s (at 202.6°C) making the correlation invalid beyond this value. Since the goal of such modeling is to determine the minimum ignition temperature (or equivalently maximum ignition delay time) a priori, use of such a model is not helpful since these cutoff values can only be determined experimentally. Additionally the manual nature of the injection process has the potential to produce significant discrepancies in the reported ignition delay time for these experiments since the initial interaction of the fluid droplets with the surface is likely to differ depending on droplet size, initial temperature, and injection velocity. Nevertheless Hilado and Clark's focus on the importance of the ignition delay time, effects of combustion chamber material and impurity effects on reported AIT provides further indication that the AIT is highly method dependent and not some fundamental fuel property as had been speculated early on.

The nature of the data also hampers the development of models for the prediction of the AIT based on molecular properties alone. Affens et al. (1961) used the same apparatus as Setchkin (1954) in an effort to correlate ignition behavior to chemical structure for various classes of alkane and aromatic substances. They noted some correlations between a decrease in chain length, methyl groups, unsaturation, and chain branching with an increase in the minimum AIT for aliphatic hydrocarbons as well as a correlation between existing side chains and side chain length and increased AIT for

alicyclic compounds and aromatics (Affens et al., 1961). More recently, a study by Tsai et al. (2012) attempted to fit a model to the AIT of 820 compounds reported in the DIPPR database based on a set of molecular descriptors. This approach was moderately successful (36°C mean absolute error) in reproducing experimental AIT values. Given the manual nature of the injection process and the wide range of fuel vapor pressures and viscosities examined in these studies, it is not surprising that there are significant discrepancies between test data and predictions based solely on molecular structure. Bounaceur et al. (2016) also proposed an AIT correlation with pressure and equivalence ratio based on a zero-dimensional detailed chemical kinetics simulation validated against experimental data from various AIT studies. However, this approach does not account for the heat losses and convective mixing that seems to be crucial especially in the low temperature autoignition regime. This limits the usefulness of their correlations despite good agreement with more engine-relevant shock tube data. These modeling and correlation efforts suffer from having to rely on data of uncertain origin and quality. There exist few studies which actually report the original data such as temperature traces or the specific test conditions (sample volumes, apparatus configuration, etc.) used in obtaining the reported minimum AIT value. This information would be useful for understanding which gas phase composition is most readily ignited for a given fuel as well as the sensitivity of the autoignition phenomena to fuel composition.

Although widely used in safety assessment and setting design criteria, it is apparent that the ASTM-E659 test is not always an appropriate method for evaluating industrial thermal ignition hazards. In the particular case of aircraft, most of the hot surfaces encountered are metals (steel, nickel and titanium alloys, and aluminum) rather than glass as in ASTM-E659 testing. These are important considerations since the surface material can have a significant effect on the ignition thresholds for some fuels (> 100°C variation) (Smyth, 1990). However the influence of surface material is only minor in cases where the surface is not catalytically effective and surface reactions do not dominate (Roth et al., 2017). Even more important than surface material are the differences between the confined flow within the vessel used in ASTM-E659 testing and unconfined or partially confined external flows that occur in many industrial situations. The heated surface geometry and residence time in the thermal layer (Jones & Shepherd, 2020) can be significantly different in actual hazards than in ASTM-E659 testing. This is important because fuel decomposition and the formation of the ignition kernel has been observed to take place preferentially close to the heated surface (Melguizo-Gavilanes & E.Shepherd, 2017; Melguizo-Gavilanes et al., 2017a; Melguizo-Gavilanes et al., 2017b; Coronel et al., 2019). Hot surface ignition testing like that performed by Strasser et al. (1971) are more representative of potential ignition hazards where the liquid fuel spray impinges directly on heated cylindrical and flat test targets contained within a cooler atmosphere. These studies found significantly larger ignition temperatures (>200°C) as compared to AIT data for the same fuels. Colwell and Reza (2005) made similar observations for a large number of tests with

aviation fuels and conducted using single fuel droplets incident a horizontal flat plate. For some geometries, the orientation of the heated surface has also been shown to play an important role in the ignition process. Velagala et al. (2020) studied this issue for the case of heated hemispheres in a range of orientations which resulted in distinct differences in the development of thermal plumes in the bulk flow which ultimately led to different ignition kernel locations and delay times.

Heating transients and ignition events can also occur over much longer times than the 10 minutes examined in ASTM-E659 testing. Longer duration experiments can lead to significant fuel decomposition as well as unusual ignition transients without any obvious rapid energy release (Boettcher et al., 2012). These types of tests near the autoignition threshold are therefore complicated by the existence of these longer duration, weaker ignition modes or "cool flames" which blur the traditional definition of ignition. A recent review of cool flame phenomena is given by Ju (2021). In the ASTM-E659 guidelines some general ignition criterion is given as the appearance of a luminous flame accompanied by a temperature rise of at least a few hundred degrees (International, 2005). Some further discussion is also given on cool flames and preflame reactions for cases which don't meet the ignition criteria. However, in the present study there was found to be more nuance in these near threshold reactions for many of the fuels studied, especially multi-component fuels like Jet A as will be discussed in Section 2.3. A spectrum of ignition events ranging from non-luminous slow reaction to rapid and luminous flames is observed as a function of fuel composition and amount. We have classified the events into four categories by the magnitude of the temperature rise and visible luminosity in order to summarize our results, however this classification is still subjective. The wide range of observed behavior demonstrates the complexity of autoignition and the challenges of determining a threshold temperature that is appropriate for all situations.

More recent studies of autoignition behavior of commodity fuels have been conducted using heated shock tubes and rapid compression machines (RCMs) to measure ignition delay times. In comparison to ASTM-E659 testing, these studies have well-controlled conditions and instrumentation that enables validation of chemical reaction models of ignition. However, the test gas temperatures are significantly higher (625-1381 K) than those relevant to low temperature thermal hazards and the minimum AIT conditions examined in ASTM-E659 testing. These ignition studies (Vasu et al., 2008; Wang & Oehlschlaeger, 2012; Liang et al., 2012; Zhukov et al., 2014; De Toni et al., 2017; Valco et al., 2017) have also mainly been conducted at elevated pressures (8-51 atm) which are uncharacteristic of thermal ignition hazards in aircraft and industrial hazards associated with accidental explosions. One exception is Tang et al. (2012) who studied shock tube ignition at relatively lower pressures (2-4 atm) but much higher temperatures (1100-1500 K).

The regime of low temperature and low pressure thermal ignition has been less thoroughly explored for commodity fuels with studies mainly limited to simple single component fuels like n-hexane or

dimethyl ether (Mével et al., 2019; Ju, 2021). Jet stirred reactors (JSRs) are capable of enabling the investigation of the low temperature and pressure regimes but do not result in autoignition events and so do not provide ignition delay times. Stachler et al. (2020) investigated a range of fuel mixtures and Jet A mixtures using a JSR at atmospheric pressure and temperatures as low as 460 K. However due to the short residence times in the reactor and proximity to the lean blow off limit, autoignition does not occur. Almost all autoignition data from RCM and shock tube studies are obtained for T>600K and/or P>5 atm while the regime of interest here corresponds to $T \approx$ 500K and $P \leq$1 atm. This discrepancy between the present work and these data are illustrated by Figure 1.3. Studies in the high-pressure regime therefore do not provide data which is relevant to the minimum AIT of the studied fuels at atmospheric pressure as the temperature ranges studied were far too high to observe the critical temperature threshold between ignition and non-ignition. These studies may however still provide insight into the dynamics of cool flame formation and negative-temperature-coefficient (NTC) reaction rate dependence at low pressure. However at 1 atm, the range of reported minimum AIT of jet fuels are around 483–527 K and the range for diesel fuels are 498-530 K which are both substantially below the temperature ranges from RCM and heated shock tube studies (Zabetakis, 1965; USCG, 1999; Sax, 1957). The minimum AIT has also been shown to decrease with increasing pressure which means far lower temperatures must be achieved in order to observe the transition between ignition and non-ignition (Caron et al., 1999). These studies also examined kerosene fuels (including Jet A) however with the typical wide compositional variation found in commodity supplies (Edwards, 2017). The variability in commodity fuels and the associated uncertainty in the experimental results has motivated the development of surrogate fuels as well as standardized batches of Jet A to facilitate comparison between experimental studies.

2.1.3 Surrogate Fuels

Commodity fuels like gasoline, diesel or Jet A typically consist of hundreds of different hydrocarbon species in imprecise and varying quantities, even between different batches of the same fuel. This complexity makes it difficult both to accurately reproduce experimental results across distinct fuel batches and to model the reaction mechanisms leading to ignition. As an alternative, suitably representative mixtures of hydrocarbons, called surrogate fuels, can be developed to mimic a few important commodity fuel characteristics such as laminar flame speed, ignition delay time, cetane number and distillation curve while consisting of only a handful of species in well controlled concentrations (Mueller et al., 2012; Chen et al., 2016; Kang et al., 2016; Alekseev et al., 2017; Kim & Violi, 2018). This makes surrogates much more amenable to experimental reproducibility as well as numerical modeling because the species and reaction pathways to consider are both far fewer in number and typically much better understood than they are for many components of the commodity fuel. Several surrogate fuels have been developed in the literature to mimic Jet A

ignition behavior at high pressures and a range of temperatures similar to the studies previously mentioned (T=645-1750K at 8.5-20atm). These surrogate fuel studies have used the existing shock tube and RCM data from the previously mentioned studies (Wang & Oehlschlaeger, 2012; Valco et al., 2017) as sources of validation of their proposed surrogate blends (Dean et al., 2007; Dooley et al., 2010; Chen et al., 2016). Few if any of these detailed surrogate studies have been performed in the low-temperature (<600 K) and low pressure regime of autoignition likely due to the scarcity of data available in this regime for model validation. Some simple fuels like n-hexane have been studied extensively at these conditions (Mével et al., 2019) but these studies have not yet been performed on larger hydrocarbon molecules that are more characteristic of Jet A. For this reason, it is unclear if the previously developed surrogates are relevant to autoignition of Jet A at low pressure and temperature conditions.

Two Jet A surrogates from the literature have been identified in this study for their relevance to matching ignition behavior as well as for their simplicity in composition. These surrogates are (1) the Aachen surrogate (Honnet et al., 2009): n-Decane/1,2,4-Trimethylbenzene, (80/20 wt%), and (2) the JI surrogate (Chen et al., 2016): n-Dodecane/Isocetane/Trans-decalin/Toluene, (0.3/0.36/0.246/0.094 mol%). These surrogates were formulated in an effort to match high-temperature and high-pressure autoignition behavior of Jet A so it is crucial to determine if their usefulness can be extended to Jet A studies focused on the low temperature and low pressure regime of thermal ignition. This is indeed one of the main goals of the present study. Figure 1.3 illustrates the discrepancy between these literature surrogates and the regime of interest in this study for relevance to ignition hazards in aircraft. To validate these surrogates' ignition behavior in the regime of interest, two well-controlled and extensively studied (Edwards, 2017) blends of Jet A were also examined: POSF-4658 and POSF-10325. These fuel blends also provide a quantifiable baseline for comparison with the surrogate samples on a chemical level which is shown in Table 2.1. It is immediately clear from Table 2.1 that all mixtures here contain only alkanes and aromatics in large proportions with the alkanes by far accounting for the largest percentage of the total mixture. Both surrogates also roughly maintain these proportions while neglecting some of the more complex molecules present in Jet A like branched alkanes, cyclo alkanes, napthalenes, and cycloaromatics. Additionally while the overall molecular formula of Jet A and molecular diversity is more closely matched by the JI, the ratio of hydrogen/carbon or H/C is still matched fairly well by the Aachen. These chemical comparisons are useful in explaining some of the ignition results presented in this study.

In studying multi-component liquid fuels like these surrogates and Jet A, there are several difficulties one must be aware of. The major challenge in performing experiments in particular is the discrepancy between the gas phase and liquid phase compositions owing to differences in vapor

Table 2.1: Comparison between composition of Jet A blends and surrogate fuels.

		% by Weight			
		POSF-4658	**POSF-10325**	**Aachen Surrogate**	**JI Surrogate**
Alkanes	n-Alkanes	19	19.98	80	29.17
	iso-Alkanes	31.34	29.69	-	46.53
	cyclo-Alkanes	28.42	31.79	-	-
	Total	78.76	81.46	80	75.7
Aromatics	Alkylbenzenes	13.69	12.9	20	4.94
	Alkylnapthalenes	1.76	2.34	-	-
	Cycloaromatics	5.79	3.29	-	19.41
	Total	21.24	18.53	20	24.35
Avg. Molecular Formula		$C_{11.69}H_{22.62}$	$C_{11.4}H_{22.1}$	$C_{9.77}H_{19.7}$	$C_{12.49}H_{25.22}$
H/C ratio		1.935	1.939	2.016	2.019

pressure of the individual species. This is especially important in this work as all ignition takes place in the vapor phase. Therefore in order to appropriately match the Jet A ignition behavior with a surrogate, it is the vapor phase composition that must be matched. This approach is taken in the literature with the computational formulation of the JI surrogate which was designed to match the distillation curve of Jet A in order to match both droplet evaporation and ignition behavior (Chen et al., 2016). However, Farouk et al. (2019) studied preferential evaporation for a multi-component fuel droplet and found that composition was highly dependent on droplet size which was not accounted for in the JI surrogate formulation. It is unclear if this consideration is important in the present work as many of the fuel samples used in the ASTM-E659 testing formed a pool at the bottom of the apparatus which slowly evaporated throughout the test time rather than being fully vaporized as droplets during the injection process. Other surrogate studies like that of the Aachen surrogate instead simply attempted to reduce to as few representative components as possible and to roughly capture the properties of the alkanes and aromatics with one compound of each without a comprehensive analysis of the physical chemistry at play in the mixture (Honnet et al., 2009).

When producing these fuel blends for experimental use, the vapor pressure differences between the individual components also makes precision mixing difficult especially in the case of JI where the vapor pressure of toluene is much higher than the other compounds. This difference will also lead to some change in the liquid composition over time since the higher vapor pressure compounds are evaporated much more readily. To mitigate this, the samples were stored in a refrigerated flammables storage unit (ABS Model T9FB2195387) so as to minimize this vapor loss over time.

2.2 Methodology

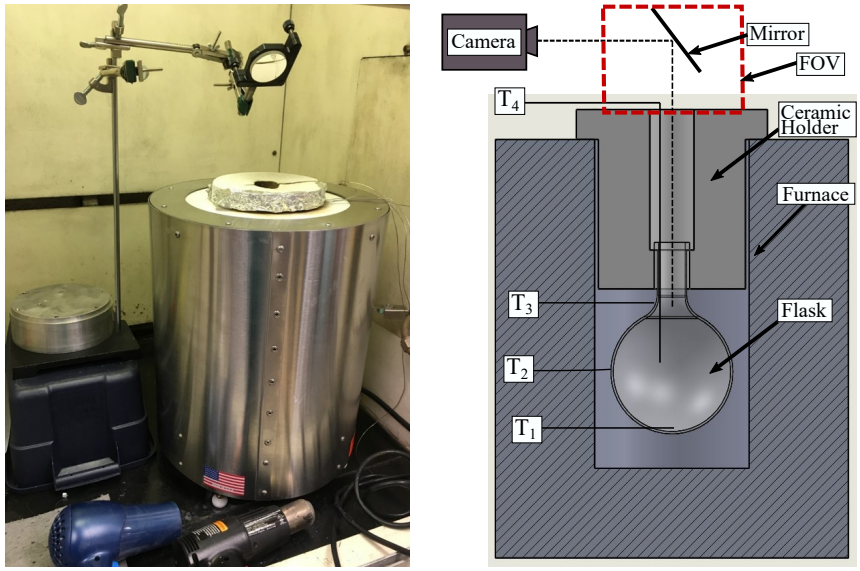

(a) (b)

Figure 2.1: (a) ASTM-E659 test apparatus. (b) Schematic showing a cross section of the internal heated region with thermocouple locations highlighted and camera field of view (FOV).

2.2.1 Procedure

The procedure and testing apparatus employed in this study was the same as that described in the ASTM-E659 standardized test specification for the determination of the AIT but the test method is also briefly discussed here. The test apparatus is shown in Figure 2.1 along with a schematic representation of the combustion vessel contained within the furnace. A small liquid sample of the fuel to be tested was injected via syringe into a uniformly heated 500 mL flask containing room air and left open to the atmosphere. The lights were turned out and the sample was observed via a mirror mounted above the flask opening using a Phantom VR3746 high speed camera which was manually triggered upon ignition of the sample. The gas temperature within the flask was also recorded and monitored during each test in order to determine the extent of self heating occurring in the sample and to provide a secondary indication of ignition via the presence of a sharp temperature spike. This was also used to obtain a measure of ignition delay time, τ_{ign} which was defined as the time between fuel injection and ignition. Typically these events were easily distinguished in the temperature profile with the injection corresponding to a steep temperature drop by a few degrees and the ignition evidenced by a sharp temperature rise. However, as will be discussed in Section 2.3.1, some temperature profiles did not exhibit such a sharp spike in temperature which led to the classification of multiple distinct ignition modes.

Each test was limited by the specification to no more than 10 minutes, at which point if ignition had

not yet been observed then a non-ignition case is recorded. If instead a flame suddenly appeared or the temperature profile indicated some steep temperature increase then an ignition or cool flame event was recorded. However, in many cases it would become clear that the sample was not going to ignite long before the 10 minute limit as self heating typically only lasted for around five minutes after injection for the substances studied here. After the gas temperature leveled off, it was usually evidence that a limit had been reached and the temperature would begin to decay. In these cases, the sample was observed for an additional two minutes after the level off and if the decay continued then the test was considered as a non-ignition case and preparation for the next test would begin. There were a few instances with where this approach failed and ignition was sometimes still observed after the gas temperature had begun to decay but in these cases the decay was only about 1°C and the decay period less than ten seconds before the rapid temperature spike from ignition. An example of this behavior is provided in Figure B.3 (b) for n-decane. Preparation for the next test included the use of a hot air gun or blow dryer applied to the top of the apparatus for up to 30 seconds in order to purge the flask of any remaining ignition products or unburnt fuel. Following purging, temperature adjustments were made via a temperature controller and the furnace was allowed to return to equilibrium at the new set temperature. This would typically take up to 45 minutes at which point a new test could begin.

It was found that the time for the apparatus to return to thermal equilibrium was significantly increased if the temperature was changed more than a few degrees at a time between tests so in order to maximize the number of tests that could be performed for a given substance, the procedure for determining the next set of conditions to test as laid out in the ASTM-E659 test specification was modified slightly. The specified procedure was to choose some sample volume, initially 0.1 mL of the substance and test various temperatures depending on the result of the previous test (i.e. if the previous test ignited (did not ignite) then drop (raise) the temperature 3°C). Once this was done for a given sample volume, the same iterative procedure was then used with a modified sample volume starting at the minimum temperature found from the previous volume. This approach was found to be inefficient as the time for the apparatus to equilibrate after each temperature change was typically over an hour. A more efficient procedure was found by setting the apparatus at a fixed temperature and testing a wide range of sample volumes at this temperature before proceeding to raise or lower the temperature. In this way, the effect of composition could be more easily studied. Additionally using the ignition delay time data, the effective range of sample volumes could be narrowed with each successive temperature level studied since a sample volumes with a shorter τ_{ign} indicated that it was more reactive than a sample volume with a longer ignition delay at the same temperature and thus further from the AIT. Using this data as an indication of sample volumes that would continue to react at lower temperatures allowed the range of ignitable compositions to be reduced in order to produce more finely spaced data points in the minimum AIT region.

A procedure for periodic cleaning of the flask was also employed throughout testing. This procedure consisted of elevating the furnace control temperature to 600°Cand holding for 1 — 2 hours. This was typically necessary only after many tests with high vapor pressure fuels and after only a handful of tests for heavy fuels and commodity fuel samples. The need for cleaning was determined visually by the mirror above the furnace opening. When the flask bottom was becoming opaque from residue buildup then the cleaning procedure was taken. Cleaning using laboratory solvents like isopropanol, methanol, or acetone were found to be insufficient for this purpose. Instead elevating the flask to a sufficiently high temperature for a short period was found to be capable of slowly burning off the residue. A maximum set point of 600°Con the temperature controller was used as the maximum value for this to avoid flask deformation as discussed in Section 2.3.2 and shown in Figure 2.9.

2.2.2 Equipment

The furnace used was a Mellen CV12 crucible furnace with 5.25-in (133 mm) diameter by 8-in (200 mm) deep cylindrical heated volume capable of achieving temperatures up to 1250°C. A PID controller (Love Controls series 16B) system was used to set the furnace at the desired temperature and was accurate to 1°C. A schematic cross section of the apparatus is shown in Figure 2.1b which illustrates the location of the 500 mL round bottom borosilicate flask within the heated volume along with the four thermocouples used to monitor the temperature evolution during a test. The flask was suspended and secured in the furnace by means of an insulating ceramic holder fabricated using a fused silica casting compound.

The casting compound used was silica based Cotronics Rescor 750 which consisted of both a powder and liquid activator compound mixed in an adjustable ratio to control the consistency of the liquid ceramic during casting. Several mold materials were tested using this compound and a silicone based mold release agent including 3D printed PLA, urethane, and molding clay. Ultimately the PLA molds were found to be too rigid to allow for removal of the cast component without severe damage to the component. Urethane molds had the additional difficulty of the mold also being easily damaged during removal of the casting. Using molding clay to create the mold was ultimately found to be the preferred approach due to its ease of removal from the casting and ability to easily recreate the mold after it is destroyed in the removal process. A 3D printed PLA model of the insulating holder was fabricated and used as a model for the clay molding process to ensure the cast component would stay true to the design. The mold was created by applying the clay in pieces to the outer surface of the 3D printed model, cutting out the model, and finally smoothing out the inner surfaces of the mold and repairing the crack created by cutting out the mold. The model was covered in saran wrap during this process so the clay wouldn't easily stick to the surface. This would allow for easy removal of the model from the clay mold. Poly-carbonate sheets were applied to each of the four external faces of the clay mold and c-clamps were applied

to these in order to counteract the hydrodynamic forces within the mold during pouring. Figure 2.2 illustrates the final step in this procedure where the compound was set to cure for 1-2 days in the mold before being removed. Upon removal, the components were cured in a standard ceramic kiln at 1750°F to remove any remaining moisture and increase strength.

The locations of the four type K thermocouples are also shown in the schematic in Figure 2.1b with the gas temperature being read from T_4 which was suspended approximately in the center of the flask volume. Preliminary tests to characterize the apparatus showed that the location of the gas phase thermocouple within the volume had little effect on the reading (±0.5°C) providing indication of temperature uniformity within the flask at elevated temperatures. The thermocouples were constructed from 36 gauge (0.127 mm diameter) wire and sheathed in stainless steel for protection. The temperatures at the bottom, side, and neck of the flask's outer wall were monitored via T_1,T_2,and T_3 respectively. The temperature of the flask wall was much less uniform than that of the gas, with typical variations of up to 5°C when set near 250°C and 15°C above 400°C. This is likely physical and due to the low thermal conductivity of borosilicate glass which can result in significant temperature gradients with a nonuniform heat input to the flask surface. The heating elements of the furnace are closer to the side of the flask so it is expected and observed that T_2 is consistently larger than T_1 and T_3. Since the gas convects within the flask it seems this region is much more uniform. The non-uniformity in flask surface temperature therefore does not seem to

Figure 2.2: (left) Casting compound and 3D printed model of insulating holder (right) Ceramic curing in clay mold.

have a significant effect on AIT.

Temperature profiles were recorded from the time of injection through any self heating or ignition event using an OMEGA HH520 four channel data logger calibrated to the nearest 0.1°C up to 600°C and 1°C for higher temperatures. All channels were sampled at 1 Hz as per the ASTM-E659 specification although some simple heat transfer calculations showed that the responsiveness of the thermocouples may be 2 orders of magnitude faster than this for similar free convection flows. 34-gauge thermocouple (0.0063-in or 0.16 mm diameter) wires were used in early tests but were eventually replaced by the test standard 36 gauge components. There was no discernible change in temperature readings and this is attributed to the data logger acquisition rate dominating the response of the temperature measurement system. Reported experimental errors were estimated based on both the standard error limits for type K thermocouples and the reported error of the HH520 datalogger itself.

2.2.3 Surrogate Fuel Preparation

An early attempt at mixing the surrogates was made using a Tree Model HRS3100 scale calibrated to the nearest 0.001 g to weigh out the individual compounds, but this method proved unreliable as shown by GC-FID (Gas Chromatography with Flame Ionization Detector) measurements (Sund, 2019). The details of this GC-FID setup are fully described in the report by Sund. Some results for the JI surrogate are shown in Figure 2.3. The first batch of surrogate used a mixture of Trans- and Cis-decalin (the AITs of these isomers are similar) and the mixture is much easier to obtain in

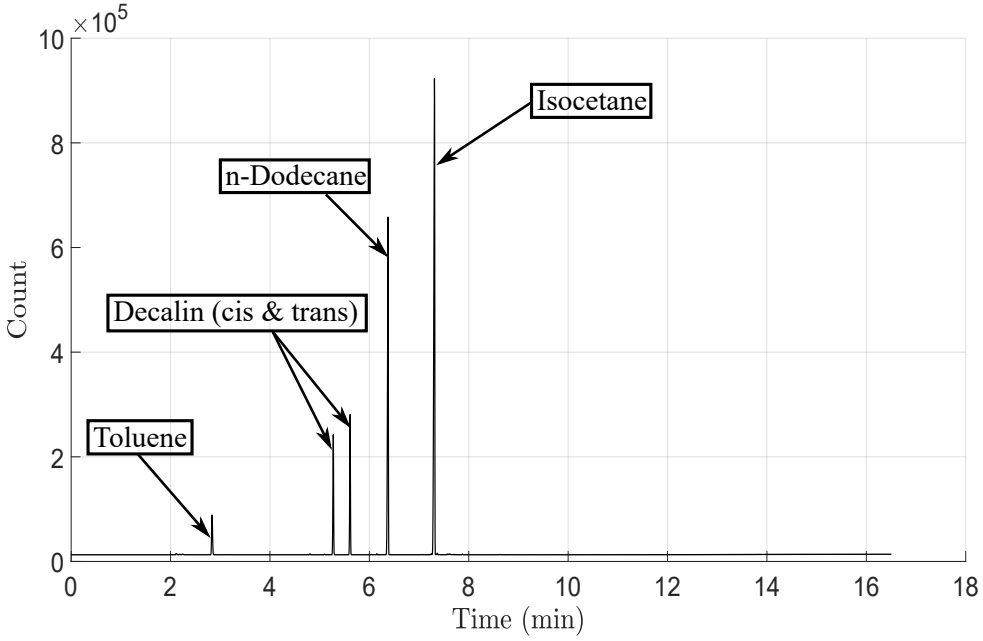

Figure 2.3: JI surrogate (Batch 1) results from GC-FID analysis.

Table 2.2: JI surrogate (Batch 1) results from GC-FID analysis.

	Mass fraction			Vapor Pressure[a] (kPa)
Fuel	**Target**	**Measured**	**% Error**	-
n-Dodecane	0.2915	0.2980	2.24	0.012
Isocetane	0.4651	0.4643	0.15	0.004
Decalin	0.1940	0.2066	6.49	0.116
Toluene	0.0494	0.0310	37.2	2.903

[a] Evaluated at T = 20°C (Sund, 2019).

larger quantities than either isomer individually. The second batch of the surrogate which was used for the AIT testing used only the Trans-decalin isomer. From the integration of the area under each of the peaks, the corresponding mass fractions of each calibrated component was determined. The mass fractions obtained in the GC-FID analysis as well as target values are shown in Table 2.2.

The results showed that for the JI surrogate, two of the four components had relatively large percent errors in their measured mass fractions (Toluene and Decalin). These two components also both happened to have the smallest target mass fractions and Toluene in particular had the highest vapor pressure by far at room temperature. As a result, it was determined that there were two possible factors at play in producing such larger errors: (1) inaccurate mixing and (2) poor sealing/storage of the fuel batch. To address these issues, two changes were made in mixing the second batch of JI, namely (1) the use of pipettes to measure out the components volumetrically, and (2) the use of higher quality storage vessels (PTFE lined caps) and a chemical refrigerator to maintain the batch at a low temperature in order to lower the vapor pressure of the entire mixture and mitigate the preferential loss of lighter compounds over time. The second batch was mixed on a volumetric basis using graduated pipettes into a large 146 mL total batch in order to minimize volume measurement errors especially in the more dilute components. This batch was then stored in an ABS flammable storage refrigerator maintained at 3°C and smaller quantities were extracted for use in the autoignition experiments.

2.3 Results

2.3.1 Classifications

Throughout the range of ignition tests conducted here, there were 4 distinct ignition modes observed along with non-ignition cases. These ignition behaviors were classified as (I) Ignition, (II) Cool Flame, (III) Non-Luminous Cool Flame, and (IV) Rapid Reaction. These were distinguished using a combination of visual evidence as well as the reading of the gas phase thermocouple (T_4). Qualitatively the differences between these modes are summarized in Table 2.3. This classification is limited mainly to qualitative descriptors since the temperature rises and timescales for the same

ignition mode can vary substantially between two different fuels or even different compositions of the same fuel. For instance mode III ignition events for n-decane were seen to produce a temperature rise of 50-200°C on timescales of between one and a half and three and a half minutes for various fuel volumes while for Jet A these events were only capable of 25-70°C temperature increases on similar timescales. A set of temperature traces from ignition testing with Jet A (POSF-4658) is shown in Figure 2.4. Here the traces are aligned such that t=0 corresponds to the injection time as determined by a drop in the bottom thermocouple signal T_1. There is a clear trend that as the flask temperature is decreased, the ignition delay time increases and generally the temperature rise is decreased. This is not always the case (as in Shot 13 in Figure 2.4) since variability in injection and mixing processes can lead to differences in the location of the ignition kernel within the heated volume. Additionally this produces inhomogenous regions where flame temperatures and burning velocities are different within the gas volume. As a consequence, although the thermocouple is placed in the same physical location, it is generally at a variable distance from the ignition point which can lead to small differences in delay time and temperature measurements if the flame is not fully formed by the time it reaches the thermocouple. The temperature measurements also in general depend on the properties of the nearby gas region which unavoidably differ between shots. Additional data of this form is also presented in Appendix B for each of the fuels studied.

Luminosity was determined via the use of high speed video capture of the approximate field of view shown as the red rectangle in the schematic of Figure 2.1b. A representative time series of images and temperature traces for each of the first three ignition modes is shown in Figure 2.5. The thermocouple traces display the difference between the initial gas temperature and the peak temperature measured by T_4 and are used to define the peak temperature rise. In some cases the visual evidence alone was not sufficient to distinguish between ignition modes I and II so the thermocouple trace was used for classification. Mode II ignition was always characterized by a longer ignition delay time as well as a lower peak temperature as compared to mode I events for the same fuel. Mode III also had a far longer timescale than the other modes which further

Table 2.3: Classifications of various ignition behaviors observed in ASTM-E659.

Ignition Mode	**Name**	**Luminosity**	**Temperature Rise (ΔT)**	**Timescale for reaction**
I	Ignition	Large	Large	5 sec - 2.5 mins
II	Cool Flame	Small	Small	15 sec - 4 mins
III	Non-Luminous Cool Flame	None[a]	Large	1 - 5 mins
IV	Rapid Reaction	None	Small	30 sec - 2 mins
-	Non-Ignition	None	<15°C	> 4 - 5 mins

[a] Faint glow only visible to naked eye and small puff of smoke.

distinguished it from the other modes. Mode IV was unique in that the reaction delay occurred on a similar timescale as that of a normal mode I ignition but resulted in a small temperature spike, in some cases comparable to non-ignition cases.

For the mode I events, the images show that the initial explosion progresses rapidly and the flame quickly expands out the top opening of the flask before burning out. For the case shown in Figure 2.5, the first image shows an ignition kernel forming within the flask as observed in the mirror followed by a series of images showing the flames expansion into the region above the testing apparatus in a period of around 14ms. The final three images show the longer period over which the flame in the outer region becomes extinguished while the gas within the flask continues to burn. All four thermocouple traces show a quick rise, for T_4 this is of order 100°C. The rapid decay following the peak is due to the expulsion of the products from the open top as well as heat transfer to the vessel.

For mode II events, it was typically observed that the ignition event is less energetic and the flame remains confined to the interior of the flask which is indicative of a low pressure rise which is consistent with the measured low temperature rise. For the Mode II case in Figure 2.5, a faint ignition kernel is seen in the mirror followed by a more gradual increase in luminosity over the next few images. In the fourth mode II image a dark central region of soot formation is observed which grows to extinguish the flame in the final two images. Mode II was primarily observed in compounds with high ignition temperatures (> 400°C) including the aromatics and iso-cetane. The T_4 thermocouple trace shows a pronounced drop due to the cooling effect of vaporization of

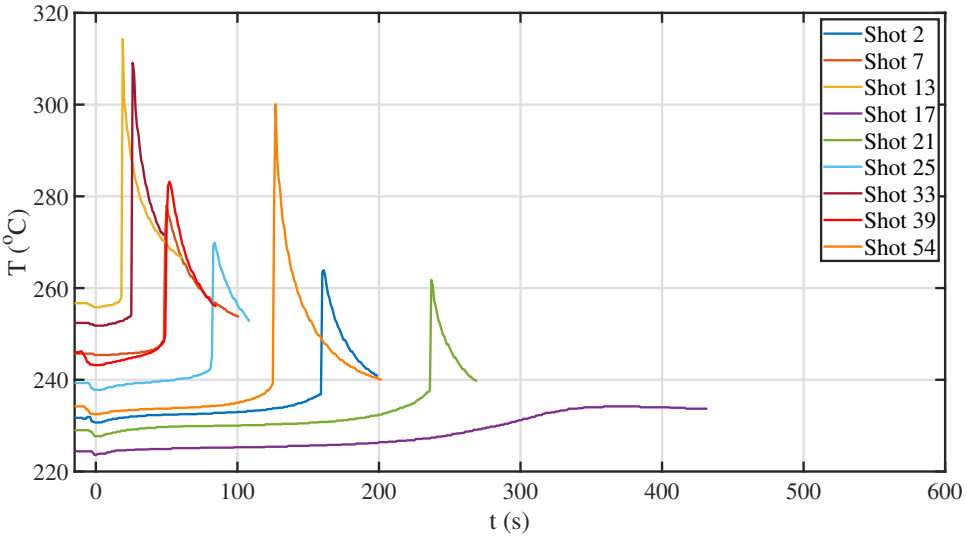

Figure 2.4: Jet A Temperature time curves for a 0.3 ml injection volume at a range of gas temperatures.

the liquid fuel with possible contribution from endothermic reactions, followed by a slow rise to a peak with maximum rise of less than 25∘C. The liquid fuel apparently puddles on the bottom of the vessel and vaporization results in a decrease in the temperature measured by T_1 followed by a slow return to the ambient value.

Mode III ignition events were more prevalent in heavier hydrocarbon species and were indicated by a brief and dim glow visible to the naked eye only in complete darkness. Alternatively, a puff of smoke escaping from the flask could also be observed in these cases and was much easier to record with the current setup. A series of images for mode III is shown in Figure 2.5. In the first image the background and mirror holding apparatus is entirely unobstructed but after a few hundred milliseconds a puff of smoke becomes visible beginning with the second image which persists over the next set of images for well over 1000 ms before dissipating fully in the final image. A temperature drop associated with fuel vaporization is observed on T_1 with a gradual return to ambient temperature. After a delay of about 210s, a temperature rise associated with exothermic reaction is observed on all four thermocouples with a maximum rise of about 25°C observed on T_4.

Mode IV was similarly non-luminous but was distinguished by a much smaller temperature rise and shorter timescale for the peak temperature to be reached as compared to mode III. These events were observed primarily for multi-component mixtures including the Jet A blends and surrogate fuels.

These complex ignition modes make it difficult to define exactly what the word "ignition" means in the context of this test since there is no clear distinction between ignition and non-ignition. This non-binary ignition behavior has been observed in other studies and the ASTM-E659 specification describes the expected behavior for cool flames in the current apparatus (International, 2005). Boettcher et al. (2012) saw a dramatic difference in ignition behavior depending on heating rate in a vessel with transient heating of n-Hexane-air mixtures from room temperature to temperatures above the AIT. For slow heating rates, non-explosive reaction with no obvious ignition but a rapid decrease in fuel concentration occurred and for faster heating rates, explosive ignition with rapid pressure and temperature increase occurred along with a rapid decrease in the fuel concentration. These highly distinct ignition modes may be related to the variety that have been observed in the present work. The non-binary ignition classifications we have adopted enables a fuller description of the test results and allows a more nuanced description of "ignition". The thermocouple traces accompanying each of these ignition cases are shown in Figure 2.5.

The results of the ASTM-E659 ignition testing are presented here for each of the alkanes, aromatics, Jet A batches, and surrogates studied. These data are summarized for each fuel by separate plots containing each ignition test as a data point in the temperature-composition space. Also plotted are the reported AIT values from literature sources discussed in Section 2.1.1 and cited in Table 2.4.

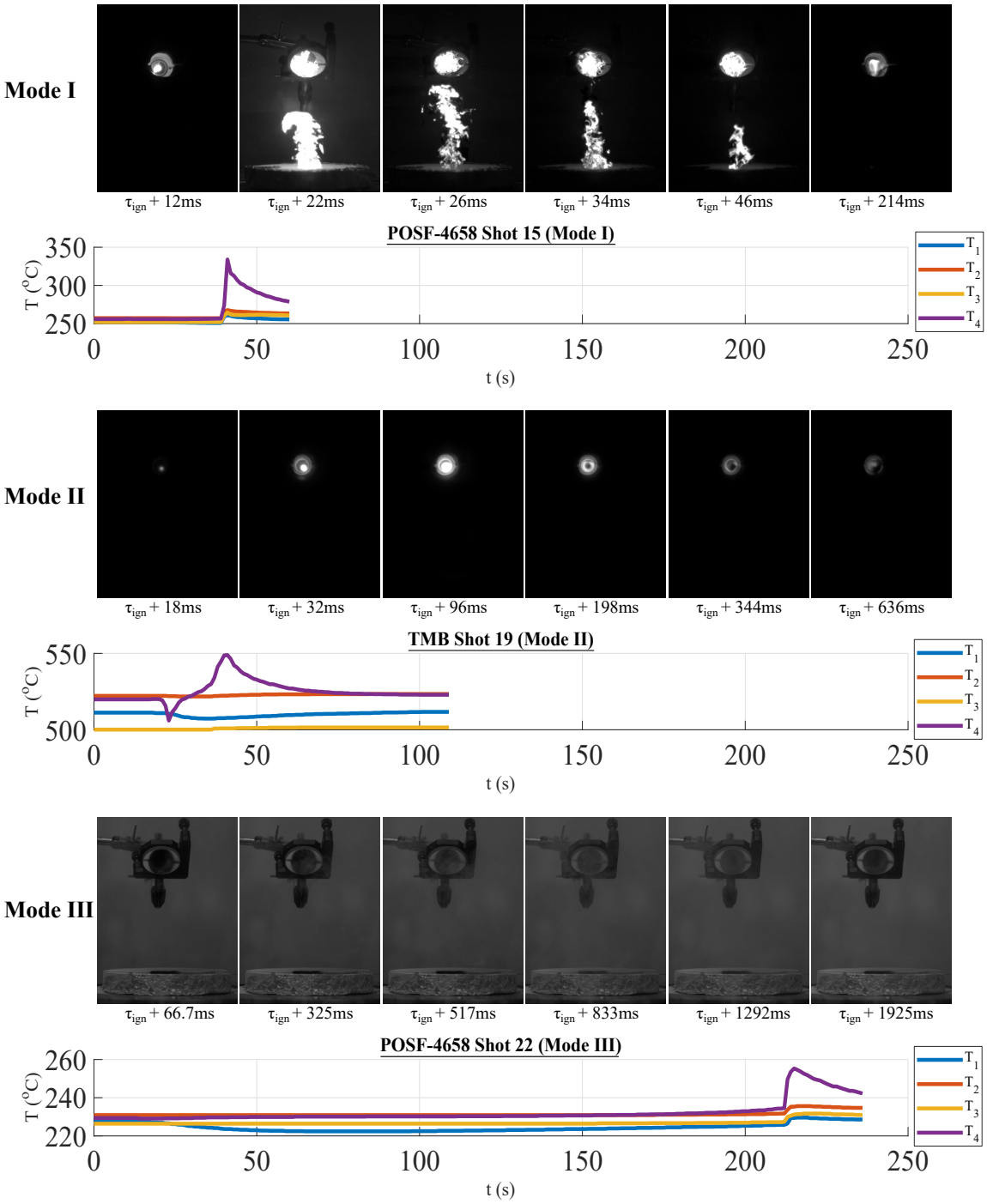

Figure 2.5: Representative ignition events for 3 distinct ignition modes: (I) Ignition, (II) Cool flame, (III) and Non luminous cool flame (Note these correspond to POSF-4658 Shot 15, TMB Shot 19, and POSF-4658 Shot 22).

However, these numbers are always reported as a global minimum with no associated composition given so these values are plotted as constant lines across the compositional domain. This does not accurately reflect the expected and observed compositional dependence of the minimum AIT value. The peak temperature rise during each test (ΔT) was also recorded and is shown here for most fuels. The global minimum AIT measured from each of the fuels as well as the corresponding test conditions are also summarized in Table 2.4 for convenience.

A global equivalence ratio (ϕ) was defined in order to more easily compare results from fuels of different structure and molecular weight by putting the seemingly arbitrary fuel volumes into context. This ϕ is defined based on the vapor space for each fuel sample as if the fuel mass were fully vaporized and mixed homogeneously with air and is calculated by Equation (2.2).

$$\phi = \frac{m_{fuel}/(\rho_{air} V_{flask})}{(F/A)_{stoich}} \tag{2.2}$$

Here m_{fuel} is the fuel mass, V_{flask} is the flask volume, ρ_{air} is the air density, and $(F/A)_{stoich}$ is the stoichiometric fuel to air mass ratio. Using this parameter, it is much easier to see what the effect of having a fuel rich ($\phi > 1$) or fuel lean ($\phi < 1$) mixture is on the ignition behavior and to interpret the different ignition modes.

2.3.2 Alkanes

Three normal alkanes (n-hexane, n-decane, and n-dodecane) were studied along with one branched alkane (iso-cetane, also known as 2,2,4,4,6,8,8-heptamethylnonane). These compounds were chosen for study because they are the molecular components for both of the surrogate fuels studied (Aachen and JI). n-Hexane was also chosen for study due to extensive previous work from our group on n-Hexane ignition in various test conditions, see Boettcher et al. (2012), Boettcher et al. (2013), Mével et al. (2014), and Coronel et al. (2018), Mével et al. (2019).

The first fuel studied was n-Hexane for this reason and some early attempts were made to perform statistical analysis on the ignition results in a similar manner to previous spark ignition studies (Bane et al., 2013). For this reason much of the data was obtained for the same composition and the overall parameter space was not well explored. However as can be seen in Figure 2.6a and some of the other samples studied, there is minimal variability in the outcome of ignition events near the auto ignition temperature. The temperature range bounding ignition and non-ignition is typically contained within 5-10°C. This makes statistical analysis challenging since this temperature interval is comparable to the measurement error of the temperature data acquisition system. An example of statistical analysis performed on the n-Hexane data are presented in Figure 2.6b. The experimental data points were used to compute the logistic curve and 95% confidence limits as described by Bane

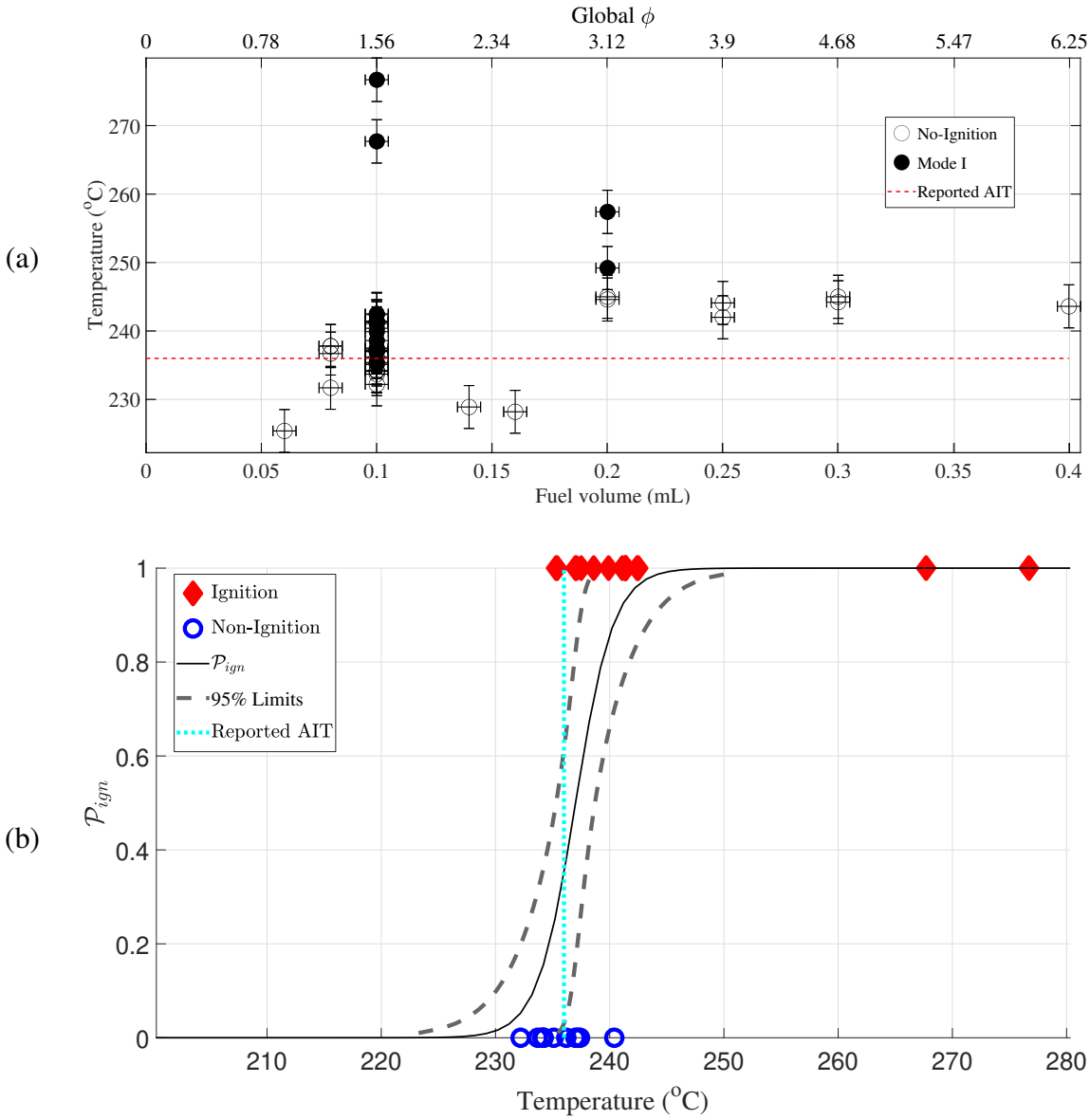

Figure 2.6: (a) n-hexane ignition testing results and (b) n-hexane ignition statistical analysis using the logistic function (Fuel Volume = 0.1mL, Global ϕ = 1.56).

et al. (2013), where $P_{ign} = 1$ indicates ignition and $P_{ign} = 0$ indicates non-ignition. The literature (NFPA, 1991) value of AIT intersects the logistic curve at 40% probability, within a few degrees of the temperature corresponding to 50% probability of ignition. Though reasonably successful in application to the n-Hexane data, statistical analysis of the data was found to problematic for other fuels where the measurement uncertainty became larger (e.g. for aromatics) or little to no crossover was observed in the outcomes of repeated trials at similar test conditions.

It was also found that certain factors like the injection location and the degree of decomposed fuel buildup on the flask surface due to repeated testing was able to impact ignition results. The

impact on AIT was not systematically explored in the present study but seemed to be only a few degrees (<5°C), which is of the same order as the measurement error and the range of ignition threshold data shown in Figure 2.6b. The fact that we have not systematically applied statistical methods to characterize the results of our ASTM-E659 testing (other than for n-Hexane) should not be taken to mean that there is no intrinsic variability in the test outcome but rather that the limited temperature measurement resolution capabilities and apparently narrow region of overlap between ignition and non-ignition for many fuels makes statistical analysis challenging. This difficulty could potentially be overcome with a much larger data set produced under more well-controlled conditions (e.g. injection location, extent of residue buildup on the flask, etc.). In any case, the variability (e.g. confidence interval) as characterized by statistical analysis is of similar order to the temperature measurement uncertainty so all results are presented using the temperature measurement uncertainty to characterize the variability in the results.

Additionally, many of our early n-Hexane tests did not make use of a data logger for thermocouple traces so peak temperature data are not available. Despite this issue, we find that for n-Hexane, there is good agreement between the literature (NFPA, 1991) AIT value (236°C) and our result ($T = 235.3 \pm 3.1$°C) obtained for a slightly rich mixture.

In the case of n-Decane, a 6°C difference is observed between the reported (NFPA, 1991; USCG, 1999) AIT of 210°C and our experimentally determined value of 204.3 ± 3.1°C . In Figure 2.7a we note some mode III ignition behavior near the AIT is also observed for globally rich mixtures with this behavior occurring over a rather broad range of temperatures near the AIT limit which seems to further broaden for even richer mixtures. In Figure 2.7b we note that the peak temperatures in many of these cases are comparable to Mode I ignition temperatures with the exception of the slightly rich mixtures ($\phi = 1.71$) while n-Decane rapidly becomes much harder to ignite closer to stoichiometric and in the lean regime.

Figure 2.8 shows similar trends to those observed for n-Decane with lean and near stoichiometric mixtures becoming harder to ignite and the rich regime producing some mode III events near the AIT limit. Figure 2.8b also shows that these peak temperatures are comparable between mode I and mode III while the highest temperature rises are again seen occurring in the slightly rich regime ($2 < \phi < 4$) with a drop off in both leaner and richer conditions. The reported (NFPA, 1991) AIT value 203°C is quite close to our experimental value 202.2 ± 3.1°C. The is consistent with the small variation in the literature values as compared to many of the other fuels studied.

In Figure 2.10, mode II events begin to dominate the rich compositional space for the iso-cetane samples which is in stark contrast to the mode I and broadening mode III regimes observed for the n-alkanes studied. Additionally it is clear that the iso-cetane sample has a much higher ignition temperature than the n-alkanes which is consistent with the connections made between chemical

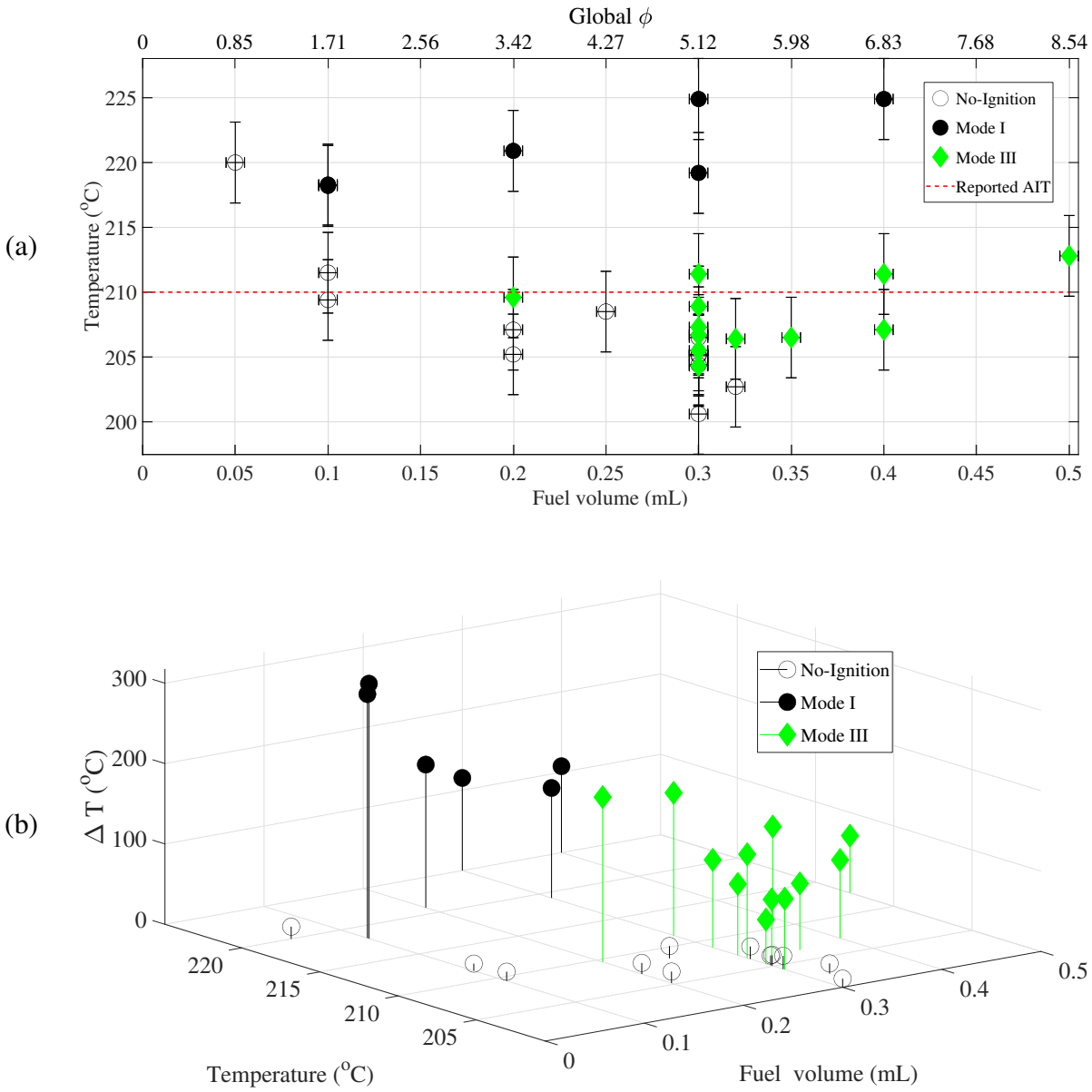

Figure 2.7: (a) n-Decane ignition testing results and (b) Peak temperature rise.

structure (branching) and AIT as laid out in the literature (Affens et al., 1961). Figure 2.10b shows that the mode II events result in much lower peak temperature rises making them easily distinguishable despite the luminosity present in both modes. As with the n-alkanes, the trend in ignition temperature with composition shows that the richer compositions are capable of ignition at much lower temperatures than the lean and near stoichiometric mixtures. An absolute minimum AIT of 395.2 ± 4.1°C was observed but we did not locate any experimental AIT values. The only literature source found for iso-cetane AIT was the DIPPR database (as noted by Sund), which

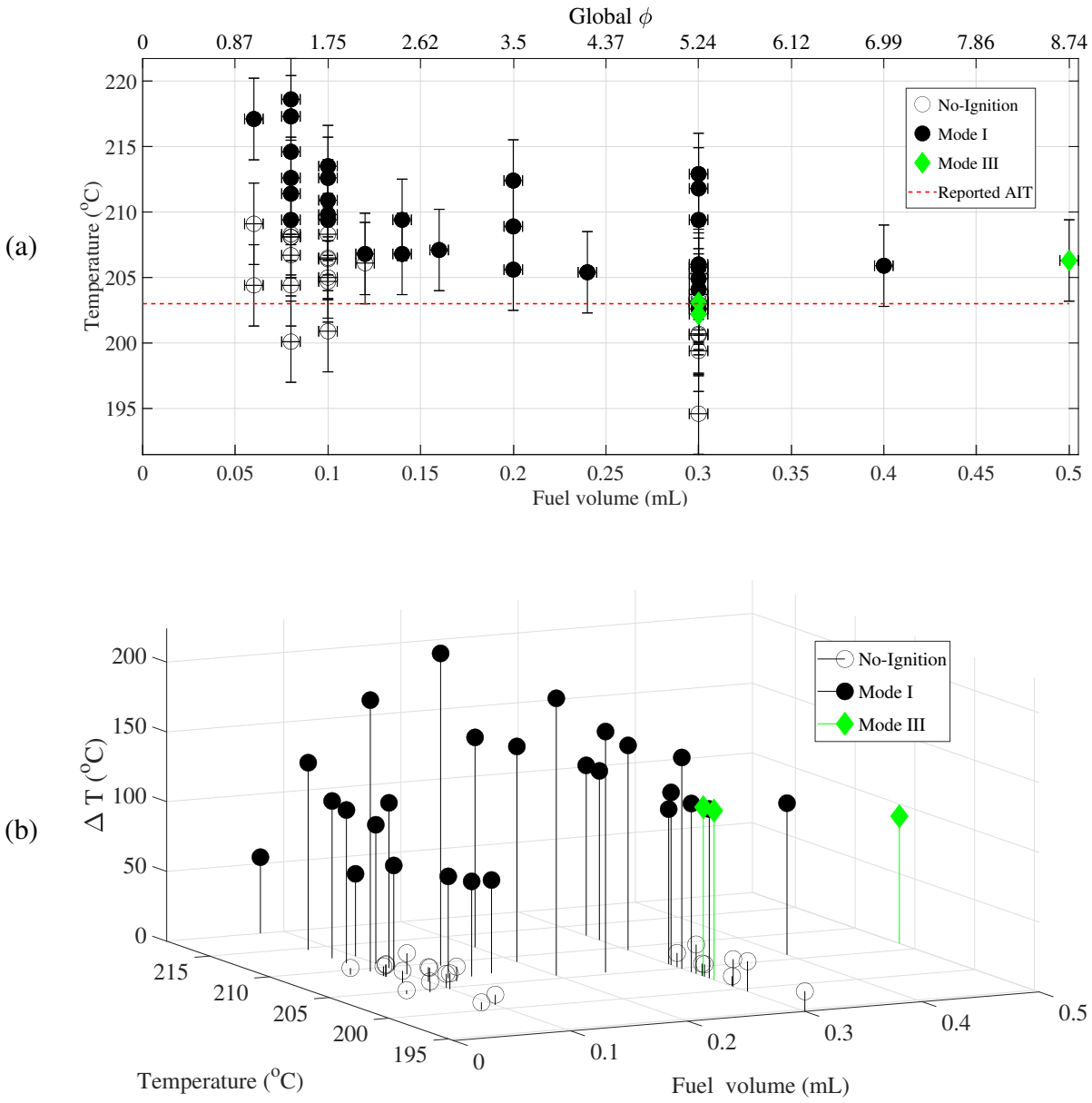

Figure 2.8: (a) n-Dodecane ignition testing results and (b) Peak temperature rise.

reported an AIT of 705°C based on a numerical study.

Some tests were indeed performed at these temperatures with rapid ignition observed, however it was also found that these conditions lead to accelerated deformation of the test flask likely due to a transition to viscoelastic behavior of the borosilicate glass at these elevated temperatures. Under the flasks own self weight, this led to a "flowing" of the glass and elongation to a non spherical geometry. In this way the standardized conditions of the test are not consistent for substances with

Figure 2.9: (left) Unused spherical flask and (right) Deformation of flask observed for T > 600°C.

AIT above a certain threshold (T > 600°C) where in fact a modified geometry of the combustion vessel becomes unavoidable. Figure 2.9 shows the comparison between an unused spherical flask with the deformed flask produced after exposure above 600°Cfor several hours. As discussed in the introduction, the apparatus has a significant impact on the ignition testing results so the elongation effect will in part lead to different results from that expected for the specified test conditions. Indeed this was observed here after the deformed flask was removed and some test conditions were repeated and showed that the deformed vessel actually allowed for ignition at lower temperatures than the spherical flask. It is not immediately clear why this is the case but it may be related to ignition behavior dependence on residence time which would be longer in the case of an elongated vessel as compared to a spherical one. The elongated geometry should allow for naturally convecting fluid particles to spend more time in the thermal boundary layer of the vessel leading to more rapid heating and perhaps accelerated low temperature chemistry leading more quickly to thermal runaway and ultimately ignition, which is consistent with recent studies (Coronel et al., 2019; Jones & Shepherd, 2020).

2.3.3 Aromatics

The aromatic compounds studied here were also chosen based on their relevance to literature surrogate fuels with two alkylbenzenes (1,2,4-trimethylbenzene or TMB and trans-decalin or trans-decahydronapthalene) as well as one cycloaromatic (toluene). It is expected based both on reported

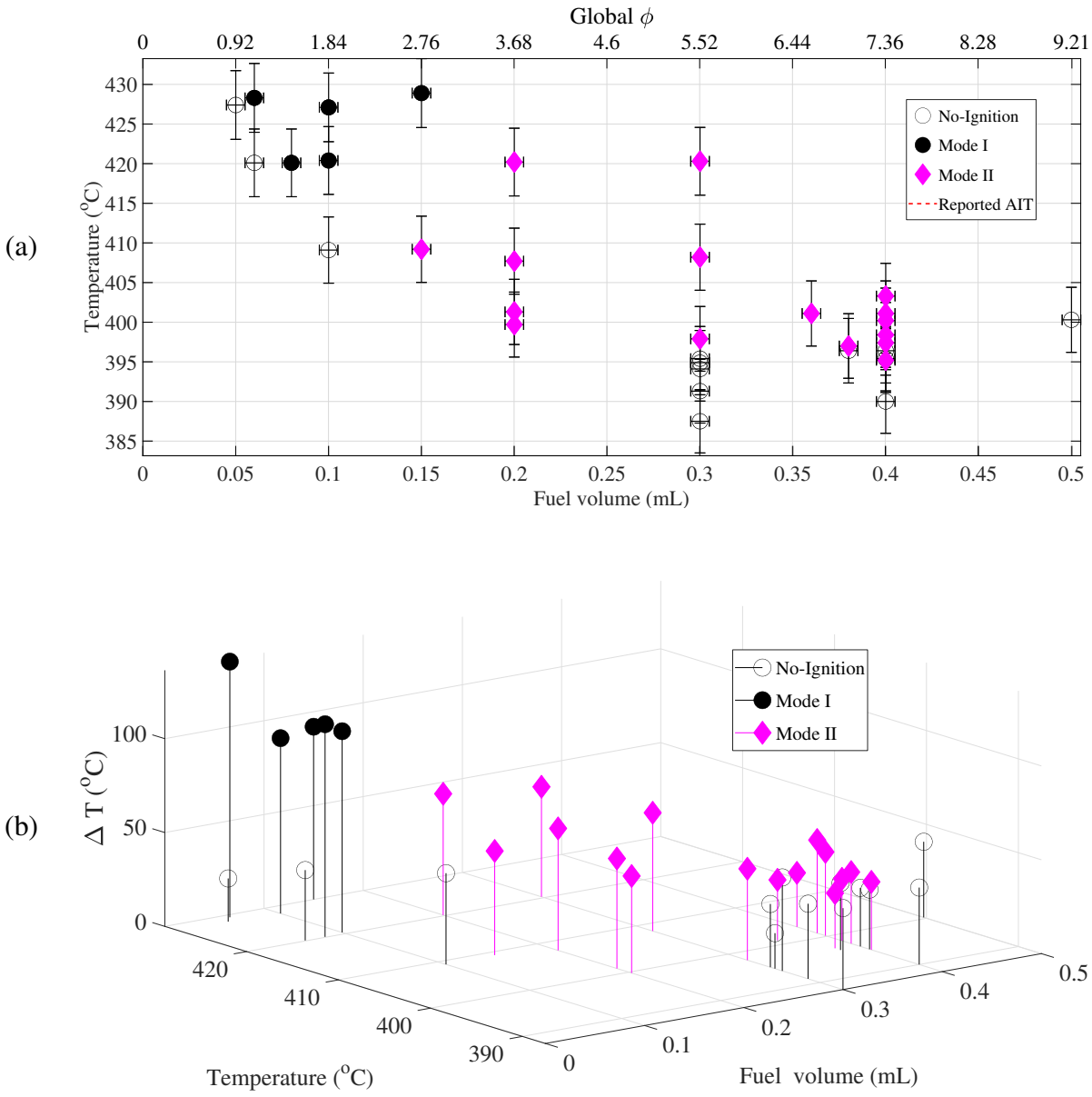

Figure 2.10: (a) Isocetane ignition testing results and (b) Peak temperature rise.

values and literature discussed in the introduction that the minimum AITs of aromatic compounds should be far greater than n-alkanes which indeed is the case here in general. Additional ignition modes were also observed for these fuels and far different trends in the parameter space as compared to those seen for alkanes.

In Figure 2.11a this difference is immediately obvious as there is a much sharper dependence on the composition with lean mixtures now proving to ignite much more readily than rich mixtures for 1,2,4-trimethylbenzene (TMB). Some mode II cool flame behavior is also seen here again with

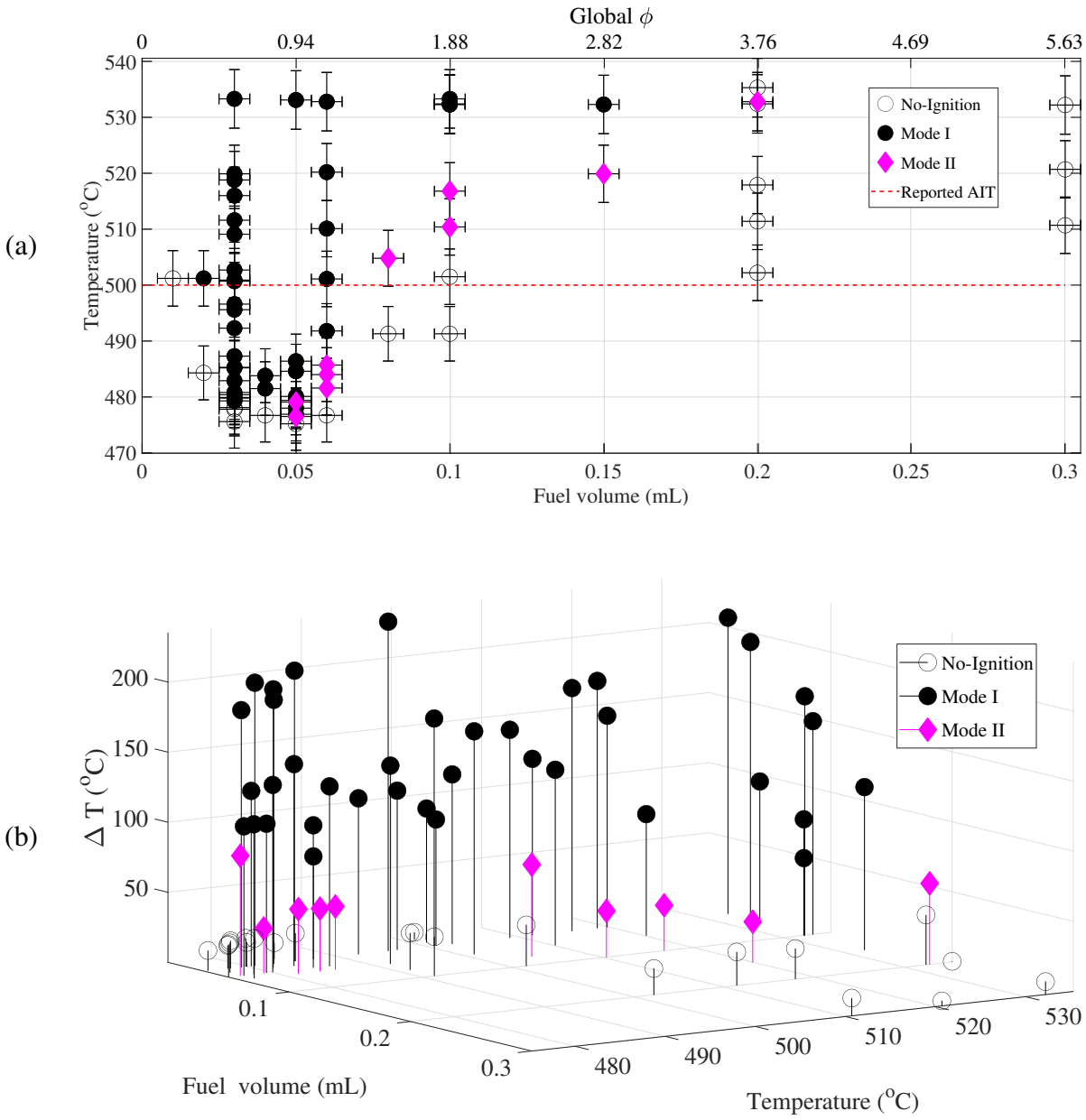

Figure 2.11: (a) 1,2,4 Trimethylbenzene ignition testing results and (b) Peak temperature rise.

far lower peak temperature rises as compared to the mode I events again allowing them to be easily distinguished in Figure 2.11b. The difference between the measured minimum AIT 476.5 ± 4.8°C and the literature (NFPA, 1991; USCG, 1999) value AIT of 500°C is significant in this case.

Figure 2.12a shows that for trans-decalin there is not a strong dependence on composition as seen for the TMB but rather a weak compositional dependence. However it is interesting that trans-decalin exhibits the widest variety of ignition modes in any of the fuels studied. The mode IV

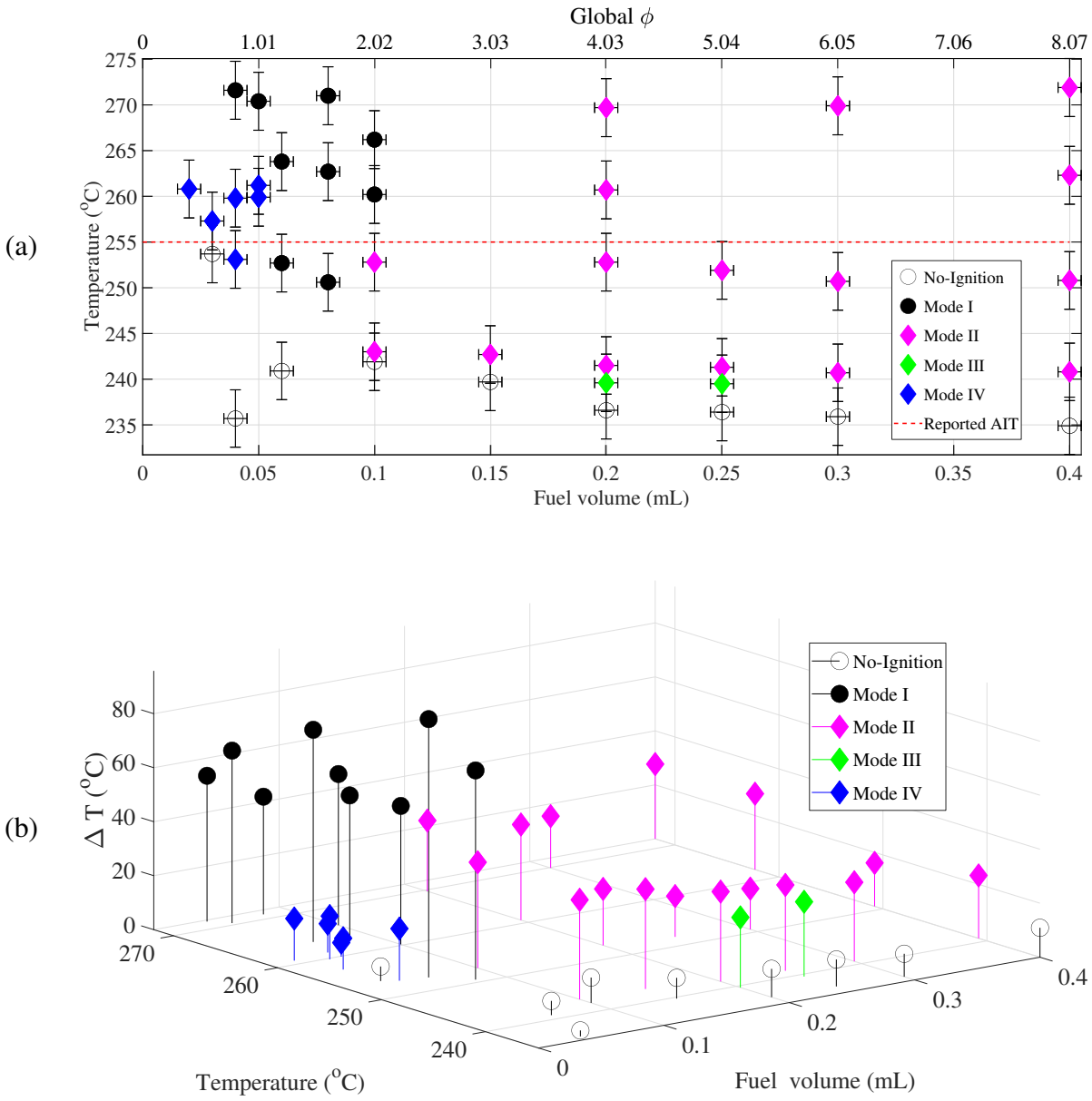

Figure 2.12: (a) Trans-decalin ignition testing results and (b) Peak temperature rise.

events are present near stoichiometric and lean conditions while both mode II and III are present in the rich regime. The distinction to be made between all of these modes can begin to be seen in Figure 2.12b where the temperature rise for mode IV events are much lower than other modes while the mode II and III are still significantly less than mode I. Further distinction is also made from luminosity observations and reaction timescales determined by the temperature traces as alluded to in Table 2.3. The minimum AIT determined in our tests is $T = 239.5 \pm 3.1$°C and the NFPA (1991) value is 255°C.

Figure 2.13a shows similar dependencies exist for Toluene as for TMB. Namely the sharp compositional dependence is evident here again with samples much more readily ignited near stoichiometry than in the extremely rich or lean regimes. The mode II events seen here are again only present in the rich regime as with the other simple fuels. Figure 2.13b illustrates the distinction between mode I and II events with lower temperature rises clearly evident for mode II events. There is a significant difference between the reported (NFPA, 1991; USCG, 1999) AIT value of 480°C and our experimental result of 508.2 ± 5.0°C.

2.3.4 Single-component fuels summary

The n-alkanes studied showed generally lower AITs than iso-cetane and the aromatics which is consistent with the connections made between chemical structure (branching, unsaturation) and AIT as laid out in Affens et al. (1961). The n-alkanes also generally exhibited lower ignition temperatures at more fuel rich conditions where mode III ignition events became dominant. Iso-Cetane also followed this trend but with mode II ignition becoming dominant at fuel rich conditions. The TMB and toluene showed an opposite trend in that the minimum AIT was generally observed at near stoichiometric or slightly lean conditions with increasingly great difficulty igniting at rich conditions. Additionally mode II ignition rapidly became dominant at even slightly rich conditions for both of these aromatics. The exception to these trends for the aromatic fuels was the trans-decalin which became more easily ignited at rich conditions with a far lower AIT around 240°C. In addition trans-decalin exhibited all four ignition modes with mode II and III both becoming dominant at rich conditions and mode IV ignition being observed only at lean conditions near the ignition threshold. The temperature rises measured were also far higher for the n-alkanes than iso-cetane or any of the aromatics.

2.3.5 Multi-component fuels

The multi-component fuels examined in this study were Jet A fuel standards (POSF-4658 and POSF-10325) and surrogate jet fuels from the literature (Aachen and JI). Some of the observed ignition behaviors of these fuels can be attributed to characteristics of their molecular components. As summarized in Table 2.1, these fuels are effectively entirely composed of alkane and aromatic compounds with the alkanes making up the bulk of the fuels which indicates that the alkane ignition behavior is expected to dominate.

POSF-4658 is a Jet A blend which has been examined extensively by a number of researchers; see Edwards (2017). Figure 2.14a shows the ignition results obtained in this study for this blend. Mode III and mode IV events are observed in the rich and lean regimes respectively which is similar to the behavior of the simple fuels. There is a good agreement between our experimental AIT of 229.0 ± 3.1°C and the accepted FAA (2018) Jet A AIT value of 232°C. This relatively low

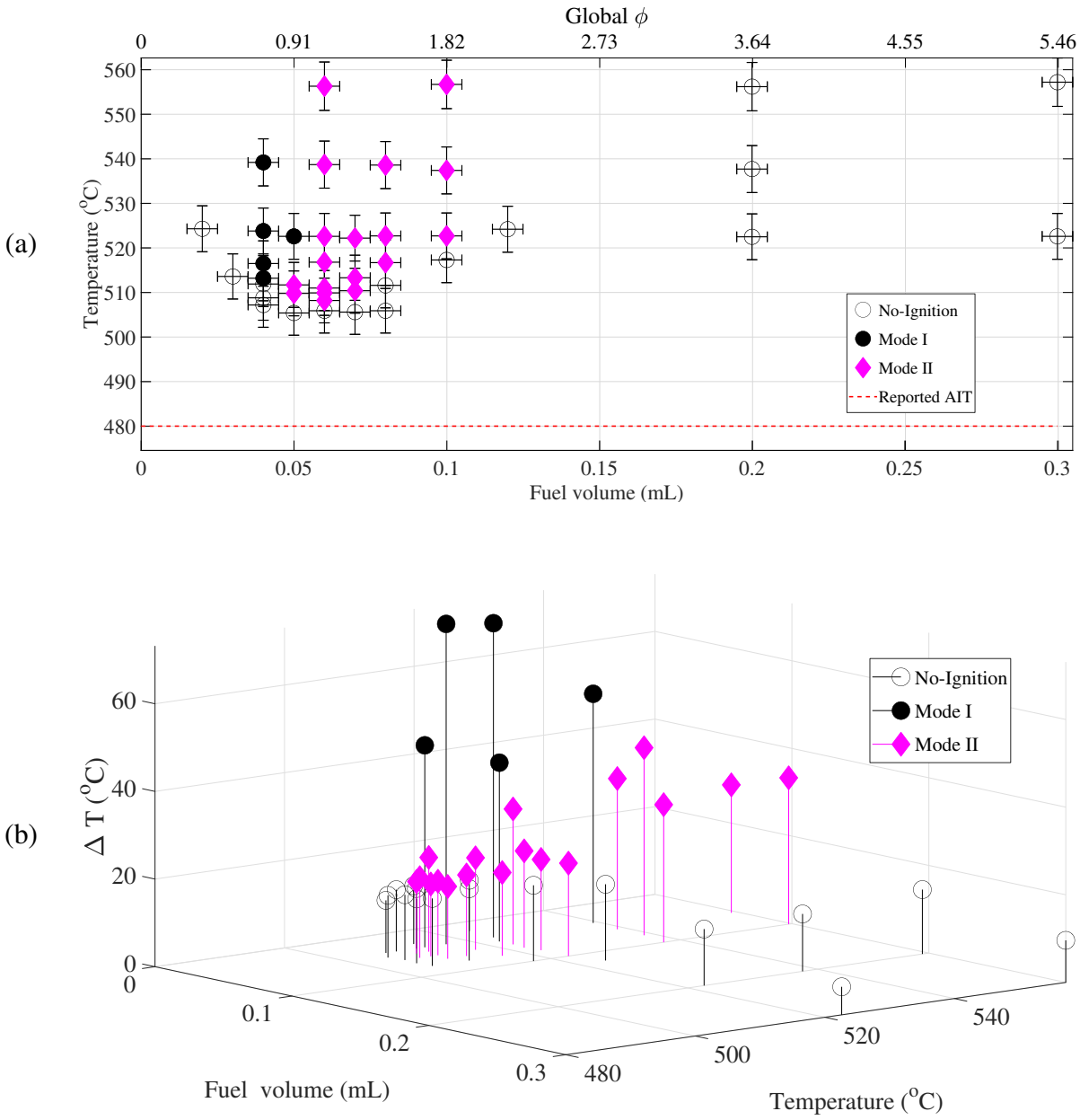

Figure 2.13: (a) Toluene ignition testing results and (b) Peak temperature rise.

AIT can likely be attributed to the alkane dominant composition of Jet A since alkanes generally exhibit AITs in this range while aromatic compounds tend to be much higher. Figure 2.14b shows temperature rises around 100°C while the mode III and IV events exhibit far lower temperature increases.

POSF-101325 shows substantially similar ignition behavior to POSF-4658, which is consistent with the modest differences in composition between the two fuel blends (Table 2.1). The POSF-10325

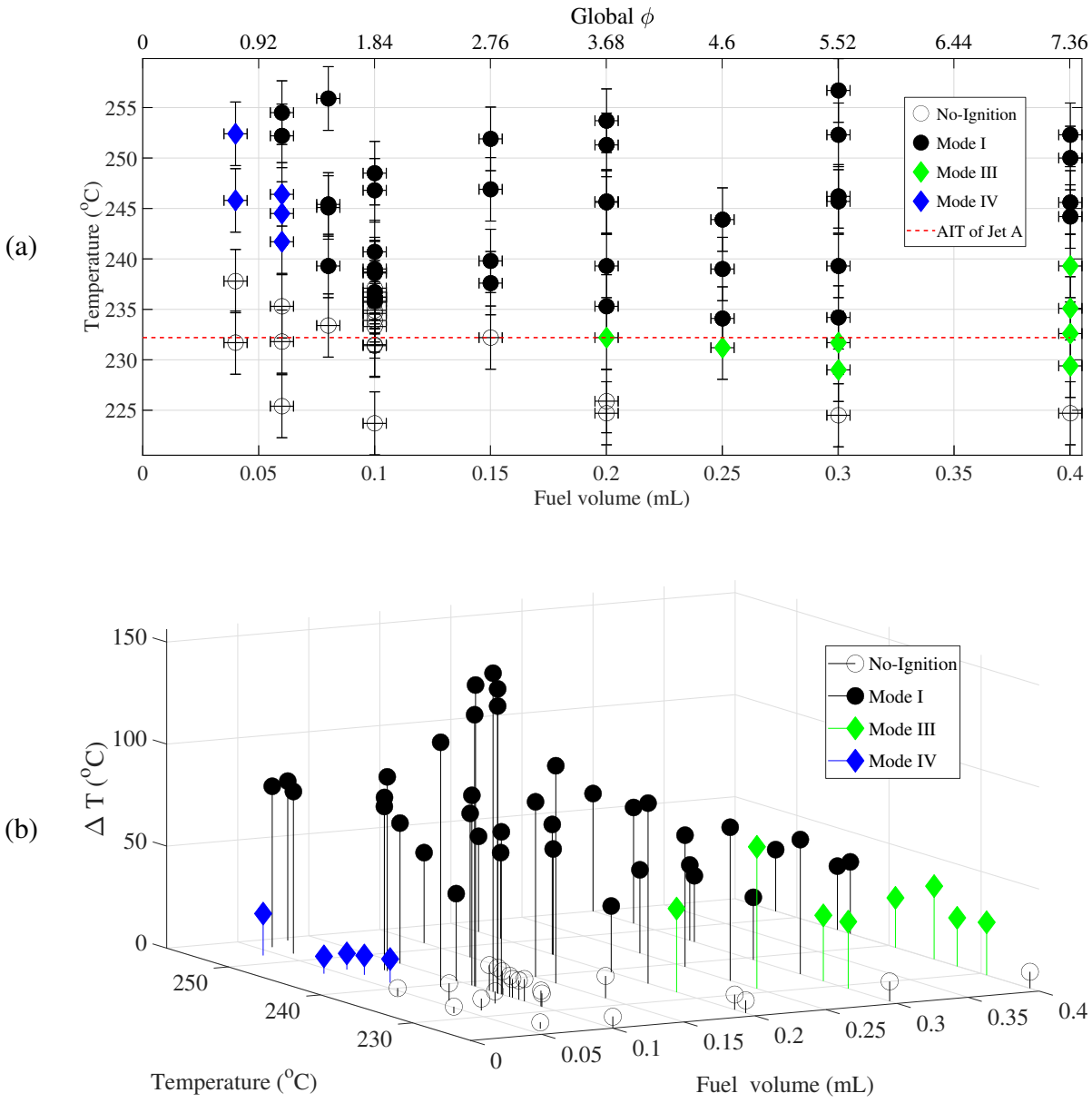

Figure 2.14: (a) POSF-4658 (Jet A) ignition testing results and (b) Peak temperature rise.

ignition data shown in Figure 2.15a is similar to Figure 2.14a but has a few minor differences. One of these differences is in the lean regime where the mode IV ignition occurs at slightly lower temperatures than for the POSF-4658. Similar to POSF-4658, the mode III events are seen in the rich regime and occur at higher temperatures for increasingly rich compositions while the minimum AIT levels off. Figure 2.15b shows that peak temperature rises for all ignition modes are similar to those seen for POSF-4658. The minimum AIT of 225.3 ± 3.1°C for POSF-4658 and agrees reasonably well with the accepted (FAA, 2018) Jet A AIT of 232°C.

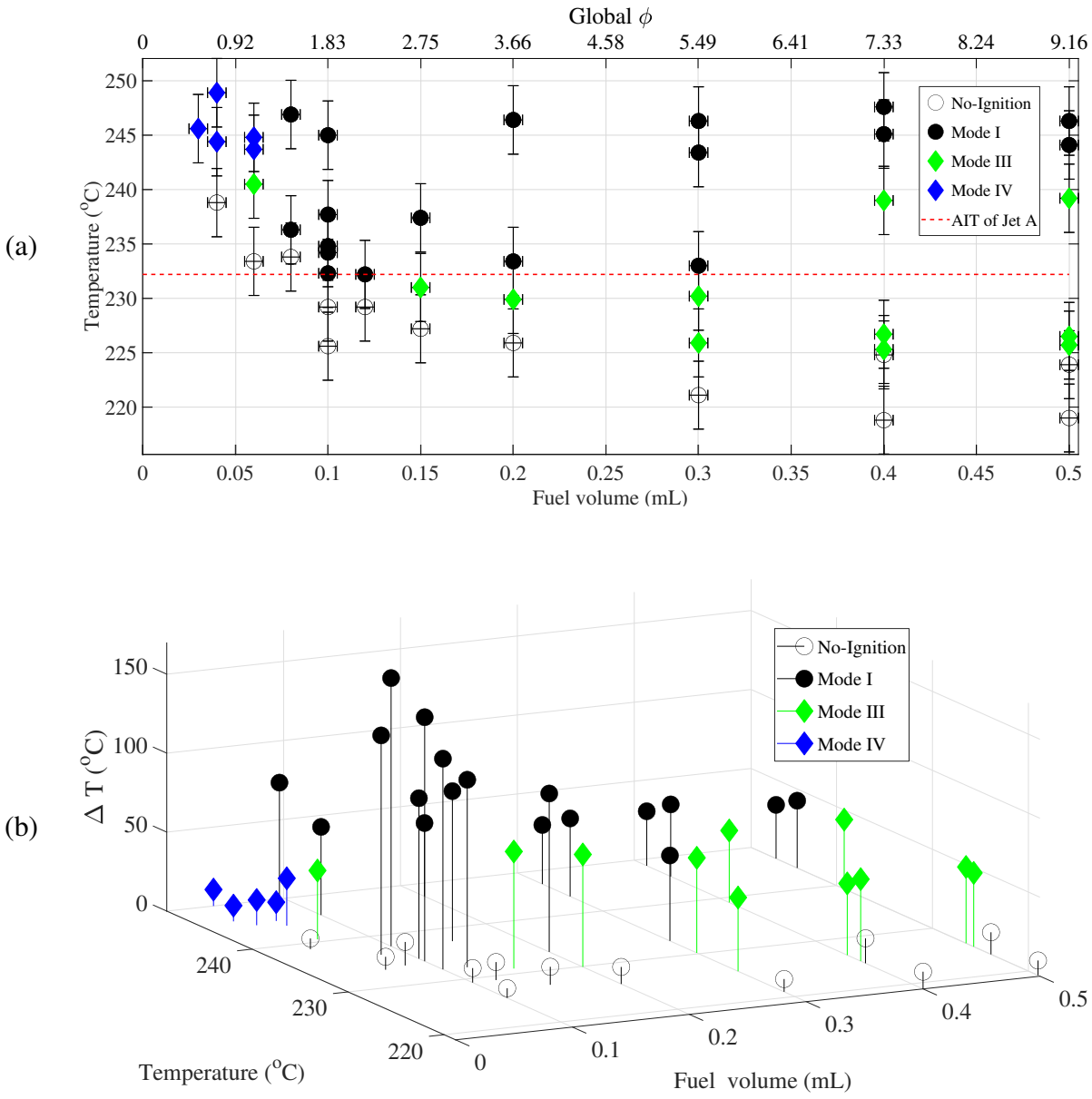

Figure 2.15: (a) POSF-10325 (Jet A) ignition testing results and (b) Peak temperature rise.

The Aachen surrogate is a simple two component blend which seems to capture the general trends from the Jet A batches while missing some details like mode IV events in the lean regime as seen in Figure 2.16a. Mode III events are generally well captured in the rich regime with this mode extending to higher temperatures for richer compositions as was seen for Jet A. The Aachen surrogate has a lower AIT value (219.0 ± 3.1°C) than the accepted (FAA, 2018) Jet A value of 232°C. Figure 2.16b shows that there is also some discrepancy in the peak temperature rise for both the mode I and III events as compared to those seen in both Figure 2.14b and Figure 2.15b.

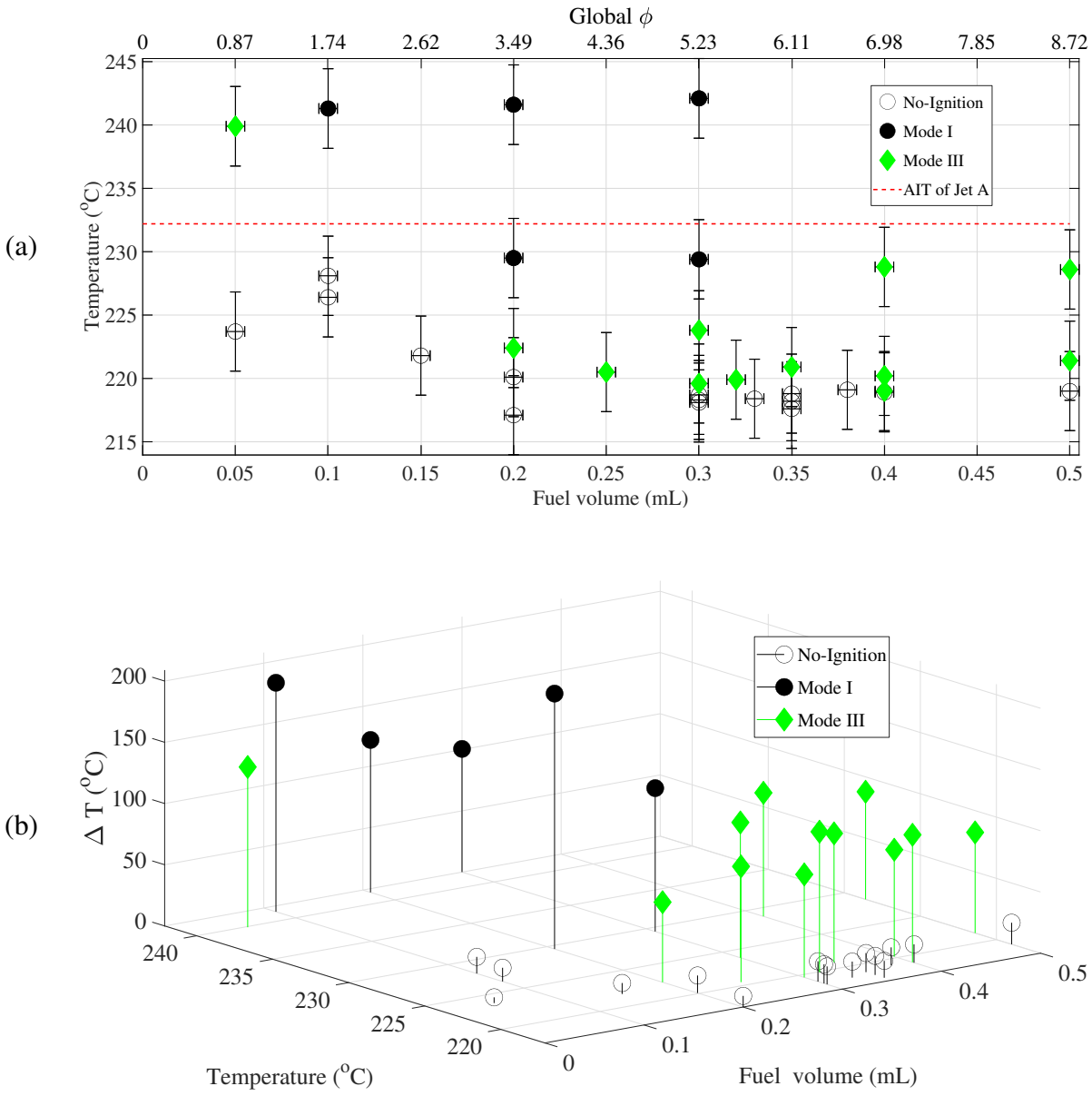

Figure 2.16: (a) Aachen surrogate ignition testing results and (b) Peak temperature rise.

The more complex JI surrogate consisting of 4 components does a much better job at reproducing the ignition behaviors found in the Jet A samples. Figure 2.17a shows the existence of mode IV events in the near stoichiometric regime along with the mode III events being maintained in the rich regime. However, these mode IV events occur at slightly richer compositions than observed for Jet A. Figure 2.17b shows another difference in that the temperature rises measured for JI are much lower than those seen in either of the Jet A samples as shown by Figure 2.14b and Figure 2.15b. The minimum AIT of 228.3 ± 3.1°C is also more consistent with the accepted (FAA, 2018) Jet A

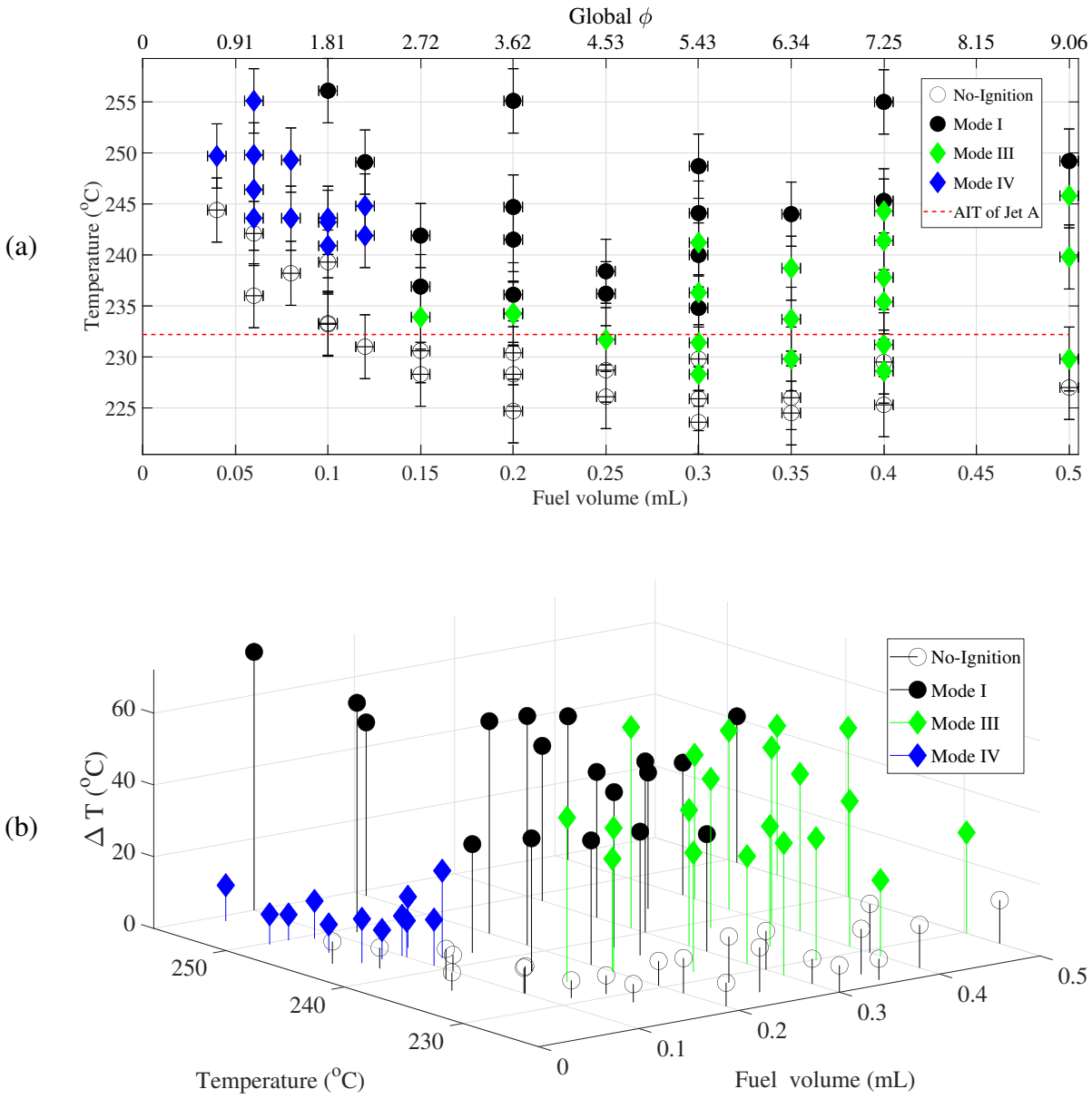

Figure 2.17: (a) JI surrogate ignition testing results and (b) Peak temperature rise.

AIT value of 232°C.

The global minimum AIT measured from each of the fuels as well as the corresponding test conditions are summarized in Table 2.4 and compared to some values reported in the literature. The differences between present results and literature values range from 1 to 7%, comparable to or larger than the estimated uncertainty of ±1%.

Table 2.4: Summary of measured minimum AIT values and corresponding test conditions.

		Measured			Literature
	Fuel	**Fuel Volume [mL]**	**Global ϕ**	**Minimum AIT [°C]**	**Reported AIT [°C]**
Alkanes	n-Hexane	0.10	1.56	235.3 ± 3.1	225[a] (236[b])
	n-Decane	0.30	5.12	204.3 ± 3.1	210[ab]
	n-Dodecane	0.30	5.24	202.2 ± 3.1	203[a]
	Isocetane	0.40	7.36	395.2 ± 4.1	-
Aromatics	1,2,4-Trimethylbenzene	0.05	0.94	476.5 ± 4.8	500[ab]
	Trans-decalin	0.25	5.04	239.5 ± 3.1	255[a]
	Toluene	0.06	1.09	508.2 ± 5.0	480[ab]
Multi component	POSF-4658	0.30	5.52	229.0 ± 3.1	232[c]
	POSF-10325	0.40	7.33	225.3 ± 3.1	232[c]
	Aachen Surrogate	0.40	6.98	219.0 ± 3.1	-
	JI Surrogate	0.30	5.43	228.3 ± 3.1	-

[a] NFPA (1991) ; [b] USCG (1999) ; [c] FAA (2018)

2.4 Conclusion

The low-temperature (< 600 K) and low pressure (≤ 1 atm) thermal ignition regime is important to industrial safety for commodity fuels but presents many challenges for combustion experimenters and modelers. This chapter examined the potential for using surrogate fuels with simple and well-controlled composition rather than samples of Jet A which can have wide variability in properties. As a first step in determining the applicability of surrogates for low temperature Jet A thermal ignition studies, we have examined the ignition behavior in the ASTM-E659 apparatus for two Jet A surrogates, their molecular components, and two standardized batches of Jet A. The origins of the ASTM-E659 method were examined along with various limitations and practical considerations associated with the empirical nature of the test.

Four distinct ignition modes were observed near the AIT threshold and were characterized using the limited diagnostic tools possible in the ASTM-E659 test. Experimental results were compared with reported minimum AIT numbers from literature sources with some data obtained showing significant discrepancies with reported AIT numbers. Branched alkanes and aromatics seemed to show more exotic ignition behavior, but overall showed higher AIT thresholds as compared to n-alkanes. The multi-component fuels exhibited ignition characteristics that appear to be dominated by n-alkanes which is consistent with the predominance of alkane components in these fuels. The two Jet A batches studied showed similar ignition behavior across the parameter space while both the Aachen and JI surrogates were able to reasonably replicate most of the Jet A ignition trends

with composition and temperature. The JI surrogate did however exhibit much better agreement for ignition thresholds in comparison with Jet A than the Aachen surrogate and was even able to reproduce the mode IV ignition events which the Aachen surrogate could not.

References

Affens, W. A., Johnson, J. E., & Carhart, H. W. (1961). Effect of chemical structure on spontaneous ignition of hydrocarbons. *Journal of Chemical & Engineering Data*, *6*(4), 613–619. https://doi.org/10.1021/je60011a041 (Cit. on pp. 27, 28, 46, 52)

Alekseev, V., Soloviova-Sokolova, J., Matveev, S., Chechet, I., Matveev, S., & Konnov, A. (2017). Laminar burning velocities of n -decane and binary kerosene surrogate mixture. *Fuel*, *187*, 429–434. https://doi.org/10.1016/j.fuel.2016.09.085 (Cit. on p. 30)

Bane, S., Ziegler, J., Boettcher, P., Coronel, S., & Shepherd, J. (2013). Experimental investigation of spark ignition energy in kerosene, hexane, and hydrogen. *Journal of Loss Prevention in the Process Industries*, *26*(2), 290–294. https://doi.org/10.1016/j.jlp.2011.03.007 (Cit. on p. 43)

Boettcher, P., Menon, S., Ventura, B., Blanquart, G., & Shepherd, J. (2013). Cyclic flame propagation in premixed combustion. *Journal of Fluid Mechanics*, *735*, 176–202. https://doi.org/10.1017/jfm.2013.495 (Cit. on p. 43)

Boettcher, P., Mével, R., Thomas, V., & Shepherd, J. (2012). The effect of heating rates on low temperature hexane air combustion. *Fuel*, *96*, 392–403. https://doi.org/10.1016/j.fuel.2011.12.044 (Cit. on pp. 29, 41, 43)

Bounaceur, R., Glaude, P.-A., Sirjean, B., Fournet, R., Montagne, P., Vierling, M., & Molière, M. (2016). Prediction of auto-ignition temperatures and delays for gas turbine applications. *Journal of Engineering for Gas Turbines and Power*, *138*(2), 021505. https://doi.org/10.1115/1.4031264 (Cit. on p. 28)

Caron, M., Goethals, M., De Smedt, G., Berghmans, J., Vliegen, S., Van't Oost, E., & van den Aarssen, A. (1999). Pressure dependence of the auto-ignition temperature of methane/air mixtures. *Journal of Hazardous Materials*, *65*(3), 233–244. https://doi.org/10.1016/S0304-3894(99)00004-7 (Cit. on p. 30)

Chen, X., Khani, E., & Chen, C. (2016). A unified jet fuel surrogate for droplet evaporation and ignition. *Fuel*, *182*, 284–291. https://doi.org/10.1016/j.fuel.2016.05.114 (Cit. on pp. 30–32)

Colwell, J. D., & Reza, A. (2005). Hot surface ignition of automotive and aviation fluids. *Fire Technology*, *41*(2), 105–123 (Cit. on p. 28).

Coronel, S., Lapointe, S., & Shepherd, J. (2019). Boundary layer ignition modeling, 10 (Cit. on pp. 28, 48).

Coronel, S., Melguizo-Gavilanes, J., Mével, R., & Shepherd, J. (2018). Experimental and numerical study on moving hot particle ignition. *Combustion and Flame*, *192*, 495–506. https://doi.org/10.1016/j.combustflame.2018.02.027 (Cit. on p. 43)

CRC. (1983). *Handbook of aviation fuel properties*. Coordinating Research Council. (Cit. on p. 26).

De Toni, A., Werler, M., Hartmann, R., Cancino, L., Schießl, R., Fikri, M., Schulz, C., Oliveira, A., Oliveira, E., & Rocha, M. (2017). Ignition delay times of Jet A-1 fuel: Measurements in a high-pressure shock tube and a rapid compression machine. *Proceedings of the Combustion Institute*, *36*(3), 3695–3703. https://doi.org/10.1016/j.proci.2016.07.024 (Cit. on p. 29)

Dean, A., Penyazkov, O., Sevruk, K., & Varatharajan, B. (2007). Autoignition of surrogate fuels at elevated temperatures and pressures. *Proceedings of the Combustion Institute*, *31*(2), 2481–2488. https://doi.org/10.1016/j.proci.2006.07.162 (Cit. on p. 31)

Dooley, S., Won, S. H., Chaos, M., Heyne, J., Ju, Y., Dryer, F. L., Kumar, K., Sung, C.-J., Wang, H., Oehlschlaeger, M. A., Santoro, R. J., & Litzinger, T. A. (2010). A jet fuel surrogate formulated by real fuel properties. *Combustion and Flame*, *157*(12), 2333–2339. https://doi.org/10.1016/j.combustflame.2010.07.001 (Cit. on p. 31)

Edwards, J. T. (2017). Reference jet fuels for combustion testing. *55th AIAA Aerospace Sciences Meeting*. https://doi.org/10.2514/6.2017-0146 (Cit. on pp. 30, 31, 52)

FAA. (2018, September 24). FAA AC 25.981-1D: Fuel tank ignition source prevention guidelines. (Cit. on pp. 52, 54–56, 58).

Farouk, T., Won, S. H., & Dryer, F. (2019). Investigating the role of preferential vaporization during sub-millimeter sized multi-component jet fuel surrogate droplet combustion (Cit. on p. 32).

Hattwig, M., & Steen, H. (2004). 3.1.6.2 Autoignition temperature (AIT). *Handbook of explosion prevention and protection* (pp. 301–304). Wiley-VCH Verlag GmbH & Co. KGaA. (Cit. on p. 27).

Hilado, C. J., & Clark, S. W. (1972). Discrepancies and correlations of reported autoignition temperatures. *Fire Technology*, *8*(3), 218–227. https://doi.org/10.1007/BF02590545 (Cit. on p. 27)

Honnet, S., Seshadri, K., Niemann, U., & Peters, N. (2009). A surrogate fuel for kerosene. *Proceedings of the Combustion Institute*, *32*(1), 485–492. https://doi.org/10.1016/j.proci.2008.06.218 (Cit. on pp. 31, 32)

International, A. (2005). ASTM-E659: Standard test method for autoignition temperature of liquid chemicals. (Cit. on pp. 26, 29, 41).

Jones, S., & Shepherd, J. E. (2020). Thermal ignition of n-hexane mixtures by vertical cylinders. *Proceedings of the 13th International Symposium on Hazards, Prevention and Mitigation of Industrial Explosions (ISHPMIE 2020)* (Cit. on pp. 28, 48).

Ju, Y. (2021). Understanding cool flames and warm flames. *Proceedings of the Combustion Institute*, *38*(1), 83–119. https://doi.org/10.1016/j.proci.2020.09.019 (Cit. on pp. 29, 30)

Kang, D., Kalaskar, V., Kim, D., Martz, J., Violi, A., & Boehman, A. (2016). Experimental study of autoignition characteristics of Jet-A surrogates and their validation in a motored engine and a constant-volume combustion chamber. *Fuel*, *184*, 565–580. https://doi.org/10.1016/j.fuel.2016.07.009 (Cit. on p. 30)

Kim, D., & Violi, A. (2018). Hydrocarbons for the next generation of jet fuel surrogates. *Fuel*, *228*, 438–444. https://doi.org/10.1016/j.fuel.2018.04.112 (Cit. on p. 30)

Liang, J., Wang, S., Hu, H., Zhang, S., Fan, B., & Cui, J. (2012). Shock tube study of kerosene ignition delay at high pressures. *Science China Physics, Mechanics and Astronomy*, *55*(6), 947–954. https://doi.org/10.1007/s11433-012-4723-8 (Cit. on p. 29)

Melguizo-Gavilanes, J., Boeck, S., Mevel, R., & Shepherd, J. (2017a). Hot surface ignition of stoichiometric hydrogen-air mixtures. *J. Hydrogen Energ.*, *42*(11), 7393–7403. https://doi.org/10.1016/j.ijhydene.2016.05.095. (Cit. on p. 28)

Melguizo-Gavilanes, J., Coronel, S., Mével, R., & Shepherd, J. (2017b). Dynamics of ignition of stoichiometric hydrogen-air mixtures by moving heated particles [Preprint, published version available at http://dx.doi.org/10.1016/j.ijhydene.2016.05.206.]. *International Journal of Hydrogen Energy*, *42*(11), 7380–7392 (Cit. on p. 28).

Melguizo-Gavilanes, J., & E.Shepherd, J. (2017). *Effect of Orientation on the Ignition of Stoichiometric Ethylene Mixtures by Stationary Hot Surfaces* [Paper No. 981, 26th International Colloquium on the Dynamics of Explosions and Reactive Systems, Boston, MA, 30 July – 4 August 2017]. (Cit. on p. 28).

Mével, R., Chatelain, K., Boettcher, P., Dayma, G., & Shepherd, J. (2014). Low temperature oxidation of n-hexane in a flow reactor. *Fuel*, *126*, 282–293. https://doi.org/10.1016/j.fuel.2014.02.072 (Cit. on p. 43)

Mével, R., Rostand, F., Lemarié, D., Breyton, L., & Shepherd, J. (2019). Oxidation of n-hexane in the vicinity of the auto-ignition temperature. *Fuel*, *236*, 373–381. https://doi.org/10.1016/j.fuel.2018.09.009 (Cit. on pp. 30, 31, 43)

Mueller, C. J., Cannella, W. J., Bruno, T. J., Bunting, B., Dettman, H. D., Franz, J. A., Huber, M. L., Natarajan, M., Pitz, W. J., Ratcliff, M. A., & Wright, K. (2012). Methodology for formulating diesel surrogate fuels with accurate compositional, ignition-quality, and volatility characteristics. *Energy & Fuels*, *26*(6), 3284–3303. https://doi.org/10.1021/ef300303e (Cit. on p. 30)

NFPA. (1991). *Fire protection guide to hazardous materials.* (10th ed.). National Fire Protection Association. (Cit. on pp. 26, 44, 45, 50–52, 58).

Robinson, C., & Smith, D. (1984). The auto-ignition temperature of methane. *Journal of Hazardous Materials*, *8*(3), 199–203. https://doi.org/10.1016/0304-3894(84)85001-3 (Cit. on p. 26)

Roth, D., Häber, T., & Bockhorn, H. (2017). Experimental and numerical study on the ignition of fuel/air mixtures at laser heated silicon nitride particles. *Proceedings of the Combustion Institute*, *36*(1), 1475–1484. https://doi.org/10.1016/j.proci.2016.05.054 (Cit. on p. 28)

Sax, N. I. (1957). *Dangerous properties of industrial materials* (1st ed.). Reinhold Publishing Corporation. (Cit. on pp. 26, 30).

Setchkin, N. (1954). Self-ignition temperatures of combustible liquids. *Journal of Research of the National Bureau of Standards*, *53*(1), 49. https://doi.org/10.6028/jres.053.007 (Cit. on pp. 26, 27)

Smyth, K. C. (1990). *Short-duration autoignition temperature measurements for hydrocarbon fuels* (NIST IR 4469). National Institute of Standards and Technology. Gaithersburg, MD. https://doi.org/10.6028/NIST.IR.4469. (Cit. on p. 28)

Stachler, R., Heyne, J., Stouffer, S., & Miller, J. (2020). Lean Blowoff in a Toroidal Jet-Stirred Reactor: Implications for Alternative Fuel Approval and Potential Mechanisms for Autoignition and Extinction. *Energy & Fuels*, *34*(5), 6306–6316. https://doi.org/10.1021/acs.energyfuels.9b01644 (Cit. on p. 30)

Strasser, A., Waters, N. C., & Kuchta, J. M. (1971, November). *Ignition of Aircraft Fluids by Hot Surfaces under Dynamic Conditions* (AFAPL-TR-71-86). Bureau of Mines. (Cit. on p. 28) PMSRC Report No. 4162.

Sund, S. M. (2019). *Thermal ignition of surrogate jet fuels* (Master's Thesis in Process Technology). University of South-Eastern Norway. (Cit. on pp. 37, 38, 46).

Tang, H.-C., Zhang, C.-H., Li, P., Wang, L.-D., Ye, B., & Li, X.-Y. (2012). Experimental study of autoignition characteristics of kerosene. *Acta Physico-Chimica Sinica*, *28*(4), 787–791 (Cit. on p. 29).

Tsai, F.-Y., Chen, C.-C., & Liaw, H.-J. (2012). A model for predicting the auto-ignition temperature using quantitative structure property relationship approach. *Procedia Engineering*, *45*, 512–517. https://doi.org/10.1016/j.proeng.2012.08.195 (Cit. on p. 28)

USCG. (1999). Chemical hazard response information system (CHRIS). *United States Coast Guard* (Cit. on pp. 26, 30, 45, 50, 52, 58).

Valco, D. J., Min, K., Oldani, A., Edwards, T., & Lee, T. (2017). Low temperature autoignition of conventional jet fuels and surrogate jet fuels with targeted properties in a rapid compression machine. *Proceedings of the Combustion Institute*, *36*(3), 3687–3694. https://doi.org/10.1016/j.proci.2016.05.032 (Cit. on pp. 29, 31)

Vasu, S. S., Davidson, D. F., & Hanson, R. K. (2008). Jet fuel ignition delay times: Shock tube experiments over wide conditions and surrogate model predictions. *Combustion and Flame*, *152*(1-2), 125–143. https://doi.org/10.1016/j.combustflame.2007.06.019 (Cit. on p. 29)

Velagala, S., Raval, P., Chowhan, S. C. S., Esmaeelzade, G., Beyer, M., & Grosshans, H. (2020). Simulation of the flow of an explosive atmosphere exposed to a hot hemisphere. *Proceedings of the 13th International Symposium on Hazards, Prevention and Mitigation of Industrial Explosions (ISHPMIE 2020)*. https://doi.org/10.7795/810.20200724 (Cit. on p. 29)

Wang, H., & Oehlschlaeger, M. A. (2012). Autoignition studies of conventional and Fischer–Tropsch jet fuels. *Fuel*, *98*, 249–258. https://doi.org/10.1016/j.fuel.2012.03.041 (Cit. on pp. 29, 31)

Zabetakis, M. G. (1965). *Flammability characteristics of combustible gases and vapors* (BM–BULL-627, 7328370). Bureau of Mines. Washington D.C. https://doi.org/10.2172/7328370. (Cit. on pp. 26, 30)

Zakel, S., Brandes, E., & Schröder, V. (2019). Reliable safety characteristics of flammable gases and liquids – The database CHEMSAFE. *Journal of Loss Prevention in the Process Industries*, *62*, 103914. https://doi.org/10.1016/j.jlp.2019.07.002 (Cit. on p. 26)

Zhukov, V. P., Sechenov, V. A., & Starikovskiy, A. Y. (2014). Autoignition of kerosene (Jet-A)/air mixtures behind reflected shock waves. *Fuel*, *126*, 169–176. https://doi.org/10.1016/j.fuel.2014.02.036 (Cit. on p. 29)

Chapter 3

LOW PRESSURE AND NITROGEN DILUTION EXPERIMENTS

3.1 Introduction

As introduced in Chapter 1 there is an important distinction to be made between ignition by heated vessels and heated surfaces. Chapter 2 involved the use of a heated vessel and hot air atmosphere for ignition testing. This chapter instead explores a hot surface and cold premixed flammable atmosphere ignition test for which mixture effects have not been thoroughly evaluated in the literature. A thorough understanding of the effects of pressure and nitrogen dilution on thermal ignition are of particular interest to the aviation sector and are thus the focus of these experiments.

Extensive testing of various fuels has already been presented in Chapter 1 and in (Jones, 2020) for the experimental facility used in this chapter. In the present study we have again focused on n-hexane, using this as a surrogate for aviation kerosene. Many other fuels are of interest in evaluating potential industrial hazards. For this study, we have also performed a limited number of ignition experiments with hydrogen and ethylene to enable comparisons with data from experiments with smaller heated surface area (Boeck et al., 2017) as well as the typical autoignition temperature (AIT) criteria (International, 2005).

3.1.1 Motivation

Sub-atmospheric mixtures and mixtures with reduced oxygen concentration are of particular importance for aircraft fuel tank flammability reduction (FAA, 2017). Aircraft fuel tanks are vented to the atmosphere and pressures can be as low as 17 kPa (0.17 atm) at cruise altitudes of up to 13 km (43 kft). In order to minimize fuel tank flammability, nitrogen-enriching systems have been developed (Moravec et al., 2006), tested (Cavage & Summer, 2008) and are now extensively used in commercial aircraft. These systems are designed to reduce the oxygen concentration below the limiting value (approximately 12% by volume at ground level) for flammability. It is therefore of interest to understand how thermal ignition events are affected by variations in pressure and oxygen concentration. Summer (2004) used high-energy spark ignition and hot ($\approx$ 1000 K) surfaces to establish limiting oxygen concentrations at sub-atmospheric pressures. However, the hot surface tests used a fixed geometry and surface temperature and did not quantify the ignition threshold dependence on pressure and oxygen concentration.

The effect of pressure on thermal ignition thresholds has primarily been studied only at elevated pressures, for example Hirsch and Brandes (2005). Zabetakis (1965) report that flammability

limits of alkane/air mixtures have a negligible dependence on pressure down to about 200 Torr. Brandes et al. (2017a, 2017b) studied ignition with elevated oxygen concentration (21-100%) and alternative oxidizers (N_2O) at atmospheric pressure. Those experiments involved internal natural convection (heated vessels) rather than external convection (heated surfaces). Ignition by external natural convection at reduced pressure was studied by Ono et al. (1976) who examined thermal ignition by small vertical hot plates (1.5 - 9 cm^2) at initial pressures between 0.13 and 1.0 atm. Ono et al. (1976) developed a semi-empirical correlation between ignition temperature, surface height, and pressure for laminar natural convection. With the exception of Summer (2004), two factor combinations of low pressure and oxygen content have not been systematically examined in previous studies.

The present study is an external natural convection experiment where the ignition source is a vertical cylinder. These experiments build upon the work performed by Jones and Shepherd (2021) who investigated thermal ignition by vertical cylinders and the effects of both length and surface area on ignition. Jones' study explored ignition source surface areas ranging from 25 to 200 cm^2 for stoichiometric n-hexane/air mixtures as well as Jet A samples and surrogates. Jones and Shepherd (2021) demonstrated that contrary to previous attempts at correlating thermal ignition thresholds with area, in external natural convection there is only a modest decrease in the ignition threshold with increased surface area. Therefore, the present study used only the largest cylinder from Jones and Shepherd (2021), labelled 200A (length = 25.4 cm (10 in), diameter = 2.54 cm (1 in), surface area = 202.58 cm^2 (31.4 in^2)) using stoichiometric hydrogen/air, ethylene/air mixtures, and n-hexane/oxygen/nitrogen mixtures at reduced pressures.

3.2 40L Vessel Experimental Methodology

The experimental setup is identical to that described by Jones and Shepherd (2021) and in more detail by Jones (2020). The ignition source, cylinder 200A, is a vertical cylinder constructed from 304 stainless steel tubing and heated resistively using a Magna Power XR5-600 computer controlled DC power supply. A natural convection flow develops around the exterior of the cylinder surface during the heating process. The experiments are conducted inside a 40 L cylindrical combustion vessel with a 30.4 cm inner diameter and a height of 66.0 cm. The cylinder is held in place in the center of the combustion vessel with a copper support structure as shown in Figure 3.1. The support structure both mechanically stabilizes the heated surface and provides a path for electrical current to flow from. The cylinder temperature is monitored using a custom built two-color (or two-wavelength) pyrometer as well as a 24 gauge K-type thermocouple welded to the center of the cylinder. The thermocouple is not present for all tests as prolonged exposure to high temperatures tended to rapidly oxidize the wires which degraded the measurement accuracy and weakened the spot weld which eventually led the thermocouple to become disconnected from the surface during

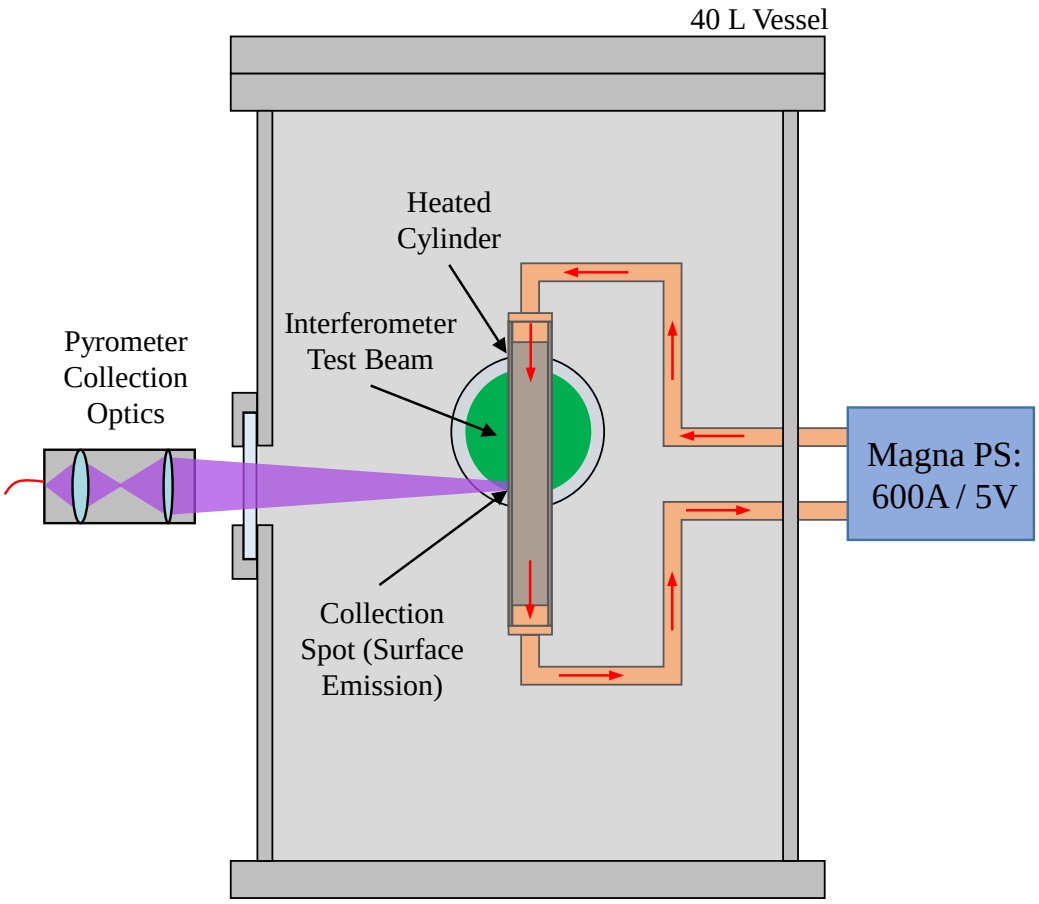

Figure 3.1: Schematic of heated cylinder setup.

testing. For this reason, the pyrometer is found to be more reliable and is used in a feedback control loop with the power supply to maintain a set surface temperature. This technique is discussed in more detail in Section 3.3.2. This heating system is operated remotely via LabVIEW and the control loop is only initiated after an initial ramping period where the current supplied is fixed. The ends of the cylinder are water cooled using a NESLAB system III heat exchanger whose flow rate is adjusted using a ball valve and volumetric flow controller. This system extracts the heat that otherwise would be conducted into the support structure during testing. This is necessary so hot spots are not formed on the support structure resulting in additional buoyant plumes interfering with the desired laminar flow field. This is also important for preserving axisymmetry in the flow which is crucial in post processing interferograms for quantitative field data as described in Section 3.3.3. A modified Mach-Zehnder interferometer in conjunction with a Phantom V7100 high speed camera was used to visualize ignition and make some quantitative measurements of the gas surrounding the hot cylinder for nonreactive mixtures (100% N_2). Details of this technique are found in Jones and Shepherd (2020) and a brief summary of this technique is found in Section 3.3.3. Additional color

visualization was also performed using the slow motion video setting on an iPhone 6 camera which can achieve a frame rate of 240 fps. This was sufficient to observe a few frames of the ignition and flame propagation and was a qualitative supplement to the higher sensitivity and higher speed interferometer imaging.

The method of partial pressures was used to control the gas conditions for each shot. The vessel was evacuated to less than 0.1 Torr before the start of the filling process. The fuel was then added using either a syringe in the case of liquid fuels or a gas supply system for gaseous fuels. Nitrogen and oxygen were then added independently in appropriate amounts to make the desired fuel/air mixture. A capacitive pressure gauge (MKS model 121A-01000B) with an accuracy of 0.1 Torr is used to monitor the pressure during filling. After the vessel was filled, a fan mixer was turned on for three minutes to promote mixing of the gases and then turned off for three minutes to allow the gases to settle and produce a quiescent mixture at the start of each test. The test time was limited to 300 s in order to prevent recirculation of the gas through the heated boundary layer. At the end of the test time if there had been no ignition, then the test was ended manually and was recorded as a non-ignition result. In the cases where ignition occurred, the data acquisition system was triggered by a thermally-protected, piezoresistive pressure transducer (Endevco 8530B-200) which was used to record pressure rise during the test. The magnitude of the pressure rise and the appearance of a flame in the interferometer imaging were used to determine if ignition took place.

Ignition data were analyzed statistically by the logistic method, assigning to each shot a binary outcome variable of 0 or 1, representing a non-ignition and ignition result respectively. Details of the logistic approach can be found in Bane et al. (2011) and Jones (2020). Outcome data paired with the surface temperature (T_w) of each test demonstrate that there are both ignition and non-ignition cases at a given temperature near the ignition threshold. This overlap can be attributed to intrinsic uncertainty related to the ignition process as well as typical small experimental parameter (composition, temperature, heating ramp profile, etc.) variability for tests nominally at the same initial conditions. The temperature corresponding to an ignition probability of 50% ($\mathcal{P}_{ign}$=0.5) is reported as the ignition temperature (T_{ign}).

3.3 Surface Temperature Measurements

3.3.1 Thermocouples

Thermocouples were used during ignition testing and troubleshooting efforts as a comparison with the pyrometer measurements. The principles of thermocouple measurement are summarized well in Quinn (1990). A thermocouple consists of two dissimilar metal alloys forming an electrical junction. This junction produces a voltage that is dependent on the temperature at the junction as described by the Seebeck effect. The thermocouples used here were 24 gauge type K wire and

constructed in the same way as described in Jones (2020). The thermocouples were welded to the surface of the cylinder using a capacitance welder (DCC Corporation HotSpot I). It was found that the quality of this weld can have a significant impact on the measured surface temperature. If poor thermal contact was achieved then significant contact resistance can cause a spuriously low temperature reading. However welding is necessary since alternative joining methods like thermally conductive epoxies, adhesives, and solder cannot withstand the temperatures of interest for this ignition testing. An Analog Devices 5B37 Isolated Thermocouple Input unit was also used in each thermocouple line to protect the data acquisition system from potential damage by the large currents present in the heating system. Typically only one of these thermocouple lines was used during ignition testing.

The principal difficulties in using these thermocouple measurements are twofold. First the presence of a thermocouple weld bead on an otherwise uniformly smooth cylinder can potentially cause early onset of ignition by either forming a localized hot spot or by "tripping" the flow into the turbulent regime leading to an increased thickness of the thermal layer. This was not a significant issue for these test in particular,however it is still an important consideration for similar experiments.

The second difficulty arises from the particular configuration of the heating system. The large DC currents used as the source of heating in this experiment can induce a small voltage difference at the thermocouple weld which must be accounted for. The current coupling can be seen in the measurement signal when current is turned off where a sharp step in the signal is typically observed. Jones (2020) proposes a method for correcting for this current coupling effect through a linear calibration as shown in Equation (3.1):

$$T_{corrected} = T_{raw} + \Delta T \,, \tag{3.1}$$

where $\Delta T = c_1 I + c_2$ is the induced temperature difference determined by calibration with ΔT values obtained for six discrete current inputs. This approach is reasonable, however the calibration corrected signal still produces a spike during the transient current shutoff period. c_2 must also be sufficiently small so the raw and corrected signals agree with no current applied. The degree of current coupling also depends on minute details of the weld such as the quality of the electrical contact of the weld and wire orientation. As a consequence such a calibration would need to be repeated routinely as the weld ages and the wires bend through the course of ignition testing. Instead here a two point calibration is used for each shot independently. Firstly it is clear that $T_{corrected} = T_{raw}$ at the initial temperature during the test, where $I = 0$, so $\Delta T(I = 0) = 0$. The second point is obtained at the end of the ignition test when current ($I_{pre-shutoff}$) is shut off. The sharp jump in the thermocouple signal during the shutoff period provides the temperature

difference. Therefore $c_1 = \frac{\Delta T(I_{pre-shutoff})}{I_{pre-shutoff}}$. By doing the calibration for each shot independently in this way, variations due to the small changes in weld features over the course of ignition testing can be eliminated. Nevertheless this approach still only works when there is good thermal contact between the weld and surface of interest so over the course of many heating cycles the thermocouple weld must inevitably be remade.

These are referred to as aging effects and are the result of oxidation and differential thermal expansion. Oxidation of the individual wires at high temperatures degrades the quality of the measurement due to the change in thermometric properties of the wires that are integral to accurate conversion of the voltage measurements to temperatures using standard conversion tables. Additionally thermal cycling of the surface can cause the weld to develop microcracks which weaken the connection over time due to differential thermal expansion between the wire and surface materials. Conductive losses to the thermocouple wires can also decrease the temperature of the surface under measurement leading to nonuniformities that are mainly significant for applications involving objects with low thermal mass and/or requiring large gauge thermocouple wires.

3.3.2 Two-Color Pyrometry

Pyrometery is an attractive technique for temperature measurement for many reasons. For this application the primary benefits are (1) the elimination of any flow disturbances introduced by spot welding a thermocouple wire to an otherwise uniformly smooth cylinder surface and (2) independence of the measurement from surface currents induced by the heating system. Additional benefits of this technique are that the achievable sampling rate of this technique is also much faster than the thermal response time of any reasonably sized thermocouple wires. Rates up to 100 KHz were found to be possible with the pyrometer described here. Typically temperatures of at least 700 - 800 K are required for this approach to be useful since at lower temperatures the signal to noise ratio is small. This is a consequence of the inverse exponential dependence of radiative emission intensity on surface temperature for a given wavelength which is illustrated by Equation (3.9) and Figure 3.2 in the following section. This is one main drawback of this technique for use in lower temperature applications. Other difficulties include optical alignment sensitivities and sensitivity to variations in surface emissivty with wavelength and temperature leading to difficulties in calibration. To obtain a reliable and comparable set of temperature measurements both the thermocouple and the pyrometer were each used during most ignition tests.

3.3.2.1 Theory

The theory and derivation of Planck's law presented here can be found in many heat transfer textbooks or chapters covering radiative heat transfer. The presentation here is adapted from

(Michalski & Michalski, 2001) and (Coronel, 2016).

The radiant intensity of a body L is the heat flux per unit area emitted from the surface that is reabsorbed by the surface itself. This can be expressed as the ratio of heat flux $d\Phi$ emitted from an infinitesimal element of the surface dA as in Equation (3.2).

$$L = \frac{d\Phi}{dA} \tag{3.2}$$

The spectral dependence of the radiant intensity can be determined by taking the intensity produced by an infinitesimal element $d\lambda$ of the full wavelength spectrum. The spectral radiant intensity L_λ is thereby obtained in Equation (3.3).

$$L_\lambda = \frac{dW}{d\lambda} \tag{3.3}$$

Planck's law gives the spectral *radiance* of a blackbody as a function of temperature in Equation (3.4).

$$L_{\lambda,b}(T) = \frac{c_1}{\lambda^5 \left(e^{c_2/\lambda T} - 1\right)} \tag{3.4}$$

with

$$c_1 = 2\pi hc^2 \quad \text{and} \quad c_2 = hc/k_B\,. \tag{3.5}$$

Here $L_{\lambda b}(T)$ is the spectral radiant intensity (typical units of $\frac{\mathrm{W}}{\mathrm{sr\ m^2}\mu\mathrm{m}}$, c_1 and c_2 are the first and second radiation constants given by Equation (3.5), h is Planck's constant, c is the speed of light in a vacuum, and k_B is Boltzmann's constant. Integrating Equation (3.4) over the unit sphere or equivalently multiplying by the total solid angle of 4π sr gives the total spectral *irradiance* $E_{\lambda,b}(T)$ of a blackbody as in Equation (3.6):

$$E_{\lambda,b}(T) = \frac{C_1}{\lambda^5 \left(e^{c_2/\lambda T} - 1\right)}\,. \tag{3.6}$$

Here C_1 now includes the constant factor of 4π so $C_1 = 8\pi hc^2$. The integration eliminates the sterradian units so $E_{\lambda,b}(T)$ simply has units of $\frac{\mathrm{W}}{\mathrm{m^2}\mu\mathrm{m}}$. The spectral irradiance is plotted for a range of temperatures in Figure 3.2. The maximum irradiance shifts to lower wavelengths as the temperture is increased and for the temperatures of interest for ignition the maximum occurs in the near to medium infrared (IR) between approximately $1 - 4\ \mu$ m. These are therefore the

targeted wavelengths for the two color pyrometer measurements since the signal to noise ratio will be maximized.

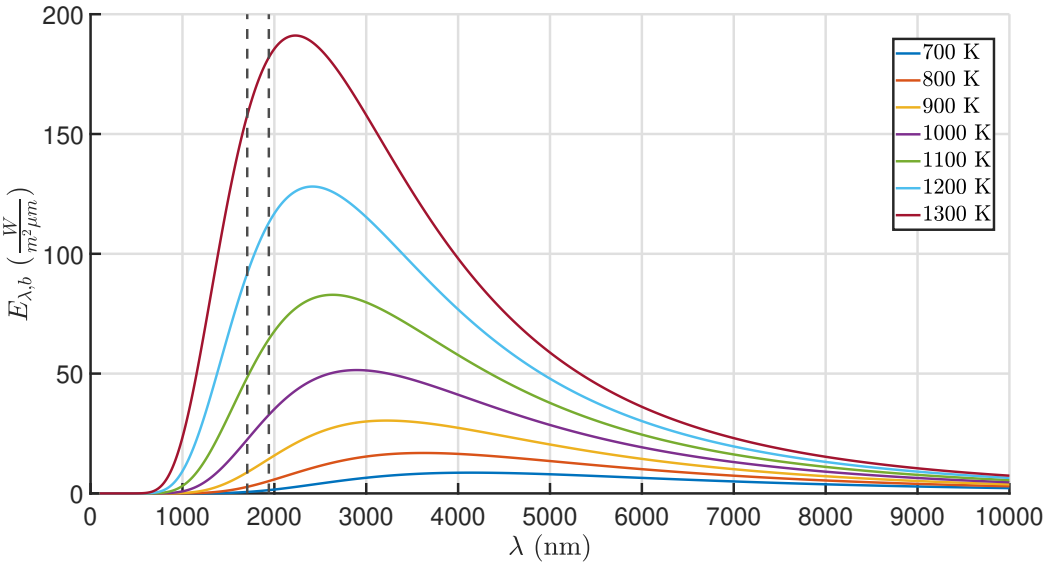

Figure 3.2: Spectral irradiance of blackbody at various temperatures. The dotted lines show the center wavelengths of the filters used for the two color pyrometer used in this work.

For non-ideal radiating bodies a spectral emissivity is introduced ϵ_λ such that $E_\lambda(T) = \epsilon_\lambda E_{\lambda,b}(T)$. Further simplification can be implemented by using the Wien approximation such that our new equation is Equation (3.7). This is valid since in the IR spectrum $\lambda T \ll c_2$. The errors in making this approximation are typically much less than 1% for the range of wavelengths and temperatures of importance here and in general for radiation pyrometry (Michalski & Michalski, 2001).

$$E_\lambda(T) \approx \epsilon_\lambda \frac{C_1}{\lambda^5 \left(e^{c_2/\lambda T}\right)} \tag{3.7}$$

Integration of $E_\lambda(T)$ over a region center on λ as in Equation (3.8) yields the total intensity I of the radiation in that region. The entire spectrum ($0 \leq \lambda \leq \infty$) yields Equation (3.8)

$$I(T) = \int_{\lambda-\Delta\lambda/2}^{\lambda+\Delta\lambda/2} \epsilon_\lambda \frac{C_1}{\lambda^5 \left(e^{c_2/\lambda T}\right)} d\lambda \,. \tag{3.8}$$

If the integration region $\Delta\lambda$ is small (e.g. for a narrow bandpass filter) then Equation (3.8) can be approximated as Equation (3.9)

$$I(T) = \epsilon_\lambda \frac{C_1}{\lambda^5} \exp(-c_2/\lambda T)\Delta\lambda \,. \tag{3.9}$$

Applying Equation (3.9) to two distinct wavelength regions about λ_1 and λ_2 and taking the ratio of intensities I_1/I_2 yields Equation (3.10)

$$\frac{I_1}{I_2} = \frac{\epsilon_{\lambda_1}}{\epsilon_{\lambda_2}} \frac{\lambda_2^5}{\lambda_1^5} \frac{\Delta\lambda_1}{\Delta\lambda_2} \exp\left(\frac{c_2}{T\left(\frac{1}{\lambda_1} - \frac{1}{\lambda_2}\right)} \right). \tag{3.10}$$

Finally taking the natural logarithm of Equation (3.10) yields an equation of the form

$$\ln\left(\frac{I_1}{I_2}\right) = A/T + B \tag{3.11}$$

with

$$A = \frac{c_2}{\left(\frac{1}{\lambda_1} - \frac{1}{\lambda_2}\right)} \quad \text{and} \quad B = \ln\left(\frac{\epsilon_{\lambda_1}}{\epsilon_{\lambda_2}} \frac{\lambda_2^5}{\lambda_1^5} \frac{\Delta\lambda_1}{\Delta\lambda_2} \right). \tag{3.12}$$

Equation (3.11) is the theoretical basis which underpins the use of two color pyrometry for temperature measurement. It relates the surface temperature of a body T to the intensity ratio of two emitted light at two wavelengths. This intensity ratio can be measured using two photodetectors and a calibration of this measured ratio with a known temperature source will yield values for A and B.

Inspecting Equation (3.12) we find that all that remains in A are known constants c_2, λ_1, and λ_2. B contains also mostly known constants λ_1, λ_2, $\Delta\lambda_1$, and $\Delta\lambda_2$ however $\frac{\epsilon_{\lambda_1}}{\epsilon_{\lambda_2}}$ is unknown a priori. If the surface under measurement is assumed to be a gray body, e.g. emissivity is independent of wavelength, then this ratio is just unity and B is a constant. The gray body assumption need only to be valid for the wavelengths used for measurement ($\epsilon = \epsilon_{\lambda_1} = \epsilon_{\lambda_2}$) not over the entire spectrum. If λ_1 is close to λ_2 then this is typically the case for most materials. However in practice λ_1 and λ_2 cannot be arbitrarily close together since the bandpass filters used to isolate the wavelengths have some uncertainty in center wavelength and additional transmission spectrum outside of the desired wavelength.

Previous extensive testing (documented in Jones, 2020) using comparisons with thermocouple data indicates that this gray body assumption is indeed valid for oxidized, high temperature 304 stainless steel surfaces. However the material properties and surface oxidation conditions can change depending on the time at temperature and surrounding. An illustrative example of this is discussed in Section 3.4.1 for hydrogen/air tests where the oxidation state changes and begins to deviate from gray body behavior. In those cases calibration with a blackbody source is not

valid and alternative calibration methods should be explored such as use of the surface itself and a thermocouple for calibration. This is the approach taken in later experiments presented in Chapter 7. High emisssivity ceramic spray coatings capable of withstanding high temperatures were also found to be commercially available and may provide a suitable alternative to a reliance on developing a useful oxidization state at the surface.

3.3.2.2 Two-color Pyrometer Construction

The Pyrometer used in this work is shown schematically in Figure 3.3 and originates from Jones (2020) which built off previous designs in Coronel (2016) and Boeck et al. (2017). This design consists of a light collection head which passes light to an optical detector system via a fiber optic cable. This construction technique enables easy alignment since the collection head is small and can be moved independently of the larger and more sensitive components like the photo detectors.

The light emitted from the hot surface is collected by the pyrometer head which consists of an arrangement of two lenses (C1 and C2) designed to focus the light onto the tip of a 1 mm multimode silica fiber optic cable (FC). The region of light collected by the pyrometer head is referred to as the "spot size" which in this case was determined to be approximately 0.32 cm (0.126 in) in diameter at a distance of approximately 38.1 cm (15 in) from surface to collection head. The 1mm fiber optic cable is relatively large in diameter in order to maximize light transmission and consequently the signal captured by the photodetectors (D1 and D2). The output of the cable is then focused using a single plano convex lens (L1) and split into two beams using a longpasss dichroic mirror (BS) with a cut on wavelength of λ_{cut} = 1800 nm. This is designed such that the light is

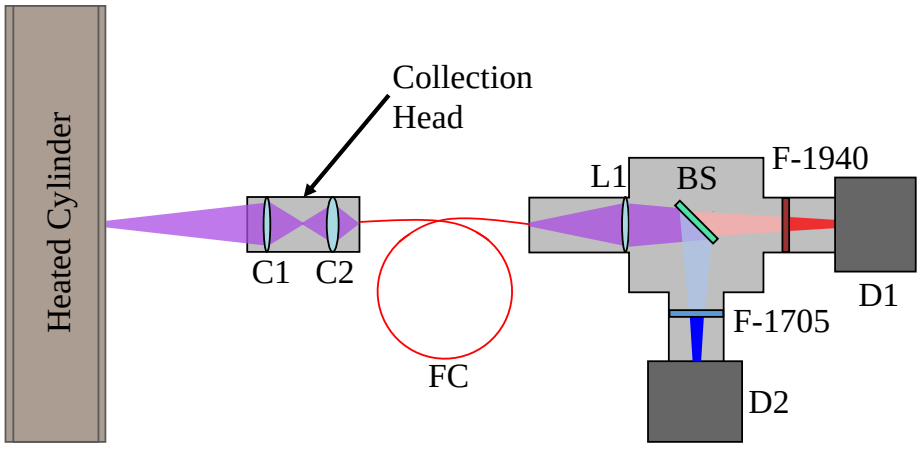

Figure 3.3: Schematic of pyrometer construction with detectors, filters and collection optics shown. C1 and C2: Collection lens 1 and 2, FC: Fiber optic cable, L1: Body lens 1, BS: Longpass dichroic mirror, F-1940/1705: Bandpass filter cetnered at 1940/1705 nm, D1 and D2: Photodetectors.

focused on the 1 mm active area of the photodetectors. Longer wavelengths are transmitted through the mirror (1850 - 2100 nm) while shorter wavelengths are reflected (1500 - 1750 nm). Each beam is then independently filtered using narrow bandpass filter centered at 1940 nm (F-1940, 105 nm FWHM) and 1705 nm (F-1705, 97 nm FWHM) respectively. These beams are projected onto two photodetectors (D1 and D2; Model PDA10DT) which produce a voltage signal in response to light intensity. The ratio of these voltage signals, I_1/I_2, is then used to determine surface temperature using Equation (3.13) obtained from the theory described in Section 3.3.2.1.

$$T = \frac{A}{\ln\left(\frac{I_1}{I_2}\right) - B} \tag{3.13}$$

Values for constants A and B are obtained via calibration with a surface at known temperature. For the experiments in this chapter a blackbody source (Process Sensors BBS1200) was used for these calibrations. A temperature measurement from an unknown surface can then be obtained using the measured voltage ratio through Equation (3.13) assuming the surface is a graybody over the measured wavelengths. An alternative calibration technique using the surface of interest as the calibration source is described in Chapter 7. A complete components list for the pyromter is also included in Appendix C.1.

3.3.3 Interferometer

Interferometery is a technique that is useful in many applications but here is leveraged for its ability to measure changes in the index of refraction of a flow field. Interferometers have been used for such purposes since as early as the late 19th century. Merzkirch (1987) describes in detail the history and fundamental principles behind interferometry as well as theory that allows for quantitative evaluation of interference patterns into useful spatially resolved data like density and temperature. For this work, an interferometer was used primarily to visualize thermal boundary layers and ignition phenomenon.

Jones developed a novel variation of the Mach-Zehnder interferometer which was also used in these tests. This design was unique in that the reference beam was passed through a single-mode polarization preserving optical fiber to traverse the lab bench which both simplified the optical system alignment and protected it from stray currents in the laboratory which would degrade the quality of the interferograms. The reader is referred to Jones (2020) for a detailed description of this diagnostic tool. A schematic of this unique setup is also reproduced in Figure 3.4

The system produces a 4 in diameter field of view (FOV) which enabled visualization of the cylinder and entirety of the thermal boundary layer on both sides. A Phantom V711 high speed camera was

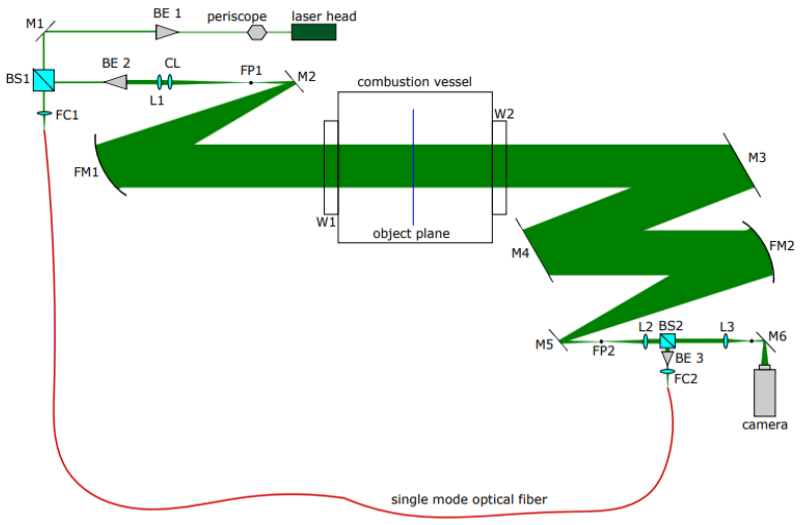

Figure 3.4: Schematic of the interferometer setup illustrating the location of key optical components. Adapted from Jones (2020).

used to record these interferograms at frame rates up to 10,000 fps at a resolution of 864 x 800 pixels. The effective resolution obtained in this fashion was approximately 9px/mm.

3.4 Results and discussion

A summary of all conditions studied are given in Table 3.1. Ignition thresholds for hydrogen and ethylene were obtained at only one condition, 1 atm and normal air composition and stoichiometric ratios of fuel to air. Ignition thresholds for n-hexane were obtained for a range of initial pressures and nitrogen dilution levels. The initial pressures were chosen based on various altitudes in the standard atmosphere (e.g. P_0 = 1, 0.7, 0.466, and 0.238 atm corresponding to altitudes of 0, 10 kft, 20 kft, and 35 kft respectively). A range of values for the nitogen fraction in air (β) were also chosen to range from normal air to highly diluted mixtures near the flammability limit. The n-hexane mixture compositions were defined by $\phi C_6H_{14} + 9.5(O_2 + \beta N_2)$. Previous work on thermal ignition by Boeck et al. (2017) has shown minimal dependence of ignition threshold on equivalence ratio (ϕ) for n-hexane away from the flammability limits. This was confirmed in the present study by some preliminary testing on n-hexane mixtures (ϕ = 0.88, 1, 1.6, β = 3.76, P_0 = 1 atm) with ignition temperature thresholds of 1020 K which are consistent with previous work by Jones (2020) and is well within the experimental uncertainty bounds of the pyrometer and logistic regression analysis. This is important since the stoichiometric partial pressure o fn-hexane is relatively low (2.16%) so relatively small filling errors can produce a large change in ϕ. The composition used was stoichiometric for all future n-hexane tests presented in this study. Complete shot data for these experiments are presented in Appendix D.

Table 3.1: Summary of all experimental conditions and reported ignition temperatures (T_{ign}) with 95% confidence limits (95% CL) from logistic regression. Note that the uncertainty bounds on the pyrometer are much larger in all cases (± 30 K). All conditions are stoichiometric (ϕ = 1.0).

		β X_{O_2}(%)	3.76 (20.6)	5.64 (14.8)	7.52 (11.6)	
Fuel	P_0 (atm)					
n-hexane	1.0		1020 ±4	1045 ±6	1066 ±3	T_{ign} (K) 95% CL (K)
	0.7		1060 ±5	1078 ±5	1098 ±3	T_{ign} (K) 95% CL (K)
	0.466		1091 ±5	1119 ±3	1128 ±4	T_{ign} (K) 95% CL (K)
	0.238		1143 ±4	1153 ±5	1171 ±1	T_{ign} (K) 95% CL (K)
hydrogen	1.0		982 ±13	- -	- -	T_{ign} (K) 95% CL (K)
ethylene	1.0		996 ±6	- -	- -	T_{ign} (K) 95% CL (K)

3.4.1 Hydrogen/Air

Hydrogen/air mixtures introduced some unexpected challenges that were not present in previous experiments working with n-hexane, Jet A, or surrogate fuels. After several tests with hydrogen mixtures, we observed a large discrepancy in the temperatures recorded by the thermocouple and the pyrometer which had been in good agreement (±10 K) in the n-hexane and ethylene tests. Comparison with thermocouple data indicated that the pyrometer measurement was about 50 K higher than the actual surface temperature. The reason became apparent upon visual inspection of the heated surface as illustrated in Figure 3.5. A reddish-orange oxide layer had formed on top of the gray-black oxide that normally persists on the surface for heating in air and other hydrocarbon combustion testing. This layer is likely composed of Fe_3O_4 (gray) and Fe_2O_3 (red) or one of many possible hydrated iron oxides (such as FeO(OH),$Fe_2H_2O_4$, $Fe(OH)_3$) which will subsequently be referred to as "rust". No chemical analysis was conducted to confirm which oxides were present however these are well known compounds and common oxidation states for steel alloys.

Additional testing with n-hexane/air mixtures in the presence of this rusty surface was conducted and it also seems that this surface condition had some catalytically inhibiting effect on ignition. For actual surface temperatures (as measured by thermocouples) up to 1100 K stoichiometric n-hexane/air mixtures were unable to ignite. These same mixtures typically ignited around 1020 K in the presence of the gray oxidized surface. This observation is consistent with results reported by Hilado and Clark (1972) for autoignition experiments conducted in the presence of ferric oxide

Figure 3.5: Comparison of the surface conditions observed in these experiments. (left) Polished stainless steel (middle) Typical oxide layer built up on surface after being held for 5 - 10 mins above 1000 K in an air atmosphere and (right) Surface after approximately 5 hydrogen ignition tests.

powder. For paraffinic hydrocarbons the effect of the oxide was to increase the AIT while for aromatics, alcohols, ketones, and other oxides the effect was the opposite. For n-hexane the reported AIT was increased by 89 °C with the addition of ferric oxide. This is consistent with the present work's observation of at least an 80 °C increase for n-hexane.

The "rust" build-up could be removed along with the gray oxide layer using sandpaper, revealing the underlying polished steel surface. Before further testing using the pyrometer, the gray oxide layer then had to be rebuilt by holding the cylinder at an elevated temperature (1000 K) for 5-10 minutes in an air atmosphere. Once this was done the pyrometer readings agreed with the welded thermocouple (within ±10 K). We therefore speculate that the differences in the wavelength dependence of the emissive properties of the rusty surface and the gray oxidized steel are the cause of this discrepancy. The rusted surface apparently is not a gray body between 1705 - 1940 nm and there is substantial variation in the emissivity for the two wavelengths measured by the pyrometer.

The sensitivity of the surface temperature measurement to wavelength dependent emissivity is substantial as can be illustrated through Equation (3.13). For example a 3% increase $\left(\frac{\epsilon_{\lambda_1}}{\epsilon_{\lambda_2}} = 1.03\right)$ will contribute an additional 0.03 to the constant B. This change corresponds to an approximately 40 K difference in T_w for a nominal surface at T_w = 1000 K. This is illustrated by the two calibration curves shown in Figure 3.6. This difference is comparable to the observed discrepancy of 50 K between the pyrometer and thermocouple measurements on the rusty surface at similar temperatures ($\simeq$ 1000K). Note that both curves in Figure 3.6 have similar slopes and are comparable to the predicted reposes from a blackbody source however the intercept difference is large. This is attributed mainly to differential attenuation from optical components laid out in Figure 3.3.

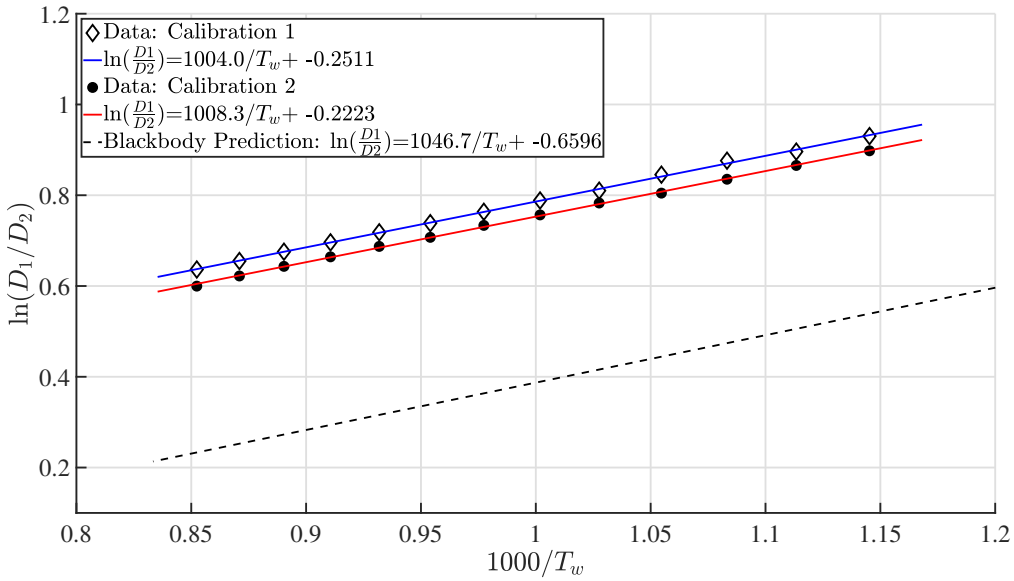

Figure 3.6: Example of two pyrometer calibration curves where B differs by 0.03 and A is the same. The difference in temperature between these two lines is about 40 K at T_w = 1000 K. The difference in B between the two calibrations is primarily due to sensitivity to alignment factors, especially the quality of the fiber coupling to the pyrometer collection head. The blackbody curve is computed from the curves in Figure 3.2.

This 3% emissivity difference is speculative but reasonable over a 235 nm wavelength range, however reliable data for spectral emissivity of rusty 304 stainless steel could not be found to definitively confirm this trend at the measured wavelengths and temperatures. The surface disruption and rust was found to develop for non-ignition cases as well as cases with ignition. This indicated that there was some significant reaction of hydrogen taking place near the surface in addition to the obvious potential of high temperature oxidation by water vapor in the post-combustion environment. This was also observable through a gradual decline in vessel pressure over the testing period. Similar declines were also evident in ignition cases in the lead-up to ignition. This can be seen in Figure 3.7 near the end of a non-ignition test but the drop was also evident in ignition cases in the lead-up to ignition.

This observation was in opposition to the gradual pressure rise observed in tests with other fuels. A pressure rise is expected and was observed due to the bulk heating of the gas over the testing period of 300 s and slight decomposition of hydrocarbon species in the thermal boundary layer. However, decomposition of H_2 should lead to a decrease in total number of moles in the gas phase which would result in a decreasing pressure. The pressure data and surface change both indicate that there is significant low temperature decomposition for hydrogen.

The procedure employed in performing the hydrogen tests therefore had to be modified to account for

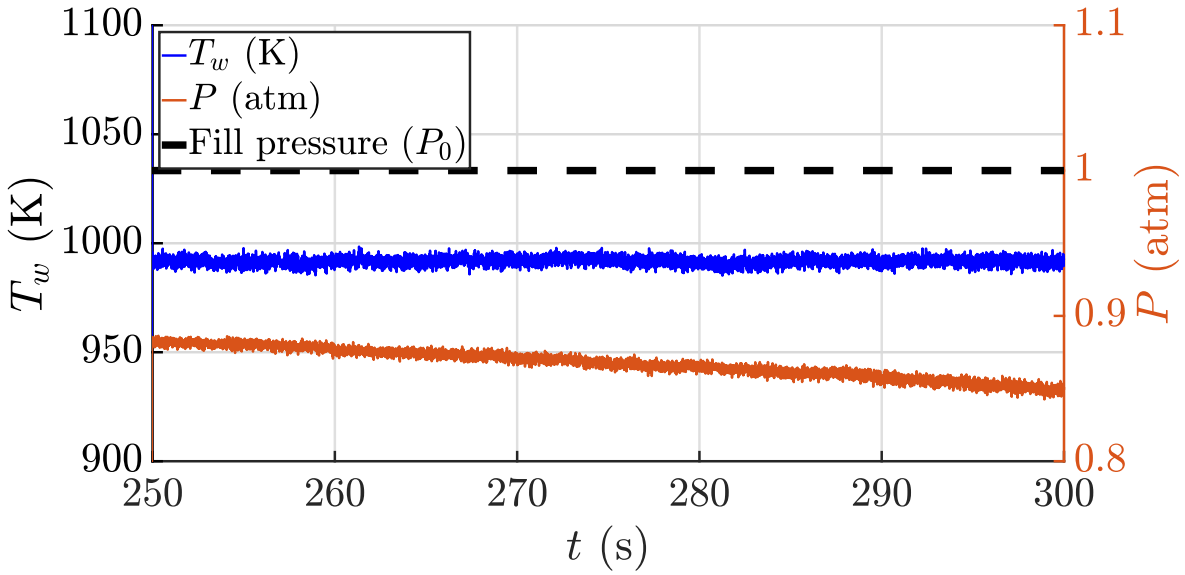

Figure 3.7: Gradual pressure drop recorded over 300s testing period for non-ignition case (H_2/air).

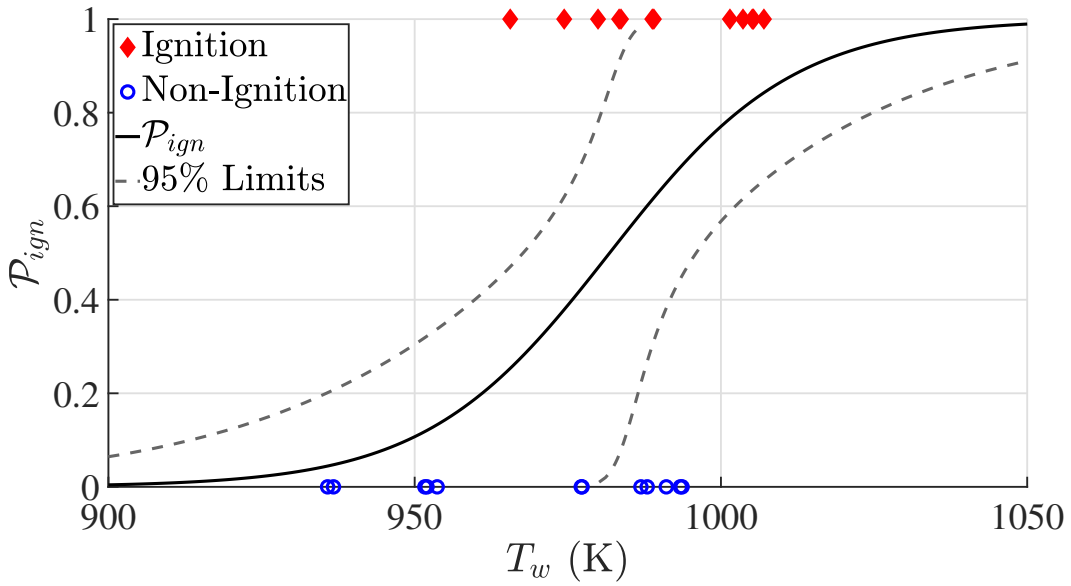

Figure 3.8: Probability of ignition ($\mathcal{P}_{ign}$) vs surface temperature (T_s). The probability curve and 95% confidence limits for the fit are found using logistic regression of stoichiometric hydrogen/air ignition data.

the heater surface changes. After each shot, the hot ignition products were immediately evacuated to minimize time exposed to the hot post-combustion products. Additionally, the surface was "cleaned" with sandpaper after every 5 shots and the gray oxidation layer was built back up before doing additional testing. Ignition kernels formed near the middle of the cylinder which was unique in that previously studied hydrocarbon fuels formed ignition kernels near the top of the heated

surface (Jones, 2020). The results of the ignition testing were fit using a logistic regression and the results are shown in Figure 3.8. The ignition temperature was 982 ± 30 K. This corresponds to an ignition probability of 50% with the uncertainty determined by the pyrometer measurements.

3.4.2 Ethylene-Air

With the experience gained from the hydrogen tests, the ethylene/air shots were monitored closely for anomalous system behavior but none was observed. Ignition kernels formed near the top of the cylinder as was the case with other hydrocarbon fuels. Near the ignition threshold, ignition events often appeared to be instigated by small perturbations and fluid ejections from the boundary layer. These ejected hot fluid pockets travel upward to the top of the cylinder where they are able to mix with hotter fluid at the top of the heated surface where the thermal layer is thickest. It is unclear what role these ejections play in the early stages of ignition but they may contain some partially reacted mixture that would aid in instigating ignition and may promote mixing of fluid in the thermal layer. In these cases the ignition kernel seems to form out of frame above the interferometer's field of view for these shots. These ejections were also observed for n-hexane mixtures and nonreactive mixtures (pure nitrogen) so it seems they may be purely fluid mechanical in origin. Some examples of these events are presented in Appendix E.2. Indeed these may be early indications of occasional turbulent transition as will be discussed more extensively in Chapter 6. The ignition data are presented in Figure 3.9 and again fit with a logistic regression. The ignition temperature is 996 ± 30K as determined by the 50% probability of ignition with the uncertainty determined by the pyrometer measurements.

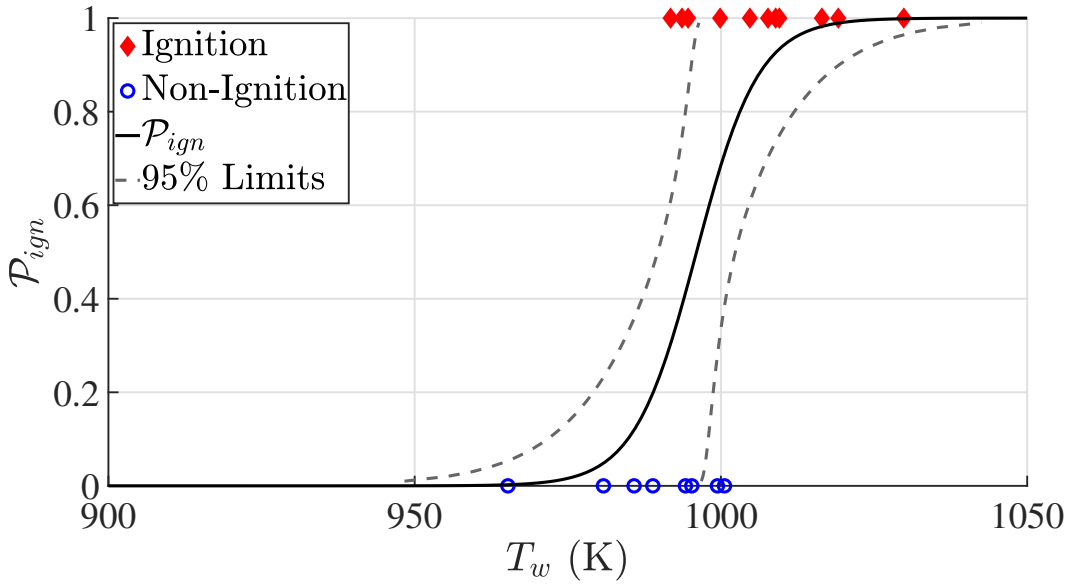

Figure 3.9: Logistic regression of stoichiometric ethylene/air ignition data.

3.4.3 Sub-atmospheric n-hexane/oxygen/nitrogen mixtures

A two factor factorial experimental approach was taken to study 12 total test conditions consisting of mixtures of stoichiometric n-hexane/oxygen/nitrogen. The two factors under investigation were initial pressure and nitrogen dilution (equivalently, oxygen concentration). Each test condition was repeated at least 12 times to produce a statistically significant data set which could be reliably analyzed using the logistic regression approach. Full results are shown in Figure 3.10 for all tests. These results demonstrate that decreasing pressure at fixed nitrogen dilution (constant β) results in increasing ignition temperatures. Similarly, increasing nitrogen dilution (β) at fixed initial pressure results in increasing ignition temperatures.

Figure 3.11 plots the ignition temperatures at fixed pressures against β. The ignition temperatures shown in this plot are those corresponding to 50% ignition probability as determined by the logistic curves shown in Figure 3.10. The error bars correspond to the uncertainty in the pyrometer readings which are estimated based on the 95% confidence intervals of the linear fit to the calibration data.

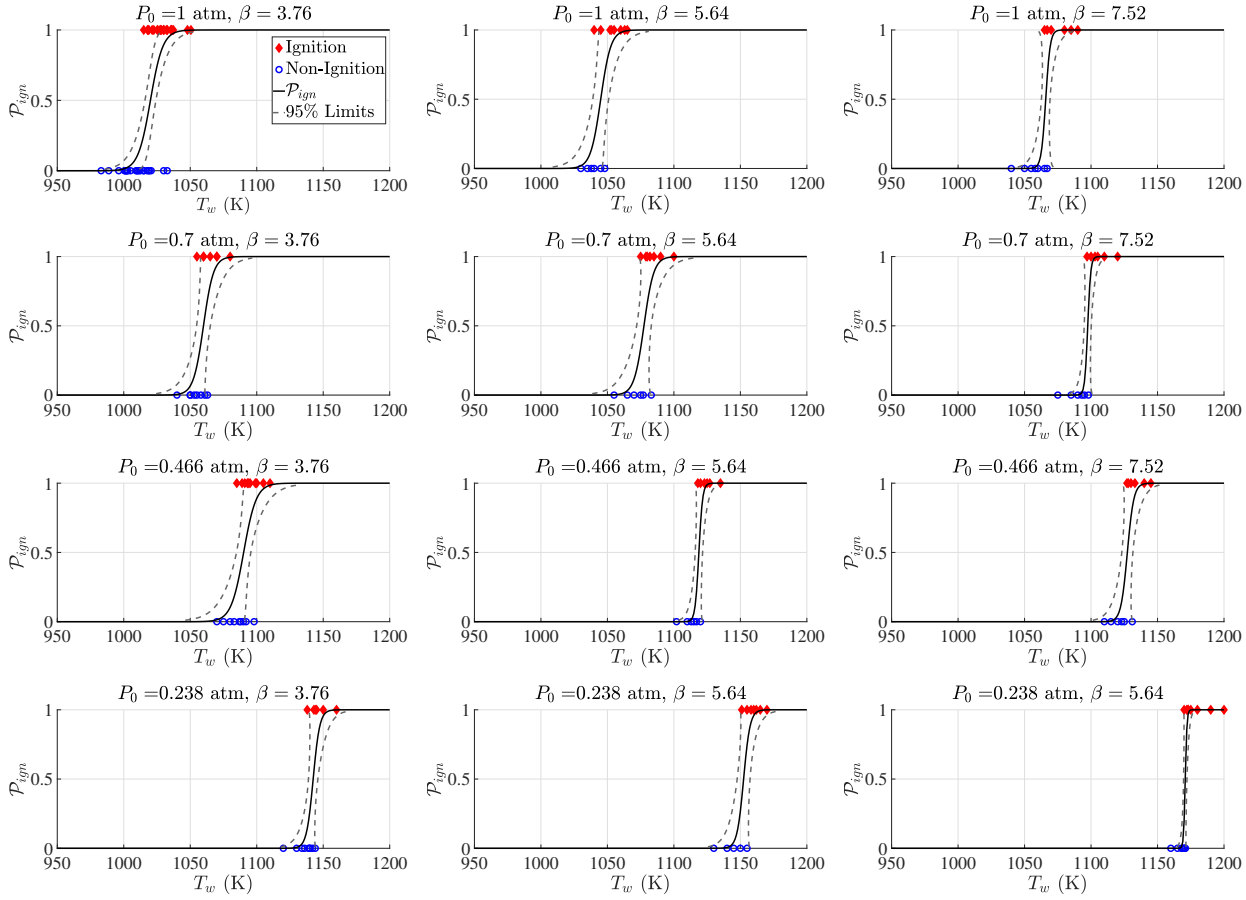

Figure 3.10: Ignition data and logistic regression for n-hexane/air mixtures at combinations of P_0 = 1, 0.7, 0.466, 0.238 atm and β = 3.76, 5.64, 7.52 (X_{O_2} = 20.6, 14.8, 11.6%). Pressure decreases from top to bottom and β increases from left to right.

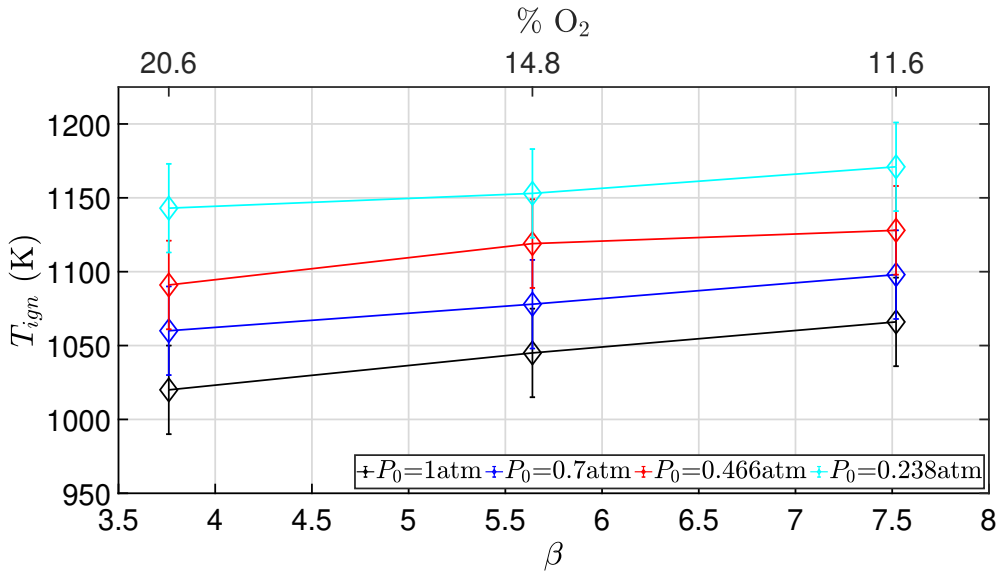

Figure 3.11: Summary of ignition threshold temperatures vs β and O_2 concentration for each pressure condition.

This error is ± 30 K in this case which is much larger than the uncertainty resulting from the logistic regression fitting of the ignition data which is on the order of ± 3 - 7 K in the cases shown in Figure 3.10. Ignition temperatures for all pressures show a similar trend with β and vice versa. There does not appear to be any significant interaction between pressure and β effects on ignition thresholds in these experiments. Ignition was achieved for all pressures at 11.6% O_2. This is in contrast to the results of Summer (2004) where limiting oxygen concentrations (LOC) of at least 14% were found for tests with a heated surface (~ 350 cm^2) at temperatures up to about 1050 K using Jet fuels. The pressure for these tests was not stated. Summer's study primarily used a low-power arc of relatively short duration (1 s) and in those tests a LOC of around 12% was reported for sea level and increasing up to 14.5% for pressures corresponding to 40 kft altitude. Coward and Jones (1952) report a minimum LOC of 11.9% for n-hexane with nitrogen as the inerting agent. However this minimum was for slightly rich mixtures whereas for stoichiometric mixtures the LOC was 13.4%. Coward and Jones's approach to determining flammability was the Explosion Tube Method and did not involve ignition by a hot surface but used a spark or an open flame. A detailed experimental exploration of the LOC with the 200A cylinder as an ignition source is presented in Section 3.5 where our mixtures are systematically diluted at P_0 = 1 atm.

Figure 3.12 shows representative pressure traces obtained from an ignition experiment at each of the test conditions near the ignition thresholds. The plots show a reduction in peak pressure and decrease in the rate of pressure rise (dP/dt) with increasing β. The decrease in peak pressure with increasing β and decreasing initial pressure is consistent with the thermodynamics of the

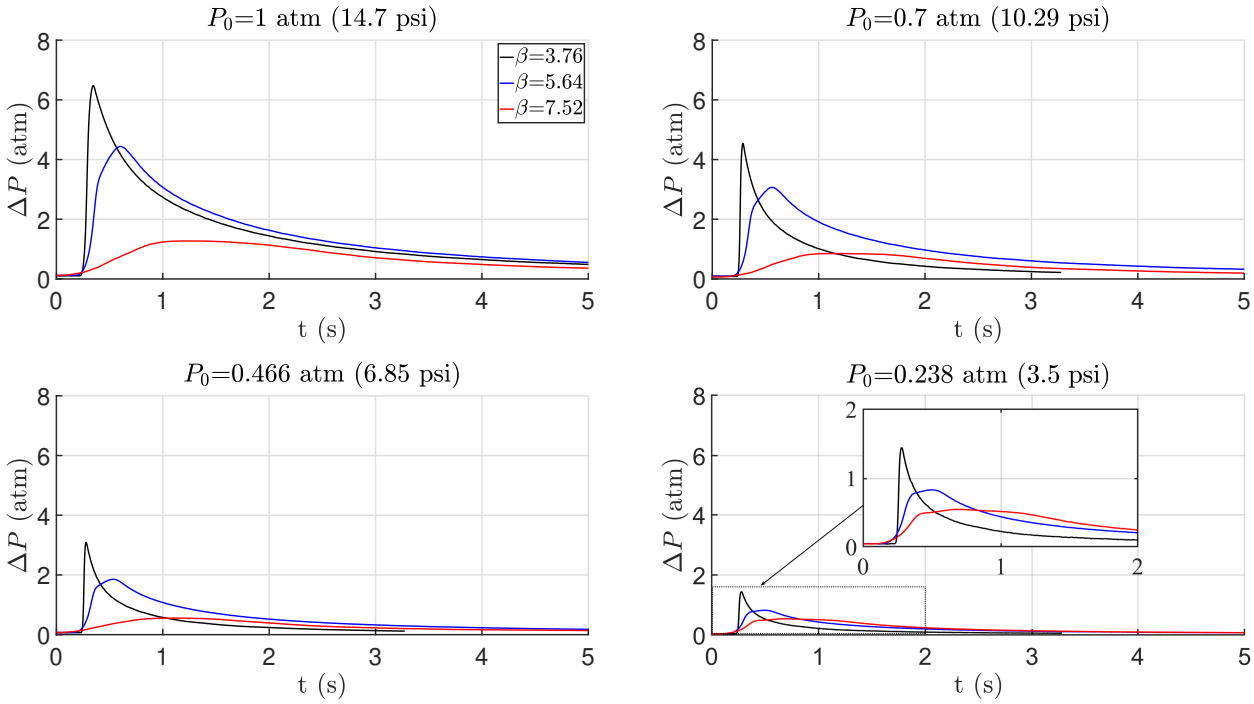

Figure 3.12: Representative pressure traces from ignition in each of the sub-atmospheric n-hexane conditions. Note the reduced y-axis scale for the P_0 = 0.238 atm case.

combustion process and the dependence of flame speed on mixture composition. These effects becomes especially evident at lower pressures. For example in the $P_0 = 0.466$ atm, $\beta = 7.52$ case the flame speed is much lower than in mixtures with lower β at the same P_0. This causes an increased duration of the pressure transient as the flame propagates more slowly through the combustion chamber. This also leads to increased heat loss from the flame causing lower peak temperatures and pressures. More dilute mixtures also have lower energy content and consequently lower flame temperatures and peak adiabatic combustion pressures.

All other factors being the same, the peak pressure should scale directly with the initial pressure so that the ratio of peak pressure to initial pressure should depend mainly on β and have only a modest dependence on initial pressure.

The decrease in pressure rise rate with increasing β is consistent with the decrease in observed and computed flame speeds for diluted mixtures. The magnitudes of the pressure rises can be compared to thermodynamic estimates as well as the peak pressure data from Summer (2004). For more dilute mixtures and at lower pressure, the effects of heat transfer and buoyancy on the flame are more pronounced, resulting in significant departures of the measured peak pressures from the adiabatic, constant-volume, complete-combustion (AICC) estimates as shown in Table 3.2. As anticipated from thermodynamic analysis of adiabatic combustion, the AICC pressure ratios are only modestly

dependent on initial pressure and a decreasing function of increasing dilution, $P_{AICC}/P_0 \approx 9.5$, 8.0 and 7.0 for β = 3.76, 5.64 and 7.52 respectively.

In contrast with the results in Summer (2004), our measured peak pressures are substantially higher for even the lowest O_2 concentration (11.6%) condition and pressure (0.238 atm) tested. The peak pressure rises reported by Summer at oxygen concentrations 1-2% higher than his LOC values were on the order of 0.4 to 2.5 psi (.027 to 0.17 atm). One key difference in test procedure that may explain this is that in Summer's tests the combustion products are vented early in the ignition process where our vessel remains closed throughout. The peak pressure rises in the present tests for the lowest O_2 concentration ranged from 7.3 to 17.2 psi (0.50 to 1.17 atm) for initial pressures between 0.238 and 1 atm. We also observed consistent ignition at an oxygen concentration of 11.6% at an initial pressure equivalent to 35 kft whereas Summer reported a limiting O_2 concentration of 14% at this altitude.

There are multiple factors for these differences in peak pressure and flammability limits observed in the present tests and those of Summer (2004). Our test facility used a single component gaseous fuel (hexane) with precise control over the fuel concentration rather than using the vaporization of liquid jet fuel/hexane mixtures and total hydrocarbon characterization reported by Summer. We also tested at a fixed equivalence ratio and it appears from the measurements reported by Summer that the equivalence ratio was increasing with decreasing altitude and pressure with a large variability in measured hydrocarbon concentration for tests at similar conditions. Our ignition system and mixing methods as well as the geometry of combustion vessel are significantly different than used by Summer (2004). All of these factors are known to contribute to differences in observed flammability limits.

Table 3.2: Thermodynamic estimates (AICC) and measurements of peak combustion pressure (atm) observed in the n-hexane testing as a function of β and initial pressure P_0.

	β X_{O_2}(%)	3.76 (20.6)	5.64 (14.8)	7.52 (11.6)	
P_0 (atm)					
1.0		9.58 7.48	8.08 5.44	6.95 2.28	AICC Experiment
0.7		6.67 5.24	5.64 3.77	4.86 1.55	AICC Experiment
0.466		4.41 3.56	3.74 2.32	3.23 1.02	AICC Experiment
0.238		2.23 1.69	1.90 1.06	1.65 0.78	AICC Experiment

3.4.3.1 Ono Correlation

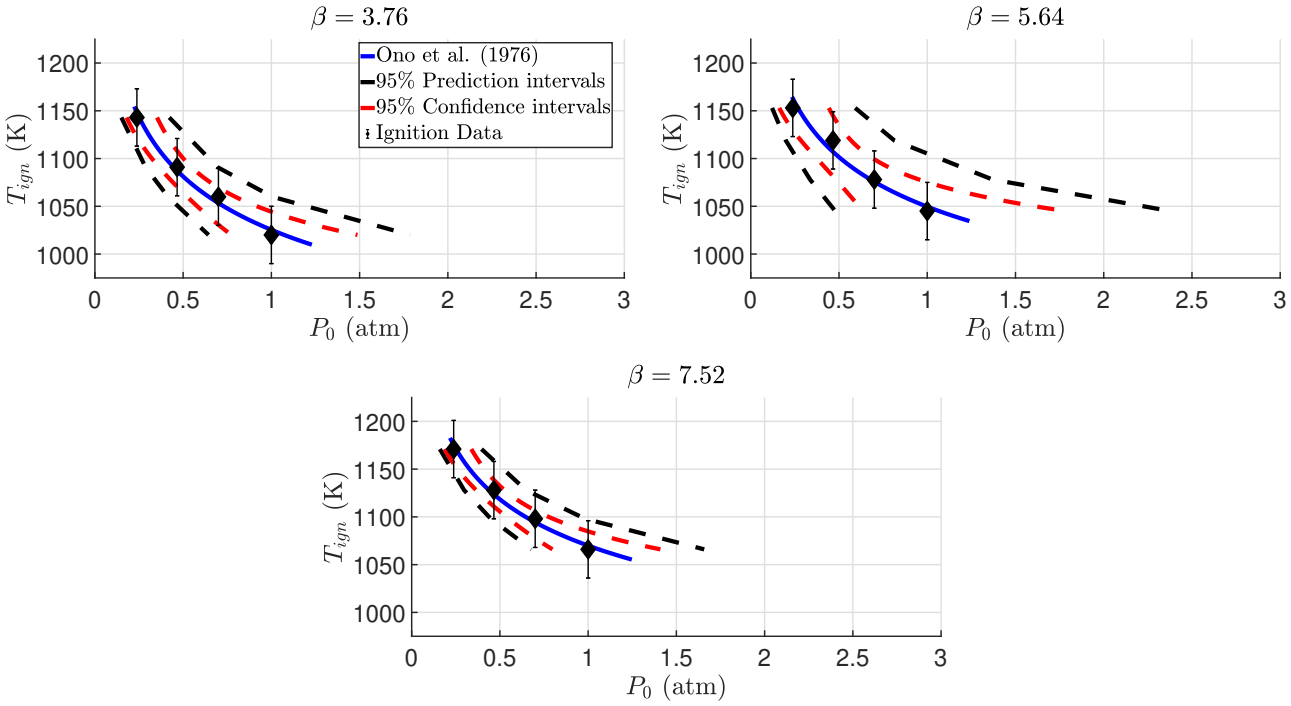

Figure 3.13: Ignition temperature vs initial pressure for β = 3.76, 5.64, and 7.52 (X_{O_2} = 20.6, 14.8, 11.6%). The blue line is the semi-empirical correlation derived by Ono et al. (1976). The red and black dashed lines are the 95% confidence and prediction intervals computed from the linear regression.

Ono et al. (1976) proposed a semi-empirical correlation for their work with a small heated flat plate. This has the form shown in equation 3.14 where n is a fuel-dependent constant, H is the flat plate vertical length, T_{ign} is the ignition temperature, and P_0 is the initial pressure of the flammable mixture.

$$\ln(P_0^{n-1} H^{1/2}) = \frac{C_1}{T_{ign}} + C_2 \tag{3.14}$$

A least-squares fit is performed to determine the constants C_1 and C_2 using the ignition data for varying pressure at a fixed β. We note that n and H are both constant for our cases so these values are absorbed into the regression coefficients. The resulting relationship T_{ign} as a function of P_0 is shown in Figure 3.13. The fit of the Ono et al. model to the present data gives confidence to the use of this model in extrapolating atmospheric pressure ignition data to lower pressures. Previous examination of this model by Jones and Shepherd (2021) demonstrated the validity of this correlation for extrapolating data obtained for a given height H over at least one order of magnitude for atmospheric n-hexane/air mixtures. Further work is needed and in progress in our laboratory to

ground this correlation in fundamental properties of the flammable mixture in order to make this a more predictive tool.

3.4.4 Ignition Testing Summary

The results of the logistic regression of the ignition testing for each of the fuels is summarized in Table 3.3. The reported ignition temperatures are also compared with those reported from previous studies using a small cylinder and the ASTM-E659 method respectively (Boeck et al., 2017; Martin & Shepherd, 2021; Zabetakis, 1965). These results are also plotted in Figure 3.14 where the trend seems to be increasing ignition temperatures with fuel size in the case of external flow experiments. The opposite seems to be true for the internal flow AIT test, however caution should be taken in giving any merit to the H_2 and C_2H_4 data since the AIT numbers for these are likely found using a different apparatus that the ASTM-E659.

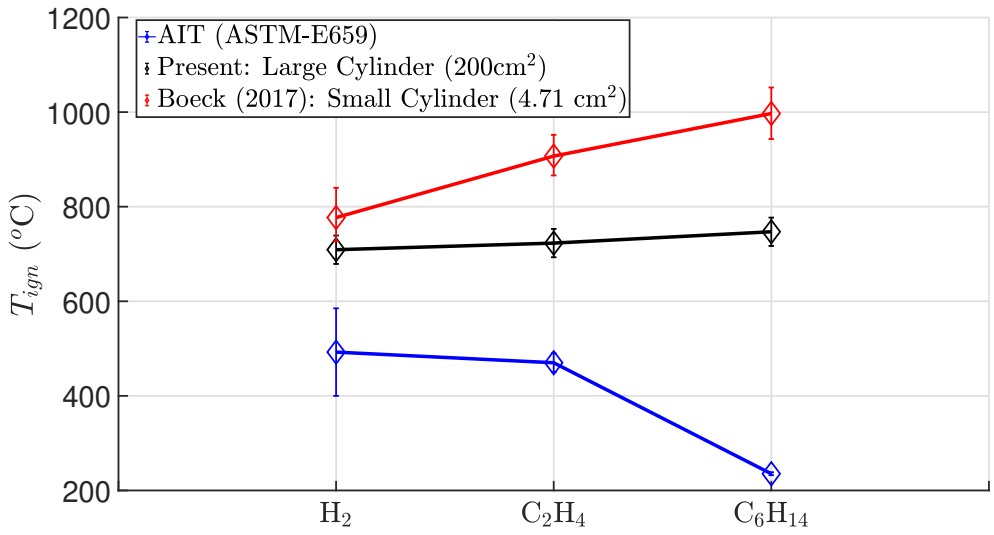

Figure 3.14: Comparison of ignition temperatures for the three fuels studied with alternative ignition test methods. Error bars for H_2 and C_2H_4 ignition data represents range of values typically reported in literature.

3.5 Limiting Oxygen Concentration (LOC) Experiments

As mentioned in Section 3.1.1, nitrogen-enriching systems have been developed and are now extensively used in commercial aircraft to inert the ullage space of the fuel tanks(Moravec et al., 2006; Cavage & Summer, 2008). For these systems to be effective, lower and upper flammability limits (LFL and UFL, respectively) are useful definitions on the limiting fuel concentrations in air that produce a propagating flame. The progressive addition of an inert gas like Nitrogen to a fuel/air mixture causes the narrowing of these limits until the mixture is no longer combustible. This

Table 3.3: Ignition temperatures for all fuels as compared with previous work. Boeck et al. (2017) used a 10 mm X 10 mm cylinder. AIT values for the gaseous fuels are of uncertain provenance and the method used in obtaining these data are not always clear. [a] Zabetakis (1965) [b] Martin and Shepherd (2021).

Ignition test	Ignition source	H_2	C_2H_4	C_6H_{14}
AIT	500 mL heated flask	673 K [a]	763 K [a]	508.3 ± 3.1 K[b]
Boeck et al. (2017)	1cm x 1cm cylinder	1050 ± 30 K	1180 ± 30 K	1270 ± 30 K
Present work	2.54 cm x 25.4cm cylinder	982± 30 K	996± 30 K	1020± 30 K

approach leads to another definition, that of the limiting oxygen concentration (LOC) which is the minimum O2 concentration in a mixture of fuel, air, and an inert gas which produces a propagating flame. Previous studies have focused on visible detection of flame propagation to determine the LOC rather than entirely eliminating combustion events such as localized combustion or cool flames. Historical data has typically been generated via the use sparks or passing of an open flame as ignition sources (Coward & Jones, 1952). These are highly localized and transient ignition sources which differ from heated surfaces where the ignition source is spatially distributed and can be present for extended periods of time. For such cases, previous experiments using a propagating flame criteria may not be sufficient to predict explosive limits from such sources and provide a sufficient design LOC to cover all potential ignition hazards. More recent work (Zlochower & Green, 2009) and the current standards like the ASTM E681 and ASTM-E2079 (ASTM International, 2015, 2019) instead use large spherical vessels and more quantifiable metrics like a 7 % explosion over pressure for determination of these limits. However again in these apparatus a spark ignition system is used.

It is therefore of interest to apply the current experimental apparatus to the evaluation of flammability of n-hexane in nitrogen inerted atmospheres in the hopes of determining an LOC) using a hot surface ignition source. Summer (2004) have reported the LOC for heated surface ignition, in addition to spark ignition, however under significantly different circumstances and only for Jet A mixtures. Ignition definition in these experiments is also somewhat more empirical and determined typically by the blowing of a pressure relief mechanism like a rupturing foil diaphragm as described in Summer (2004). The results in Section 3.4.3 clearly show that as a mixture becomes diluted the flame character and explosion properties are entirely different from what is seen in undiluted cases. The explosion over pressure is significantly reduced and the transient is elongated. Close to the LOC a pressure relief mechanism may not respond to these pressure transients and produce an artificially higher LOC than intended. For this section we consider $\beta > 7.52$ where the same trend continues in that the flame speeds drastically reduce causing longer pressure transients and lower peak pressures to be produced. Some examples of this are shown in Figure 3.15 for $\beta = 8.25$ and $\beta = 8.6$. The already reduced pressure signal of $\beta = 7.52$ is also shown for comparison. In these

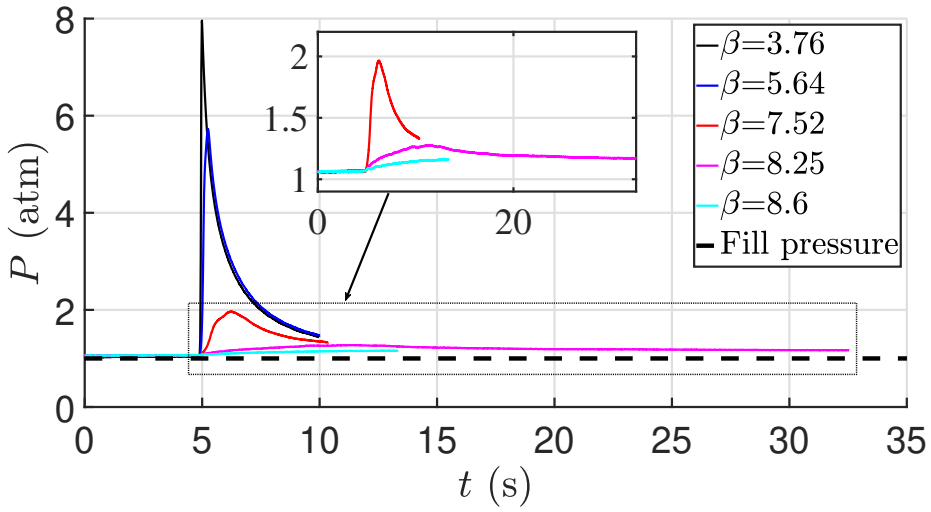

Figure 3.15: Pressure traces for increasing β. Peak pressure rise becomes lower as LOC is reached and pressure transient is highly elongated owing to slow flame speed, puffing flames, and buoyancy stratification of gas within the vessel. The time offset on the x axis here is arbitrary and the pressure traces for all cases are offset to coincide where there is a sharp increase indicative of ignition.

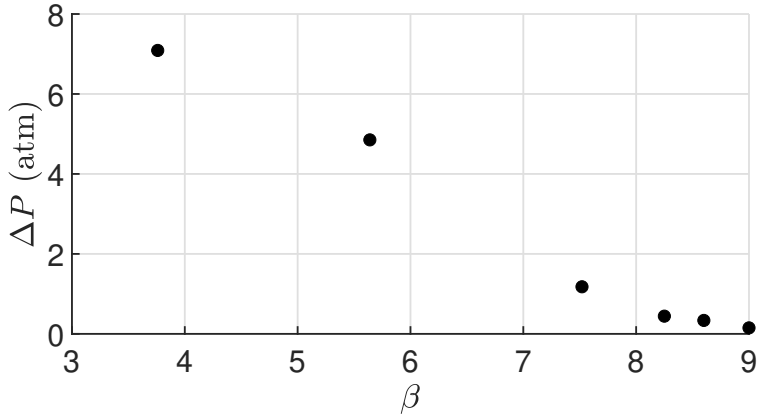

Figure 3.16: Peak pressure rise decrease for increasing β. No sharp threshold is reached, flame speed, pressure rise, and temperature simply gradually drop and approach nonreactive values.

cases the pressure increase due to ignition is reduced to less than 0.5 atm. Additionally there is a long period beyond the initial ignition event where pressure continues to rise. For example in the β = 8.25 case this occurs between 22 and 29 s. This is a result of the severely reduced flame speed competing with the natural convection flow velocity such that propagation into the bulk gas becomes difficult even near the hot surface. Far away from the surface, the bulk gas is far too cold and energy content is so low that flame propagation is impossible. Instead the bulk gas must be entrained into the hot surface where reaction can occur. A layer of hot unreacted gas is also built up in the top of the vessel above the ignition source and remains unreacted until it recirculates to the

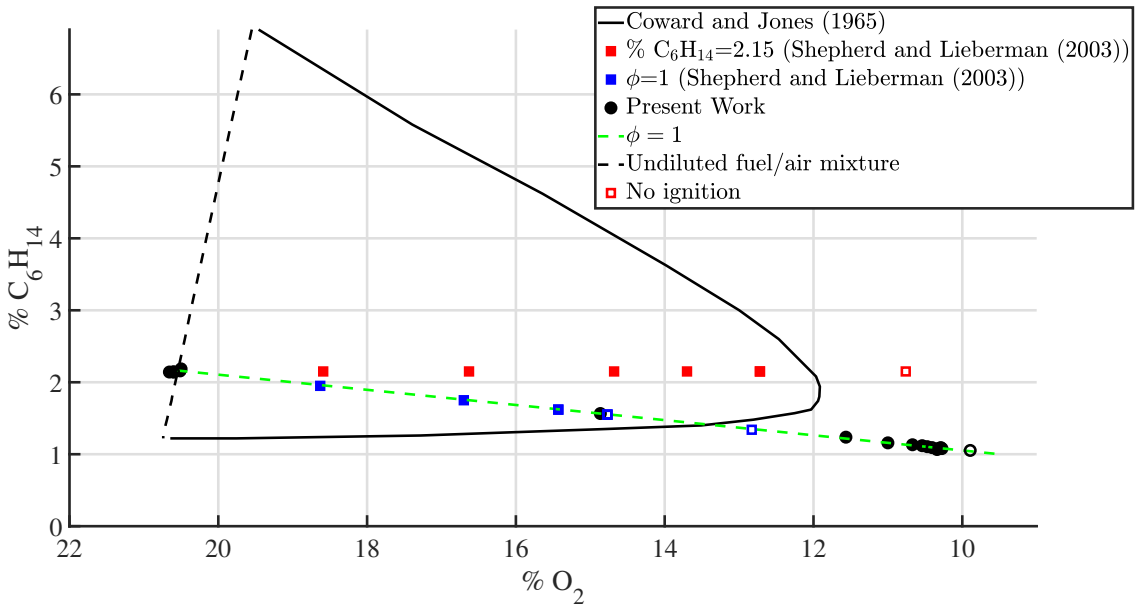

Figure 3.17: Comparison of limiting oxygen concentration (LOC) data from Coward and Jones (1952) and an unpublished internal experimental study by Shepherd and Lieberman. Closed symbols represent flammable mixtures and open symbols nonflammable.

lower portion of the vessel as it is slowly displaced by hotter combustion products. The comparably long time scales required for complete recirculation of the bulk gas into the heated region are the reason for these elongated pressure transients. In undiluted case the large flame speeds produce the dominant timescale as rapid processing of the entire vessel volume by the flame occurs long before recirculation become important. Near the LOC these non-ideal effects cause incomplete combustion of the gas in the combustion vessel and again challenge the definition of ignition and flammability limits that are relevant to hazard evaluation.

Interesting flame phenomena are observed as β increases. Section 3.5 shows an example sequence of frames for cases with a range of β = 8.6 . The flame speed becomes drastically reduced such that the velocity in the natural convection boundary layer is of comparable speed to the flame speed resulting in a puffing flame phenomenon occurring near the hot surface. The period of this puffing is likely related to the rate of entrainment into the boundary layer of fresh reactants from the cold bulk gas. This phenomenon is also likely responsible for the gradual pressure rise observed after the initial spike as observed in Figure 3.15. Figure 3.16 shows peak pressure rises (ΔP) as a function of β or equivalently X_{O_2}. There is a gradual decline in (ΔP) up to β = 9 after which point no appreciable pressure rise can be distinguished for higher values of β. This is therefore the LOC reported for these ignition experiments. This is comparably lower to the value of 13.4% given by Coward and Jones for stoichiometric n-hexane mixtures at 1 atm and even the lowest value

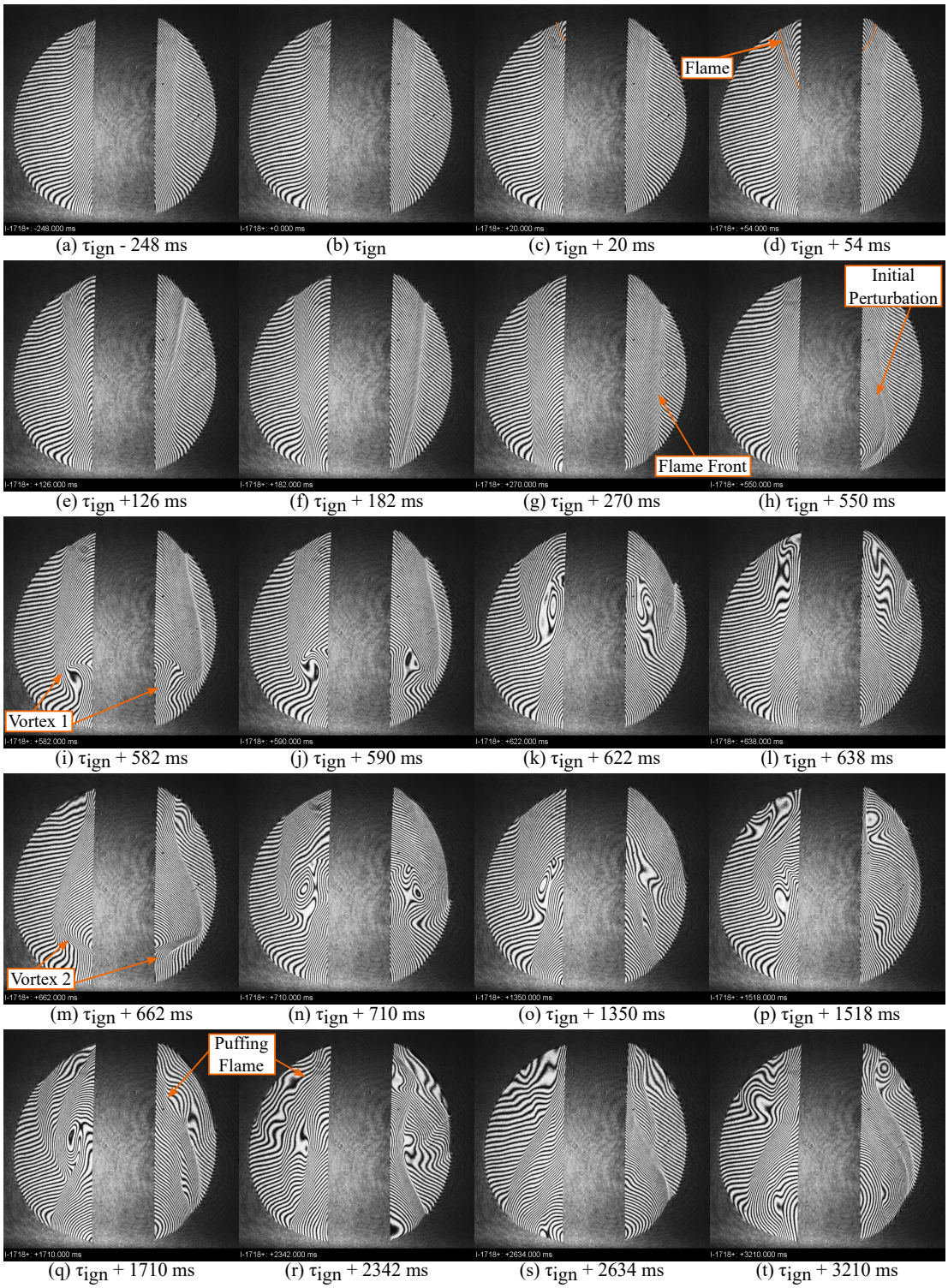

(a) τ_{ign} - 248 ms (b) τ_{ign} (c) τ_{ign} + 20 ms (d) τ_{ign} + 54 ms

(e) τ_{ign} +126 ms (f) τ_{ign} + 182 ms (g) τ_{ign} + 270 ms (h) τ_{ign} + 550 ms

(i) τ_{ign} + 582 ms (j) τ_{ign} + 590 ms (k) τ_{ign} + 622 ms (l) τ_{ign} + 638 ms

(m) τ_{ign} + 662 ms (n) τ_{ign} + 710 ms (o) τ_{ign} + 1350 ms (p) τ_{ign} + 1518 ms

(q) τ_{ign} + 1710 ms (r) τ_{ign} + 2342 ms (s) τ_{ign} + 2634 ms (t) τ_{ign} + 3210 ms

Figure 3.18: Example of puffing flame phenomenon near the LOC. Shot 493: β = 8.6, T_w=1200 K, P= 1 atm. (b) Ignition occurs above the FOV. The flame propagates into frame beginning along the top left edge. (c)-(g) Flame propagation through boundary layer. At (g) the flame is unable to propagate into cold bulk gas. (h)-(l) Vortex formation and propagation upwards. (m)-(t) Repeated vortex formation and shedding from surface aka "puffing" on timescale of seconds.

of 11.9% found for $\phi \approx 1.5$. Coward and Jones used a 150 cm vertical tube ignited by a spark or open flame for the determination of LOC and considered the limits where a freely propagating flame was produced in the tube. It is not explicitly clear what measurement techniques were used for determination of a propagating flame in these experiments beyond visual means. Cases where a stationary or "cap" of flame is produced are not considered flammable mixtures in those experiments. These differences are likely to result in different thresholds since the ignition source is more localized and the criteria for a flammable mixture more restrictive.

The puffing buoyant flames seen in Section 3.5 are readily observed beyond 11.6 % O_2 (β = 7.52) due to natural convection competition with the burning velocity. These flames slowly propagate into the bulk gas so are still considered to be flammable for our purposes. However even the limit of 11.6% contains clearly propagating flames and is well beyond the limiting curve as shown in Figure 3.17. In this study the pressure signal is used for the LOC cutoff and as evidenced by Figure 3.15 and section 3.5, a non propagating locally puffing flame can be obtained using the present method and still produces a measurable pressure rise. Cases like this were likely impossible in the experiments conducted by Coward and Jones (1952) since a much smaller combustion volume and localized ignition source were used so a slightly lower LOC would be expected. Data from unpublished internal experiments in a rectangular 11.25 L explosion vessel using a spark ignition system is also presented in Figure 3.17. A limited number of tests with constant stoichiometry and constant fuel concentration were conducted and showed reasonable agreement with the data from Coward and Jones (1952). Both sets of data were obtained for P_0 = 0.493 atm (50 kPa) while the present data and Coward and Jones data were obtained for P_0 = 1 atm. The effect of reduced pressure is generally to narrow the range of flammability limits by both raising the LOC and lowering the rich limit.

3.6 Conclusions

These experiments show that both decreasing pressure and increasing nitrogen dilution lead to increasing thermal ignition thresholds in n-hexane-air mixtures. These studies were carried out with a single type and size of ignition source, a heated vertical cylinder which produced an external laminar natural convection flow. Ignition thresholds increased over 100 K with a decrease in pressure from 1 to 0.238 atm. The effect of nitrogen dilution on ignition temperature at constant initial pressure was much smaller, within the range of uncertainty of the instrumentation. However, the nitrogen dilution substantially decreased the overpressure and maximum rate of pressure rise. In contrast to previous studies we were able to obtain ignition for oxygen concentrations as low as 11.6% for all initial pressures that were examined. The dependence of ignition temperature threshold on initial pressure is consistent with the correlation suggested by Ono et al. (1976).

Tests with hydrogen and ethylene were consistent with the trends of ignition temperature threshold dependence on fuel and the decrease in ignition temperature with increasing vertical height of the hot surface. This was consistent with the observations of Jones and Shepherd (2021) for n-hexane and Ono et al. (1976) for a range of fuels. Tests with hydrogen also demonstrated that surface reactions — not observed in tests with hydrocarbon fuels — had a significant effect on the wavelength dependence of thermal emission. The accumulation of a reddish-orange oxide layer was observed indicating some hydrated iron oxides were being formed at the surface. We had to monitor the surface condition and use a cleaning regimen in order to obtain reliable surface temperature measurements using optical pyrometry. Chapter 7 will present an alternative calibration method for cases where the oxide layer is problematic for pyrometry.

Limiting oxygen concentration (LOC) testing was also conducted using the same vertical cylinder heated to 1200 K. Buoyancy effects dominated as the LOC was approached however somewhat propagating puffing flames were observed for oxygen concentration as low as 10.3%. This value is lower than that reported for more traditional ignition sources in the literature. This difference is thought to be a result of the use of a spatially distributed, long duration ignition source producing fluid motion and sustained heating that is absent in other experiments. The pressure transients in these experiments were also much longer in duration and produced far lower peak values due to the slow flame speeds competing with buoyancy effects in complete burning of the vessel mixture.

References

ASTM International. (2015). ASTM E681-09: Test Method for Concentration Limits of Flammability of Chemicals (Vapors and Gases). https://doi.org/10.1520/E0681-09R15. (Cit. on p. 86)

ASTM International. (2019). ASTM E2079-19: Test Methods for Limiting Oxygen (Oxidant) Concentration in Gases and Vapors. https://doi.org/10.1520/E2079-19. (Cit. on p. 86)

Bane, S., Shepherd, J., Kwon, E., & Day, A. (2011). Statistical analysis of electrostatic spark ignition of lean H2/O2/Ar mixtures. *International Journal of Hydrogen Energy*, *36*(3), 2344–2350. https://doi.org/10.1016/j.ijhydene.2010.05.082 (Cit. on p. 66)

Boeck, L., Meijers, M., Kink, A., Mével, R., & Shepherd, J. (2017). Ignition of fuel–air mixtures from a hot circular cylinder. *Combustion and Flame*, *185*, 265–277. https://doi.org/10.1016/j.combustflame.2017.07.007 (Cit. on pp. 63, 72, 74, 85, 86)

Brandes, E., Hirsch, W., & Stolz, T. (2017a). *Zündtemperaturen in anderen Oxidationsmitteln als luft; Projekt – Zündtemperaturen brennbarer Flüssigkeiten bei erhöhtem Sauerstoffanteil im O2+N2-Gemisch* [EN: Ignition Temperatures In oxidants other than air; Project - Ignition temperatures of flammable liquids with increased oxygen content in the O2+N2 mixture]. PTB Braunschweig. (Cit. on p. 64).

Brandes, E., Hirsch, W., & Stolz, T. (2017b). *Zündtemperaturen in anderen Oxidationsmitteln als luft; Projekt – Zündtemperaturen brennbarer Flüssigkeiten in Luft+N2O-Gemisch* [EN: Ignition Temperatures In oxidants other than air; Project - Ignition temperatures of flammable liquids in air+N2O mixture]. PTB Braunschweig. (Cit. on p. 64).

Cavage, W. M., & Summer, S. (2008, February). *A Study of the Flammability of Commercial Transport Airplane Wing Fuel Tanks* (Final Report DOT/FAA/AR-08/8). Federal Aviation Administration. William J. Hughes Technical Center, Atlantic City International Airport, NJ. (Cit. on pp. 63, 85).

Coronel, S. A. (2016). *Thermal Ignition Using Moving Hot Particles*. California Institute of Technology. (Cit. on pp. 69, 72).

Coward, H., & Jones, G. (1952). *Limits of Flammability of Gases and Vapors* (BM–BULL-503). Bureau of Mines. Washington D.C. https://doi.org/10.2172/7328370. (Cit. on pp. 81, 86, 88, 90)

FAA. (2017, April). *Operator Information for Incorporating Fuel Tank Flammability Reduction Requirements into a Maintenance and/or Inspection Program* (Advisory Circular AC No. 120-98A CHG 1). Federal Aviation Administration. (Cit. on p. 63).

Hilado, C. J., & Clark, S. W. (1972). Discrepancies and correlations of reported autoignition temperatures. *Fire Technology*, *8*(3), 218–227. https://doi.org/10.1007/BF02590545 (Cit. on p. 75)

Hirsch, W., & Brandes, E. (2005). *Zündtemperaturen binärer Gemische bei erhöhten Ausgangsdrücken* [EN: Ignition temperatures of binary mixtures at increased outlet pressures]. PTB Braunschweig and Berlin. (Cit. on p. 63).

International, A. (2005). ASTM-E659: Standard test method for autoignition temperature of liquid chemicals. (Cit. on p. 63).

Jones, S., & Shepherd, J. E. (2020). Thermal ignition of n-hexane mixtures by vertical cylinders. *Proceedings of the 13th International Symposium on Hazards, Prevention and Mitigation of Industrial Explosions (ISHPMIE 2020)* (Cit. on p. 65).

Jones, S. M. (2020). *Thermal ignition by vertical cylinders*. California Institute of Technology. (Cit. on pp. 63, 64, 66, 67, 71–74, 79).

Jones, S. M., & Shepherd, J. (2021). Thermal Ignition by Vertical Cylinders. *Combustion and Flame*, *232*, 111499. https://doi.org/10.1016/j.combustflame.2021.111499 (Cit. on pp. 64, 84, 91)

Martin, C., & Shepherd, J. (2021). Low temperature autoignition of Jet A and surrogate jet fuel. *Journal of Loss Prevention in the Process Industries*, *71*, 104454. https://doi.org/10.1016/j.jlp.2021.104454 (Cit. on pp. 85, 86)

Merzkirch, W. (1987). *Flow visualization* (2nd ed). Academic Press. (Cit. on p. 73).

Michalski, L., & Michalski, L. (Eds.). (2001). *Temperature measurement* (2nd ed) [Rev. ed. of: Temperature measurement / L. Michalski, K. Eckersdorf, and J. McGhee. c1991]. J. Wiley. (Cit. on pp. 69, 70).

Moravec, B. L., Boggs, R. E., Graham, R. N., Grim, A., Adkins, D. A., Snow, D., & Haack, A. (2006, December). *Commercial Aircraft On-Board Inerting System* (U.S. pat. Patent No. 7,152,635 B2). (Cit. on pp. 63, 85).

Ono, S., Kawano, H., Niho, H., & Fukuyama, G. (1976). Ignition in a Free Convection from Vertical Hot Plate. *Bulletin of JSME*, *19*(132), 676–683 (Cit. on pp. 64, 84, 90, 91).

Quinn, T. (1990). THERMOCOUPLES. *Temperature* (pp. 286–331). Elsevier. https://doi.org/10.1016/B978-0-12-569681-4.50013-0. (Cit. on p. 66)

Summer, S. (2004, August). *Limiting Oxygen Concentration Required to Inert Jet Fuel Vapors Existing at Reduced Fuel Tank Pressures-Final Phase* (DOT/FAA/AAR-04/08). Federal Aviation Administration. William J. Hughes Technical Center, Atlantic City International Airport, NJ. (Cit. on pp. 63, 64, 81–83, 86).

Zabetakis, M. G. (1965). *Flammability characteristics of combustible gases and vapors* (BM–BULL-627, 7328370). Bureau of Mines. Washington D.C. https://doi.org/10.2172/7328370. (Cit. on pp. 63, 85, 86)

Zlochower, I. A., & Green, G. M. (2009). The limiting oxygen concentration and flammability limits of gases and gas mixtures. *Journal of Loss Prevention in the Process Industries*, *22*(4), 499–505. https://doi.org/10.1016/j.jlp.2009.03.006 (Cit. on p. 86)

Chapter 4

1D FLAME MODELING

4.1 Motivation

The discussion in previous chapters has thus far been dominated by the time dependent process of ignition. This process of starting with reactants and evolving in time towards production of products through the development of a steadily propagating flame is of primary importance in explosion hazard assessment. However, the time-independent steadily propagating flame which follows this ignition process is also of importance to understand due to its influence on the temperature and pressure rises during the explosion which produce the undesired thermal and structural loads acting on the system.

This chapter therefore focuses on the propagation of flames in enclosed vessels which is primarily of interest to understand the mixture effect on explosion properties observed in Chapter 3. Understanding of the dependence of flame properties on mixture variables lends insight into the observed trends in pressure traces and ignition thresholds. For this purpose, a highly simplified 1D flame model was implemented using Cantera (Goodwin et al., 2017). The model is of a one-dimensional (1D), steady state, laminar, premixed, adiabatic, freely propagating flame using detailed kinetics for n-hexane (JetSurf2) and mixture averaged transport (Wang et al., 2010). Useful outputs of this model include the adiabatic flame temperature (T_{ad}), laminar burning velocity (S_L) and flame thickness (l_f). These are fundamental properties of a premixed flame and are useful quantities in exploring correlations for thermal ignition thresholds and explosion properties. Flame properties can be computed relatively easily even for large detailed kinetic models, which are difficult to use in reactive CFD simulations of multi-dimensional flows. As an alternative, it may be possible to analyze potential and actual hazards in engineering designs based on correlations of nonreacting flow properties (such as boundary layer temperature profiles) with flame properties.

4.2 Governing Equations for 1D flames

A simple model of a low-speed one-dimensional (1D) flame is based on assuming constant pressure and the steady-flow equations for continuity, energy and species in the domain $-\infty < x < \infty$.

$$\frac{d(\rho u)}{dx} = 0 \tag{4.1}$$

$$\rho c_P u \frac{dT}{dx} = \frac{d}{dx}\left[\lambda \frac{dT}{dx}\right] - \sum_k j_k c_{P,k} \frac{dT}{dx} - \sum_k h_{f,k} W_k \dot{\omega}_k \tag{4.2}$$

$$\rho u \frac{dY_k}{dx} = -\frac{dj_k}{dx} + W_k \dot{\omega}_k \tag{4.3}$$

Here ρ is the density, u is the velocity, c_P is the specific heat capacity at constant pressure, T is the temperature, and λ is the thermal conductivity. The subscript k denotes properties relating to species k in the mixture. Therefore for each species k, j_k is the diffusive mass flux, $h_{f,k}$ is the mass specific enthalpy of formation, $c_{p,k}$ is the mass specific heat capacity, W_k is the molecular weight, $\dot{\omega}_k$ is the molar production rate, and Y_k is the mass fraction. The fluid is also assumed to be an ideal gas so

$$P = \rho R T \tag{4.4}$$

with

$$R = \frac{\tilde{R}}{W_{mix}} \quad \text{and} \quad \frac{1}{W_{mix}} = \sum_{k=1}^{N} \frac{Y_k}{W_k}\,. \tag{4.5}$$

Here R is the specific gas constant, $\tilde{R}$ is the universal gas constant, and W_{mix} is the mixture averaged molecular weight. The unburnt gas density ρ_u is given in Equation (4.6) which follows from Equation (4.4) and Equation (4.5). The properties of the unburnt and burnt gas states are identified using subscripts u and b respectively.

$$\rho_u = \frac{P_u W_{mix,u}}{R T_u} \tag{4.6}$$

The flame propagates into the unburnt mixture at some velocity denoted as S_L. This can be found using Equation (4.1) which states the mass flow rate is constant throughout the system ($\dot{m}'' = \rho u$ =constant). Equating the mass flow rate at the burnt and unburnt states yields an expression for the laminar burning velocity as in Equation (4.7).

$$S_L = \frac{\dot{m}''}{\rho_u} = \frac{\rho_b u_b}{\rho_u} \tag{4.7}$$

The system of equations is solved with the following boundary conditions on temperature and species:

$$T(x = 0) = T_u \tag{4.8}$$

$$Y_k(x = 0) = Y_{k,u} \tag{4.9}$$

$$\frac{dT}{dx}(x \to \infty) = 0 \tag{4.10}$$

$$\frac{dY_k}{dx}(x \to \infty) = 0 \tag{4.11}$$

In practice, the solution is obtained on a finite domain $0 < x < L$ that is sufficiently large that gradients are close to zero at the upstream and downstream boundaries. The model was implemented based on the Cantera `adiabatic_flame.py` example code. The solution technique is a modified Newton's method to implicitly solve for the steady state solution vectors $u(x)$, $T(x)$, $\rho(x)$, $Y_k(x)$, treating the mass flux $\dot{m}''$ as unknown (Felden, 2015; Bane, 2010).

An initial domain size w is set and discretized by N points at varying intervals. Once a solution is found on the initial domain, the grid is automatically refined near regions with large gradients, the initial domain size is increased if needed and the equations are again solved on the new domain. Using this method, convergence is sensitive to the initial conditions and solver settings. For the n-hexane/oxygen/nitrogen mixtures studied here, convergence issues only became apparent for cases with low flame speeds ($S_L \lesssim O(1$ cm/s)) or high initial temperatures ($T_u \gtrsim 930$ K). For low S_L the corresponding flames required exceedingly large domain sizes w for convergence resulting in prohibitively large computing times for convergence. Cases with $S_L \lesssim O(1$ cm/s) are also likely not physically relevant since the flame competition with buoyancy and surface curvature become so large that flame instabilities set in (as observed in Section 3.5) and the representation of such cases with a 1D flat flame speed is no useful. At high initial temperatures the gas also had a tendency to autoignite within the unburned domain region such that the unburned state and zero gradient boundary conditions could not be maintained and solutions for these cases could not be found.

Nevertheless this approach was found to be useful and robust for to evaluate a wide range of conditions varying the unburned gas conditions (T_u, P_u, β (through $Y_{k,u}$). A limited number of conditions for hydrogen/air, ethylene/air, and n-hexane/air at various equivalence ratios (ϕ) were also performed for validation and comparison with previous work. An example of the corresponding temperature ($T(x)$) and selected species ($Y_k(x)$) profiles for one mixture are plotted in Figure 4.1.

Here the location of the flame front in x and the width of the domain are arbitrary. These depend on the solution method for discretizing and refining the domain.

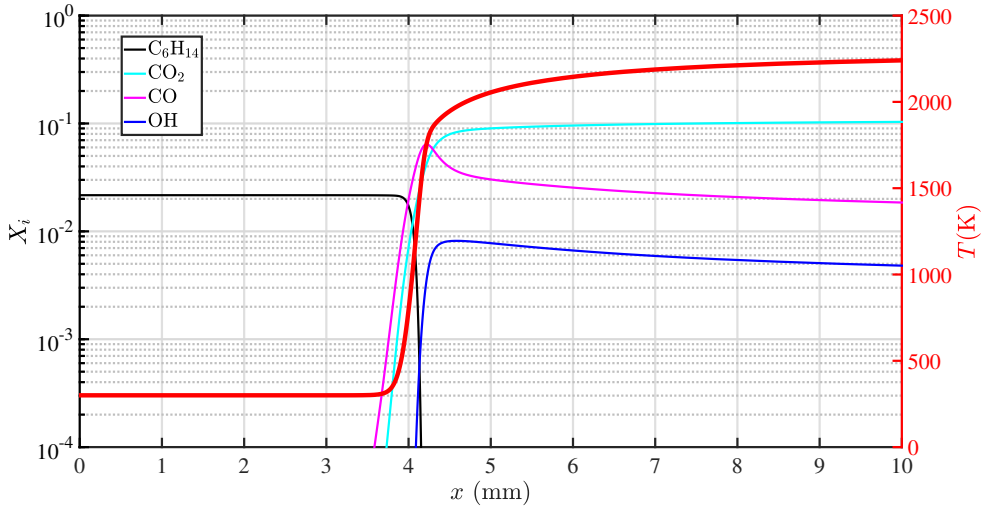

Figure 4.1: Typical structure of a converged solution for the 1D flame model.

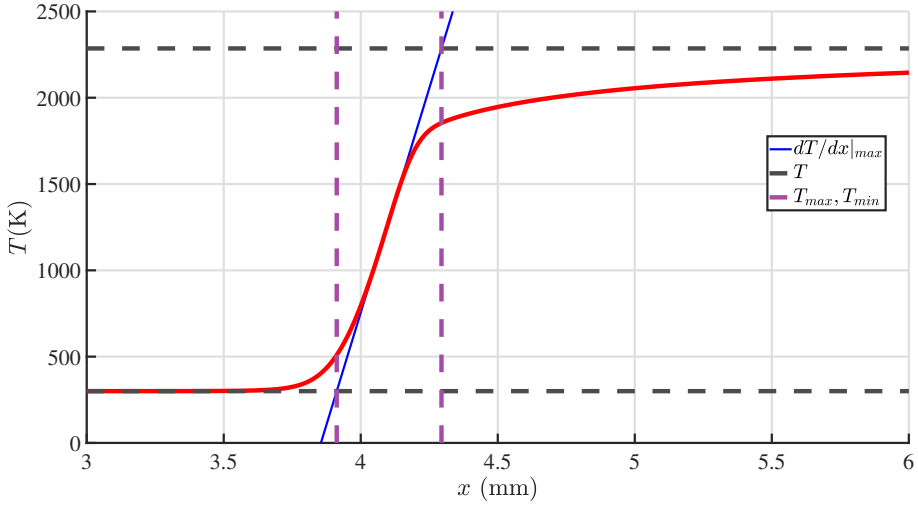

Figure 4.2: Graphical construction of the 1D flame thickness presented in the current work. Equation (4.12) can be derived from this.

The adiabatic flame temperature corresponded to the maximum temperature in the domain, $T_{ad} = T(x \rightarrow \infty = T_{max})$ which is also the burned gas temperature T_b. The temperature profile was also used to extract a flame thickness via the maximum derivative method. The construction is shown graphically in Figure 4.2 and the resulting equation is shown:

$$l_f = \frac{T_{max} - T_{min}}{\left(\frac{dT}{dx}\right)_{max}} \tag{4.12}$$

where the subscripts *max* and *min* refer to the maximum and minimum values respectively. S_L, l_f,

and T_{ad} are useful for data interpretation of the low pressure and nitrogen dilution experiments in Chapter 3 as well as for modeling attempts to correlate flame properties with ignition thresholds.

4.2.1 Simplified Laminar Flame Theory: One-Step Model

In order to gain insight into the factors governing S_L and l_f it is useful to first develop an analytical solution to the governing equations for a highly simplified case. Such simplified models are presented in many combustion textbooks and the approach here loosely follows that of Turns (1996). A model with one-step chemistry is employed which is useful in providing a means to obtain analytical expressions for S_L and l_f which clearly illustrate the important dependent variables in flame modeling. We begin by making the following additional simplifying assumptions to further reduce Equations (4.1) to (4.3) such that analytical solutions are possible.

1. Unity Lewis numbers: $Le_k = \frac{\alpha}{D_k}$=1
2. Fickian diffusion: $j_k = -\rho D \frac{dY_k}{dx}$ so $D = D_k$
3. Identical heat capacities for all species: $c_p = c_{p,k}$
4. c_p = and λ are constant
5. Mixture is stoichiometric or lean such that fuel is completely consumed in the flame

where α is the thermal diffusivity ($\alpha = \frac{\lambda}{\rho c_P}$) and D is the mass diffusivity. Item 3 implies $\sum_k j_k c_{P,k} \frac{dT}{dx}$ =0 since by definition $\sum_k j_k$ =0. Under these assumptions Equation (4.2) and Equation (4.3) become

$$\rho u \frac{dT}{dx} = \frac{d}{dx}\left[\rho \alpha \frac{dT}{dx}\right] - \frac{\sum_k h_{f,k} W_k \dot{\omega}_k}{c_P} \tag{4.13}$$

$$\rho u \frac{dY_k}{dx} = \frac{d}{dx}\left[\rho \alpha \frac{dY_k}{dx}\right] + W_k \dot{\omega}_k \tag{4.14}$$

Equation (4.13) and Equation (4.14) have the same form so the solutions will also be of the same form and differ only in the chemical source term. This means there is no need to solve both equations and we will focus our attention on the energy equation for the rest of the analysis. A one-step model as in Equation (4.15) can be employed for evaluating these terms.

$$\nu_F F + \nu_O O \rightarrow \nu_{\mathcal{P}} \mathcal{P}\,, \tag{4.15}$$

where the reactants F and O are the fuel and oxidizer respectively which transform directly into a product species P via a single exothermic reaction. The number of moles of species k in the balanced reaction are given by ν_k. The molar production rates of each species $\dot{\omega}_k$ can be expressed using Equation (4.16)

$$\dot{\omega}_k = K(T)[F]^{n_F}[O]^{n_O}\,, \tag{4.16}$$

where care must be taken in defining the sign of this rate which is negative for reactants and positive for products. We will further assume an Arrhenius form of the rate constant

$$K(T) = A\exp(-E/\tilde{R}T)\,, \tag{4.17}$$

where A is a pre-exponential factor and E is the activation energy. The molar production rates are related to the mass production rates (in units of kg/m^{3}s) through the molecular weight W_k

$$\dot{\rho}_k = W_k\omega_k = W_K K(T)[F]^{n_F}[O]^{n_O}\,. \tag{4.18}$$

To satisfy conservation of mass, the mass of the reactants must equal the mass of the products so $W_F\nu_F + W_O\nu_O = W_\mathcal{P}\nu_\mathcal{P}$. If we set the fuel mass as unity in arbitrary units $m_F = W_F\nu_F = 1$, then in terms of mass $1 + m_O = m_\mathcal{P}$. This allows the mass production rates given by Equation (4.18) to be related as

$$\dot{\rho}_F = \frac{1}{m_O}\dot{\rho}_O = \frac{-1}{m_O+1}\dot{\rho}_\mathcal{P}\,, \tag{4.19}$$

where $\dot{\rho}_F$ is the mass rate of fuel production which is negative by definition since it is consumed in the reaction. With these definitions, the chemical source term in Equation (4.13) becomes

$$-\sum_k h_{f,k}W_k\dot{\omega}_k = -\left[h_{f,F}W_F\dot{\omega}_F + h_{f,O}m_O W_F\dot{\omega}_F - h_{f,\mathcal{P}}(m_O+1)W_F\dot{\omega}_F\right] = -W_F\dot{\omega}_F\Delta H_c\,, \tag{4.20}$$

where ΔH_c is the heat of combustion of the fuel

$$\Delta H_c \equiv h_{f,F} + m_O h_{f,O} - (m_O+1)h_{f,\mathcal{P}}\,. \tag{4.21}$$

This is also useful for defining the adiabatic flame temperature where with no external heat transfer all of the excess energy produced in the reaction goes into heating the products and we obtain Equation (4.22) where the burned gas temperature is the same as the adiabatic flame temperature $T_{ad} = T_b$.

$$T_{ad} \equiv T_b = T_u + \frac{\Delta h_c}{c_P(m_O + 1)} \tag{4.22}$$

We can now substitute Equation (4.20) in for the right most term in Equation (4.13) to obtain

$$\rho u \frac{dT}{dx} = \frac{d}{dx}\left[\frac{k}{c_P}\frac{dT}{dx}\right] - W_F \dot{\omega}_F \Delta h_c \,. \tag{4.23}$$

We can now integrate Equation (4.23) under the following boundary conditions where far upstream (downstream) the temperature is that of the unburned (burned) gas and the gradients go to zero far away from the flame.

$$T(x \to -\infty) = T_u \tag{4.24}$$

$$\frac{dT}{dx}(x \to -\infty) = 0 \tag{4.25}$$

$$T(x \to \infty) = T_b \tag{4.26}$$

$$\frac{dT}{dx}(x \to \infty) = 0 \tag{4.27}$$

For simplicity a linear temperature profile which brings the gas from T_u to T_b is assumed to occur over a small distance l_f which is equivalent to the flame thickness definition used in Equation (4.12). Performing the integration and using the definition of mass flux ($\dot{m}'' \equiv \rho u$)

$$\dot{m}''(T_b - T_u) = -\frac{W_F \Delta h_c}{c_P} \int_{-\infty}^{\infty} \dot{\omega}_F \, dx \,. \tag{4.28}$$

The limits of the remaining integral can be transformed into temperature since $\dot{\omega}_F$ is only nonzero in the small region l_f where the temperature gradient was assumed to be linear. Therefore

$$\frac{dT}{dx} = \frac{T_b - T_u}{l_f} \quad \text{or} \quad dx = \frac{l_f}{T_b - T_u} dT \,. \tag{4.29}$$

The remaining integral term becomes

$$\int_{-\infty}^{\infty} \dot{\omega}_F \, dx = \frac{l_f}{T_b - T_u} \int_{T_u}^{T_b} \dot{\omega}_F \, dT \,. \tag{4.30}$$

Substituting using Equations (4.16) and (4.17) yields an expression where all of the temperature dependence is captured in the Arrhenius rate term.

$$\frac{1}{l_f} \int_{-\infty}^{\infty} \dot{\omega}_F \, dx = \frac{A[F]^{n_F}[O]^{n_O}}{T_b - T_u} \int_{T_u}^{T_b} \exp(-E/\tilde{R}) \, dT \,. \tag{4.31}$$

Integrating this expression yields the final fuel production term which is condensed using $\bar{\dot{\omega}_F}$

$$\bar{\dot{\omega}_F} = -\frac{RA[F]^{n_F}[O]^{n_O}}{E(T_b - T_u)} [\exp(-E/\tilde{R}T_b) - \exp(-E/\tilde{R}T_u)] \,. \tag{4.32}$$

Equation (4.28) now becomes

$$\dot{m}''(T_b - T_u) = -\frac{W_F \Delta h_c}{c_P} l_f \bar{\dot{\omega}_F} \tag{4.33}$$

This is now one equation for two unknowns, $\dot{m}''$ and l_f. A second equation can be obtained by following the same integration procedure with Equation (4.13) over $-\infty < x < l_f/2$ and assuming $\dot{\omega}_F = 0$ over this region. This is somewhat reasonable to assume since the reaction rate is an exponential function of the temperature (as shown by Equation (4.17)) so the highest temperature region from $l_f/2 < x < \infty$ should contain most of the reaction. In reality this assumption is likely unrealistic in most cases but is useful for now in enabling further analysis. As a further consequence, the $\exp(-E/RT_u)$ term in Equation (4.32) is also dropped since the boundary at $x \longrightarrow -\infty$ contains no chemical reaction. Using the linear temperature profile we obtain new boundary conditions at $x = l_f/2$

$$\frac{dT}{dx}(x = l_f/2) = \frac{T_b - T_u}{l_f} \quad \text{and} \quad T(x = l_f/2) = \frac{T_b + T_u}{2} \,. \tag{4.34}$$

Integrating Equation (4.13) with these yields

$$\dot{m}'' \left(\frac{T_b + T_u}{2} - T_u \right) - k/c_p \frac{T_b - T_u}{l_f} = 0 \tag{4.35}$$

$$\dot{m}'' \frac{l_f}{2} - k/c_P = 0\,. \tag{4.36}$$

Simultaneously solving Equations (4.33) and (4.36) and recalling: $\alpha = \frac{\lambda}{\rho_u c_P}$, $S_L \equiv \dot{m}''/\rho_u$ and making use of Equation (4.22) ($\Delta H_c = (m_O + 1)c_P(T_b - T_u)$) and using Equation (4.32) yields

$$S_L = \left[\frac{2\alpha\tilde{R}(m_O + 1)A[F]^{n_F}[O]^{n_O}}{E\rho_u(T_b - T_u)} \exp(-E/\tilde{R}T_b)\right]^{1/2} \tag{4.37}$$

and

$$l_f = \frac{2\alpha}{S_L} \tag{4.38}$$

$$l_f = \left[\frac{2\alpha\rho_u E(T_b - T_u)}{\tilde{R}(m_O + 1)A[F]^{n_F}[O]^{n_O} \exp(-E/\tilde{R}T_b)}\right]^{1/2}\,. \tag{4.39}$$

Equations (4.37) and (4.39) illustrate the dependencies of S_L and l_f explicitly. The dependence's in this simplified model lie in the total mass of reactants $m_O + 1$, thermal diffusivity α, molar concentrations of fuel and oxidizer $[F]$ and $[O]$, reaction orders n_k, activation energy E, pre exponential factor A, and the mixture density ρ_u and temperatures T_b and T_u. The relationship in Equation (4.38) between flame speed, flame thickness, and thermal diffusivity indicated that the numerical simulation based on detailed chemistry should produce large flame thicknesses for low flame velocities and vice versa.

In Equation (4.37) the strongest functional dependence is through the Arrhenius factor's dependence on T_b. This dependence can also be viewed in terms of T_u since they are related via Equation (4.22). This term competes with the linear temperature difference term in the denominator but overall an increase in T_u or T_b will strongly increase S_L and decrease l_f. The pressure dependence comes in through α and ρ_u using the ideal gas law and depends on the reaction order. Turns (1996) gives the following functional dependencies for pressure and temperature in this model where fluid properties k, c_P, and α are evaluated at the average temperature between burned and unburned states ($\bar{T} = (T_b + T_u)/2$) and n is the overall reaction order.

$$S_L \propto \bar{T}^{0.375} T_u {T_b}^{-n/2} \exp(-E/2\tilde{R}T_b) P^{(n-2)/2} \tag{4.40}$$

$$l_f \propto \bar{T}^{0.375} {T_b}^{n/2} \exp(E/2\tilde{R}T_b) P^{-n/2} \tag{4.41}$$

(a)

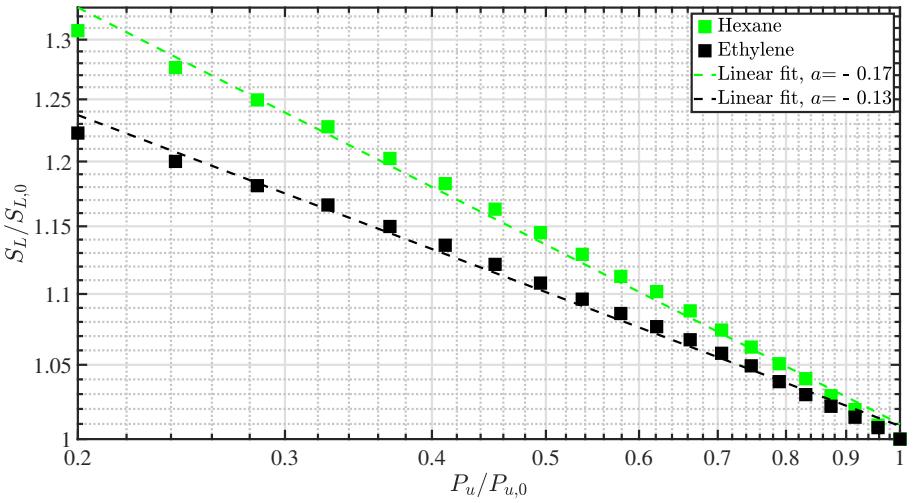

(b)

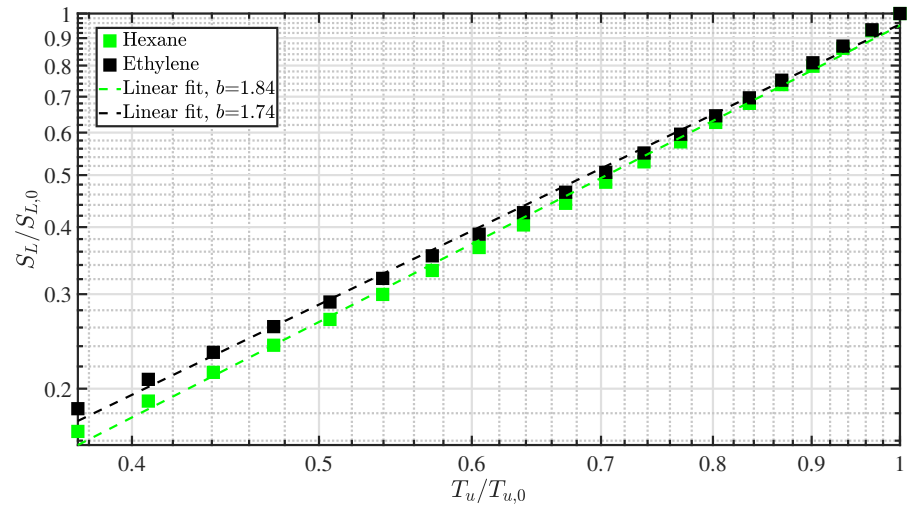

Figure 4.3: Computed laminar flame speed dependence on P_u and T_u for n-hexane and ethylene.

For binary reactions common in hydrocarbon combustion n is approximately two so it is expected that $l_f \sim 1/P_u$ and that S_L has little to no dependence on P_u. The dependence on nitrogen fraction β manifests through a decrease in the molar concentrations of fuel and a decrease in the total mass of fuel and oxidizer in the system. According to Equations (4.37) and (4.39) this should yield a weak power law dependence on β.

4.3 Modeling Results

4.3.1 Model Validation

Much experimental data exists on the laminar flame speed dependencies of P and T for many fuels but over relatively limited ranges compared to numerical capabilities particularly for large T_u (Metghalchi & Keck, 1982; Razus et al., 2000; Christensen et al., 2015; Lowry et al., 2011; Alekseev et al., 2017; Amirante et al., 2017). Most work on n-alkanes is focused on gaseous fuels like methane, ethane, ethylene, and propane, however some data exists for n-hexane over a range of pressures and temperatures (Coronel et al., 2013). Previous studies have found that the laminar flame speeds for a given equivalence ratio are similar across the range of n-alkanes from C_4 to C_7 (Davis & Law, 1998; Davis, 1998; Ji et al., 2010; Kelley et al., 2011). This is important since it suggests there exists some similarity in the dominant fuel oxidation pathways and diffusion process within the flame structure for large alkane fuels. This also implies that the dependencies on mixture properties for these fuels should also be similar and the experimental data available for all large alkanes should be useful for validation of the flame model and detailed kinetics for n-hexane air mixtures. Therefore the model validation is sought by comparison of with empirical trends of S_L with T_u and P_u. Studies have found that a reasonable empirical correlation can be found for most fuels using a power law formula of the following form:

$$\frac{S_L}{S_{L,0}} = \left(\frac{P_u}{P_{u,0}}\right)^a \left(\frac{T_u}{T_{u,0}}\right)^b \tag{4.42}$$

Table 4.1: Literature coefficients for pressure and temperature dependencies in Equation (4.42) for various fuels (values provided for stoichiometric fuel/air mixtures mixtures).

Name	Formula	a	b	Source
Hydrogen	H_2	0.26	1.26	Milton and Keck (1984)
		0.43	1.54	Iijima and Takeno (1986)
Methane	CH_4	-0.50	2.00	Andrews and Bradley (1972)
		-0.42	1.60	Iijima and Takeno (1986)
		-	1.68	Sharma et al. (1981)
Propane	C_3H_8	-0.17	2.13	Metghalchi and Keck (1980)
		-0.19	1.93	Milton and Keck (1984)
n-pentane	C_5H_{12}	-	1.43	CresciItelli et al. (1981)
n-hexane	C_6H_{14}	-0.24	2.02 [a]	Coronel et al. (2013)
iso-octane	iso-C_8H_{18}	-0.22	1.56	Gulder (1983)
Acetylene	C_2H_2	-0.06	2.00	Milton and Keck (1984)
Ethylene	C_2H_4	-	2.24	CresciItelli et al. (1979)
Propylene	C_3H_6	0.207	1.63	Razus et al. (2000)

[a] This value was not explicitly stated in Coronel et al. (2013) but obtained by fitting the data for $\phi = 0.9$.

Here the subscript 0 denotes a reference state $T_u = T_{u,0}$ and $P_u = P_{u,0}$ at which S_L is equal to a measured burning velocity $S_{L,0}$. The burning velocities of n-alkanes as a whole are well studied and some data can be found for n-hexane specifically (Davis and Law (1998) and Coronel et al. (2013) are examples). Lewis (1954) (reproduced in Gaydon and Wolfhard (1979)) showed that there is little variation in the pressure coefficient a among n-alkanes but that the coefficient is modestly dependent on $S_{L,0}$. Over the range of $S_{L,0} = 35 - 250$ cm/s a only varies from -0.1 to 0.1. For $S_{L,0}$ below this value there is an approximately linear decrease which can be extrapolated to approximately $a = -0.6$ for $S_{L,0} = 0$. For n-hexane in air at 1 atm $S_{L,0} = 37.97$ cm/s so the expected pressure dependence is $a \approx -0.05$. For ethylene in air at 1 atm $S_{L,0} = 62.87$ cm/s so $a \approx 0$. However in the model results shown in Figure 4.3 (a) these small values are not reproduced well. For n-hexane $a = -0.17$ and for ethylene $a = -0.13$ in this range.

There are clear differences between the correlations based numerical simulations and the values in Table 4.1. In part, this can be explained by the experimental methods used to obtain the data underlying these correlations. For example the pressure dependence correlation values in Gaydon and Wolfhard (1979) were measured using a spherical bomb technique. This consists of a centrally located electric spark ignition source in a spherical pressure vessel. The resulting unsteady flame propagates into unburned gas that is compressed and has a continuously increasing pressure and temperature. In addition, the spherical flame front propagation results in fluid strain (stretching) acting on the flame which must be compensated for in order to obtain the planar (unstretched) flame speed. Significant effort has been made in developing compensation methods and other techniques for measuring flame speeds but there is significant scatter in experimental data. A simple power law fit seems to be an oversimplification over a wide range of initial pressures where the pressure dependence seems to decrease for sub atmospheric pressures (see Andrews and Bradley (1972) for example). Nevertheless the general trend of a weak pressure dependence is well captured by the numerical simulation based on a detailed chemical reaction mechanism.

Christensen et al. (2015) found that detailed reaction models were generally consistent at predicting the temperature power exponent b even if deviations of the predicted flame speeds existed between models. Some data was available for n-hexane specifically and values of 1.4 - 2.3 are reported for other similar stoichiometric hydrocarbon air mixtures. Literature values of a and b for various fuels are listed in Table 4.1. This range of values agrees reasonably with the slopes fit to results in Figure 4.3 (b). For n-hexane $b = 1.86$ and for ethylene $b = 1.74$.

More abundant data is available for S_L as function of ϕ so these data were also used for direct validation with experimental values for n-hexane/air mixtures from Coronel et al. (2013) and Davis and Law (1998). Results are shown in Figure 4.4 and compare well with experimental data and previous modelling with the same JetSurf mechanism. Errors in digitizing Coronel et al.'s JetSurf

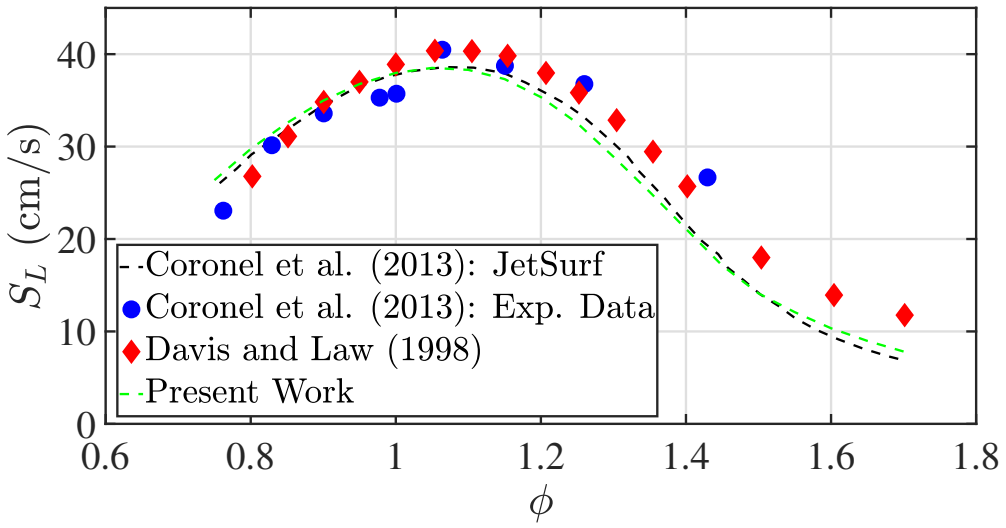

Figure 4.4: Comparison of current model with experimental and calculated S_L of n-hexane/air mixtures at standard initial conditions as a function of equivalence ratio ϕ.

curve and small differences in model inputs (T_u, P_u) are the likely reasons for the small deviations with the present work.

4.3.2 Detailed Model Results for $S_L = S_L(P_u, T_u, \beta)$ and $l_f = l_f(P_u, T_u, \beta)$

Single factor dependencies are shown in Figure 4.5 for both S_L and l_f for the mixture properties of interest. Both n-hexane and ethylene exhibit similar trends consistent with the experimental observations for hydrocarbon fuels (Davis & Law, 1998). As expected from the analysis in Section 4.2.1 and Equations (4.40) and (4.41) S_l has a weak negative dependence on P_u, a strong positive dependence on T_u, and a modest negative dependence on β. l_f has a strong negative dependence on P_u, weak negative dependence on T_u, and strong positive dependence on β. The numerical data are also well fit by a simple power law for each of these single parameter plots. Before proceeding with discussion of the overall parameter space, it is worth noting the limits of these simulations presented here and in the following sections.

For $T_u > 936$K or $\beta > 8$ and particular n-hexane mixtures, converged solutions could not be obtained. No pressure limitation was found for $P_u \geq 0.2$ atm. Failure to obtain convergence occurred for different reasons for large T_u and large β. Large values of T_u cause such rapid reaction in the region upstream of the burned gas that it is not possible to obtain a steady-state solution. This issue is illustrated in Figure 4.6 where a rapid change in the dependence of S_L on T_u is observed for $T_u > 930$ K. Examining the residuals, it is clear convergence cannot be obtained by this algorithm and the computed values of S_L are incorrect at these conditions. For $T_u > 1250$ K, the algorithm fails on the first step. By contrast, for highly diluted mixtures (large β), the flame speeds become

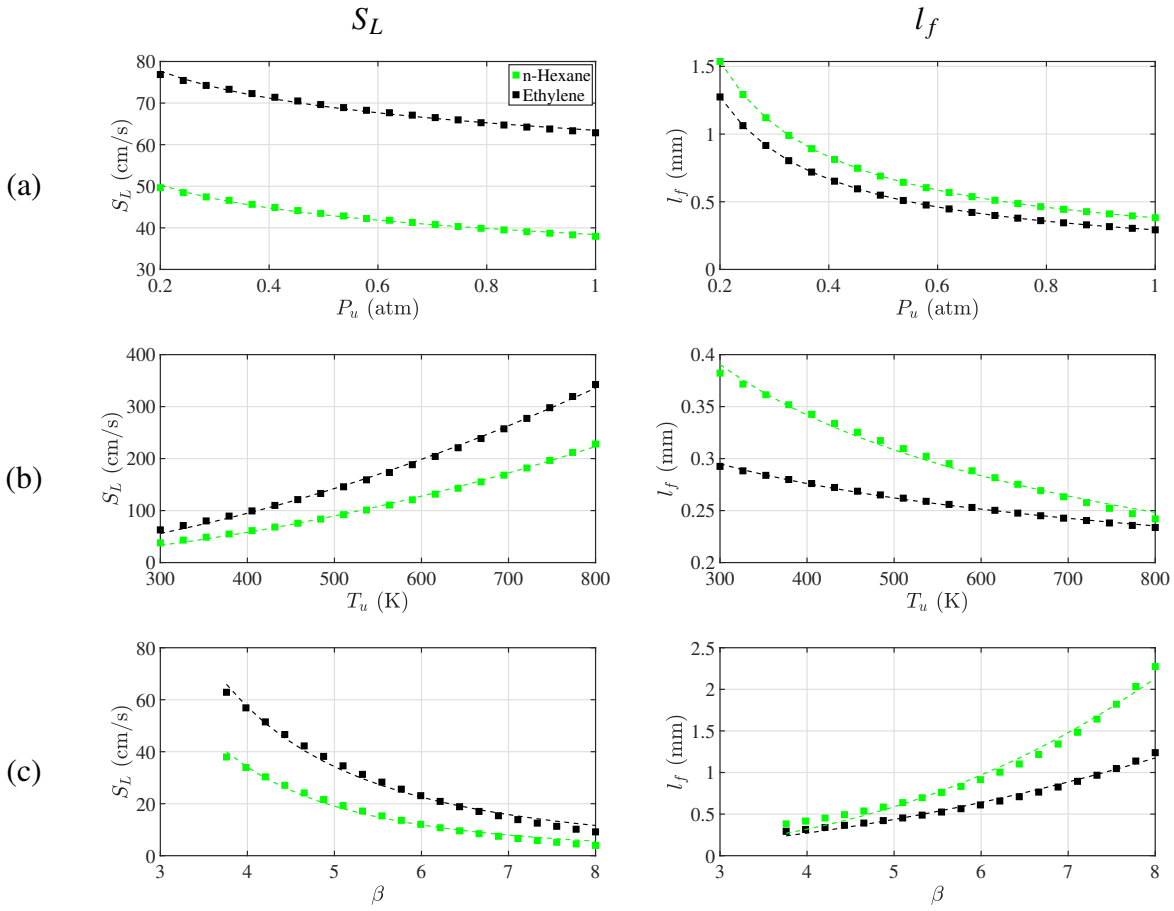

Figure 4.5: Single-factor dependence of S_L and l_f on (a) P_u (T_u = 300 K, β = 3.76) (b) T_u (P_u = 1 atm, β = 3.76) and (c) β (T_u = 300 K, P_u = 1 atm) for n-hexane and ethylene air mixtures. The symbols are data from the numerical simulations and the dashed lines are power law fits.

so low (< 5 cm/s) and thicknesses so large (> 3mm) that the domain size and number of grid points needed to solve the steady state problem becomes prohibitively large in order to obtain convergence. As a consequence, the numerical simulation results are restricted to $T_u \leq 936$ K and $\beta \leq 8$.

Figure 4.7 (a) and (b) show results for both S_L and l_f across the $P_u - \beta$ parameter space at a fixed T_u =300 K. These plots represent a total of approximately 400 discrete simulations across the parameter space and the axes are scaled to match each other. These data were then fit with polynomial surfaces to obtain the smooth contours illustrated in Figure 4.7. These plots illustrate the coupled nature of the S_L and l_f where the leftmost region of the parameter space corresponds to large S_L and small l_f while the opposite is true for the rightmost region. The relationship between S_L and l_f is not exactly inverse, because the pressure dependence has the same sign as seen in Figure 4.5 (a). Figure 4.7 (a) shows the order of magnitude decrease in S_L as mixtures are diluted from normal air β = 3.76 to β = 8. The decrease of S_L with pressure is again shown to be modest

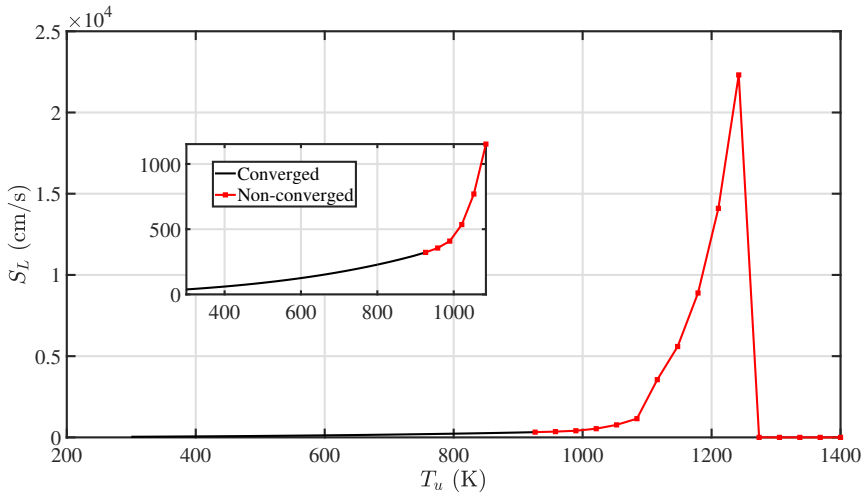

Figure 4.6: Illustration of convergence issues when excessively large values of T_u are used. For $T_u > 930$ K the cases are not converged.

especially compared to the effect of β. These effects also appear to be entirely independent as is expected. Figure 4.7 (b) shows that both effects are significant for l_f but that β is again the stronger effect with the combined low P_u and high β cases producing the thickest flames that were computed in this work. This corner region doesn't correspond to the absolute lowest S_L but is close.

Figure 4.8 shows results in the $T_u - \beta$ parameter space and contains four rows corresponding to four fixed values of P_u which are the same as those used in the experiments of Chapter 3. The left column contains plots of S_L and the right contains plots of l_f. Again each plot represents approximately 400 discrete simulations which have been fit by polynomial surfaces for smoothing. In these plots the inverse relationship of S_L and l_f is clear as the contours follow a similar character for a fixed pressure. For example in Figure 4.8 (a) the top left corner corresponds to the largest values of S_L and the smallest values of l_f. Progressing towards the lower right corner of the plot,

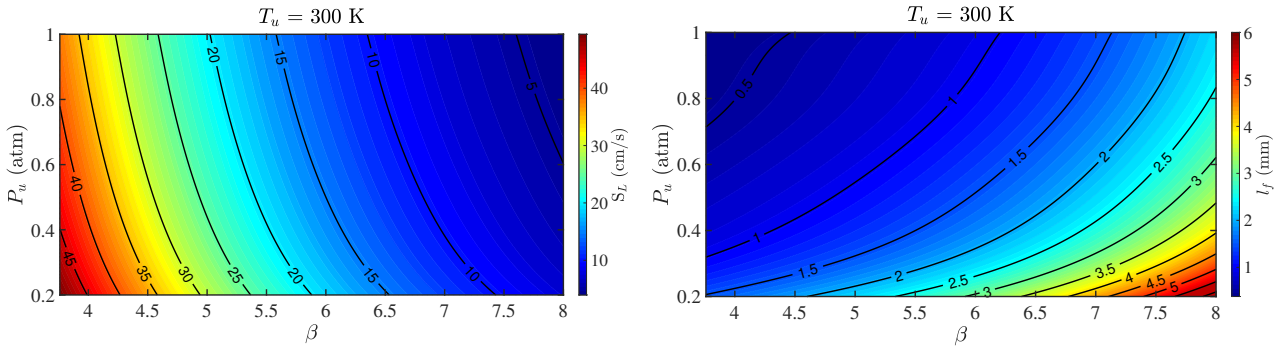

Figure 4.7: 2D colormap and contours of flame thickness for stoichiometric n-hexane air flame in the P-β parameter space (T_u = 300 K is constant).

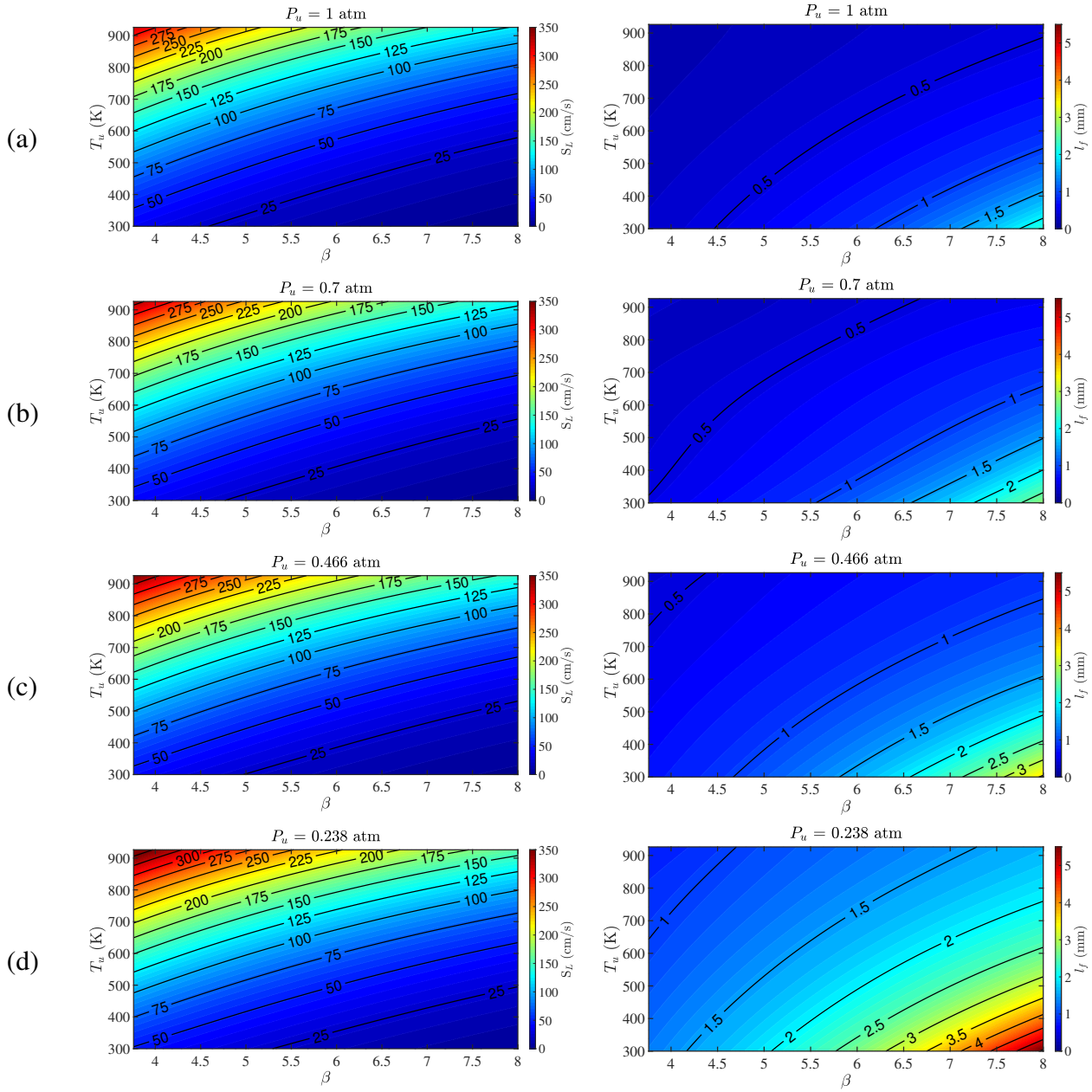

Figure 4.8: Contour plot of S_L for stoichiometric n-hexane/O_2/N_2 mixtures in the $T_u - \beta$ parameter space for (a) $P_u = 1$ atm (b)$P_u = 0.7$ atm (c) $P_u = 0.466$ atm (d) $P_u = 0.238$ atm.

S_L decreases while l_f increases until the corner is reached and the smallest S_L corresponds to the largest l_f. This is the same trend seen in Figure 4.8 (b) (c) and (d) which indicates that for a fixed pressure the relationship between S_L and l_f is inversely proportional and similar at all pressures.

4.4 Thermal Ignition Correlation Using 1D Flame Properties

In order for an ignition kernel to form in the boundary layer next to a heated surface, the kernel must develop at a sufficient distance from the surface so that the heat losses to the surface are sufficiently smaller than the heat release due to reaction. This process can be viewed as a competition between timescales for chemical reaction and timescales for heat loss close to the surface. The ignition kernel grows rapidly and develops into an expanding flame which propagates through the test gas in the explosion vessel and produces a measurable pressure and temperature rise. This process can again be viewed as a competition between timescales of energy release in the flame front and heat loss processes during flame propagation. The goal in this section is to compute these timescales using the 1D flame properties computed in this chapter and to relate the ignition and explosion processes to these timescales.

4.4.1 Time and Length Scales for Ignition and Flame Propagation Processes

The rate of chemical energy generation is typically described via the use of an ignition delay time τ_{ign} which can also be computed using detailed kinetics in a zero-dimensional, constant-pressure adiabatic explosion in Cantera. Alternatively a chemical timescale can be computed from the 1D flame properties directly as the ratio of the flame thickness and flame speed ($\tau_{flame} = l_f/S_L$). This is a characteristic timescale for the flame propagation and describes the time for the flame to propagate a distance of l_f. Using Equation (4.38) one can also find that $\tau_{flame} = l_f^2/(2\alpha) = 2\alpha/S_L^2$ which implies that only one flame quantity is actually needed along with an appropriate α to compute this timescale. However this result was developed from a highly simplified model using one-step kinetics and it is likely not enough in reality to relate l_f and S_L in such a simple way. It is also unclear at what conditions α should be evaluated for this relation to hold in practice. Thus the direct relation $\tau_{flame} = l_f/S_L$ and τ_{ign} are the two chemical timescales considered here for attempts at ignition data correlation.

There are several ways to characterize heat losses during kernel formation and flame propagation. A flame thermal diffusion timescale can be defined using the flame thickness and thermal diffusivity α_w evaluated at the wall ignition temperature, $\tau_{diff,flame} = l_f^2/\alpha_w$. It will be shown later by comparison with model data that this is indeed distinct from the τ_{flame} that would be computed from Equation (4.38). In the hot surface ignition, the heat transfer within the thermal boundary layer defines a characteristic thickness. It has been observed in studies of thermal ignition problems of premixed mixtures that the ignition kernel forms near the surface, typically where the thermal layer is thickest. In the case of a laminar boundary layer over a vertical hot surface, the thickest region is at the top of the surface. The thermal layer profile for a vertical cylinder can be measured experimentally using interferometry (in a nonreactive flow such as 100% N_2 atmosphere as described in Section 3.3.3 and Jones (2020)), or using CFD with an inert mixture. Using ignition data for

diluted low pressure mixtures from Chapter 3, the properties of the steady-state natural convection boundary layer profiles at the point of ignition are computed by setting the wall temperature equal to that corresponding to ignition for a given mixture. Results of such simulations and simpler models based on similarity solutions (Jones, 2020) for a vertical flat plate presented in Chapter 1 are in reasonable agreement with the interferometer measurements. From the similarity models of laminar natural convection on a vertical flat plate, the thermal boundary layer thickness dependence on height x is given by

$$\delta_T = \eta_{\delta_T} \left(\frac{4 T_\infty \nu_\infty^2}{\Delta T g} \right)^{1/4} x^{1/4}, \tag{4.43}$$

where η_{δ_T} is the value of the similarity variable used to define the edge of the thermal boundary as discussed in Chapter 1. This relationship is approximate as it is based on the linearized (Boussinesq model) version of the buoyancy term in the momentum equation. The detailed analysis of Jones (2020) showed that the result of the approximate Boussinesq analysis in Equation (4.43) gives the correct trends and is useful for estimating δ_T with modest errors for large ΔT.

The boundary layer thickness is evaluated using Equation (4.43) by assuming the ignition location is at the top of the hot cylinder $x = H$. This length scale can be used to define the extent of the region in which ignition can take place as well as the magnitude of the thermal gradient near the wall. Combining this with the thermal diffusivity produces a timescale for diffusion of thermal energy in the wall-normal direction, $\tau_{diff,BL} = {\delta_T}^2/\alpha$. Here α could be reasonably evaluated at the wall temperature or at the film temperature $T_{film} = (T_w + T_\infty)/2$. However the ignition location is exceedingly close to the hot surface so the wall temperature is the most relevant temperature and should be chosen for this property evaluation. The ignition takes place so close the surface that the convective motion is unimportant during the ignition transient and the flow velocity in the boundary layer and associated convective time scale are also irrelevant during the ignition event. In the experiments described in Chapter 3, the variation in gas composition and observed variation in ignition temperature will result in modest variations in δ_T. The most significant changes will be due to the pressure dependence of $\nu_\infty \propto P^{-1}$ which implies that all other factors being the same $\delta_T \propto P^{-1/2}$.

Additional timescales become relevant as the flame expands into the bulk gas and heat losses during this process will significantly influence the pressure history. The characteristic time needed for a laminar flame to propagate throughout the vessel is $\tau_{prop,flame} = V^{1/3}/S_L$ where $V^{1/3}$ is a characteristic vessel length scale. From experimental data, a characteristic propagation time can be estimated as the maximum pressure rise rate normalized by some reference pressure like the ambient or peak pressures. If we normalize using the ambient fill pressure P_0, then $\tau_P = P_0/(dP/dt_{max})$.

Table 4.2: Time scales for chemical, heat transfer, and pressure transients during ignition and flame propagation.

$$\text{Chemical}: \quad \tau_{ign} \sim \exp(E/\tilde{R}T), \quad \tau_{flame} = \frac{l_f}{S_L} \tag{4.44}$$

$$\text{Heat Transfer}: \quad \tau_{diff,flame} = \frac{{l_f}^2}{\alpha_w}, \quad \tau_{diff,BL} = \frac{{\delta_T}^2}{\alpha_w} \tag{4.45}$$

$$\text{Pressure}: \quad \tau_{prop,flame} = \frac{V^{1/3}}{S_L}, \quad \tau_P = \frac{P_0}{dP/dt_{max}}, \quad \tau_{P,FWHM} = FWHM(P_{explosion}) \tag{4.46}$$

The duration of the pressure transient also gives another characterization of the explosion time and can be quantified using the full width at have max (FWHM) of the pressure pulse, $\tau_{P,FWHM}$.

The various time scales are summarized in Table 4.2. Note that the ignition delay time scale is only notional and was actually computed using a detailed reaction mechanism as are the flame properties. The pressure time scales are computed from the experimental data.

All of the timescales of interest are summarized in Equations (4.44) to (4.46) and example magnitudes for these quantities are plotted in Figure 4.9. These timescales correspond to the experimental conditions for n-hexane with (a) β =3.76 (b) β =5.64, and (c) β =7.52. The four points on each individual curve correspond to the four ambient pressure conditions for the experiments. An appropriate choice of temperature is necessary to ensure the computed timescales are relevant to the problem at hand. For example for processes taking place close to the heated surface properties should be computed at some elevated temperature rather than the ambient gas condition of 300 K. Near the surface either T_{ign} or T_{film} are most appropriate. In Figure 4.9, τ_{ign} were computed using T_{ign}, S_L and l_f were evaluated at T_u = 800 K, δ_T was evaluated at the film temperature, and α was evaluated at T_{ign}. The only exception was $\tau_{prop,flame}$ where S_L was evaluated at T_u = 300 K. Evaluation of S_L and l_f at T_{ign} is not possible unless the model data is extrapolated beyond where converged solutions exist. Instead a well converged case of T_u = 800 K was chosen as representative of an elevated temperature close to the hot surface which is relevant to evaluating the chemical timescale in that region. τ_P and τ_{FWHM} were obtained using the experimental pressure traces presented in Figure 3.12.

Notably there is a large difference between the two chemical timescales at these temperatures, τ_{flame} is much smaller than τ_{ign} for all of the experimental conditions. τ_{ign} is the result of homogeneous explosion computation with no heat transfer or species diffusion in the lengthy induction period prior to explosion. τ_{flame} incorporates the effects of thermal and species diffusion so that reactions are occurring ahead of the flame under much higher temperature and radical concentrations, resulting

(a)

(b)

(c)

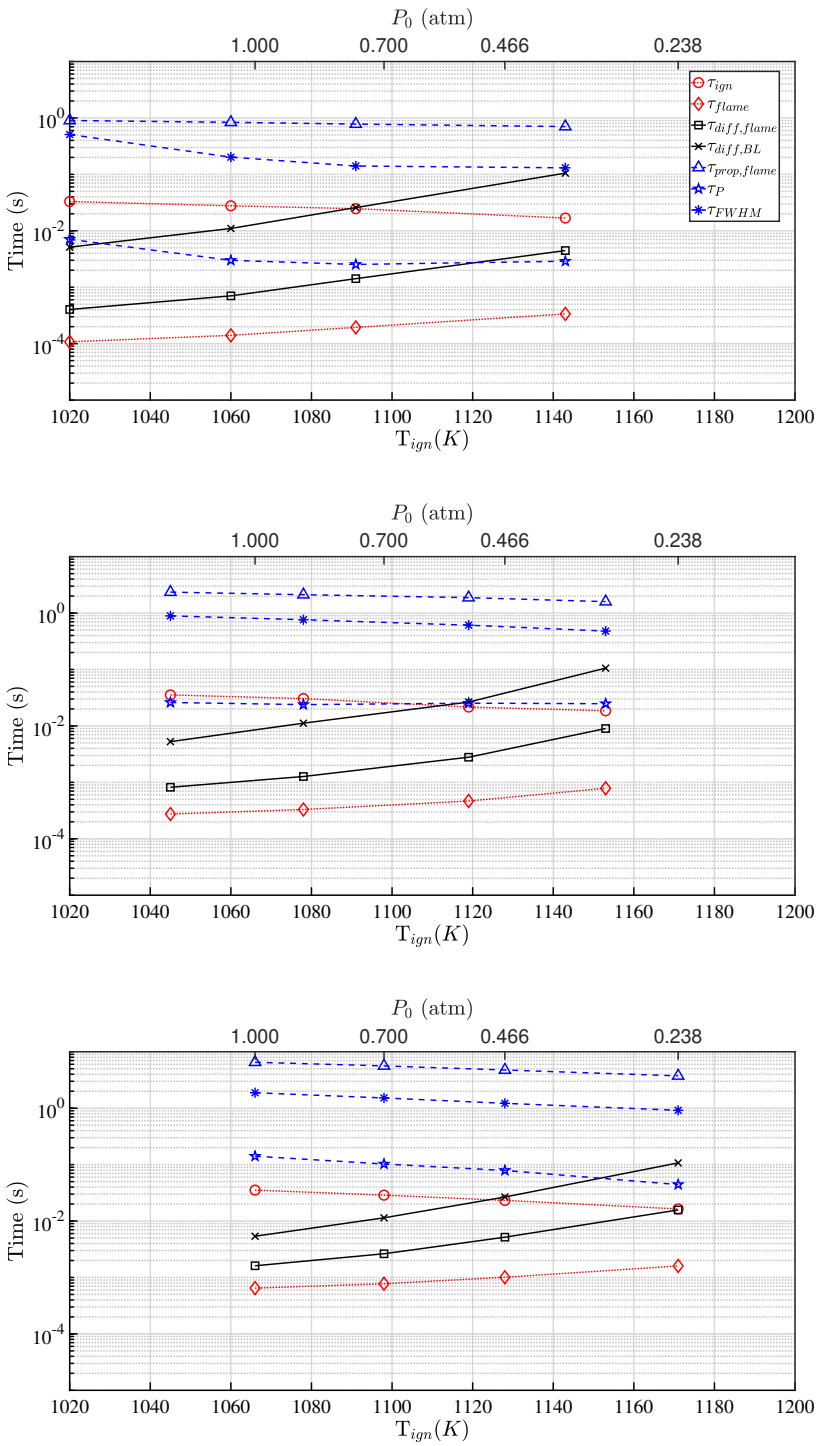

Figure 4.9: Comparison of timescales for n-hexane with with (a) β = 3.76 (b) β = 5.64, and (c) β = 7.52 for ignition conditions at range of pressures (1.0, 0.7, 0.466, 0.238 atm). The red, black, and blue lines correspond to chemical timescales in Equation (4.44), Equation (4.45), and Equation (4.46) respectively.

in significantly shorter characteristic times. The diffusion time scales are also relatively small and most comparable to τ_{flame} across all twelve conditions. Finally the timescales relevant to the flame propagation process and developed explosion pressure are all much larger than the other groups. This is not unexpected as the length and time scales involved in flame propagation and heat transfer throughout the volume are orders of magnitude larger that the local properties in the boundary layer or flame.

A nonlinear regression analysis was performed seeking a functional dependence of ignition thresholds and explosion properties on all of these timescales. Also included was a non-dimensional length scale which was formed using l_f and δ_T as the chemical and heat transfer length scales respectively. Independent variables used were a normalized wall temperature at ignition T^*=T_w/T_{ad} and the normalized peak pressure rise during the explosion, $P^* = (P_{AICC} - P_{max})/P_{AICC}$. A product series of each group parameterized by a power law exponent was used as the assumed functional form. For the ignition problem, an additional geometric factor of D/H was found to be useful in correlating ignition data from cylinders of different sizes than the 200A like those of Jones and Shepherd, 2020. The form of these fitting functions are shown in Equations (4.47) and (4.48).

$$T^* = B_1 \left(\frac{H}{D}\right)_1^d \left(\frac{lf}{\delta_T}\right)_1^c \prod_{\{\forall j > i\}} \prod_i \prod_j \left(\frac{\tau_i}{\tau_j}\right)^{b_1(i)} \tag{4.47}$$

$$P^* = B_2 \left(\frac{lf}{\delta_T}\right)_2^c \prod_{\{\forall j > i\}} \prod_i \prod_j \left(\frac{\tau_i}{\tau_j}\right)^{b_2(i)} \tag{4.48}$$

Here B_k, c_k, d_k and $b_k(i)$ are just fitting coefficients. An iterative procedure was performed using the function `lsqcurvefit` in Matlab to progressively eliminate irrelevant terms from the product. In regression of T^* data it was found that a single non-dimensional timescale (τ_i/τ_j) was sufficient to fully collapse the experimental data and eliminate all dependencies. That this is possible indicates that there are only two competing processes which describe the hot surface ignition problem fully. For P^* a satisfactory correlation was unable to be found using this approach. This is likely due to the large change in the relative importance of each of the physical processes across the range of pressures and diluted mixtures spanned by the data. These complications are not retained in the regression analysis in reducing to only one or two relevant time or length scales. Consequently only the T^* correlation is the focus of further discussion.

Results from this analysis are shown in Figure 4.10. T^* follows a linear trend with the non-dimensional parameter χ however a small intercept value is retained in rounding of the exponent values. This indicates that all dependencies of the independent variable have been accounted for in

the construction of the dependent variable. The additional inclusion of a relevant geometric factor (H/D) also enabled a good regression of other cylinder data from Jones and Shepherd (2020). This parameter is however a constant for the mixture varying data which all used the 200A cylinder and can be dropped to obtain the same regression fit for only the data from Chapter 3. All of the mixture variations in these data are accounted for in the other two terms, the non dimensional length and time scales.

The ratio of $\tau_{flame}/\tau_{diff,BL}$ was found to be the dominant competition underling the ignition process. This physically can be thought of as representing the competition between heat release and diffusive heat losses within the thermal boundary layer. τ_{ign} and $\tau_{diff,flame}$ were found to be relatively uncorrelated to the ignition data. τ_{ign} is relatively large at the wall temperatures and doesn't seem to be able to describe the much more rapid energy release which is described by an already burning flame and captured by τ_{flame}. Additionally $\tau_{diff,flame}$ is unimportant since the timescale for these losses are also comparatively large across the experimental conditions as shown by Figure 4.9.

This competition is also captured by the length scale ratio l_f/δ_T seemingly independently in χ. However by using the definitions of the timescales and rearranging terms it can be shown that χ is effectively a single non-dimensional parameter which depends only on α, l_f, S_L, and δ_T (neglecting the geometric factor)

$$\chi = 1.2\left(\frac{H}{D}\right)^{0.03}\left(\frac{\alpha^{1/4}l_f^{5/4}}{\delta_T^{3/2}S_L^{1/4}}\right)^{1/5} . \tag{4.49}$$

4.5 Summary and Implications for Explosion Testing

This chapter discussed a simplified one-dimensional model using detailed kinetics for flame propagation in gaseous mixtures. Analysis of a one-step kinetic model and literature experimental data for a range of fuels provided insight into the expected dependencies of flame properties. The detailed model was implemented in Cantera and various ambient mixture conditions evaluated to provide insight into the explosion properties observed in Chapter 3. One and two parameter functionality was presented for laminar flame speed (S_L) and flame thickness (l_f) as a function of the unburned gas conditions. Notably the strong dependence of flame speed on temperature illustrates clearly why the flame front is experimentally observed to rapidly and preferentially propagate in the boundary layer near the heated cylinders in Chapter 3. This is the region where there is a large thermal gradient and larger absolute temperature values than exist in the bulk gas. In the low pressure and nitrogen dilution data we also noted a significant decrease in the severity of the explosions namely in the peak pressure rise rate ($\frac{dP}{dt}_{max}$), peak absolute pressure (P_{max}) and duration of the pressure

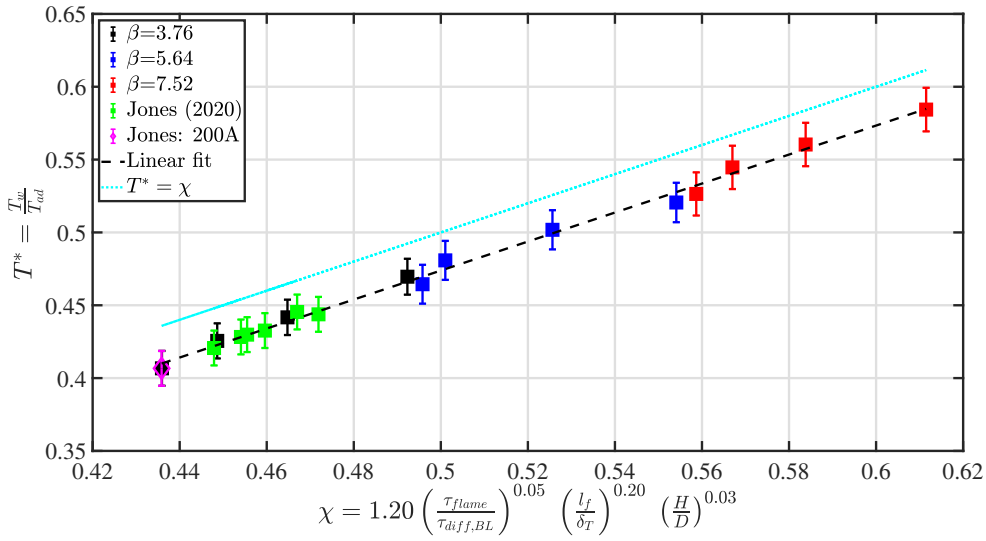

Figure 4.10: Regression fitting for cylinder ignition data with flame model and boundary layer properties. Note the linear fit has a slop of one with a small negative y intercept value.

transient (P_{FWHM}). This again is a consequence primarily of the flame propagation properties. The flame speeds are lower for nitrogen diluted cases which mean there is more time for heat losses to take effect and further decelerate the flame as it propagates. The mixtures also have less energy content per unit mass so overall result in lower flame temperatures and consequently pressure as observed in the experimental pressure traces.

A correlation with experimental ignition thresholds from Chapter 3 was achieved by considering the important timescales during both the ignition and flame propagation processes. A nonlinear regression analysis revealed that the ignition temperature (T^*) for these mixtures are able to be predicted by a single non-dimensional timescale and non-dimensional length scale parameter. Attempts to correlate the maximum pressure increase (P^*) using the same approach was found to be unpromising likely due to oversimplification of many competing processes. This is a useful development which enables the prediction of ignition thresholds from parameters extracted from a highly simplified flame model and the theoretical scaling of the laminar boundary layer developed around a hot surface. Such an approach could prove useful for correlating data from other hot surface ignition sources and other fuels. Additionally, since flame properties can be computed relatively easily even for highly detailed kinetic models, this presents a benefit to avoid use of a detailed ignition model in reactive CFD simulations models of complex geometries. This relation between purely thermodynamic quantities, flame properties, and boundary layer thickness to ignition thresholds should therefore prove useful for applying thermal ignition data obtained from idealized conditions and simplified geometries to more complex engineering designs of components in flammable leakage zones of aircraft and industrial facilities.

References

Alekseev, V., Soloviova-Sokolova, J., Matveev, S., Chechet, I., Matveev, S., & Konnov, A. (2017). Laminar burning velocities of n -decane and binary kerosene surrogate mixture. *Fuel*, *187*, 429–434. https://doi.org/10.1016/j.fuel.2016.09.085 (Cit. on p. 104)

Amirante, R., Distaso, E., Tamburrano, P., & Reitz, R. D. (2017). Laminar flame speed correlations for methane, ethane, propane and their mixtures, and natural gas and gasoline for spark-ignition engine simulations. *International Journal of Engine Research*, *18*(9), 951–970. https://doi.org/10.1177/1468087417720018 (Cit. on p. 104)

Andrews, G., & Bradley, D. (1972). The burning velocity of methane-air mixtures. *Combustion and Flame*, *19*(2), 275–288. https://doi.org/10.1016/S0010-2180(72)80218-9 (Cit. on pp. 104, 105)

Bane, S. (2010). *Spark Ignition: Experimental and Numerical Investigation With Application to Aviation Safety*. California Institute of Technology. (Cit. on p. 96).

Christensen, M., Nilsson, E., & Konnov, A. (2015). The temperature dependence of the laminar burning velocities of methyl formate + air flames. *Fuel*, *157*, 162–170. https://doi.org/10.1016/j.fuel.2015.04.072 (Cit. on pp. 104, 105)

Coronel, S., Mével, R., Vervisj-Kljakic, P., Boettcher, P., Thomas, V., Chaumeix, N., Darabiha, N., & Shepherd, J. (2013). *Laminar Burning speed of n-hexane mixtures* [Proceedings of th Eighth Join US Sections Meeting of the Combustion Institute, Park City, USA, May 21 2013.]. (Cit. on pp. 104, 105).

CresciItelli, S., Meli, S., Russo, G., & Tufano, V. (1981). Laminar Burning Velocity of n-Pentane-Methanol-Air Mixtures. *Chimica & L Industria*, *63*(2), 8–12 (Cit. on p. 104).

CresciItelli, S., Russo, G., & Tufano, V. (1979). Measurements of Laminar Burning Velocity in Closed Vessels - Near-Limit Mixtures. *Quaderni Dell Ingegnere Chimico Italiano*, *15*(5-6), 45–51 (Cit. on p. 104).

Davis, S. G., & Law, C. (1998). Determination of and Fuel Structure Effects on Laminar Flame Speeds of C_1 to C_8 Hydrocarbons. *Combustion Science and Technology*, *140*(1-6), 427–449. https://doi.org/10.1080/00102209808915781 (Cit. on pp. 104–106)

Davis, S. (1998). *An experimental and kinetic modeling study of the pyrolysis and oxidation of selected carbon (3-8) hydrocarbons*. Princeton University. (Cit. on p. 104).

Felden, A. (2015). CANTERA Tutorials: A series of tutorials to get started with the python interface of Cantera version 2.1.1. (Cit. on p. 96).

Gaydon, A. G., & Wolfhard, H. G. (1979). *Flames, their structure, radiation, and temperature* (4th ed. rev) ["A Halsted Press book." Includes indexes]. Chapman & Hall ; Wiley : Distributed in the U.S.A. by Halsted Press. (Cit. on p. 105).

Goodwin, D. G., Moffat, H. K., & Speth, R. L. (2017). *Cantera: An Object-oriented Software Toolkit for Chemical Kinetics, Thermodynamics, and Transport Processes* [Version 2.4.0]. https://doi.org/10.5281/zenodo.170284. (Cit. on p. 94)

Gulder, Ö. L. (1983). Laminar Burning Velocities of Methanol, Isooctane and Isooctane/Methanol Blends. *Combustion Science and Technology*, *33*(1-4), 179–192. https://doi.org/10.1080/00102208308923674 (Cit. on p. 104)

Iijima, T., & Takeno, T. (1986). Effects of temperature and pressure on burning velocity. *Combustion and Flame*, *65*(1), 35–43. https://doi.org/10.1016/0010-2180(86)90070-2 (Cit. on p. 104)

Ji, C., Dames, E., Wang, Y. L., Wang, H., & Egolfopoulos, F. N. (2010). Propagation and extinction of premixed C5–C12 n-alkane flames. *Combustion and Flame*, *157*(2), 277–287. https://doi.org/10.1016/j.combustflame.2009.06.011 (Cit. on p. 104)

Jones, S., & Shepherd, J. E. (2020). Thermal ignition of n-hexane mixtures by vertical cylinders. *Proceedings of the 13th International Symposium on Hazards, Prevention and Mitigation of Industrial Explosions (ISHPMIE 2020)* (Cit. on pp. 114, 115).

Jones, S. M. (2020). *Thermal ignition by vertical cylinders*. California Institute of Technology. (Cit. on pp. 110, 111).

Kelley, A., Smallbone, A., Zhu, D., & Law, C. (2011). Laminar flame speeds of C5 to C8 n-alkanes at elevated pressures: Experimental determination, fuel similarity, and stretch sensitivity. *Proceedings of the Combustion Institute*, *33*(1), 963–970. https://doi.org/10.1016/j.proci.2010.06.074 (Cit. on p. 104)

Lewis, B. (1954). *Selected Combustion Problems*. London. (Cit. on p. 105).

Lowry, W., De Vries, J., Krejci, M., Petersen, E., Serinyel, Z., Metcalfe, W., Curran, H., & Bourque, G. (2011). Laminar Flame Speed Measurements and Modeling of Pure Alkanes and Alkane Blends at Elevated Pressures. *Journal of Engineering for Gas Turbines and Power*, *133*(9), 091501. https://doi.org/10.1115/1.4002809 (Cit. on p. 104)

Metghalchi, M., & Keck, J. (1980). Laminar burning velocity of propane-air mixtures at high temperature and pressure. *Combustion and Flame*, *38*, 143–154. https://doi.org/10.1016/0010-2180(80)90046-2 (Cit. on p. 104)

Metghalchi, M., & Keck, J. C. (1982). Burning velocities of mixtures of air with methanol, isooctane, and indolene at high pressure and temperature. *Combustion and Flame*, *48*, 191–210. https://doi.org/10.1016/0010-2180(82)90127-4 (Cit. on p. 104)

Milton, B., & Keck, J. (1984). Laminar burning velocities in stoichiometric hydrogen and hydrogenhydrocarbon gas mixtures. *Combustion and Flame*, *58*(1), 13–22. https://doi.org/10.1016/0010-2180(84)90074-9 (Cit. on p. 104)

Razus, D., Oancea, D., & Ionescu, N. (2000). Burning velocity determination by spherical bomb technique. II: Propylene-air mixtures of various compositions, pressures and temperatures. *Revue Roumaine de Chimie*, *45*, 319–330 (Cit. on p. 104).

Sharma, S., Agrawal, D., & Gupta, C. (1981). The pressure and temperature dependence of burning velocity in a spherical combustion bomb. *Symposium (International) on Combustion*, *18*(1), 493–501. https://doi.org/10.1016/S0082-0784(81)80055-0 (Cit. on p. 104)

Turns, S. R. (1996). *An introduction to combustion: Concepts and applications*. McGraw-Hill. (Cit. on pp. 98, 102).

Wang, H., Dames, E., Sirjean, B., Sheen, D., Tango, R., Violi, A., Lai, J., Egolfopoulos, F., Davidson, D. F., Hanson, R. K., Bowman, C., Law, C. K., Tsang, W., Cernansky, N., Miller, D., & Lindstedt, R. (2010, September 19). *A high-temperature chemical kinetic model of n-alkane (up to n-dodecane), cyclohexane, and methyl-, ethyl-, n-propyl and n-butyl-cyclohexane oxidation at high temperatures, JetSurF version 2.0,* (Cit. on p. 94).

Chapter 5

CONFINED AUTOIGNITION TEST (CAT) FACILITY DESIGN AND ANALYSIS

5.1 Motivation and Design Considerations

The hot surface ignition experiments described in Chapter 3 and previous studies at Caltech with heated cylinders in cold atmospheres were limited to small surfaces and relatively large confining vessels (Jones & Shepherd, 2020; Boeck et al., 2017; Boettcher et al., 2013; Mével et al., 2016). Comparatively many industrial hazards have a larger range of hot surface sizes and extent of confinement. Larger surfaces will result in turbulent flow in the boundary layers next to the hot surface and confinement will result in recirculating flow within the vessel. Recirculation of the flammable atmosphere and entrainment into the boundary layer adjacent to the hot surface can result in significant slow reactant depletion prior to ignition. Furthermore, the interaction of the recirculating flow with the boundary layers, particularly on the hot wall, can result in turbulent motion not just within the boundary layer but throughout the vessel.

Review of studies by other researchers (discussed in Chapter 1) indicates a lack of systematic experiments with hot surface areas comparable to actual industrial ignition hazards. Sufficiently tall hot surfaces are anticipated to result in transitional and fully turbulent natural convection flows. Transition from laminar to turbulent flow in natural convection boundary layers on vertical heated surfaces is typically observed between $Ra_H = 10^8 - 10^9$ and $Ra_H \propto H^3$, where H is the surface vertical height. The effect of turbulent flow on thermal ignition thresholds has not previously been explored in a systematic fashion.

Also lacking are systematic studies on hot-surface ignition within confining combustion vessels with recirculation times sufficiently short such that there is substantial depletion of reactants prior to or entirely in place of classical rapid ignition events. Small vessel combustion testing typically consists of non-premixed liquid fuel injection into a hot gas volume, as in Chapter 2. Some studies have also been conducted on premixed, heated atmosphere and vessel ignition (Boettcher et al., 2012) at temperatures comparable to the AIT. In those tests there was a strong dependence of heating rate on ignition dynamics, especially timescales for fuel consumption, pressure rise, and temperature rise. Similar heating rate effects are also expected to occur with highly confined isolated hot surface and a cold atmosphere experiments.

The proposed Confined Autoignition Test (CAT) was designed to study these previously unexplored conditions. This chapter focuses on the design of this ignition testing facility which encompasses

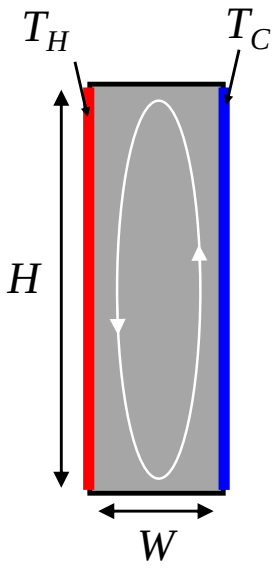

Figure 5.1: Schematic of buoyancy driven cavity flow problem with isothermal walls. For an annular channel $W = r_o - r_i$.

a relatively large range in heated surface heights H while enabling a wide range of flow regimes: laminar, transitional, and fully turbulent. This facility enables examination of the effects of turbulence, confinement, and heating rate. The test vessel consists of an axisymetric cavity formed by two concentric cylinders. The inner cylinder is heated via resistive heating in the same manner as described in Chapter 3. The outer cylinder walls are also cooled with water pumped via a NESLAB heat exchanger to maintain a cold isothermal boundary condition. The top and bottom walls are similarly cooled for this purpose and to protect the brazed joints on the inner cylinder ends as in Chapter 3. This configuration produces an axisymmetric variation of the classical buoyancy driven cavity flow with isothermal walls as illustrated in Figure 5.1.

Similar nonreactive natural convection flows have been explored extensively for relatively low temperature differences ($\Delta T = T_H - T_C$) and are typically characterized by three non-dimensional groups: aspect ratio ($A = H/W$), Prandtl number (Pr), and Rayleigh number (Ra_H) (or equivalently Grashof number Gr_H). Prandtl number is important for distinguishing gaseous from liquid-filled channels. Chenoweth and Paolucci (1986) explored this parameter space for the case of an enclosed square channel and found that a rich variety of flows can be achieved across this parameter space including fully developed independent boundary layers, interacting boundary layers, and turbulence. The extent of these flow regimes are shown in Figure 5.2. Note Chenoweth and Paolucci (1986) used Ra_W instead of Ra_H but their parameter space can be transformed using the relation $Ra_H = A^3 Ra_W$ as discussed later. For short cylinders (low Ra_H and small A) the flow is expected to be fully laminar and to produce steady secondary fluid motion in the channel. For long cylinders (high Ra_H and

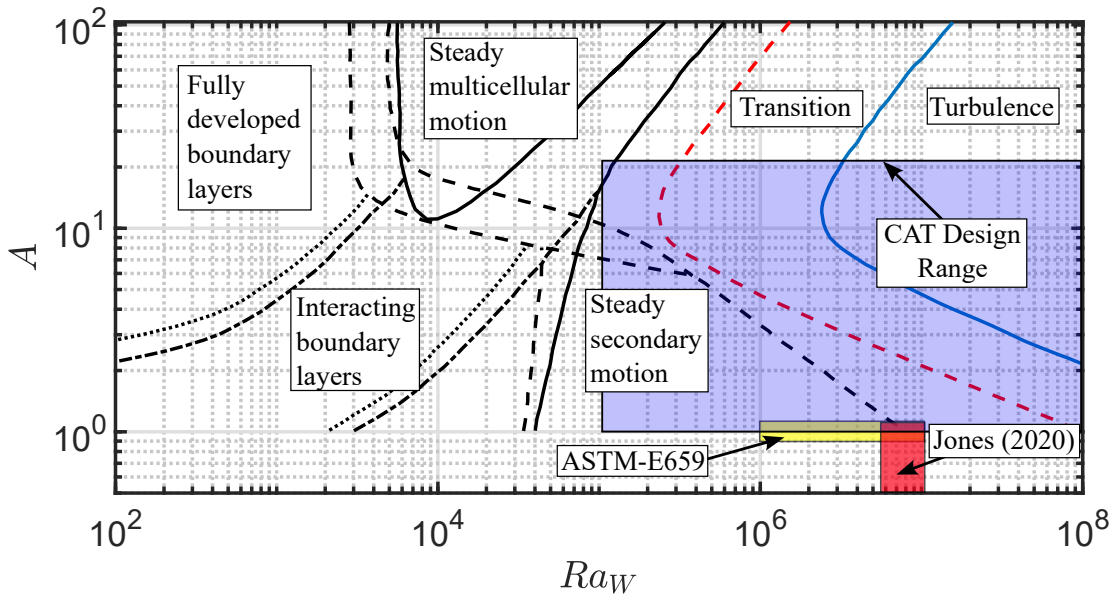

Figure 5.2: Reproduced parameter space results of Chenoweth and Paolucci (1986) plotted with parameter values for previous ignition experiments and planned design range for CAT.

large A) fully developed boundary layers transition to produce intricate recirculation patterns such as steady multi-cellular, counter-rotating vortex structures before transitioning to turbulence as Ra_H increases (Chenoweth & Paolucci, 1986). For the case of an enclosed annulus, the flow is also expected to be influenced somewhat by the curvature via the ratio d/D of the diameters of the heated cylinder (d) and confinement vessel (D) however was not studied systematically here. The nature of the flow is likely to influence the thermal ignition behavior of a flammable mixture due to the influence of the temperature history of a given fluid particle on the rate of reaction (Jones, 2020). Additionally the onset of boundary layer turbulence increases the boundary layer growth rate thus reducing thermal gradients and heat loss from gas phase reactions near the heated surface.

5.2 Design Targets for Non-dimensional Groups

The relevant design parameters are the Rayleigh (or Grashof) number

$$Ra_H = \frac{g\beta(T_w - T_\infty)H^3}{\nu\alpha}\,, \tag{5.1}$$

and the aspect ratio of the annulus

$$A = H/W\,. \tag{5.2}$$

Preliminary estimates of the required range of values for these parameters were based on the parametric study of Chenoweth and Paolucci (1986). Using the definition of A allows us to transform the original plot, Figure 5.2, for the A and Ra_W parameter space into A and Ra_H via

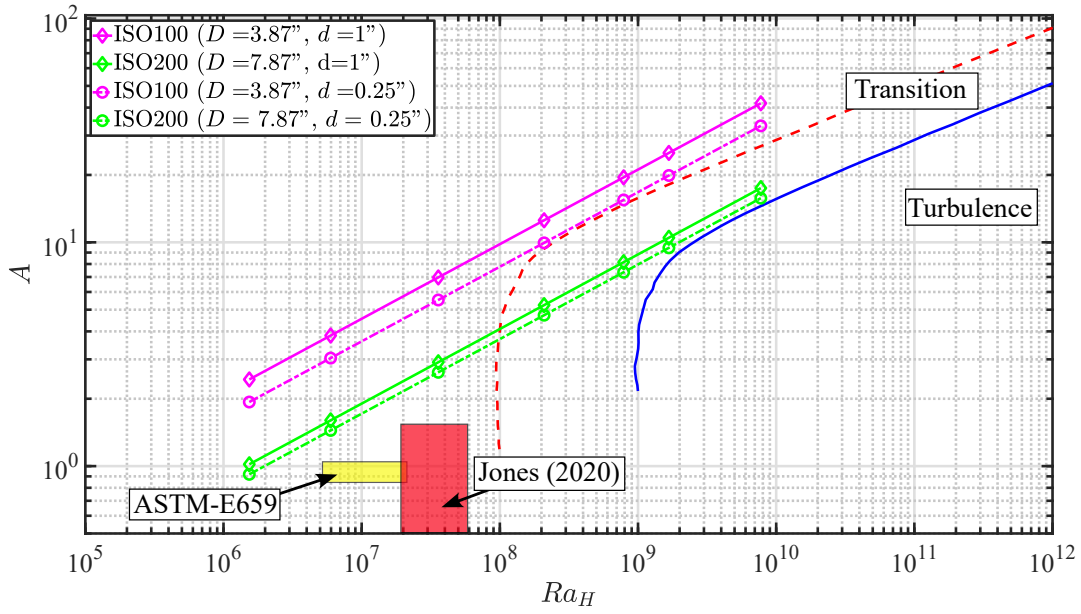

Figure 5.3: Preliminary design geometries for CAT plotted in the A-Ra_H parameter space. T_w =1100 K is used here with a range of H = 3.5 - 60 in. The narrow ISO100 and ISO200 tubes enable A and Ra_H values larger than those used by (Jones, 2020) by up to an order of magnitude. The "Transition" and "Turbulence" curves indicate respectively the approximate experimentally and numerically observed conditions for the onset and fully developed turbulent flow on vertical cylinders (Chenoweth & Paolucci, 1986).

the relation $Ra_H = A^3 Ra_W$. This is more appropriate as we intuitively expect H to be the key parameter determining the onset of turbulent flow in vertical natural convection. The resulting transformed parameter space is shown in Figure 5.3 together with the range of parameters used in previous studies.

From these plots it is clear that the previous study of Jones and Shepherd (2020) as well as other Caltech studies were in the laminar, low-aspect ratio regime. In order to test in the turbulent and/or high aspect ratio, the design target is therefore the upper rightmost region of the A and Ra_H parameter space. Our primary restriction here was designing a facility to fit vertically within the lab space (e.g. $H \leq 60$ in.). A limitation on the channel width was also necessary since some space is required to place instrumentation within the vessel in practice. Thus a minimum outer tube diameter of 3 in. is considered.

Modularity in the design was also desired and helpful for achieving a wide range of test conditions in a simple and economical manner. Standardized stainless steel vacuum tubes with ISO flanges were a source of inspiration for this and provided a source of sample dimensions to consider. Ultimately these were not used in the final vessel design due primarily to the uncertainty in the

ability of the sealing flanges to maintain integrity under impulsive pressure rise typical of an explosion. Dimensions corresponding to the ISO100 (ID = 3.87 in.) and ISO200 (ID = 7.87 in.) were used for reference here. The inner cylinder diameter also plays a small role in A and values of d = 0.25 and 1 in. were considered. Regions of the plot covered by these geometrical ranges are shown in Figure 5.3 with an assumed surface temperature of T_w = 1100 K. From this plot it is clear that the choice of inner cylinder radius has only a minimal effect on the experimental location in this parameter space and so was neglected for these considerations. It is also clear that even the nearly factor of 2 increase in channel width between the ISO100 and ISO200 tubes, there is only minimal difference in the aspect ratio for the cylinder heights of interest. Therefore only one vessel diameter needed to be designed for to cover the desired A range. Values of H considered here ranged from 3.5 to 60 in, and covered the laminar to turbulent transition region in the reference ISO channels. This range of heights also allowed A to be varied by more than an order of magnitude. It was anticipated that real world effects would enhance the turbulent transition process and enable full turbulence at lower Ra_H than predicted. Surface roughness due to oxide growth, boundary layer interactions with the unsteady flow produced during the initial transient heating period, and previously unconsidered effects of large temperature differences (non-Boussinesq flow regime) all enhance turbulence.

5.3 Heating Model for determination of Cylinder Dimensions

The first design challenge was to understand the feasibility of heating long cylinders to expected temperatures required for ignition testing. A target value of T_w = 1100 K was set for this effort which was based on experience with ignition experiments for similar mixtures and smaller cylinders (Chapter 3) A parametric study of a simple lumped-mass heating model was conducted assuming a similar resistive heating method as implemented in Chapter 3. The model treats the cylinder as a resistor with Joule heating imposed by an applied current and losses due to radiation, convection, and conduction. The goal of this analysis was to determine the range of geometries of hollow cylindrical tubes that can be heated to T_w = 1100 K using the previously implemented MagnaPower DC power supplies (XR5-600 and XR5-375) available in the laboratory. In addition to single power supply configurations, these units can also be arranged in series (parallel) to augment maximum supply voltage (current). The current (voltage) limitation is determined by the lowest value between the two supplies. Therefore with two units, we could construct three potential power sources to consider:

1. Single power supply (XR5-600): 600A/5V
2. Series (XR5-600 + XR5-375): 375A/10V
3. Parallel (XR5-600 + XR5-375): 975A/5V

The maximum voltage V and current I define the design constraints. The dependent design parameters of interest are the cylinder radius (r), wall thickness (t), and height (H). The relationship of the design parameters to the power supply constraints was determined using the heating model. The model was based on a power balance in Equation (5.3) and engineering models of the Joule heating and heat transfer processes implemented in Equation (5.4).

$$P_{in} = P_{convection} + P_{radiation} + P_{conduction} \tag{5.3}$$

$$I^2R = hA_s\left(T_w - T_\infty\right) + \sigma\epsilon A_s\left({T_w}^4 - {T_\infty}^4\right) + 2kA_c\overline{\frac{dT}{dx}} \tag{5.4}$$

Here I is the DC current supplied to the circuit, R is the resistance of the heated cylinder, h is the convective heat transfer coefficient, A_s is the heated surface area, T_w is the surface or wall temperature, T_∞ is the ambient temperature, σ is the Stefan–Boltzmann constant, ϵ is the surface emissivity, A_{cond} is the conductive heat transfer area, and k is the thermal conductivity. The conductive term is approximate, implementing an average temperature gradient ($\overline{\frac{dT}{dx}}$) based on previous work by Jones (2020) using one-dimensional models to define a length L_{edge} where the conductive losses are important. Jones found the conductive losses were confined to only the outermost 2-in. region on both cylinder ends in practice. Between these regions, the temperature reached a uniform value. The gradient was not constant over the end region, so a conservative modeling approach was taken by using a smaller L_{edge} value representative of the linear portion of the gradient. For the present analysis, L_{edge} = 1.5 in. This loss occurs on both ends which accounts for the factor of two because the conductive heat transfer area A_{cond} is defined for one end of the cylinder.

For modeling purposes, we consider a similar design as the cylinder in Chapter 3 which had a soldered copper plug on the tube ends used as contact surfaces for the support system. The cross-sectional area of these plugs in contact with the 304SS tube can be taken as A_{cond}, assuming good thermal contact via press fit and soldering. This contact area is shown schematically in Figure 5.4. The conductive losses are limited by the low thermal conductivity of 304SS at this contact joint, so this is the k used for modeling. The estimation of the conduction losses in the 200A cylinder is

$$P_{conduction} = 2k_{avg}A_{cond}\left(\frac{T_w - T_\infty}{L_{edge}}\right).$$

Using the parameter values

$$\begin{aligned} k_{avg} &= 20\ \mathrm{W \cdot m^{-1} \cdot K^{-1}}, \\ A_{cond} &= 8.17 \times 10^{-4}\ \mathrm{m^2}, \\ T_w - T_\infty &= 800\ \mathrm{K}, \\ L_{edge} &= 0.0381\ \mathrm{m}, \end{aligned}$$

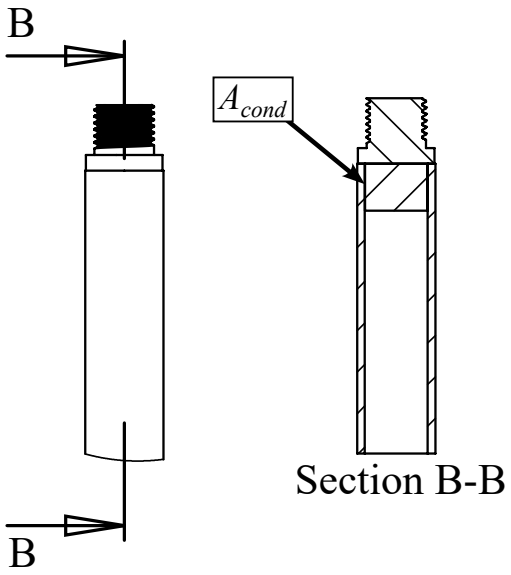

Figure 5.4: Surface area for end conductive losses.

the conductive losses are

$$P_{conduction} = 686 \text{ W} .$$

These conductive losses can be compared with Jones (2020) who estimated them to be approximately 200 W at each end (400 W total). This compares reasonably with the simplified and conservative approximation taken here. If the entire conduction region is used (L_{edge} = 2 in) then the estimate becomes $P_{conduction}$ = 515 W. A_{cond} is also likely overestimated in this model since the copper plugs are actually tapered away from the cylinder wall as seen in Figure 5.4. This large gap along with potential for regions of poor filling with the solder filler metal means the actual A_{cond} may be significantly smaller. The thermal conductivity is also a function of temperature, $k = k(T)$, and assuming a constant value here is also an approximation. An average value of $k_{avg} = (k(1100\,\text{K}) + k(300\,\text{K}))/2$ was used here. The thermal energy losses in Equation (5.4) are dominated by the radiation loss term for typical ignition values of T_w = 900 - 1100 K so that errors in the estimates of the conduction and convection losses do not significantly affect the model results. A constant value of A_{cond} corresponding to that of the 200A cylinder is assumed for simplicity and the value was refined to correspond to the final design of cylinder connections in Section 5.4.2.1.

The cylinder resistance can be computed by assuming a uniform temperature along the cylinder and across the thickness

$$R(T) = \frac{\rho_e(T)H}{A_c} . \tag{5.5}$$

The electrical resistivity is ρ_e, A_c is the cross-sectional area of the cylinder wall, and H is the cylinder height. The explicit dependence of ρ_e on temperature is important in this model since for

stainless steel in the temperature range 300 — 1100 K, the electrical resistivity increase by nearly a factor of two. A_c for a hollow cylindrical tube is given in Equation (5.6), assuming r is the outer radius and t is the wall thickness.

$$A_c = \pi r^2 - \pi(r-t)^2 = 2\pi rt - \pi t^2 \,. \tag{5.6}$$

For a thin-wall tube this can be approximated as

$$A_c = 2\pi rt \,. \tag{5.7}$$

The cylinder exterior surface area A_s is

$$A_s = 2\pi rH \,. \tag{5.8}$$

The total resistance can be expressed in term of the geometric parameters by substituting Equation (5.6) into Equation (5.5)

$$R(T) = \frac{\rho_e(T)H}{2\pi rt - \pi t^2} \,. \tag{5.9}$$

Finally substituting Equation (5.9) into Equation (5.4) and solving for I yields

$$I(r,t) = 2\pi r\sqrt{\frac{t}{\rho_e}\left(1-\frac{t}{2r}\right)}\sqrt{h(T_w - T_\infty) + \sigma\epsilon\left({T_w}^4 - {T_\infty}^4\right) + 2k_{avg}\frac{A_{cond}}{2\pi rH}\left(\frac{T_w - T_\infty}{L_{edge}}\right)} \tag{5.10}$$

where the dependence on r, t, and H have been made explicit. The dependence on H can be neglected except for short cylinders. Using Ohm's law, $V = IR$, to obtain the voltage drop across the cylinder allows us to substitute for $I = V/R$ in Equation (5.4) and solve for V. This yields equation Equation (5.11) with the dependence on r, t, and H written explicitly.

$$V(r,t,H) = H\sqrt{\frac{\rho_e}{t\left(1-\frac{t}{2r}\right)}}\sqrt{h(T_w - T_\infty) + \sigma\epsilon\left({T_w}^4 - {T_\infty}^4\right) + 2k_{avg}\frac{A_{cond}}{2\pi rH}\left(\frac{T_w - T_\infty}{L_{edge}}\right)} \tag{5.11}$$

The results can be simplified to give approximate scaling relationships for a thin-walled tube, neglecting conduction and convection losses. The current required to reach a given temperature is

$$I \propto r\sqrt{t} \,,$$

the voltage required is

$$V \propto \frac{H}{\sqrt{t}} \,,$$

and the total power required is

$$P_{in} = IV \propto rH \,.$$

The convective heat transfer coefficient h is estimated using the Nusselt number (Nu_H) correlation for laminar flow on a vertical cylinder (Boetcher, 2014).

$$Nu_H = -0.06211 + 0.5441 {Ra_H}^{1/4} + 0.6123 \left(\frac{H}{2r}\right) \quad 10^2 < Ra_H < 10^9 , \tag{5.12}$$

and the heat transfer coefficient is

$$h = \frac{k_f Nu_H}{H} , \tag{5.13}$$

where k_f is the film (average) temperature representative of the average conditions within the thermal boundary layer. Typical values of h for laminar flow are on the order of 1 to 15; at $Ra_H = 10^{11}$, turbulent flow is estimated to increase h by a factor of 2. The magnitude of the convection and radiation terms and the total power input in Equation (5.3) are shown in Figure 5.5. At typical ignition temperatures of 900 to 1100 K, the radiation heat transfer is clearly the dominant heat transfer mode with convection and conduction (not shown in the plot) an order magnitude lower. Transition to turbulent flow for the taller cylinders is expected to have a modest effect on the power balance that can be neglected for the purposes of sizing the cylinders and power supplies.

For metals, ϵ depends strongly on the degree of surface oxidation, oxide composition and surface temperature. From experience, we know that at the temperatures being targeted there is significant oxidation of 304 SS consisting primarily of a dark grey to black composition, presumably magnetite (Fe_3O_4). This is expected to yield a relatively high emissivity (ϵ = 0.7 - 0.95). The values of the coefficients h and ϵ used in the model can be adjusted using by comparison with data from testing

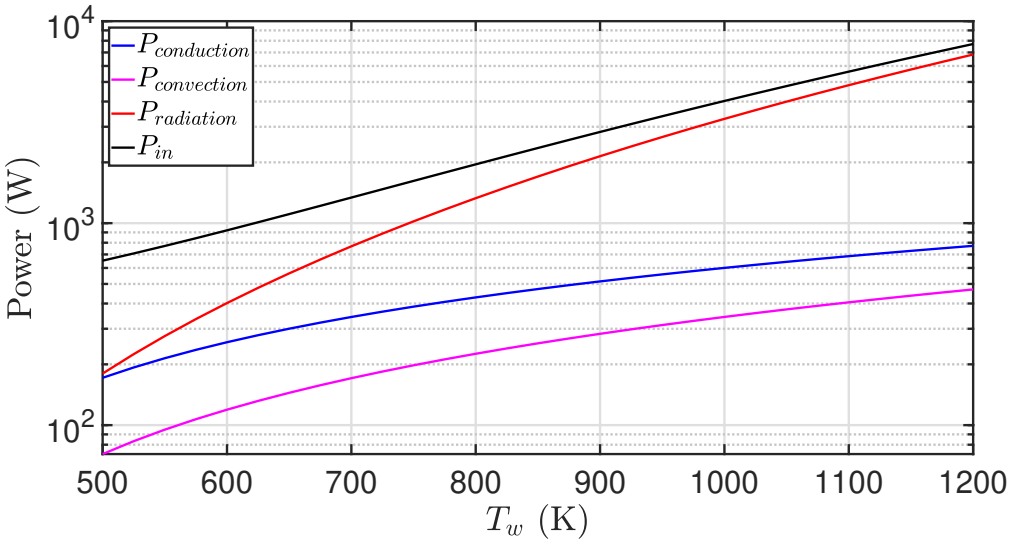

Figure 5.5: Comparison of input power, convective, conductive, and radiation loss terms for 36-in. tall, 1-in. diameter cylinder assuming laminar convection.

described in Chapter 3 using the measured I, V, T_w, and cylinder geometry (r,t,H). The results of the model with adjusted constants are shown in Figure 5.6.

5.3.1 Model Results

The geometric design space of this model can be understood using isosurfaces of constant I and V in 3D space where each axis represents a geometric parameter. This plot is shown in Figure 5.7. The intersection of an I isosurface and V isosurface bound the design space for a given power supply configuration. The volume "behind" the I surface and "under" the V surface give the geometric design space. For a fixed height, the parameter space can be visualized on a 2D plot with t and r as axes as shown in Figure 5.8. The region of these plots for which $t \geq r$ is not physical and left blank. Contours of constant I and V can be plotted in this space and we see that the geometric design space is bounded between the maximum I and V contours defined by the choice of power supply. The most restrictive geometry will be that with largest H we can select the largest H we want experimentally and find what cross-sections are possible in the corresponding 2D contour plot. From here we can find solutions matching available standard tubing dimensions from stainless steel suppliers. Here we find that for H = 36 in., a tube with r = 0.25 in. and t = 0.049 in. is in the design space so we choose this for the CAT design. This is a standard size available in 6-ft lengths of 304 stainless steel.

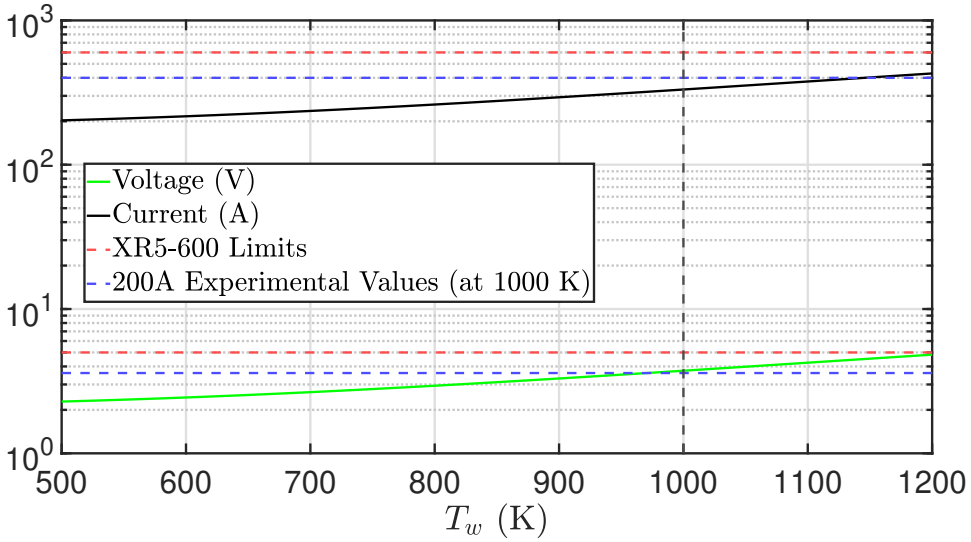

Figure 5.6: Validation of heating model using testing data obtained in 200A cylinder experiments.

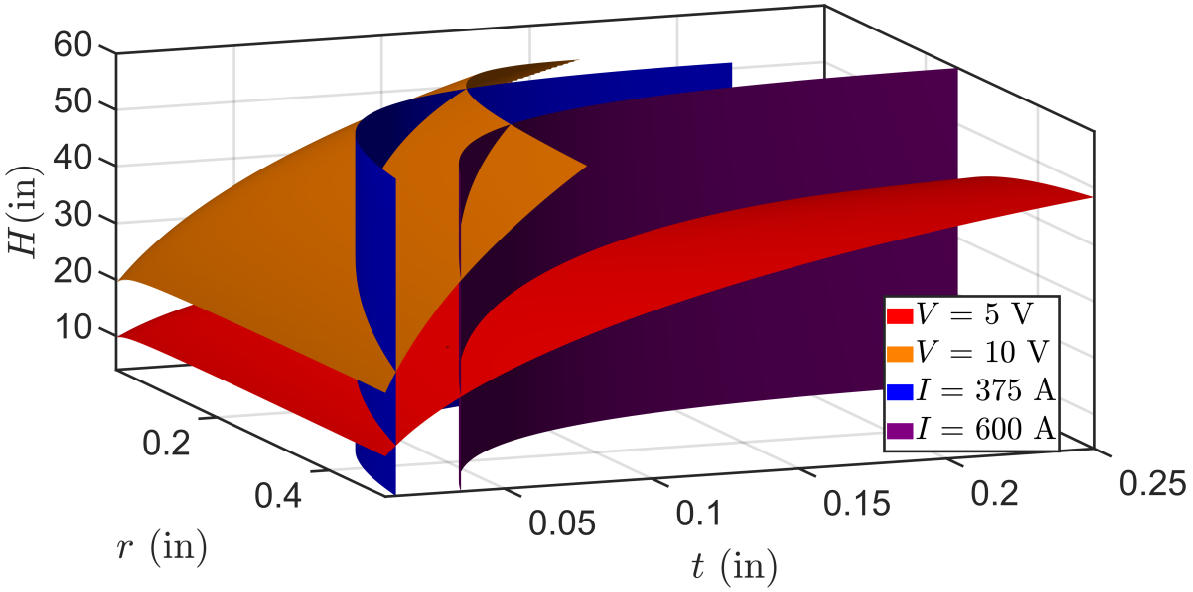

Figure 5.7: Contour plots of constant I and V as a function of the three geometric parameters: r, t , H. The intersection of any I and V surfaces give the bounding surface for the use of the corresponding power supply configuration. Here T_w = 1100 K was used.

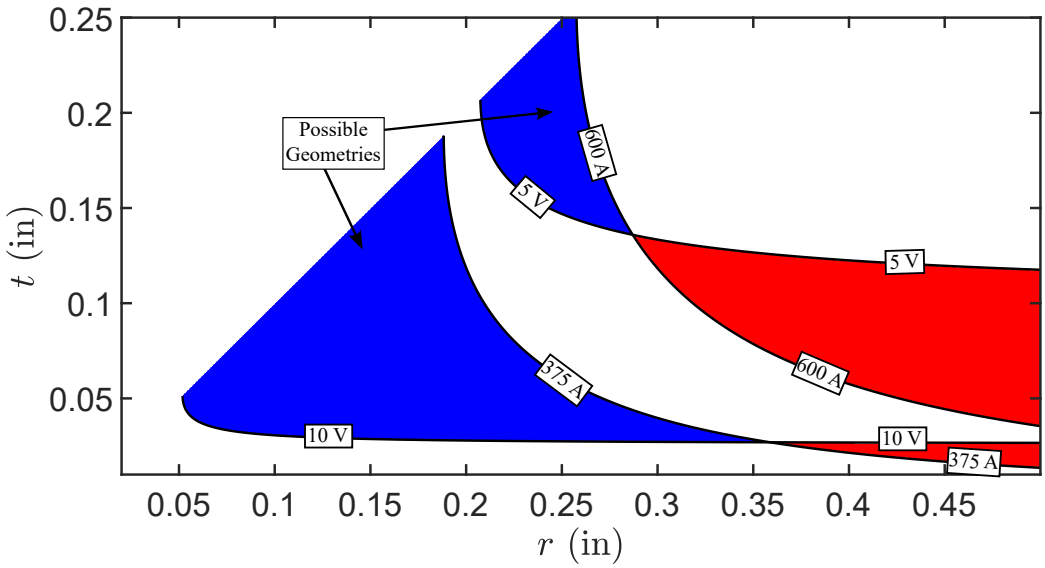

Figure 5.8: Contour plots of constant current and voltage as a function of the cross-sectional geometric parameters: r and t for fixed H = 36 in and T_w = 1100 K. The blue shaded areas between contours show the possible t and r values to satisfy the heating model for single power supply (600A/5V) or Series (385A/10V). The geometries in the red shaded regions satisfy neither the current nor voltage requirements.

5.3.2 Transient Heating Model

Being able to obtain rapid heating rates is desirable in ignition testing. To compare with the results of (Jones, 2020) and Chapter 3, similar times to steady state (60 - 90 s) and overall test times (300 s) are required. To examine this issue, a simple transient heating model Equation (5.14) is used to estimate the time varying temperature of the lumped-mass system developed in Section 5.3.

$$\frac{dT_w}{dt} = \frac{P_{net}(T)}{\rho V c_P}\,, \tag{5.14}$$

P_{net} is the net power input, ρ is the density of 304 stainless steel, V is the volume of the heated cylinder metal, and c_P is the specific heat at constant pressure. This equation is integrated numerically to determine the time evolution of the surface temperature T_w. Results from this model are compared with bench top experiments for two different cross-sections in Section 5.3.4.

5.3.3 Modeling Assumptions and Limitations

The heating model makes several assumptions including: a constant cylindrical cross-section of the heated surface, uniform surface temperature, negligible resistance in power supply wires, simplified conduction heat losses through the electrodes, no radiation returned to surface, and only dissipation of electrical input power as heat in the cylinder. The model parameters can be adjusted and the model refined but as will be shown in Section 5.3.4 the model is adequate for the design study and replicates experimental data with reasonable fidelity.

Wire resistance One important practical issue is that model has assumed negligible resistance in the power supply wires. The 4/0 10-ft cables that will be used to connect the power supply to the CAT electrodes have a measured room-temperature resistance of 0.70 mΩ each. This 1.40 mΩ is non-negligible compared to the typical cylinder resistance which is on the order of between 1-10 mΩ at room temperature. This resistance can be included in the model as shown in Equation (5.15). The resistance of the wires will increase slightly at high current operation during long duration tests because of heat dissipation, resulting in a wire temperature increase on the order of 10°C.

$$R(T) = \frac{\rho_e(T) H}{2\pi r t - \pi t^2} + R_{wire}\,, \tag{5.15}$$

where $R_{wire} = 1.4\ m\Omega$. Accounting for the wire resistance will result in a modest decrease in the power available to heat the cylinder and a reduction in the maximum voltage drop.

Radiant Heat Transfer At the temperatures of interest, 900 - 1100 K, there is substantial power in the thermal radiation which is primarily absorbed in the surrounding water-cooled outer cylindrical vessel of the CAT. However, the outer aluminum cylinder will be partially reflective and some fraction of the incident thermal radiation will reflect back to the hot cylinder surface. The surface

properties of the inner surface of the outer cylinder are not known and the most we can say is that the reflected radiation with be a combination of specular and diffuse reflection of incident radiation, direct emission for the cold surface being negligible.

Some of the reflected radiation will be absorbed by the hot cylinder, reducing the net radiant power transfer Q from the hot cylinder. We do not have enough knowledge of surface radiative properties to carry out accurate computations so instead we will bound the magnitude of this effect by using two simple models of radiant heat transfer and assumptions about surface properties. Based on past experience, the surface of an aged (oxidized) hot cylinder will have a emissivity between 0.7 and 0.95 with a modest dependence on wavelength. The reflectivity of the inner surface of the outer cylinder is unknown. At the level of approximation appropriate for this design study, we will also idealize the geometry to be two infinite concentric cylinders. If we assume that the outer cylinder is a specular reflector, the net radiant power transfer is (Table 9.1, Siegel & Howell, 1981)

$$Q = A_1 \sigma \frac{T_1^4 - T_2^4}{\frac{1}{\epsilon_1} + \frac{1}{\epsilon_2} - 1} , \tag{5.16}$$

where subscript 1 refers to the inner cylinder and subscript 2 to the outer cylinder. If the outer surface is a gray, diffuse reflector

$$Q = A_1 \sigma \frac{T_1^4 - T_2^4}{\frac{1}{\epsilon_1} + \frac{A_1}{A_2}\left(\frac{1}{\epsilon_2} - 1\right)} . \tag{5.17}$$

In both cases, the surface of the inner cylinder can be either gray and diffuse or a specular reflector. The net radiative power transfer can be simplified at high inner cylinder temperatures, as $(T_2/T_1)^4 \ll 1$ and can be written as

$$Q = A_1 \epsilon_1 \sigma T_1^4 \, (1 - F) \ , \tag{5.18}$$

where F is the fraction of emitted radiation that is incident on the inner cylinder due to reflection by the outer cylinder. For a specular outer surface

$$F = \frac{\epsilon_1 (1 - \epsilon_2)}{\epsilon_1 + \epsilon_2 (1 - \epsilon_1)} . \tag{5.19}$$

For a gray, diffuse outer surface with typical CAT design values of $A_1/A_2 = 1/4$

$$F = \frac{1}{4} \frac{\epsilon_1 (1 - \epsilon_2)}{\epsilon_2 + \frac{1}{4}\epsilon_1 (1 - \epsilon_2)} . \tag{5.20}$$

The value of Q is an improved estimate of the radiation transfer term $P_{radiation}$ in Equation (5.4). The larger the value of F, the lower the amount of electrical power required to maintain the surface

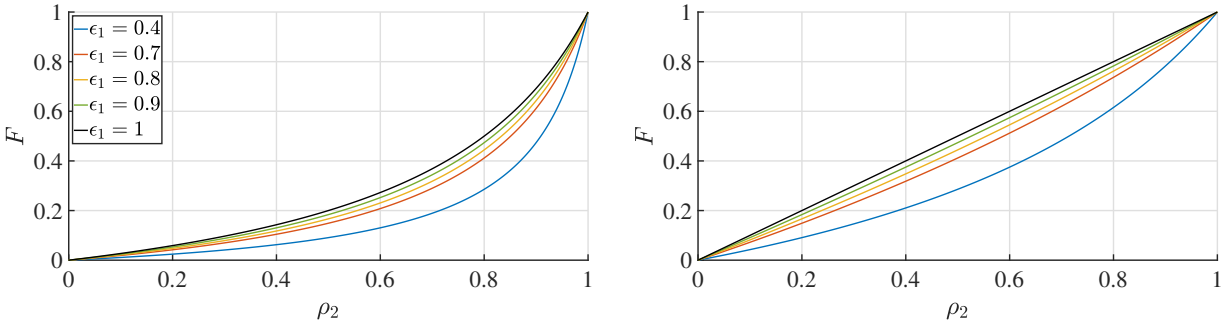

Figure 5.9: Reflected radiation fraction F as a function of inner cylinder emissivity (ϵ_1) and outer cylinder reflectivity (ρ_2). (a) Gray-diffuse outer cylinder. (b) Specular outer cylinder.

at a given temperature. Evaluation of the F expressions as a function of the surface properties, shown in Figure 5.9, indicates that F is a weak function of the inner cylinder emmissivity and a strong function of the outer cylinder reflectivity $\rho_2 = 1 - \epsilon_2$. A wide range of values of F are possible depending on the reflectivity and the actual magnitude would have to be evaluated by experimental measurement. In any case, these results indicate that reflection of radiation by the outer cylinder will enhance rather than degrade the performance of the power supplies in achieving the temperatures of interest.

Uniform Surface Temperature The validity of assuming a uniform axial surface temperature is conventionally evaluated by computing Biot number, which is the ratio of the thermal losses to the environment by convection to the conduction losses along the axis. However, in the present case, the dominant heat transfer process to the environment is thermal radiation for the central region of the cylinder. Convection is negligible at ignition conditions and conduction is only significant in the end region of the cylinder over the length L_{edge}. So the conventional Biot number approach is not appropriate and a more sophisticated approach is needed. Experiments and analysis based on a one-dimensional model of heat transfer was carried out by Jones (2020). This work confirmed the axial uniformity of the central region for sufficiently tall cylinders and high temperatures.

5.3.4 Benchtop Experiments for Model Verification

Prior to design of an ignition vessel, we verified the results of the heating model using a simple bench-top experiment. A commercial 304SS tube with dimensions of r = 0.25 in. t = 0.049 in. and H= 48 in. was used for this purpose. Copper fixtures were fabricated to clamp onto the outer surface of the tube to provide a means of electrical connection with power supply cables and to mechanically support the tube. These electrodes were cooled using water circulated through the NESLAB heat exchanger. The supports were isolated thermally and electrically using 0.25-in.

thick fiberglass blocks (Garolite G-10/FR4). A CAD model of the fixture is shown in Figure 5.10 together with an image of the actual tube wtih T_w = 1100 K.

The height of the top copper clamp could be adjusted to test different cylinder lengths without needing to cut the cylinder. Only the cylinder material between the electrodes acted as a resistor in the circuit. For the results shown a cylinder height of H = 36 in. was used. The pyrometer described in Section 3.3.2 was used to measure the surface temperature at an approximate height of 6 in. above the bottom support. This measurement was also used in a feedback (PID) control loop to hold the surface temperature constant. A type-K thermocouple was also welded to the surface at the same height as the pyrometer measurement but on the opposite side of the cylinder. The thermocouple provided an independent measurement of temperature at high temperatures and a means of data collection at low temperatures that were outside the range of the pyrometer.

A thicker 304SS tube with a cross-section of r = 0.5 in. and t = 0.188 in. was also tested (labelled v1 in Figure 5.11). The larger cross-section reduced the supply voltage requirement below the 5 V threshold for a single power supply. Use of a single power supply would reduce system complexity

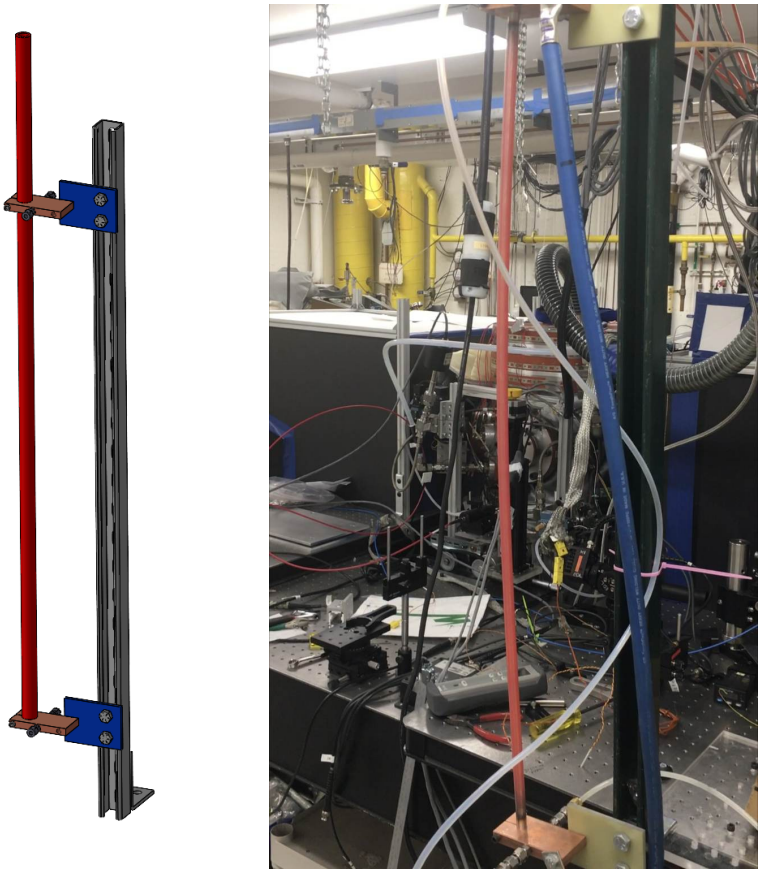

Figure 5.10: Bench-top cylinder heating experiment for validation of heating model. Bowing of the cylinder is apparent at 1100 K due to thermal stresses and the constrained ends.

and enable use of higher currents if this cross-section were found to be viable. These tests were used to examine the fidelity of the transient heating model. The thicker tube had a much larger mass as compared to the smaller cross-section so required a commensurately larger amount of input energy to increase its temperature. Figure 5.11 illustrates this point and demonstrated the ability of the simple transient heating model in predicting surface temperatures.

Large heating rates are typically desired in ignition testing and for reasonable comparisons to be made with the results of Jones (2020) and Chapter 3, similar times to steady state (60 - 90s) and overall test times (300s) are desired. The previously selected r = 0.25 in. , t = 0.049 in. , and H = 36 in. cylinder is a viable option for achieving these targets and used for further analysis. These benchtop experiments also illustrated a previously overlooked consideration of the significant thermal strain produced in these large cylinders. With the cylinder ends being fully constrained, this can lead to stress loadings which are sufficient to induce thermal buckling as shown by the noticeable curvature of the benchtop cylinder in Figure 5.10. Thus another outcome of this testing was the understanding that an axially free support (e.g. only provides a normal reaction source, no axial force) would be required to prevent this buckling. This will be addressed in detail in Section 5.4.2.1.

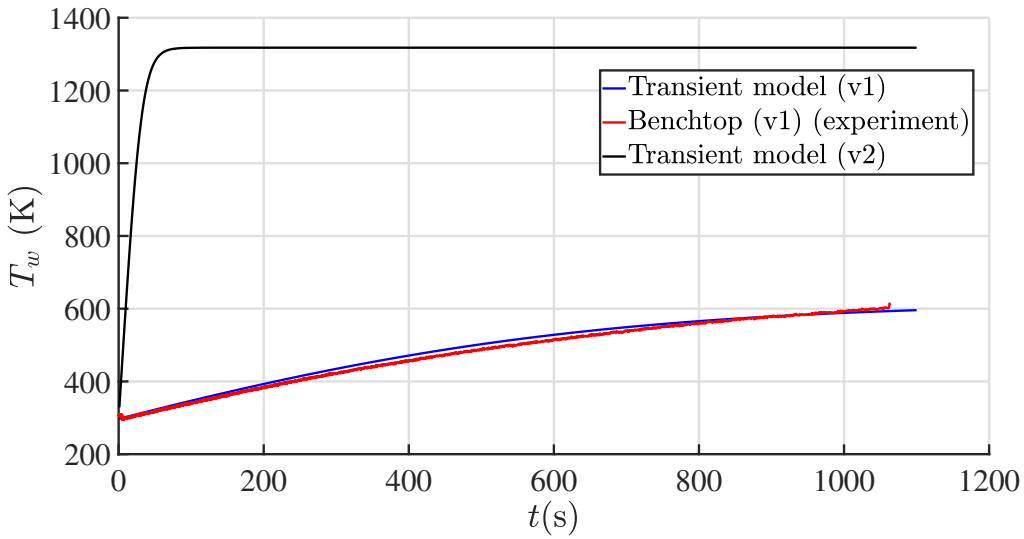

Figure 5.11: Bench-top cylinder heating experimental temperature data compared to transient heating model. v1 corresponds to a cross section selected for the single XR5-600 power supply and v2 for the thinner cross section (r = 0.25 in. , t = 0.049 in. , and H = 36 in.) using the series configuration for larger voltage. v2 is the geometry adapted for the final design.

5.4 CAT CAD Design and Unique Features

Several important designs considerations have been discussed already and additional concerns will be presented here. The final design underwent several early iterations until the final design was ultimately settled on. These design iterations will be discussed briefly here where relevant to the final design choice.

5.4.1 Preliminary Design Considerations

The previously mentioned ISO100 tubes were used in initial designs but were ultimately entirely replaced with custom machined tubes manufactured from 6061 Aluminum. This was chosen to have better control over discrete lengths, feedthrough ports, windows, sealing design, and flange surfaces. These ISO flanges do not have standard O-ring grooves and instead rely (Figure 5.12) on a centering ring to hold the O-ring on the surface which seals only for negative pressure differences ($P_{internal} \leq P_{external}$).

This design is not expected to hold positive pressure differences and could result in failure for explosion testing where $P_{internal} > 6$ atm is expected. Additionally this sealing scheme results in a discontinuous internal diameter which could trip the outer boundary layer of the channel into turbulence. Machinable ceramic plates (MACOR) were also considered for use as top and bottom boundary surfaces in order to simulate adiabatic surface conditions as used in some studies of vertical channel flows. Instead isothermal boundary conditions were chosen so cooled metal tubes end caps were used instead.

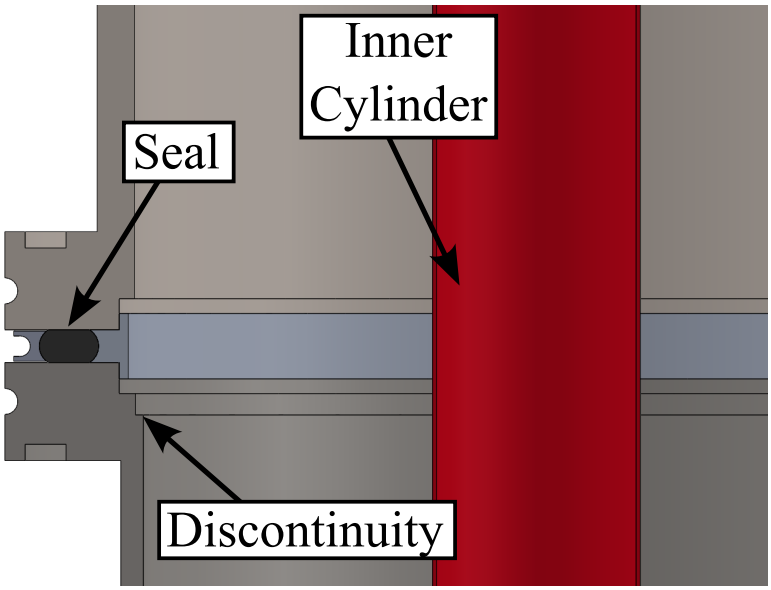

Figure 5.12: Sealing scheme for ISO flanges illustrating discontinuity of inner diameter and centering ring for holding O-ring in place of a groove.

The use of an optically clear material for a single tube section was considered. This was desirable for direct visualization of the flame propagation and potential shadowgraph and schlieren techniques. Optically clear acrylic or glass were both considered. To enable schlieren visualization, the cylindrical lensing effect of a curved tube must be compensated for. This could be done using a carefully aligned system with corrective lenses on either side of the tube as in Kaiser et al. (2013). A more interesting approach was taken by Fujikawa et al. (1988) who designed the optical compensation into the tube itself. The inner surface still consisted of a cylindrical profile of desired diameter but the outer surface is defined parametrically using a model derived from geometrical optics. The model was derived by requiring:

1. Tangent rays at inner and outer surfaces are parallel
2. Solution is smooth and satisfies (1.) for all rays
3. The optical path length is identical for all rays through the surface

Figure 5.13 illustrates these constraints and provides a schematic for the model variables. The parametric definition of the outer surface is given by Equations (5.21) and (5.24).

$$x = r_0 \cos t + t_1 \cos \theta_1 \tag{5.21}$$

$$x = r_0 \sin t + t_1 \sin \theta_1 \tag{5.22}$$

$$\theta_1 = t - \arcsin \frac{\sin t}{n} \tag{5.23}$$

$$t_1 = \frac{t_0(n-1)}{(n - \cos t - \arcsin \frac{\sin t}{n})} \tag{5.24}$$

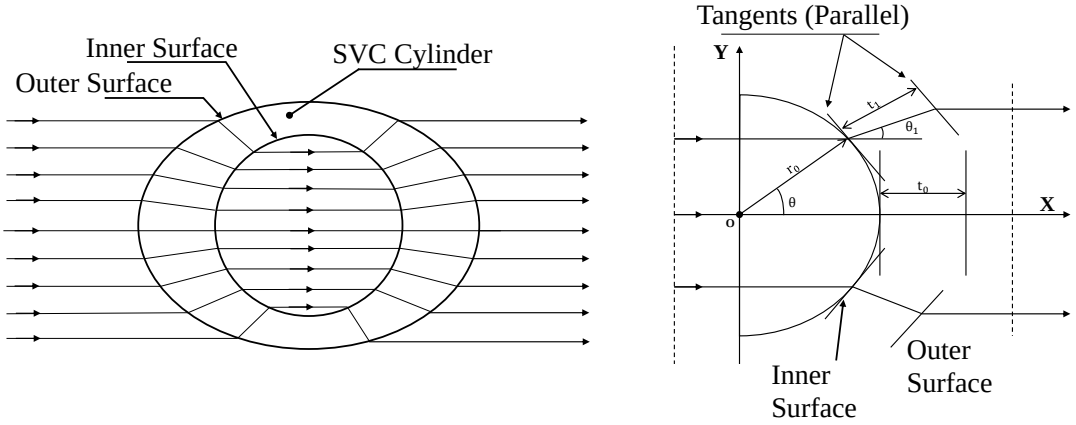

Figure 5.13: Side view collimating (SVC) cylinder of Fujikawa et al. for optical correction of a curved surface used for visualization inside a cylinder. (Recreated from Fujikawa et al., 1988).

This model was successfully employed on a machined acrylic piece for visualization of combustion in a piston cylinder (Fujikawa et al., 1988). However these tests were only conducted for short periods (< 30 s) with small heating loads from the flame so the acrylic did not melt. In the CAT tests, the heat input to the outer vessel will occur over a longer period of time (300 s) from sustained thermal emission from the inner cylinder at 1100 K. A low thermal conductivity material like acrylic will rapidly heat in this situation and can soften, become deformed, and ultimately melt (T_{melt} = 160°C) eliminating any optical quality gained by the intricately machined outer surface. For use in the CAT experiment the SVC cylinder would therefore have to be machined out of a higher temperature material like quartz glass. While many sophisticated glass machining companies exist now, costs and lead times for such a piece even of modest size (5 in. × 5 in.) were prohibitively large. Additionally the surface finish desired for optical correction is 0.01 mm as outlined in Fujikawa et al. (1988). This is simply not achievable from any commercial glass fabrication service found readily. Even the values of 0.08 mm and 0.13 mm achieved by Fujikawa et al. for an acrylic piece were not feasible for some glass machining services. This approach was ultimately considered unpromising and unnecessary for the CAT since optical access was only required in the region close to the heat surface which could be achieved using flat windows affixed to flanges on a metal tube.

5.4.2 Final Design

Figure 5.14 shows the final design points on the *Ra-A* parameter plot discussed previously. It is anticipated that experimental nonidealities will facilitate turbulent transition at lower parameter values than obtained in the numerical study of the parameter space by Chenoweth and Paolucci (1986) so attaining the transitional regime is sufficient for the final design. Six discrete points are chosen which span the desired range of conditions and were chosen in such a way that the modular construction is optimal. This means that the outer vessel only requires the minimum number of total pieces to construct all configurations. For six discrete lengths, a total of six pieces are required at minimum for the outer vessels. This cannot be done with fewer components and can be easily proven by considering that one unique vessel is required for each length as a minimum constraining condition (e.g. cannot have a number of vessel sizes greater than the number of individual pieces). One piece of each desired length would be one obvious approach but would require each piece to be outfitted with gas and instrumentation feedthroughs, window flanges, and cooling lines. This would increase machining costs for the longest pieces ($L > 18$ in.). The cost and material footprint of such an approach are much greater than for modular construction. The six conditions that were chosen are outlined in Table 5.1. The inner diameter of the outer vessel is chosen as 4 in. for these calculations and the desired input I is used to compute the resulting V and time to steady state (t_{steady}) based on the model in Section 5.3 for T_w = 1100 K.

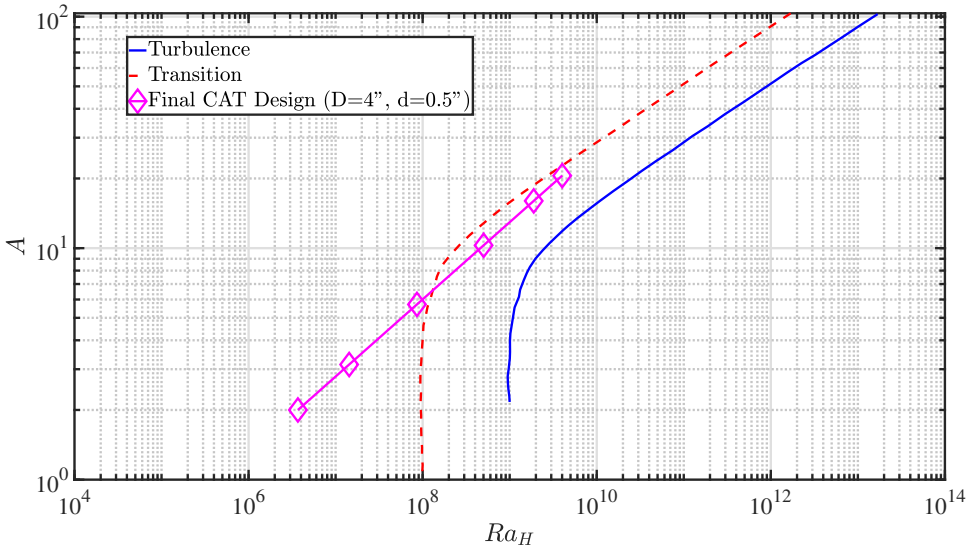

Figure 5.14: Design space for CAT plotted in the *Ra*-*A* parameter space. Comparisons with previous work of Jones show that the aspect ratio and Rayleigh numbers are increased by two orders of magnitude.

By changing the height of this channel the channel aspect ratio ($A = H/W$) is also changed. This choice of a single outer vessel diameter was made for design simplicity and ease of component manufacturing however channels of different width could also be studied with additional component fabrication if desired. This change in height also enables significant changes in achievable Rayleigh numbers since Ra scales like H^3. Previous studies have predicted transition to turbulence around $Ra = 10^8$ - 10^9. Assuming comparable ignition thresholds ($\simeq$ 1000 K) to previous vertical cylinder studies (Chapter 3), the height required to achieve $Ra_H = 10^9$ is around 30 in. This was set as a minimum design goal.

Table 5.1: CAT Cylinders and corresponding parameters of interested for ignition testing.

Cylinder label	**Heated Length (in)**	A	**Surface Area (cm^2)**	Ra_W	Ra_H	**I (A)**	**Volts (V)**
H4	3.5	2	35.5	4.61×10^5	3.69×10^6	500	3.04
H6	5.5	3.14	55.7	4.61×10^5	1.43×10^7	500	3.66
H10	10	5.71	101.3	4.61×10^5	8.60×10^7	450	4.56
H18	18	10.29	182.4	4.61×10^5	5.02×10^8	375	5.67
H28	28	16.00	283.8	4.61×10^5	1.89×10^9	375	8.01
H36	36	20.57	364.8	4.61×10^5	4.01×10^9	375	9.88

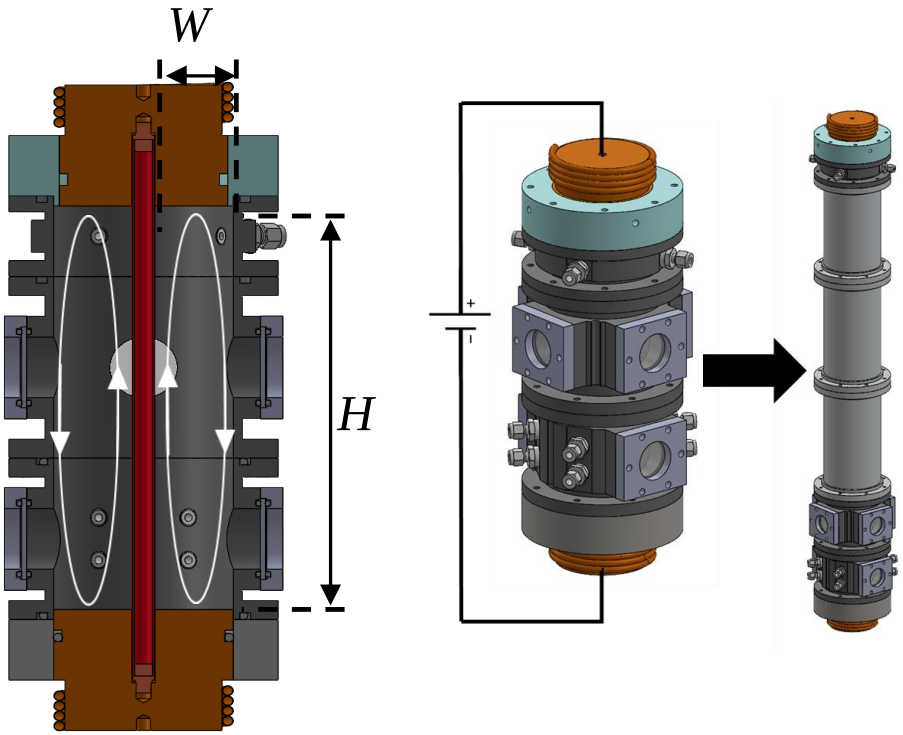

Figure 5.15: CAD model of CAT assembled in small and large configurations. The cross-section illustrates the expected channel flow configuration with a large recirculation region for low aspect ratio cases.

5.4.2.1 Outer Vessel

Figure 5.15 illustrates the final design of the assembled CAT vessel. This is shown using a CAD model for both a small (H10) and large (H36) cylinder assembly. The outer vessel consists of modular pieces machined out of 6061 aluminum tubes of 4 in. ID which is similar to the ISO100 tube dimensions. Three unique tubes were designed for feedthrough and optical access while three tubes had no additional features. Sealing between each piece was achieved using static O-ring face seals contained on flanges that were machined into the ends of each piece. For most pieces this groove was only necessary on the top surfaces since the bottom mating surface would be placed against the top groove of the piece below it. Only the bottom gas feedthrough piece featured O-ring grooves on both the top and bottom surface since it was the only piece used in all configurations, including on its own in the smallest configuration with the H4 cylinder. Eight feedthrough ports and two opposing 1-in. diameter windows were included in this gas feedthrough piece. This provided enough access for gas feedthrough, mixing, vacuum, gas phase thermocouple, a static pressure gauge, and a dynamic pressure gauge. This left room for two additional feedthroughs for surface

thermocouple feedthroughs and other equipment as desired. In all but the smallest configuration, the top feedthrough collar was also used and enabled four additional feedthrough ports. This collar was necessary to ensure mixing of the full gas volume during the fill procedure for high aspect ratio configurations. If the mixing lines were placed too close together (e.g. both on the bottom gas feedthrough piece) then the volume above this region would mix primarily through diffusion since it is not directly in the pumping volume of the mixing pump. Additional optical access was also provided by the final unique tube which contained two sets of opposing 1 in. windows. This was used in all configurations higher than H = 5.5 in. and enabled visualization of a range of heights for the longest cylinder by simply rearranging this tubes location in the stack of modular pieces.

Calcium Fluoride (CaF_2) windows were chosen due to their wide transmission range (> 90% for 0.2-7 μm) and durability. Of particular interest in this experiment are the ranges 1700-1940 nm for the two-color IR pyrometer use, 306 nm for OH* chemiluminescence, and 3.93 μm for C-H bond absorption spectroscopy. Plate stress calculations were also conducted for a clamped CaF_2 windows with 1.5 in. diameter optical aperture and assuming uniforming loading under the same conditions previously mentioned for explosion pressure of 6 atm. Although not a structural material, these calculations for CaF_2 are useful in conservatively establishing a stress state for a given window thickness. The equation for maximum stress in a clamped circular plate under uniformly distributed load is

$$\sigma_{max} = \frac{3Pr^2}{4t^2}\,, \tag{5.25}$$

where P is the uniform load (up to 5 atm during explosion), r is the radius of the plate, and t is the plate thickness. CaF_2 material properties are ν = 0.26 and E= 75.8 GPa. Fracture strength for CaF_2 reportedly has large variation from σ_F = 34.1 ± 15.1 MPa for roughly finished pieces to σ_F = 157.2 ± 13.7 MPa for optically polished material.[1] Rearranging Equation (5.25) and solving for the minimum thickness

$$t_{min} = \sqrt{\frac{3Pr^2}{4\sigma_F}} \tag{5.26}$$

To determine t_{min} with this formula, a fracture strength has to be specified. Although we selected highly polished samples, a conservative approach is to use the worst case σ_F = 19 MPa which yields a result of t_{min}=2.694 mm. For t=5 mm a maximum stress of only σ_{max} = 5.52 MPa is reached. This results in a factor of safety of 3.4 in even this most conservative case. If instead the more appropriate value for a polished sample is taken, σ_F = 157.2 ± 13.7 MPa, then the factor of safety becomes much larger. 50.8 mm diameter, 5 mm thick CaF_2 windows were therefore deemed acceptable and were sourced from Edmund Optics. Additional design consideration was given to the O-ring grooves used to seal these windows such that there would be no glass-to-metal contact.

[1] "Calcium Fluoride Physical and Chemical Properties" (2003).

In particular the grooves are made shallower and wider and these adjustments can be seen in the design drawings in Appendix F.

The bottom and top boundaries were massive copper electrodes sealed using dynamic O-ring gland seals. These electrodes allowed the inner heated cylinders to be threaded directly into the electrode with a short, low-resistance path to the power supply cables. The copper electrodes were each cooled using three loops of copper tubing soldered to a grooved surface outside the vessel. This cooling enabled the high thermal conductivity copper to maintain the desired isothermal boundary conditions. The top electrode was electrically isolated from the vessel walls using a plate made of plastic (Delrin Acetal Resin) fabricated with a narrow lip to match the inner diameter of the outer vessel. Four equally spaced set screws were used to hold this electrode fixed in the insulating plate. The bottom electrode was not electrically insulated from the vessel since the corresponding fitting plate was fabricated from 6061 aluminum. This was done since the thermal expansion of the tube would cause the bottom electrode to displace vertically and expose a portion of this bottom support plates inner surface. With a low melting point and low thermal conductivity, a concern was that a plastic surface would soften or melt when exposed to the radiating cylinder and propagating flames. This would degrade the quality of the gland seal allowing for gas leakage or resistance to the cylinder expansion. The integrity of this moving or "roller" support was necessary to prevent axial stress buildup in the cylinder which could cause buckling as will be discussed in the following section.

5.4.2.2 Inner Heated Cylinder

Inspiration for the inner heated cylinder design was found in Jones (2020) and ultimately a similar approach was taken. A cooper threaded insert was press fit and brazed on each of the open ends to enable a reliable threaded connection to each electrode. These inserts were required to be sealed on the ends, provide high electrical conductivity, and have superior joint strength and integrity. To achieve these goals, a high temperature vacuum brazing process was chosen and provided by Scarott Metallurgical services. The braze used was a high temperature Nickel alloy (brazing temp 1925 - 1950°F). These temperatures are far in excess of those expected for the ignition experiments except in the transient flame front which should not propagate in the gap and reach this joint as will be discussed. Additionally the joint area are in direct threaded contact with the large copper electrodes which should act as a large heat sink and maintain near-isothermal conditions at these joints even during sustained heating periods.

This design also differed from this previous work in that the cylinder ends were offset 1.5 in. into the electrodes at each end. This was done in an effort to eliminate the edge effects on surface temperature from the test vessel volume and produce a more uniform temperature on the inner tube.

This offset required some insulation from the electrode surface and a physical ceramic insulation sleeve was considered. This sleeve was ultimately abandoned in favor of a narrow air gap since air has a low thermal conductivity. This also enables unrestricted thermal expansion of the inner tube which would cause cracking of a ceramic sleeve. This choice also introduced the consideration of ignition and/or flame propagation in this narrow gap. Ignition in this volume would be unlikely due to reduced surface temperatures caused by the cooled boundary and large surface area for heat loss from any pocket of reacting gas. Flame propagation can also be eliminated if the gap is sufficiently narrow (e.g. below the flame thickness). For 1 atm stoichiometric n-hexane/air, the flame thickness is 0.38 mm (0.15 in.). The gap size is designed is therefore designed to be less than this value and at room temperature it is nominally 0.254 mm (0.01 in.). This gap will shrink as the inner cylinder is heated and thermally expands in the radial dimension from 0.5 in. (at 300 K) to 0.5069 in. (at 1100 K). The tolerance of the cylinder outer diameter was initially 0.5 in. ± 0.005 in. Accounting for this, the maximum diameter is nominally 0.5074 in. which results in a gap size of 0.16 mm (0.0063 in.). This is well below the flame thickness for the mixtures under study so flame propagation into this gap should not occur. This is important to protect the brazed joints at the cylinder ends from exposure to high temperatures.

The previously mentioned design of the bottom electrode provided a "roller" support which allowed for axial expansion of the cylinder in order to prevent thermal buckling. Using Equation (5.27), we can estimate the linear thermal expansion for each of the cylinders at a maximum temperature of 1100 K.

$$\Delta L = L_0 \alpha \Delta T \tag{5.27}$$

where ΔT is the temperature increase, L_0 is the initial length, α is the mean linear thermal expansion coefficient, and ΔL is the increase in length. Using a mean value[2] of $\alpha = 18.8\times10^{-6}$ K^{-1} for 304SS, ΔL is estimated for each of the six cylinders and reported in Table 5.2 for ΔT = 800 K. For these calculations L_0 is the heated length. These results illustrate the significant role thermal expansion plays especially in the tallest experiments where over 0.5 in. of expansion is expected (and observed)! To ensure integrity of the gland seal during all of these tests, the bottom sealing plate must have a thickness greater than this worst case expansion (0.5414 in.) and the seal must be located on this surface such that it has sufficient distance to traverse when at elevated temperature. The adopted design features a 1.5 in. thick plate and a maximum gland seal travel distance of 0.95 in.

As a consequence of the use of a "roller" support on the bottom, the heated cylinders act as structural components in this experiment. These cylinders must therefore support pressure and vacuum loading in the interior volume (e.g. 1 atm static compression pressure under vacuum and

[2] *High-Temperature Characteristics of Stainless Steels* (n.d.)

Table 5.2: Critical buckling loads and maximum linear thermal expansion for CAT cylinders, evaluated at 1100 K.

Cylinder label	Heated Length (in.)	Unsupported Length (in.)	P_{cr} (lbf)	ΔL (in.)
H4	3.5	6.8	2028	0.0526
H6	5.5	8.8	1999	0.0827
H10	10	13.3	1908	0.1504
H18	18	21.3	1654	0.2707
H28	28	31.3	1172	0.4211
H36	36	39.3	756	0.5414

up to approximately 6 atm of dynamic pressure due to combustion events as estimated from 40 L vessel experiments). However the dynamic loading is expected to be lower in CAT due to reactant depletion and additional heat loss to isothermal boundaries. The pressure force acting on the surface of the bottom electrodes is the loads considered here. The weight of the bottom electrode is also supported by the cylinder but is negligible compared to these other forces (10 lb). The area over which the pressure acts is the area of the bottom support surface, taken to be 12.37 in.^{2} (A= $\pi(r^2 - r_i^2)$ with r = 2 in. and r_i = 0.25 in.). This results in a compressive load of P_{vac} = 181.8 lbf (808.6 N) under vacuum and an impulsive tensile load of P_{max} = 908.9 lbf (4043.2 N) during a 1 atm n-hexane air explosion.

Stress and buckling calculations for these conditions with fixed-fixed boundary conditions were conducted for the design dimensions previously stated. The critical buckling load (P_{cr}) is

$$P_{cr} = \frac{\pi^2 E I^2}{KL} \tag{5.28}$$

and the moment of inertia is

$$I = \frac{\pi}{4}\left(r_o^4 - r_i^4\right) \tag{5.29}$$

E is Young's modulus, I is the area moment of inertia given by Equation (5.29), L is the unsupported column length, and K is an effective length factor which depends on the boundary conditions. For room temperature 304 stainless steel, E= 28 $\times 10^6$ psi (193 GPa) and for fixed-fixed boundaries, K =0 .65. The cross-sectional area is A_c = 0.069 in^2 (44.791 mm^2) and the area moment of inertia I = 0.001786 in^4 (743.39 mm^4). Neglecting other loading sources such as pressure forces from the explosion on the tube directly and assuming the load is applied symmetrically on the bottom support, only axial loading will be present in the tensile case. In this case the stress state is given by $\sigma_{max} = P_{max}/A_c$.

At room temperature the yield stress of 304SS is σ_y = 30 ksi (207 MPa). However at ignition conditions, the temperature is expected to be as high as 1000 - 1100 K. Stainless steels soften at

elevated temperatures and the yield stress at these temperatures is reduced to between 13.8 ksi (at 975 K) and 9.9 ksi (at 1089 K) *High-Temperature Characteristics of Stainless Steels* (n.d.). The tensile strength is similarly reduced to between 35 ksi (at 97 5K) and 18 ksi (at 1089 K). The maximum stress expected from this loading is 13.1 ksi and is higher than this reduced yield strength, however still lower than the tensile strength. Plastic deformation is therefore possible in the heat affected region of the cylinders due to the explosive loading. However in practice there is significant friction force due to the gland seal which will support some of this load especially under asymmetric loading. Deviation from the symmetric loading assumption will produce a moment on the bottom electrode which will transfer the loading into the outer vessel through friction with the vessel wall. Additionally, at elevated temperatures a support piece is located just below the bottom electrode position to prevent significant yielding from occurring.

5.5 Component Fabrication: Cooling System

All individual components were machined in house by the GALCIT machine shop including the outer vessel pieces, electrodes inner heated cylinders, mounting shelf, supports, and isolation plates. As previously mentioned a high temperature vacuum brazing process was used to seal the heated cylinders to the copper threaded inserts. The final remaining portion of the component fabrication was the joining of cooling lines to the copper electrodes and aluminum vessel walls to enable control of a room temperature isothermal boundary condition on these surfaces. A NESLAB system III heat exchanger was planned to be used as in Chapter 3. However the challenge here was determining how to attach the cooling water lines to large surface areas ensuring good thermal contact so incident heat absorbed from the inner surface radiation is exceeded. Several methods were explored including conductive adhesive tapes, thermal adhesives, thermal pastes, brazing and soldering. Welding is not possible with the thin walled 1/4-in. tubing used as cooling lines since puncturing of these lines difficult to avoid. These methods are compared in Table 5.3 comparing thermal conductivity, structural considerations, ease of fabrication, etc.

This table shows that most cooling options actually provide relatively poor thermal conductivity like thermally conductive adhesive tape and pads which are typically used in electronics. Slightly larger values are advertised for thermally conductive epoxies however all of these methods rely on the application of only a thin layer of material between the joining surfaces to minimize thermal resistance. Additional curing at elevated temperatures (65 - 95°C) is also recommended for these epoxies to improve mechanical properties. High performance thermal pastes are typically used in CPU and GPU cooling solutions but are not themselves a structural material, instead relying on a clamping force with the paste simply improving thermal contact. These could be used with a series of hose clamps or a structural epoxy for structural support but still provide relatively poor conduction. Preliminary tests with these materials were conducted on simple test pieces of

Table 5.3: Comparison of joining techniques for cooling lines.

Joining Method	**Thermal Conductivity ($W \cdot m^{-1} \cdot K^{-1}$)**	**Melting Temperature (°C)**	**Structural Strength**	**Ease of Fabrication**
Thermally Conductive Adhesive Tapes/Pads	0.6-1	-	Poor	High
Thermal Paste	12	-	None	Med
Thermally conductive epoxy*	1.87	-	Good	Med
Brazing (85/15 Zn/Al)	110	382-452	Excellent	Low
Soldering	50-65	171-227	Good	Low

* Numbers here are for Cotronics Duralco 4525 but representative of other commercial epoxies.
Values for thermal conductivity are approximate and intended to be representative of the options found specifically for this work.
Melting temperatures given represent a range for the specific alloys considered in this work.

aluminum and copper tubing as pictured in Figure 5.16. This was done to evaluate structural strength and cooling capabilities under heating load from a heat gun held at close range. These samples were put under heating load both with cooling water pumped through the tubing at approximately 1 gal/min and with zero flow rate. The results of these tests show little effect when cooling flow was applied. The maximum temperatures and cooling rate after the heat load was removed were similar between these cases. The epoxy joints were however found to be structurally reliable for affixing the cooling lines in place.

Brazing and soldering are two related approaches where the base metal work pieces are heated to the melting point of a filler allow which is applied to the joining region typically using a flux to prevent oxidation. These methods are distinguished by the melting point of the filler metals used. The cutoff of $T_{melt} = 450°C$ typically distinguishes these two processes with lower (higher) melting points being typical of soldering (brazing). These filler alloys tend to have the largest thermal conductivity of any methods used here since they are pure metallic compounds. The structural integrity of these joints is also superb. The challenge in these methods however is the high working temperatures which are problematic for large work pieces. The heat can be applied either via torch or an industrial furnace. Industrial vacuum furnaces are typically required to braze large pieces due to the high heating loads required. Aluminum pieces are also notoriously difficult to use in the processes so are not accepted by many industrial operations. A commercial “low temperature” aluminum brazing material was found (85/15 Zn/Al), however in testing on one work piece the

required working temperatures were still to high to achieve even with an acetylene-oxygen torch. The much higher temperature required for brazing is simply too difficult to achieve and maintain with a single torch process.

Torch soldering was found to be the most effective and suitable fabrication method for these components due to the relatively large thermal conductivity of the filler metal (> 50 W$\cdot$ m$^{-1}\cdot$ K^{-1}) and ease of fabrication for large pieces. The top and bottom electrodes were solid copper cylindrical pieces with 3-in. diameter recesses cut out for joining of cooling tubing. Four loops of 1/4-in. copper tubing were coiled around the region and soldered using a rosin core 60/40 (Pb/Sn) solder along with additional flux paste applied periodically. Hose clamps were also applied to each of the tubing coils to prevent thermal expansion of the 1/4-in. tubing from creating a large gap between the surfaces which would not be fill able with solder. A propane/air torch was used to heat the work piece to the melting temperature of the solder. Due to the large thermal mass of the work pieces this required up to 10-15 min of preheating with the torch. At sufficiently high temperatures (just above the solder melting point) it was found that the solder would readily flow from the top coil to the bottom, wetting and filling the joining interface along the way. This enabled ample use of hose clamps without worry of obstructing access to the joining interface for solder application. Once sufficient solder had been applied, the work piece was left to cool down slowly in the lab environment. This was necessary to prevent differential thermal expansion during cooling from causing crack formation in the solder joints. The finished components are shown in Figure 5.17.

Aluminum is notoriously difficult to join using soldering/brazing methods however through experimentation we found a suitable low temperature solder material and flux for aluminum joining

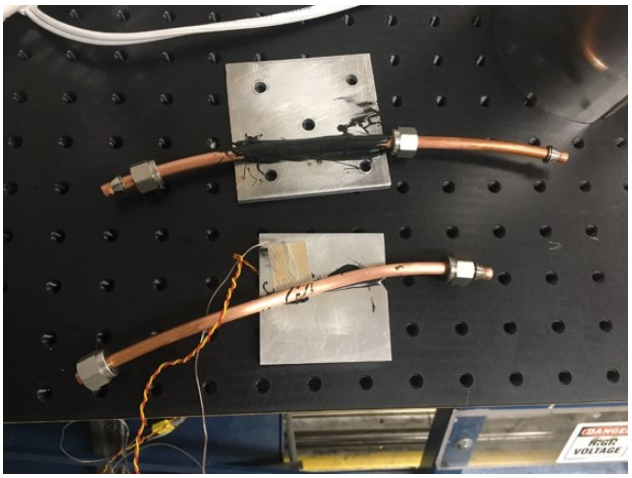

Figure 5.16: Thermal epoxy samples. The bottom sample had a thin layer of Duralco 4525 thermal epoxy applied between the joining surfaces. The top sample utilized a thermal pad compressed between the tubing and aluminum plate with thermal epoxy used for structural support.

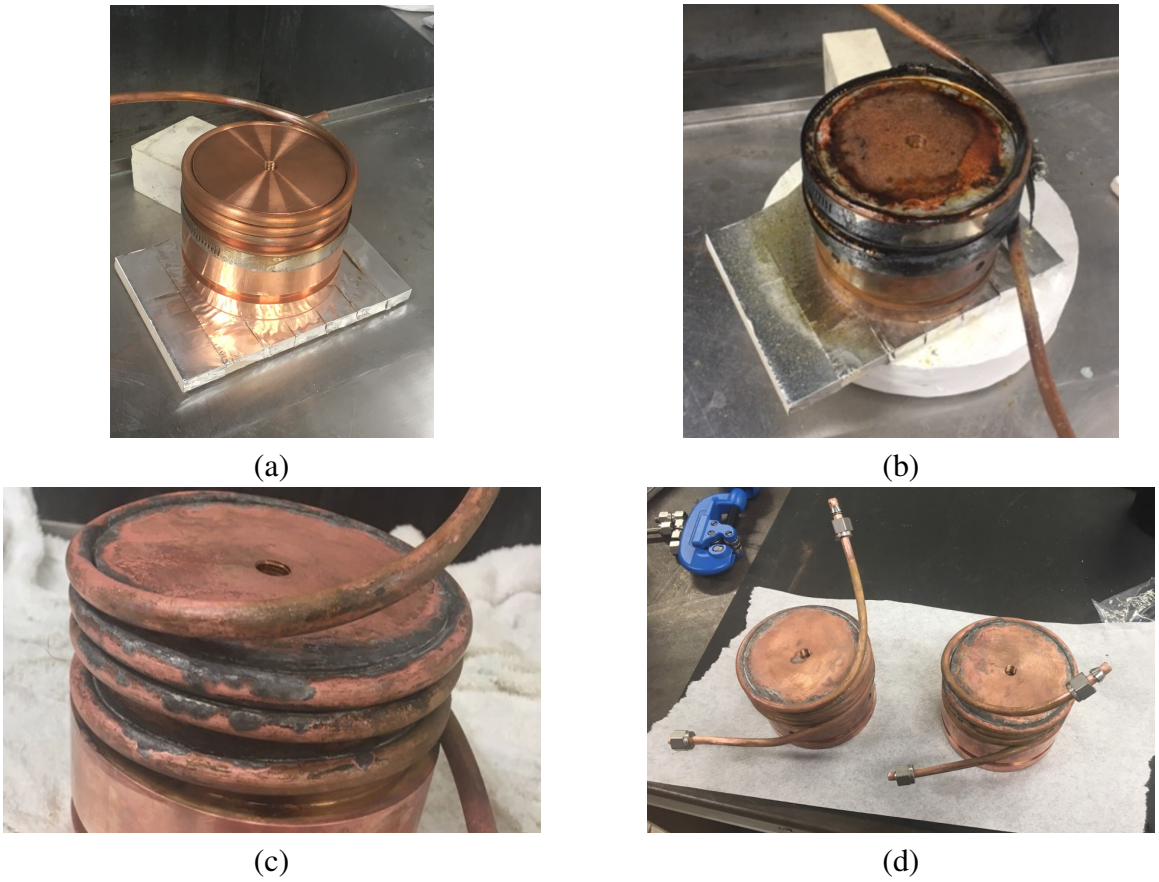

(a) (b)

(c) (d)

Figure 5.17: Soldering of cooling lines to copper supports. (a) Fixture for soldering using hose clamps and insulating ceramic piece as a platform. (b) Application of solder to all tubing coils. (c) Removal of hose clamps and cleaning performed sequentially with isopropyl alcohol, vinegar, and water baths. (d) Finished copper support pieces.

which is commercially available consisting of 95/4.8/0.2 (Sn/Cu/Ag). The key however is the use of the correct flux in ample quantities to ensure proper joining (Superior NO. 1265 flux paste). Test pieces were fabricated using 6061 aluminum brackets and aluminum 1/4-in. tubing however the 1/4-in. tubing was easily melted or punctured by the torch head and found to produce a far weaker joint to 1/4-in. copper tubing on a separate piece of the same aluminum bracket material. Therefore 1/4-in. copper tubing was also used as cooling lines for these aluminum pieces. Figure 5.18 shows pictures of these sample pieces along with sample copper-copper joints.

Due to the larger solder melting point and larger surface area of the work pieces as compared to the copper electrodes, a preheat oven was necessary to efficiently raise the temperature of the work piece to achieve good solder joints. A Yamato DKN 400 was used and set to 270°C which was well above the solder melting point to account for some cooling during transfer out of the oven and the rapid cooling taking place while torch soldering. It was also necessary to work in a fume

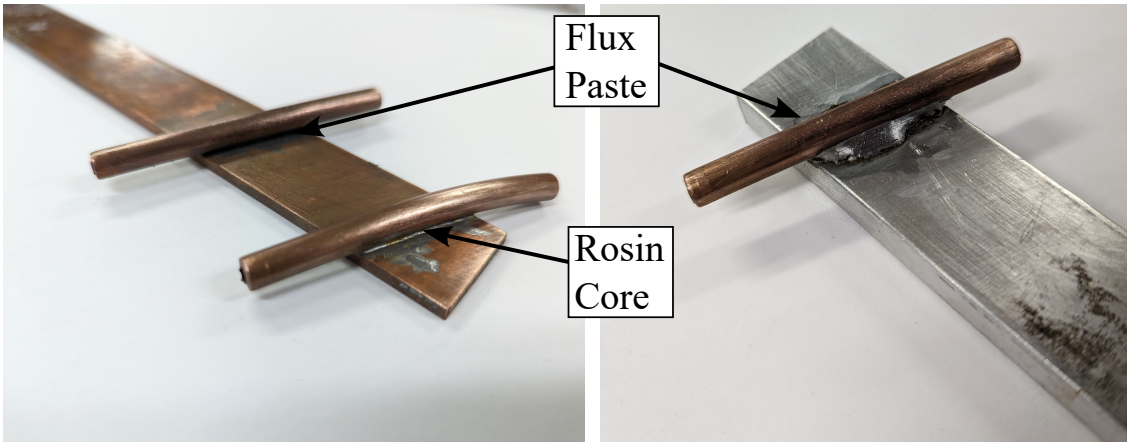

Figure 5.18: Sample 1/4" copper tubing soldered to copper and 6061 aluminum bars showing sample solder joints with the desired characteristics. Superior NO. 1265 flux paste was used for both samples along with a separate solder using a rosin flux core solder.

hood since the flux paste readily produced large quantities of smoke at elevated temperature and in fact had a smoke point lower than the melting point of the solder. Several cycles of heating in the oven and local heating with the propane torch were necessary to cover all joining regions of a single pieces with sufficient solder. These difficulties contributed to reducing the joint quality for these pieces as compared to the copper electrodes. However since both base metals have large thermal conductivities, even a small amount of solder metal between these components would greatly improve the heat transfer as compared to a simple tube clamp scheme or thermal epoxy that otherwise would have been used. The finished components are shown in Figure 5.19. The effectiveness of the cooling system was evaluated for long test periods in Section 5.6.

5.5.1 PVC Cooling Water Distribution System

To maintain an isothermal boundary, a sufficient flow rate through the 1/4-in. tubing lines had to be maintained. This is difficult since frictional losses in narrow tubing rapidly diminish the mass flow rate even for high capacity pumps. For a length of 40 ft of 1/4 in. tubing a pressure loss of 100 kPa is expected. This is the achievable pressure by the NESLAB pump so no net flow rate would result from such a system. To obtain a greater flowrate, a 1 in. diameter PVC piping system was fabricated to deliver cooling water directly next to the CAT facility. The larger diameter pipe significantly decreased the frictional losses and enabled sufficient large flow rates. In addition, 5 parallel connections of the 1/4-in. cooling lines to the PVC piping were used further minimize the pressure losses. Using parallel circuits enabled higher flow rates than if the entire length of 1/4 in. tubing coils were connected in one loop. This pvc system can be seen pictured in Figure 7.1 for reference.

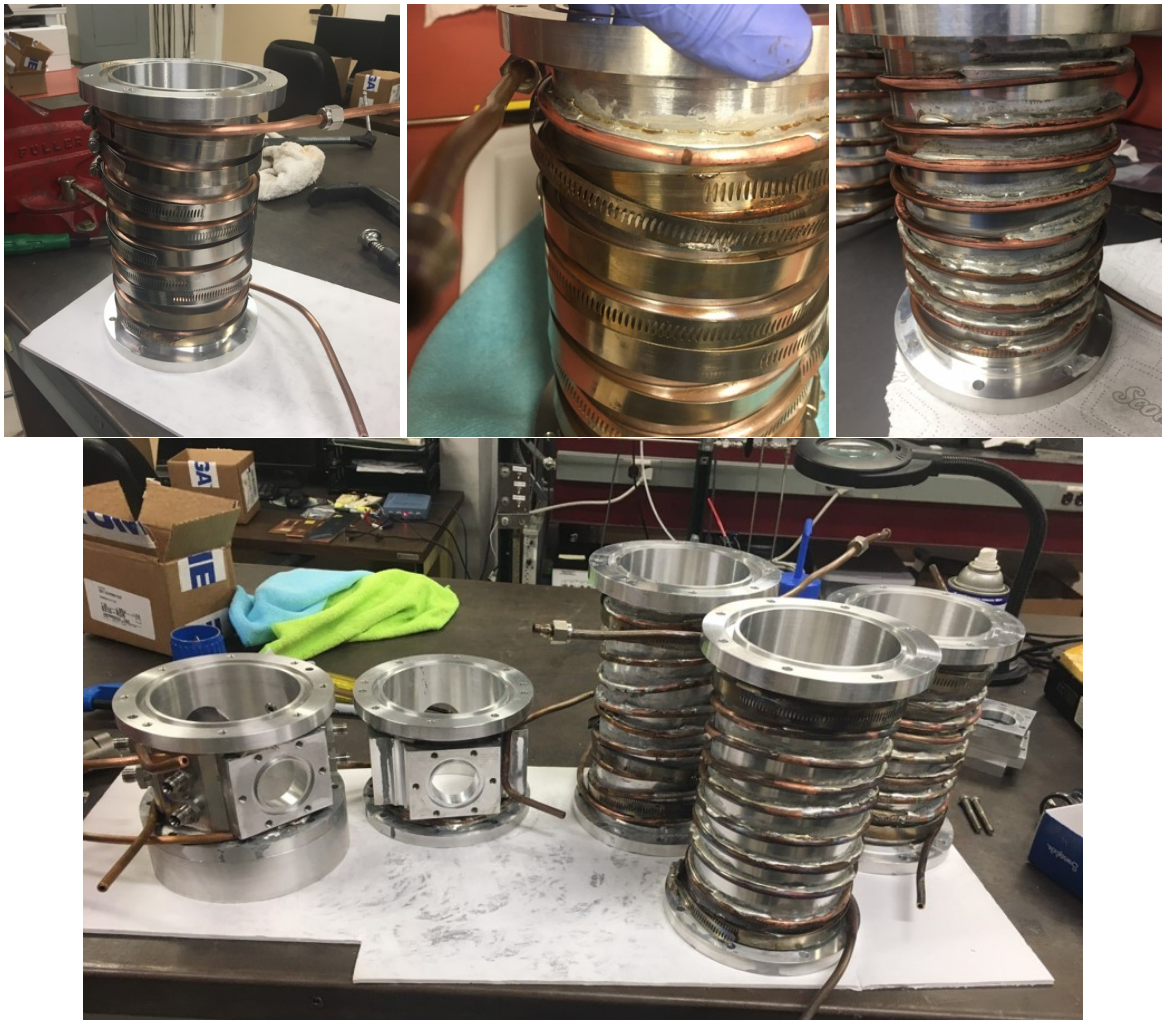

Figure 5.19: Stages of soldering of aluminum outer tubes and final results. (left) Fixture of tubing coils using hose clamps. (middle) Close-up of one solder joint. (right) Final work piece after all joints soldered and clamps removed. (bottom) All of the soldered outer vessel pieces.

5.6 Cylinder Characterization

Prior to ignition testing it was desired to experimental verify the heating model and ensure desired temperature metrics could be achieved. This was performed using a series of bench top experiments mentioned previously. Additionally characterization of the surface temperature under heating loading was desirable to properly understand the conditions present in the planned ignition testing. Visualization of the natural convection flow field around each cylinder was also desired in order to contextualize any differences in ignition thresholds, better understand temperature uniformity data, and directly observe and quantify transitional and turbulent cases. This visualization is presented separately in Chapter 6.

5.6.1 Temperature Measurements

The primary metric to define threshold in thermal ignition testing is the surface temperature. It is prudent then to ensure the temperature distribution of the cylinders used here are well characterized prior to reporting ignition results. Three distinct methods were used for measurement of the surface temperature:

1. 5 K type thermocouples
2. Two-color IR pyrometery (1900/1740 nm)
3. Two-color visible imaging pyrometry using a Nikon D200 camera (636/532nm)

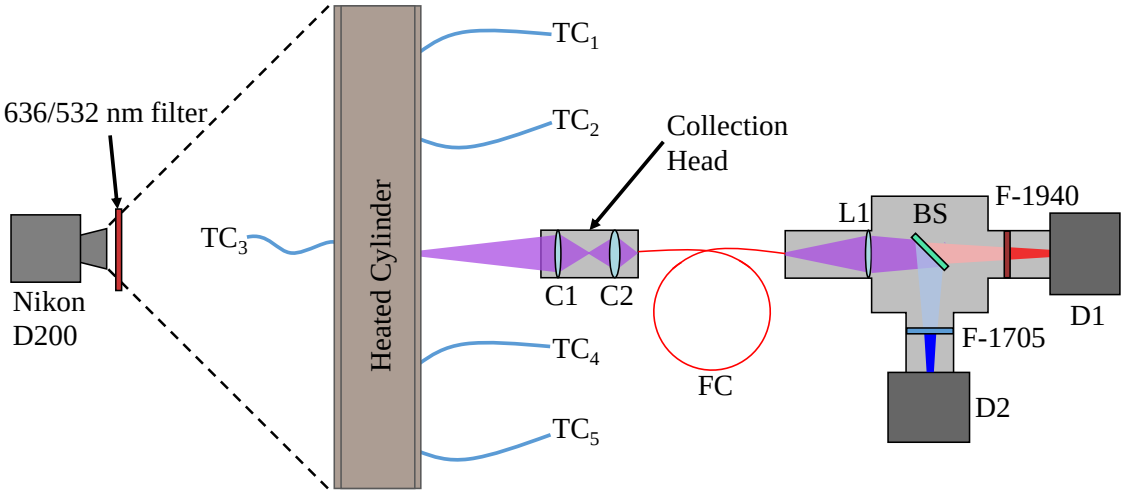

Figure 5.20: Schematic of system used to measure surface temperature measurements of heated cylinders.

A schematic of this temperature measurement system is shown in Figure 5.20. These measurements were repeated for each cylinder presented in Table 5.1. A series of 5 24 gauge K type thermocouples were welded directly to the cylinder surfaces at evenly spaced increments near the central region and near the boundaries. An Analog Devices 5B37 Isolated Thermocouple Input unit was used in each thermocouple line to protect the data acquisition system from potential damage by the large currents present in the heating system. These thermocouples lines were calibrated using a Yokogawa CA71 multi function calibrator. This was used to send a stepped series of 15 discrete signals in the range of 0 - 45 mV corresponding to temperatures from 0 to 1100 °C for K-type thermocouples. The measured values were then converted to temperature using standard thermoelectric voltage conversion tables for type K thermocouples. The results of the calibration are shown in Figure 5.22. A precision spot welder was used to form a bead which was welded to

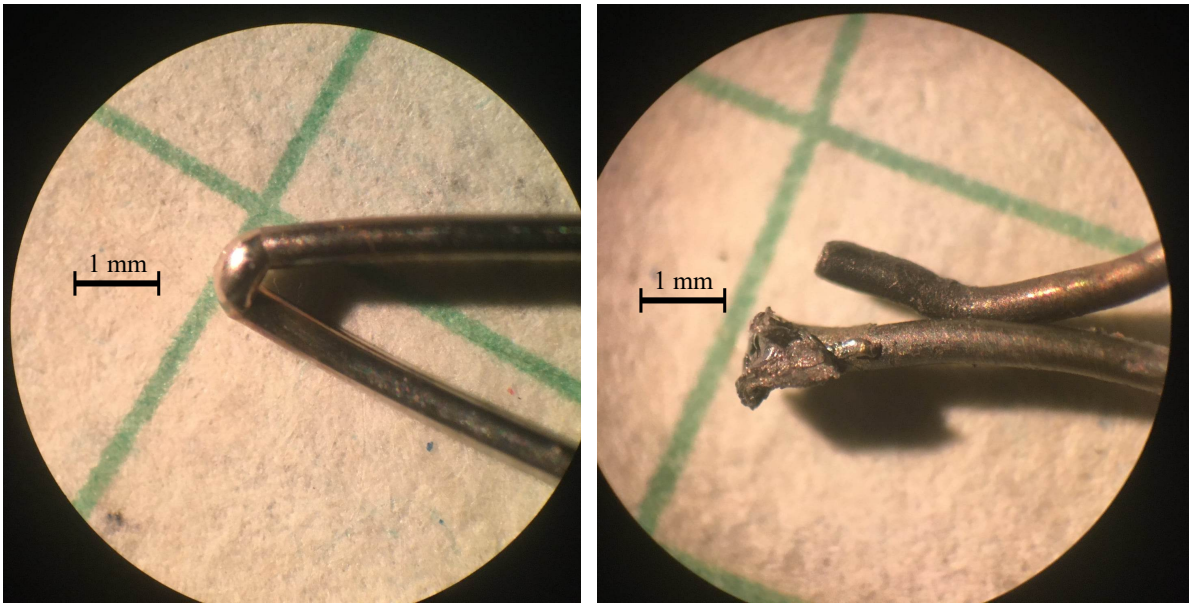

Figure 5.21: (left) Images of well formed thermocouple joined and (right) heavily oxidized thermocouple wire.

the cylinder surface using a DCC Corporation HotSpot I. This was necessary to enable attaching of thermocouples in-situ rather than requiring disassembly for thermocouples to be repaired. The beads were inspected for quality under a microscope and an example of a well formed, unheated thermocouple bead is shown in Figure 5.21. Figure 5.21 also shows the same wire after several heating cycles welded to the cylinder surface illustrating a large degree of oxidation. This oxidation is an aging effect which can cause increasing measurement errors due to the change in resistivity of the wires as the extent of oxidation is increased. For this reason, only a few heating cycles were performed before the thermocouples were detached and the welds redone with fresh portions of the wire.

The principles of the two-color IR pyrometer have already been discussed extensively in Section 3.3.2. This device was previously used with an automated translation stage in Jones (2020) to characterize cylinders of up to 10 in. length. However here the cylinders are much larger and a translation stage with 36 in. of travel was not readily available. Consequently for this study this device is simply used as to provide a point measurement at a fixed height, typically about 5 in. from the bottom support.

An alternative approach to measure a distributed temperature field is using pyrometry with a distributed sensor consisting of many discrete outputs. This can be done using a commercial camera sensor such as a Nikon D200 camera with a CCD sensor which is sensitive in the range of 400 - 700 nm. Most consumer cameras are only sensitive in the visible range so the wavelengths used in the two-color method are different than used in the IR pyrometer. This approach can

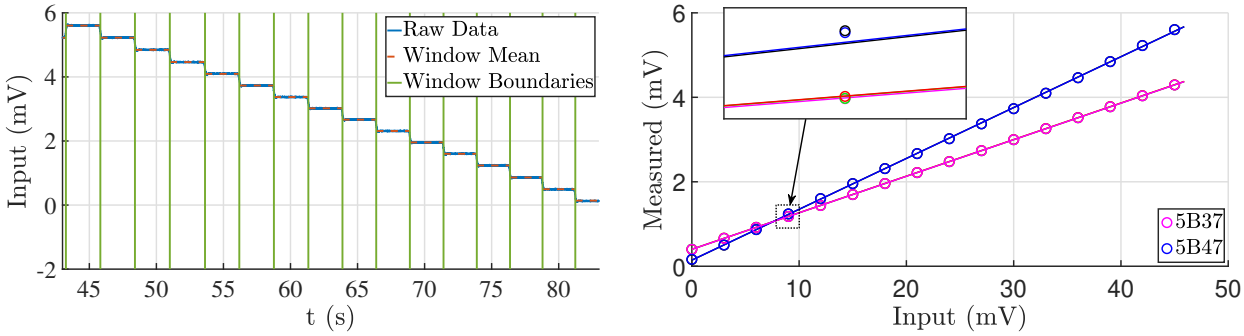

(a) (b)

Figure 5.22: (a) Stepped input voltage applied in 2.5s windows to each thermocouple line. (b) Measured response curves for each of five total thermocouple lines. Measurements for each group of data points are on top of each other for the same isolator unit (3 of 5B37 and 2 of 5B47).

be problematic for low-temperature measurements because there is little emission in the visible spectrum. This is expected from Planck's law of blackbody radiation where the emitted light intensity increases with T^4. Figure 5.23 shows that for temperatures near 1000 K there is sufficient visible emission for two-color pyrometry in the visible range.

Blackbody emission can also be used to predict the expected response of the two-color pyrometry method for any two wavelengths. The expected response curve is found by using the surface temperature and corresponding intensities in Equation (3.11). The result is shown in Figure 5.24 where the linear response seen in previous calibrations is predicted and compares favorably to previous calibrations of the IR pyrometer due to a higher measurement sensitivity to T_w. Using

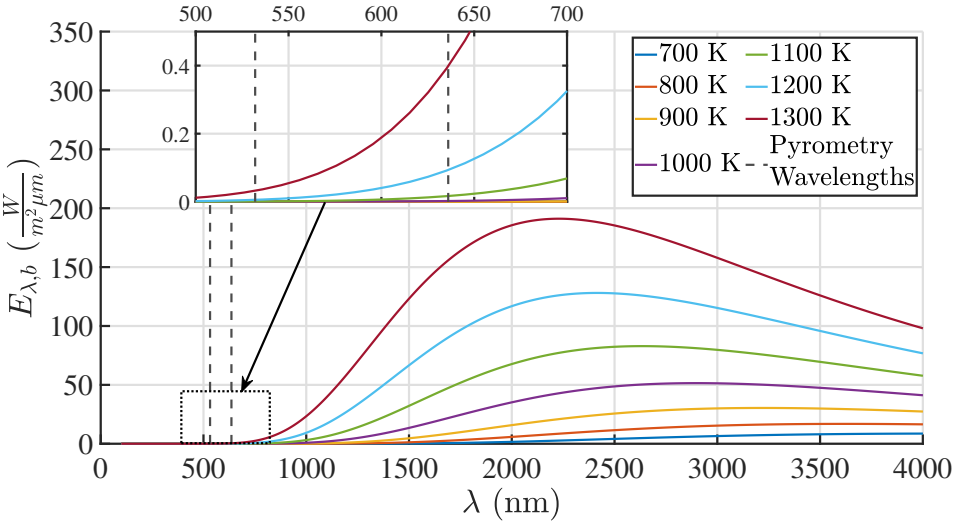

Figure 5.23: Spectral irradiance of an ideal blackbody as predicted by Planck's law. The inlet box shows the visible spectrum and the wavelengths used for imaging pyrometry.

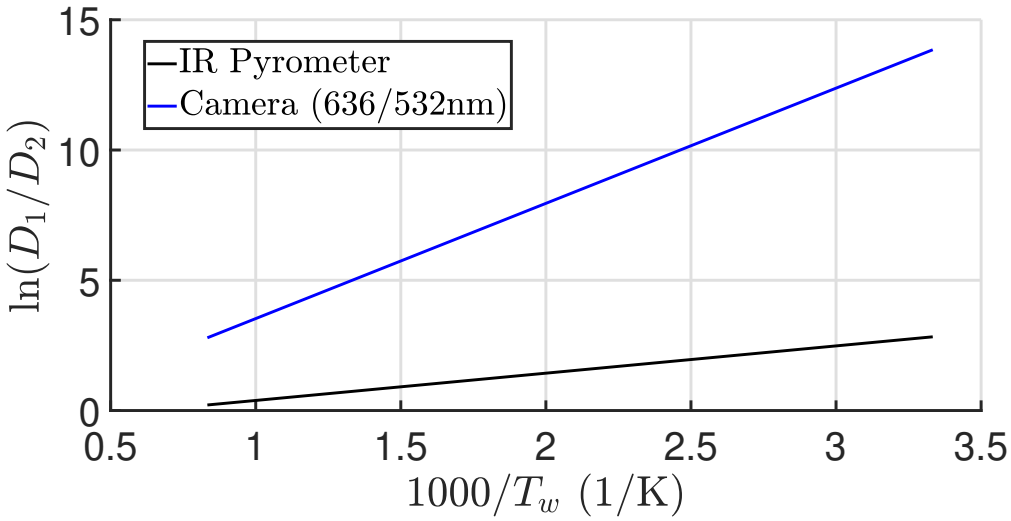

Figure 5.24: Predicted response of camera sensor for visible wavelengths (636/532nm) and IR pyrometer prediction as compared to typical calibration curve.

visible wavelengths shows a larger slope than the in the IR due to the large curvature in the visible portion of the blackbody curve. This means in theory that the measured response to a given temperature change is larger for a visible two-color pyrometer system. This increased sensitivity should lend itself to an improved method for temperature measurement, however this is likely only realizable for high-temperature surfaces where large enough signal-to-noise ratio can be established.

Two cameras were tried for this method, a Nikon D200 and a PCO.2000. Their relevant specifications are compared in Table 5.4. It was desirable to use the PCO.2000 since it contained a monochrome sensor and had a larger bit depth than the D200. However there were unresolved measurement errors which will be discussed in the following paragraphs which made it unsuitable for use in this application. A monochrome sensor is desired since all pixels can be used to measure response in any wavelength of the entire range of the sensor sensitivity. Color camera sensors consist of a Bayer filter overlaid on a monochrome sensor which results in a mosaic tiling of pixels with alternating wavelength sensitivities. In the case of the D200 a RGB filter is present as illustrated in Figure 5.25. The resulting response on each of the three channels is also shown. Use of this Bayer filter directly for isolating the color response for use in pyrometry is not ideal since there is significant overlap in the wavelength sensitivity range of these channels. Separate narrow

Table 5.4: Comparison of cameras used for imaging pyrometry.

Model	**Sensor Type**	**Bit Depth**	**Resolution**	**Monochrome**
Nikon D200	CCD	12	3,872 × 2,592	No
PCO.2000	CCD (Cooled)	14	2048 × 2048	Yes

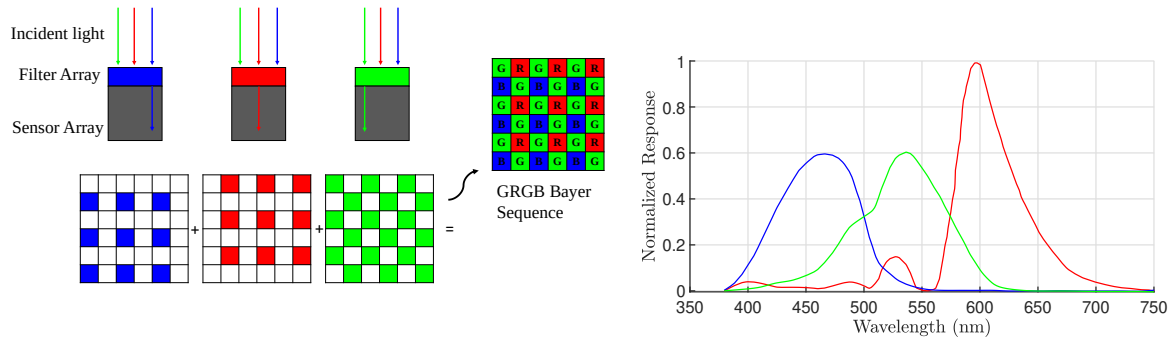

Figure 5.25: (left) Construction of RGB Bayer filter on D200 sensor and (right) response curves for resulting RGB channels. Response data from Toś (2016).

bandpass filters in front of the camera lens are instead used to better isolate the wavelengths of interest. Figure 5.25 also shows that only a fraction of the pixels are sensitive to a given wavelength range designated by the RGB color model. In this case only 25% of the pixels are responsive to blue, a separate 25% to red, and 50% to green. Therefore if looking at 636 nm light, only the red pixels will respond which reduces the effective pixel count to 75% of the full sensor. This must also be accounted for in processing of the image and "demosaicing" of the raw pixel arrangement must be performed to separate the desired red pixels from the non-responding channels.

To isolate the two wavelengths of interest, bandpass filters at 636 nm and 532 nm (both with 10 nm FWHM) were used in sequential individual images. This approach is reliable assuming the object of interest is at a steady state over the imaging time for both exposures. Calibration of this technique was performed using a blackbody radiation source (Process Sensors BBS1200) set from 600 - 900^{o}C in 25^{o}C increments with the aperture fully opened to 1 in. diameter. Each image of the blackbody source was processed to extract the mean pixel value of the central portion of the open blackbody aperture. These values were then taken in a ratio with the corresponding image of the same temperature source obtained with the other filter. During calibration, the ISO, aperture, and lens settings remained constant. The shutter speed was varied during calibration in order to test pixel response linearity. This is important since the shutter speed required for imaging a real surface may be different than calibration and not known a priori. With a linear pixel response this means the calibration curve should be independent of shutter speed and can be adjusted from measurement to calibration. This linearity can be seen in Figure 5.26 for both the 636 nm and 532 nm wavelengths on the D200 and PCO.2000 cameras. The slopes for each wavelength differ and can be taken in the intensity ratio used for calibration instead of using only one discrete exposure.

Typical calibration curves are shown in Figure 5.27 for the D200 camera. The measured slope compares well with the expected response curve in Figure 5.24. The absolute values differ slightly due to real world factors like using an imperfect blackbody, light absorption by the camera lens, and

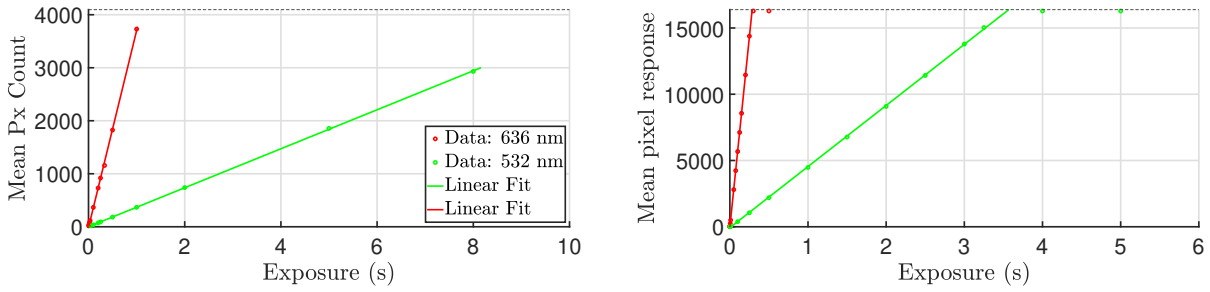

(a) (b)

Figure 5.26: Example of pixel linearity to shutter speed for (a) Nikon D200 and (b) PCO.2000. The blackbody temperature was constant T = 900°C for all exposures presented here. The linear fit excludes exposure values where the sensor was saturated or where the pixel count was too low.

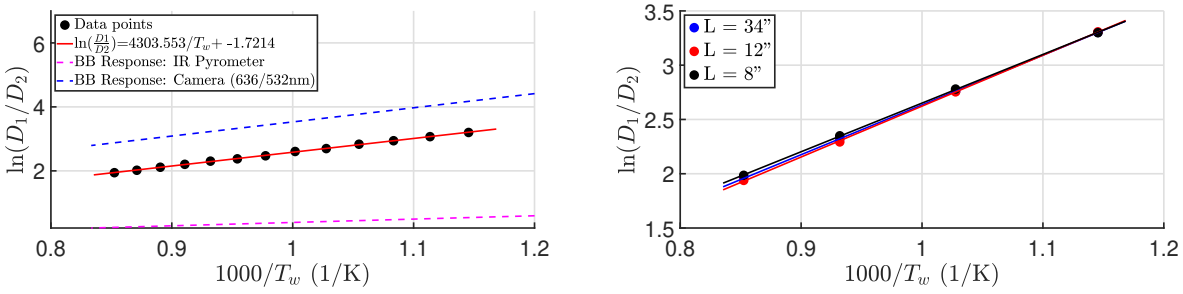

(a) (b)

Figure 5.27: (a) Calibration of Nikon D200 using blackbody source and compared with predicted blackbody response. (b) Comparison of calibrations at different offset distances L between camera lens and blackbody source. There are some differences at high temperatures for different offset distances and lens settings.

the real response characteristics of the camera sensor. The calibration is also relatively insensitive to distance from the source except at high temperatures as illustrated Figure 5.27. The lens settings for each of these distances were also adjusted and may contribute to the observed differences.

When attempting to use the PCO.2000 in the same calibration approach, the response of the sensor differed significantly. The issue is illustrated in Figure 5.28 where there doesn't seem to be a measurable response in intensity ratio with temperature for this camera. This is of course problematic for use in a two-color pyrometer measurement system. All aspects outside of the camera used in the calibration were the same including distance from the source, the lens used, and lens settings. It was found that the linearity of the pixel response held for all temperatures as seen in Figure 5.26 so this was not the source of the error. It seemed that the sensor response somehow depended on the intensity of the source since this response deviates strongly from the expected blackbody response. The reason for this lack of measurable response therefore remains a mystery

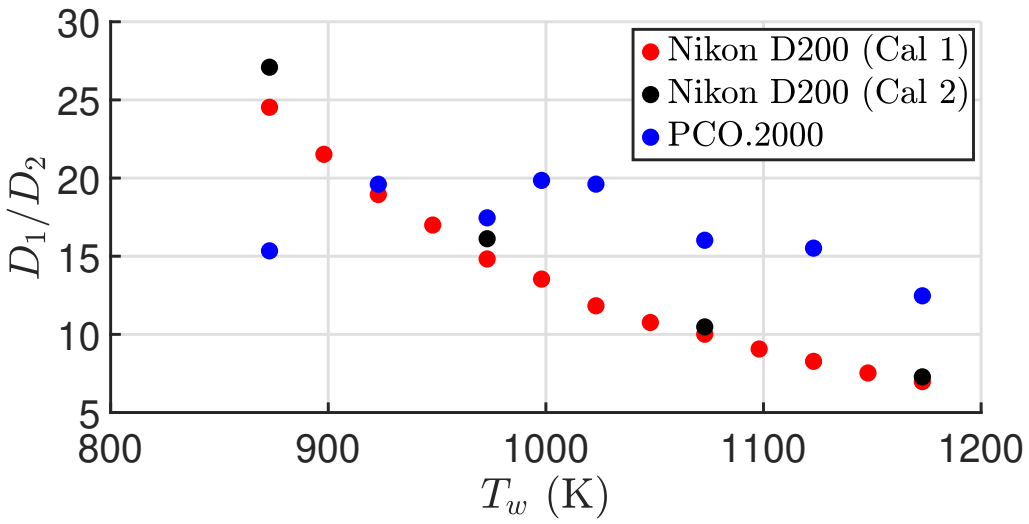

Figure 5.28: Comparison of PCO.2000 and Nikon D200 for Imaging Pyrometry. Cal1 and Cal2 are two separate calibration allignments with Nikon D200.

that may only be explainable by the construction of the sensor to which we do not have detailed descriptions or data on. For this reason use of this camera was abandoned in favor of the Nikon D200 for the measurements presented for cylinder characterization.

5.6.1.1 Cylinder Temperature Uniformity

These measurements were repeated for each cylinder length in Table 5.1. The results are presented in Figure 5.29. Significant differences between the pyrometer and thermocouple measurements is shown for some cases. For the short cylinders (Represented by H6) this is likely a result of small pointing errors and relatively large thermal gradients on the surface due to conduction at the vertical boundaries. For the long cylinders the variation in oxide development is the main issue and will be discussed further and calibrated for as presented in Section 7.2.1. For short cylinders there exist large temperature gradients due to thermal conduction at the boundaries. The H10 and H18 cylinders were highly uniform across the cylinder height (within 10 — 15K). However the H28 and H36 cylinders showed a relatively large decrease in temperature in the top region (uniformly lower, not decreasing). This can be attributed to the large increase in turbulent convection for these longer cylinders that will be plainly evident in the flow visualization presented in Chapter 6. Turbulent convection increases the convective heat transfer coefficient significantly and in Section 5.3 an estimation of a factor of 2 increase was used for design. In the upper region of these cylinders where the flow is fully turbulent, the heat balance changes from that in the laminar region since the input current density is approximately constant through the length of the cylinder. This was not originally considered in the design but is a natural and unavoidable process when doing these larger

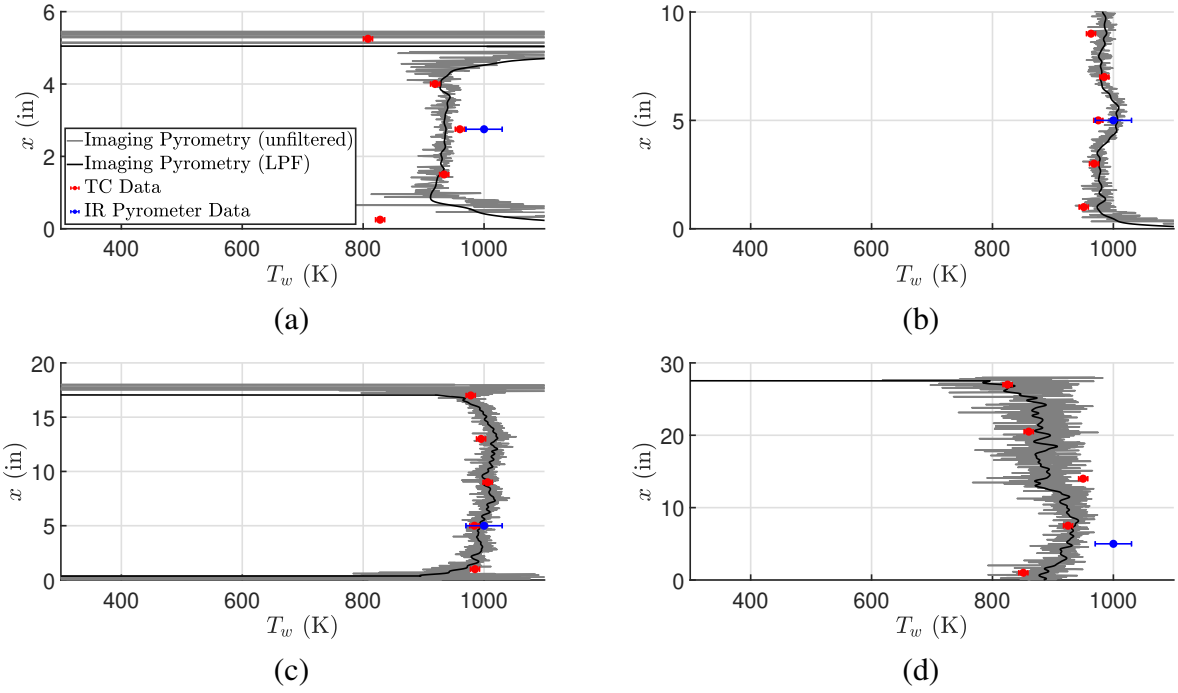

Figure 5.29: Temperature profiles for each of the CAT cylinders designed in this chapter (a) H6 (b) H10 (c) H18 (d) H28. H4 and H36 results are not included here but are similar to H6 and H28 results respectively.

scale experiments consisting of both laminar and turbulent regions of heat transfer. This makes quantification of ignition using a single surface temperature difficult. The hottest temperature region (in the laminar flow) can be selected for conservative design or alternatively input power required for may be useful. Overall the H4, H6, H10, and H18 cylinders are considered uniform and can be well characterized by a single temperature. The H28 and H36 cylinders will be characterized by the temperature near the bottom (e.g. the laminar region) and a corrective factor for the temperature at the top can be taken to be approximately -50 K. Input powers leading to ignition will also be presented and discussed as metrics for ignition threshold determination.

References

Boeck, L., Meijers, M., Kink, A., Mével, R., & Shepherd, J. (2017). Ignition of fuel–air mixtures from a hot circular cylinder. *Combustion and Flame*, *185*, 265–277. https://doi.org/10.1016/j.combustflame.2017.07.007 (Cit. on p. 120)

Boetcher, S. K. S. (2014). *Natural Convection from Circular Cylinders*. Springer International Publishing. https://doi.org/10.1007/978-3-319-08132-8. (Cit. on p. 128)

Boettcher, P., Menon, S., Ventura, B., Blanquart, G., & Shepherd, J. (2013). Cyclic flame propagation in premixed combustion. *Journal of Fluid Mechanics*, *735*, 176–202. https://doi.org/10.1017/jfm.2013.495 (Cit. on p. 120)

Boettcher, P., Mével, R., Thomas, V., & Shepherd, J. (2012). The effect of heating rates on low temperature hexane air combustion. *Fuel*, *96*, 392–403. https://doi.org/10.1016/j.fuel.2011.12.044 (Cit. on p. 120)

Calcium Fluoride Physical and Chemical Properties. (2003). (Cit. on p. 141).

Chenoweth, D. R., & Paolucci, S. (1986). Natural convection in an enclosed vertical air layer with large horizontal temperature differences. *Journal of Fluid Mechanics*, *169*, 173–210. https://doi.org/10.1017/S0022112086000587 (Cit. on pp. 121–123, 138)

Fujikawa, T., Ozasa, T., & Kozuka, K. (1988). Development of Transparent Cylinder Engines for Schlieren Observation, 881632. https://doi.org/10.4271/881632 (Cit. on pp. 137, 138)

High-Temperature Characteristics of Stainless Steels. (n.d.). Nickel Institute, American Iron and Steel Institute. (Cit. on pp. 143, 145).

Jones, S., & Shepherd, J. E. (2020). Thermal ignition of n-hexane mixtures by vertical cylinders. *Proceedings of the 13th International Symposium on Hazards, Prevention and Mitigation of Industrial Explosions (ISHPMIE 2020)* (Cit. on pp. 120, 123).

Jones, S. M. (2020). *Thermal ignition by vertical cylinders*. California Institute of Technology. (Cit. on pp. 122, 123, 125, 126, 131, 133, 135, 139, 142, 152).

Kaiser, S. A., Salazar, V. M., & Hoops, A. A. (2013). Schlieren measurements in the round cylinder of an optically accessible internal combustion engine. *Applied Optics*, *52*(14), 3433. https://doi.org/10.1364/AO.52.003433 (Cit. on p. 137)

Mével, R., Melguizo-Gavilanes, J., Boeck, L., Nove-Josserand, A., Kishita, Y., Coronel, S., & Shepherd, J. E. (2016). Ignition of hydrogen-air mixtures by a localized stationary hot surface, 17 (Cit. on p. 120).

Siegel, R., & Howell, J. R. (1981). *Thermal radiation heat transfer* (2d ed). Hemisphere Pub. Corp. (Cit. on p. 132).

Toś, C. (2016). The Use of a Modified Camera for the Classification of Sedimentary Rocks. *Photogrammetrie - Fernerkundung - Geoinformation*, *2016*(4), 191–210. https://doi.org/10.1127/pfg/2016/0299 (Cit. on p. 155)

Chapter 6

NON-BOUSSINESQ NATURAL CONVECTION ON A VERTICAL CYLINDER WITH LARGE WALL TEMPERATURES

6.1 Motivation

An understanding of the flow field surrounding a heated surface is necessary to study the conditions leading to ignition in the thermal boundary layer and the subsequent flame propagation. One of the main goals in the design of the CAT experiments described in Chapter 5 is to enable experimentation of transitional and turbulent thermal ignition. This is of interest since the effect of turbulence on thermal ignition problems has not been well studied. With this in mind an experimental approach was taken using visualization tools to study the flow field produced by the cylinders used in CAT testing.

6.2 Background

Most existing work on natural convection flows by vertical heated surfaces and in narrow channels has been limited to the Boussinesq regime wherein temperature differences are assumed to be linearly proportional to density differences ($\Delta\rho = -\rho_0\beta\Delta T$). This is only a valid assumption in cases where temperature gradients are small (Tritton, 1988). In these cases only the density variation is important to consider and only when multiplied by $\boldsymbol{g}$ since other accelerations are small ($|D_{\boldsymbol{u}}/Dt| \ll \boldsymbol{g}$). Consequently the variation in fluid properties is also neglected. For large temperature differences, density variations cannot be linearized with temperature and fluid property variation with temperature becomes significant, especially for gases. In those cases the low Mach number approximation can still typically be made however density differences are significant so that $\nabla \cdot \boldsymbol{u} \neq 0$. Paolucci (1982) derived a widely applicable set of governing equations for flows with variable fluid properties applying the low Mach number approximation and applied this approach to various problems including natural convection flow in a cavity (Chenoweth & Paolucci, 1986). Even in studies where the Boussinesq approximation is not made, the temperature differences investigated are still modest compared to the present work ($T_w \leq 698$ K, Cairnie and Harrison (1982)). Additionally the length scales investigated are relatively small which result in small Grashof (Gr) and Rayleigh (Ra) numbers due to the cubic dependence on vertical length. The accepted wisdom suggests that transition to turbulence occurs in the range of Ra = $10^8 - 10^9$ and even larger values for high aspect ratio channels (Gebhart et al., 1988; Chenoweth & Paolucci, 1986).

The Boussinesq approximation is implicitly included in the classical definitions of Ra and Gr

$$Gr_H = \frac{g\beta(T - T_\infty)H^3}{\nu^2}\,, \tag{6.1}$$

$$Pr = \frac{\nu}{\alpha}\,, \tag{6.2}$$

$$Ra_H = Gr_H Pr = \frac{g\beta(T - T_\infty)H^3}{\nu\alpha}\,. \tag{6.3}$$

For an ideal gas, the coefficient of thermal expansion $\beta = T^{-1}$. In vertical channel flows $T - T_\infty$ is replaced by the temperature difference between the hot and cold channel walls, $T_H - T_C$. A more generalized approach to characterizing the buoyancy term in the numerator would be to use density difference ($\Delta\rho$) directly

$$Gr_H^{NB} = \frac{g(\rho_\infty - \rho)H^3}{\rho\nu^2}\,, \tag{6.4}$$

$$Ra_H^{NB} = GrPr = \frac{g(\rho_\infty - \rho)H^3}{\mu\alpha}\,, \tag{6.5}$$

where the kinematic viscosity is ν and the absolute viscosity $\mu = \rho\nu$. Here the superscript NB is used to denote Non-Boussinesq formulations. Fluid properties (α,β,ν) are conventionally evaluated at the film temperature defined as the average temperature between the hot wall and cold fluid or cold wall in channel flows:

$$T_{film} = \frac{T_w + T_\infty}{2} \tag{6.6}$$

Cantera (Goodwin et al., 2017) is used to compute the thermodynamic properties of air and a stoichiometric mixture of n-hexane and air using a database of realistic thermochemical and transport parameters. These properties are used to calculate Gr, Pr, and Ra as a function of hot wall temperature (T_w) for a chemically frozen flow with $P = 1$ atm, $T_\infty = 296$ K and $L = 1$ m. Figure 6.1 (a) and (b) shows that there is reasonable agreement of the Boussinesq and non-Boussinesq formulations for small values of T_w. However significant differences between these definitions exist for $T_w > 400$ K. Both formulations predict a maximum in Ra and Gr with increasing wall temperature and a fixed length scale. Because $Ra(T)$ and $Gr(T)$ are not monotonically increasing functions of T_w, a prescribed value of these nondimensional parameters corresponds to two distinct physical states. This can prove problematic when trying to use these values to define a physical regime change such as laminar-turbulent transition.

This feature of $Ra(T)$ and $Gr(T)$ are consequences of the property value dependencies on temperature as shown in Figure 6.1 (d). $\beta(T)$ is a strictly decreasing function while $\alpha(T)$ and $\nu(T)$ are strictly increasing. These terms therefore all serve to compete with the linearly increasing ΔT term and dominate at high T_w. The constant property formulation of nondimensional groups where the

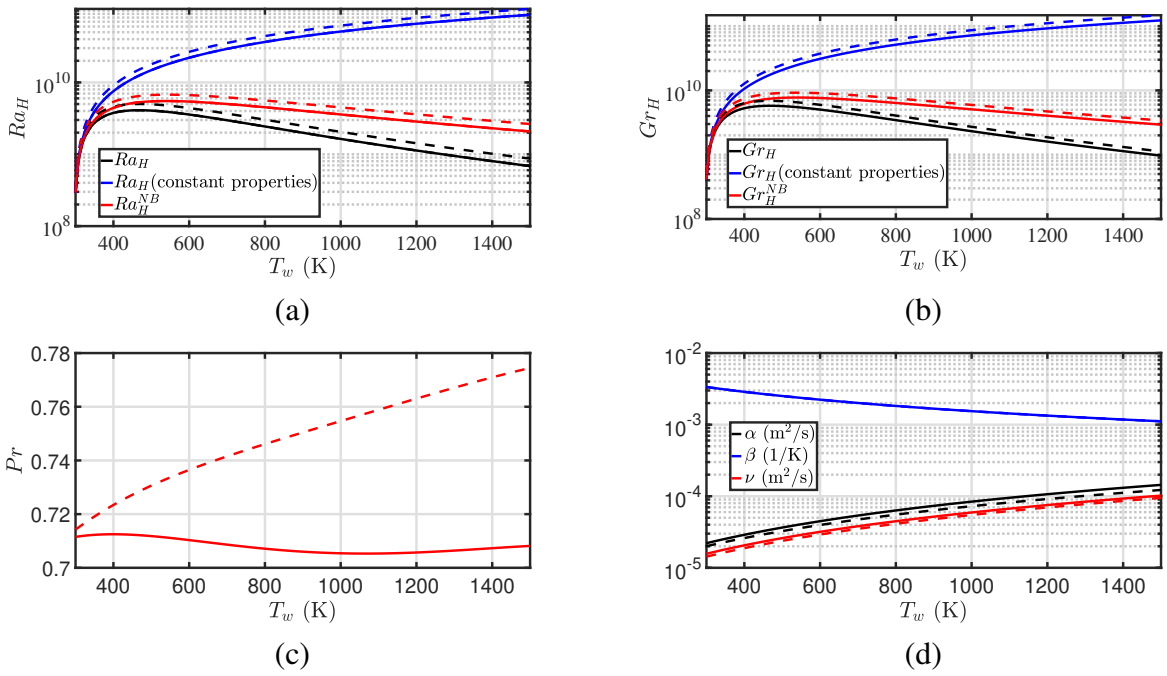

Figure 6.1: (a) Comparison of different formulations for Ra and (b) Gr. (c) Pr vs T_w and (d) Thermodynamic property values. Dotted lines are for chemically frozen stoichiometric n-hexane air mixtures and solid lines are for air. β is identical for both mixtures.

fluid properties are naively evaluated at a fixed temperature does not exhibit the local maximum for this reason. It is worth noting that for liquids like water where ν is a strongly decreasing function of temperature and α and β exhibit minimal temperature dependence, the local maximum does not exist. This implies that there is a fundamental difference in how these nondimensinal groups should apply to gas and liquids and highlight the importance of Pr which are much larger for liquids. For a full description of laminar-turbulent transition the use of Gr or Ra alone is therefore insufficient to apply generally to all fluids. The remaining discussion will focus on Ra for simplicity but the same conclusions apply to Gr since they are related. The remaining sections explore the relevance of Ra in defining laminar-turbulent transition in an experimental system with large vertical surfaces and large ΔT.

6.3 Visualization System

A double-pass shadowgraph and schlieren flow visualization system was constructed. The shadowgraph used a retroreflective screen and the schlieren used a 8.5 in.-diameter, 1400 mm focal length mirror as reflective elements. These visualization systems are shown schematically in Figure 6.2. It was desirable to use both visualization systems since the shadowgraph method enabled large fields of view while the schlieren enabled enhanced sensitivity which improved visualization of the steady laminar boundary layers and enabled high resolution imaging of the flow structures in the

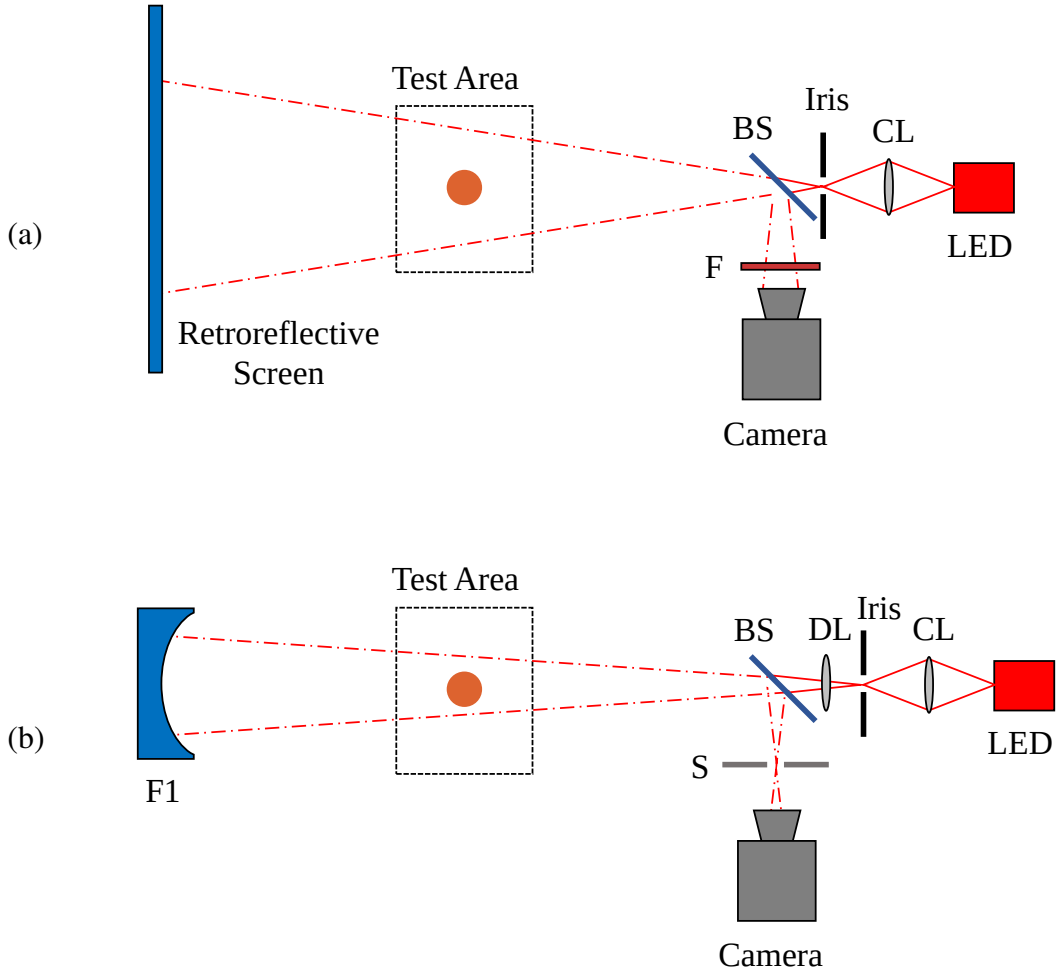

Figure 6.2: (a) Schematic of the shadowgraph visualization system. (b) Schematic of schlieren visualization system. CL: Condenser Lens, BS: Beam Splitter, F: Bandpass filter (636 nm), DL: Dall null corrector lens, F1: Parabolic Mirror , S: Schlieren Stop.

transitional flow region. As shown in Figure 6.2 the light source was a red LED whose intensity was controlled by a variable current power supply. The light was focused onto an iris using a short-focal-length condenser lens (CL) for both systems, the imaging optical components varied slightly between the two setups. The camera used in both systems was a Phantom V711 high speed camera. The optical system was built in such a way that the light source and imaging plane could be translated vertically to enable visualisation of different regions along the cylinder length.

6.3.1 Shadowgraph Imaging

The complete shadowgraph system is illustrated in Figure 6.2 (a). Light from the iris passed through a 50/50 cubic beamsplitter. The expanding beam illuminated a test area of approximately 1 m^2. The shadow of the object in the test area was projected onto the reflective screen placed downstream

of the test area. Light rays from this screen are reflected back along their incident path to the beamsplitter where half of the light is directed towards the camera. A commercial Nikon lenses (f = 100 - 210mm adjustable) was used to magnify and focus the image of the screen onto the camera sensor. The camera optical axis was offset angle by 5-10°from the perpendicular to the main optical axis to eliminate stray internal reflections from the light source optics and beam splitter. A 636 nm bandpass filter was also used to filter out emitted radiation from the cylinder. The field of view in this setup was large enough that no vertical translation was necessary to visualize different regions of the cylinder. Simply adjusting the magnification of the Nikon lens was sufficient.

The reflection screen was a 3M® Scotchlite Reflective High Temperature Vinyl (HTV) material. This material is retro-reflective meaning incident light rays are returned along their original path. This is enabled by the presence of microscopic spherical glass beads embedded in the vinyl material. A picture of the material under high magnification is shown in Figure 6.3. The retroreflective property allows for a high gain return of incident light rays to the imaging plane of the camera with no need for a downstream focusing optic.Hargather and Settles (2009) used this technique in order to eliminate double imaging resulting from placing the camera off axis from the light source in classical direct shadowgraph systems. Using this technique also enables lower exposure times and higher frame rates than a traditional diffuse screen due to the high return gain. To obtain high quality images, careful alignment is required to make the object and its shadow coincident in the image plane.

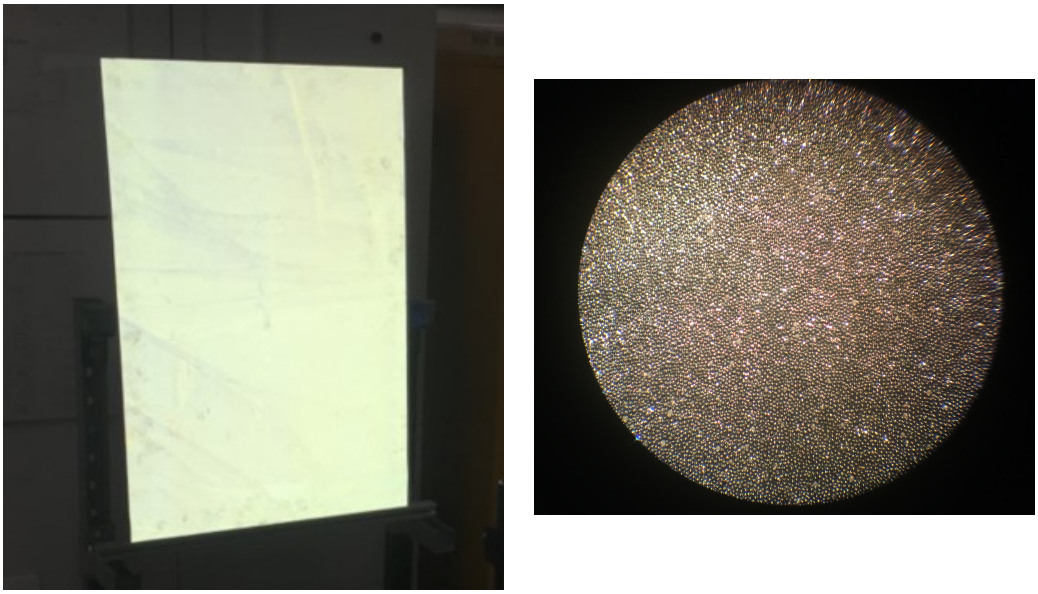

(a) (b)

Figure 6.3: (a) Image of the retroreflective screen using flash photography and (b) Region under high magnification using a microscope. The spherical beads are $\lesssim 100\mu$m in diameter.

6.3.2 Schlieren Imaging

The schlieren system is illustrated in Figure 6.2 (b). This system used a corrective lens placed between the iris and beamsplitter in order to minimize off-axis aberrations across the imaging field. The lens was located between the light source and the beamsplitter. A narrower illumination region was produced in the test region than for the shadowgraph system . An 8.5-in. diameter, 1400 mm focal length parabolic mirror was used as the focusing optic in this system. The light reflected from the mirror returned through the beamsplitter where one-half of the light was directed toward the camera. The schlieren focus was formed on the camera side of the beamsplitter where the schlieren stop was placed. This stop was an adjustable iris to enable sensitivity to gradients in all directions. A commercial Nikon lenses (f = 55 mm) was used to magnify and focus the image plane of the test area onto the camera sensor. A bandpass filter was not required because lower exposure times were possible with much greater light intensity than the shadowgraph system.

An 4-in. diameter field of view was produced with this system. Vertical translation of the light source and camera along with the schlieren mirror was used to obtain images of various elevations. This was challenging to align properly since the optical axes had to be precisely co-linear for good image quality. The mirror used was mounted with a fairly course kinematic mount on a large steel support placed on the ground since the system could not fit on the optical bench due to the long focal length of the mirror. Two height regimes were successfully used for this system: one in the laminar region around 2 - 6 in from the bottom of cylinders and the other in a region of 8 - 12 in where the onset of instability and transition to turbulence was typically observed to occur for the temperature regime of interest.

Settles (2001) discusses the implementation of a similar double-pass schlieren system using a 1 m parabolic mirror. This includes a brief discussion of the corrective optic element called a *Dall null corrector* and its implementation. Dall (1953) originated this method and provides a detailed description of the requirements. A simple plano-convex lens can be used as the corrector. Using Dall's analysis, an off-the-shelf f = 75 mm plano-convex lens was selected and placed at the calculated distance of 44.45 mm from the point light source. Careful alignment of the optical axes of the mirror, lens and point light source are essential in eliminating the double image. Figure 6.4 shows a comparison of the image with and without the Dall corrective lens. Without the corrective optic, the aberrations due to off-axis rays causes the return image to shift towards the center of the mirror. Despite these improvements, the corrective optic was also found to produce a distributed focus and poor performance with mono-directional (knife edge) schlieren stop. The double imaging correction was only maintained if an iris was used for this purpose. Otherwise cutting off light from one side preferentially reintroduced a double image in that direction.

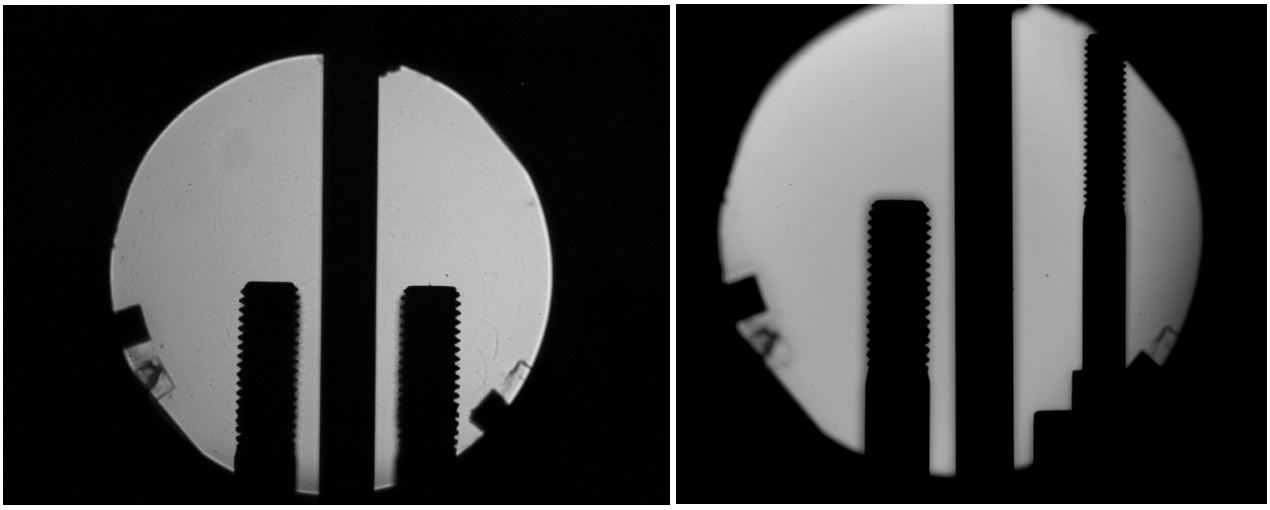

(a) (b)

Figure 6.4: (a) Uncorrected schlieren field. Off axis aberration cause the image of the bolt threads to be shifted toward the mirror center. (b) Corrected imaging field with Dall null corrector.

6.3.3 Cylinder Setup

To perform imaging the cylinders were placed in the large copper electrode pieces described in Chapter 5 and suspended in the test area. The cylinders were only supported at the top electrode via a tube clamp and the bottom electrode hung free to allow unconstrained thermal expansion of the cylinders during these tests. Care was taken to ensure the cylinders hung fully vertically prior to each test as there was some slop in the threaded connections of the cylinders with the electrodes and clamp supports. This allowed some small angular deviation from vertical which had to be prevented. This is important because if cylinder axis is inclined relative to the vertical, gravity would cause asymmetry due to the buoyancy force not being parallel to the cylinder wall. When the cylinder is not aligned vertically, then early flow separation and transition to turbulence can occur. Care also had to be taken to protect the exposed cylinders from various lab currents such as from electronic equipment fans, AC ducts, breathing, and human motion to minimize the perturbations introduced from the lab environment. Fans and vents were blocked off and human presence in the room during imaging was forbidden.

The optical pyrometer described in Chapters 3 and 5 was used in a feedback control loop to maintain constant wall temperatures during testing. The pyrometer head was aligned at the center of H4, H6 and H10 cylinders and at a nominal height of 6 in. as measured from the bottom surface for the H18, H28, and H36 cylinders. The use of the pyrometer was only possible for $T_w > 800$ K due to rapidly diminished signal to noise ratio for surfaces below this temperature. For cases with $T_w < 800$ K a type K thermocouple was used in a pseudo feedback-control method. The thermocouple welded to

the cylinder and a constant current input applied for heating until a constant value was measured on the thermocouple. The current was then shut off temporally to determine the actual surface temperature (to eliminate the current offset produced when $I \neq 0$ as described in Chapter 3). The same input current was then reapplied until the same constant value was measured on the thermocouple as in the first heating cycle. Finally the thermocouple was detached to eliminate its influence on the fluid motion and a video was captured.

6.3.4 Image Processing using Proper Orthogonal Decomposition (POD)

A combination of the visualized disturbances being relatively weak, resolution limitations of the high speed camera, and the reflective screen not producing perfectly uniform background resulted in poor contrast images especially for low temperature differences. To improve the image quality, a Proper Orthogonal Decomposition (POD) toolbox (Masullo, 2023; Mendez et al., 2017) was used to remove the common background modes from the raw videos. Removal of the first two modes was typically sufficient for this application but removal of four modes was necessary for some of the lowest temperature cases discussed in later sections (e.g. 555 K, 625 K). All images using this processing method had four modes removed and the contrast stretched afterwards. Figure 6.5 shows an example of a raw shadowgraph image with non-uniform background intensity and the same image after POD background removal and contrast stretching.

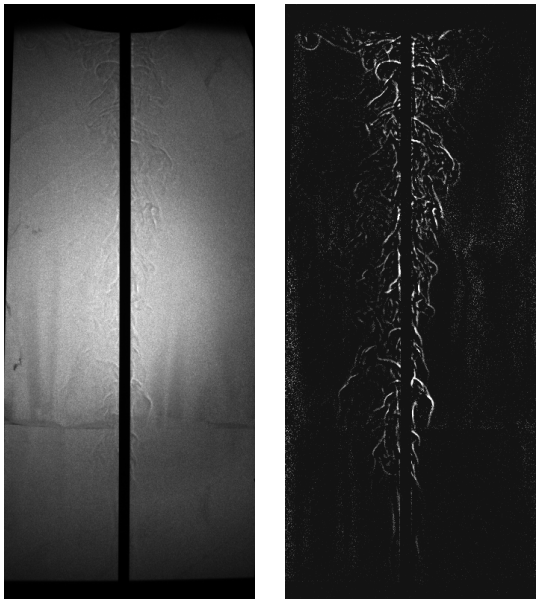

(a) (b)

Figure 6.5: (a) Raw shadowgraph image of H28 cylinder at T_w = 950 K showing non-uniform background intensity. (b) Same image after removal of first 4 background modes using POD and contrast stretching.

6.4 Flow Field Visualization Results

6.4.1 Dependence on Vertical Height

A case study of all cylinder lengths was conducted (H4, H6, H10, H18, H28 and H36) using shadowgraph imaging. For these tests T_w = 1000 K was used to approximate the expected temperatures required in the CAT ignition experiments. This revealed the limitations in the visualization of steady laminar natural convection boundary layers by the shadowgraph method. Shadowgraphy is sensitive to the second spatial derivative of refractive index which for constant composition gases is proportional to the density (e.g. $\frac{\partial^2 n}{\partial x^2} \propto \frac{\partial^2 \rho}{\partial x^2}$). The raw images therefore contain information about $\frac{\partial^2 \rho}{\partial x^2}$ in the flow and for laminar boundary layers this is small since the temperature gradient in the boundary layer doesn't vary substantially which makes for a low contrast shadowgraph image. However, for transitional and turbulent flows, $\frac{\partial^2 \rho}{\partial x^2}$ is much larger and the flow structures within the boundary layer and ejected into the bulk fluid are readily observed in the shadowgraph images.

Figure 6.6 presents representative schlieren images of the H4 and shadowgraph images of the H6 cylinders. These images show the centrally located cylinder surrounded by a narrow boundary layer. The edge of the boundary layer is the bright white band running vertically in frame and slightly offset on either side of the surface. At the top of the frame the flow impinges on the upper electrode, turns radially and forms a boundary layer on the upper surface as indicated by the horizontal white line. For the H4 and H6 cases the flow was always laminar in the vertical surface boundary layer with occasional periods of instability likely excited by small lab currents and quickly damped out. Over long testing periods ($\leq$ 10 mins) at constant T_w the flow features did not vary substantially.

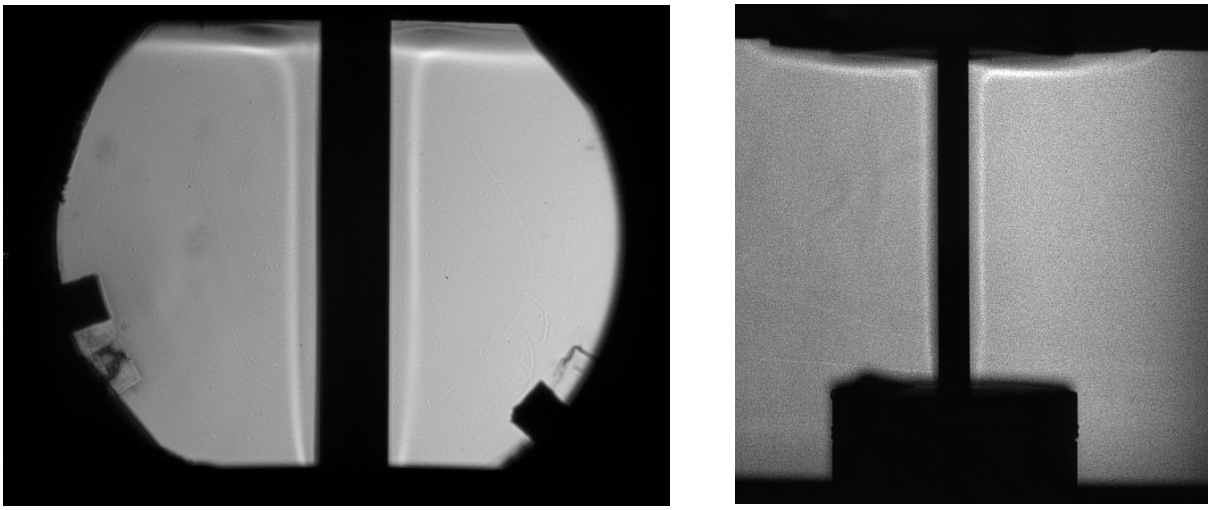

(a) (b)

Figure 6.6: (a) Schlieren visualization of the H4 cylinder and (b) Shadowgraph visualization of H6 cylinder. Both surfaces are at T_w = 1000 K.

The H10 cylinder was a transitional case where there are occasional long periods ($O(10\,\mathrm{s})$) of steady laminar flow. These periods were routinely interrupted by small boundary layer perturbations. Rather than being damped out as in the H4 and H6 cases, these perturbations were amplified and resulted in turbulent motion with quite prominent unsteady flow features resembling the roller or large-eddy structures observed in many other turbulent shear flows. These eddy structures typically traveled up the cylinder a short distance before ejecting into the bulk fluid and forming large plumes of heated turbulent fluid which required relatively long times to dissipate. High-resolution schlieren images of the structures developed in the transitional region are also shown in Figure 6.7. Comparatively, the flow along the 10-in. long cylinder (200A) in Chapter 3 appeared fully laminar in almost all cases. Some reasons for this discrepancy are that the 200A cylinder is enclosed in the 40 L and fully isolated from lab currents, the actual heated length is less (6.5 in) when accounting for the conduction zones near the ends, the boundary conditions for fluid entertainment are "smoother" because the end supports have smaller profiles, and the 200A is twice the diameter of the present cylinders so the curvature effect of the present cylinders is greater.

Consideration was given to using a glass-walled enclosure to eliminate the most likely disturbance source (lab currents) and maintain the ability to perform flow visualization. A preliminary exploration of this idea was made using a non optical quality 10-in.-long, 4-in.-ID glass cylinder with the H10 cylinder to mimic the CAT vessel dimensions. This configuration also resulted in unsteady flow and eddy structures near the top boundary. A partially enclosed metal shell was also used to estimate the effects of lab currents and showed similar structure to the unconfined case. However without a full enclosure, the potential still exists for currents to enter through holes in the enclosure necessary for pyrometry and visualization. In any case, sufficient confinement is expected to alter the fluid mechanics beyond simply eliminating stray lab currents and it has been shown than confinement can suppress the onset of turbulence at least for low ΔT flows (Chenoweth & Paolucci, 1986).

The flow around the H18 cylinder appears to be entirely turbulent above the point of laminar-turbulent transition for $T_w = 1000$ K with occasional formation of the large eddy structures observed in the H10 case. The H28 and H36 cylinder flows are similar with larger flow structures and occasional complete separation of the flow from the upper surface. A reduced region of approximately 2 to 28 in and 10 - 36 in were visible in the field of view for the H28 and H36 cylinders respectively. Sample images of each of the H28 cylinder are shown in Figures 6.8 and 6.9. Qualitative comparison suggests a consistent laminar-turbulent transition region near a height of 8 - 12 in. for $T_w = 1000$ K. This occurs for $Ra_H \sim 10^7$ which is an order of magnitude lower than typically accepted values of $Ra_H \sim 10^8 - 10^9$ for laminar-turbulent transition in natural convection flows over a vertical surface .

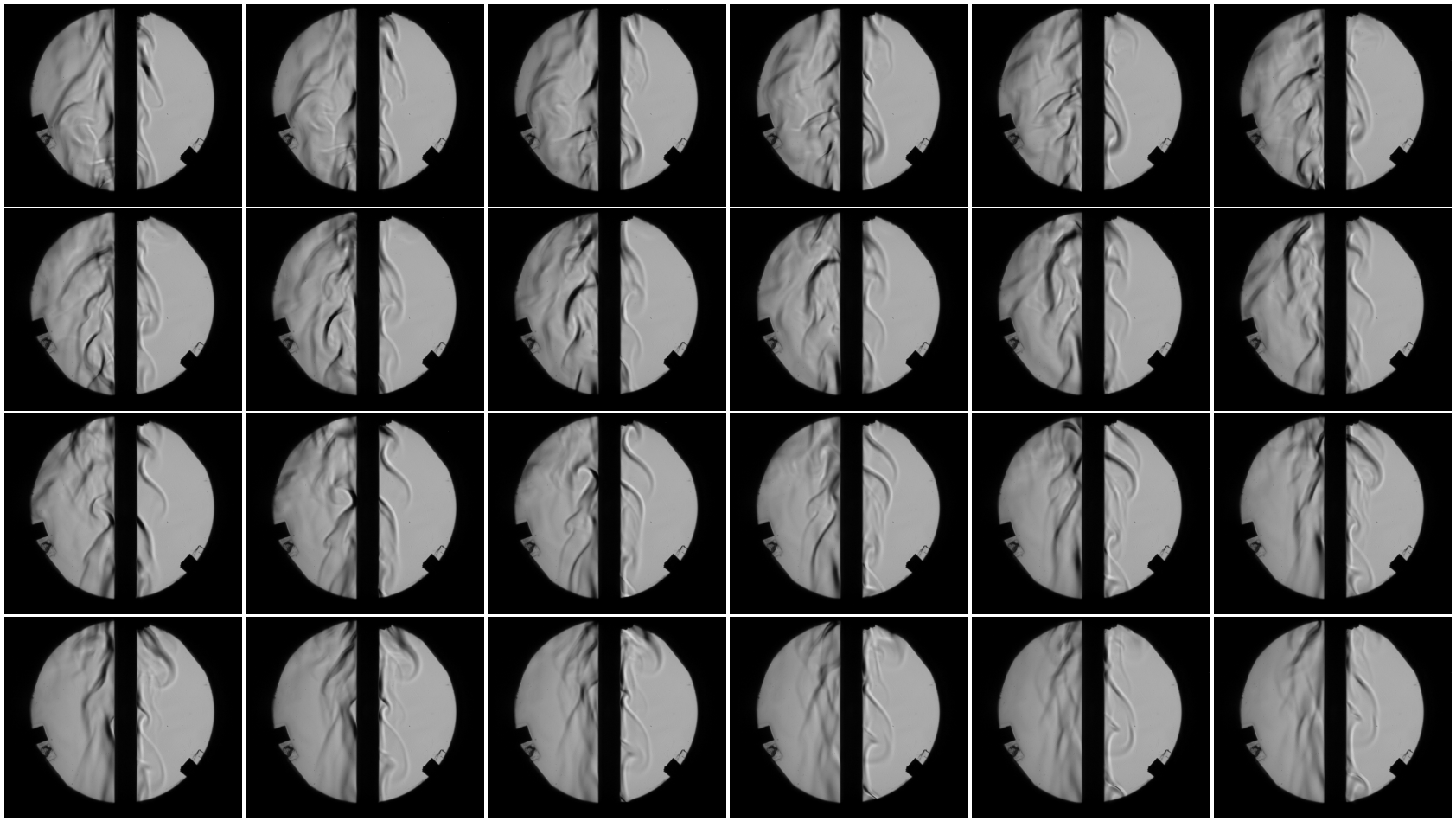

Figure 6.7: Schlieren visualization of the roller or large-eddy structures formed in the transition region. The field of view is approximately $8 < x < 12$ along the vertical length of the H36 cylinder at T_w = 1000 K. Δt between frames is 1/60 s.

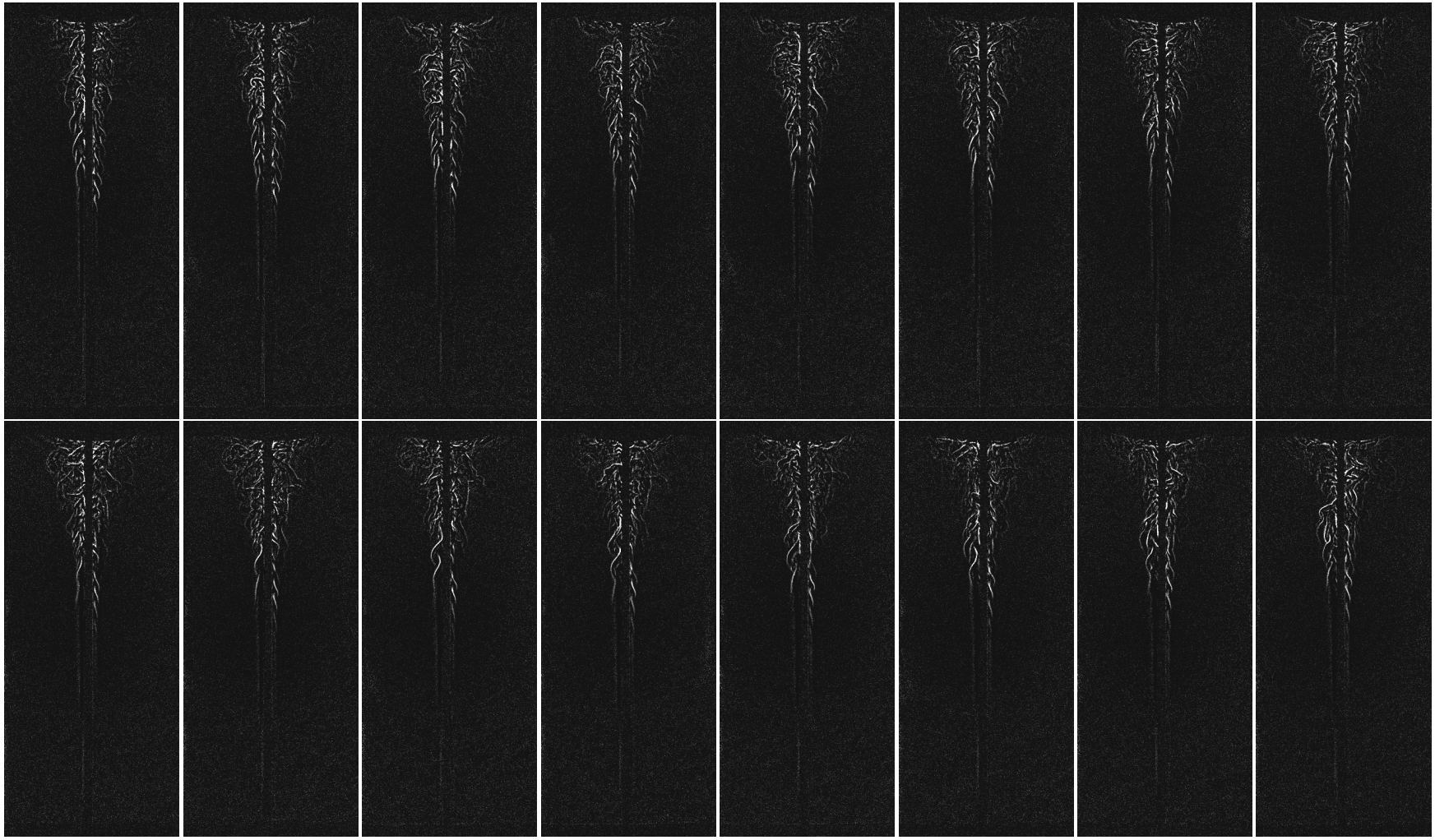

Figure 6.8: Processed Shadowgraph image sequence from T_w = 555 K for H28 cylinder. Fluctuations and transition is mostly located in the upper region of the surface. Early vortex formation is seen occurring over the course of many frames on the right side of the cylinder near the middle of the frame. Δt between frames is 1/30 s. Note: Images have been brightened and contrast stretched for presentation.

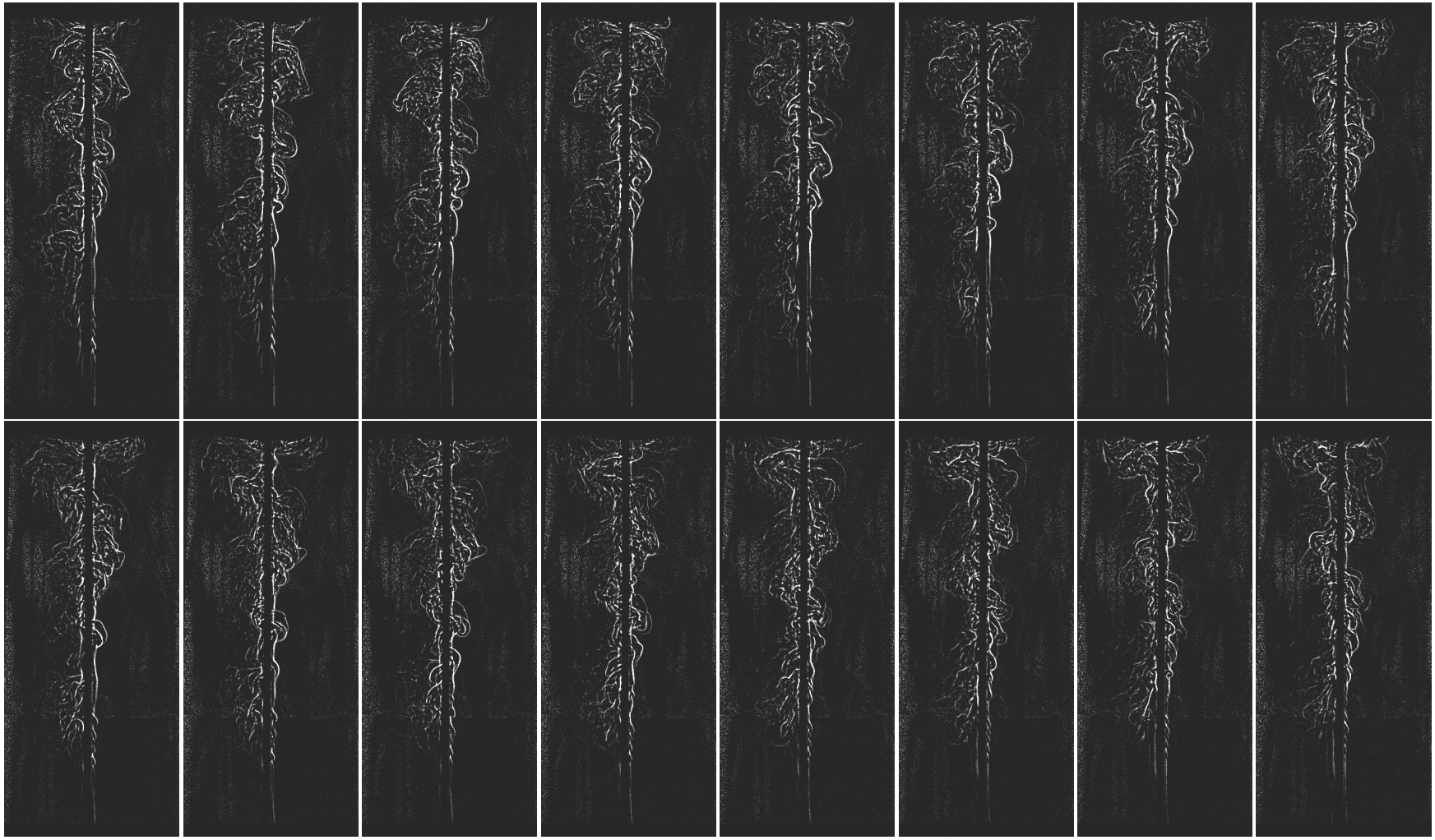

Figure 6.9: Processed Shadowgraph image sequence from T_w = 1015 K for H28 cylinder. Fluctuations and transition occur along the length of the cylinder. Incipient roll up vortices form in the bottom of the frame and quickly amplify to larger scale turbulence and ejection of fluid into the bulk. Δt between frames is 1/30 s. Note: Images have been brightened and contrast stretched for presentation.

6.4.2 Dependence on Temperature

To ascertain the influence of temperature on the flow regime, a detailed study of the near full field image of the H28 cylinder was conducted. The H36 cylinder was too large to fully visualize in a single FOV using the system described here, however the H28 case was fully visible in the field of view[1] but was near the physical limitations of the imaging system. The raw videos contained 5476 frames captured at 120 fps which represents a duration of 45.6 s for each video. The reflective screen covered a region of approximately 800 × 336 pixels on the sensor. This resolution and number of frames was found to be sufficient for use of the POD algorithm for common mode background removal in all but the lowest T_w cases where the flow disturbances were exceedingly weak. Wall temperatures in the range 450 K< T_w < 1150 K were targeted for study here.

The procedure described in Section 6.3.3 for low-temperature, steady-state control was used for cases where T_w < 800 K. TC1 was placed at the same height as the pyrometer (approximately 6 in. from the bottom) while additional thermocouples (TC4 and TC5) were also placed in the upper region of the cylinder at heights of 24 and 25 in. from the bottom surface as measured at room temperature. These were also attached and removed along with TC1 in the same way as described in Section 6.3.3. These readings illustrate there is a physical temperature gradient within the cylinder which was previously observed and discussed in Section 5.6.1.1. This difference is a consequence of the convective term in the energy balance being larger in the turbulent region and reducing the cylinder temperature when the input power is held constant.

The input current density is constant since the cylinder cross section is uniform along the axis resulting in uniform power dissipation along the length of the cylinder. The turbulent flow region

[1]The bottom ~2 in. of the temperature cylinder was obstructed by the support frame. This omitted region contains mostly laminar flow features and is unimportant for the subsequent analysis

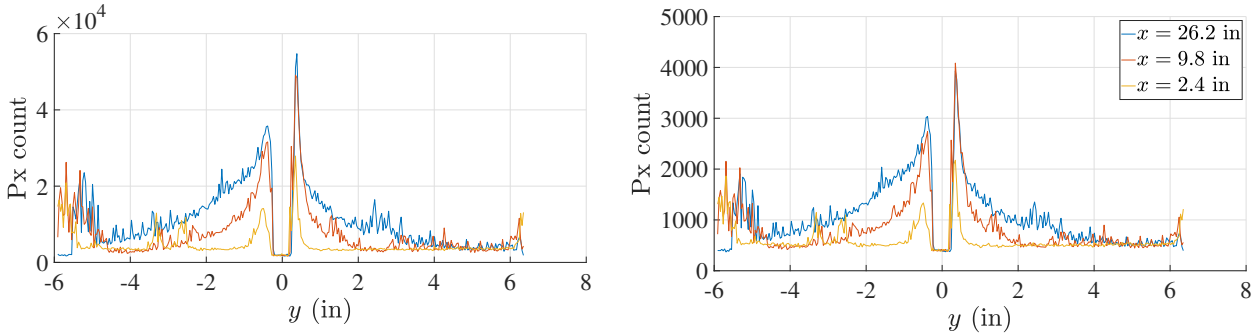

Figure 6.10: (a) Profiles of mean flow pixel counts and (b) Profiles of average fluctuation pixel counts at the same heights.

has a larger convective heat transfer coefficient than in the bottom laminar region and consequently the steady state temperature is lower than that in the laminar region. This gradient decreases somewhat at lower temperatures but is still significant and typically between 30 - 50 K. This temperature gradient could in theory be eliminated using a cylinder with varying wall thickness or multiple discrete and independently controlled heat sources. However these options were not pursued since the goal of this study was to understand the flow developed over these specific cylinders designed for the CAT experiments.

Example sequences of images are shown in Figure 6.8 for 555 K and Figure 6.9 for 1015 K. These images have been processed using the POD background removal tool and contrast stretched for presentation (Masullo, 2023; Mendez et al., 2017). These examples show that the boundary layer instabilities, large eddy structure, and other turbulent flow features move downstream (vertically upward) as the surface temperature is decreased. From Equation (6.3) it is clear that Ra_H has a cubic dependence on length scale and from Figure 6.1that Ra_H decreases with decreasing temperature for large T_w (e.g. large ΔT). Therefore qualitatively the 555 K images show that laminar-turbulent is occurring at higher values of Ra_H as compared to the 1015 K images. The next sections focus on attempts to quantify this difference by quantitatively identifying the laminar-turbulent region from these videos.

6.4.2.1 Intensity Fluctuations and Intermittency

In an effort to quantify the observed flow features, the POD processed images were further processed by computing the mean flow and subtracting from the POD processed frames to extract images with only the fluctuations in intensity. The mean was computed from the full 5476 frames for each case. The images remaining from the subtraction of this mean flow contain information about the fluctuations in the second derivative of density, $\left(\frac{\partial^2 \rho}{\partial x^2}\right)'$, which are exceedingly small. However the POD background removal retains appreciable signal-to-noise ratio across the flow field. A comparison of the horizontal slices of the mean and fluctuation images at various heights are shown in Figure 6.10. These profiles illustrate the growth in both the mean flow and fluctuations as vertical distance is increased. These profiles also indicate that the intensity fluctuations increase as wall normal distance is decreased. All profiles are relatively noisy especially far from the cylinder center and at the cylinder surface.

To further quantify the intensity fluctuations, concepts from turbulent flow analysis were used. A common approach in the study of transitional and turbulent flows is to define an intermittency function defined as the fraction of time where a region of the flow experiences turbulent fluctuations (Emmons, 1951; Jiménez, 2006). Intermittency measurements are typically made using velocity data however here we apply this to the intensity fluctuations in the images. The intensity fluctuations

Table 6.1: Summary of conditions for temperature dependence study with H28 cylinder.

Condition	T_w **(K)**	T_{pyr} **(K)**	**TC$_1$ (K)**	**Const. Current (A)**	**TC$_4$** (K)	**TC$_5$ (K)**
1	1140	1140	1140	-	-	1100
2	1015	1015	1015	-	-	965
3	950	950	950	-	915	920
4	850	850	850	-	815	820
5	745	-	745	150	696	706
6	625	-	625	120	585	590
7	555	-	555	100	520	525
8 [a]	445	-	445	75	-	415

[a] This condition was visualized successfully however it was too noisy to be useful for quantitative processing.

are due to the temperature gradients creating index refraction gradients so computing intermittency in the intensity fluctuations is a proxy for the intermittency of the underlying unsteady flow that creates the temperature gradients.

The procedure outlined here applies to all conditions in Section 6.4.2.1 and the sample data shown is for images corresponding to $T_w = 950$ K. Firstly the raw fluctuations in pixel intensity are analyzed across each pixel in the image. Figure 6.11 shows pixel intensities as functions of time for locations near the wall at three different heights. The intensity of the fluctuations are larger in magnitude which again indicates a growth in fluctuation intensity with vertical distance. Examination of the time signals in Figure 6.11 makes it clear that there are intermittent fluctuations at all heights, even within the laminar regime near the bottom of the surface. This is similar to what is described in the literature for measurable velocity fluctuations in transitional flows and lends validity to idea of using intensity fluctuation intermittency to infer fluid mechanical intermittency.

We define γ as the fraction of test time t_{tot} where the pixel intensity value I is above a certain threshold value $I_{threshold}$ which we choose

$$\gamma(x, y) = \frac{t(I > I_{threshold})}{t_{tot}} . \tag{6.7}$$

This is a scalar quantity which is defined for each pixel given by a spatial coordinate pair (x, y). Here y is the wall normal coordinate and x is the coordinate parallel to the surface. In principle any value between 0 and the camera bit depth can be selected but may alter the resulting analysis. A threshold value of zero will indicate turbulence at all points in the flow where the pixel is not perfectly black. A value equal to the camera bit depth would require saturation at all times to indicate turbulence. Veerasamy and Atkin (2020) suggest a selection based on the intensity of fully laminar

perturbations. The laminar fluctuations grow downstream until they reach onset of transition where there are additional, sparse, large perturbations attributed to turbulent spots. Beyond this region the laminar perturbations are progressively overcome by more frequent turbulent fluctuations until sufficiently far downstream when the turbulent perturbations have completely overtaken the laminar perturbations. Since the objective of this work is to identify the transitional region, the maximum laminar perturbation value is difficult to determine since we don't a priori know where transition occurs. Therefore for practical purposes a threshold value based on the fluctuations at $x = 2$ in. is used for all temperature cases studied here.

To quantify the intermittency change along the cylinder we can integrate Equation (6.7) in the wall normal direction to obtain an integrated intermittency as a function of vertical height

$$\Gamma(x) = \int \gamma(x, y) dy \,. \tag{6.8}$$

This provides a single numerical value to quantify the fluctuation values at each location along the length of the cylinder. The region close to the top boundary is eliminated for further analysis since there is a measurable change in flow structure due to the effect of the top support electrode on the flow. The cutoff height was determined by a local maximum in the inflection point of the $\Gamma(x)$ profile. The resulting values of $\Gamma(x)$ were then normalized by the maximum value of $\Gamma(x)$ through

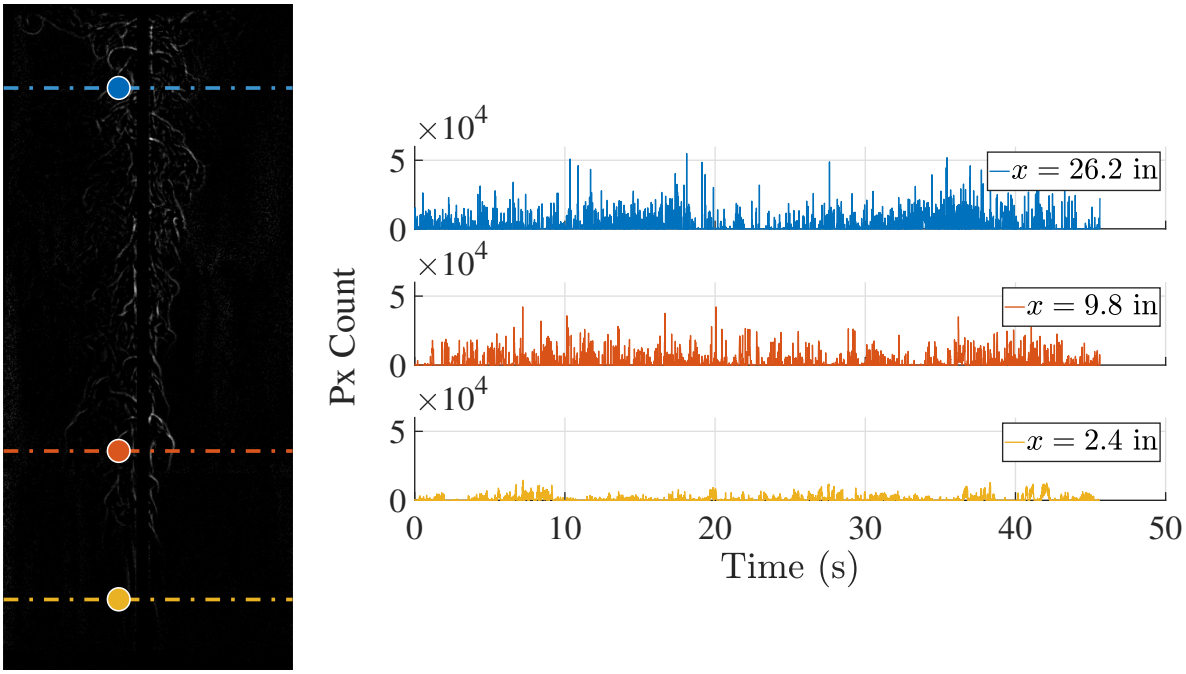

Figure 6.11: Fluctuation intensity as a function of time at three vertical locations. The data are sampled at a wall normal distance of approximately 0.37 in (9.3 mm).

the region

$$\Gamma^*(x) = \frac{\Gamma(x)}{(\Gamma(x))_{max}}\,. \tag{6.9}$$

This normalization is necessary for quantitative comparison with results obtained at different values of T_w since the absolute value of the shadowgraph fluctuations as measured by pixel intensities vary with temperature. The resulting Γ^* functions for each of the cases in Section 6.4.2.1 are shown in Figure 6.12. The profiles are consistent with an initial region of slow growth of integrated intermittency with downstream distance followed by a transition to a more rapid growth, followed by an inflection point and decrease in growth, leveling off at relatively constant value. Variations near the top of the cylinder are the effect of the upper electrode on the flow and are not relevant for analysis here. The key features vary with wall temperature except for large values of T_w where the profiles collapse to a single normalized shape. For low temperatures, the rapid growth region and inflection point occur further downstream along the length of the cylinder (at larger x values) with decreasing temperature.

The $\Gamma^*(x)$ profiles in Figure 6.12 are noisy and to reduce this, were processed by fitting with piecewise cubic smoothing splines. An example is shown in Figure 6.13(a). These smoothing functions was then numerically differentiated, Figure 6.13(b) to locate particular features in the $\Gamma^*(x)$ profiles for each condition. The first local maximum in the curvature was found in all cases which corresponded to the sudden change in growth rate of $\Gamma^*(x)$. This is identified as the start of the transition region since fluctuations begin to grow rapidly. Further upstream an inflection point was also found where the slope reaches a maximum and curvature changes from positive to negative. After this point the fluctuation growth begins to slow and the flow becomes fully turbulent with constant integrated intermittency along the remaining surface length. The location

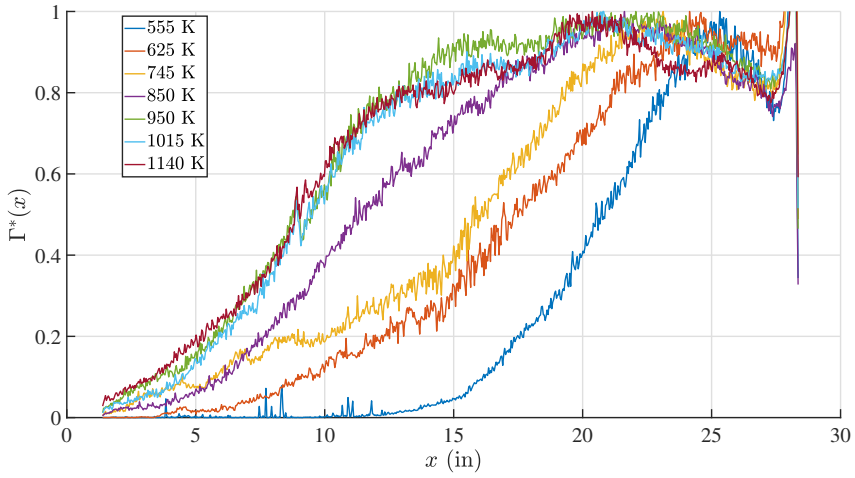

Figure 6.12: Γ^* for varying T_w on H28 cylinder.

of these two points are used to bound the transitional region. We take the first critical point as the transitional height and use it to compute Ra_H^{NB}. The results for all temperatures are shown in Figure 6.14 (a) and (b). These show that both H_{trans} and $Ra_{H,trans}^{NB}$ decreases as T_w increases. This result makes clear that the use of Ra_H^{NB} as defined this way is not useful in predicting the onset of turbulence across a range of temperatures.

One alternative approach is to use a length scale more relevant to the boundary layer like the boundary layer thickness δ_T. Values for this quantity are not known a priori so simulation tools or the laminar laminar flat plate similarity solution of Ostrach (1953) and Sparrow and Gregg (1958) can be used for estimation. The transition heights found in these experiments are needed to compute the Gr_H values which δ_T depends on as in Equation (1.32). These values are shown in Figure 6.14 (c) and show an inverse dependence on temperature similar to H_{trans}. $\delta_{T,trans}$ was then be used as an alternative length scale for use in definitions of transitional Ra evaluated using a constant property formulation as is relevant to the definition of the similarity variable.

The values for $Ra_{\delta_T,trans}$ computed this way are also presented in Figure 6.14 (d) and are somewhat less dependent on temperature due to the more similar length scale across the cases studied. Across the temperature range studied this quantity still decreases but only by approximately a factor of 2 whereas $Ra_{H_{trans}}^{NB}$ varies by a factor of 100. Thus for these non-Boussinesq large temperature difference cases this approach using boundary layer thickness provides a more consistent transition criterion than the traditional approach using the axial height.

6.4.3 Effect of Imposed Flow Disturbance

In order to improve our understanding of the intermittency observed due to natural transition in these experiments, we created early transition of the boundary layer with the use of a trip wire.

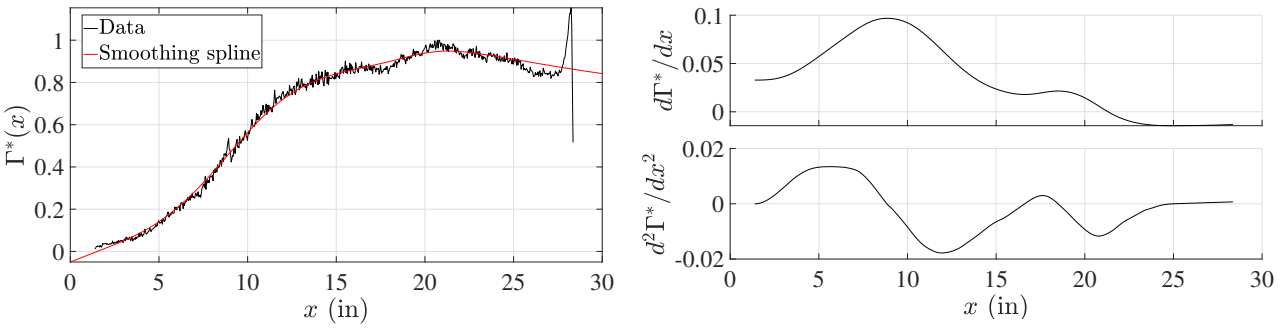

Figure 6.13: (a) Cubic smoothing spline applied to Tw = 1015 K data. (b) Numerical first and second derivatives of smoothing function used to find critical points.

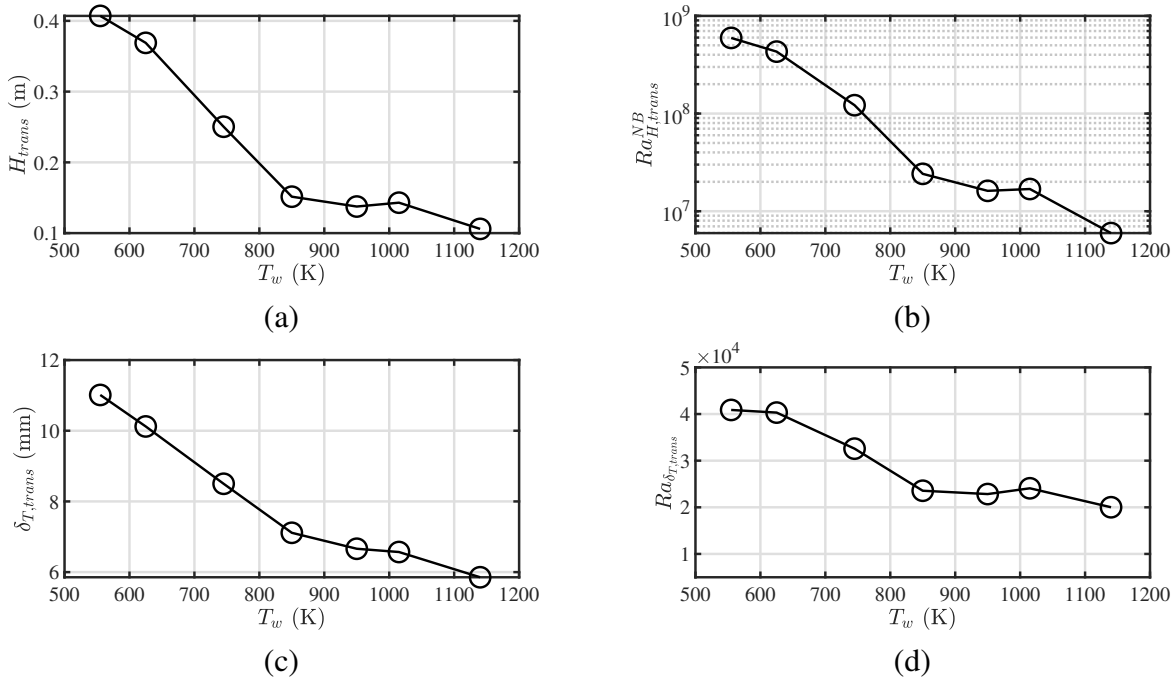

Figure 6.14: (a) Vertical height where transition occurs (b) Ra_H^{NB}. (c) δ_T as calculated for a laminar flat plate using $Gr^{NB}_{H_{trans}}$ and (d) $Ra^{NB}_{\delta_T}$. Plots (a) (b) and (d) show a strong dependence on temperature while plot (c) is only modest.

This was of interest to aid in identifying the features of a transition point since we know precisely where it should occur with a trip wire. A 12 gauge copper wire was wrapped around the cylinder at a height of 12 in. for additional testing at a limited number of temperature regimes of interest. This height was chosen as it is below the natural transition region for low temperature cases and within the transitional regime for moderate temperature cases. One potential issue with this approach is that the wire itself is also conductively heated by the surface and consequently contributes to the thermal boundary layer profile by altering the heating profile within the boundary layer in addition to disturbing the velocity profile as intended.

Three of the same temperature conditions from the un-tripped experiments were explored using the trip wire and the same analysis was performed on the resulting videos to extract $\Gamma^*(x)$ profiles for each case. The results are shown in Figure 6.15 where each un-tripped temperature profile is plotted in red with the tripped case at the same temperature plotted in black. Figure 6.15 shows that for the 555 K case the wire is below the natural transition region so the flow is readily tripped at the wire. Appreciable fluctuations are also seen below this height since the velocities are low and fluctuations can propagate upstream relatively quickly. Some effect of this is also observed in the 745 K case as well where the rapid growth is initiated slightly further upstream than in the untripped case. In the 850 K case however the first transition point remains unchanged and the

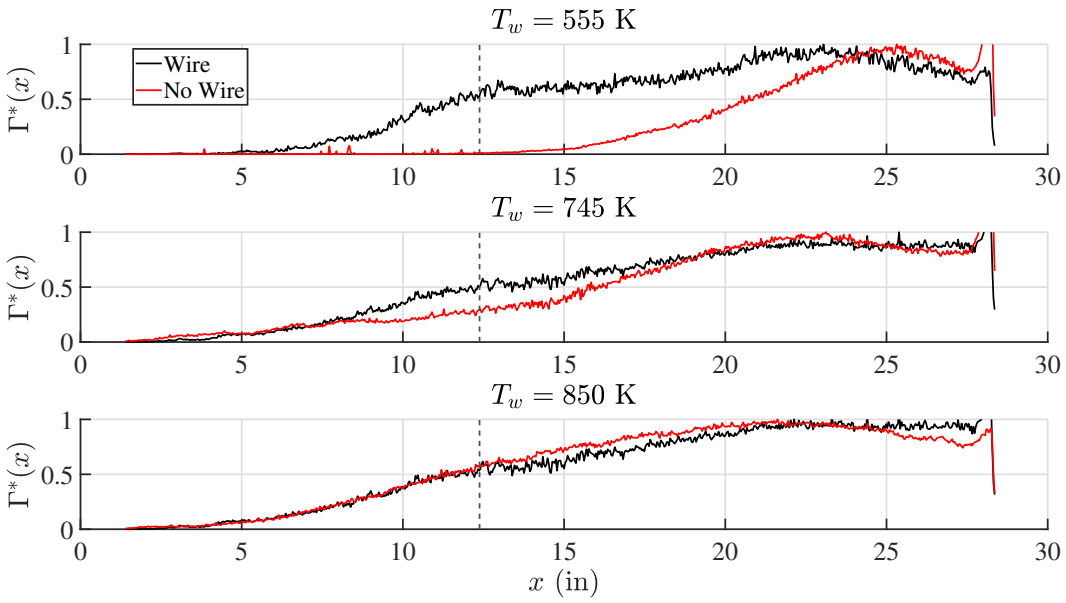

Figure 6.15: Effect of trip wire on onset of turbulence for T_w = 555 K, 745 K, and 850 K. The vertical dotted line denotes the location of the wire.

effect of the wire is not significant since the flow is already mostly turbulent by the wire location. Smaller gauge wires were attempted to be used at similar heights and found to be unable to produce any effect on the measured flow field. This illustrates that a large physical disturbance is required to prematurely trip the flow. As a result, in the un-tripped experiments there is likely little to no effect of small surface defects from uneven oxide or residual thermocouple beads on the transition point.

6.5 Summary

An examination of the dominant non dimensional parameters in natural convection flows illustrated that there is a fundamental difference in these parameters and their dependence's on temperature for large temperature differences in gases. For these cases $Ra(T)$ and $Gr(T)$ exhibits a maximum close to where the Boussinesq approximation becomes invalid. Beyond this critical temperature Ra and Gr are decreasing functions of temperature. However, the onset of boundary layer instability and transition from laminar-to-turbulent flows are observed to monotonic functions of temperature and so are not correlated with the Ra or Gr for large values of the wall temperature. Further experiments and analysis are required to develop appropriate non-dimensional figures of merit useful for correlating laminar-turbulent transition in these flows.

An experimental characterization of the flow field around the CAT cylinders was conducted to measured and interpret the flow field implications on ignition testing. Experiments were conducted

to visualize the flow fields near for these large ΔT vertical surfaces. To enable this effort a dual purpose double-pass schlieren and shadowgraph system was developed and implemented and a high speed camera was used to capture short-exposure, long-duration videos of the unsteady flow fields. To quantify the flow field images a POD background removal tool was implemented and the flow field fluctuations were extracted by subtracting the mean flow from long duration videos.

An intermittency function was then defined to quantify the fluctuations of image intensity and to characterize the transition region as a function of temperature. The results showed that the transitional Ra decreases as a function of temperature and is therefore not useful for predicting transition. Instead a critical thermal layer thickness $\delta_{T,c}$ was estimated based on the laminar theory for a vertical flat plate. Using this as an alternative length scale allowed $Ra_{\delta_{T,c}}$ to be defined and showed a more consistent value for the measured transitional regions in these experiments.

References

Cairnie, L., & Harrison, A. (1982). Natural convection adjacent to a vertical isothermal hot plate with a high surface-to-ambient temperature difference. *International Journal of Heat and Mass Transfer*, *25*(7), 925–934. https://doi.org/10.1016/0017-9310(82)90068-0 (Cit. on p. 160)

Chenoweth, D. R., & Paolucci, S. (1986). Natural convection in an enclosed vertical air layer with large horizontal temperature differences. *Journal of Fluid Mechanics*, *169*, 173–210. https://doi.org/10.1017/S0022112086000587 (Cit. on pp. 160, 169)

Dall, H. (1953). A Null Test for Paraboloids [Rev. ed. of: Amateur telescope making, advanced : a sequel to Amateur telescope making. 1937]. In A. G. Ingalls (Ed.), *Amateur Telescope Making* (pp. 149–153). Scientific American. (Cit. on p. 165).

Emmons, H. W. (1951). The Laminar-Turbulent Transition in a Boundary Layer-Part I. *Journal of the Aeronautical Sciences*, *18*(7), 490–498. https://doi.org/10.2514/8.2010 (Cit. on p. 174)

Gebhart, B., Jaluria, Y., Mahajan, R. L., & Sammakia, B. (1988). *Buoyancy induced flows and transport: Reference edition*. Hemisphere Publ. Corp. (Cit. on p. 160).

Goodwin, D. G., Moffat, H. K., & Speth, R. L. (2017). *Cantera: An Object-oriented Software Toolkit for Chemical Kinetics, Thermodynamics, and Transport Processes* [Version 2.4.0]. https://doi.org/10.5281/zenodo.170284. (Cit. on p. 161)

Hargather, M. J., & Settles, G. S. (2009). Retroreflective shadowgraph technique for large-scale flow visualization. *Applied Optics*, *48*(22), 4449. https://doi.org/10.1364/AO.48.004449 (Cit. on p. 164)

Jiménez, J. (2006). Intermittency in Turbulence. *Encyclopedia of Mathematical Physics* (pp. 144–151). Elsevier. https://doi.org/10.1016/B0-12-512666-2/00368-0. (Cit. on p. 174)

Masullo, A. (2023). *POD-based background removal for Particle Image Velocimetry* (Version 1.0.0). (Cit. on pp. 167, 174).

Mendez, M., Raiola, M., Masullo, A., Discetti, S., Ianiro, A., Theunissen, R., & Buchlin, J.-M. (2017). POD-based background removal for particle image velocimetry. *Experimental Thermal and Fluid Science*, *80*, 181–192. https://doi.org/10.1016/j.expthermflusci.2016.08.021 (Cit. on pp. 167, 174)

Ostrach, S. (1953, January 1). *An Analysis of Laminar Free-Convection Flow and Heat Transfer About a Flat Plate Parallel to of the Generating Body Force* (Technical Report No. 1111). NACA. (Cit. on p. 178).

Paolucci, S. (1982). *On the Filtering of Sound from the Navier-Stokes Equations* (Sandia Report SAND82-8257). Sandia National Laboratories. Livermore CA. (Cit. on p. 160).

Settles, G. S. (2001). *Schlieren and shadowgraph techniques: Visualizing phenomena in transparent media*. Springer. (Cit. on p. 165).

Sparrow, E. M., & Gregg, J. (1958). The Variable Fluid-Property Problem in Free Convection. *Transactions of the ASME*, *80*, 879–886 (Cit. on p. 178).

Tritton, D. J. (1988). *Physical fluid dynamics* (2nd ed, pp. 163–196). Clarendon Press ; Oxford University Press. (Cit. on p. 160).

Veerasamy, D., & Atkin, C. (2020). A rational method for determining intermittency in the transitional boundary layer. *Experiments in Fluids*, *61*(1), 11. https://doi.org/10.1007/s00348-019-2856-5 (Cit. on p. 175)

Chapter 7

CONFINED AUTOIGNITION TEST (CAT) IGNITION TESTING

7.1 Motivation

This chapter presents the results and methodology for ignition testing in the facility that was developed and characterized in Chapter 5 and Chapter 6. As discussed in earlier chapters, the motivation behind these experiments is to bridge an experimental and knowledge gap between heated surface and heated vessel experiments. New results are presented on ignition under conditions of high Rayleigh numbers for a hot vertical cylinder in a cold flammable atmosphere. The Rayleigh numbers are sufficiently large that transition from laminar to turbulent flow will occur in the natural convection boundary layer and turbulent flow will exist above the transition region. The surrounding vessel is also much smaller relative to the hot surface area than in previous testing, leading to the possibility of recirculation and mixing of partially reacted fuel during long duration tests. The conditions are relevant to a wider range industrial hazards than previous studies and provide a unique data set for evaluating theories of hot surface ignition.

7.2 Experimental Methodology

The experimental procedure for mixture preparation and data acquisition follows closely that discussed in Chapter 3. A brief summary is presented here along with a discussion of differences in the diagnostics used. Two configuration of the assembled facility are shown in Figure 7.1. The assembled vessel is used for a series of ignition tests before the configuration is altered. The facility is mounted on a steel uni-strut frame purpose-built on an optical bench with access to gas feed lines and diagnostic equipment. The frame supports a horizontal shelf elevated approximately 8 in. from the optical table surface. The CAT vessel is placed on this shelf over a centrally located hole that allows translation of the bottom electrode resulting from the thermal expansion of the cylinder during heating. The shelf supports only the outer body of the vessel. Tube clamps are also used to secure the vessel and are mounted in the steel uni-strut frame at the bottom most flange and at the top most for the A20 configuration to prevent tipping due to the elevated center of mass. Pneumatically-actuated solenoid valves are mounted on the support frame to control the vacuum, mixing, and gas feed lines. A secondary support is placed underneath the bottom electrode during testing in order to prevent possible over-extension of the heated cylinders.

All results presented here are for stoichiometric n-hexane/air mixtures at an initial pressure P_0 = 1 atm. The method of partial pressures was used to control the gas conditions for each shot. The vessel was evacuated to less than 0.1 torr before the start of the filling process. The fuel was then

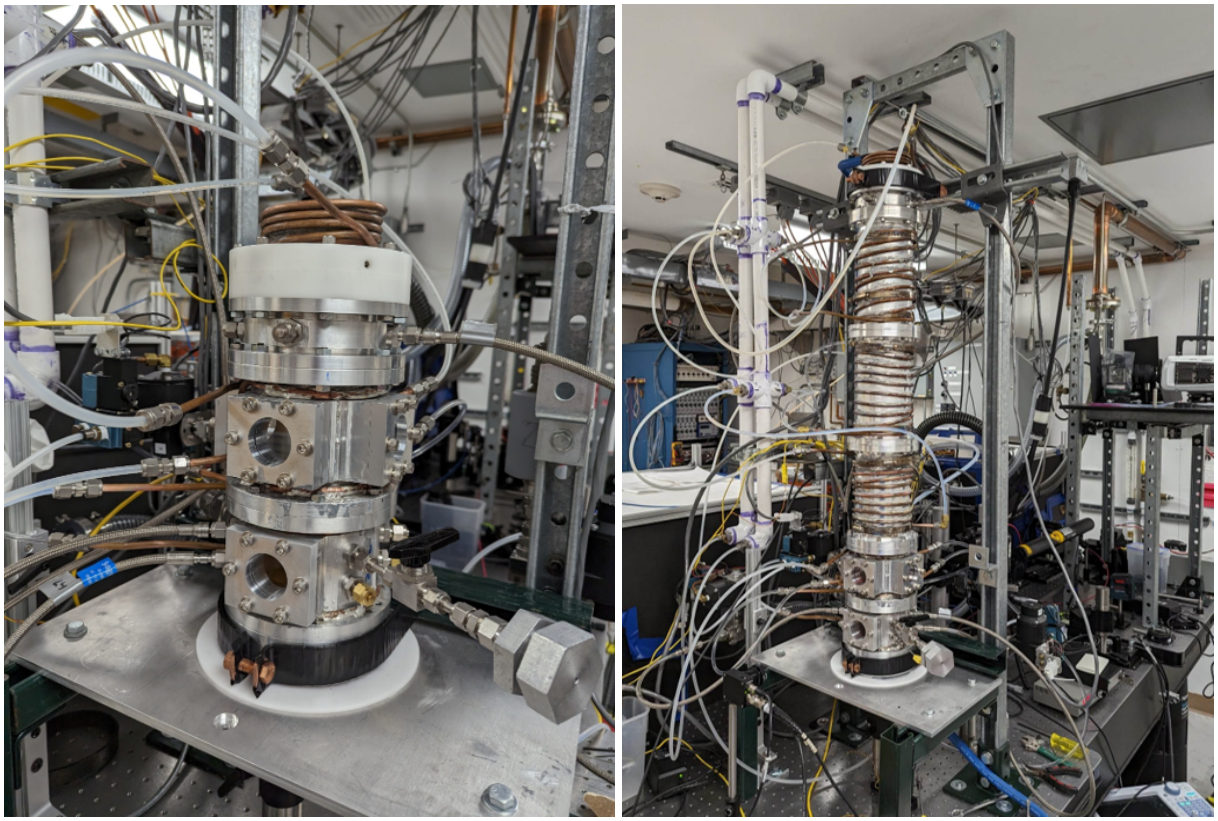

Figure 7.1: The CAT in AR5 (left) and AR20 (right) configurations.

added using a syringe through a septum port in the lower feedthrough section. Nitrogen and oxygen were then added independently in appropriate amounts to make the desired fuel/air mixture. A capacitive pressure gauge (MKS model 121A-01000B) with a readout accuracy of 0.01 kPa was used to monitor the pressure during filling. After the vessel was filled, a mixing pump was turned on for three minutes to promote mixing of the gases and then turned off for three minutes to allow the gases to settle and produce a quiescent mixture at the start of each test. The test time was initially limited to 300 seconds for comparisons with results in Chapter 3 and Jones (2020). However this

Table 7.1: CAT configuration labels, hot surface and vessel dimensions for ignition testing. AR is the channel aspect ratio. SA is the surface area of the heated cylinder. Ra_H values correspond to T_w = 1100 K.

CAT Configuration Label	**Cylinder label**	**Heated Length (in)**	AR	SA (**cm**^{2})	V (**L**)	Ra_H
A5	H10	10	5.71	101.3	2.03	3.65 E+07
A10	H18	18	10.29	182.4	3.65	2.13 E+08
A20	H36	36	20.57	364.8	7.30	1.70 E+09

was found to be an unsuitable limitation for this experimental configuration. For later tests the test time was determined by the measurements obtained from C-H bond absorption measurement. The tests were only ended once the fuel had been completely consumed or the absorption signal reached a steady state. At the end of the test time if there had been no ignition, then the test was ended manually and was recorded as a non-ignition result.

In the cases where ignition occurred, the data acquisition system was triggered by a thermally-protected, piezoresistive pressure transducer (Kulite XT-190) which was used to record pressure rise during the test. A type K thermocouple probe was also placed in the bottom feedthrough collar for all configurations and offset approximately 5 cm from the surface of the cylinder at a height of approximately 1.2 in. as measured from the bottom surface at room temperature. For the longer configuration (AR20) an additional piezoresistive pressure transducer (Endevco 8530B-200) was placed in the top feedthrough collar along with another type K thermocouple probe placed again approximately 5 cm from the cylinder surface and 0.75 in. from the top boundary. The magnitude of the pressure rise, appearance of a flame in imaging, and the C-H absorption measurement were used to determine if ignition took place and to characterize the events. The CAT configurations summarized in Table 7.1 are fewer than contemplated in Chapter 5 and tested in Chapter 6 due to the challenges encountered in ignition testing.

7.2.1 Temperature measurements

The same two-color pyrometer discussed in Section 3.3.2 is used here but with a new calibration approach. At first, calibration using our standard technique with the blackbody source was attempted using new CaF_2 windows. This resulted in a different set of constants for Equation (3.11) than previously obtained due to the different relative absorption of this material as compared to the N-BK7 windows used in the 40 L vessel. In addition, the consistent oxide layer observed in previous work did not develop readily on the cylinder surfaces. The consistency and uniformity of the oxide layer is essential for pyrometry.

Although the tube material (304SS) was sourced from the same vendor (Mccmaster Carr) as used for fabrication of the 200A cylinder, the preferred oxide development was much more varied in the newer tubes. This could be a result of many factors involved in the fabrication of the cylinders or the different process (brazing vs. soldering) used for joining of the copper end pieces to the tubes. The precise composition of the stainless alloy, humidity, mechanical polishing, chemical cleaning, and residual oxides present in the initial microstructure are known to significantly alter the preferred oxidation mode (Guillamet et al., 1993; Nasrazadani & Raman, 1993; Lille & Jargelius-Pettersson, 2000; Huang et al., 2020).

Another factor may be the higher flow velocities induced by the longer tubes. Lille and Jargelius-

(a) (b)

Figure 7.2: (a) Example of oxide developed on the upper portion of H28 cylinder. (b) Oxidation variation developed on cylinders heated to 1000 K in air. The right most cylinder is an ideal oxidation state for using the gray body assumption. From right to left the oxidation state becomes less ideal and the variations are the result of flow conditions and surface preparation.

Pettersson (2000) found that modest flow velocities (4.5 mm s^{-1}) greatly affect the size of the oxide grains. Sufficiently uniform and gray oxides were eventually reproducible for the H4, H6, H10, and H18 cylinders after mechanical roughening of the surfaces with sandpaper and cleaning with isopropyl alcohol and water. For the longer cylinders (H28 and H36) where there are large differences in the flow conditions along the surface due to the transition to turbulent flow observed in Chapter 6, a difference in the oxide structure in the turbulent region is anticipated and was observed. Figure 7.2 (a) shows an examples of the typical oxide layer developed on the upper portion of these cylinders. Figure 7.2 (b) shows a comparison with the desired oxides formed on shorter cylinders. The difference in flow conditions seemed to be the dominant mechanism producing these irregular oxide patterns and prevented development of a uniform oxide on the long cylinders. These differences are important since the oxide composition and grain size effect the high-temperature surface spectral properties that are crucial in pyrometric measurement techniques.

To address the oxide issue and improve the reliability of the pyrometer measurements, a new

(a)

(b)

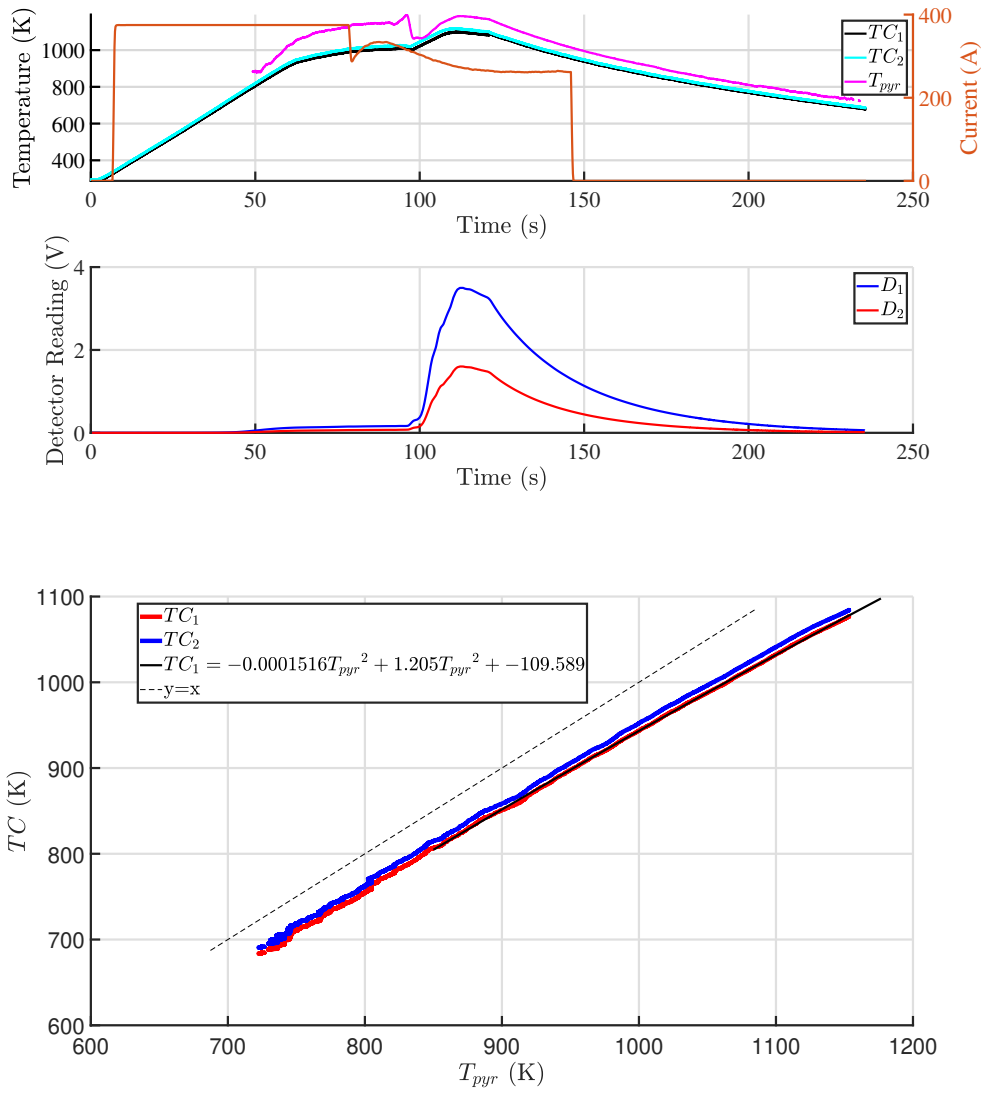

Figure 7.3: Example of one test used for obtaining calibration data for A20 configuration. The data plotted in (b) corresponds to the portion of time after the current is shut off and reaches a value of 0 in (a). Two simultaneous thermocouple measurements are shown to illustrate the reliability and variability range in thermocouple values.

calibration approach[1] was taken using the radiation from the hot cylinder surface with one or more thermocouples as the reference datum for the calibration. To do this, up to three 24-gauge, type K thermocouples were welded to the opposite side of the cylinder from the pyrometer and located in close proximity (within approximately 1 in.). The calibration was done with the cylinder assembled in the CAT vessel to enable heating using the resistive heating system and to account for all potential influences from effects such as optical alignment quality, surface emissivity changes,

[1]We thank James Craig for suggesting this technique and sharing his observations on pyrometric methods.

(a)

(b)

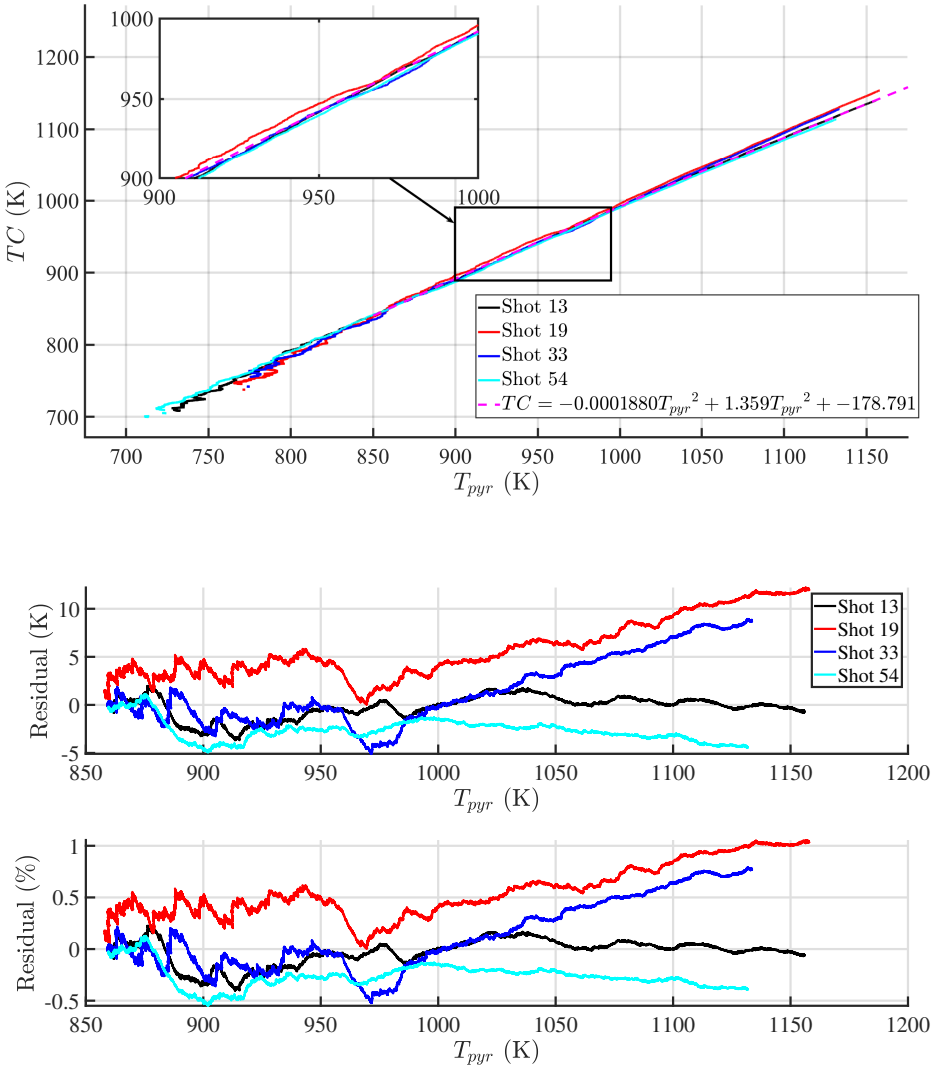

Figure 7.4: Calibration data for measurement system over the lifetime of tests with the A5 configuration (a) overlaid data for all tests plotted with calibration curve from Shot 13 data. (b) residuals in both magnitude and relative percentage from calibration curve. Note the shot numbers indicate the CAT shot number just prior to the calibration. The residuals are less than 1% in all cases indicating the consistency and reliability of in situ calibration.

and any stray internal reflections from the interior surface of the vessel reaching the collection optics of the pyrometer. By performing the calibration in situ, the variation in physical property values (emissivity as a function of temperature and wavelength) are now incorporated directly into the calibration, circumventing the problems encountered when using the blackbody calibration method.

The calibration was achieved by first heating the cylinder to a temperature between 1150 and 1200

K as measured by the thermocouples (accounting for current coupling). Then by shutting off the supplied current the cylinder would cool back to room temperature over the course of a few minutes. During this period with $I = 0$ there is no current coupling present in the thermocouple measurements so the output can be reliably used to calibrate the pyrometer photo detector response using Equation (3.11). Alternatively a correction factor to the original calibration determined by the blackbody source could be applied although this is less precise. An example of one of the tests used for calibration of the A20 configuration is shown in Figure 7.3. Using a reasonable sampling rate of 1-20 kHz in this period provided a large number of calibration points over a relatively short period of time as compared to the typically few discrete points that are used for fitting with a blackbody. This also enabled multiple calibrations to be performed in quick succession to test repeatability. These repeat tests were limited to up to five heating cycles in order to minimize the influence of thermocouple aging effects on these calibrations.

The main drawbacks of this method are (1) a reliance on the accuracy and repeatability of the thermocouple measurements of surface temperature and (2) an assumption that the surface oxide layer is stable such that the optical properties don't drift over many heating cycles and combustion tests. Multiple thermocouple probes were used in each calibration for comparison amongst each other in order to assess their accuracy and repeatability. Typically the three thermocouples agreed within ±10 K, disagreement can likely be attributed to weld quality issues previously discussed in Chapter 3. Calibration was periodically checked between ignition shots to determine if the surface conditions changed enough to have significant effects on the pyrometer temperature measurement.

An initial oxide change was typically found after a few combustion tests, likely owing to some surface reactions of combustion products or radical species. To develop a consistent oxide layer, a set of "dummy" combustion tests were conducted prior to data collection shots. After doing this, significant calibration drift was not observed, indicating a stable oxide layer was formed and was not affected by additional heating or exposure to combustion products. This is illustrated in Figure 7.4 showing a comparison of calibration measurements carried out throughout combustion testing with the AR5 configuration. The residuals from the initial calibration curve are shown for the original calibration data and data obtained by checking the calibration after a number of shots. These residuals are relatively small across the temperature range of interest, especially compared to typical uncertainties attributed to calibrations with the Blackbody source which are on the order of ± 30 K. Based on these measurements we attribute a maximum uncertainty of ± 15 K to the temperature measurements in these experiments.

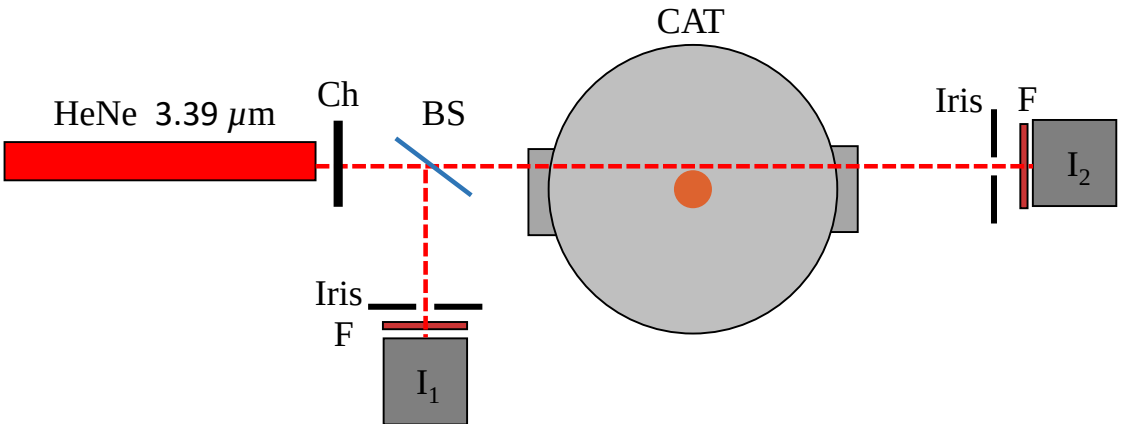

Figure 7.5: Schematic of C-H bond laser system. For all measurements the lower set of windows was used (Approximately 1.75 in. from bottom surface). Ch: Chopper, BS: Beam Splitter, F: Bandpass filter, I_1: Reference detector, I_2: Signal detector.

7.2.2 C-H bond Absorption

The C-H bonds present in hydrocarbon molecules readily absorb in the IR spectrum and provide a convenient method of measuring their concentration Jaynes and Beam (1969), Drallmeier (2003), and Klingbeil et al. (2006). This technique has been applied in many studies of combustion and low-temperature fuel oxidation. The system used for the present measurements has been developed and used by Boettcher et al. (2012) and Mével et al. (2012), Mével et al. (2019) for slow heating rate combustion and lower temperature oxidation studies of various hydrocarbon species. The present implementation is shown schematically in Figure 7.5. It consists of a 2 mW 3.39 μm He-Ne laser (Thorlabs H339P2) with an output beam diameter of 1 mm. The beam was passed through an optical chopper (Stanford Research Systems SRS540) running at 300 Hz to prevent the photo detectors from saturating. Two fixed gain PbSe photo detectors (Thorlabs PDA20H-PbSe) were used for measurements and are sensitive in the range of 1.5 μm $< \lambda <$ 4.8 μm. A 50/50 beam splitter was used to divide the light between the reference detector (I_1) and a signal detector (I_2) located on the opposing side of the CAT vessel. The reference detector was used to account for temporal variations in laser intensity and high frequency noise. In front of each detector was placed a narrow band pass filter with CWL = 3.33 μm and FWHM = 150 nm (Thorlabs FB3330-150). In front of each of the filters an adjustable iris (Thorlabs SM1D12D) was used to narrow the optical aperture and eliminate noise from diffuse light entering the detector. The combination of filter and iris was implemented primarily to prevent detection of emitted radiation from the heated surface which is significant in the measurement wavelength range at elevated temperatures. The iris had the added benefit of enabling control of the signal level via slight adjustment of the aperture size.

When a test gas with molecules containing C-H bonds are injected in the CAT vessel there is a

change in measured intensity at I_2 due to absorption of some portion of the 3.39 μm light by the test gas. This change in signal is proportional to the undisturbed incident intensity (I^o) and depends on the path length (L) of the test gas region, volumetric molar density of the absorbing species (n, units of mol/volume) and the absorption cross section ($\sigma_{\nu,i}$) of the species i at the specified frequency ν. This relationship is expressed by the Beer–Lambert law

$$\frac{I(L)}{I(0)} = \exp\left(-Ln_i\sigma_{\nu,i}\right) \tag{7.1}$$

to relate the intensity decrease through a slab of absorbing molecules of thickness L. The absorption is measured from the variation of the reference beam $I_1(t)$ and and the signal beam $I_2(t)$ after correcting for the losses of the optical components such as the beam splitter, windows in the test section, and filters. These losses can be determined by measuring the intensity ratio I_2^o/I_1^o with no absorption in the test cell, i.e., $n_i = 0$. The ratio of the detector signals when there is absorption will be

$$\frac{I_2(t)}{I_1(t)} = \frac{I_2^o}{I_1^o}\exp\left(-Ln_i\sigma_{\nu,i}\right) \tag{7.2}$$

Rearranging Equation (7.2) yields an expression for n_i as a function of the intensity ratios

$$n_i = \frac{1}{\sigma_{\nu,i}L}\left[\ln\left(\frac{I_1(t)}{I_2(t)}\right) - \ln\left(\frac{I_1^o}{I_2^o}\right)\right] \tag{7.3}$$

If there is a single absorbing species, then the ideal gas law $P = n\tilde{R}T$ can be used to express the concentration n_i in terms of the mole fraction $X_i = n_i/n$ or partial pressure $P_i = X_iP$, using the measured total pressure P and temperature T.

$$n_i = X_i\frac{P}{\tilde{R}T}$$

The mole fraction can be computed from the absorption measurements as

$$X_i = \frac{\tilde{R}T}{P\sigma_{\nu,i}L}\left[\ln\left(\frac{I_1(t)}{I_2(t)}\right) - \ln\left(\frac{I_1^o}{I_2^0}\right)\right] \tag{7.4}$$

The cross section $\sigma_{\nu,i}$ is specific to a particular molecule. For a mixture of absorbing species, each with concentrations n_i, the argument of the exponential in Equation (7.2) contains the sum

$$n\sum_i X_i\sigma_{\nu,i}$$

Except at the outset of a test, the identity and amounts of absorbing species are unknown for the duration of an ignition test where absorbing species are being formed and consumed continuously. We therefore adopt the strategy of computing and reporting an *equivalent* fuel mole fraction X^*_{fuel}.

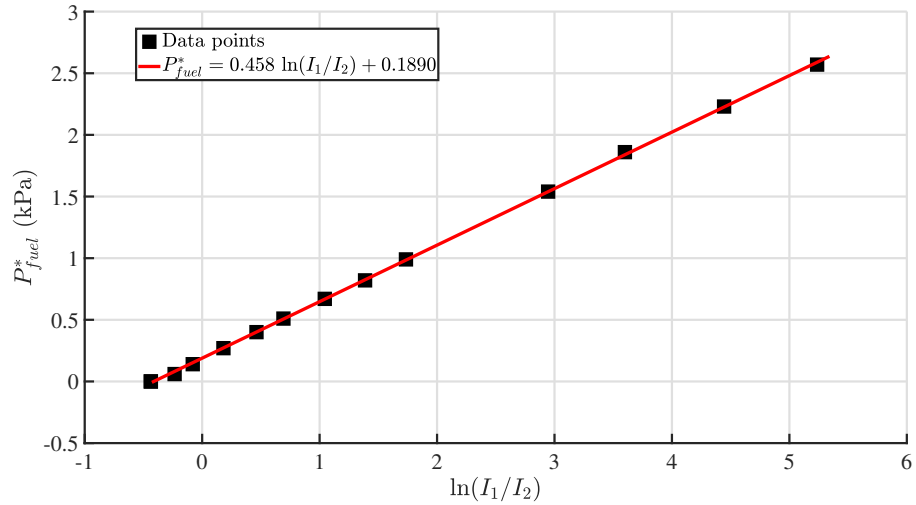

Figure 7.6: Sample in situ calibration for C-H bond absorption measurements in terms of n-hexane fuel partial pressure.

In situ calibration of the optical system was made by injecting known quantities of fuel into the CAT vessel, measuring the resulting intensity ratio I_1/I_2 and reducing the data by fitting to the functional form of Equation (7.4) in terms of the fuel partial pressure, P^*_{fuel}. The ratio I^o_1/I^o_2 is measured under vacuum where $X^*_{fuel} = 0$. An example of a calibration curve obtained from this approach is shown in Figure 7.6. An effective cross section can be computed from the slope of the calibration curve using linear regression and is consistent with the cross section of n-hexane measured by Mével et al. (2012).

Note that this is a line of sight integrated measurement technique across the entire path length of approximately $L = 5.2$ in. between the vessel windows. This is much larger than the boundary layer thickness which is less than 0.5 in at this location. Since n-hexane in particular has a large σ_ν, only a small concentration of n-hexane (close to sotichiometric conditions at 1 atm) is sufficient to fully absorb all of the emitted light. The dynamics of the fuel decomposition near the surface are therefore obstructed and are likely occurring at a faster rate than is being measured with this technique. The absorption signal will only change once a sufficient amount of the bulk gas has circulated through the boundary layer region and begun to decompose. These measurements therefore inform us about the rate of fuel decomposition in the bulk gas rather than within the boundary layer region.

7.2.3 Detector Alignment and Signal Processing

Detector output signals of up to 10 V were possible but were adjusted to a slightly lower value (typically 9 V) using the iris and neutral density filters to prevent potential signal saturation if the alignment drifted significantly over time. A sample set of the raw signals obtained in this way are

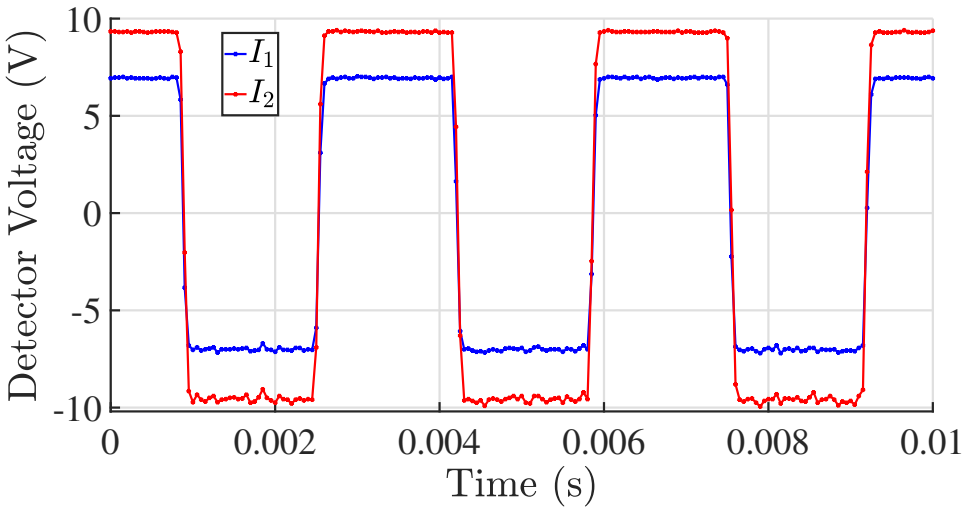

Figure 7.7: Raw data for laser absorption measurements with no fuel.

shown in Figure 7.7. The raw signal was then post-processed by isolating the square wave peaks by windowing at the chopper frequency in order to isolate the signal high portions of the raw data to perform averaging of the signal within each window. This approach gave an effective sampling rate of 300 Hz as determined by the chopper frequency.

To produce useful results, care also had to be taken in precise alignment of the photodetectors to produce consistent results and stable signals. The adjustable irises were helpful in achieving this since the beam diameter (1 mm) and active region of the detector are both small (2×2 mm). The laser beam intensity is low so making use of IR sensitive detector cards for alignment was difficult. Using a narrow aperture during alignment aided in ensuring the detectors were aligned orthogonal to the beam path. This was found to be important since even a modest incidence angle can produce a nonuniform exposure of the laser to the active detector area. Due to the nonuniform distribution of beam intensity and overlap of the beam on the active detector area, a slight misalignment can amplify system sensitivity to small beam pointing fluctuations. Small fluctuations in the output angle from the laser head can result in relatively large fluctuations in beam output location at large distances from the laser.

For the present setup, I_2 is approximately 1 m from the laser head meaning a pointing drift on the order of 0.1 mm at the location of the signal detector is possible with only a 1 mrad beam pointing fluctuation. This is enough to cause signal fluctuations on the order of 5% if the beam is close to the edge of the active sensor area. This is the same amplitude of commonly observed fluctuations with poor alignment as shown in Figure 7.8 (a). These fluctuations occur with a period of 1 to 5 minutes depending on the degree of misalignment. The sensitivity to such fluctuations is much smaller on the reference detector which is located relatively close to the beam output. However

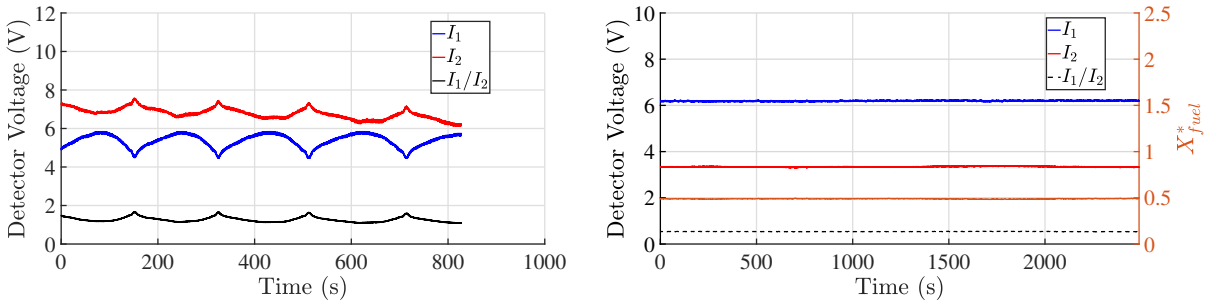

Figure 7.8: Example of absorption detector data obtained from (a) poor alignment and (b) precise alignment. The signals in (a) are obtained with no fuel present and in (b) were obtained after injecting the vessel with a small volume of n-hexane (P^*_{fuel} = 0.52 kPa).

when fluctuations did appear on I_1 they were occasionally out-of-phase with those on I_2, which indicated the origin of these fluctuations was not simply in the intensity fluctuations of the source beam. Obtaining stable performance and minimizing fluctuations was only achieved after precise alignment of the optical components. In Figure 7.8 (b), the signal obtained after precise alignment is shown to be stable over long periods of time, which is necessary for the slow heating rate cases discussed in the following section.

7.3 Results and Discussion

Based on previous experience in the 40 L vessel, two classes of testing were originally planned:

1. Steady state: T_w =const.
2. Transient: dT_w/dt =const.

where T_w is the surface temperature of the cylinder as measured from a height of approximately 6 in. from the bottom surface using the optical pyrometer described in Section 3.3.2. Case 1 corresponds to a constant surface temperature following a short transient warm-up period and Case 2 to a constant heating rate. In each case the pyrometer was used in a feedback control loop to control the cylinder surface temperature or heating rate.

7.3.1 Steady-State Tests

The original plan was to perform steady-state testing using a similar procedure to that in Chapter 3. However, following preliminary tests, it was found that due to the small volume of the vessels and short recirculation times there was significant depletion of the reactants during the initial transient heating period prior to reaching the set point point temperature selected for the test. As

a consequence, even at the highest heating rates it was not possible to reach a set temperature and have some dwell time prior to ignition without incurring depletion of the fuel.

The amount of depletion and type of ignition event was found to depend strongly on the heating rate and the set point temperature. For rapid heating rates with set points that exceed the threshold temperature for ignition, abrupt ignition and a rapid explosion transient was observed after a critical T_w was reached. For slow heating rates or set point temperatures less than a critical T_w, no abrupt ignition or explosion transient was observed but substantial reaction did occur as evidenced by the decrease in effective fuel concentration (X^*_{fuel}) with time. Intermediate cases of abrupt ignition following some amount of reaction depletion were also observed for slow heating rates and T_w exceeding the ignition temperature before the fuel is completely depleted.

The influence of heating rate was not unexpected and has been observed in previous studies on thermal ignition, although in a different temperature range and test configuration than the CAT. Boettcher et al. (2012) observed a similar sensitivity of the test outcome to heating rate in long-duration (up to 2500 s), low temperature (up to 540 K) heated vessel tests with constant low heating rates up to 15 K/min. Below a critical heating rate, complete depletion of fuel without explosive reaction was observed once a sufficiently high temperature was reached. Above a critical heating rate, some depletion of the fuel took place but ignition and rapid flame propagation was observed above a critical temperature that was lower than in the non-explosive case. The effect of heating rate was explained by considering the competition between heat transfer and chemical reaction, with buoyancy-driven flow influencing the location of ignition and time to explosion (Melguizo-Gavilanes et al., 2019).

An example of two types of test outcomes are shown in Figure 7.9 for a set point of T_w = 1000 K in both cases. An initial heating ramp was set by specifying a constant current in both cases. After T_w reached 90% of the set value, a PID feedback control loop activated to modulate the current in order to approach the set point without overshoot. As discussed further in the next section, ignition can occur for $T_w < 1000$ K in the larger configurations (A10 and A20) but $T_w \geq 1050$ was required for ignition in the shorter configuration A5. For this reason, ignition is observed in Figure 7.9 (a) but not in Figure 7.9 (b).

In the A10 test shown in Figure 7.9 (a), the onset of fuel consumption and decrease of X^*_{fuel} begins for $T_w > 750$ K and proceeds nearly linearly until approximately 125 s where the rapid combustion event occurs. The explosion is evidenced by a rapid pressure transient to a peak of 5.8 atm and rapid depletion of X^*_{fuel} to a low residual value within a short period. T_{pyr} also shows a sharp decrease in this region due to saturation of the photo detectors by emission from the flame front passing in front of the cylinder surface. Although approximately one-half of the fuel is consumed during the heating period, sufficient fuel remains in the mixture to result in abrupt ignition and rapid flame

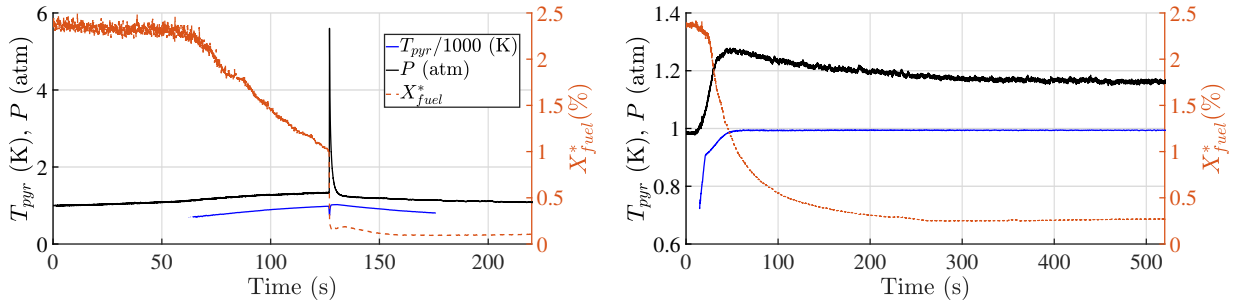

Figure 7.9: Example of two type of results for steady-state heating tests. (a) A10 with T_w = 1000 K. Ignition occurs on transient heating period at T_w = 989 K. (b) A5 with T_w = 1000 K. Ignition does not occur during the transient heating period and the reactants are slowly consumed.

propagation as evidenced by the rapid pressure transient and peak pressure following ignition.

In Figure 7.9(b) after T_{pyr} reached the set point of 1000 K at ~50 s, the temperature remained constant until the end of the test. Depletion of the fuel began shortly before the set point was reached and continued until 250 s, reaching a residual value of X^*_{fuel} = 0.2 %. The pressure trace initially showed a steady increase due to heat transfer and increase of temperature of the constant volume gas mixture. The ideal gas law predicts that pressure will be proportional to the average gas temperature for slow heating, $P \propto \overline{T_{gas}}$. The pressure reaches a peak value during the initial period of fuel consumption and then slowly decreases, approaching the final value at 500 s. The variation in pressure is due to a combination of heat transfer, chemical reaction and condensation processes.

Chemical reactions can either increase or decrease the pressure. The peak pressures of up to 7-8 atm produced in explosive ignition events are a consequence of rapid flame propagation resulting in the conversion of chemical energy into gas thermal energy without significant energy loss by heat transfer. Heat transfer from the combustion products takes place by thermal radiation from the hot CO_2 and H_2O and convective heat transfer to the cold walls, resulting in the decay of the peak pressure after ignition as observed in Figure 7.9(a).

The pressure changes in a case like Figure 7.9(b) are the consequence of the interaction of chemical reaction, heat transfer, and condensation. Consider the balanced reaction for complete combustion of n-hexane in air to form the stable products CO_2 and H_2O

$$C_6H_{14} + 9.5\,(O_2 + 3.76\,N_2) \rightarrow 7\,H_2O + 6\,CO_2 + 35.72\,N_2 \tag{7.5}$$

If the water does not condense, there is a net increase of 2.5 moles of gas resulting in a final pressure increase of 5.4% after the temperature has returned to the initial value. If the water does condense, there is a net decrease of 4.5 moles of gas resulting in final pressure reduction of 10%.

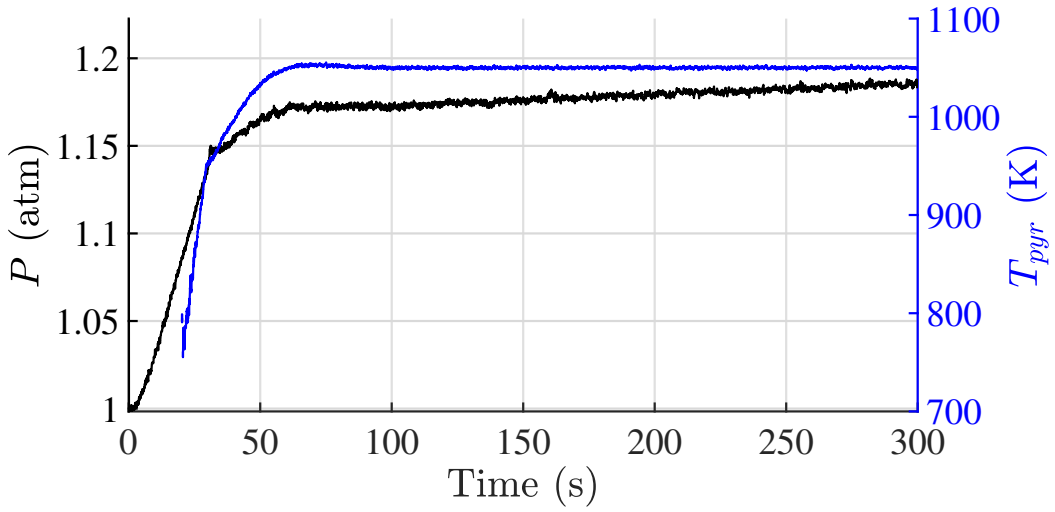

Figure 7.10: Pressure increase due to heating alone. CAT configuration A5 with 100% N_2 and the same heating rate as in Figure 7.9(b).

Incomplete combustion and low-temperature reactions of the fuel result in the creation of a number of intermediate species that tend to increase the pressure unless these species condense on the cold walls.

There is also a measurable effect on pressure during long duration tests in small volumes due to the increase in the average gas temperature. Heat transfer from the gas to cold walls of the CAT is effective at removing almost all of the thermal energy deposited into the gas. However, due to the finite rate of heat transfer, at steady-state conditions for long heating periods there is small but measurable pressure rise. The magnitude of the thermal pressure rise is shown in Figure 7.10 which illustrates a case with the same heating rate as that of the A5 case shown in Figure 7.9(b) but in a 100% N_2 environment to avoid any effects of chemical reaction. The effect of the heating is a nearly linear increase in pressure to the final equilibrium value approximately 20% higher than the initial value. The combination of chemical reaction, heat transfer and condensation effects makes it challenging to draw quantitative conclusions from the measured pressures for the long-duration tests without abrupt ignition.

7.3.2 Transient Heating

A series of transient heating tests explored the effects of heating rate and set point temperature observed during the tests of the steady state ignition procedure. Transient heating tests are classified in terms of slow ($\lesssim 2$ K·s^{-1}) and fast ($\gtrsim 2$ K·s^{-1}) heating rates.

For slow heating rates, the feedback control scheme was similar to that used in steady state testing but the control parameter was a specified heating rate dT_w/dt. This control system was initiated

only after sufficient signal was emitted from the surface so temperature measurement using the pyrometer was possible. This occurred for $T_w > 750$ K so this was used as the threshold for activating the control loop. The initial heating period to $T_w = 750$ K was performed using a constant input current, chosen to approximate the desired end heating rate.

For fast heating rates, a constant current input was sufficient to produce an approximately constant heating rate. This was preferable to using a control loop since the time delay for the control loop to stabilize after the initial heating to T_w =750 K was significant relative to the total test time. This is important because the depletion of reactants during this stabilization period will alter the ignition results. For slow heating rates the stabilization period was short relative to the total test time so the use of a feedback control system did not significantly affect the ignition results.

The achievable heating rates depend on the total thermal mass of the system and the energy balance as discussed in Chapter 5. Since the input power is proportional to the current, the maximum current available determines the maximum achievable heating rate. For the A5 configuration larger

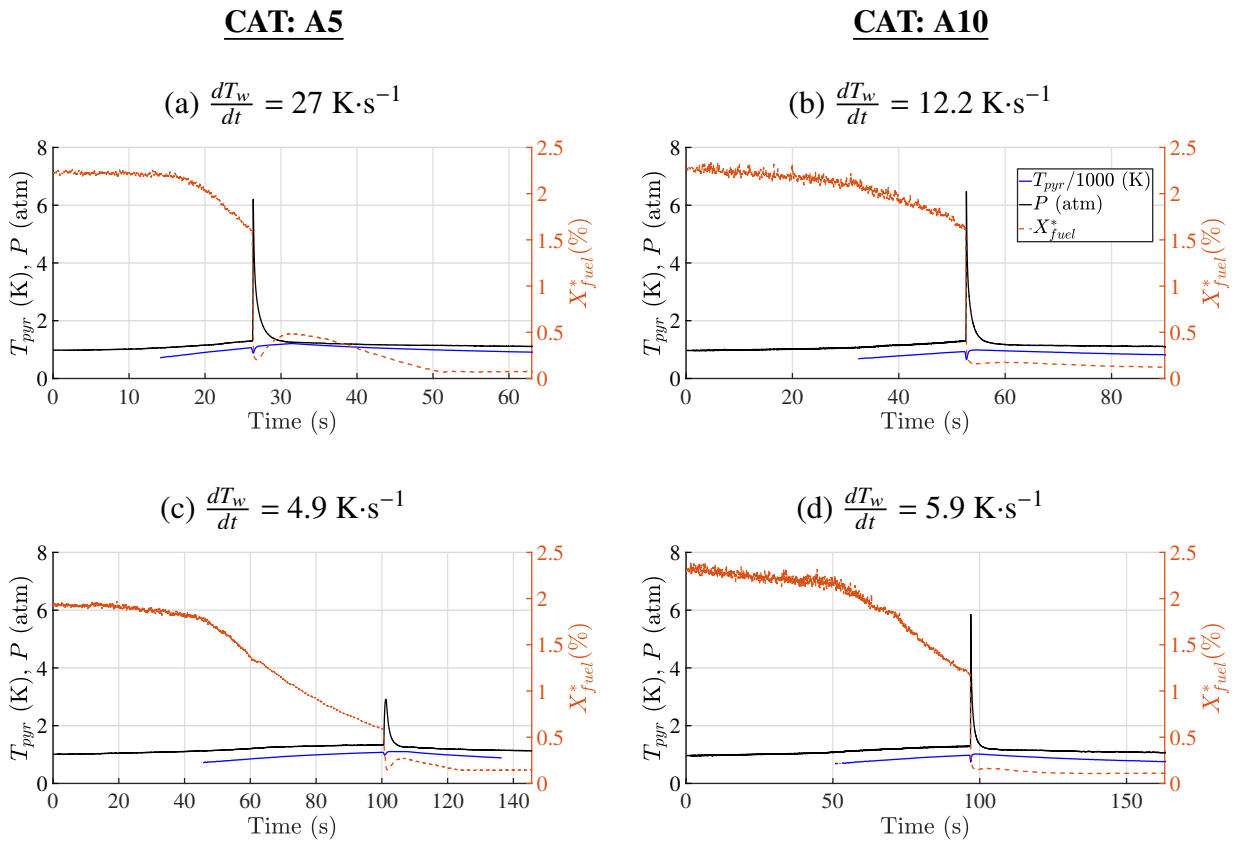

Figure 7.11: Example shot data for transient ignition cases. Left (right) column corresponds to A5 (A10) configuration. (a) and (b) are fast heating rates and (c) and (d) are moderate heating rates.

heating rates were achievable since a single 5 V and 600 A power supply was capable of being used. For the A10 and A20 cases however the voltage requirements were larger such that the use of two 5 V power supplies in series was necessary and limited the output current to 375 A. In practice the maximum heating rates achieved with the A10 and A20 configurations was approximately 12 K·s^{-1}. With the A5 configuration heating rates up to approximately 29 K·s^{-1} were achievable. Heating rates as low as 5 K·min^{-1} (0.083 K·s^{-1}) were also achieved using the control scheme described.

Figure 7.11 shows example shot data for fast (a, b) and moderate (c, d) heating rates with ignition for both the A5 and A10 configurations. For large heating rates the reactant depletion is small prior to ignition so for explosions above some critical heating rate, the depleted fraction at ignition is similar. This can be seen by a comparison of (a) and (b) which show a similar amount of depletion prior to explosion despite a large difference in heating rate. For moderate heating rates there is appreciable depletion of reactants prior to the main combustion event. This produces a decrease in the explosion pressure and and pressure rise rate as a result of slower flame speeds and lower energy content in the partially-reacted mixture. The pressure rise in (c) is much smaller than (d) despite similar heating rates. This is due to a significant increase in flame speed which is attributed to turbulent conditions in the upper region of the vessel which contributes to producing flame speeds in excess of the laminar flame speed of the mixture. This will be become apparent with detailed examination and comparison of properties of the pressure traces as discussed in later sections.

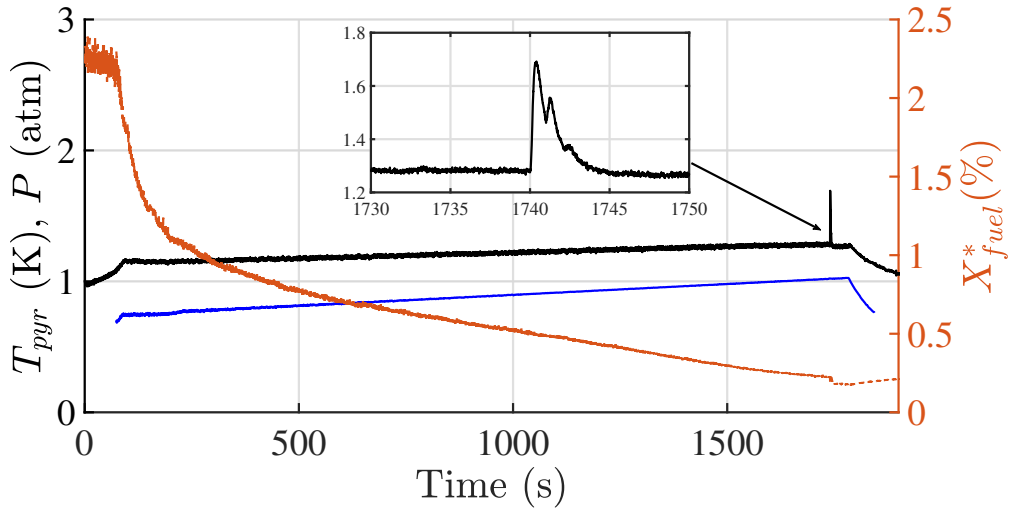

Figure 7.12: Slow heating rate case leading to delayed ignition in A10 configuration, Shot 91: dT_w/dt = 10 K·min^{-1} (0.17 K·s^{-1}). Inset box shows zoomed in region where ignition occurs after long heating time. Two pressure peaks are evident and explained by two sequential ignition events corresponding to flames seen in Figure 7.13.

For slow heating rates there is significant depletion of the reactants prior to the rapid explosion event as shown in Figure 7.12. Consequently the peak pressure of the transients are even smaller than in the moderate heating rate cases. For near critical cases, multiple small pressure peaks are observed over a few seconds. These are the result of multiple ignition and propagating flame events occurring sequentially. Visualization of these events illustrates that the pressure peaks are caused by flames which propagate within the thermal boundary layer. An example sequence of images of

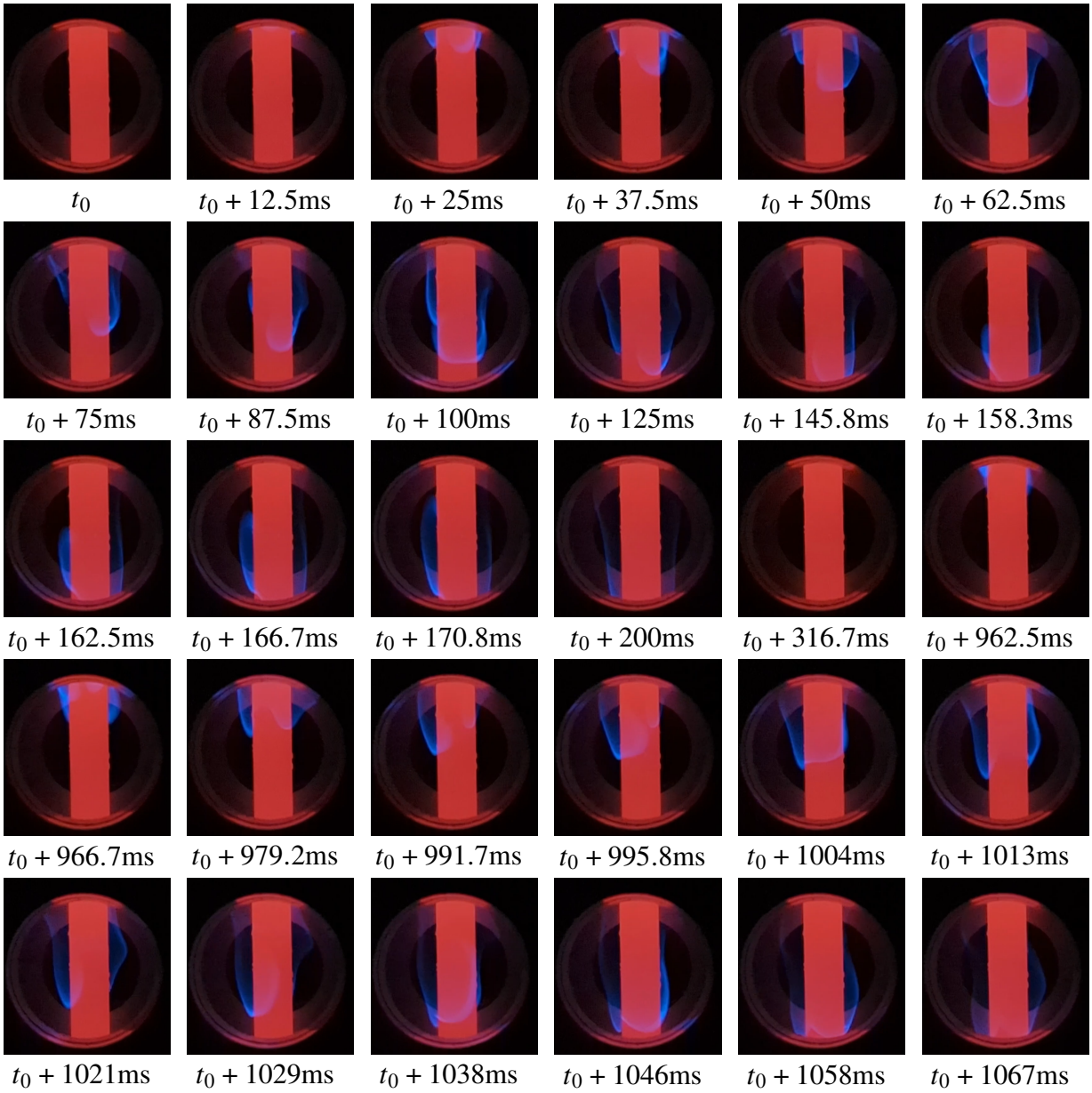

Figure 7.13: Flame propagating within the boundary layer in Shot 91. Approximate field of view: H = 5.25-6.75 in. 240 fps (Pixel 7 camera).

such an event is shown in Figure 7.13. Flames are initiated out of view of the window, likely near the top of the vessel where the thermal layer is thickest and where there is a stagnation region at the intersection of the boundary layer with the top surface. The flame propagates downward through the field of view while simultaneously moving in the azimuthal direction about the centrally-located cylinder. The first event is observed for about 200 ms within the field of view. A second flame is then observed 700 ms later and is observed for over 100 ms. These two events correspond to the dual pressure peaks observed in Figure 7.12. A third, even weaker pressure pulse is also observed following these two. This likely corresponds to a third flame event which does not propagate fully along the cylinder and into the field of view.

This phenomenon is the result of a highly unsteady flame front and a weakly reactive mixture where flame propagation is only possible in the heated region close to the cylinder surface due to the strong dependence of flame speed on temperature. However, within the boundary layer the buoyancy-induced velocity is comparable to the burning velocity in these mixtures. As a consequence, flame motion is quite irregular in comparison to the 40 L vessel tests, with "spinning and puffing" motions of a highly-curved flame front. Outside the boundary layer in the cold gas, the mixture has reduced reactivity due to extensive reactant depletion so flames are not observed to propagate in this region. Below a certain critical heating rate rapid explosion events no longer occur at all and the reactants instead just deplete to some residual value after long periods of time, similar to Figure 7.9(b). This is the result of near complete depletion of the reactive species in the

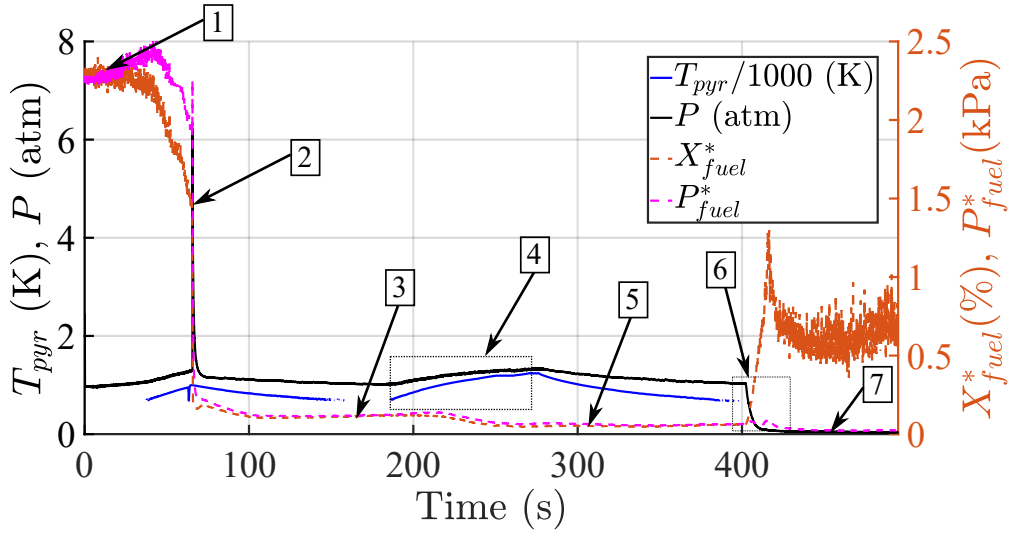

Figure 7.14: Example signal traces from a typical shot showing residual C-H absorption after a fast explosion. (1) Fill fraction: X^*_{fuel} = 2.23% (2) Explosion: X^*_{fuel} = 1.47% (3) Post explosion residual: X^*_{fuel} = 0.12% (4) Secondary heating ramp (5) Residual: X^*_{fuel} = 0.06% (6) Evacuation period (7) Post Evacuation: P^*_{fuel} < 0.01 kPa. Note at (7) X^*_{fuel} is noisy since the total pressure P in Equation (7.4) is close to 0.

mixture after sufficiently long periods of time at elevated temperature. For these configurations, the critical heating rate was found to be about 5 K·min^{-1} (0.083 K·s^{-1}).

In all cases a small residual signal in X^*_{fuel} of 0.1 to 0.2% remains after the explosion events and slow heating shots without explosion. Further investigation was conducted to attempt to determine the nature of the product mixture by repeated cycles of heating following the initial test. The process is shown in Figure 7.14. After a rapid heating rate over the first 50 s, an explosion occurs at (2) consuming most of the fuel. After the bulk gas cools, a steady residual value of X^*_{fuel} = 0.1% remains at (3), this is typical. At (4) a secondary heating cycle is then conducted where T_w is rapidly brought to 1200 K as measured by T_{pyr}. During this heating event, X^*_{fuel} begins to decrease from the residual value indicating further breakdown of the remaining absorbing species. At (5) the gas has cooled and a residual of X^*_{fuel} = 0.05% still remains. At (6) the vessel is then evacuated and X^*_{fuel} again decreases. This portion can be attributed to absorbing species which are non-reactive such as water vapor. The final residual at (7) is less than 0.01% and decreases to less the limit of detection as condensed products are vaporized and evacuated from the vessel. While H_2O has a relatively small absorption cross section at 3.39 μm, the combustion process generates a significant amount and some of it will remain in the gas phase.

The reactive portion of the residual signal at (3) is probably composed of aldehydes, alcohols, and organic acids. These species are formed in appreciable quantities in both spark engines (Zervas et al., 2001) and premixed flames (Zervas, 2005). Battin-Leclerc et al. (2007) successfully modeled and predicted the formation of organic acids in premixed propane flames at atmospheric pressure. They used this model to qualitatively study the pre-ignition phase in a Homogeneous Charge Compression Ignition (HCCI) engine with temperatures around 1000 K which are comparable to those in the boundary layer of the present experiments. The model suggests that the acids derive from aldehydes of the same structure via addition of hydroxyl and carbonyl groups. Smaller hydrocarbons and other intermediates were observed by Mével et al. (2019) during the long-duration oxidation of hexane-air in heated vessel experiments at 450 - 500 K. Measurements of species in flow reactor experiments (Mével et al., 2014) between 400 - 1000 K showed a large number of hydrocarbon fragments were generated during the decomposition of n-hexane. Numerical simulations (Mével et al., 2014; Mével et al., 2019) of both studies with detailed chemical reaction mechanisms predicted the formation of a wide range of major products and intermediate species including carbonyls in the form of hydroperoxy-ketones. Further evidence of the reactivity of the residual mixtures was evident in the long-duration (up to 2 hr) heated vessel (up to 500 K) tests of Mével et al. who were able to ignite propagating flames in these mixtures with a localized hot surface (a glow plug with a surface temperature of 1300 K). Significant peak pressures (60% of the adiabatic complete combustion value) were observed, indicating that a large number of hydrocarbon fragments and

partially oxidized intermediates were present. Due to the higher temperatures within the boundary layer of the hot cylinder in the CAT test these species are apparently destroyed during long duration tests.

The intermediate compounds have appreciable absorbance at 3.39 μm. A simulation of the absorbance of intermediates like formaldehyde, acetaldehyde, ethanol, methanol, formic acid, and acetic acid was conducted using Spectraplot(Goldenstein et al., 2017) and yielded a relative absorbance of each species in relation to the absorbance of hexane $b_k = A_k/A_{hexane}$. The largest contributors are ethanol $b_k = 0.2087$, formaldehyde $b_k = 0.0913$, and formic acid $b_k = 0.0.087$. If a large proportion of the residual is formaldehyde (CH_2O) as suggested by Zervas (2005) then

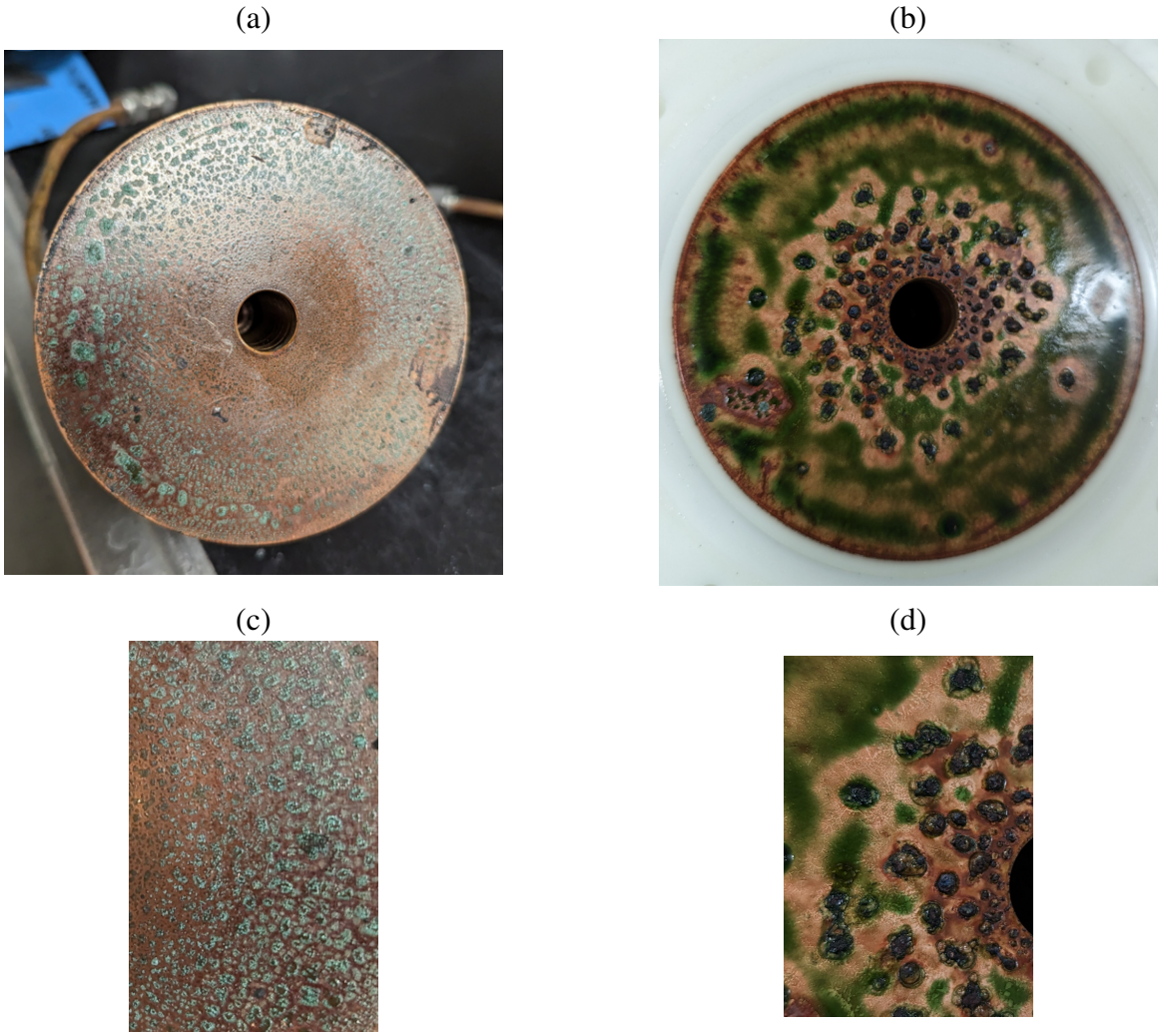

Figure 7.15: Corrosive residue present on (a) bottom surface and (b) top surface after several shots with A20 configuration. (c) and (d) are higher magnification images showing details of the corrosion morphology. Note: In (a) and (b) the central hole is 0.52" in diameter.

we can assume most of the absorption is due to this species. A mole fraction of approximately X_{CH_2O} = 0.5476% is required to account for the residual signal of X^*_{fuel} = 0.05% . In isooctane burner flames the reported concentration of CH_2O was approximately 400 ppm (X_{CH_2O} = 0.040%) which is not sufficient alone to account for the residual absorption not attributable to water vapor (Zervas, 2005). However given that those concentrations are measured in a premixed burner, the temperatures are much higher and conditions much different than those in the present experiment. The lower temperatures and longer heating times will preferentially form low temperature partially oxidized intermediates like CH_2O in larger quantities than in a burner flame (Ju, 2021). Additional combined contributions from other aldehydes, alcohols, and acids as well as other species like dimethyl ether which are present in relatively small quantities can likely account for the remaining absorption.

Additional evidence of the residual species is presented in Figure 7.15 which illustrates the condensed residue and resulting corrosion on the top and bottom isothermal surfaces of the vessel after several combustion tests. Copper readily oxidizes in the presence of oxygen and water and this process is accelerated by high temperatures. This typically results in a verdigris patina that develops on copper surfaces over time and has a deep blue green color . This is similar to what is observed in the bottom surface visualized in Figure 7.15(a) and (c). These images show discrete spots of accelerated oxidation likely due to the formation and evaporation of water droplets in the post combustion environment and under vacuum. Figure 7.15 (b) and (d) show a different oxidation structure with a dark green solution visible across most of the surface and localized deposits of black oxide as large as a 2 mm in diameter. These black oxide deposits become smaller close to the inner cylinder and do not form in the outer region of the surface indicating there is some ambient temperature dependence to their formation. The dark green solution is likely a dissolved solution of verdigris in an organic acid like formic or acetic acid.[2] These intermediate products of low temperature combustion reactions are derived from aldehydes of the same structure. These species can be formed in the thermal boundary layer near the cylinder surface and be convected to the top of the vessel where a portion is condensed onto the cooled isothermal walls. Over the course of many experiments these deposits build up in appreciable quantities. The black oxide beads are likely formed from concentrated regions of these condensed products which then burn in later experiments. The presence of these compounds on the copper surfaces is unlikely to affect the ignition results since ignition takes place close to the heated surface.

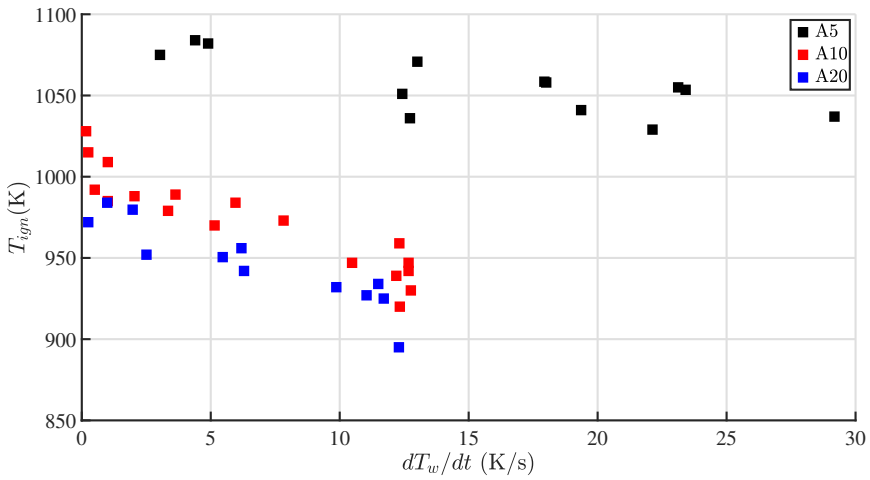

Figure 7.16: Summary plots of ignition temperatures vs. heating rate for all transient shots.

7.3.3 Shot summary

Summary plots of the ignition temperatures obtained at various heating rates for all three configurations are shown in Figure 7.16. Figure 7.16 shows that for similar heating rates there is a much lower critical surface temperature for ignition to occur in the larger configurations (A10 and A20) as compared to A5. Some dependence on height is expected since the laminar thermal boundary layer size scales with $H^{1/4}$ and thick boundary layers are predicted to result in lower ignition temperatures (Laurendeau & Caron, 1982; Law & Law, 1979). The dependence on height was studied experimentally by Jones (2020) and Ono et al. (1976) for laminar flow. These anf other laminar flow data are compared with the CAT experiments in Figure 7.17. The Ono et al. correlation is consistent with data from cylinders of the same diameter obtained by Jones and smaller cylinders of Boeck et al. (2017) and Melguizo-Gavilanes et al. (2016). The correlation is also consistent with data from cylinders of other diameters (Jones, 2020) and at lower pressure (Chapter 3) as well as the A5 configuration. The data obtained from the larger cylinder configurations A10 and A20 disagrees either the Ono et al. correlation or the trend of the data from the laminar flow tests with shorter surfaces. We attribute these differences for A10 and A20 CAT configurations to transition from laminar to turbulent flow on the upper part of the cylinder where ignition is most likely to occur. The analysis of Ono et al. (1976) assumes a laminar boundary layer and substantially over predicts the ignition temperature. At present, there is no theory or simulations to guide the development of models for ignition in turbulent, natural convection boundary layers.

[2]Interestingly there seems to be some connection of this process to the synthesise of paint pigments. Methods of extracting green and blue pigments through the creation of various copper oxides involving some combination with organic acids (typically acetic) have been described across history (50 -1750 AD) and have been studied using modern techniques (Buse et al., 2019).

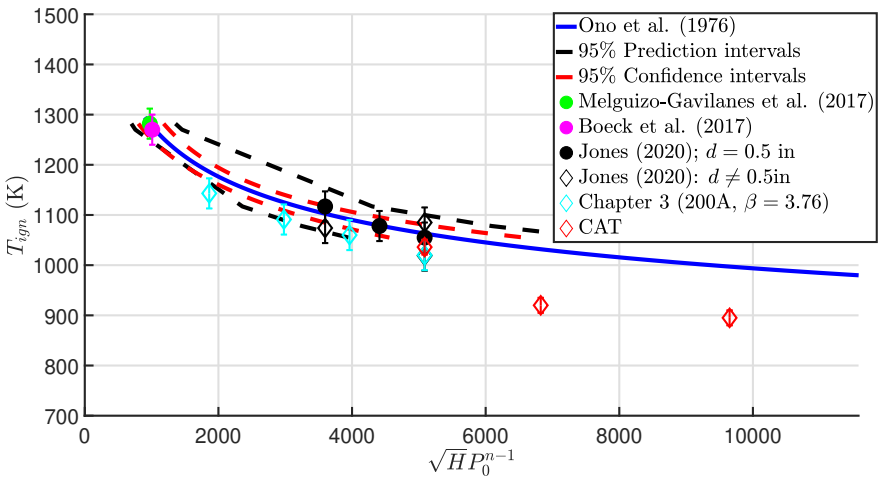

Figure 7.17: Comparison of present data with that of Jones (2020), Melguizo-Gavilanes et al. (2016), Boeck et al. (2017), and Chapter 3 for n-hexane air ignition by vertical cylinders. The fit from Ono's correlation was produced only using the data from Jones (2020) with filled in symbols which correspond to cylinders of the same diameter as CAT (d = 0.5 in). The value of n = 1.7 is the same as used by Ono et al. (1976) for methane and propane.

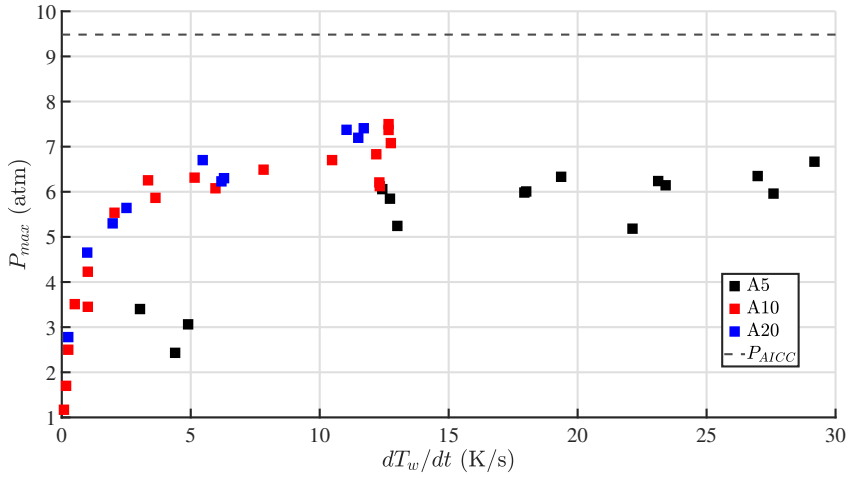

Figure 7.18: Summary plot of peak pressure vs. heating rate for all transient shots.

For lower heating rates cases in Figure 7.16, the higher ignition temperatures are a consequence of the depleted mixtures at the time of ignition as shown in Figures 7.11 and 7.12. The mixture in the boundary layer is less reactive and has a lower energy content due to the long duration of the test causing extensive depletion of the fuel. A higher temperature will be required to compensate for the decrease in reactivity and form an ignition kernel within the boundary layer.

The effect of this depletion is also evident in examination of the maximum pressure in the explosions

plotted in Figure 7.18. The slow to moderate heating rate cases for a given configuration show a significant decrease in the peak explosion pressure as a result of the reactant depletion in the vessel. The energy remaining in the mixture is decreased slowly until the point of ignition so that when it occurs, the unburned mixture being processed by the flame is less exothermic and produces lower flame temperatures and slower flame speeds which contribute to the decrease in explosion pressure.

The effect of turbulence can also explain the trends in Figure 7.18 where the maximum pressures achieved in the A10 and A20 cases are consistently higher than in the laminar A5 case for all heating rates. For example at 12 $K \cdot s^{-1}$ the A10 and A20 experiments consistently show maximum pressures of 7 - 8 atm while the A5 configurations produce pressures closer to 6 atm for the same heating rates. To understand why this gap exists it is useful to compare with the idealized adiabatic, isochoric, complete combustion (AICC) pressure (P_{AICC}) for the stoichiometric n-hexane air mixture. This idealized pressure is never achieved in experiments due to radiative and convective heat transfer from the hot products to the cold vessel during flame propagation. The loss in thermal energy during flame propagation will reduce the peak temperature and proportionally the peak pressure at the end of the combustion process. Losses are more significant for more slowly propagating flames and vessels with large surface area to volume ratios (Kunz, 1998).

In the A10 and A20 configurations the flames were observed to propagate faster and thus have less heat loss than the A5 configuration. In addition, the surface to volume ratio is also larger for the A5 configuration than for A10 and A20, which further increases the heat loss rate. We expect that the flames are faster due to the contribution of turbulence in the unburned gas created by the transition to turbulence in the boundary layers of the A10 and A20 cylinders. The turbulence in the boundary layer is expected to spread throughout the flow due to the natural convection recirculation pattern in the enclosed vessel. Turbulence will distort the initially laminar flame front generated during ignition, increasing the flame surface area and effective burning rate. The fluid motion induced by the flame further increases the turbulence level providing a feedback mechanism that results in flame acceleration (Ciccarelli & Dorofeev, 2008). This provides an explanation for the observed increases in peak explosion pressure for the A10 and A20 cases where turbulent flow is anticipated in the upper part of the vessel.

Figure 7.19 provides an additional indication of the increased flame speed in A10 and A20 tests. Significantly larger values of the maximum rate of pressure rise $(dp/dt)_{max}$ are observed in the A10 and A20 configurations than in the laminar cases. Additionally there is a modest gap between the A10 and A20 cases at large heating rates (12 $K \cdot s^{-1}$) which can be explained by the additional time for turbulent flame acceleration in the larger A20 vessel. There is also significant scatter and some cases with appreciably larger $(dp/dt)_{max}$ values in the A5 configuration at high heating rates. This is likely a consequence of the transitional nature of the A5 cases which was observed

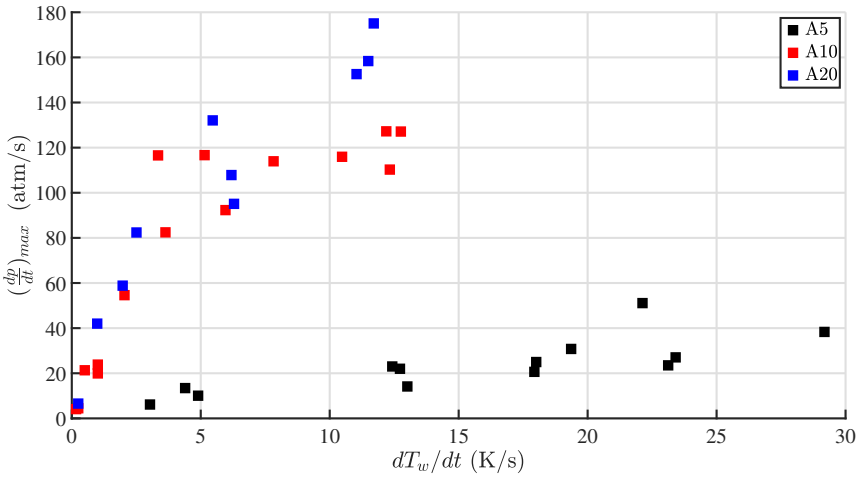

Figure 7.19: Peak pressure rise rate vs. heating rate for all shots.

in Chapter 6. At high heating rates there is a shorter time for the flow to respond to the changes in surface temperature so there is additional unsteadiness in the bulk gas. This can contribute to some turbulent flame acceleration, however over a relatively shorter period due to the small vessel size. We can estimate the effective flame speed in the experiments using the nondimensional pressure rise coefficient of Kunz (1998)

$$K_g' = \left(\frac{dp}{dt}\right)_{max} V^{1/3} \frac{1}{\Delta p_{max} S_{u,exp}} \tag{7.6}$$

where $\Delta p_{max} = P_{AICC} - p_{max}$ and $S_{u,exp}$ is the experimentally determined effective burning speed. We obtain $S_{u,exp}$ using this relation as in Equation (7.7)

$$S_{u,exp} = \left(\frac{dp}{dt}\right)_{max} V^{1/3} \frac{1}{\Delta p_{max} K_g'} \tag{7.7}$$

where the only unknown quantity is K_g'. Kunz shows there is minimal scatter in this quantity for a wide range of vessel sizes (1.84 < V < 1180 L) especially for low flame Reynolds numbers (Re_f = $S_{u,exp}, V^{1/3}/\nu$). For most conditions 8 < K_g' < 16 however for small vessels with $Re_f > 10^4$, K_g' seems to converge to a lower value. It is difficult to estimate this quantity a priori for the present experiments but it is simply a scaling factor in our estimation of $S_{u,exp}$. For the configurations of interest here the nominal unburned mixtures are the same and vessel sizes are similar so we can reasonably assume K_g' is a constant for all configurations. However we can also attempt to estimate Re_f by assuming a nominal value of $S_{u,exp}$ to obtain a consistent correlation. The initial rapid flame propagation in the heated boundary layer region is expected to dominate the development of the pressure transient. Therefore a reasonable assumption of a nominal value of $S_{u,exp}$ = 200 cm/s

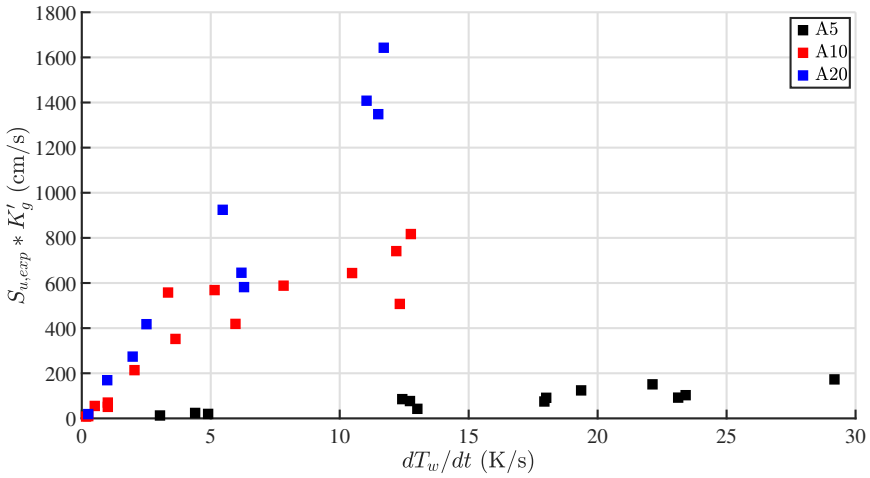

Figure 7.20: Summary plot of effective flame speeds as determined by implementation of Kunz's nondimensional pressure rise coefficient K'_g.

can be made which is representative of this region (Chapter 4). This yields $Re_f \simeq O(10^4)$ which indicates $K'_g \simeq 4$ for vessels of similar size to those used here (Kunz, 1998).

Figure 7.20 shows the estimates of the $S_{u,exp} * K'_g$ for these mixtures. This plot shows that for constant K'_g, there is a significant increase in flame speeds observed for the turbulent cases. For heating rates of approximately 12 K·s^{-1} there is an order of magnitude difference between the A5 and A10 configurations. This degree of difference in the flame speeds is expected for turbulent flame acceleration and for purely laminar flames would only be expected for large differences in unburned gas temperature. There is also an approximate factor of two increase between the A10 and A20 configurations around 12 K·s^{-1} heating rates. This is the same as the geometric factor of 2 increase in the cylinder length and vessel volumes for these two cases. This suggests there is a direct relationship between the increase in flame speed and the length of propagation. This is consistent with the idea of turbulent flame acceleration as the underlying mechanism for trends in pressure rise rate for the A10 and A20 configurations.

7.4 Conclusions

This chapter presented experimental results from a previously unexplored type of ignition experiment where effects of turbulence and confinement are significant. These effects were found to influence both ignition thresholds and explosion properties exhibited by pressure traces. The design of this experiment was discussed extensively in Chapter 5 and the flow regimes were visualized in Chapter 6 which lent insight into interpretation of the ignition results. The oxidation of the cylinders, especially H28 and H36, was found to be nonuniform and deviated from gray body

behavior in some cases. The different near surface flow structure as a result of turbulent transition was proposed as one possible explanation for this. A new approach to calibration of the temperature measurements obtained from the pyrometer was necessary to account for these oxide variations. This was done using reference thermocouples welded to the particular surface of interest.

C-H bond absorption measurements were implemented and lent insight into the depletion rate of reactive species in the gas volume during cylinder heating. For slow heating rates it was found that depletion of the C-H bonds in the volume occurred at a slow enough rate that classical ignition events would not occur. For moderate heating rates some depletion still occurred prior to the rapid explosion reaction which mostly consumed the remaining fuel. This had the effect of weakening the explosion as evidenced by lower peak pressures, pressure rise rates and slower flames. For fast enough heating rates little to no reactant depletion occurred and the largest peak pressures and pressure transients were observed. In most cases, residual absorption of the 3.39 μm light indicated the presence of weakly reactive hydrocarbons in the gas mixture. It was proposed that there is significant formation of aldehydes, alcohols, and organic acids in the gas volume which remain after the explosion. Some of these compounds condensed out of the gas phase onto the cooled vessel walls and resulted in enhanced corrosion of the top copper surface relative to the bottom.

Comparison of the ignition thresholds using existing data and correlations for laminar boundary layer ignition indicated that the data for the A10 and A20 configurations were inconsistent with previous laminar flow ignition studies. Additional examination of resulting explosion pressure transients across all configurations indicated the existence of two explosion regimes for these experiments. A laminar regime exists for small enough cylinders where the flow throughout the vessel remains mostly laminar so there is not typically a significant effect of flame acceleration. For larger heights corresponding to larger Ra flows the turbulent instabilities generated in the boundary layer fill the volume and results in a significant turbulent flame acceleration. This increased the severity of explosions resulting from these ignition events as measured by the steep increase in rate of pressure rise and closer approach to P_{AICC}. To build on these experiments, additional small cylinder configurations could be tested such as using the H4 and H6 cylinders to further explore the laminar regime. Exploration of larger heating rates for the A10 and A20 configurations would also be desirable in order to confirm the observations in the A5 case of minimal dependence of ignition thresholds and pressure transients on heating rates from 12 to 30 K·s^{-1}.

References

Battin-Leclerc, F., Konnov, A. A., Jaffrezo, J. L., & Legrand, M. (2007). To Better Understand the Formation of Short-Chain Acids in Combustion Systems. *Combustion Science and Technology*, *180*(2), 343–370. https://doi.org/10.1080/00102200701740782 (Cit. on p. 202)

Boeck, L., Meijers, M., Kink, A., Mével, R., & Shepherd, J. (2017). Ignition of fuel–air mixtures from a hot circular cylinder. *Combustion and Flame*, *185*, 265–277. https://doi.org/10.1016/j.combustflame.2017.07.007 (Cit. on pp. 205, 206)

Boettcher, P., Mével, R., Thomas, V., & Shepherd, J. (2012). The effect of heating rates on low temperature hexane air combustion. *Fuel*, *96*, 392–403. https://doi.org/10.1016/j.fuel.2011.12.044 (Cit. on pp. 190, 195)

Buse, J., Otero, V., & Melo, M. (2019). New Insights into Synthetic Copper Greens: The Search for Specific Signatures by Raman and Infrared Spectroscopy for Their Characterization in Medieval Artworks. *Heritage*, *2*(2), 1614–1629. https://doi.org/10.3390/heritage2020099 (Cit. on p. 205)

Ciccarelli, G., & Dorofeev, S. (2008). Flame acceleration and transition to detonation in ducts. *Progress in Energy and Combustion Science*, *34*(4), 499–550. https://doi.org/10.1016/j.pecs.2007.11.002 (Cit. on p. 207)

Drallmeier, J. A. (2003). Hydrocarbon absorption coefficients at the 339-*M*m He-Ne laser transition. *Applied Optics*, *42*(6), 979. https://doi.org/10.1364/AO.42.000979 (Cit. on p. 190)

Goldenstein, C. S., Miller, V. A., Mitchell Spearrin, R., & Strand, C. L. (2017). SpectraPlot.com: Integrated spectroscopic modeling of atomic and molecular gases. *Journal of Quantitative Spectroscopy and Radiative Transfer*, *200*, 249–257. https://doi.org/10.1016/j.jqsrt.2017.06.007 (Cit. on p. 203)

Guillamet, R., Lopitaux, J., Hannoyer, B., & Lenglet, M. (1993). Oxidation of stainless steels (AISI 304 and 316) at high temperature. Influence on the metallic substratum. *Le Journal de Physique IV*, *03*(C9), C9-349-C9–356. https://doi.org/10.1051/jp4:1993935 (Cit. on p. 185)

Huang, X., Xiao, K., Fang, X., Xiong, Z., Wei, L., Zhu, P., & Li, X. (2020). Oxidation behavior of 316L austenitic stainless steel in high temperature air with long-term exposure. *Materials Research Express*, *7*(6), 066517. https://doi.org/10.1088/2053-1591/ab96fa (Cit. on p. 185)

Jaynes, D. N., & Beam, B. H. (1969). Hydrocarbon Gas Absorption by a HeNe Laser Beam at a 339-μ Wavelength. *Applied Optics*, *8*(8), 1741. https://doi.org/10.1364/AO.8.001741 (Cit. on p. 190)

Jones, S. M. (2020). *Thermal ignition by vertical cylinders*. California Institute of Technology. (Cit. on pp. 184, 205, 206).

Ju, Y. (2021). Understanding cool flames and warm flames. *Proceedings of the Combustion Institute*, *38*(1), 83–119. https://doi.org/10.1016/j.proci.2020.09.019 (Cit. on p. 204)

Klingbeil, A. E., Jeffries, J. B., & Hanson, R. K. (2006). Temperature- and pressure-dependent absorption cross sections of gaseous hydrocarbons at 3.39 *M*m. *Measurement Science and Technology*, *17*(7), 1950–1957. https://doi.org/10.1088/0957-0233/17/7/038 (Cit. on p. 190)

Kunz, O. (1998). *Combustion characteristics of hydrogen-and hydrocarbon-air mixtures in closed vessels*. University of Stuttgart. Germany. (Cit. on pp. 207–209).

Laurendeau, N. M., & Caron, R. N. (1982). Influence of hot surface size on methane-air ignition temperature. *Combustion and Flame*, *46*, 213–218 (Cit. on p. 205).

Law, C. K., & Law, H. K. (1979). Thermal-ignition analysis in boundary-layer flows. *Journal of Fluid Mechanics*, *92*, 01 (Cit. on p. 205).

Lille, C., & Jargelius-Pettersson, R. F. A. (2000). Factors affecting the oxidation mode of stainless steels. *Materials at High Temperatures*, *17*(2), 287–292. https://doi.org/10.1179/mht.2000.17.2.016 (Cit. on p. 185)

Melguizo-Gavilanes, J., Boettcher, P., Mével, R., & Shepherd, J. (2019). Numerical study of the transition between slow reaction and ignition in a cylindrical vessel. *Combustion and Flame*, *204*, 116–136. https://doi.org/10.1016/j.combustflame.2018.12.036 (Cit. on p. 195)

Melguizo-Gavilanes, J., Nové-Josserand, A., Coronel, S., Mével, R., & Shepherd, J. (2016). Hot surface ignition of n-hexane mixtures using simplified kinetics. *Combustion Science and Technology*, *188*(11-12), 2060–2076 (Cit. on pp. 205, 206).

Mével, R., Boettcher, P., & Shepherd, J. (2012). Absorption cross section at 3.39μm of alkanes, aromatics and substituted hydrocarbons. *Chemical Physics Letters*, *531*, 22–27. https://doi.org/10.1016/j.cplett.2012.01.069 (Cit. on pp. 190, 192)

Mével, R., Chatelain, K., Boettcher, P., Dayma, G., & Shepherd, J. (2014). Low temperature oxidation of n-hexane in a flow reactor. *Fuel*, *126*, 282–293. https://doi.org/10.1016/j.fuel.2014.02.072 (Cit. on p. 202)

Mével, R., Rostand, F., Lemarié, D., Breyton, L., & Shepherd, J. (2019). Oxidation of n-hexane in the vicinity of the auto-ignition temperature. *Fuel*, *236*, 373–381. https://doi.org/10.1016/j.fuel.2018.09.009 (Cit. on pp. 190, 202)

Nasrazadani, S., & Raman, A. (1993). Formation and Transformation of Magnetite (Fe_3O_4) on Steel Surfaces Under Continuous and Cyclic Water Fog Testing. *CORROSION*, *49*(4), 294–300. https://doi.org/10.5006/1.3316052 (Cit. on p. 185)

Ono, S., Kawano, H., Niho, H., & Fukuyama, G. (1976). Ignition in a Free Convection from Vertical Hot Plate. *Bulletin of JSME*, *19*(132), 676–683 (Cit. on pp. 205, 206).

Zervas, E. (2005). Formation of organic acids from propane, isooctane and toluene/isooctane flames. *Fuel*, *84*(6), 691–700. https://doi.org/10.1016/j.fuel.2004.11.012 (Cit. on pp. 202–204)

Zervas, E., Montagne, X., & Lahaye, J. (2001). C_1-C_5 Organic Acid Emissions from an SI Engine: Influence of Fuel and Air/Fuel Equivalence Ratio. *Environmental Science & Technology*, *35*(13), 2746–2751. https://doi.org/10.1021/es000237v (Cit. on p. 202)

Chapter 8

SUMMARY AND CONCLUSIONS

The goal of this work was to expand the understanding of thermal ignition problems by investigating previously unexplored issues through experimentation. The studied issues included the use of representative commodity fuels and multi-component surrogates in thermal ignition testing, ignition and flame propagation in highly-diluted mixtures and low pressures, effects of large heated sources in highly confined vessels, and the study of laminar, transitional, and turbulent natural convection flows with large wall temperatures. The value of this work is in improving the design, regulation and certification of aircraft components and evaluating thermal ignition hazards in industrial processes involving flammable substances.

The goals were met via the implementation of three distinct experimental approaches:

1. The ASTM-E659 autoignition test method: Chapter 2
2. Ignition by laminar natural convection flow around a vertical cylinder: Chapters 3 and 4
3. The confined autoignition test (CAT): Chapters 5 to 7

The study of the ASTM-E659 test method provided for the first time, a detailed study with extensive documentation of the results for samples of representative aviation fuels, individual components and surrogate blends. The study also demonstrated how surrogates compare to actual fuels in the thermal ignition regime. Most importantly, this study documented the wide range of possible ignition behavior and the limitations of the AIT method as basis for aircraft certification.

The study of ignition by laminar natural convection examined two key issues: the effect of nitrogen dilution (reduced oxygen concentration) and reduced pressure ignition thresholds and explosion development. These tests provided for the first time, quantitative data on thermal ignition in conditions relevant to modern aircraft fuel tank designs, which use inerting by nitrogen-enriched air to reduce or eliminate fuel flammability hazards.

The confined autoignition testing examined for the first time, the key issue of how turbulence and confinement combine to influence hot surface ignition thresholds. To address this regime, the CAT facility was designed and experiments conducted to understand the onset of boundary layer instabilities and turbulent transition for large (up to 1 m tall) hot vertical cylinders. The effects of these flow phenomena on ignition thresholds and explosion properties were previously

unknown. In addition, the introduction of a large degree of confinement (large heated surface area to volume ratio) in CAT enabled severely reduced recirculation times and increased the prevalence of low temperature chemical reactions prior to combustion. Overall this experiment provided a bridge between the purely nonpremixed heated vessel type experiments (ASTM-E659) and external laminar flow heated surface experiments.

A summary of the observations made in this study are as follows:

1. There is an important distinction to be made between heated vessel and heated surface ignition experiments.
2. There exists a lack of transparency of conditions under which AIT numbers were obtained and little to no published raw data for most substances.
3. Surrogate fuels can accurately capture the autoignition thresholds and regimes of cool flame ignition modes of Jet A.
4. There is a modest effect of nitrogen inerting and pressure reduction on reducing ignition thresholds but a strong reduction in flame speed and the severity of the pressure transient.
5. The laminar boundary layer ignition problem can be correlated using one-dimensional flame model properties by considering the balance between chemical energy generation and heat diffusion in the thermal boundary layer region.
6. The presence of highly unsteady flames propagating within thermal boundary layers for highly diluted or highly confined configurations with low heating rate.
7. The onset of boundary layer instability and turbulent transition for non-Boussinseq natural convection flows with large temperature differences is not predicted by the conventional definition of a critical Rayleigh number based on surface height Ra_H.
8. Transition from laminar to turbulent flow on a hot vertical cylinder reduces the ignition threshold temperature and increases the severity of resulting explosions via flame acceleration.
9. The effect of confinement around a hot surface can lead to recirculation and pre-combustion reactions such that the ignition threshold temperature and severity of explosion depend on the heating rate.
10. For certain combinations of heating rates and maximum temperatures, only slow reactions occur and explosive ignition events are not observed.

8.1 Future Work

This study leaves open many avenues for future work in thermal ignition. The approach to autoigniton testing with the ASTM-E659 apparatus presented in Chapter 2 can be implemented for additional liquid fuels of interest to other groups within the realm of aviation and beyond. Sustainable aviation fules (SAF) and aircraft hydraulic fluids (Skydrol) are of particular immediate interest in this testing. Additional experimental developments designed at understanding the physical processes underpinning the ASTM-E659 autoignition test would also be invaluable in future attempts to model and simulate the heated vessel ignition process. The formation of droplets, vaporization and diffusion of the fuel into the air, convective motion and the potential impingement of the fuel on the hot flask surface currently make this a challenging situation to model. The fuel-air mixture is likely to be highly nonuniform as is the temperature distribution due to the cooling effects of fuel vaporization. Design of a heated vessel experiment with optical access and well controlled injection process would enable visualization tools like schlieren, particle image velocimetry (PIV), phosophr thermometry, and OH* chemiluminescence among others to be implemented and greatly enhance understanding of the heated vessel ignition process.

Additional testing with confined experimental facilities like the CAT in Chapter 5 and Chapter 7 with different fuels and mixtures would be valuable in developing an database of experimental ignition values for confined ignition. Experiments with much higher heating rates on the order of 100 K/s could also provide an interesting avenue of research to verify the plateau in ignition thresholds and explosion properties for fast heating rates. These would be possible with the implementation of a more powerful heating system such as the use of two XR5-600 power supplies in parallel for short cylinders and in series for longer cases requiring higher voltage. For fast enough heating rates, no measurable reactant consumption would occur prior to ignition and this should produce the lowest ignition temperatures achievable in those experiments. The use of a fully transparent outer vessel section as discussed in Section 5.4 would enable additional measurement techniques like schlieren, particle image velocimetry (PIV), and OH* chemiluminescence. These tools would be useful in further studying mixing, reactant depletion, and ignition kernel formation and location and the unstable boundary layer confined flame observed for low heating rates. Gas sampling for use in gas chromatography would also be useful for quantitatively determining the composition of the residual mixture present in most CAT explosion tests.

Improvements to high temperature measurement techniques are also a clear area in need of further development. High emissivity ceramic spray coatings have potential for producing a more stable and uniform surface condition for use in pyrometry. These coatings can even be used with non metallic surfaces enabling even more varied approaches to ignition testing. A multiwavelength pyrometer (spectral pyrometer) which uses a spectrally resolved photo detector as the measurement device

is also a potential improvement over the two-color pyrometers used here. By measuring a wide spectral response and comparing to idealized blackbody curves the temperature can be determined and emissivity measurements can be made. Using this tool any degradation in the surface condition would be more obvious than with only two wavelengths being captured. Coupling this tool with a stable ceramic coating of known emissivity would likely provide a robust approach and would be an improvement over current methods.

The flow features observed in Chapter 6 also certainly warrant additional exploration experimentally and numerically. In general a reevaluation of the non-dimensional groups of relevance to non-Boussinesq vertical surface flows and channel flows is warranted since Ra_H alone does not seem to be a useful indicator of turbulent transition. One avenue for this is the implementation of computational fluid dynamics (CFD) tools for simulating nonreacting flow fields in exposed and highly confined non-Boussinesq natural convection flows similar to those experimentally explored here for the CAT experiments. The particle paths and temperature time histories of the bulk gas could also be explored to understand the reaction depletion process observed in CAT. The temperature time histories of nonreacting seed particles could then be used in a 0D detailed kinetic model to study the reaction progression in the boundary layer region. Turbulent transition for non-Boussinesq natural convection flows could also be explored with such tools and modern computing capabilities. This would be useful in interpreting the transitional flow fields observed experimentally. Reactive simulations can also be implemented for imposed turbulent cases using simplified kinetics and could be useful in understanding the drop in ignition thresholds observed in experiments.

Experimental quantification of the effect of turbulent intensity on ignition thresholds and explosion properties would further supplement this work. An experiment with variable forced convection could produce a high degree of turbulent intensity for this purpose. The use of similar large surfaces as studied here would likely be best suited to such experiments since the relatively large thermal mass would prevent strong temperature gradients from forming on the surface due to nonuniform turbulent convective heat transfer. Measurements of turbulent intensity present in the A10 and A20 CAT configurations would be useful in establishing a relevant range of values to target. The use of a simpler ignition system like a spark with a high aspect ratio tube with forced turbulence could also inform the turbulent flame acceleration process present in those cases. A final goal of modelling the ignition process in turbulent boundary layers would require these data and a better understanding of the relationship between turbulent intensity and thermal ignition thresholds.

Appendix A

ASTM-E659: IGNITION DATA

This section summarizes the data obtained using the ASTM-E659 autoignition temperature test for n-hexane, n-decane, n-dodecane, isocetane, 1,2,4-trimethylbenzene, toluene, trans-decalin, Jet A (POSF-4658), Jet A (POSF-10325), Aachen surrogate, and JI surrogate. V_{inj} is the volume of fuel injected given in mL and used to compute Global ϕ based on mixing with 500 mL of air. Furnace temperature is the set point of the furnace control unit while flask Temperature is the initial gas temperature as measured by T_4. The Ignition Mode entry is 0 for a no-ignition case test, 1 for a Mode I ignition, 2 for Mode II ignition, 3 for Mode III ignition, and 4 for Mode IV ignition. τ_{ign} is the delay time between end of injection and appearance of flame typically defined by maximum rate of temperature rise. Maximum temperature is measured by T_4.

A.1 n-Hexane

Table A.1: ASTM-E6559 autoignition shots: n-Hexane

Shot	V_{inj} **(mL)**	**Global** ϕ	**Furnace Temp. (°C)**	**Flask Temp. (°C)**	**Ignition Mode**	τ_{ign} **(s)**	**Max Temp. (°C)**
1	0.10	1.56	250	237.0	0	-	-
2	0.10	1.56	300	276.7	1	5.5	-
3	0.10	1.56	280	267.7	1	9.4	-
7	0.20	3.12	260	249.2	1	18.0	-
8	0.20	3.12	250	245.0	0	-	-
9	0.25	3.90	250	242.0	0	-	-
10	0.30	4.68	260	245.0	0	-	-
14	0.20	3.12	280	257.4	1	13.9	-
17	0.20	3.12	260	244.6	0	-	-
18	0.25	3.90	260	244.1	0	-	-
19	0.30	4.68	260	244.2	0	-	-
20	0.40	6.25	260	243.6	0	-	-
21	0.10	1.56	260	239.9	1	51.0	-
22	0.10	1.56	260	242.4	1	48.3	-
23	0.10	1.56	250	237.2	0	-	-
24	0.10	1.56	260	237.0	1	55.6	-

Table A.1: ASTM-E6559 autoignition shots: n-Hexane (continued)

Shot	V_{inj} **(mL)**	**Global** ϕ	**Furnace Temp. (°C)**	**Flask Temp. (°C)**	**Ignition Mode**	τ_{ign} **(s)**	**Max Temp. (°C)**
25	0.10	1.56	260	241.4	1	41.4	-
26	0.10	1.56	260	240.4	0	-	-
27	0.10	1.56	260	241.4	1	46.9	-
28	0.10	1.56	260	242.5	1	51.5	-
29	0.10	1.56	250	234.2	0	-	-
30	0.10	1.56	250	234.2	0	-	-
31	0.10	1.56	255	236.2	0	-	-
32	0.08	1.25	255	237.8	0	-	-
33	0.08	1.25	255	237.8	0	-	-
34	0.10	1.56	255	237.4	0	-	-
35	0.10	1.56	255	237.5	1	53.0	-
36	0.08	1.25	255	236.7	0	-	-
37	0.10	1.56	250	233.7	0	-	-
38	0.10	1.56	260	241.1	1	48.5	458.9
39	0.10	1.56	260	241.3	1	47.2	578.7
40	0.10	1.56	260	241.4	1	45.4	521.3
41	0.10	1.56	250	234.1	0	-	245.6
42	0.10	1.56	255	237.1	1	54.6	523.2
43	0.10	1.56	252	235.1	0	-	-
44	0.10	1.56	250	238.6	1	46.5	497.9
45	0.10	1.56	245	235.3	1	63.8	504.1
46	0.10	1.56	245	235.4	1	61.3	529.3
47	0.10	1.56	240	232.2	0	-	242.7
48	0.08	1.25	240	231.7	0	-	237.3
49	0.14	2.19	240	228.9	0	-	238.3
50	0.16	2.50	240	228.2	0	-	238.6
51	0.06	0.94	240	225.4	0	-	230.6

A.2 n-Decane

Table A.2: ASTM-E6559 autoignition shots: n-Decane

Shot	V_{inj} **(mL)**	**Global** ϕ	**Furnace Temp. (°C)**	**Flask Temp. (°C)**	**Ignition Mode**	τ_{ign} **(s)**	**Max Temp. (°C)**
1	0.10	1.71	240	218.3	1	59.7	521.8
2	0.05	0.85	240	220.0	0	-	235.2
3	0.20	3.42	240	220.9	1	47.6	398.9
4	0.30	5.12	240	224.9	1	38.3	340.1
5	0.40	6.83	240	224.9	1	34.7	332.4
6	0.10	1.71	230	218.2	1	64.3	535.3
7	0.30	5.12	230	219.2	1	57.0	356.0
8	0.10	1.71	220	211.5	0	-	220.4
9	0.30	5.12	220	211.4	3	95.5	388.8
10	0.20	3.42	220	209.6	3	119.9	414.7
11	0.30	5.12	220	206.7	3	151.7	335.7
12	0.35	5.98	220	206.5	3	160.4	289.3
13	0.30	5.12	215	204.3	3	217.3	292.4
14	0.20	3.42	215	205.2	0	-	219.6
15	0.10	1.71	220	209.4	0	-	220.8
16	0.40	6.83	220	211.4	3	88.1	324.5
17	0.50	8.54	220	212.8	3	86.2	283.9
18	0.25	4.27	212	208.5	0	-	223.7
19	0.20	3.42	212	207.1	0	-	220.9
20	0.40	6.83	212	207.1	3	168.3	304.3
21	0.30	5.12	212	208.9	3	128.3	317.8
22	0.30	5.12	207	200.6	0	-	211.4
23	0.30	5.12	210	205.1	0	-	218.7
24	0.30	5.12	211	205.2	0	-	217.3
25	0.30	5.12	212	206.5	0	-	222.1
26	0.30	5.12	211	207.3	3	152.8	295.8
27	0.30	5.12	211	205.5	3	199.2	260.4
28	0.32	5.46	210	206.4	3	174.6	276.6
29	0.32	5.46	208	202.7	0	-	215.4
30	0.30	5.12	212	204.4	0	-	220.9

A.3 n-Dodecane

Table A.3: ASTM-E6559 autoignition shots: n-Dodecane

Shot	V_{inj} **(mL)**	**Global** ϕ	**Furnace Temp. (°C)**	**Flask Temp. (°C)**	**Ignition Mode**	τ_{ign} **(s)**	**Max Temp. (°C)**
1	0.10	1.75	240	213.5	1	54.8	-
2	0.08	1.40	240	217.3	1	53.7	-
3	0.06	1.05	230	217.1	1	59.0	-
4	0.10	1.75	225	200.9	0	-	208.1
5	0.10	1.75	225	204.7	0	-	215.9
6	0.10	1.75	225	210.9	1	85.9	310.2
7	0.08	1.40	225	212.6	1	80.2	325.3
8	0.10	1.75	220	209.8	1	91.5	328.1
9	0.08	1.40	220	209.4	1	99.3	403.9
10	0.10	1.75	215	206.5	0	-	216.8
11	0.08	1.40	215	200.1	0	-	205.6
12	0.10	1.75	220	205.0	0	-	215.0
13	0.10	1.75	220	208.3	0	-	223.3
14	0.06	1.05	220	209.1	0	-	213.9
15	0.08	1.40	215	204.4	0	-	212.1
16	0.06	1.05	215	204.4	0	-	207.2
17	0.08	1.40	230	206.7	0	-	215.2
18	0.08	1.40	230	214.6	1	67.5	348.8
19	0.08	1.40	218	208.1	0	-	217.2
20	0.12	2.10	218	206.1	0	-	216.6
21	0.08	1.40	230	218.6	1	42.9	273.2
22	0.08	1.40	220	211.4	1	75.5	321.2
23	0.08	1.40	215	208.1	0	-	216.5
24	0.08	1.40	215	208.3	0	-	215.2
25	0.10	1.75	230	212.6	1	49.2	271.7
26	0.10	1.75	220	209.4	1	84.9	284.0
27	0.10	1.75	215	206.4	0	-	216.6
28	0.12	2.10	215	206.8	1	114.6	279.9
29	0.14	2.45	215	206.8	1	105.9	274.9

Table A.3: ASTM-E6559 autoignition shots: n-Dodecane (continued)

Shot	V_{inj} **(mL)**	**Global** ϕ	**Furnace Temp. (°C)**	**Flask Temp. (°C)**	**Ignition Mode**	τ_{ign} **(s)**	**Max Temp. (°C)**
30	0.16	2.80	215	207.1	1	100.9	273.9
31	0.14	2.45	220	209.4	1	83.1	433.2
32	0.20	3.50	220	212.4	1	75.8	362.9
33	0.20	3.50	215	208.9	1	103.4	363.3
34	0.20	3.50	210	205.6	1	135.3	404.3
35	0.24	4.19	210	205.4	1	133.2	378.1
36	0.30	5.24	210	205.8	1	122.9	329.5
37	0.40	6.99	210	205.9	1	123.1	314.6
38	0.50	8.74	210	206.3	3	166.2	297.5
39	0.30	5.24	205	204.9	1	144.9	356.3
40	0.30	5.24	205	203.7	0	-	224.6
41	0.30	5.24	205	203.0	0	-	211.8
42	0.30	5.24	205	200.6	0	-	220.2
43	0.30	5.24	207	203.2	0	-	211.9
44	0.30	5.24	208	205.3	0	-	215.4
45	0.30	5.24	208	194.6	0	-	209.0
46	0.30	5.24	210	200.7	0	-	207.8
47	0.30	5.24	225	212.9	1	88.5	334.9
48	0.30	5.24	225	211.8	1	90.2	333.1
49	0.30	5.24	225	209.4	1	92.0	356.1
50	0.30	5.24	213	206.0	1	137.6	317.1
51	0.30	5.24	211	204.1	1	157.6	324.9
52	0.30	5.24	211	202.6	1	169.8	323.9
53	0.30	5.24	211	203.1	3	152.4	324.2
54	0.30	5.24	208	202.2	3	161.6	323.5
55	0.30	5.24	207	199.4	0	-	221.1

A.4 Isocetane

Table A.4: ASTM-E6559 autoignition shots: Isocetane

Shot	V_{inj} **(mL)**	**Global** ϕ	**Furnace Temp. (°C)**	**Flask Temp. (°C)**	**Ignition Mode**	τ_{ign} **(s)**	**Max Temp. (°C)**
1	0.20	3.68	750	738.0	1	0.0	820.1
2	0.10	1.84	720	711.0	1	0.0	761.4
3	0.10	1.84	690	682.0	1	0.0	725.2
4	0.10	1.84	650	642.0	1	0.0	827.4
5	0.10	1.84	600	596.0	1	0.0	645.1
6	0.10	1.84	570	564.6	1	0.2	656.3
7	0.10	1.84	540	535.0	1	1.0	626.2
8	0.10	1.84	480	475.4	1	6.7	607.1
9	0.10	1.84	460	453.8	2	8.2	501.2
10	0.20	3.68	460	452.6	2	6.4	500.9
11	0.20	3.68	440	433.2	2	8.7	484.7
12	0.30	5.52	440	433.2	2	12.0	475.9
13	0.10	1.84	440	427.1	1	20.0	520.5
14	0.05	0.92	440	427.4	0	-	450.4
15	0.06	1.10	440	428.3	1	58.7	564.5
16	0.15	2.76	440	428.9	1	12.0	520.9
17	0.30	5.52	430	420.3	2	16.5	478.9
18	0.20	3.68	430	420.2	2	14.8	484.8
19	0.10	1.84	430	420.4	1	28.7	527.6
20	0.06	1.10	430	420.1	0	-	457.6
21	0.08	1.47	430	420.1	1	45.7	533.4
22	0.20	3.68	420	407.7	2	25.0	472.7
23	0.30	5.52	420	408.2	2	20.0	471.2
24	0.10	1.84	420	409.1	0	-	457.7
25	0.15	2.76	420	409.2	2	31.1	464.7
26	0.20	3.68	410	401.3	2	33.1	459.9
27	0.40	7.36	410	401.1	2	27.6	450.7
28	0.30	5.52	395	387.5	0	-	430.9
29	0.30	5.52	400	391.3	0	-	431.3
30	0.40	7.36	400	390.0	0	-	431.0

Table A.4: ASTM-E6559 autoignition shots: Isocetane (continued)

Shot	V_{inj} **(mL)**	**Global** ϕ	**Furnace Temp. (°C)**	**Flask Temp. (°C)**	**Ignition Mode**	τ_{ign} **(s)**	**Max Temp. (°C)**
31	0.30	5.52	405	394.1	0	-	443.9
32	0.20	3.68	410	399.7	2	35.4	451.4
33	0.50	9.21	410	400.3	0	-	440.6
34	0.40	7.36	410	400.2	2	25.1	444.8
35	0.30	5.52	407	397.9	2	28.9	446.6
36	0.40	7.36	407	397.4	2	25.4	435.5
37	0.40	7.36	404	395.2	2	27.7	431.4
38	0.30	5.52	404	394.9	0	-	413.8
39	0.30	5.52	420	395.4	0	-	429.1
40	0.40	7.36	420	396.4	0	-	427.6
41	0.40	7.36	435	403.3	2	17.5	432.1
42	0.40	7.36	420	398.4	2	23.5	431.4
43	0.40	7.36	420	395.4	0	-	427.2
44	0.38	7.00	423	397.0	2	23.7	426.4
45	0.38	7.00	423	396.4	0	-	432.1
46	0.36	6.63	430	401.1	2	19.6	433.3

A.5 1,2,4-Trimethylbenzene (TMB)

Table A.5: ASTM-E6559 autoignition shots: 1,2,4-Trimethylbenzene (TMB)

Shot	V_{inj} **(mL)**	**Global** ϕ	**Furnace Temp. (°C)**	**Flask Temp. (°C)**	**Ignition Mode**	τ_{ign} **(s)**	**Max Temp. (°C)**
1	0.10	1.88	550	532.3	1	9.6	587.4
2	0.15	2.82	550	532.3	1	9.1	648.6
3	0.20	3.76	550	532.4	0	-	568.0
4	0.30	5.63	550	532.2	0	-	541.4
5	0.20	3.76	550	535.3	0	-	535.7
6	0.10	1.88	550	532.3	1	13.4	615.1
7	0.20	3.76	550	532.8	2	14.3	590.6
8	0.10	1.88	550	532.4	1	9.3	702.9
9	0.06	1.13	550	532.8	1	9.1	633.8
10	0.05	0.94	550	533.1	1	8.5	731.3
11	0.03	0.56	550	533.3	1	7.6	744.5
12	0.10	1.88	550	533.3	1	8.5	685.4
13	0.03	0.56	535	516.0	1	14.3	689.2
14	0.10	1.88	535	516.8	2	15.8	549.2
15	0.20	3.76	535	517.9	0	-	539.8
16	0.30	5.63	535	520.7	0	-	524.3
17	0.03	0.56	535	518.8	1	18.3	695.1
18	0.06	1.13	535	520.2	1	12.5	606.8
19	0.15	2.82	535	519.9	2	14.4	548.9
20	0.03	0.56	535	519.9	1	13.2	670.6
21	0.03	0.56	525	511.6	1	16.2	637.4
22	0.10	1.88	525	510.4	2	18.0	543.3
23	0.20	3.76	525	511.4	0	-	535.4
24	0.06	1.13	525	510.1	1	18.2	635.5
25	0.30	5.63	525	510.7	0	-	523.4
26	0.03	0.56	525	509.1	1	20.3	657.4
27	0.03	0.56	515	502.7	1	21.4	623.7
28	0.06	1.13	515	501.1	1	22.1	660.3
29	0.10	1.88	515	501.5	0	-	530.7
30	0.20	3.76	515	502.2	0	-	520.9

Table A.5: ASTM-E6559 autoignition shots: 1,2,4-Trimethylbenzene (TMB) (continued)

Shot	V_{inj} **(mL)**	**Global** ϕ	**Furnace Temp. (°C)**	**Flask Temp. (°C)**	**Ignition Mode**	τ_{ign} **(s)**	**Max Temp. (°C)**
31	0.03	0.56	515	500.9	1	22.5	591.0
32	0.02	0.38	515	501.2	1	24.2	596.8
33	0.01	0.19	515	501.2	0	-	506.4
34	0.03	0.56	515	500.7	1	22.0	663.0
35	0.03	0.56	510	496.6	1	27.0	610.3
36	0.03	0.56	510	495.6	1	23.7	730.6
37	0.03	0.56	505	492.3	1	30.3	603.6
38	0.06	1.13	505	491.8	1	27.3	633.1
39	0.10	1.88	505	491.3	0	-	519.3
40	0.08	1.50	505	491.3	0	-	517.7
41	0.03	0.56	500	487.3	1	38.6	560.7
42	0.06	1.13	500	485.7	2	35.2	530.8
43	0.05	0.94	500	486.4	1	40.0	614.6
44	0.03	0.56	500	485.3	0	-	505.3
45	0.03	0.56	498	485.2	1	40.4	692.6
46	0.05	0.94	498	484.6	1	36.0	586.3
47	0.02	0.38	498	484.3	0	-	496.1
48	0.06	1.13	498	484.0	2	42.1	528.8
49	0.04	0.75	498	483.8	1	42.6	627.6
50	0.03	0.56	495	480.8	1	49.1	682.7
51	0.06	1.13	495	481.6	2	42.9	527.7
52	0.04	0.75	495	481.5	1	48.4	680.3
53	0.03	0.56	490	475.6	0	-	490.1
54	0.05	0.94	490	475.2	0	-	498.5
55	0.03	0.56	492	477.8	0	-	494.4
56	0.05	0.94	492	476.9	1	54.9	583.3
57	0.06	1.13	492	476.7	0	-	505.4
58	0.04	0.75	492	476.7	0	-	498.0
59	0.03	0.56	494	479.3	1	51.4	662.7
60	0.05	0.94	494	479.1	2	52.8	511.1
61	0.03	0.56	498	478.1	0	-	497.8

Table A.5: ASTM-E6559 autoignition shots: 1,2,4-Trimethylbenzene (TMB) (continued)

Shot	V_{inj} **(mL)**	**Global** ϕ	**Furnace Temp. (°C)**	**Flask Temp. (°C)**	**Ignition Mode**	τ_{ign} **(s)**	**Max Temp. (°C)**
62	0.03	0.56	496	482.9	1	45.9	671.1
63	0.03	0.56	493	479.9	0	-	497.1
64	0.03	0.56	493	480.4	1	47.0	605.4
65	0.03	0.56	493	479.8	0	-	500.1
66	0.05	0.94	493	480.1	1	46.4	613.8
67	0.05	0.94	492	479.4	1	47.1	585.9
68	0.05	0.94	492	478.0	1	49.1	585.1
69	0.05	0.94	491	476.5	2	51.9	562.2
70	0.08	1.50	520	504.8	2	20.6	570.5

A.6 Trans-decalin

Table A.6: ASTM-E6559 autoignition shots: Trans-decalin

Shot	V_{inj} **(mL)**	**Global** ϕ	**Furnace Temp. (°C)**	**Flask Temp. (°C)**	**Ignition Mode**	τ_{ign} **(s)**	**Max Temp. (°C)**
1	0.10	2.02	290	266.3	2	25.2	290.6
2	0.20	4.03	290	269.7	2	21.1	295.9
3	0.30	6.05	290	269.9	2	18.6	289.1
4	0.05	1.01	290	270.4	1	21.6	334.3
5	0.04	0.81	290	271.6	1	20.6	325.6
6	0.08	1.61	290	271.0	1	20.0	314.6
7	0.40	8.07	290	271.9	2	14.3	299.6
8	0.06	1.21	280	263.8	1	32.1	342.4
9	0.02	0.40	280	260.8	4	63.1	276.4
10	0.03	0.61	280	257.3	4	82.1	268.9
11	0.10	2.02	280	260.2	1	38.8	311.5
12	0.20	4.03	280	260.7	2	34.8	296.1
13	0.04	0.81	280	259.8	4	59.6	275.8
14	0.05	1.01	280	261.2	4	-	271.9
15	0.08	1.61	280	262.7	1	34.9	316.6
16	0.40	8.07	280	262.3	2	23.7	290.4
17	0.10	2.02	270	252.8	2	74.5	292.0
18	0.20	4.03	270	252.8	2	58.9	273.7
19	0.08	1.61	270	250.6	1	110.6	328.1
20	0.40	8.07	270	250.7	4	-	266.1
21	0.30	6.05	270	250.7	4	-	264.4
22	0.06	1.21	270	252.7	1	99.4	348.4
23	0.04	0.81	270	253.1	4	114.3	272.4
24	0.25	5.04	270	251.9	2	58.3	267.0
25	0.03	0.61	270	253.7	0	-	259.1
26	0.20	4.03	260	236.6	0	-	247.1
27	0.10	2.02	260	243.0	2	237.5	279.9
28	0.20	4.03	260	241.5	2	182.4	274.8
29	0.10	2.02	260	241.9	0	-	251.3
30	0.06	1.21	260	240.9	0	-	246.2

Table A.6: ASTM-E6559 autoignition shots: Trans-decalin (continued)

Shot	V_{inj} **(mL)**	**Global** ϕ	**Furnace Temp. (°C)**	**Flask Temp. (°C)**	**Ignition Mode**	τ_{ign} **(s)**	**Max Temp. (°C)**
31	0.15	3.03	260	242.7	2	194.2	279.7
32	0.25	5.04	260	241.3	2	167.6	273.1
33	0.30	6.05	260	240.7	2	165.6	270.0
34	0.40	8.07	260	240.8	2	152.8	264.1
35	0.30	6.05	250	235.9	0	-	244.4
36	0.40	8.07	255	234.9	0	-	245.8
37	0.04	0.81	255	235.7	0	-	237.9
38	0.25	5.04	255	236.4	0	-	246.4
39	0.15	3.03	258	239.7	0	-	247.4
40	0.20	4.03	258	239.6	3	278.8	265.6
41	0.25	5.04	258	239.5	3	231.7	267.2
42	0.30	6.05	270	250.7	2	59.5	265.8
43	0.40	8.07	270	250.8	2	62.6	266.9
44	0.10	2.02	290	266.2	1	22.7	322.2
45	0.05	1.01	280	259.9	4	-	265.1

A.7 Toluene

Table A.7: ASTM-E6559 autoignition shots: Toluene

Shot	V_{inj} **(mL)**	**Global** ϕ	**Furnace Temp. (°C)**	**Flask Temp. (°C)**	**Ignition Mode**	τ_{ign} **(s)**	**Max Temp. (°C)**
1	0.10	1.82	550	522.7	2	93.2	543.9
2	0.20	3.64	550	522.5	0	-	535.4
3	0.30	5.46	550	522.6	0	-	529.0
4	0.06	1.09	550	522.6	2	85.8	553.5
5	0.08	1.45	550	522.7	2	84.8	543.4
6	0.12	2.18	550	524.2	0	-	541.6
7	0.04	0.73	550	523.8	1	91.4	595.5
8	0.02	0.36	550	524.3	0	-	535.9
9	0.05	0.91	550	522.6	1	86.7	563.4
10	0.07	1.27	550	522.2	2	85.2	544.3
11	0.10	1.82	565	537.4	2	48.3	568.8
12	0.20	3.64	565	537.7	0	-	550.8
13	0.06	1.09	565	538.7	2	46.0	573.1
14	0.04	0.73	565	539.2	1	48.1	591.5
15	0.08	1.45	565	538.6	2	46.9	581.4
16	0.30	5.46	580	557.2	0	-	566.8
17	0.20	3.64	580	556.2	0	-	570.9
18	0.10	1.82	580	556.7	2	27.5	590.1
19	0.06	1.09	580	556.3	2	26.4	585.5
20	0.10	1.82	540	517.3	0	-	534.6
21	0.06	1.09	540	516.8	2	85.7	537.8
22	0.04	0.73	540	516.5	1	89.3	589.6
23	0.08	1.45	540	516.7	2	80.0	535.7
24	0.04	0.73	530	507.2	0	-	519.2
25	0.06	1.09	530	509.9	2	104.1	526.4
26	0.08	1.45	530	505.9	0	-	521.3
27	0.06	1.09	535	511.0	2	98.8	527.9
28	0.04	0.73	535	511.9	0	-	525.6
29	0.08	1.45	535	511.6	0	-	528.0
30	0.05	0.91	535	511.7	2	97.5	533.2

Table A.7: ASTM-E6559 autoignition shots: Toluene (continued)

Shot	V_{inj} **(mL)**	**Global** ϕ	**Furnace Temp.** **(°C)**	**Flask Temp.** **(°C)**	**Ignition Mode**	τ_{ign} **(s)**	**Max Temp.** **(°C)**
31	0.07	1.27	535	513.3	2	91.3	531.8
32	0.03	0.55	535	513.6	0	-	526.9
33	0.04	0.73	535	513.2	1	98.0	559.3
34	0.06	1.09	530	505.9	0	-	520.8
35	0.05	0.91	530	505.4	0	-	519.6
36	0.07	1.27	530	505.6	0	-	520.3
37	0.06	1.09	534	508.2	2	98.9	526.5
38	0.05	0.91	533	509.8	2	101.4	526.2
39	0.07	1.27	533	510.4	2	95.0	526.9
40	0.04	0.73	533	508.8	0	-	522.9

A.8 Jet A (POSF-4658)

Table A.8: ASTM-E6559 autoignition shots: Jet A (POSF-4658)

Shot	V_{inj} **(mL)**	**Global** ϕ	**Furnace Temp. (°C)**	**Flask Temp. (°C)**	**Ignition Mode**	τ_{ign} **(s)**	**Max Temp. (°C)**
1	0.10	1.84	250	231.5	0	-	239.2
2	0.30	5.52	250	231.7	3	124.4	263.9
3	0.20	3.68	250	232.2	3	195.5	273.1
4	0.06	1.10	250	231.8	0	-	237.6
5	0.40	7.36	250	232.6	3	160.5	256.3
6	0.10	1.84	265	246.8	1	47.1	315.6
7	0.30	5.52	265	245.7	1	50.0	278.1
8	0.06	1.10	265	246.4	4	60.1	254.3
9	0.20	3.68	265	245.7	1	55.1	309.3
10	0.40	7.36	265	245.6	1	47.3	276.8
11	0.08	1.47	265	245.4	1	56.4	329.9
12	0.06	1.10	275	254.5	1	30.4	333.2
13	0.30	5.52	275	256.7	1	23.0	314.3
14	0.20	3.68	275	253.7	1	28.7	300.5
15	0.08	1.47	275	255.9	1	29.5	334.0
16	0.10	1.84	240	223.7	0	-	229.3
17	0.30	5.52	240	224.5	0	-	234.2
18	0.20	3.68	240	224.7	0	-	230.9
19	0.40	7.36	240	224.7	0	-	232.8
20	0.06	1.10	240	225.4	0	-	228.3
21	0.30	5.52	245	229.0	3	239.2	261.8
22	0.40	7.36	245	229.4	3	198.7	255.3
23	0.15	2.76	245	232.2	0	-	243.1
24	0.04	0.74	245	231.7	0	-	234.9
25	0.30	5.52	255	239.3	1	87.1	269.9
26	0.20	3.68	255	239.3	1	76.7	271.7
27	0.40	7.36	255	239.3	3	71.8	263.6
28	0.10	1.84	255	235.8	1	131.7	315.4
29	0.06	1.10	255	235.3	0	-	243.8
30	0.10	1.84	270	248.5	1	42.8	323.1

Table A.8: ASTM-E6559 autoignition shots: Jet A (POSF-4658) (continued)

Shot	V_{inj} **(mL)**	**Global** ϕ	**Furnace Temp.** (°C)	**Flask Temp.** (°C)	**Ignition Mode**	τ_{ign} **(s)**	**Max Temp.** (°C)
31	0.40	7.36	270	250.0	1	34.2	-
32	0.06	1.10	270	252.2	1	39.7	331.5
33	0.30	5.52	270	252.3	1	30.6	309.1
34	0.40	7.36	270	252.3	1	36.2	282.4
35	0.20	3.68	270	251.3	1	37.7	293.4
36	0.04	0.74	270	252.4	4	40.8	272.8
37	0.15	2.76	270	251.9	1	38.6	296.2
38	0.15	2.76	260	246.9	1	52.2	317.3
39	0.30	5.52	260	246.2	1	56.0	283.2
40	0.06	1.10	260	244.5	0	-	254.0
41	0.08	1.47	260	245.1	1	67.0	340.1
42	0.40	7.36	260	244.2	1	63.9	279.4
43	0.20	3.68	260	245.6	1	60.6	297.3
44	0.25	4.60	260	243.9	1	65.4	284.7
45	0.04	0.74	260	245.8	0	-	254.3
46	0.10	1.84	255	240.7	1	88.3	283.3
47	0.06	1.10	255	241.7	0	-	253.3
48	0.15	2.76	255	239.8	1	94.4	325.6
49	0.08	1.47	255	239.3	1	116.9	359.2
50	0.25	4.60	255	239.0	1	86.3	303.5
51	0.04	0.74	252	237.8	0	-	241.7
52	0.10	1.84	252	238.7	1	122.6	371.7
53	0.15	2.76	250	237.6	1	106.3	344.1
54	0.30	5.52	247	234.2	1	130.9	300.1
55	0.08	1.47	247	233.4	0	-	239.3
56	0.40	7.36	248	235.1	3	130.1	270.9
57	0.20	3.68	248	235.3	1	139.1	323.6
58	0.25	4.60	248	234.1	1	149.1	309.2
59	0.10	1.84	248	233.3	0	-	244.2
60	0.25	4.60	242	231.2	3	213.3	300.7
61	0.20	3.68	238	225.9	0	-	233.3

Table A.8: ASTM-E6559 autoignition shots: Jet A (POSF-4658) (continued)

Shot	V_{inj} **(mL)**	**Global** ϕ	**Furnace Temp.** **(°C)**	**Flask Temp.** **(°C)**	**Ignition Mode**	τ_{ign} **(s)**	**Max Temp.** **(°C)**
62	0.10	1.84	245	231.4	0	-	237.8
63	0.10	1.84	250	236.2	1	158.8	376.9
64	0.10	1.84	247	233.9	0	-	243.3
65	0.10	1.84	248	234.6	0	-	243.7
66	0.10	1.84	249	236.2	0	-	248.7
67	0.10	1.84	250	235.7	0	-	247.1
68	0.10	1.84	252	238.6	1	118.3	386.3
69	0.10	1.84	248	234.9	0	-	245.2
70	0.10	1.84	251	237.1	0	-	249.6
71	0.10	1.84	253	239.0	1	106.0	332.1
72	0.10	1.84	249	236.2	1	159.7	385.3
73	0.10	1.84	250	236.7	1	143.1	392.8

A.9 Jet A (POSF-10325)

Table A.9: ASTM-E6559 autoignition shots: Jet A (POSF-10325)

Shot	V_{inj} **(mL)**	**Global** ϕ	**Furnace Temp. (°C)**	**Flask Temp. (°C)**	**Ignition Mode**	τ_{ign} **(s)**	**Max Temp. (°C)**
1	0.10	1.83	265	245.0	1	56.9	300.8
2	0.06	1.10	265	244.8	4	58.8	256.7
3	0.20	3.66	265	246.4	1	46.4	292.8
4	0.40	7.33	265	247.6	1	37.3	282.1
5	0.30	5.49	265	246.3	1	42.2	283.7
6	0.08	1.47	265	246.9	1	41.1	327.2
7	0.50	9.16	265	246.3	1	41.1	280.3
8	0.10	1.83	250	229.2	0	-	238.4
9	0.30	5.49	250	230.2	3	134.4	290.4
10	0.10	1.83	250	234.8	1	106.4	336.4
11	0.20	3.66	250	233.4	1	97.5	333.7
12	0.08	1.47	250	233.8	0	-	248.7
13	0.10	1.83	240	225.6	0	-	231.8
14	0.30	5.49	240	225.9	3	248.1	272.6
15	0.20	3.66	240	225.9	0	-	236.7
16	0.40	7.33	240	226.7	3	240.7	272.1
17	0.50	9.16	240	226.5	3	225.4	274.8
18	0.40	7.33	232	218.8	0	-	229.7
19	0.50	9.16	232	219.0	0	-	228.4
20	0.30	5.49	235	221.1	0	-	229.2
21	0.50	9.16	238	223.9	0	-	237.9
22	0.40	7.33	238	224.8	0	-	240.6
23	0.50	9.16	239	225.7	3	244.8	272.4
24	0.40	7.33	239	225.3	3	219.7	277.2
25	0.20	3.66	245	229.9	3	145.4	301.1
26	0.15	2.75	245	231.0	3	154.6	305.1
27	0.08	1.47	255	236.3	1	117.2	375.2
28	0.10	1.83	255	237.7	1	80.0	407.5
29	0.15	2.75	255	237.4	1	65.1	332.4
30	0.40	7.33	255	239.0	3	67.3	284.6

Table A.9: ASTM-E6559 autoignition shots: Jet A (POSF-10325) (continued)

Shot	V_{inj} **(mL)**	**Global** ϕ	**Furnace Temp. (°C)**	**Flask Temp. (°C)**	**Ignition Mode**	τ_{ign} **(s)**	**Max Temp. (°C)**
31	0.50	9.16	255	239.2	3	56.3	283.1
32	0.40	7.33	260	245.1	1	38.1	290.7
33	0.50	9.16	259	244.1	1	40.1	286.7
34	0.06	1.10	259	243.7	4	49.9	273.7
35	0.30	5.49	259	243.4	1	36.1	292.8
36	0.04	0.73	259	244.4	4	55.3	260.4
37	0.06	1.10	248	233.4	0	-	241.6
38	0.30	5.49	249	233.0	1	105.0	287.1
39	0.10	1.83	249	234.2	1	118.1	388.7
40	0.10	1.83	245	232.3	1	157.8	365.7
41	0.12	2.20	245	232.2	1	143.7	350.9
42	0.12	2.20	240	229.2	0	-	240.6
43	0.15	2.75	240	227.2	0	-	238.6
44	0.04	0.73	250	248.9	4	54.4	259.3
45	0.03	0.55	250	245.6	4	80.0	255.6
46	0.06	1.10	250	240.5	3	74.5	284.1
47	0.04	0.73	250	238.8	0	-	245.6

A.10 Aachen Surrogate

Table A.10: ASTM-E6559 autoignition shots: Aachen Surrogate

Shot	V_{inj} **(mL)**	**Global** ϕ	**Furnace Temp. (°C)**	**Flask Temp. (°C)**	**Ignition Mode**	τ_{ign} **(s)**	**Max Temp. (°C)**
1	0.10	1.74	240	226.4	0	-	237.6
2	0.10	1.74	240	228.1	0	-	241.7
3	0.20	3.49	240	229.5	1	82.3	438.1
4	0.30	5.23	240	229.4	1	77.8	346.5
5	0.40	6.98	240	228.8	3	81.8	329.7
6	0.50	8.72	240	228.6	3	80.8	316.5
7	0.10	1.74	255	241.3	1	36.2	428.3
8	0.05	0.87	255	239.9	3	48.0	370.8
9	0.20	3.49	255	241.6	1	33.8	366.1
10	0.30	5.23	255	242.1	1	31.9	342.7
11	0.30	5.23	230	223.8	3	147.0	334.3
12	0.20	3.49	230	222.4	3	167.3	287.8
13	0.40	6.98	230	220.2	3	184.0	307.5
14	0.50	8.72	230	221.4	3	161.7	303.6
15	0.35	6.11	230	220.9	3	167.3	326.2
16	0.25	4.36	230	220.5	3	182.0	315.0
17	0.30	5.23	225	218.3	0	-	234.0
18	0.35	6.11	225	217.6	0	-	231.4
19	0.20	3.49	225	217.1	0	-	226.2
20	0.30	5.23	228	219.6	3	204.0	303.7
21	0.20	3.49	228	220.1	0	-	234.4
22	0.40	6.98	225	219.0	3	200.1	323.1
23	0.30	5.23	225	218.7	0	-	235.3
24	0.35	6.11	225	218.8	0	-	234.4
25	0.50	8.72	225	219.0	0	-	236.6
26	0.40	6.98	225	218.9	0	-	233.9
27	0.32	5.58	225	219.9	3	173.5	334.8
28	0.30	5.23	223	218.1	0	-	232.8
29	0.35	6.11	223	218.2	0	-	233.8
30	0.33	5.76	223	218.4	0	-	231.5

Table A.10: ASTM-E6559 autoignition shots: Aachen Surrogate (continued)

Shot	V_{inj} **(mL)**	**Global** ϕ	**Furnace Temp. (°C)**	**Flask Temp. (°C)**	**Ignition Mode**	τ_{ign} **(s)**	**Max Temp. (°C)**
31	0.38	6.63	224	219.1	0	-	233.8
32	0.15	2.62	225	221.8	0	-	230.8
33	0.05	0.87	230	223.7	0	-	228.4

A.11 JI Surrogate

Table A.11: ASTM-E6559 autoignition shots: JI Surrogate

Shot	V_{inj} **(mL)**	**Global** ϕ	**Furnace Temp. (°C)**	**Flask Temp. (°C)**	**Ignition Mode**	τ_{ign} **(s)**	**Max Temp. (°C)**
1	0.10	1.81	250	233.2	0	-	240.8
2	0.30	5.43	250	234.8	1	142.7	267.5
3	0.20	3.62	250	234.3	3	162.4	265.7
4	0.40	7.25	250	235.4	3	141.5	279.2
5	0.06	1.09	250	236.0	0	-	241.1
6	0.10	1.81	260	243.6	4	83.1	254.7
7	0.40	7.25	260	244.3	3	68.2	284.4
8	0.20	3.62	260	244.7	1	64.2	303.9
9	0.30	5.43	260	244.1	1	69.2	284.7
10	0.06	1.09	260	246.4	4	119.5	254.3
11	0.10	1.81	270	256.1	1	32.5	328.1
12	0.40	7.25	270	255.0	1	35.7	295.0
13	0.06	1.09	270	255.1	4	42.1	265.1
14	0.20	3.62	270	255.1	1	26.5	303.4
15	0.10	1.81	255	243.2	4	82.1	253.4
16	0.20	3.62	255	241.5	1	94.7	305.4
17	0.30	5.43	255	241.2	3	70.5	297.2
18	0.06	1.09	255	242.1	0	-	247.9
19	0.15	2.72	255	241.9	1	79.8	272.2
20	0.40	7.25	255	241.4	3	83.2	291.2
21	0.20	3.62	252	236.1	1	118.7	270.8
22	0.30	5.43	252	236.3	3	103.2	274.2
23	0.40	7.25	252	237.8	3	111.3	286.5
24	0.10	1.81	252	239.3	0	-	243.9
25	0.15	2.72	252	236.9	1	126.4	273.9
26	0.08	1.45	252	238.2	0	-	246.6
27	0.25	4.53	252	238.4	1	102.8	281.7
28	0.35	6.34	252	238.7	3	110.9	280.3
29	0.20	3.62	248	234.2	3	158.2	274.3
30	0.15	2.72	248	233.9	3	189.7	279.7

Table A.11: ASTM-E6559 autoignition shots: JI Surrogate (continued)

Shot	V_{inj} **(mL)**	**Global** ϕ	**Furnace Temp. (°C)**	**Flask Temp. (°C)**	**Ignition Mode**	τ_{ign} **(s)**	**Max Temp. (°C)**
31	0.25	4.53	248	236.2	1	124.8	270.7
32	0.10	1.81	245	233.3	0	-	240.4
33	0.35	6.34	245	233.7	3	149.3	267.2
34	0.20	3.62	242	230.4	0	-	237.3
35	0.30	5.43	242	229.8	0	-	240.6
36	0.25	4.53	242	228.7	0	-	241.6
37	0.40	7.25	242	229.5	0	-	243.1
38	0.25	4.53	243	231.7	3	184.6	264.9
39	0.15	2.72	243	230.6	0	-	235.8
40	0.12	2.17	243	231.0	0	-	235.9
41	0.35	6.34	243	229.8	3	240.8	263.9
42	0.20	3.62	240	228.3	0	-	238.1
43	0.15	2.72	240	228.3	0	-	233.4
44	0.30	5.43	240	228.3	3	231.8	265.1
45	0.35	6.34	237	226.0	0	-	238.7
46	0.30	5.43	237	225.9	0	-	232.9
47	0.25	4.53	237	226.1	0	-	238.6
48	0.20	3.62	237	224.7	0	-	231.3
49	0.40	7.25	237	225.3	0	-	237.3
50	0.30	5.43	236	223.6	0	-	231.1
51	0.35	6.34	236	224.5	0	-	230.4
52	0.08	1.45	260	243.6	4	-	251.8
53	0.04	0.72	260	244.4	0	-	250.6
54	0.35	6.34	260	244.0	1	65.1	282.0
55	0.12	2.17	260	244.8	4	92.3	259.0
56	0.40	7.25	260	245.3	1	62.4	282.2
57	0.50	9.06	260	245.8	3	55.2	287.4
58	0.06	1.09	260	243.6	4	-	255.9
59	0.04	0.72	265	249.7	4	-	258.1
60	0.08	1.45	265	249.3	4	58.2	259.8
61	0.06	1.09	265	249.8	4	55.2	257.0

Table A.11: ASTM-E6559 autoignition shots: JI Surrogate (continued)

Shot	V_{inj} **(mL)**	**Global** ϕ	**Furnace Temp. (°C)**	**Flask Temp. (°C)**	**Ignition Mode**	τ_{ign} **(s)**	**Max Temp. (°C)**
62	0.50	9.06	265	249.2	1	53.8	290.0
63	0.12	2.17	265	249.1	1	47.1	313.0
64	0.30	5.43	265	248.7	1	42.5	291.9
65	0.12	2.17	255	241.9	4	78.9	266.3
66	0.10	1.81	255	240.9	4	90.8	253.7
67	0.30	5.43	255	240.0	1	90.5	287.7
68	0.50	9.06	255	239.8	3	98.3	286.9
69	0.50	9.06	245	229.8	3	191.2	257.9
70	0.40	7.25	245	231.2	3	150.8	271.7
71	0.30	5.43	245	231.4	3	156.2	261.4
72	0.40	7.25	242	228.6	3	191.4	249.7
73	0.50	9.06	240	227.0	0	-	239.1

Appendix B

ASTM-E659: EXAMPLE TEMPERATURE TRACES BY FUEL

B.1 n-Hexane

B.1.1 Ignition Modes

(a)

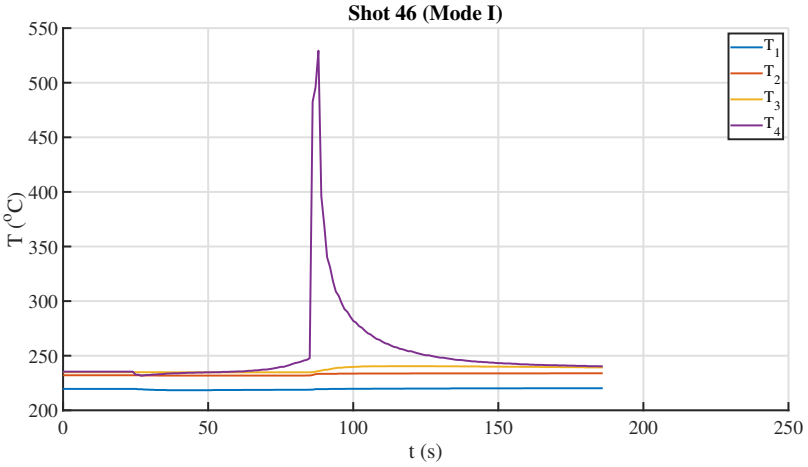

(b)

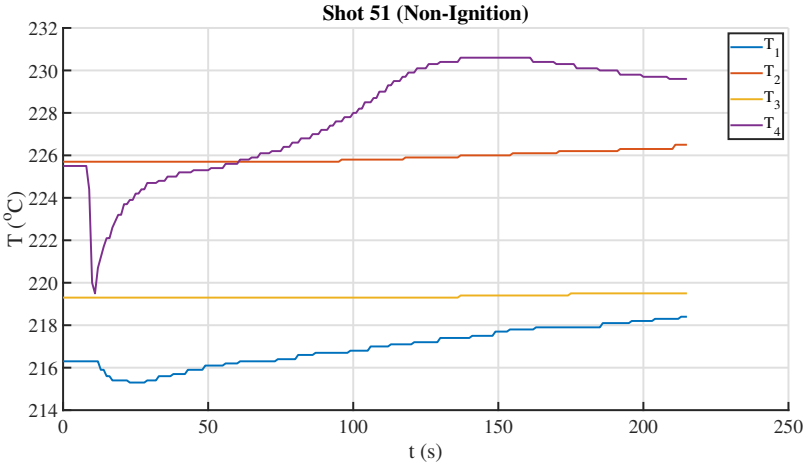

Figure B.1: Representative temperature traces for n-Hexane ignition modes. (a) Mode I Ignition and (b) Non-Ignition

B.1.2 Temperature traces by V_{inj}

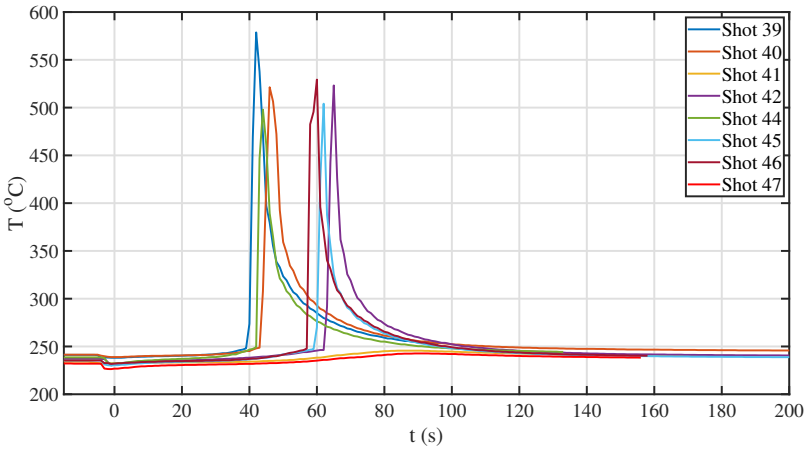

Figure B.2: Collection of temperature traces for n-Hexane shots with V_{inj} = 0.1 mL (Global ϕ = 1.56)

B.2 n-Decane

B.2.1 Ignition Modes

(a)

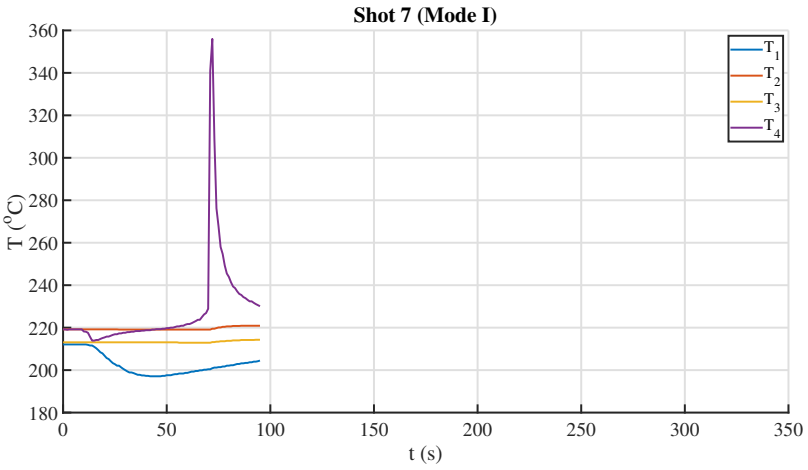

(b)

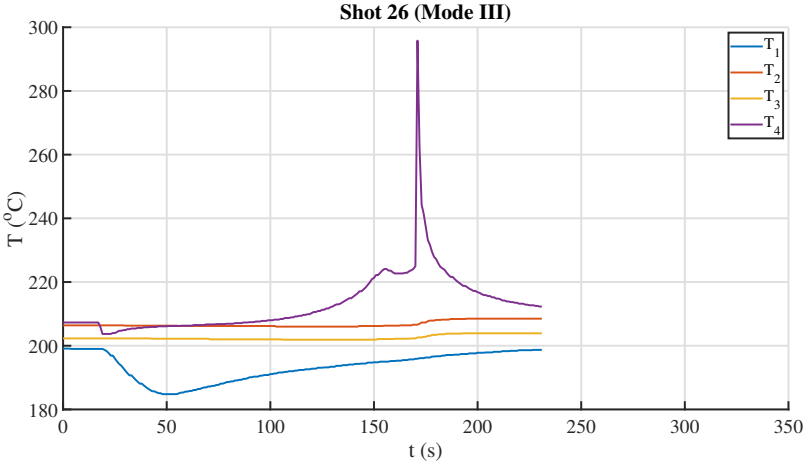

(c)

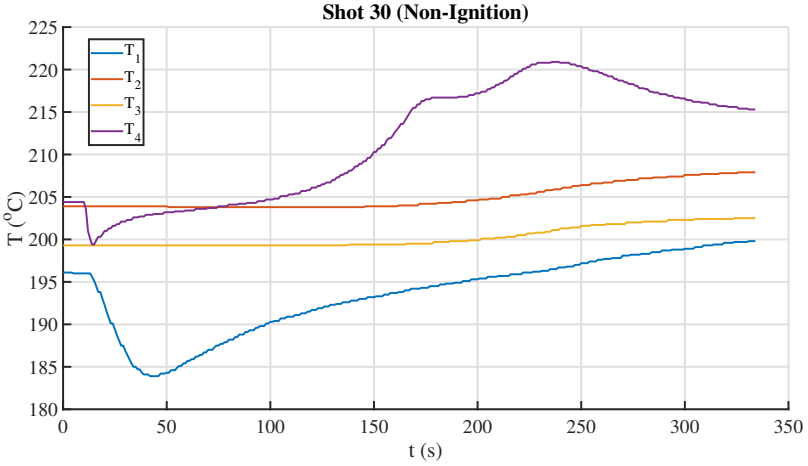

Figure B.3: Representative temperature traces for n-Decane ignition modes. (a) Mode I Ignition (b) Mode III Ignition and (c) Non-Ignition

B.2.2 Temperature traces by V_{inj}

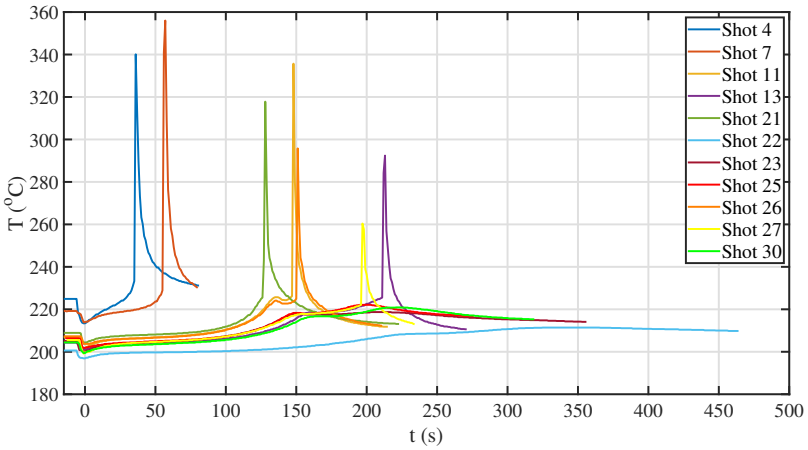

Figure B.4: Collection of temperature traces for n-Decane shots with V_{inj} = 0.3 mL (Global ϕ = 5.12)

B.3 n-Dodecane

B.3.1 Ignition Modes

(a)

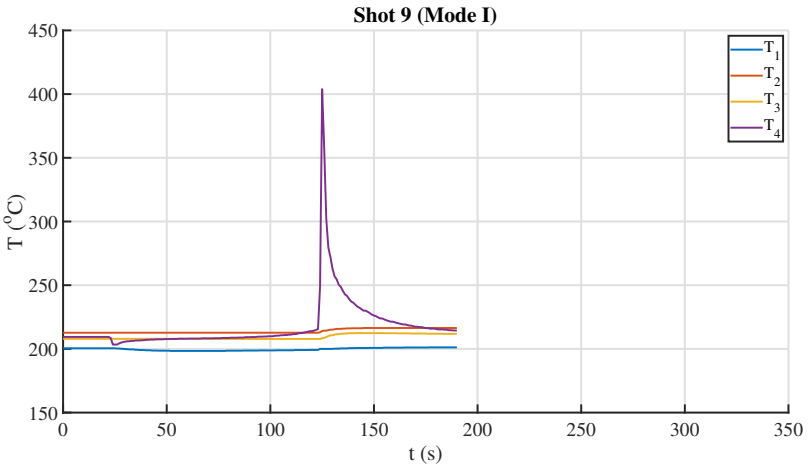

(b)

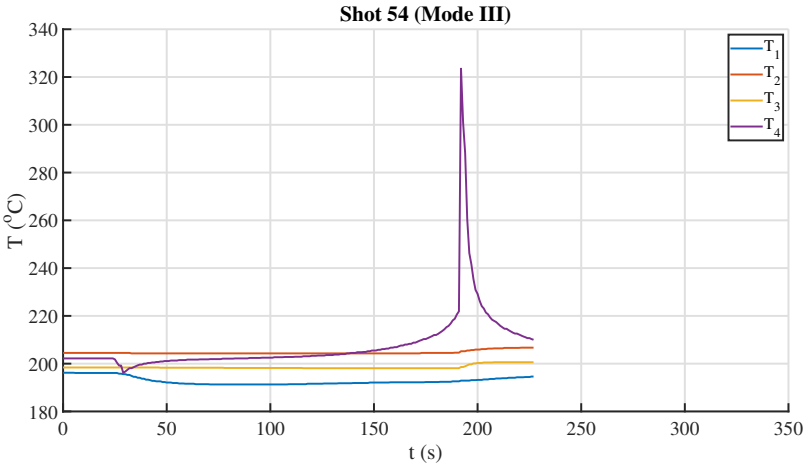

(c)

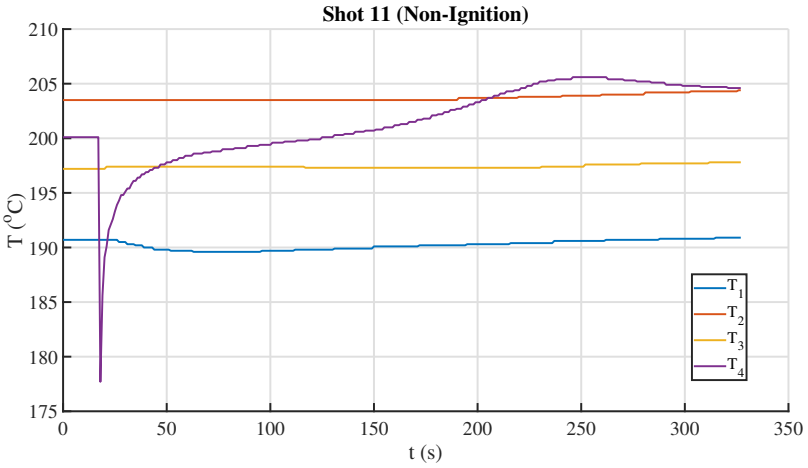

Figure B.5: Representative temperature traces for n-Dodecane ignition modes. (a) Mode I Ignition (b) Mode III Ignition and (c) Non-Ignition

B.3.2 Temperature traces by V_{inj}

(a)

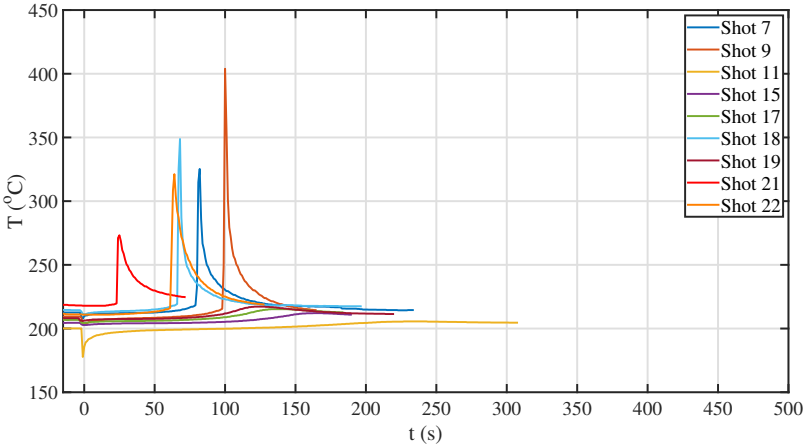

(b)

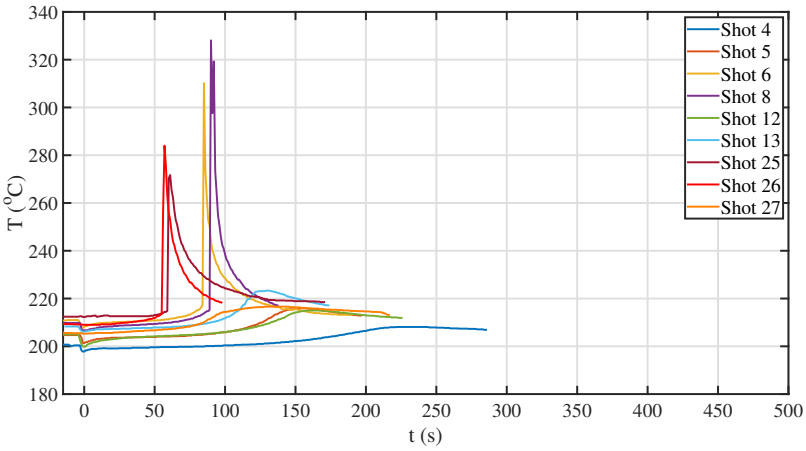

(c)

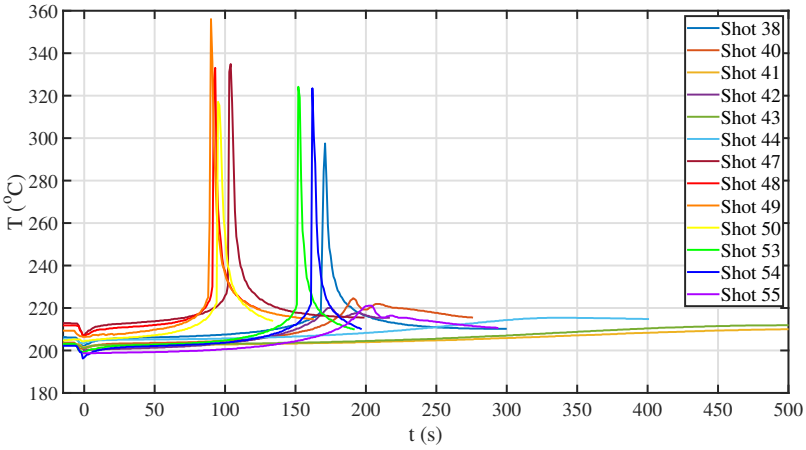

Figure B.6: Collection of temperature traces for n-Dodecane shots with (a) V_{inj} = 0.08 mL (Global ϕ = 1.40) (b) V_{inj} = 0.1 mL (Global ϕ = 1.75) (c) V_{inj} = 0.3 mL (Global ϕ = 5.24)

B.4 Isocetane

B.4.1 Ignition Modes

(a)

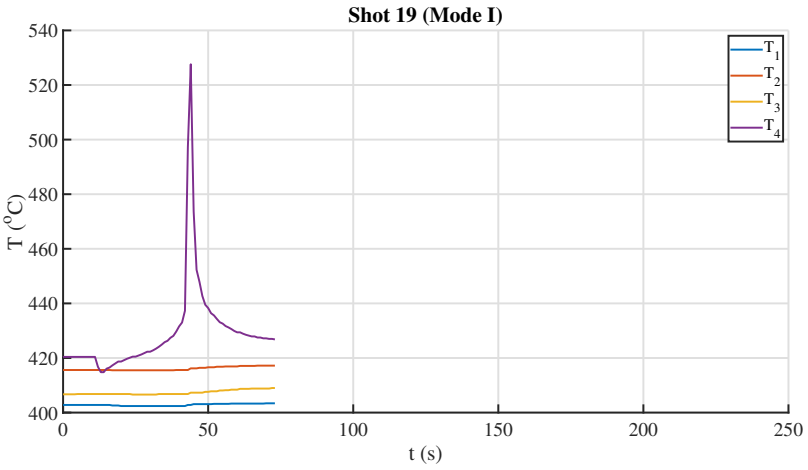

(b)

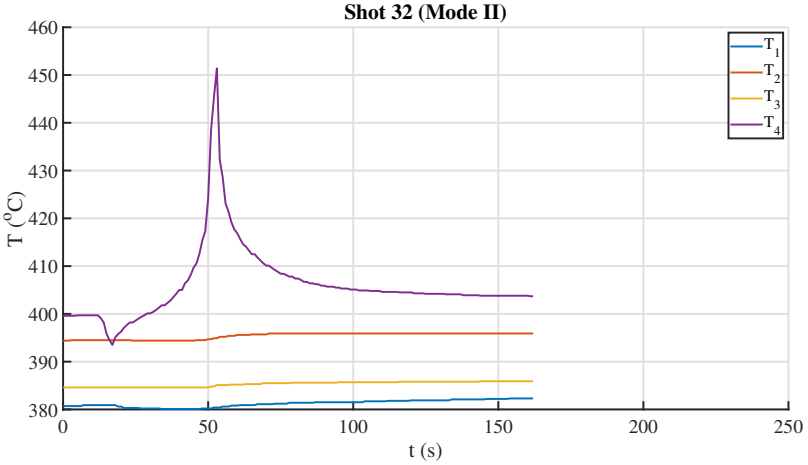

(c)

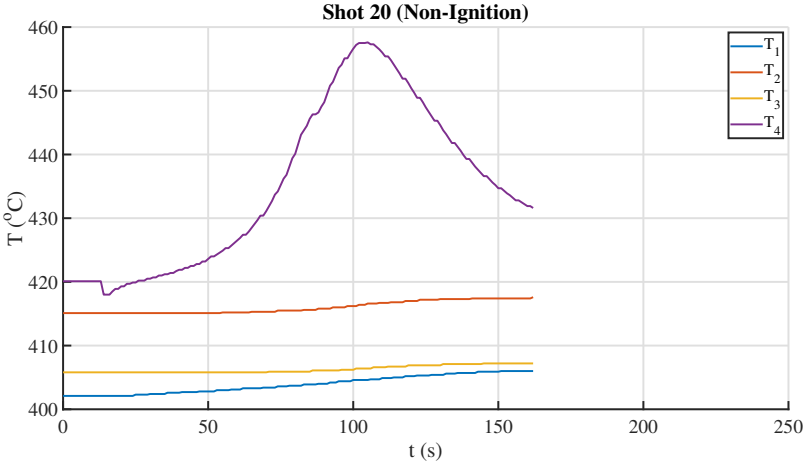

Figure B.7: Representative temperature traces for Isocetane ignition modes. (a) Mode I Ignition (b) Mode II Ignition and (c) Non-Ignition

B.4.2 Temperature traces by V_{inj}

(a)

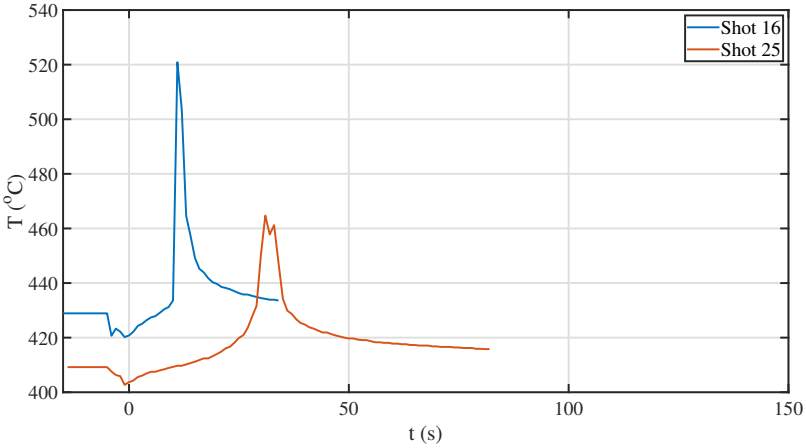

(b)

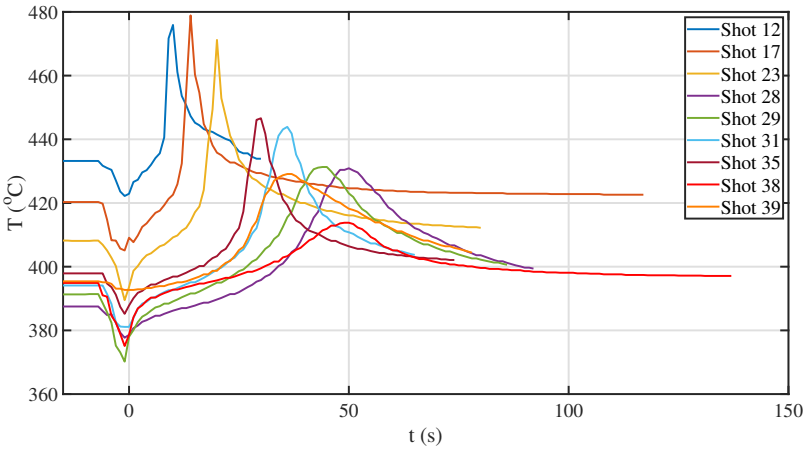

Figure B.8: Temperature profiles for Isocetane for (a) V_{inj} = 0.15 mL (Global ϕ = 2.76) and (b) V_{inj} = 0.3 mL (Global ϕ = 5.52)

B.5 1,2,4-Trimethylbenzene (TMB)

B.5.1 Ignition Modes

(a)

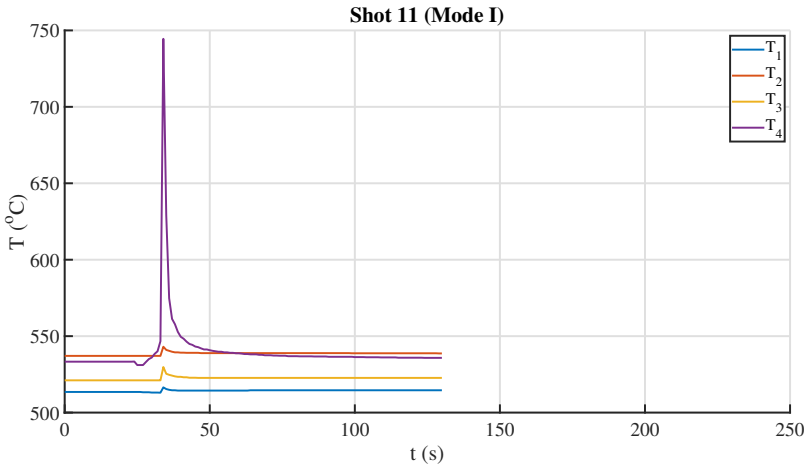

(b)

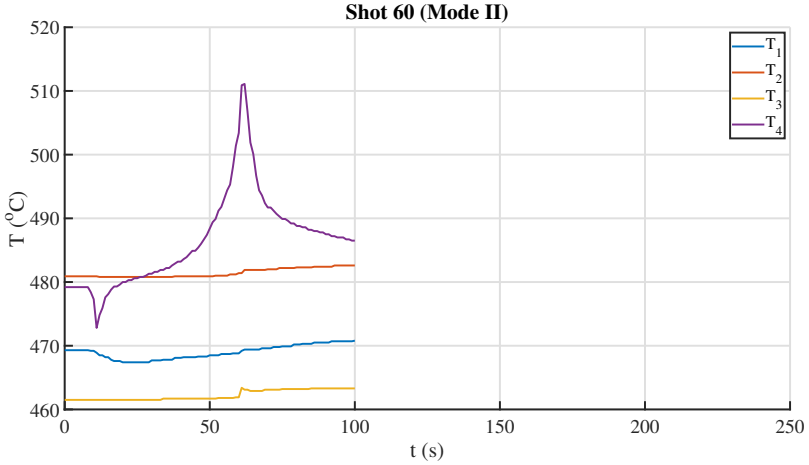

(c)

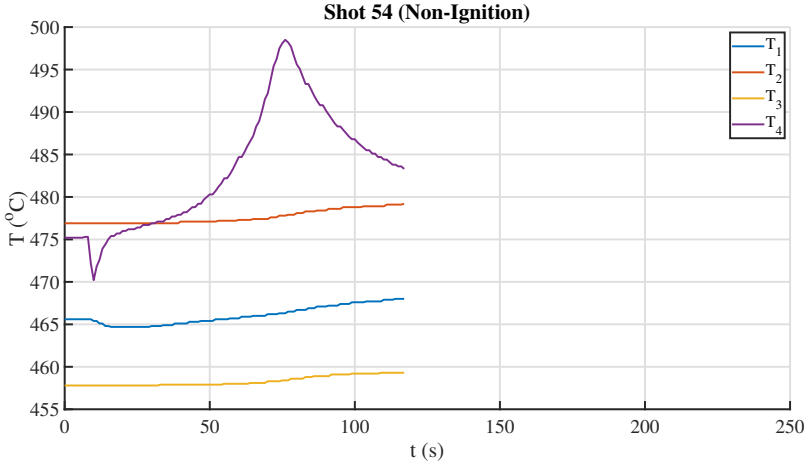

Figure B.9: Representative temperature traces for 1,2,4-Trimethylbenzene (TMB) ignition modes. (a) Mode I Ignition (b) Mode II Ignition and (c) Non-Ignition

B.5.2 Temperature traces by V_{inj}

(a)

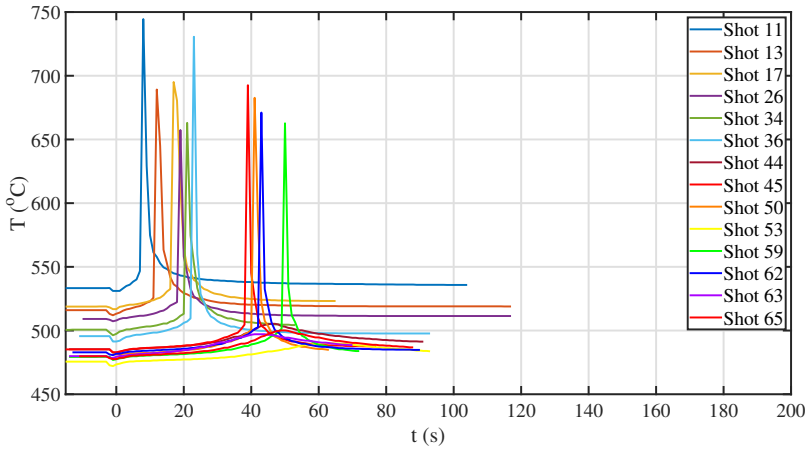

(b)

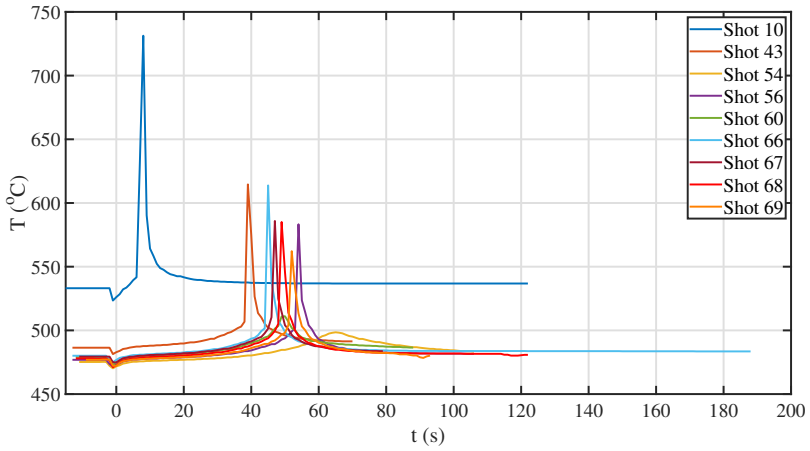

(c)

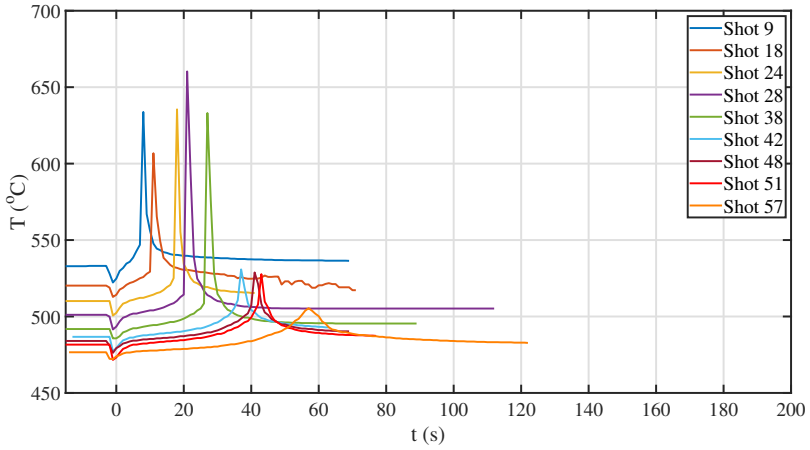

(d)

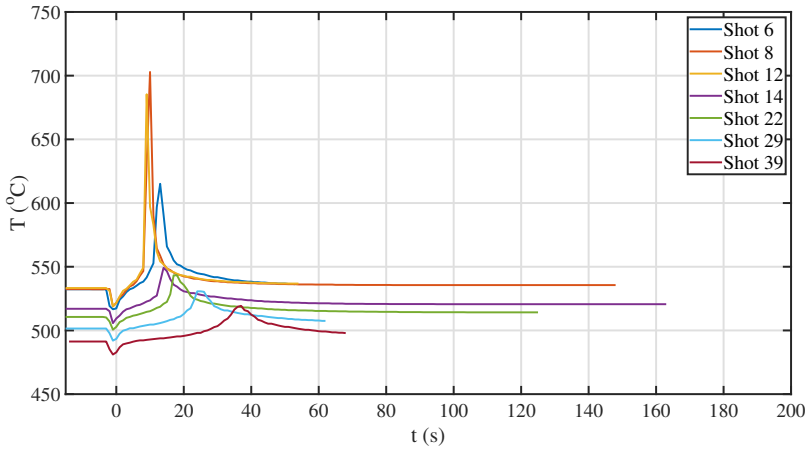

Figure B.10: Collection of temperature traces for 1,2,4-Trimethylbenzene (TMB) shots with (a) V_{inj} = 0.03 mL (Global ϕ = 0.56) ; (b) V_{inj} = 0.05 mL = 0.05 mL (Global ϕ = 0.94) ; (c) V_{inj} = 0.06 mL (Global ϕ = 1.13) and (d) V_{inj} = 0.1 mL (Global ϕ = 1.88)

B.6 Trans-decalin

B.6.1 Ignition Modes

(a)

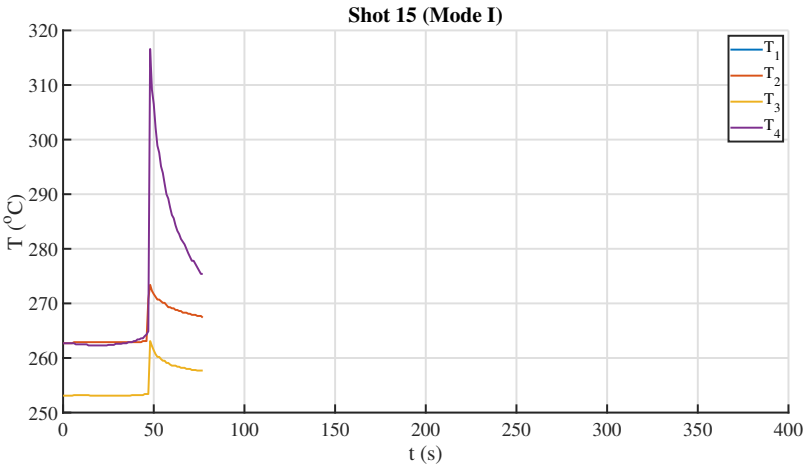

(b)

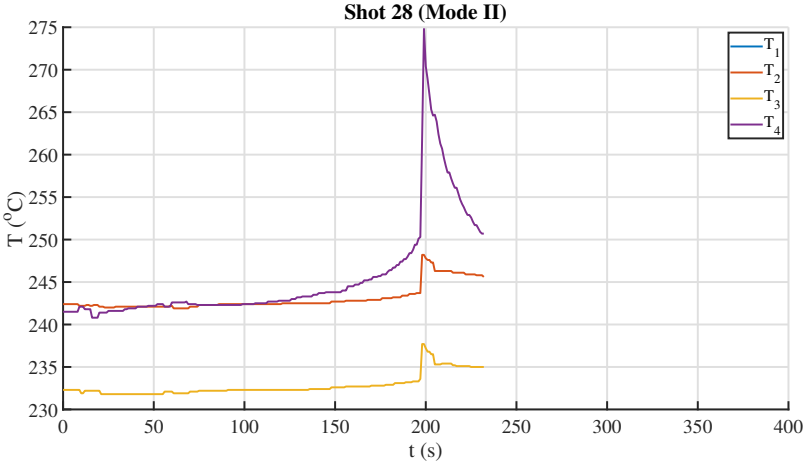

(c)

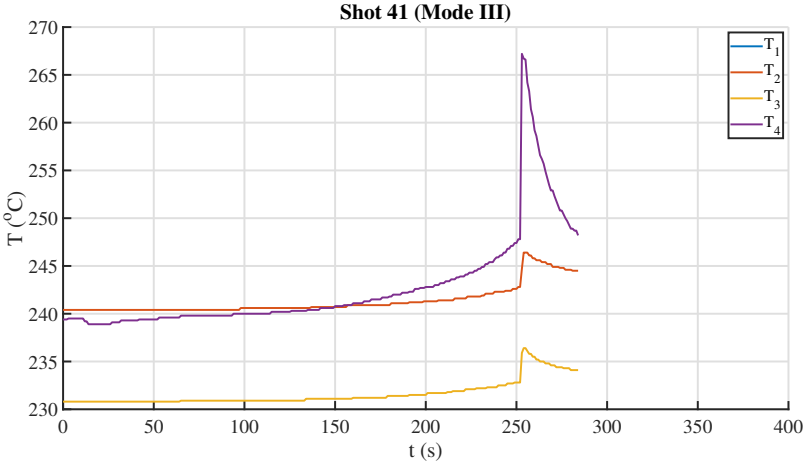

(d)

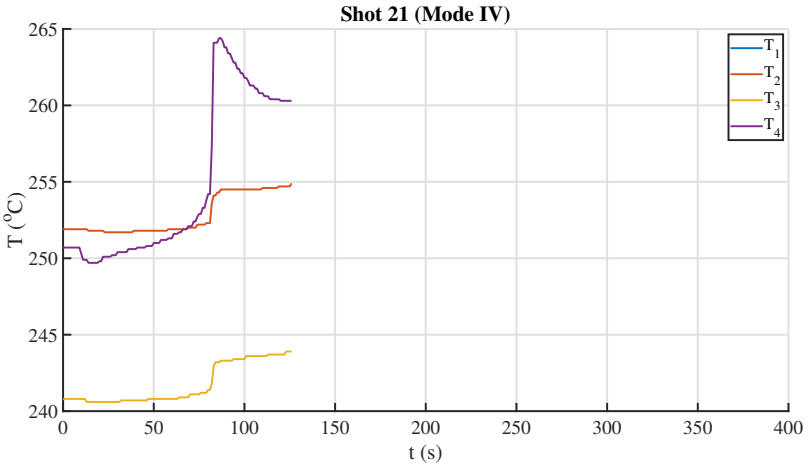

(e)

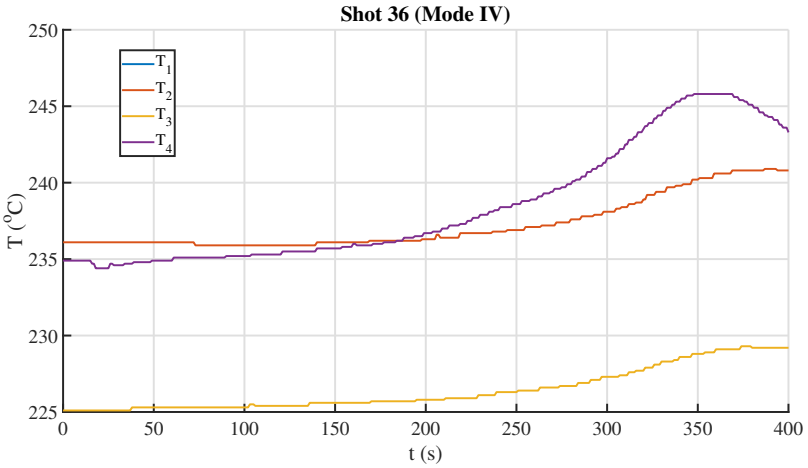

Figure B.11: Representative temperature traces for Trans-decalin ignition modes. (a) Mode I Ignition (b) Mode II Ignition (c) Mode III Ignition (d) Mode IV Ignition and (e) Non-Ignition[1]

[1]Note the extended timescale for these plots (400s) as compared to other single component fuels (250s).

B.6.2 Temperature traces by V_{inj}

(a)

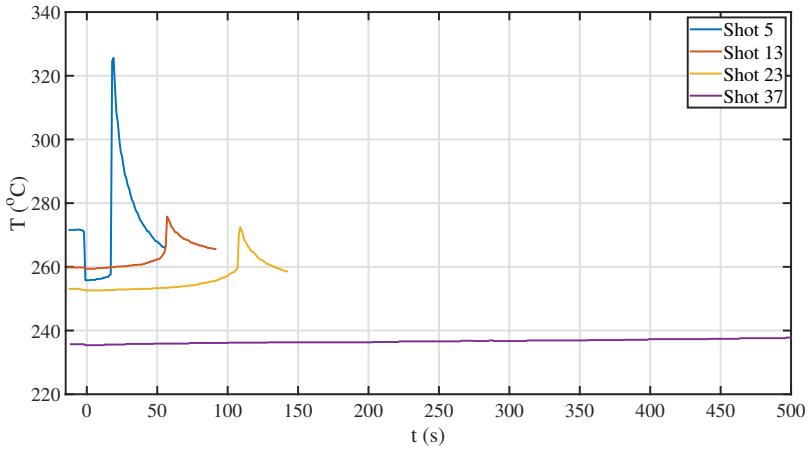

(b)

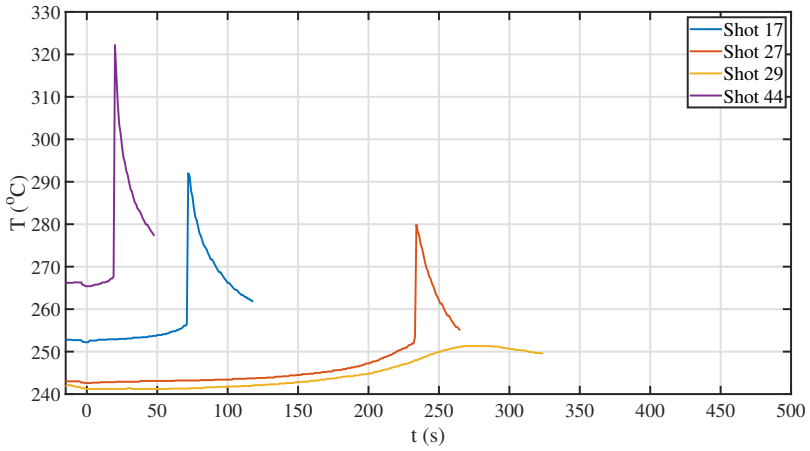

(c)

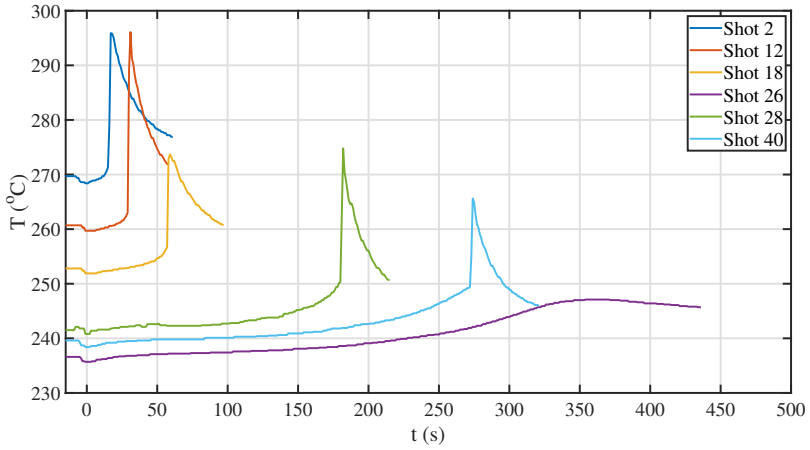

(d)

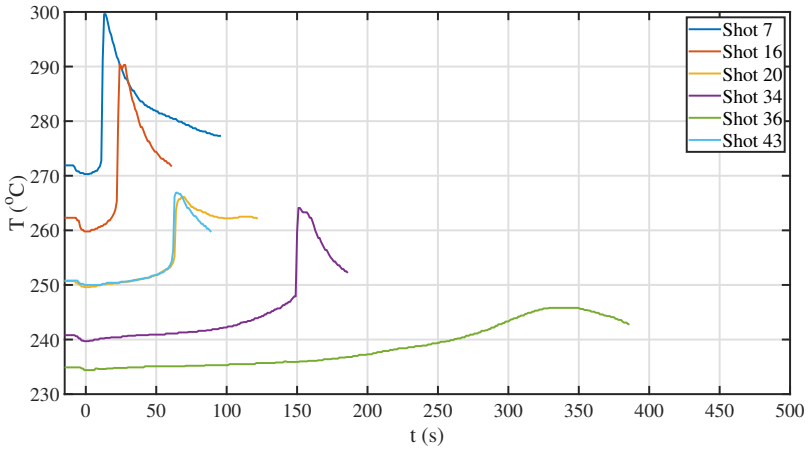

Figure B.12: Collection of temperature traces for Trans-decalin shots with (a) V_{inj} = 0.04 mL (Global ϕ = 0.81) (b) V_{inj} = 0.1 mL (Global ϕ = 2.02) (c) V_{inj} = 0.2 mL (Global ϕ = 4.03) and (d) V_{inj} = 0.4 mL (Global ϕ = 8.07)

B.7 Toluene

B.7.1 Ignition Modes

(a)

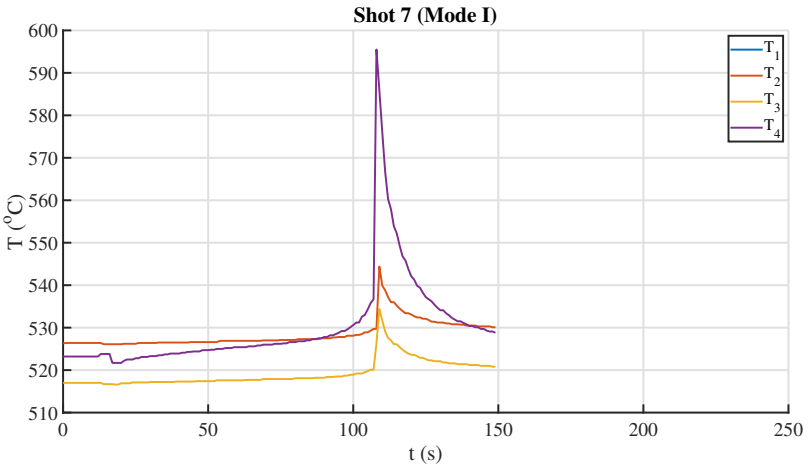

(b)

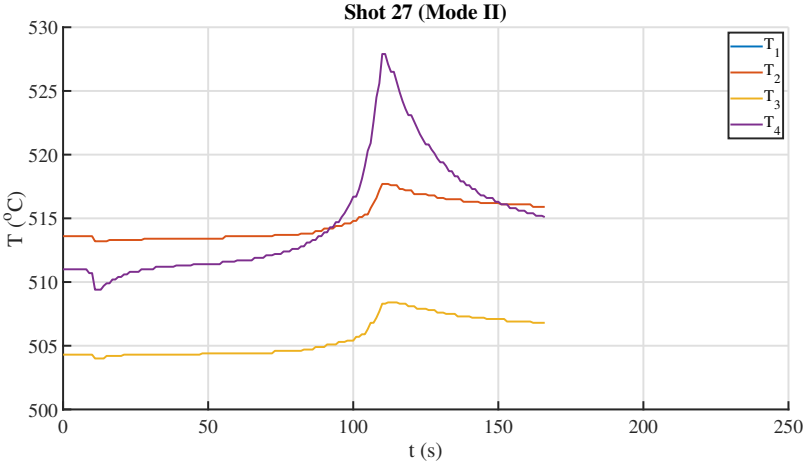

(c)

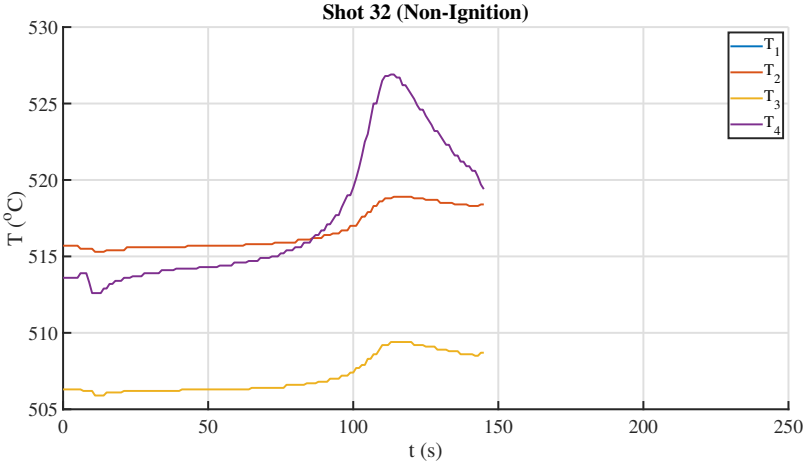

Figure B.13: Representative temperature traces for Toluene ignition modes. (a) Mode I Ignition (b) Mode II Ignition and (c) Non-Ignition

B.7.2 Temperature traces by V_{inj}

(a)

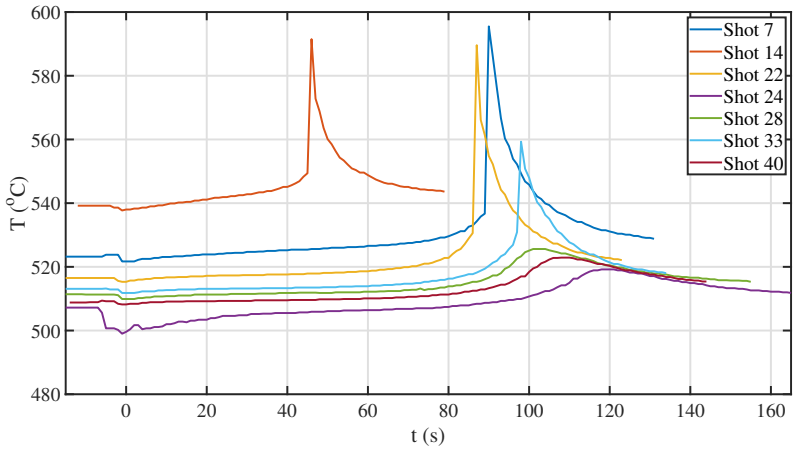

(b)

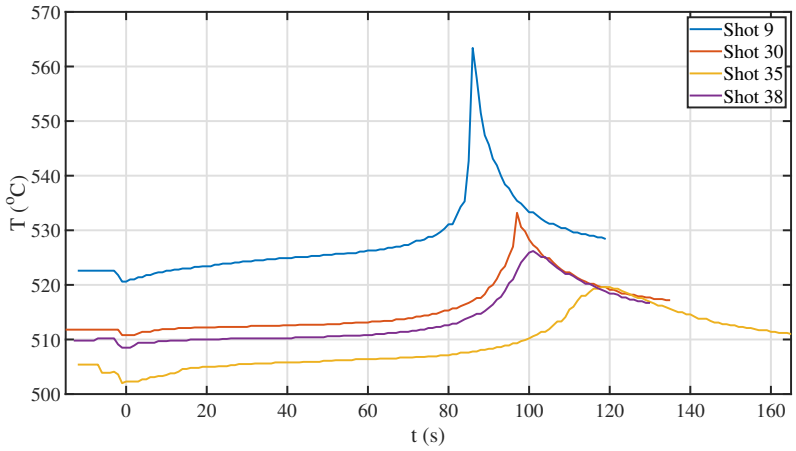

(c)

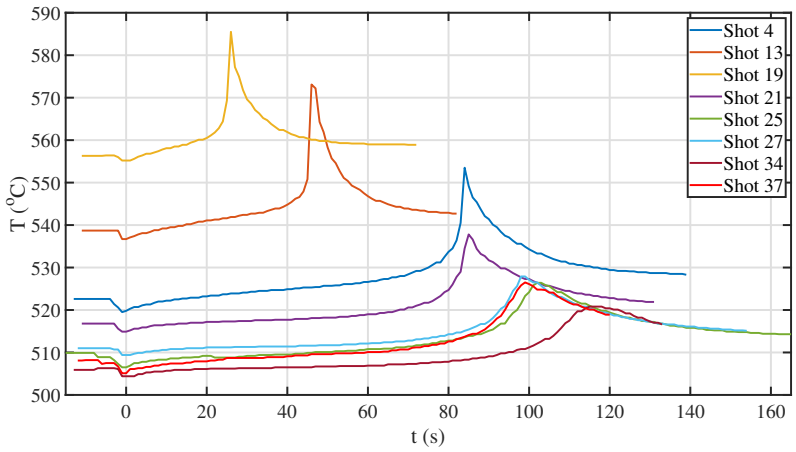

Figure B.14: Collection of temperature traces for Toluene shots with (a) V_{inj} = 0.04 mL (Global ϕ = 0.75) (b) V_{inj} = 0.05 mL (Global ϕ = 0.94) and (c) V_{inj} = 0.06 mL (Global ϕ = 1.13)

B.8 Jet A (POSF-4658)

B.8.1 Ignition Modes

(a)

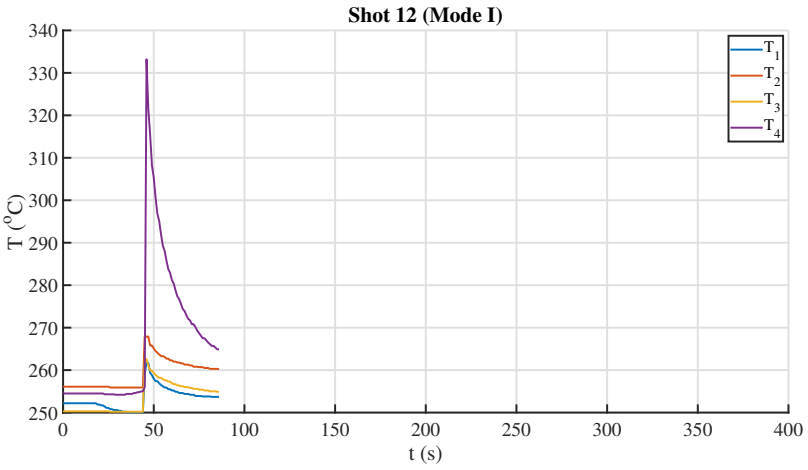

(b)

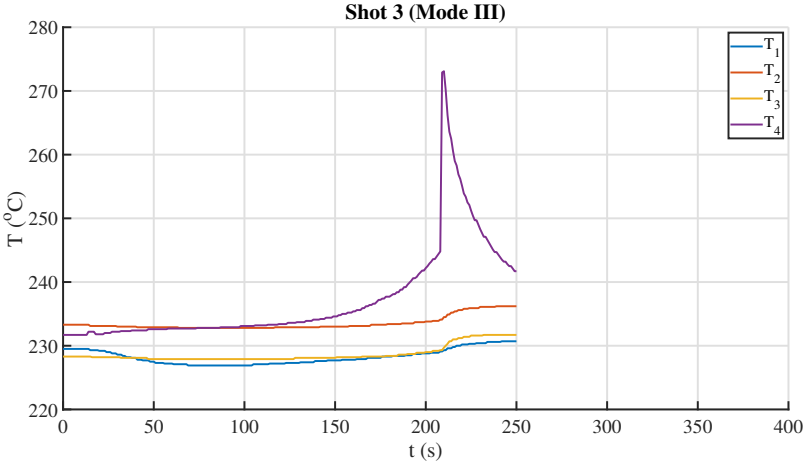

(c)

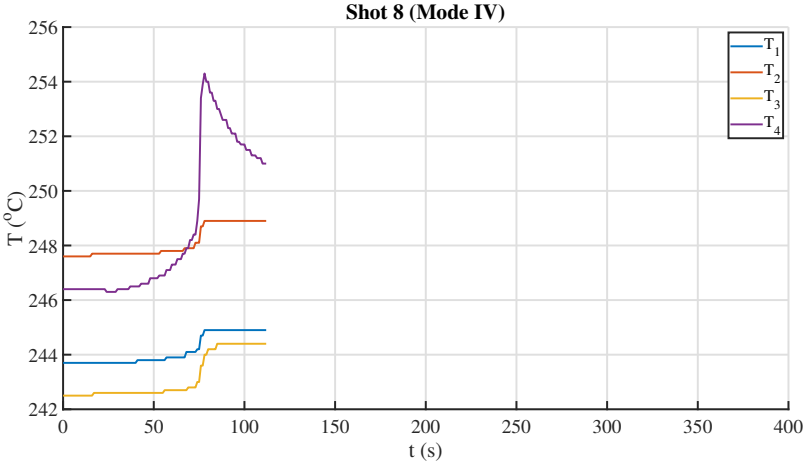

(d)

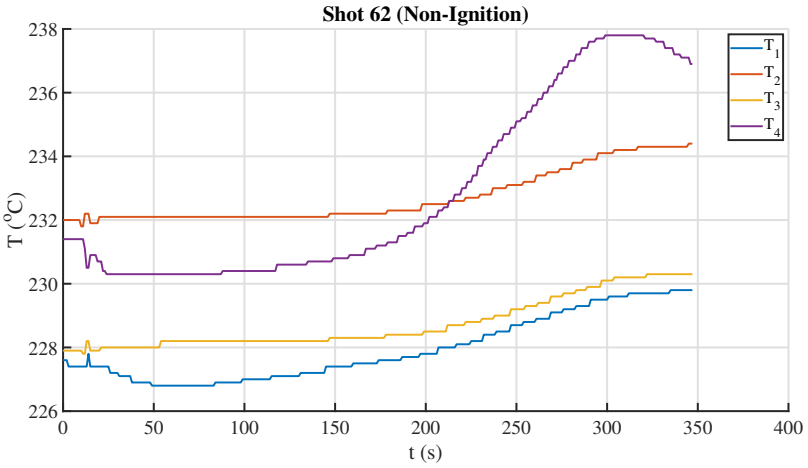

Figure B.15: Representative temperature traces for Jet A (POSF-4658) ignition modes. (a) Mode I Ignition (b) Mode III Ignition (c) Mode IV Ignition and (d) Non-Ignition [2]

[2]Note the extended timescale for multi-component fuel plots (400s) as compared to most single component fuel plots (250s).

B.8.2 Temperature traces by V_{inj}

(a)

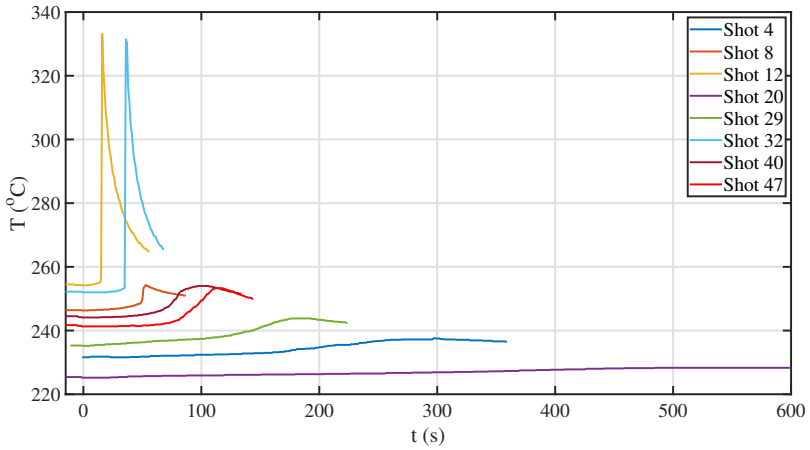

(b)

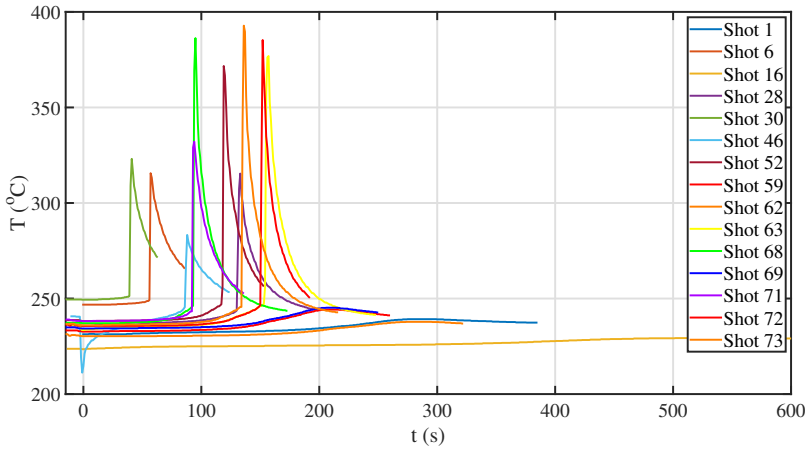

(c)

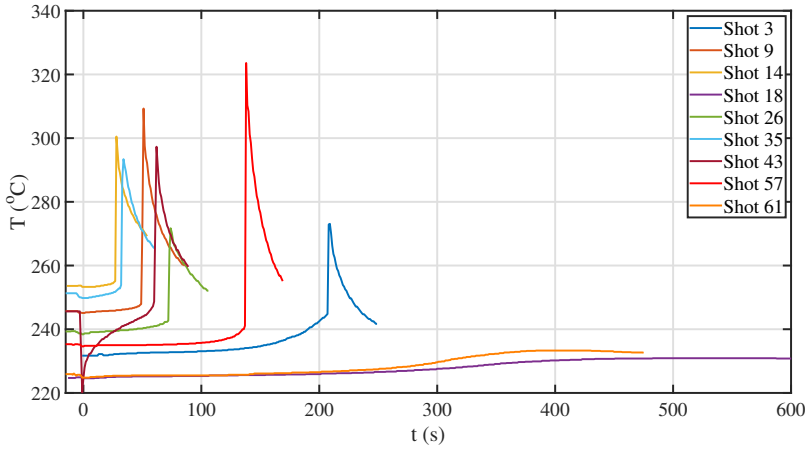

(d)

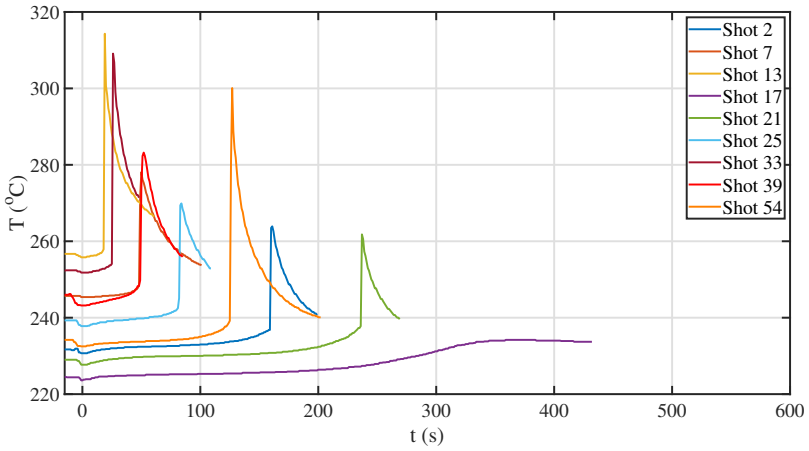

(e)

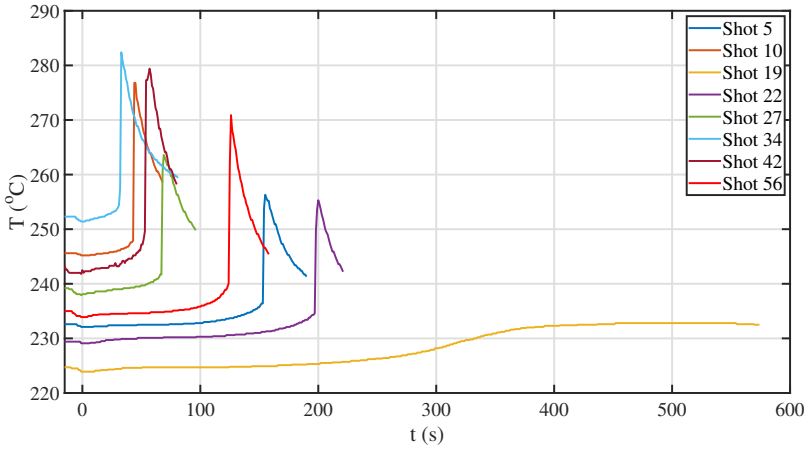

Figure B.16: Collection of temperature traces for Jet A (POSF-4658) shots with (a) V_{inj} = 0.06 mL (Global ϕ = 1.10) (b) V_{inj} = 0.1 mL (Global ϕ = 1.84) (c) V_{inj} = 0.2 mL (Global ϕ = 3.68) (d) V_{inj} = 0.3 mL (Global ϕ = 5.52) and (e) V_{inj} = 0.4 mL (Global ϕ = 7.36)

B.9 Jet A (POSF-10325)

B.9.1 Ignition Modes

(a)

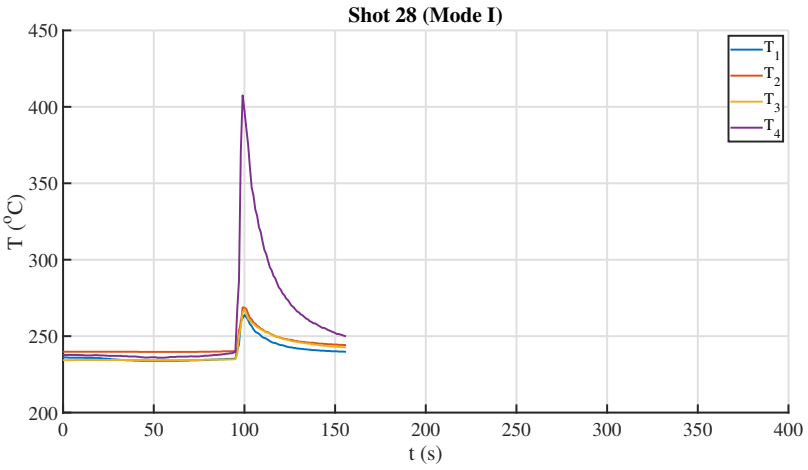

(b)

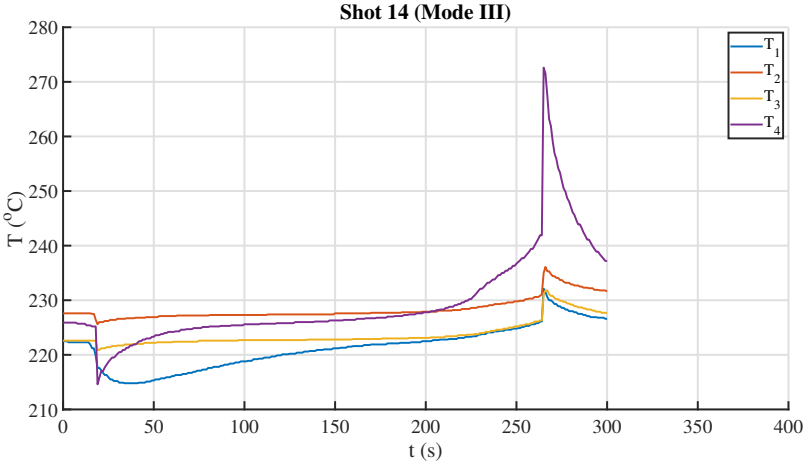

(c)

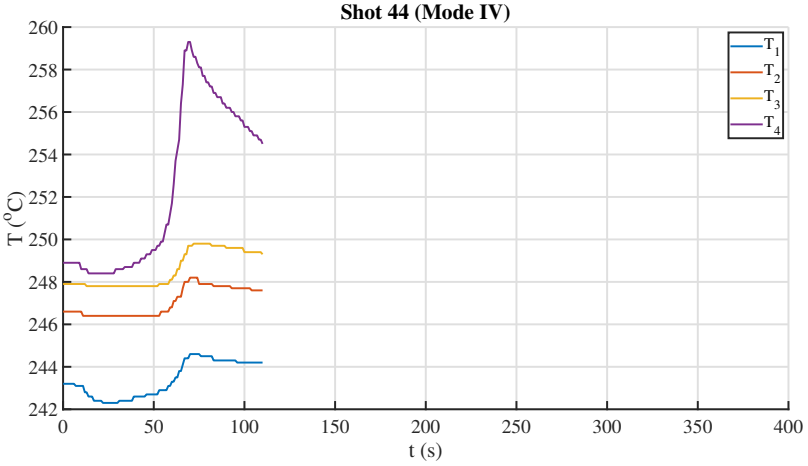

(d)

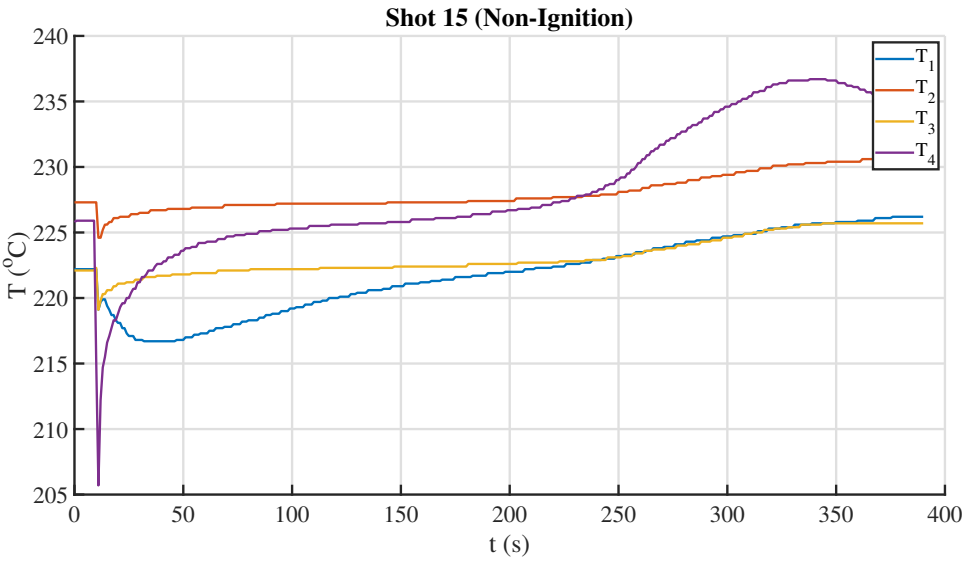

Figure B.17: Representative temperature traces for Jet A (POSF-10325) ignition modes. (a) Mode I Ignition (b) Mode III Ignition (c) Mode IV Ignition and (d) Non-Ignition

B.9.2 Temperature traces by V_{inj}

(a)

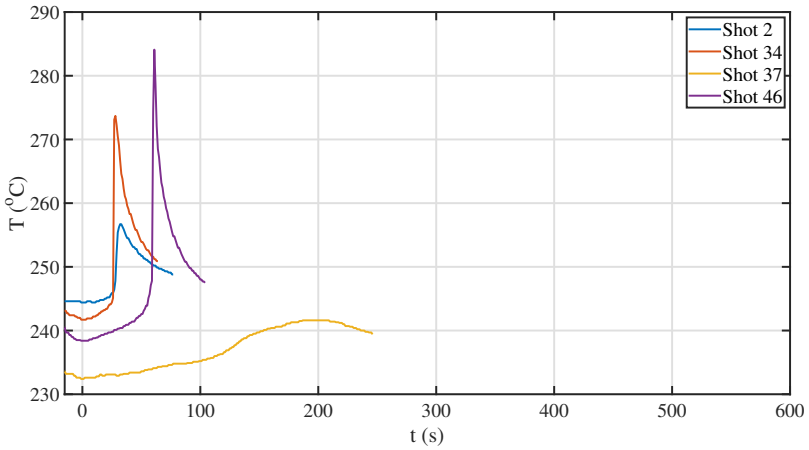

(b)

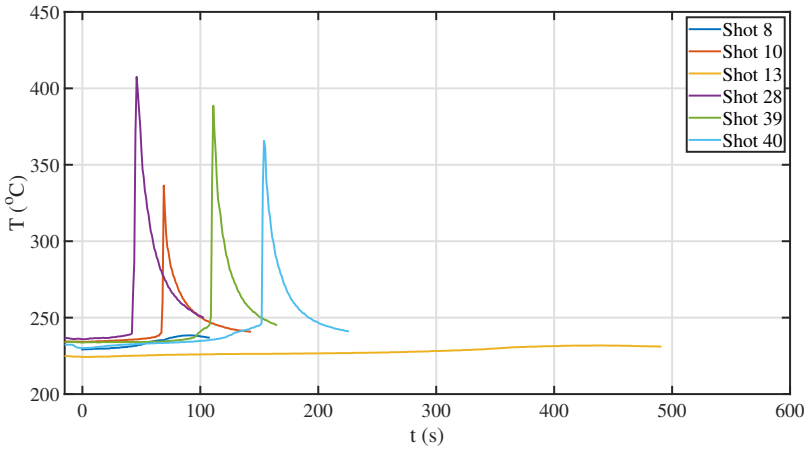

(c)

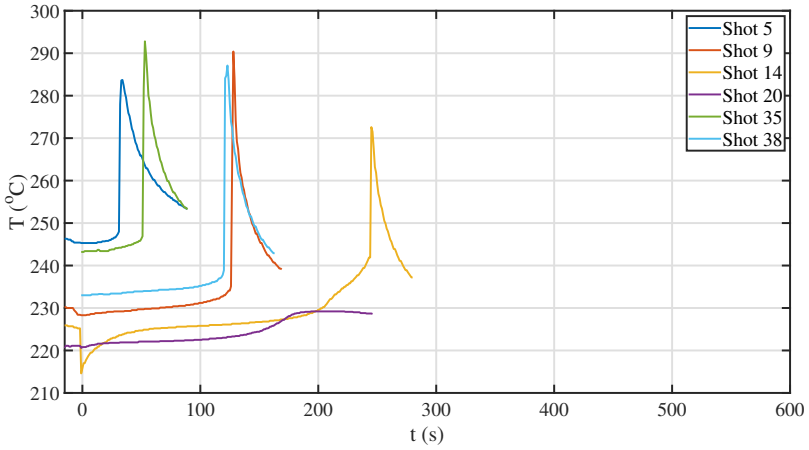

(d)

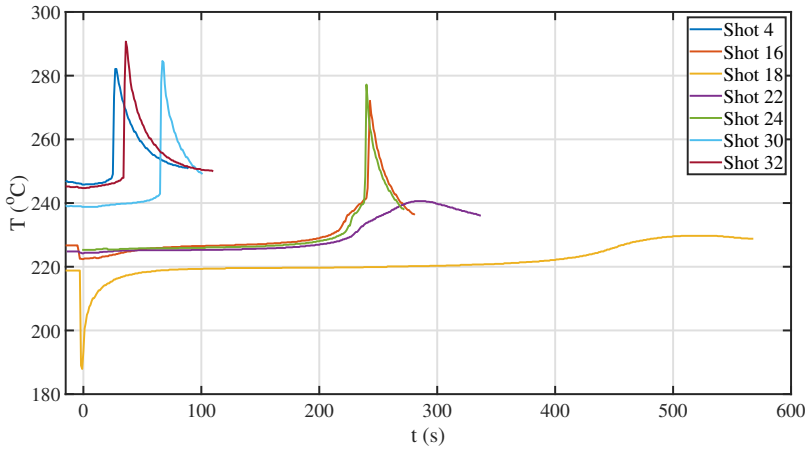

(e)

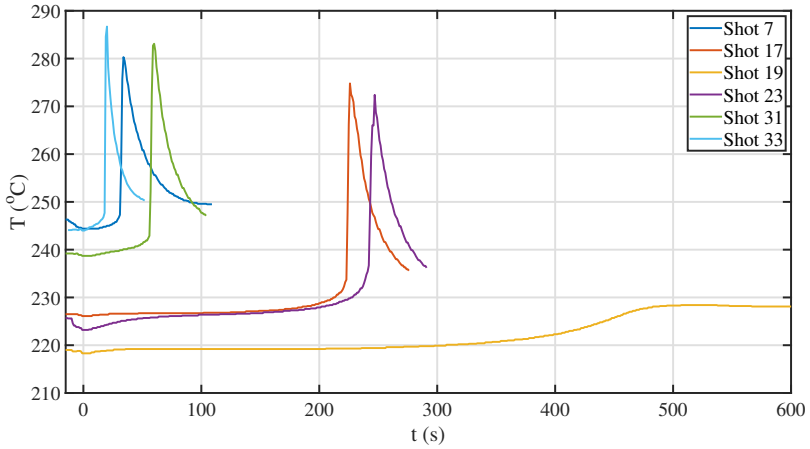

Figure B.18: Collection of temperature traces for Jet A (POSF-10325) shots with (a) V_{inj} = 0.06 mL (Global ϕ = 1.10) (b) V_{inj} = 0.1 mL (Global ϕ = 1.83) (c) V_{inj} = 0.3 mL (Global ϕ = 5.49) (d) V_{inj} = 0.4 mL (Global ϕ = 7.33) and (e) V_{inj} = 0.5 mL (Global ϕ = 9.16)

B.10 Aachen Surrogate

B.10.1 Ignition Modes

(a)

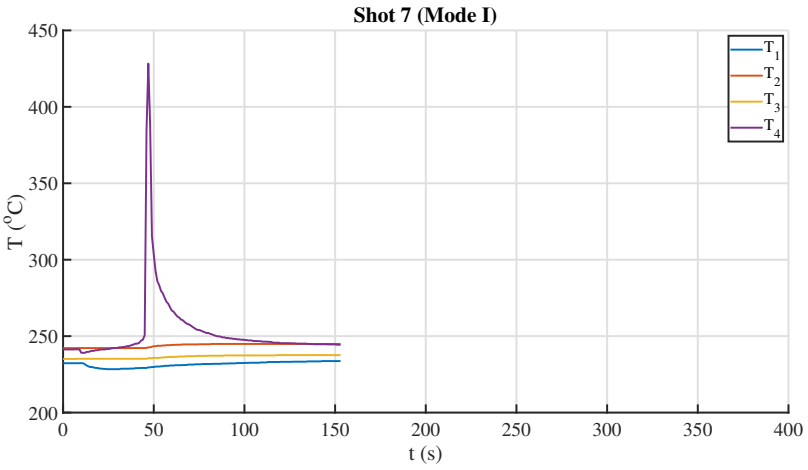

(b)

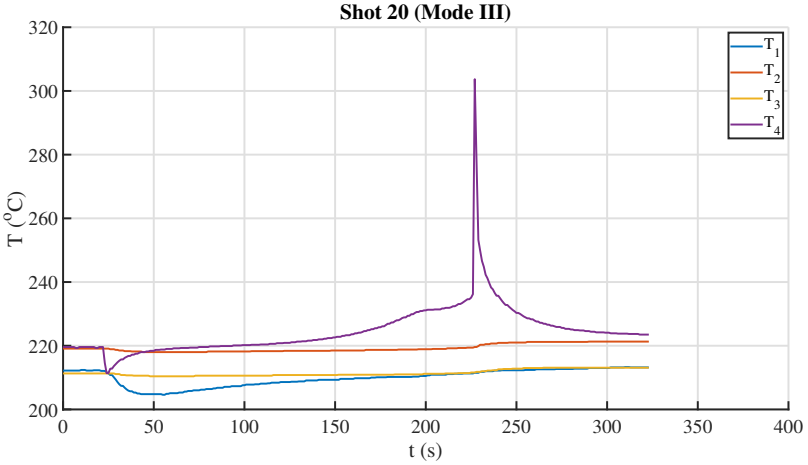

(c)

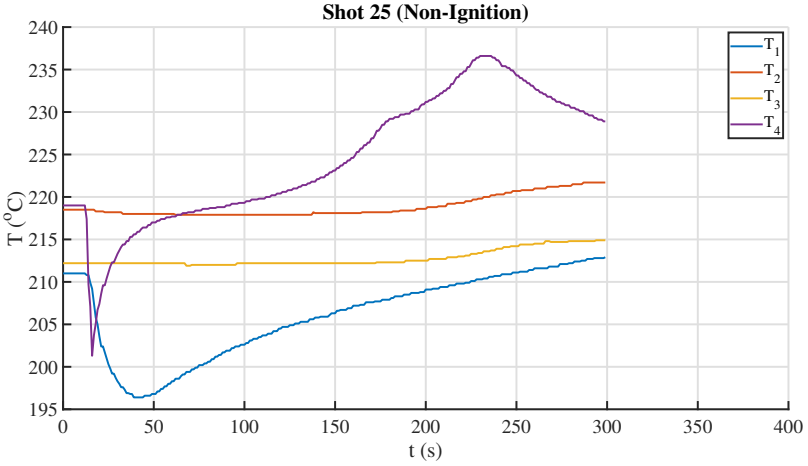

Figure B.19: Representative temperature traces for Aachen Surrogate ignition modes. (a) Mode I Ignition (b) Mode III Ignition (c) Non-Ignition

B.10.2 Temperature traces by V_{inj}

(a)

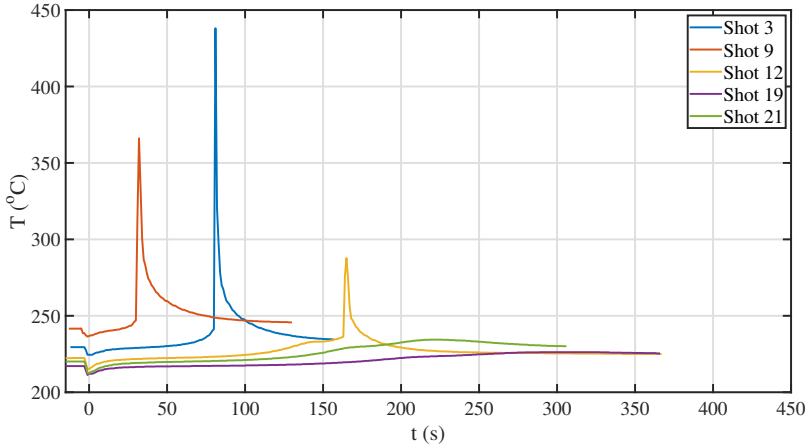

(b)

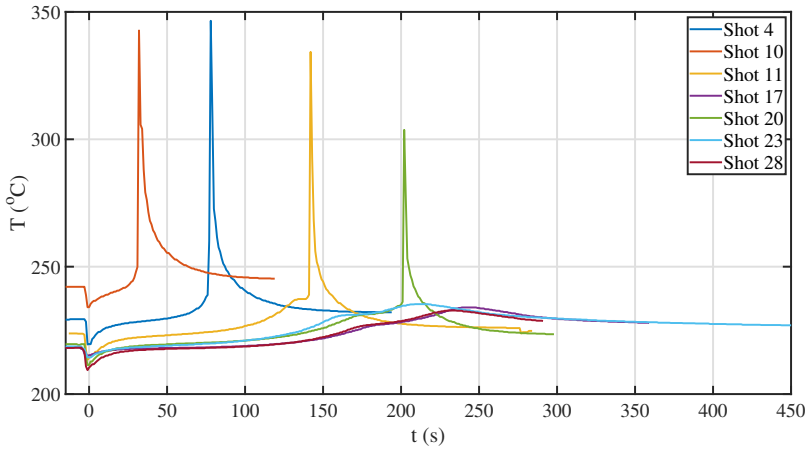

Figure B.20: Collection of temperature traces for Aachen Surrogate shots with (a) V_{inj} = 0.2 mL (Global ϕ = 3.49) and (b) V_{inj} = 0.3 mL (Global ϕ = 5.23)

B.11 JI Surrogate

B.11.1 Ignition Modes

(a)

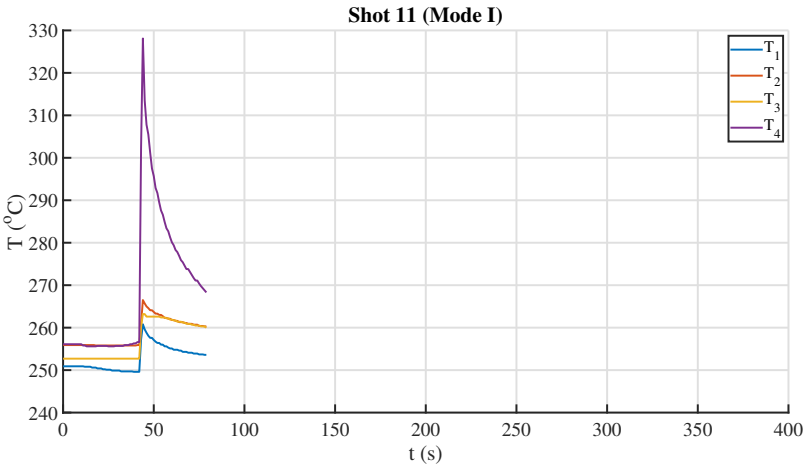

(b)

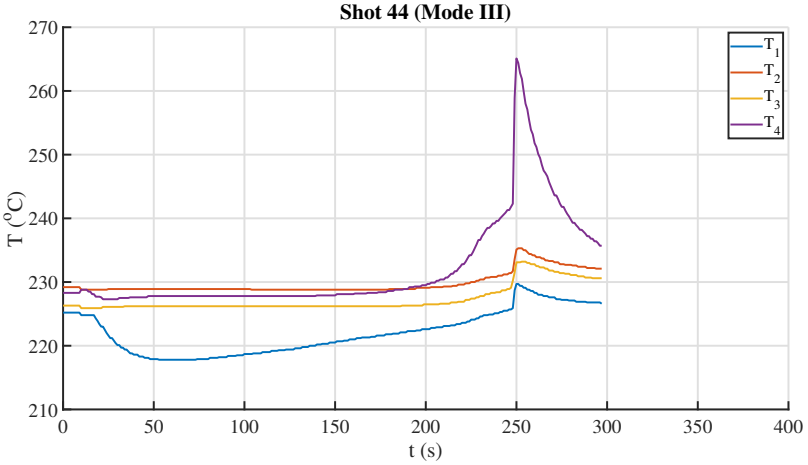

(c)

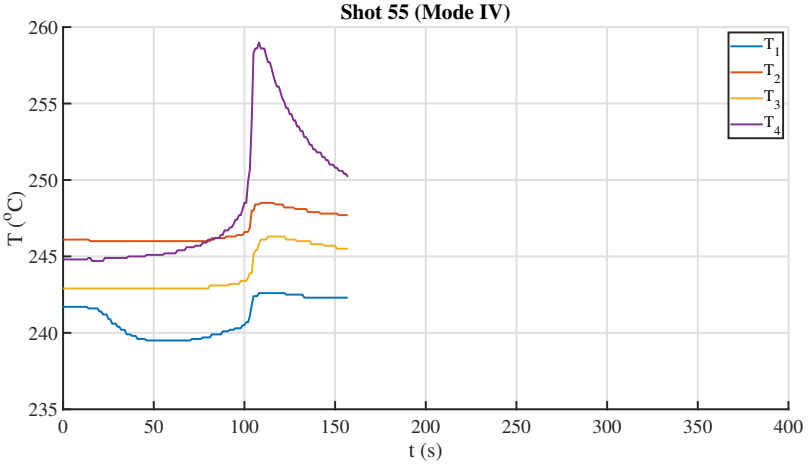

(d)

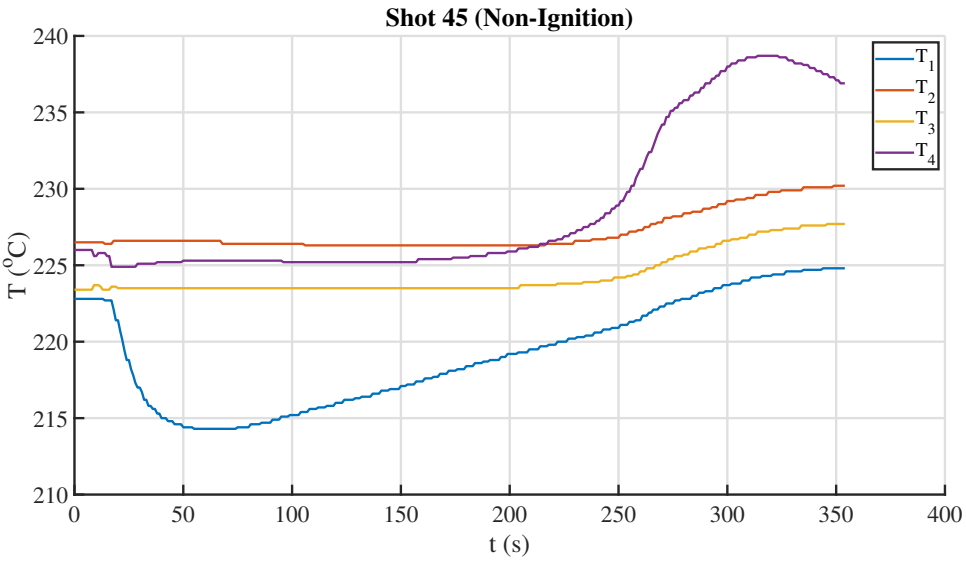

Figure B.21: Representative temperature traces for JI Surrogate ignition modes. (a) Mode I Ignition (b) Mode III Ignition (c) Mode IV Ignition and (d) Non-Ignition

B.11.2 Temperature traces by V_{inj}

(a)

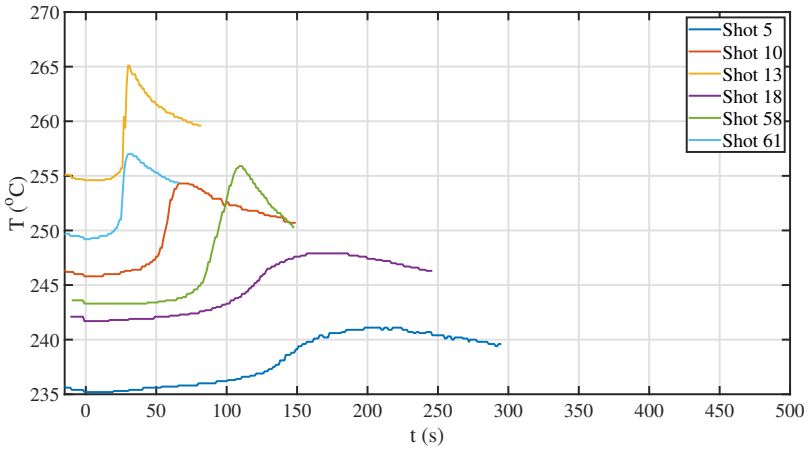

(b)

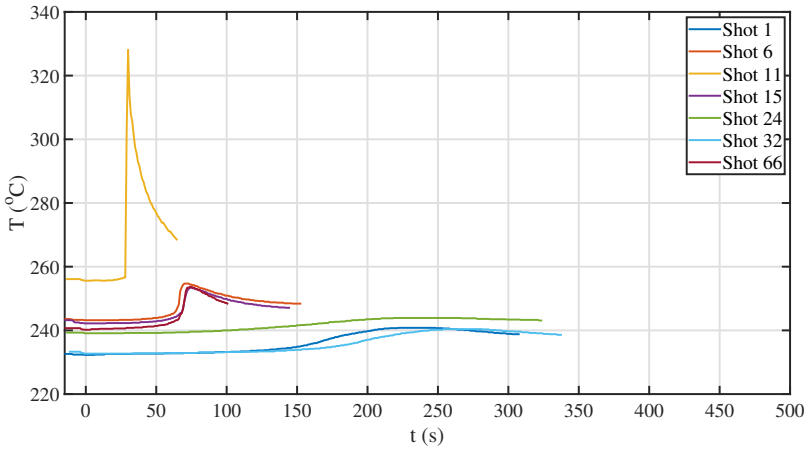

(c)

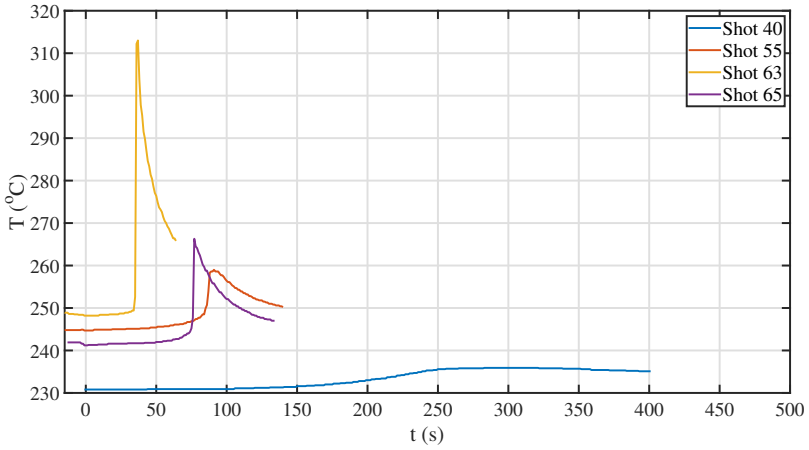

(d)

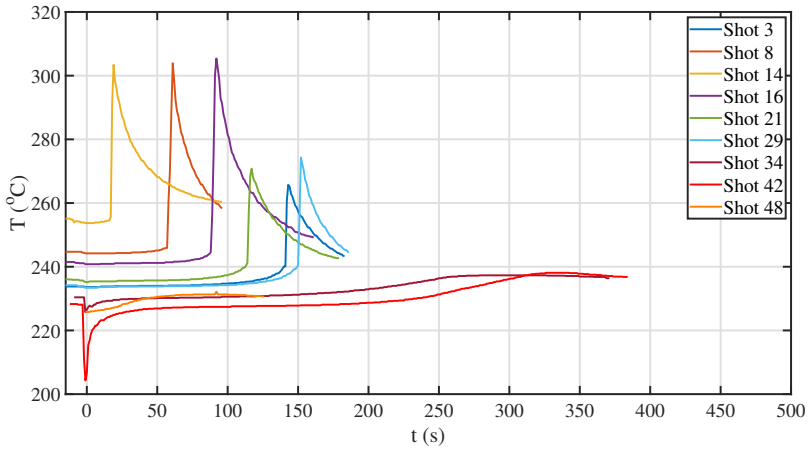

(e)

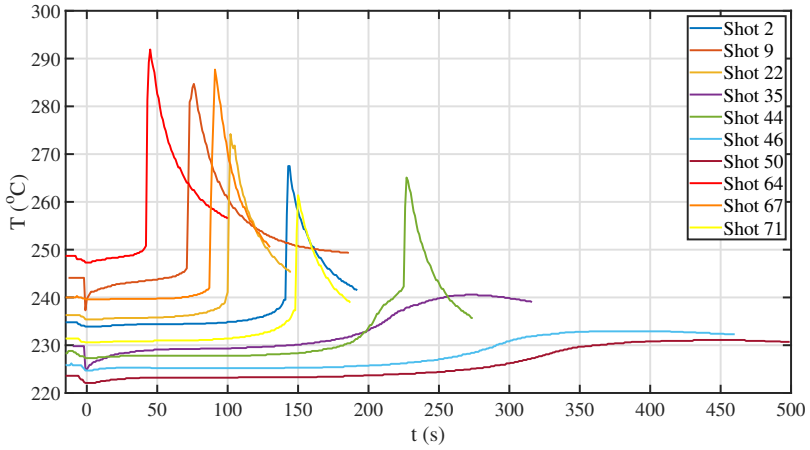

(f)

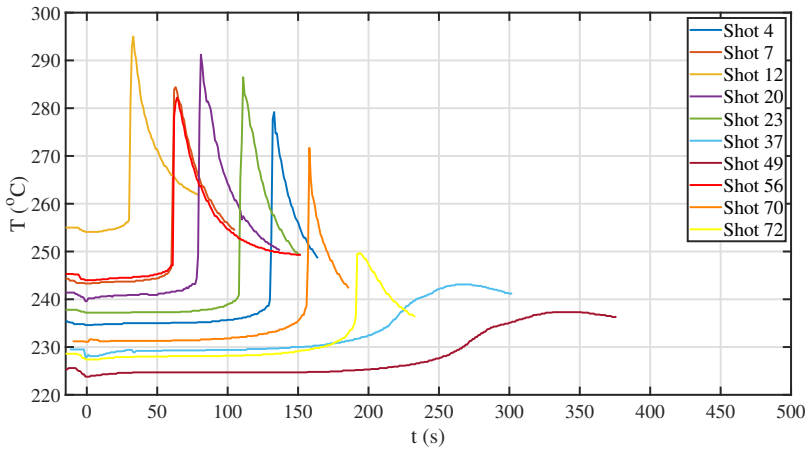

Figure B.22: Collection of temperature traces for JI Surrogate shots with (a) V_{inj} = 0.06 mL (Global ϕ = 1.09) (b) V_{inj} = 0.1 mL (Global ϕ = 1.81) (c) V_{inj} = 0.12 mL (Global ϕ = 2.17) (d) V_{inj} = 0.2 mL (Global ϕ = 3.62) (e) V_{inj} = 0.3 mL (Global ϕ = 5.43) and (f) V_{inj} = 0.4 mL (Global ϕ = 7.25)

Appendix C

COMPONENT LISTS

C.1 Two-Color IR Pyrometer Optical Components

Table C.1: List of Components used for Two-Color pyrometer

Component Label	**Component description**	**Manufacturer**	**Part number**	**Material**	**Focal Length (mm)**	**Operating Wave-length (nm)**	**FWHM (nm)**
C1	Collection Lens 1	ThorLabs	LA1134	N-BK7	60	350-2000	-
C2	Collection Lens 2	ThorLabs	LA1951	N-BK7	25	350-2000	-
FC	Multimode Fiber Optic Cable	ThorLabs	FT1000EMT	Pure Silica (Core)	-	400-2200	-
L1	Body Lens	ThorLabs	LA1608	N-BK7	75	350-2000	-
BS	Longpass Dichroic Mir-ror/Beamsplitter	ThorLabs	DMLP1800	UV Fused Silica	-	1500-2100	-
F-1705	Bandpass Filter 1705 nm	Infrared Optical Products	BP-1705-097-B	UV Fused Silica	-	-	97
F-1940	Bandpass Filter 1940 nm	Infrared Optical Products	BP-1940-105-B	UV Fused Silica	-	-	105
PD	Photodetector	ThorLabs	PDA10T	InGaAs (detector)	-	900-2570	-

Appendix D

200A CYLINDER SHOT DATA

This section summarizes the ignition data obtained using the 200A cylinder for n-hexane, hydrogen, and ethylene mixtures. This cylinder has a diameter of 2.54 cm, length of 25.4 cm, and a surface area of 200 cm^2. In the tables the I and V values correspond to those for the constant current pre-heat ramp.

The sections are grouped by fuel with Appendix D.1 encompassing all of the n-hexane tests with varying ϕ, β, and P_0. However, the Limiting Oxygen Concentration (LOC) shots for n-hexane are presented separately in Appendix D.4 where T_w = 1200 K for all tests since it is a transient test (constant heating ramp) where ignition occurs at some temperature less than T_w. Appendix D.2 and Appendix D.3 contain the data for hydrogen/air and ethylene/air mixtures respectively.

D.1 C_6H_{14}

Table D.1: C_6H_{14} ignition data for 200A cylinder.

Shot #	H **(in)**	P_0 **(torr)**	T_0 **(°C)**	I **(A)**	**Volt (V)**	ϕ	β	P_{tot} **(torr)**	$P_{C_6H_{14}}$ **(torr)**	P_{N_2} **(torr)**	P_{O_2} **(torr)**	T_w **(K)**	P_{max} **(atm)**	t_{ign} **(s)**	**Ign (0/1)**
284	10	760.3	23	420	4.2	0.88	3.76	760.7	14.3	589.4	157.0	1050	7.58		1
285	10	759.9	24	420	4.2	0.88	3.76	760.3	14.3	589.3	156.7	1025	7.38	122	1
286	10	760.7	25	420	4.2	0.88	3.76	761.4	14.5	589.1	157.8	1000			0
287	10	760.1	26	420	4.2	0.88	3.76	760.7	14.1	589.7	156.9	1010			0
288	10	761.0	26	420	4.2	0.88	3.76	761.5	14.5	589.5	157.5	1030	7.63	80	1
289	10	759.9	22	420	4.2	0.88	3.76	760.1	14.4	589.5	156.2	1020			0
290	10	760.3	24	420	4.2	1.60	3.76	760.5	26.0	579.9	154.6	1050	8.23	68	1
291	10	760.8	24	420	4.2	1.60	3.76	761.0	26.0	579.8	155.2	1000			0
292	10	759.7	26	420	4.2	1.60	3.76	760.3	26.6	579.5	154.2	1025	8.10	73	1
293	10	761.0	26	420	4.2	1.60	3.76	761.4	26.7	579.2	155.5	1010			0
294	10	760.1	23	420	4.2	1.00	3.76	760.3	16.6	587.3	156.4	1050	8.32	76	1
295	10	761.9	24	420	4.2	1.00	3.76	762.0	16.4	589.5	156.1	1000			0
296	10	760.1	26	420	4.2	1.00	3.76	760.9	16.3	587.6	157.0	1025	8.16	73	1
297	10	761.8	26	420	4.2	1.00	3.76	762.0	16.5	587.0	158.5	1010			0
317	10	759.4	23	420	4.2	0.88	3.76	760.1	14.5	589.4	156.2	1050	7.46	90	1
318	10	759.6	25	420	4.2	0.88	3.76	760.2	14.7	589.4	156.1	1030	7.41	124	1
336	10	760.9	26	420	4.2	0.88	3.76	761.0	14.7	589.2	157.1	1030			0
337	10	760.7	26	420	4.2	0.88	3.76	761.0	14.7	589.1	157.2	1035			0
362	10	759.2	26	420	4.2	1.00	3.76	760.2	16.0	587.9	156.3	1030	7.82	101	1
363	10	759.9	27	420	4.2	1.00	3.76	760.6	15.8	588.2	156.6	1010			0
364	10	532.8	23	420	4.2	1.00	3.76	533.2	11.5	412.1	109.6	1070	5.53	116	1

Table D.1: C_6H_{14} ignition data for 200A cylinder. (continued)

Shot #	H **(in)**	P_0 **(torr)**	T_0 **(°C)**	I **(A)**	**Volt (V)**	ϕ	β	P_{tot} **(torr)**	$P_{C_6H_{14}}$ **(torr)**	P_{N_2} **(torr)**	P_{O_2} **(torr)**	T_w **(K)**	P_{max} **(atm)**	t_{ign} **(s)**	**Ign (0/1)**
365	10	533.0	25	420	4.2	1.00	3.76	533.9	11.5	411.3	111.1	1050			0
366	10	531.6	24	420	4.2	1.00	3.76	532.1	11.6	411.0	109.5	1060	5.39	220	1
367	10	531.2	27	460	4.6	1.00	3.76	532.0	11.6	411.2	109.2	1040			0
368	10	532.0	30	460	4.6	1.00	3.76	532.8	11.7	411.1	110.0	1055	5.32	258	1
369	10	354.7	29	420	4.2	1.00	3.76	355.2	8.0	273.8	73.4	1100	3.63	188	1
370	10	354.1	31	420	4.2	1.00	3.76	354.8	7.9	273.6	73.3	1080			0
371	10	355.1	31	420	4.2	1.00	3.76	355.5	7.5	274.9	73.1	1090			0
372	10	356.4	22	420	4.2	1.00	3.76	356.2	7.6	274.0	74.6	1095	3.61	255	1
373	10	356.1	25	420	4.2	1.00	3.76	356.2	7.7	274.5	74.0	1093	3.59	259	1
374	10	355.2	26	420	4.2	1.00	3.76	355.2	7.7	273.8	73.7	1088			0
375	10	181.7	29	500	4.8	1.00	3.76	181.8	3.8	140.7	37.3	1130			0
376	10	182.7	29	500	4.8	1.00	3.76	182.6	4.0	140.0	38.6	1150	1.78	178	1
377	10	181.2	29	500	4.8	1.00	3.76	181.2	4.0	140.7	36.5	1140			0
378	10	182.5	31	500	4.8	1.00	3.76	182.4	4.0	140.6	37.8	1145	1.70	289	1
379	10	181.0	30	500	4.8	1.00	3.76	180.8	3.9	140.4	36.5	1142			0
380	10	181.8	22	500	4.8	1.00	3.76	181.7	3.9	139.8	38.0	1160	1.87	83	1
381	10	181.5	24	500	4.8	1.00	3.76	181.3	4.1	140.2	37.0	1144	1.78	268	1
382	10	180.8	26	500	4.8	1.00	3.76	180.7	4.0	140.1	36.6	1138	1.79	175	1
383	10	181.2	25	500	4.8	1.00	3.76	181.2	4.0	140.2	37.0	1134			0
384	10	181.8	27	500	4.8	1.00	3.76	181.8	4.0	140.4	37.4	1136			0
385	10	181.0	28	500	4.8	1.00	3.76	181.1	4.0	140.2	36.9	1140			0

Table D.1: C_6H_{14} ignition data for 200A cylinder. (continued)

Shot #	H **(in)**	P_0 **(torr)**	T_0 **(°C)**	I **(A)**	**Volt (V)**	ϕ	β	P_{tot} **(torr)**	$P_{C_6H_{14}}$ **(torr)**	P_{N_2} **(torr)**	P_{O_2} **(torr)**	T_w **(K)**	P_{max} **(atm)**	t_{ign} **(s)**	**Ign (0/1)**
386	10	183.5	26	500	4.8	1.00	3.76	183.4	4.1	140.6	38.7	1143	1.90	204	1
387	10	181.2	22	500	4.8	1.00	3.76	181.4	3.8	140.5	37.1	1139			0
388	10	180.5	26	500	4.8	1.00	3.76	180.6	4.0	140.1	36.5	1144			0
390	10	181.6	30	500	4.8	1.00	3.76	181.6	4.1	139.5	38.0	1120			0
392	10	355.0	26	500	4.8	1.00	3.76	355.3	7.7	273.7	73.9	1092			0
393	10	354.7	27	500	4.8	1.00	3.76	355.0	7.7	274.1	73.2	1098			0
394	10	355.7	28	500	4.8	1.00	3.76	355.8	7.8	274.3	73.7	1110	3.63	154	1
395	10	355.7	23	500	4.8	1.00	3.76	355.8	7.6	273.6	74.6	1105	3.66	189	1
396	10	354.8	25	500	4.8	1.00	3.76	355.0	7.6	273.8	73.6	1099	3.56	208	1
397	10	355.5	27	500	4.8	1.00	3.76	355.8	7.8	273.6	74.4	1094	3.67	96	1
398	10	355.6	26	500	4.8	1.00	3.76	355.7	7.7	273.9	74.1	1085	3.64	165	1
399	10	354.0	27	500	4.8	1.00	3.76	354.1	7.8	273.4	72.9	1070			0
400	10	354.0	29	500	4.8	1.00	3.76	354.2	7.8	273.6	72.8	1075			0
401	10	355.0	29	500	4.8	1.00	3.76	355.1	7.8	274.3	73.0	1083			0
402	10	354.8	23	500	4.8	1.00	3.76	355.0	7.6	273.9	73.5	1087			0
403	10	354.8	26	500	4.8	1.00	3.76	355.0	7.7	273.6	73.7	1091	3.63	214	1
404	10	354.6	27	500	4.8	1.00	3.76	354.8	7.9	273.5	73.4	1089	3.51	315	1
405	10	531.9	28	500	4.8	1.00	3.76	532.5	11.6	412.1	108.8	1053			0
406	10	531.8	28	500	4.8	1.00	3.76	532.4	11.5	411.3	109.6	1070	5.44	168	1
407	10	533.3	22	500	4.8	1.00	3.76	533.3	11.5	411.1	110.7	1058			0
408	10	532.0	25	500	4.8	1.00	3.76	532.5	11.7	410.9	109.9	1063			0

Table D.1: C_6H_{14} ignition data for 200A cylinder. (continued)

Shot #	H **(in)**	P_0 **(torr)**	T_0 **(°C)**	I **(A)**	**Volt (V)**	ϕ	β	P_{tot} **(torr)**	$P_{C_6H_{14}}$ **(torr)**	P_{N_2} **(torr)**	P_{O_2} **(torr)**	T_w **(K)**	P_{max} **(atm)**	t_{ign} **(s)**	**Ign (0/1)**
409	10	531.8	26	420	4.2	1.00	3.76	532.1	11.4	411.6	109.1	1061			0
414	10	759.3	22	500	4.8	1.00	3.76	760.1	15.8	588.2	156.1	1015			0
415	10	759.0	25	500	4.8	1.00	3.76	760.1	15.9	587.9	156.3	1030	7.93	75	1
416	10	759.0	25	500	4.8	1.00	4.51	759.9	14.5	610.1	135.3	1030	7.29	90	1
417	10	759.6	26	500	4.8	1.00	4.51	760.4	14.5	610.2	135.7	1020	7.10	162	1
418	10	758.8	27	500	4.8	1.00	4.51	760.1	14.5	610.5	135.1	1015			0
419	10	759.7	22	500	4.8	1.00	5.64	760.1	11.8	635.4	112.9	1040	5.57	234	1
420	10	759.2	26	500	4.8	1.00	7.52	760.3	9.4	662.5	88.4	1050			0
421	10	759.7	25	500	4.8	1.00	7.52	760.4	9.3	662.8	88.3	1070	2.44	195	1
422	10	759.4	26	500	4.8	1.00	7.52	760.2	9.3	662.9	88.0	1060			0
423	10	759.0	28	500	4.8	1.00	7.52	759.8	9.5	662.5	87.8	1065			0
424	10	759.3	23	500	4.8	1.00	7.52	759.9	9.2	662.6	88.1	1080	2.04	91	1
425	10	531.5	24	500	4.8	1.00	7.52	531.9	6.5	465.8	59.6	1120	1.51	73	1
426	10	532.0	24	500	4.8	1.00	7.52	532.4	6.6	465.0	60.8	1110	1.72	90	1
427	10	531.5	25	500	4.8	1.00	7.52	532.1	6.6	468.3	57.2	1100	1.38	262	1
428	10	531.8	27	500	4.8	1.00	7.52	532.3	6.5	464.0	61.8	1090			0
429	10	531.4	27	500	4.8	1.00	5.64	532.0	8.5	445.4	78.1	1090	4.04	128	1
430	10	531.9	28	500	4.8	1.00	5.64	532.5	8.5	444.7	79.3	1075			0
431	10	532.0	23	500	4.8	1.00	5.64	532.3	8.3	444.8	79.2	1085	4.09	120	1
432	10	532.0	24	500	4.8	1.00	5.64	532.4	8.3	444.6	79.5	1080	3.88	259	1
433	10	531.6	25	500	4.8	1.00	5.64	532.2	8.3	444.7	79.2	1070			0

Table D.1: C_6H_{14} ignition data for 200A cylinder. (continued)

Shot #	H **(in)**	P_0 **(torr)**	T_0 **(°C)**	I **(A)**	**Volt (V)**	ϕ	β	P_{tot} **(torr)**	$P_{C_6H_{14}}$ **(torr)**	P_{N_2} **(torr)**	P_{O_2} **(torr)**	T_w **(K)**	P_{max} **(atm)**	t_{ign} **(s)**	**Ign (0/1)**
434	10	354.3	27	500	4.8	1.00	7.52	354.4	4.4	310.3	39.7	1115			0
435	10	353.9	28	500	4.8	1.00	7.52	353.9	4.6	310.2	39.1	1140	1.21	116	1
436	10	354.0	28	500	4.8	1.00	7.52	354.2	4.4	309.4	40.4	1130	1.20	175	1
437	10	353.9	29	500	4.8	1.00	7.52	354.3	4.4	312.2	37.7	1120			0
438	10	354.6	22	500	4.8	1.00	7.52	354.7	4.4	309.0	41.3	1125			0
439	10	181.2	24	500	4.8	1.00	7.52	181.2	2.4	157.8	21.0	1160			0
440	10	182.1	25	550	4.9	1.00	7.52	181.9	2.3	158.7	20.9	1170			0
441	10	180.8	28	550	4.9	1.00	7.52	181.0	2.3	157.8	20.9	1200			0
442	10	758.5	29	550	4.9	1.00	3.76	760.1	16.9	587.9	155.3	1015	7.61	183	1
443	10	759.3	29	550	4.9	1.00	3.76	760.4	16.0	587.8	156.6	1005			0
444	10	181.6	22	550	4.9	1.00	5.64	181.6	2.9	151.8	26.9	1150			0
445	10	181.3	26	550	4.9	1.00	5.64	181.4	2.9	151.5	27.0	1160	1.24	294	1
446	10	181.5	28	550	5	1.00	5.64	181.5	3.1	151.5	26.9	1155			0
447	10	532.0	28	550	5	1.00	3.76	532.6	11.6	411.1	109.9	1065	5.11	289	1
448	10	531.3	22	550	5	1.00	3.76	532.0	11.3	411.4	109.3	1060	5.45	168	1
449	10	531.4	25	550	5	1.00	3.76	531.9	11.4	411.2	109.3	1050			0
450	10	531.5	26	550	5	1.00	3.76	532.1	11.5	411.3	109.3	1080	5.48	68	1
451	10	531.5	27	550	5	1.00	3.76	532.1	11.5	411.0	109.6	1055			0
452	10	181.2	26	550	5	1.00	5.64	181.1	2.9	152.3	25.9	1165	1.23	274	1
453	10	759.4	23	550	5	1.00	5.64	760.0	11.7	635.9	112.4	1035			0
454	10	759.4	25	550	5	1.00	5.64	760.3	11.8	635.6	112.9	1045			0

Table D.1: C_6H_{14} ignition data for 200A cylinder. (continued)

Shot #	H **(in)**	P_0 **(torr)**	T_0 **(°C)**	I **(A)**	**Volt (V)**	ϕ	β	P_{tot} **(torr)**	$P_{C_6H_{14}}$ **(torr)**	P_{N_2} **(torr)**	P_{O_2} **(torr)**	T_w **(K)**	P_{max} **(atm)**	t_{ign} **(s)**	**Ign (0/1)**
455	10	759.0	26	550	5	1.00	5.64	760.0	12.0	635.3	112.7	1055	5.20	281	1
456	10	758.8	26	550	5	1.00	5.64	759.8	12.0	636.5	111.3	1065	5.66	87	1
457	10	758.7	27	550	5	1.00	5.64	759.8	12.0	635.3	112.5	1060		92	1
458	10	759.3	27	550	5	1.00	5.64	760.1	12.0	635.5	112.6	1053	5.44	223	1
459	10	759.2	29	550	5	1.00	3.76	760.1	16.3	587.6	156.2	1015			0
460	10	760.1	22	550	5	1.00	3.76	760.6	15.9	588.1	156.6	1030	7.90	86	1
461	10	180.9	24	550	5	1.00	7.52	180.8	2.4	157.5	20.9	1200	0.81	168	1
462	10	188.1	24	550	5	1.00	7.52	187.9	2.4	160.1	25.4	1190	0.96	136	1
463	10	181.9	26	550	5	1.00	7.52	181.8	2.4	158.5	20.9	1180	0.76	225	1
464	10	181.3	28	550	5	1.00	7.52	181.3	2.4	157.6	21.3	1170			0
465	10	181.3	28	550	5	1.00	7.52	181.3	2.4	157.5	21.4	1175	0.79	280	1
466	10	181.0	28	550	5	1.00	7.52	181.0	2.4	158.2	20.4	1172	0.68	308	1
467	10	181.3	30	550	5	1.00	7.52	181.2	2.4	158.0	20.8	1168			0
468	10	181.3	23	550	5	1.00	7.52	181.2	2.3	158.5	20.4	1173	0.69	298	1
469	10	181.3	27	550	5	1.00	7.52	181.0	2.3	157.7	21.0	1171			0
470	10	180.8	26	550	5	1.00	7.52	180.8	2.4	158.3	20.1	1169			0
471	10	181.1	28	550	5	1.00	7.52	181.1	2.4	157.7	21.0	1173	0.75	276	1
472	10	182.9	29	550	5	1.00	7.52	183.1	2.4	157.7	23.0	1170	0.93	239	1
473	10	182.1	23	550	5	1.00	5.64	182.0	2.9	151.2	27.9	1170	1.48	105	1
474	10	181.5	24	550	5	1.00	5.64	181.4	2.9	152.7	25.8	1162	1.24	211	1
475	10	181.6	26	550	5	1.00	5.64	181.5	2.9	152.7	25.9	1158	1.23	242	1

Table D.1: C_6H_{14} ignition data for 200A cylinder. (continued)

Shot #	H **(in)**	P_0 **(torr)**	T_0 **(°C)**	I **(A)**	**Volt (V)**	ϕ	β	P_{tot} **(torr)**	$P_{C_6H_{14}}$ **(torr)**	P_{N_2} **(torr)**	P_{O_2} **(torr)**	T_w **(K)**	P_{max} **(atm)**	t_{ign} **(s)**	**Ign (0/1)**
476	10	181.3	27	550	5	1.00	5.64	181.4	2.9	151.2	27.3	1155	0.31	165	1
477	10	181.1	27	550	5	1.00	5.64	180.9	3.0	151.6	26.3	1145			0
478	10	181.0	29	550	5	1.00	5.64	181.0	3.0	152.2	25.8	1151	1.21	278	1
479	10	354.6	29	550	5	1.00	5.64	354.8	5.6	296.7	52.5	1102			0
480	10	354.2	23	550	5	1.00	5.64	354.4	5.5	297.4	51.5	1110			0
481	10	355.3	25	550	5	1.00	5.64	355.4	5.6	297.5	52.3	1120	2.68	166	1
482	10	355.3	26	550	5	1.00	5.64	355.4	5.6	299.5	50.3	1115			0
483	10	354.4	27	550	5	1.00	5.64	354.5	5.6	296.2	52.7	1125	2.74	91	1
484	10	354.1	27	550	5	1.00	5.64	354.2	5.5	296.2	52.5	1118	2.49	269	1
485	10	354.7	28	550	5	1.00	5.64	354.8	5.6	296.5	52.7	1113			0
486	10	358.8	29	550	5	1.00	5.64	359.0	5.6	296.3	57.1	1123	2.71	113	1

D.2 H_2

Table D.2: H_2/Air ignition data for 200A cylinder.

Shot #	H **(in)**	P_0 **(torr)**	T_0 **(°C)**	I **(A)**	**Volt (V)**	ϕ	β	P_{tot} **(torr)**	$P_{C_6H_{14}}$ **(torr)**	P_{N_2} **(torr)**	P_{O_2} **(torr)**	T_w **(K)**	P_{max} **(atm)**	t_{ign} **(s)**	**Ign (0/1)**
298	10	760.6	26	420	4.2	1	3.76	760.7	224.9	422.5	113.3	7.44	984	49	1
299	10	761.1	26	420	4.2	1	3.76	761.4	225.1	422.5	113.8	7.43	974	56	1
300	10	762.4	26	420	4.2	1	3.76	762.8	225.4	422.0	115.4	7.41	980	60	1
301	10	761.7	23	420	4.2	1	3.76	762.0	224.9	422.8	114.3		952		0
302	10	760.6	24	420	4.2	1	3.76	760.8	225.0	422.6	113.2		977		0
319	10	760.4	25	420	4.2	1	3.76	760.7	224.9	422.8	113.0	7.42	966	55	1
320	10	761.2	25	420	4.2	1	3.76	761.7	224.9	422.8	114.0		954		0
321	10	760.0	25	420	4.2	1	3.76	760.2	224.8	422.8	112.6		977		0
322	10	761.5	26	420	4.2	1	3.76	761.8	224.8	423.0	114.0		988		0
323	10	761.1	23	420	4.2	1	3.76	761.1	225.0	422.6	113.5	7.21	1005	62	1
324	10	759.4	24	420	4.2	1	3.76	760.2	224.8	422.7	112.7		994		0
327	10	759.9	23	420	4.2	1	3.76	760.4	224.6	423.0	112.8	7.09	1005	68	1
328	10	761.0	24	420	4.2	1	3.76	761.0	224.9	422.8	113.3	7.18	989	65	1
329	10	760.4	24	420	4.2	1	3.76	760.4	224.9	422.7	112.8		987		0
330	10	760.5	25	420	4.2	1	3.76	761.0	224.9	422.8	113.3	7.03	1001	68	1
331	10	759.3	25	420	4.2	1	3.76	759.8	225.0	422.6	112.2		993		0
332	10	759.8	23	420	4.2	1	3.76	760.0	225.0	422.6	112.4	7.06	1007	63	1
333	10	759.9	24	420	4.2	1	3.76	760.3	225.0	422.5	112.8	7.24	1004	52	1
334	10	759.6	24	420	4.2	1	3.76	760.2	225.0	422.3	112.9	7.18	989	60	1
335	10	761.0	25	420	4.2	1	3.76	761.5	225.0	422.6	113.9		991		0
338	10	759.6	26	420	4.2	1	3.76	760.0	225.0	423.0	112.0	7.46	983	60	1
358	10	759.8	23	420	4.2	1	3.76	760.2	225.1	422.5	112.6		937		0
359	10	762.2	24	420	4.2	1	3.76	762.5	225.0	422.6	114.9		936		0
360	10	761.3	25	420	4.2	1	3.76	761.5	224.8	422.8	113.9		952		0

D.3 C_2H_4

Table D.3: C_6H_{14} LOC ignition data for 200A cylinder.

Shot #	H **(in)**	P_0 **(torr)**	T_0 **(°C)**	I **(A)**	**Volt (V)**	ϕ	β	P_{tot} **(torr)**	$P_{C_6H_{14}}$ **(torr)**	P_{N_2} **(torr)**	P_{O_2} **(torr)**	T_w **(K)**	P_{max} **(atm)**	t_{ign} **(s)**	**Ign (0/1)**
339	10	759.4	26	420	4.2	1	3.76	760.0	49.8	560.7	149.5	1030	8.35	67	1
340	10	761.5	26	420	4.2	1	3.76	761.8	49.8	560.9	151.1	1019	8.46	73	1
341	10	760.8	27	420	4.2	1	3.76	761.4	49.7	561.0	150.7	1016	8.16	84	1
342	10	759.1	27	420	4.2	1	3.76	760.0	49.8	562.1	148.1	1008	8.16	90	1
343	10	758.8	28	420	4.2	1	3.76	760.0	49.8	560.9	149.3	1005	8.31	160	1
344	10	759.8	23	420	4.2	1	3.76	760.1	49.9	560.8	149.4	994	8.37	240	1
345	10	760.2	26	420	4.2	1	3.76	760.9	49.9	560.5	150.5	981			0
346	10	760.1	26	420	4.2	1	3.76	760.5	49.8	561.0	149.7	995	8.36	175	1
347	10	760.8	26	420	4.2	1	3.76	760.9	49.8	561.1	150.0	989			0
348	10	759.9	27	420	4.2	1	3.76	760.5	49.8	561.2	149.5	992	8.30	217	1
349	10	759.5	28	420	4.2	1	3.76	760.0	49.9	560.6	149.5	986			0
350	10	759.2	28	420	4.2	1	3.76	760.0	49.9	560.9	149.2	965			0
351	10	759.4	28	420	4.2	1	3.76	760.1	49.8	560.9	149.4	1000	8.00	130	1
352	10	760.0	29	420	4.2	1	3.76	760.8	49.9	560.8	150.1	994			0
353	10	761.0	23	420	4.2	1	3.76	761.2	49.8	560.8	150.6	995			0
354	10	760.2	25	420	4.2	1	3.76	760.9	49.8	561.1	150.0	1001			0
355	10	759.7	23	420	4.2	1	3.76	760.1	49.9	560.9	149.3	1009	8.36	110	1
356	10	759.6	24	420	4.2	1	3.76	760.1	49.8	560.8	149.5	1010	8.20	115	1
357	10	759.5	25	420	4.2	1	3.76	760.0	49.8	561.1	149.1	999			0

D.4 LOC: C_6H_{14}

Table D.4: C_6H_{14} LOC ignition data for 200A cylinder.

Shot #	H **(in)**	P_0 **(torr)**	T_0 **(°C)**	I **(A)**	**Volt (V)**	ϕ	β	P_{tot} **(torr)**	$P_{C_6H_{14}}$ **(torr)**	P_{N_2} **(torr)**	P_{O_2} **(torr)**	T_w **(K)**	P_{max} **(atm)**	t_{ign} **(s)**	**Ign (0/1)**
487	10	759.5	23	550	5	1.00	9.00	760.1	8.0	676.9	75.2	1200			0
488	10	759.6	25	550	5	1.00	8.50	760.1	8.3	672.7	79.1	1200			0
489	10	759.3	25	550	5	1.00	8.00	760.0	8.8	667.6	83.6	1200	1.71	45	1
490	10	759.4	22	550	5	1.00	8.25	760.1	8.6	670.4	81.1	1200	1.44	45	1
491	10	759.5	23	550	5	1.00	8.35	760.0	8.5	671.4	80.1	1200	1.36	45	1
492	10	759.5	24	550	5	1.00	8.45	760.2	8.4	672.2	79.6	1200		43	1
493	10	759.7	24	550	5	1.00	8.60	760.1	8.2	673.5	78.4	1200			1
494	10	759.3	23	550	5	1.00	3.76	760.0	16.4	587.7	155.9	1200			1
495	10	758.0	25	550	5	1.00	3.76	759.5	16.6	587.2	155.7	1200		28	1
496	10	759.5	23	550	5	1.00	5.64	760.2	11.9	635.3	113.0	1200		36	1
497	10	759.5	24	550	5	1.00	7.52	760.1	9.4	662.8	87.9	1200	2.18	41	1
498	10	759.5	22	550	5	1.00	8.60	760.1	8.2	673.6	78.3	1200	1.39		1
499	10	759.5	23	550	5	1.00	8.60	760.1	8.2	673.5	78.4	1200	1.38		1
500	10	759.9	23	550	5	1.00	8.60	760.2	8.1	673.5	78.6	1200	1.37		1
501	10	759.8	24	550	5	1.00	3.76	761.0	16.3	587.5	157.2	1200	8.07		1

Appendix E

200A CYLINDER INTERFEROGRAMS

This appendix presents interferogram image sequences for selected shots which are representative of each of the twelve n-hexane/air mixtures that were presented in Chapter 3. All combinations of P_0 = 1, 0.7, 0.466, 0.238 atm and β = 3.76, 5.64, 7.52 (X_{O_2} = 20.6, 14.8, 11.6%) are included here. Appendix E.2 presents images from cases where the boundary layer (BL) is perturbed and unsteady prior to ignition: (1) Shot 419: vortices were formed prior to ignition resulting in a highly corrugated flame front and (2) Shot 421: A weaker perturbation in the BL resulted in a corrugated flame developing relatively rapidly in contrast to typical laminar flame propagation events. Instances of these two events were uncommon and likely related to some unsteady flow disturbance due to early BL interaction with heated fluid pockets developed in the initial transient heating period. Additional Limiting Oxygen Concentration (LOC) image sequences are also included in Appendix E.2 (e.g. for β > 7.52). These conditions also show vortex formation and flame puffing over long periods similar to in Section 3.5 for β = 8.6.

Ignition kernels and flame fronts are also overlaid with dotted lines and pointed out by arrows in certain cases where the visualization is difficult (e.g. for early stages of ignition and flame propagation and low P_0 mixtures). The field of view captures the vertical range of heights of 4 – 7.5 in. In most cases the ignition kernel occurs out of frame (above, in the top 2.5 in region of the cylinder) and the flame propagates into frame giving the first indication of ignition in these sequences. All images have also been brightened for presentation.

E.1 Nitrogen enriched and low pressure n-hexane/air

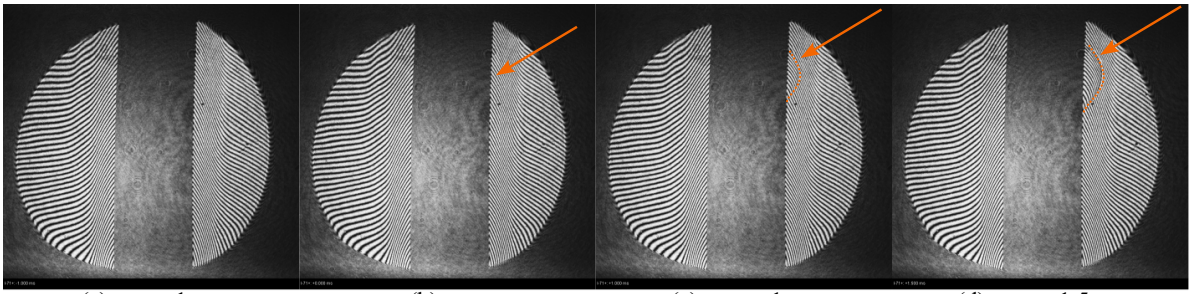

(a) τ_{ign} - 1 ms (b) τ_{ign} (c) τ_{ign} + 1 ms (d) τ_{ign} + 1.5 ms

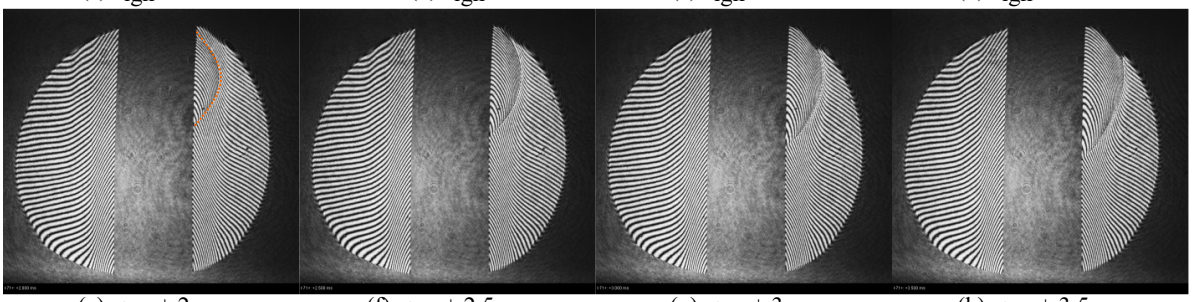

(e) τ_{ign} + 2 ms (f) τ_{ign} + 2.5 ms (g) τ_{ign} + 3 ms (h) τ_{ign} + 3.5 ms

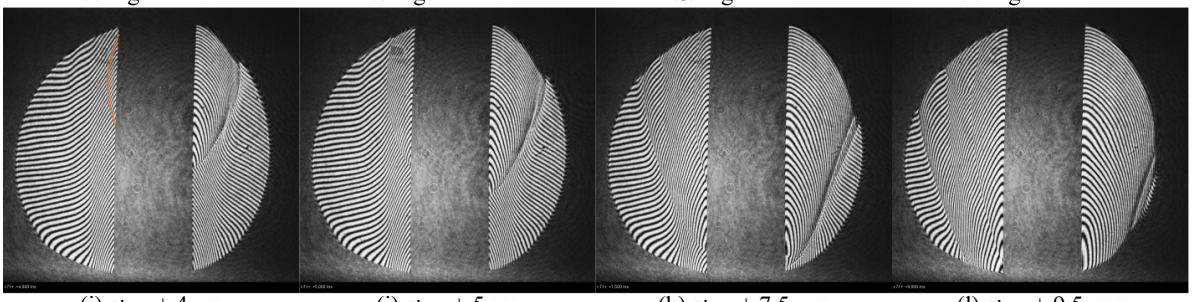

(i) τ_{ign} + 4 ms (j) τ_{ign} + 5 ms (k) τ_{ign} + 7.5 ms (l) τ_{ign} + 9.5 ms

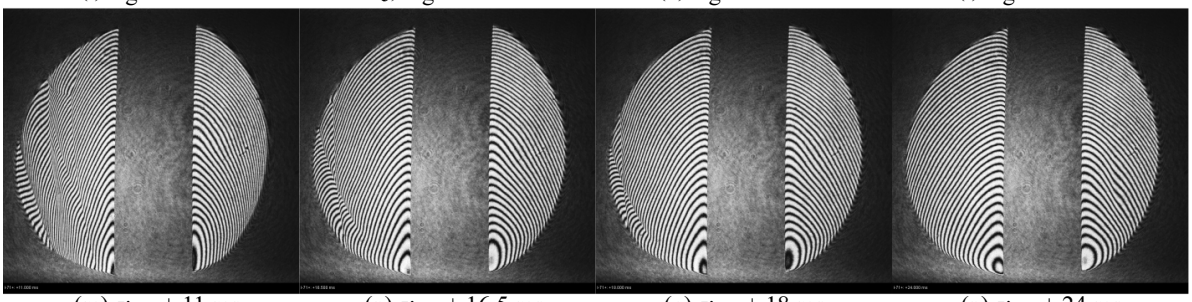

(m) τ_{ign} + 11 ms (n) τ_{ign} + 16.5 ms (o) τ_{ign} + 18 ms (p) τ_{ign} + 24 ms

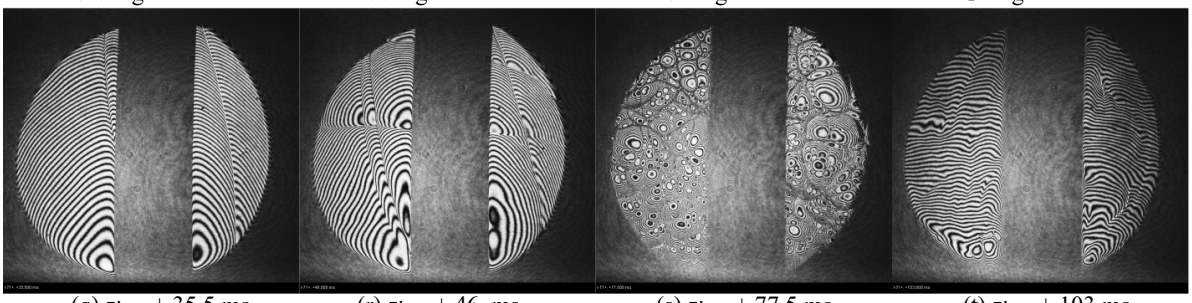

(q) τ_{ign} + 35.5 ms (r) τ_{ign} + 46 ms (s) τ_{ign} + 77.5 ms (t) τ_{ign} + 103 ms

Figure E.1: Shot 495: Interferogram image sequence for P_0 = 1 atm, β = 3.76.

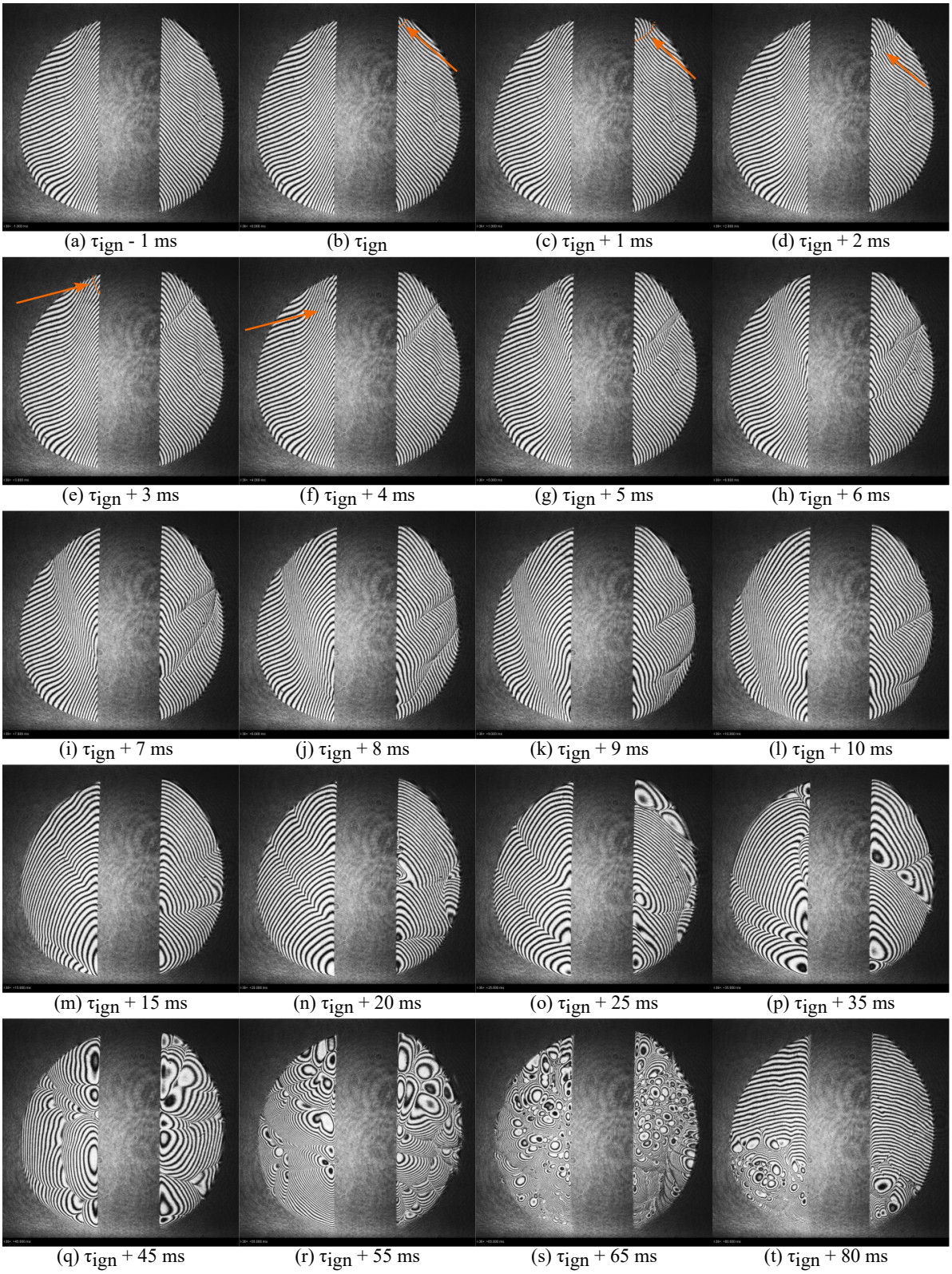

(a) τ_{ign} - 1 ms (b) τ_{ign} (c) τ_{ign} + 1 ms (d) τ_{ign} + 2 ms

(e) τ_{ign} + 3 ms (f) τ_{ign} + 4 ms (g) τ_{ign} + 5 ms (h) τ_{ign} + 6 ms

(i) τ_{ign} + 7 ms (j) τ_{ign} + 8 ms (k) τ_{ign} + 9 ms (l) τ_{ign} + 10 ms

(m) τ_{ign} + 15 ms (n) τ_{ign} + 20 ms (o) τ_{ign} + 25 ms (p) τ_{ign} + 35 ms

(q) τ_{ign} + 45 ms (r) τ_{ign} + 55 ms (s) τ_{ign} + 65 ms (t) τ_{ign} + 80 ms

Figure E.2: Shot 450: Interferogram image sequence for P_0 = 0.7 atm, β = 3.76.

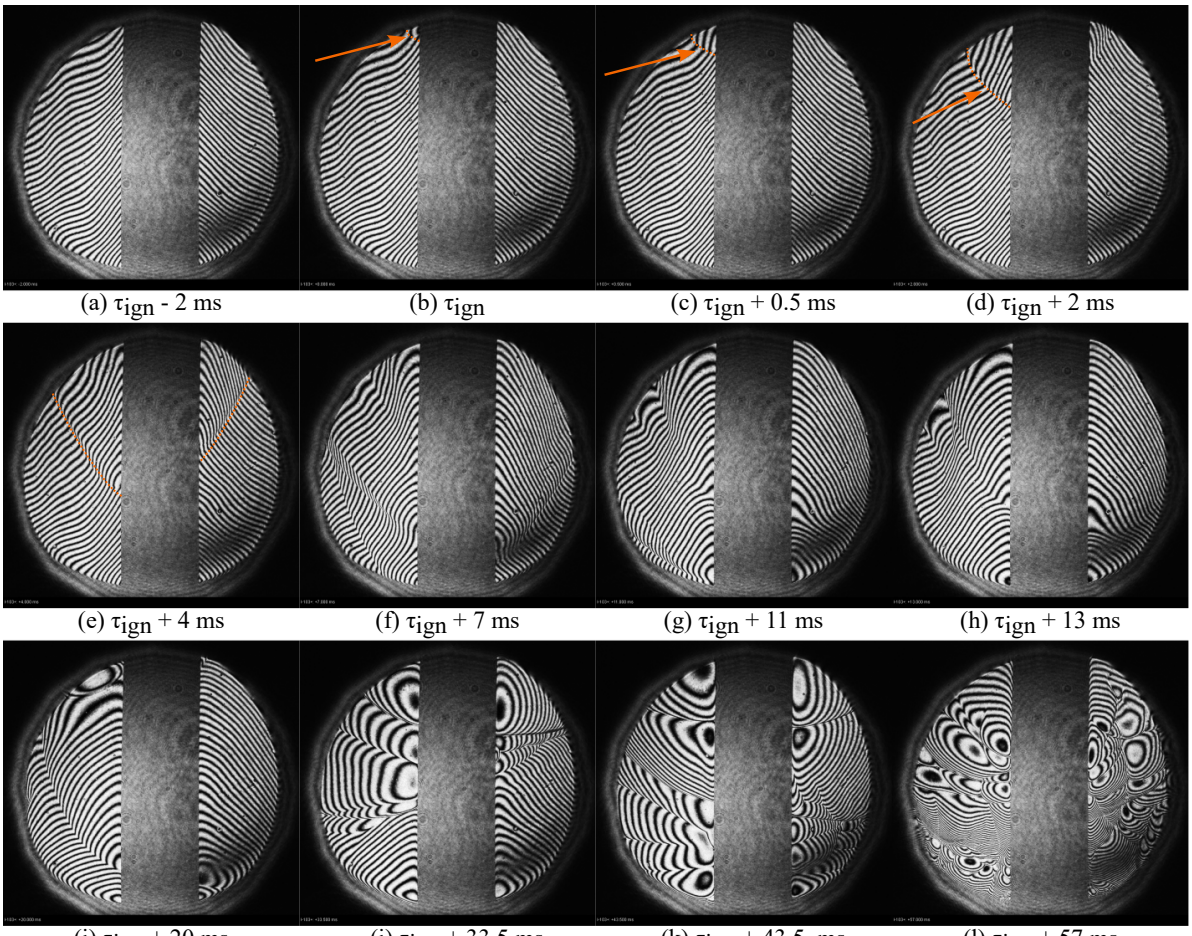

(a) τ_{ign} - 2 ms (b) τ_{ign} (c) τ_{ign} + 0.5 ms (d) τ_{ign} + 2 ms

(e) τ_{ign} + 4 ms (f) τ_{ign} + 7 ms (g) τ_{ign} + 11 ms (h) τ_{ign} + 13 ms

(i) τ_{ign} + 20 ms (j) τ_{ign} + 33.5 ms (k) τ_{ign} + 43.5 ms (l) τ_{ign} + 57 ms

Figure E.3: Shot 373: Interferogram image sequence for $P_0 = 0.466$ atm, $\beta = 3.76$.

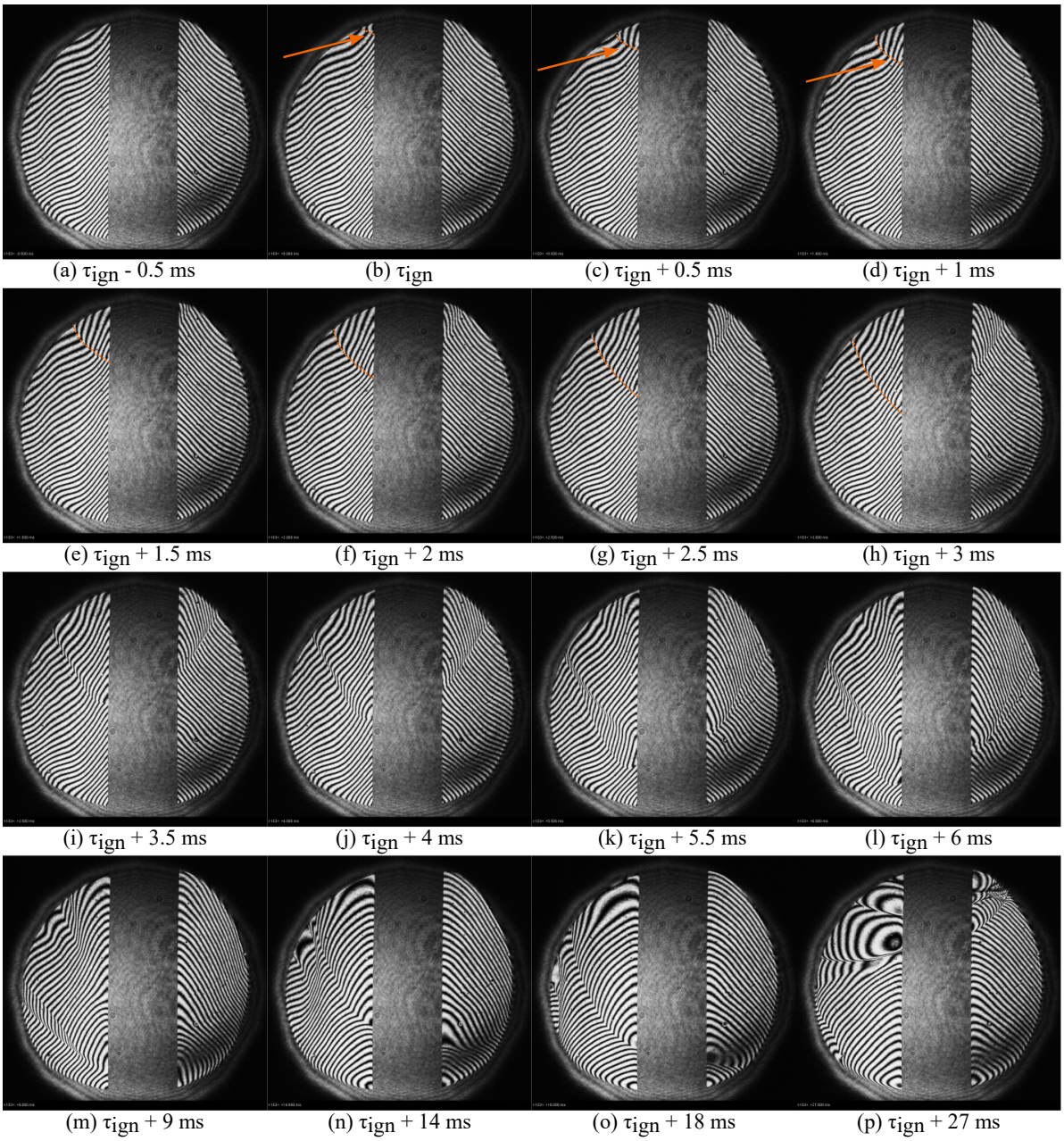

(a) τ_{ign} - 0.5 ms (b) τ_{ign} (c) τ_{ign} + 0.5 ms (d) τ_{ign} + 1 ms

(e) τ_{ign} + 1.5 ms (f) τ_{ign} + 2 ms (g) τ_{ign} + 2.5 ms (h) τ_{ign} + 3 ms

(i) τ_{ign} + 3.5 ms (j) τ_{ign} + 4 ms (k) τ_{ign} + 5.5 ms (l) τ_{ign} + 6 ms

(m) τ_{ign} + 9 ms (n) τ_{ign} + 14 ms (o) τ_{ign} + 18 ms (p) τ_{ign} + 27 ms

Figure E.4: Shot 378: Interferogram image sequence for $P_0 = 0.238$ atm, $\beta = 3.76$.

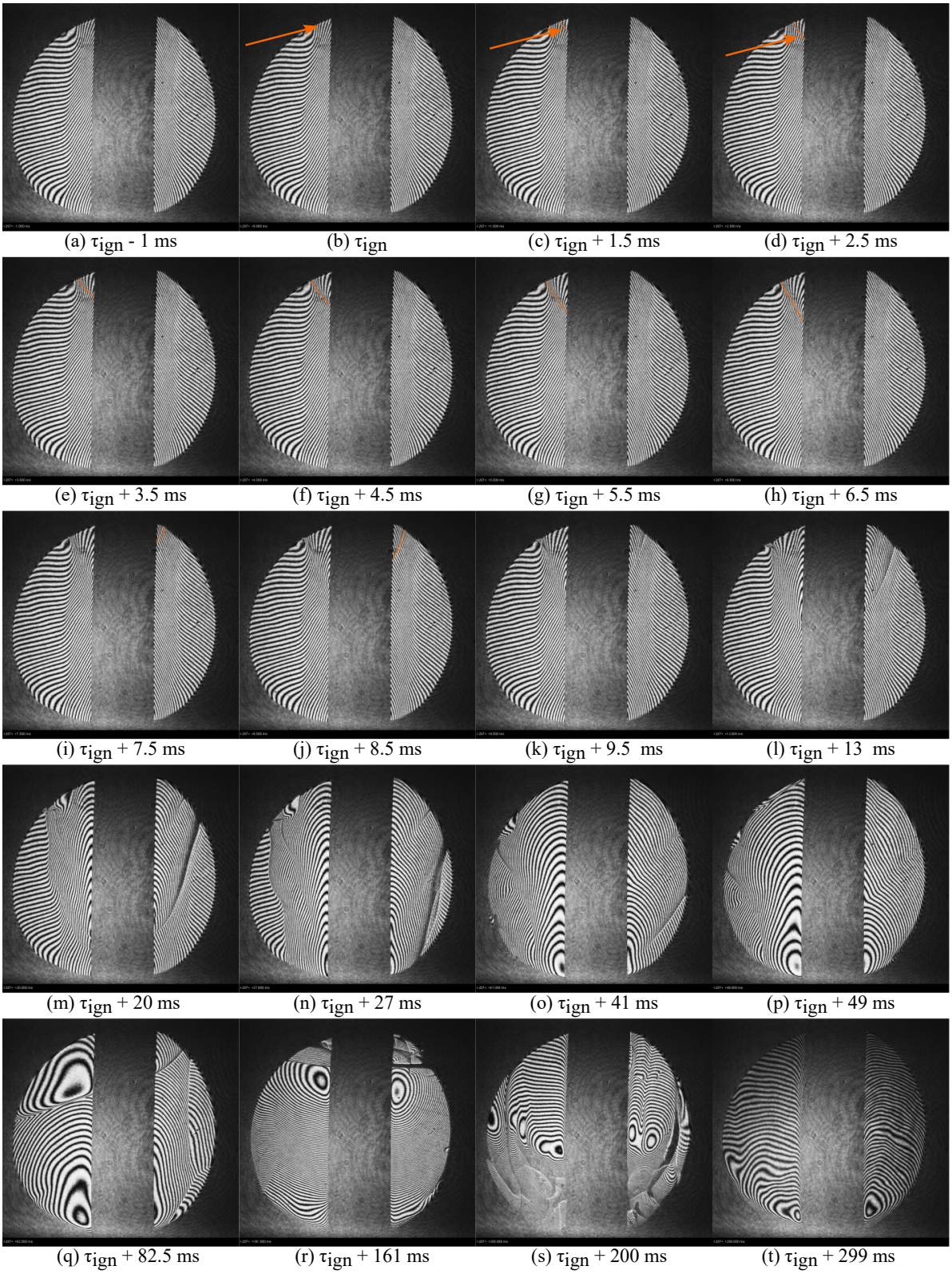

(a) τ_{ign} - 1 ms (b) τ_{ign} (c) τ_{ign} + 1.5 ms (d) τ_{ign} + 2.5 ms

(e) τ_{ign} + 3.5 ms (f) τ_{ign} + 4.5 ms (g) τ_{ign} + 5.5 ms (h) τ_{ign} + 6.5 ms

(i) τ_{ign} + 7.5 ms (j) τ_{ign} + 8.5 ms (k) τ_{ign} + 9.5 ms (l) τ_{ign} + 13 ms

(m) τ_{ign} + 20 ms (n) τ_{ign} + 27 ms (o) τ_{ign} + 41 ms (p) τ_{ign} + 49 ms

(q) τ_{ign} + 82.5 ms (r) τ_{ign} + 161 ms (s) τ_{ign} + 200 ms (t) τ_{ign} + 299 ms

Figure E.5: Shot 496: Interferogram image sequence for P_0 = 1 atm, β = 5.64.

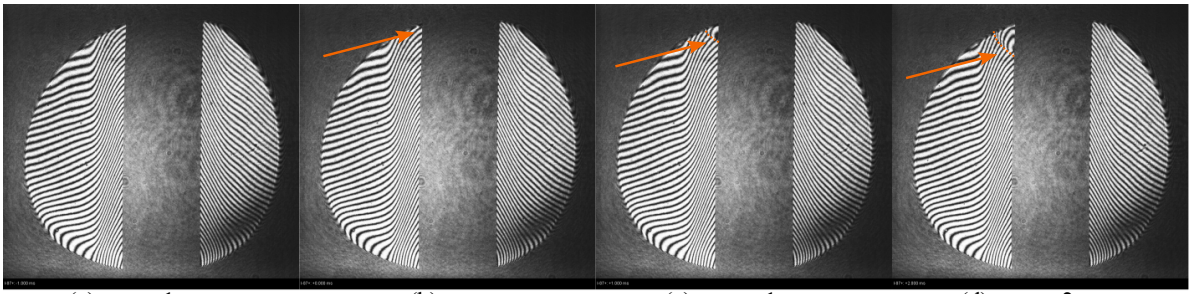

(a) τ_{ign} - 1 ms (b) τ_{ign} (c) τ_{ign} + 1 ms (d) τ_{ign} + 2 ms

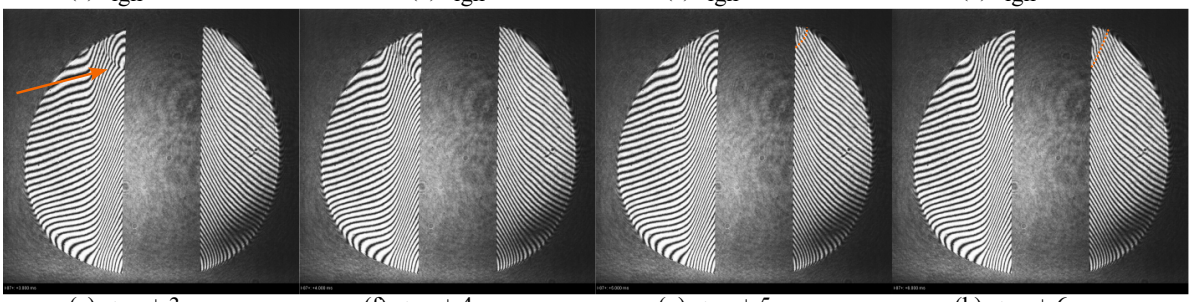

(e) τ_{ign} + 3 ms (f) τ_{ign} + 4 ms (g) τ_{ign} + 5 ms (h) τ_{ign} + 6 ms

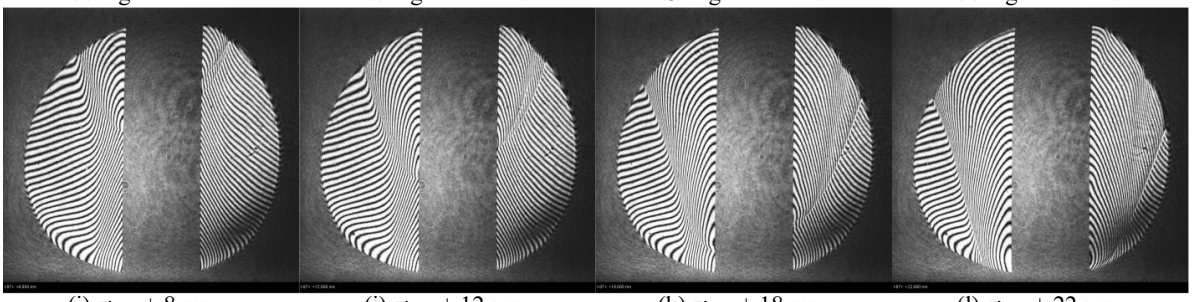

(i) τ_{ign} + 8 ms (j) τ_{ign} + 12 ms (k) τ_{ign} + 18 ms (l) τ_{ign} + 22 ms

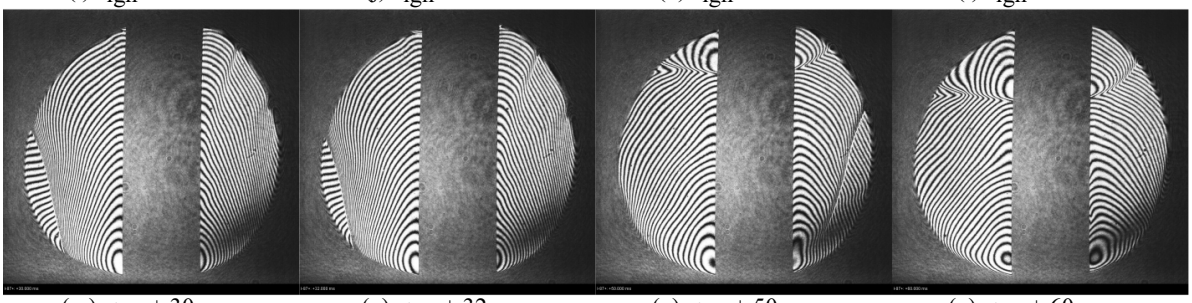

(m) τ_{ign} + 30 ms (n) τ_{ign} + 32 ms (o) τ_{ign} + 50 ms (p) τ_{ign} + 60 ms

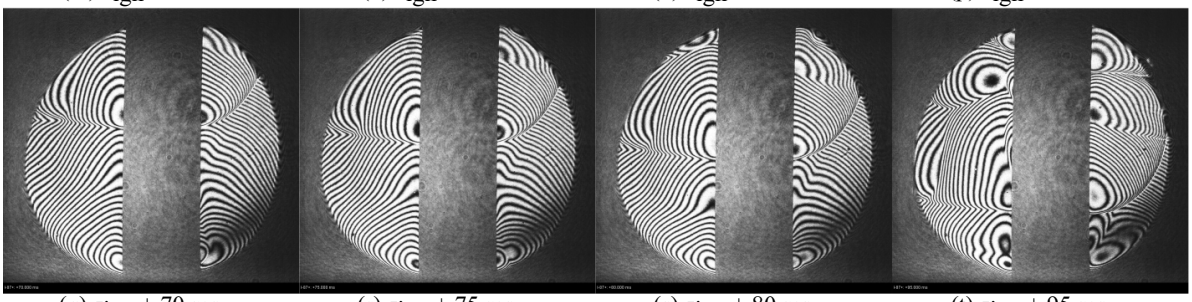

(q) τ_{ign} + 70 ms (r) τ_{ign} + 75 ms (s) τ_{ign} + 80 ms (t) τ_{ign} + 95 ms

Figure E.6: Shot 432: Interferogram image sequence for P_0 = 0.7 atm, β = 5.64.

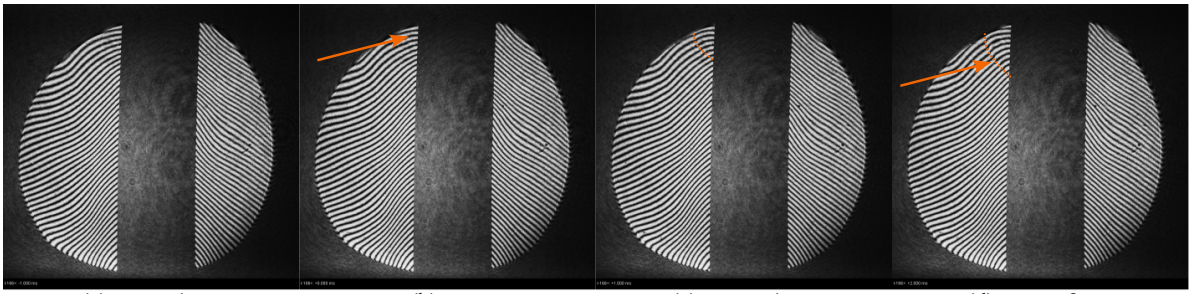

(a) τ_{ign} - 1 ms (b) τ_{ign} (c) τ_{ign} + 1 ms (d) τ_{ign} + 2 ms

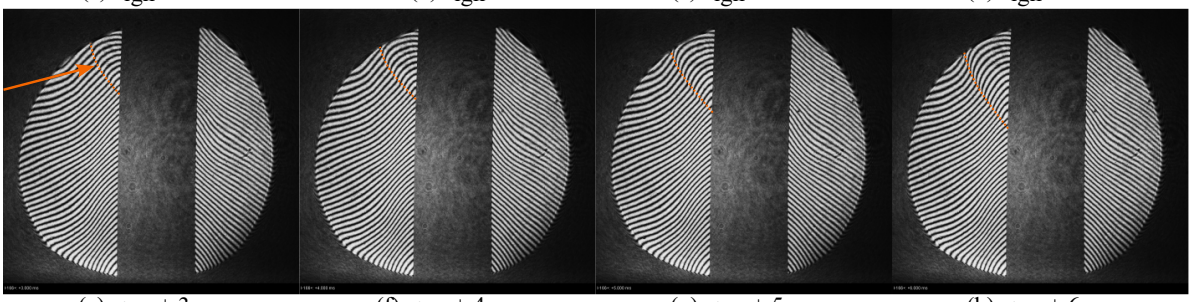

(e) τ_{ign} + 3 ms (f) τ_{ign} + 4 ms (g) τ_{ign} + 5 ms (h) τ_{ign} + 6 ms

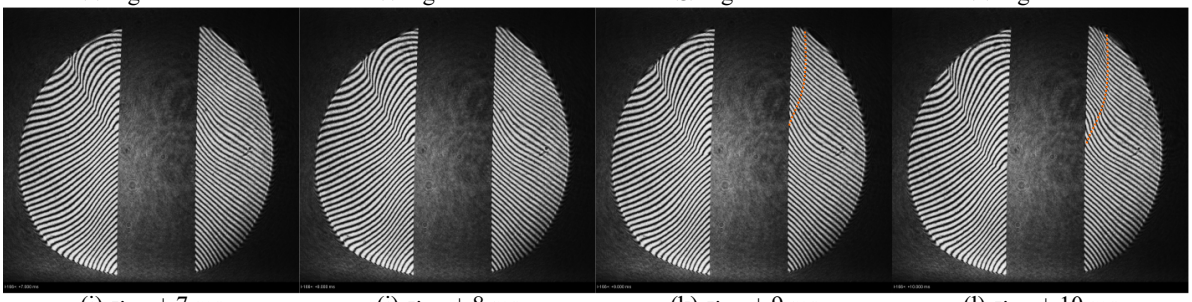

(i) τ_{ign} + 7 ms (j) τ_{ign} + 8 ms (k) τ_{ign} + 9 ms (l) τ_{ign} + 10 ms

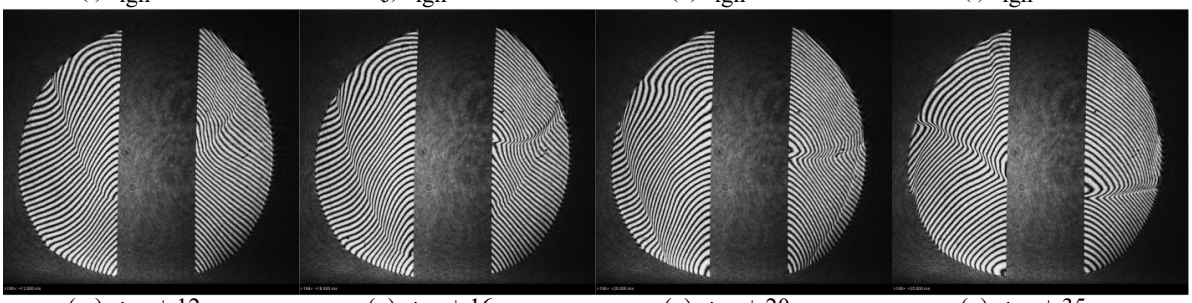

(m) τ_{ign} + 12 ms (n) τ_{ign} + 16 ms (o) τ_{ign} + 20 ms (p) τ_{ign} + 35 ms

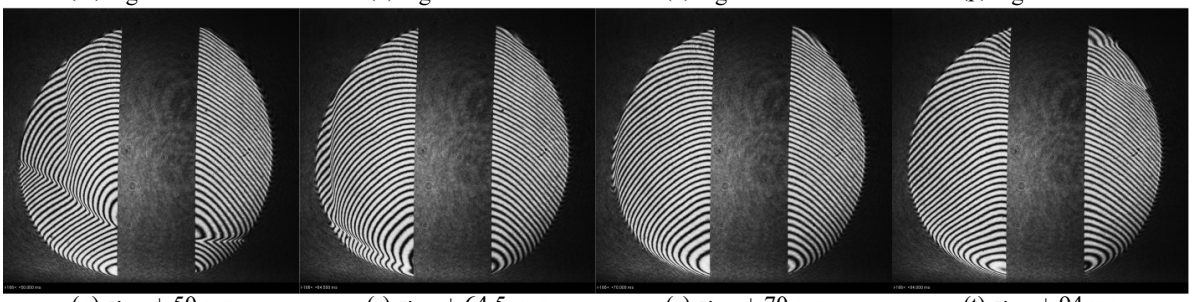

(q) τ_{ign} + 50 ms (r) τ_{ign} + 64.5 ms (s) τ_{ign} + 70 ms (t) τ_{ign} + 94 ms

Figure E.7: Shot 486: Interferogram image sequence for $P_0 = 0.466$ atm, $\beta = 5.64$.

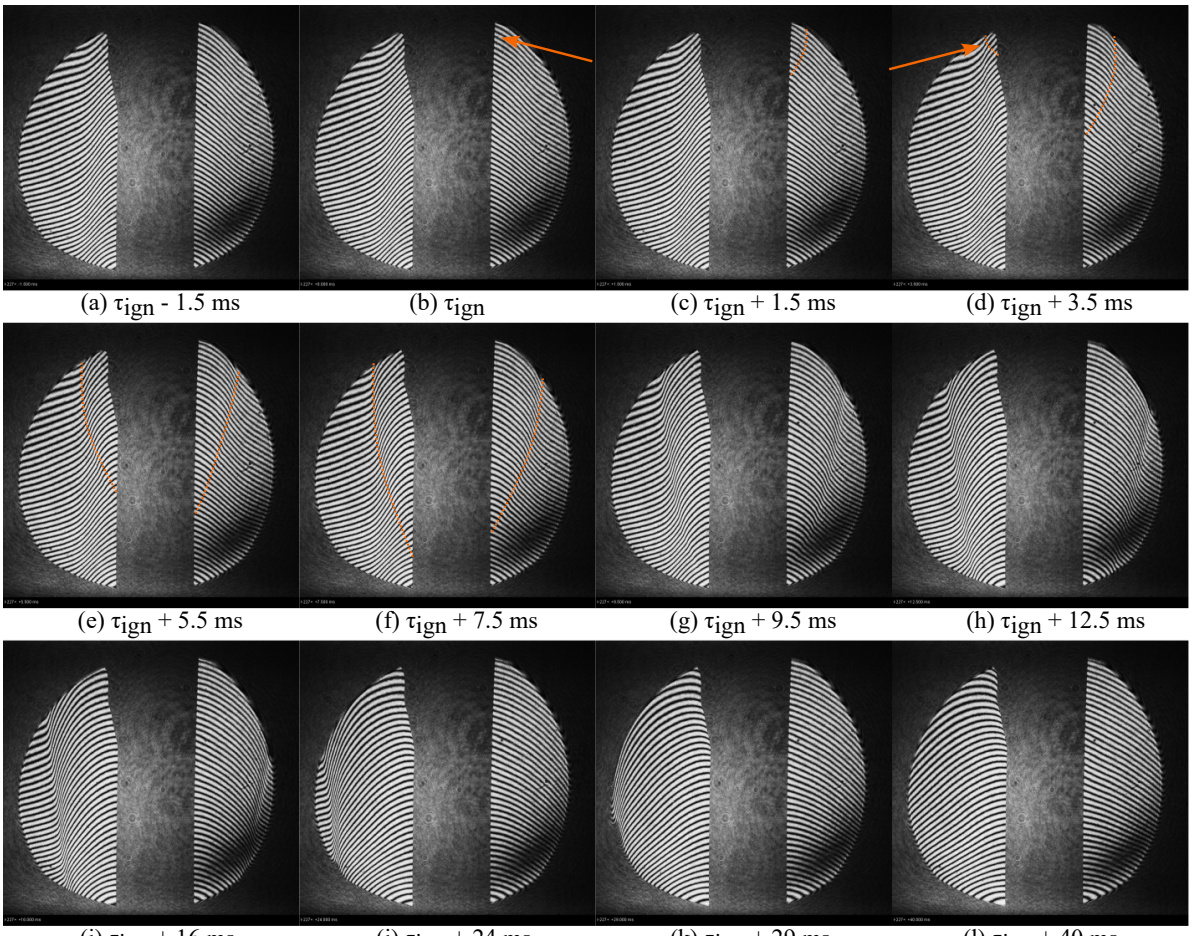

(a) τ_{ign} - 1.5 ms (b) τ_{ign} (c) τ_{ign} + 1.5 ms (d) τ_{ign} + 3.5 ms

(e) τ_{ign} + 5.5 ms (f) τ_{ign} + 7.5 ms (g) τ_{ign} + 9.5 ms (h) τ_{ign} + 12.5 ms

(i) τ_{ign} + 16 ms (j) τ_{ign} + 24 ms (k) τ_{ign} + 29 ms (l) τ_{ign} + 40 ms

Figure E.8: Shot 474: Interferogram image sequence for $P_0 = 0.238$ atm, $\beta = 5.64$.

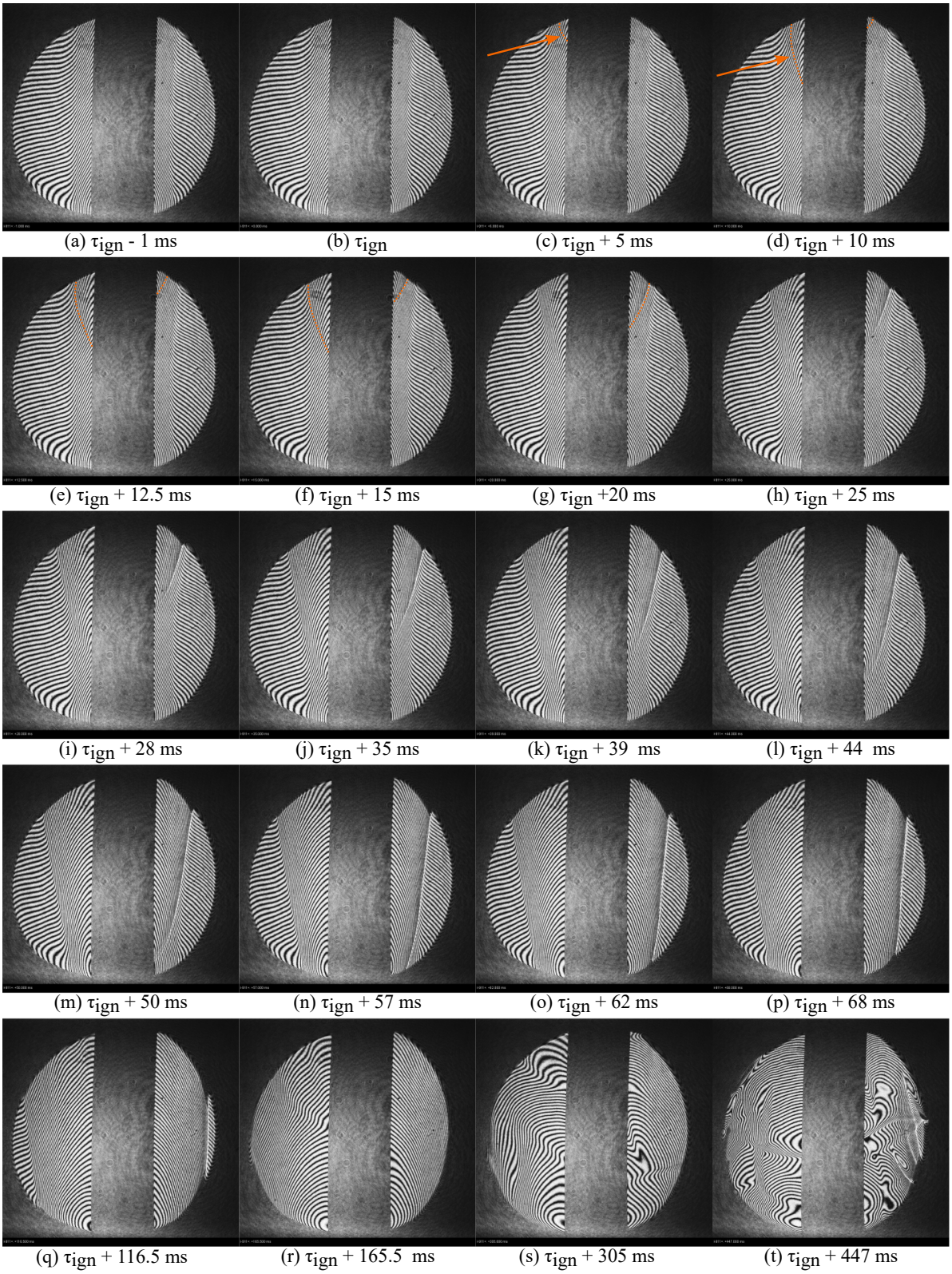

(a) τ_{ign} - 1 ms (b) τ_{ign} (c) τ_{ign} + 5 ms (d) τ_{ign} + 10 ms

(e) τ_{ign} + 12.5 ms (f) τ_{ign} + 15 ms (g) τ_{ign} +20 ms (h) τ_{ign} + 25 ms

(i) τ_{ign} + 28 ms (j) τ_{ign} + 35 ms (k) τ_{ign} + 39 ms (l) τ_{ign} + 44 ms

(m) τ_{ign} + 50 ms (n) τ_{ign} + 57 ms (o) τ_{ign} + 62 ms (p) τ_{ign} + 68 ms

(q) τ_{ign} + 116.5 ms (r) τ_{ign} + 165.5 ms (s) τ_{ign} + 305 ms (t) τ_{ign} + 447 ms

Figure E.9: Shot 497: Interferogram image sequence for P_0 = 1 atm, β = 7.52.

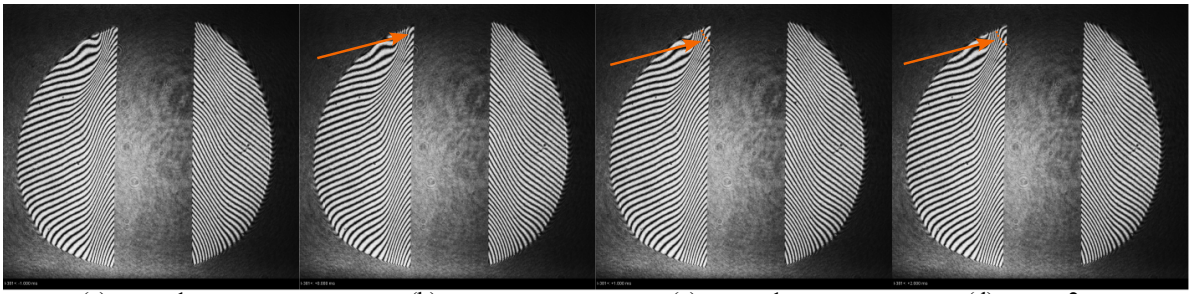

(a) τ_{ign} - 1 ms (b) τ_{ign} (c) τ_{ign} + 1 ms (d) τ_{ign} + 2 ms

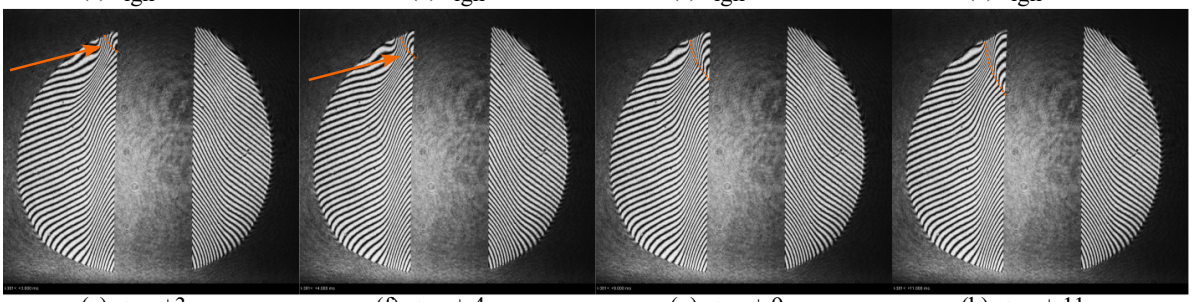

(e) τ_{ign} +3 ms (f) τ_{ign} + 4 ms (g) τ_{ign} + 9 ms (h) τ_{ign} + 11 ms

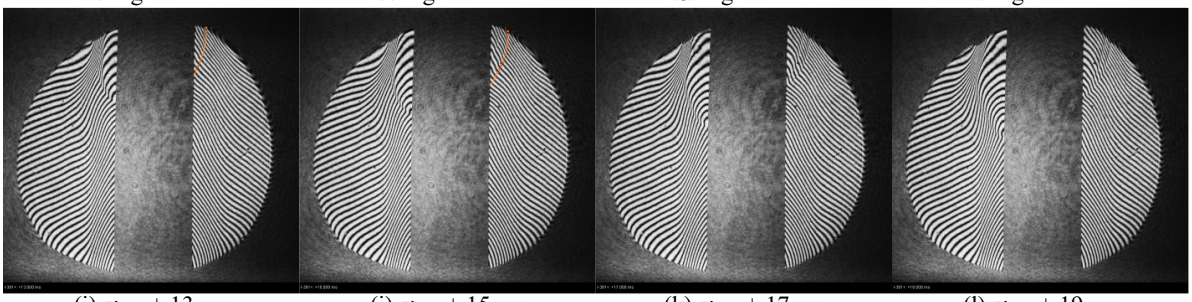

(i) τ_{ign} + 13 ms (j) τ_{ign} + 15 ms (k) τ_{ign} + 17 ms (l) τ_{ign} + 19 ms

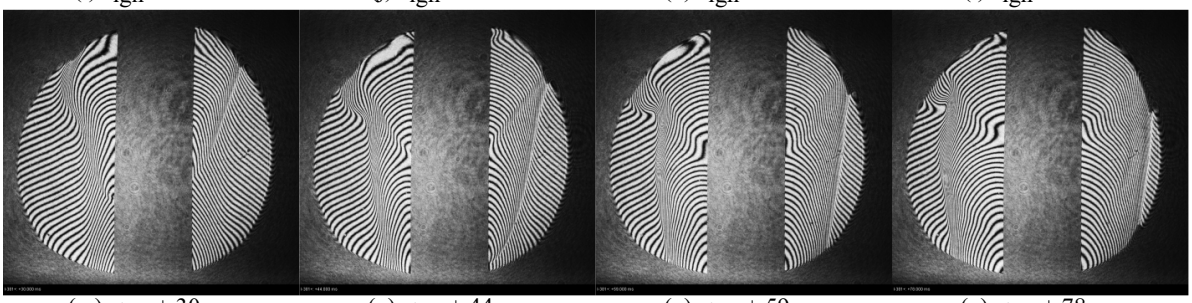

(m) τ_{ign} + 30 ms (n) τ_{ign} + 44 ms (o) τ_{ign} + 59 ms (p) τ_{ign} + 78 ms

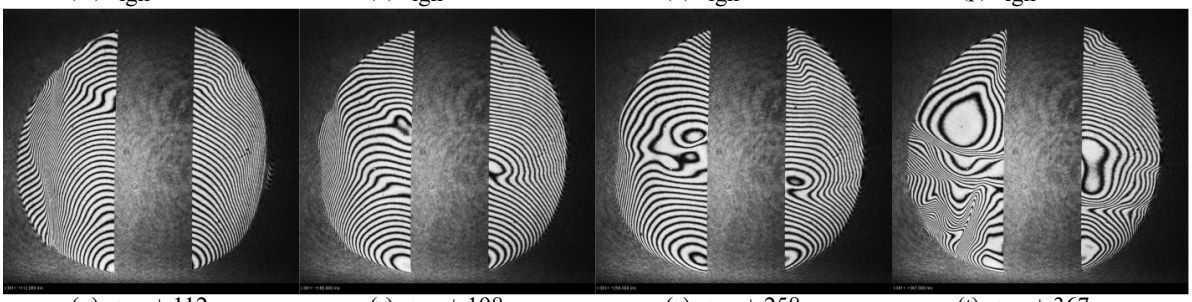

(q) τ_{ign} + 112 ms (r) τ_{ign} + 198 ms (s) τ_{ign} + 258 ms (t) τ_{ign} + 367 ms

Figure E.10: Shot 426: Interferogram image sequence for P_0 = 0.7 atm, β = 7.52.

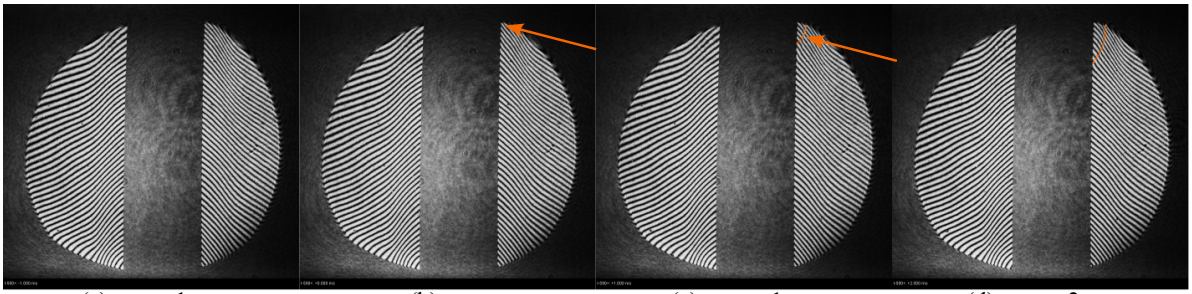

(a) τ_{ign} - 1 ms (b) τ_{ign} (c) τ_{ign} + 1 ms (d) τ_{ign} + 2 ms

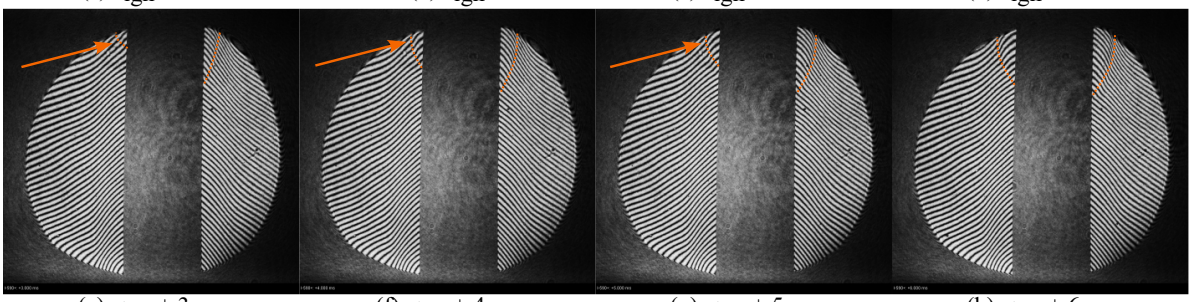

(e) τ_{ign} + 3 ms (f) τ_{ign} + 4 ms (g) τ_{ign} + 5 ms (h) τ_{ign} + 6 ms

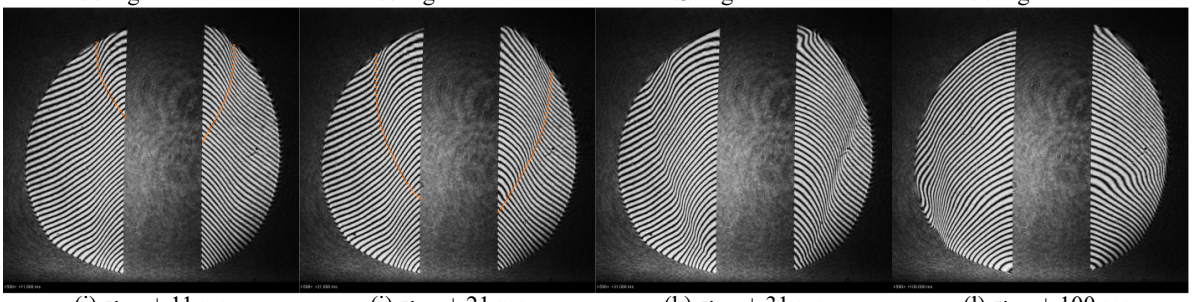

(i) τ_{ign} + 11 ms (j) τ_{ign} + 21 ms (k) τ_{ign} + 31 ms (l) τ_{ign} + 100 ms

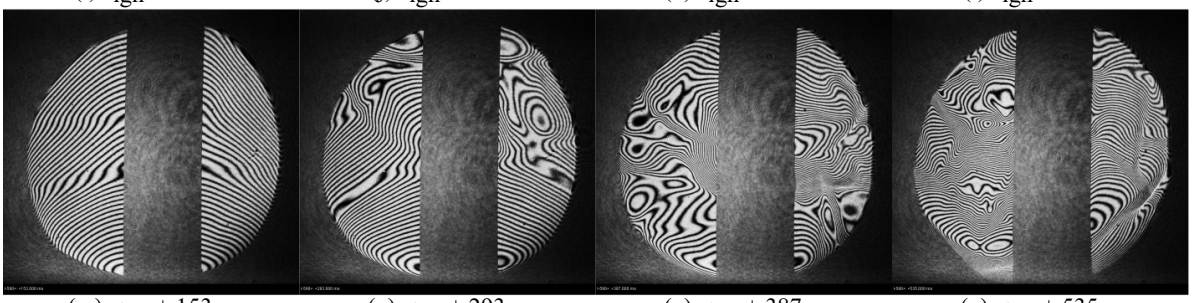

(m) τ_{ign} + 153 ms (n) τ_{ign} + 293 ms (o) τ_{ign} + 387 ms (p) τ_{ign} + 535 ms

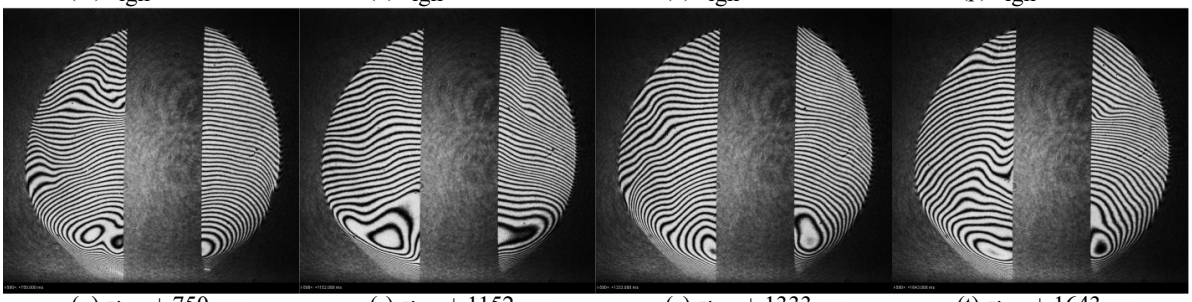

(q) τ_{ign} + 750 ms (r) τ_{ign} + 1152 ms (s) τ_{ign} + 1333 ms (t) τ_{ign} + 1643 ms

Figure E.11: Shot 435: Interferogram image sequence for P_0 = 0.466 atm, β = 7.52.

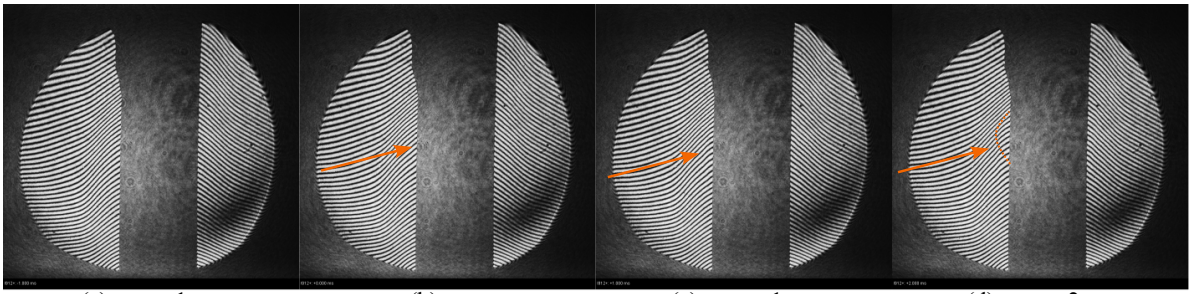

(a) τ_{ign} - 1 ms (b) τ_{ign} (c) τ_{ign} + 1 ms (d) τ_{ign} + 2 ms

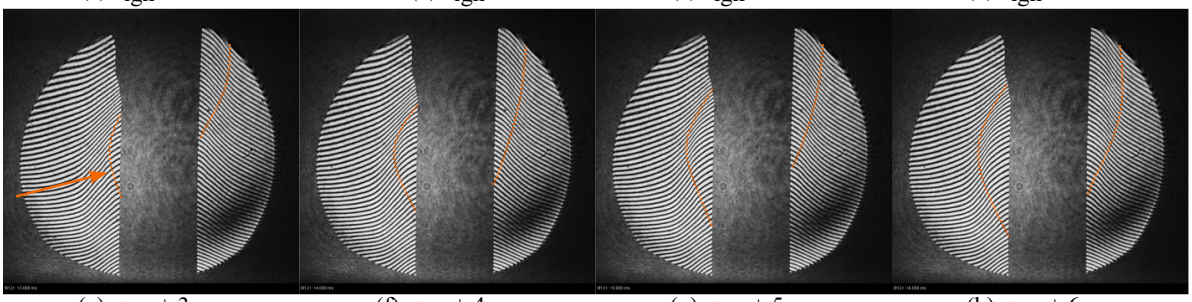

(e) τ_{ign} + 3 ms (f) τ_{ign} + 4 ms (g) τ_{ign} + 5 ms (h) τ_{ign} + 6 ms

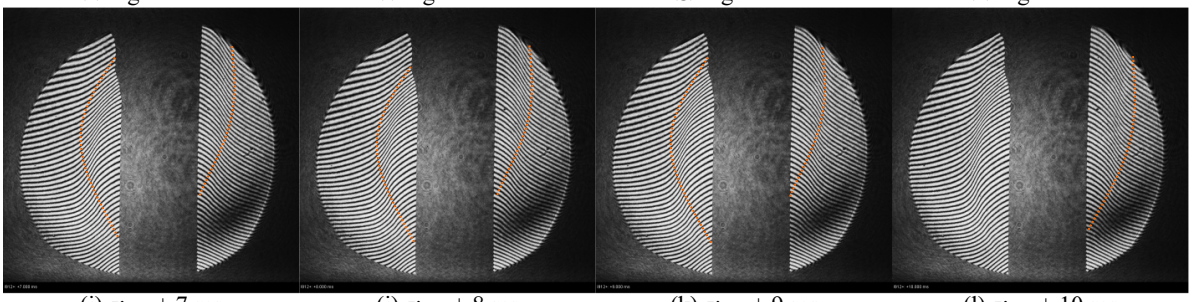

(i) τ_{ign} + 7 ms (j) τ_{ign} + 8 ms (k) τ_{ign} + 9 ms (l) τ_{ign} + 10 ms

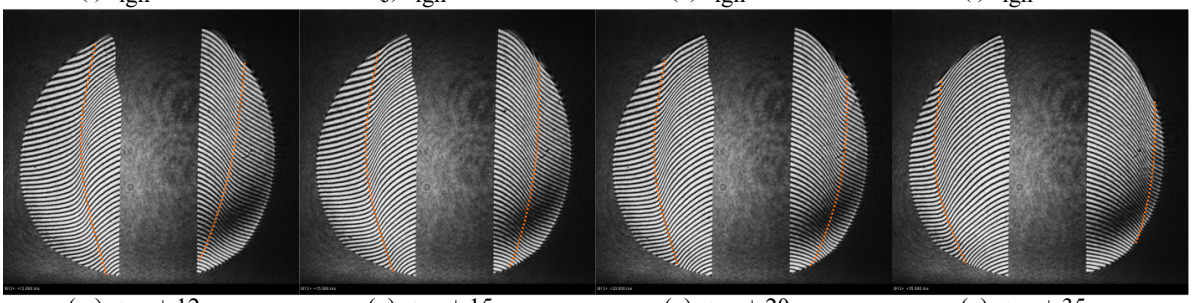

(m) τ_{ign} + 12 ms (n) τ_{ign} + 15 ms (o) τ_{ign} + 20 ms (p) τ_{ign} + 35 ms

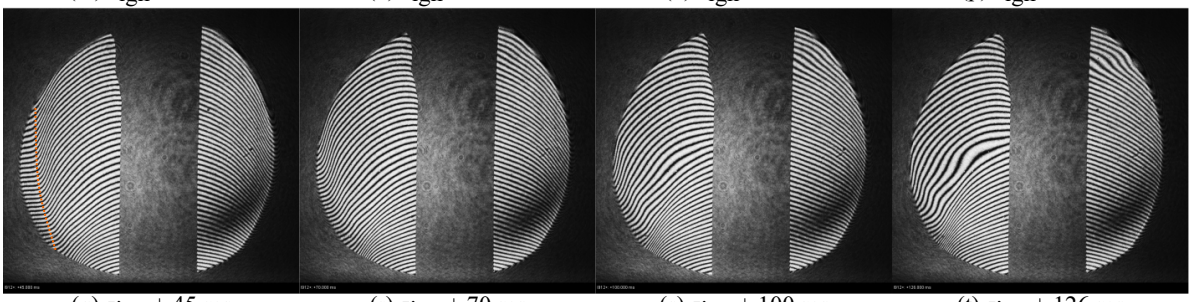

(q) τ_{ign} + 45 ms (r) τ_{ign} + 70 ms (s) τ_{ign} + 100 ms (t) τ_{ign} + 126 ms

Figure E.12: Shot 466: Interferogram image sequence for $P_0 = 0.238$ atm, $\beta = 7.52$.

E.2 Unsteady BL ignition and LOC shots

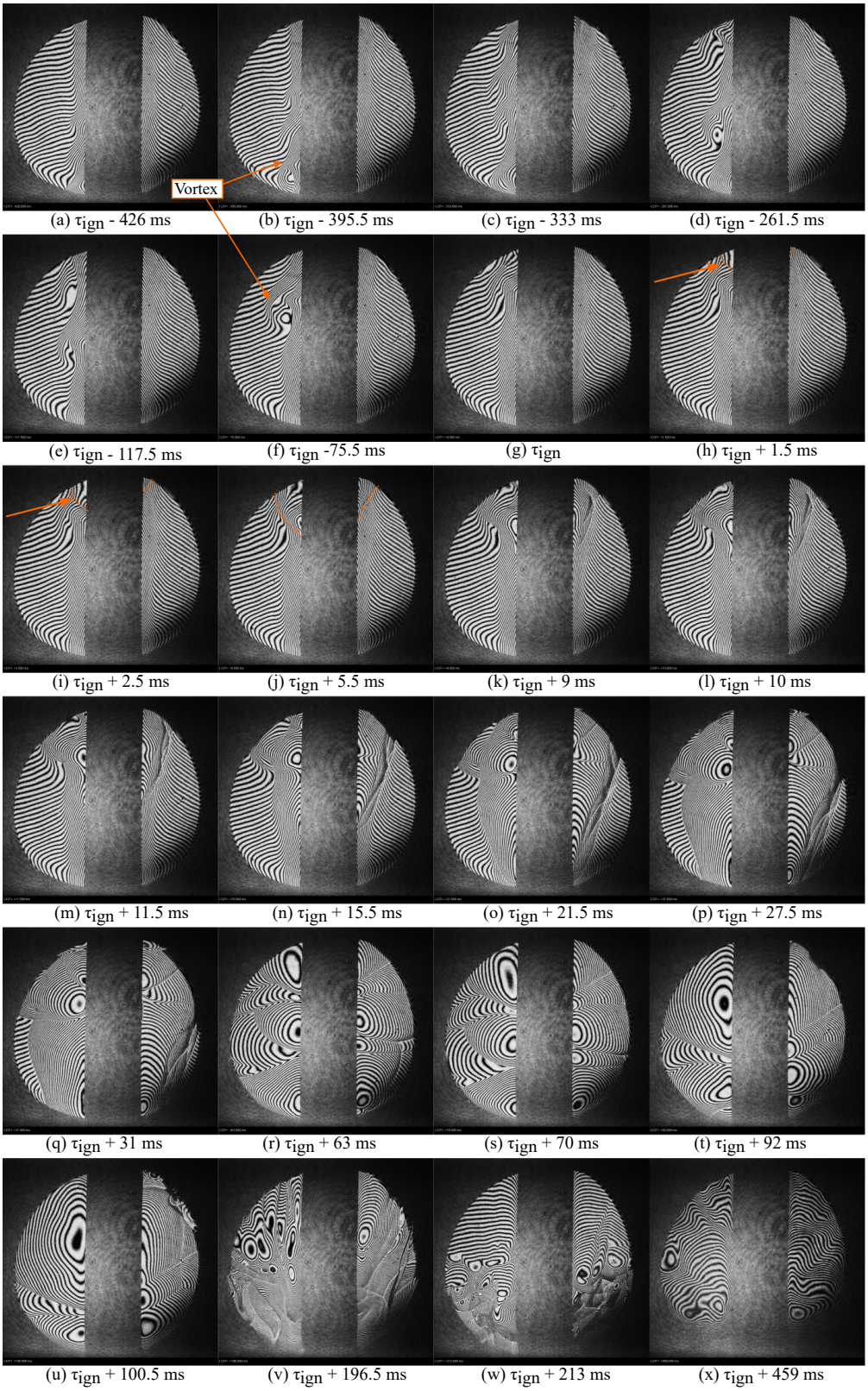

Figure E.13: Shot 419: Interferogram image sequence for P_0 = 1 atm, β = 5.64.

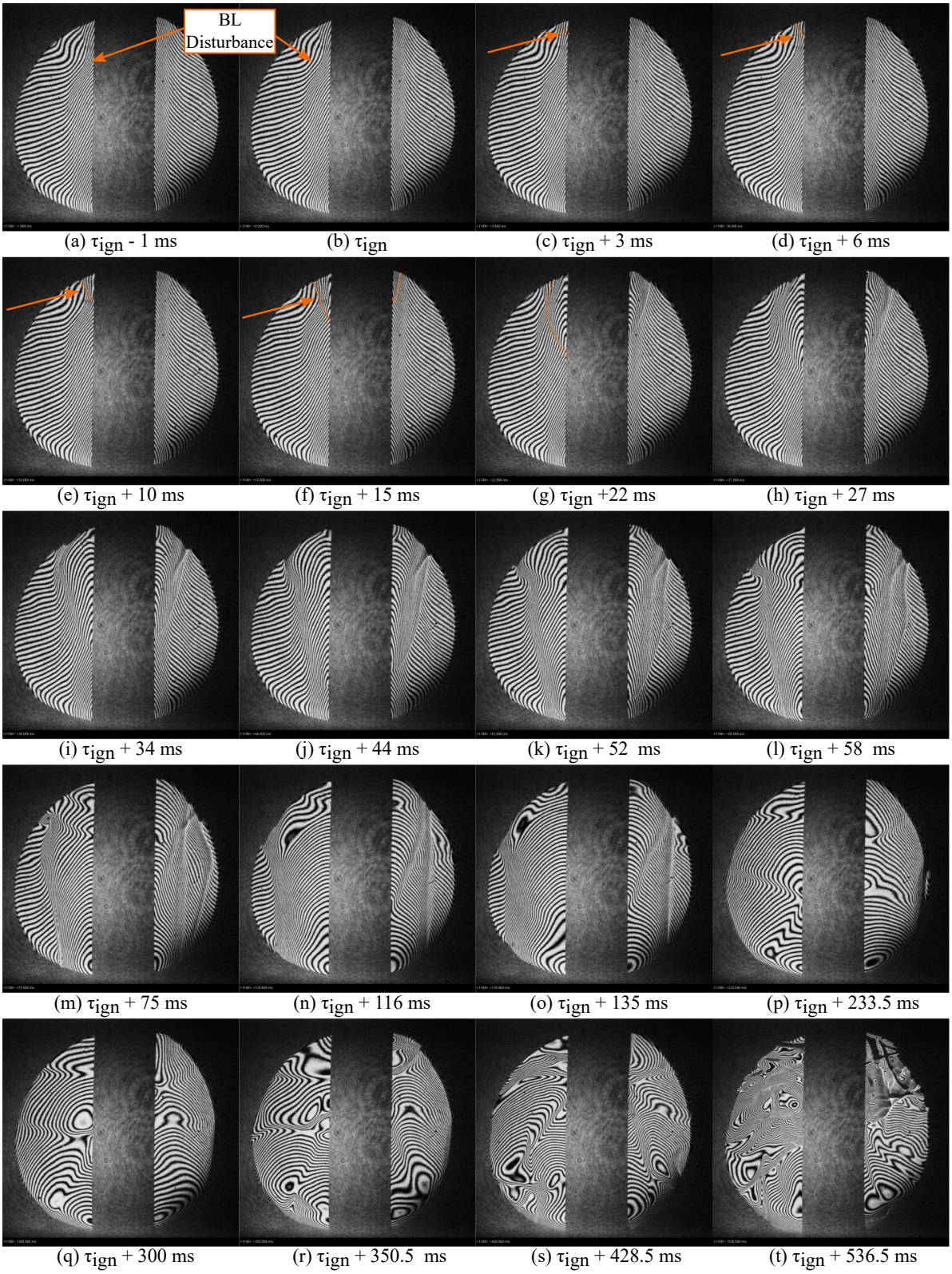

Figure E.14: Shot 421: Interferogram image sequence for P_0 = 1 atm, β = 7.52.

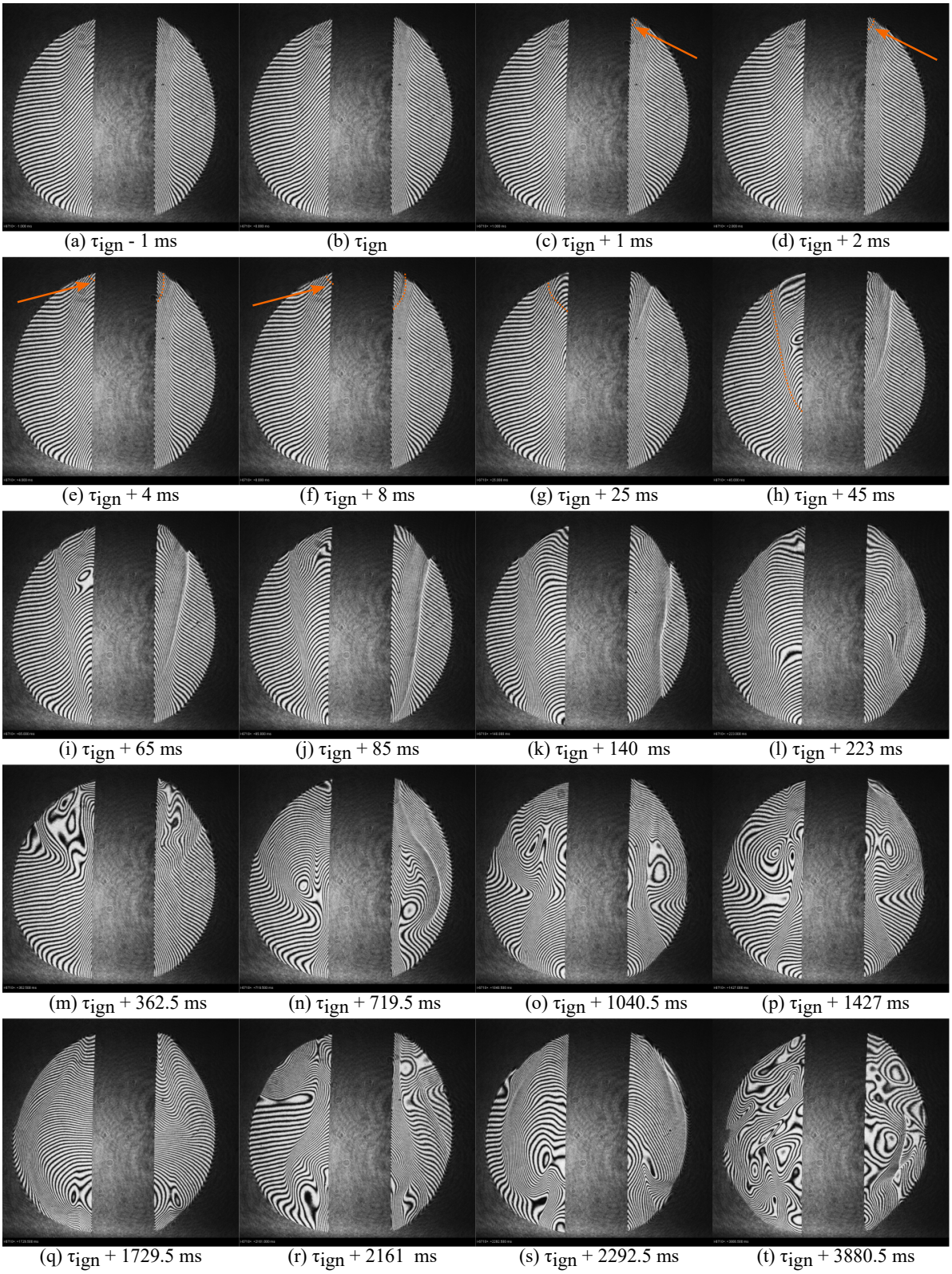

Figure E.15: Shot 489: Interferogram image sequence for P_0 = 1 atm, β = 8.0.

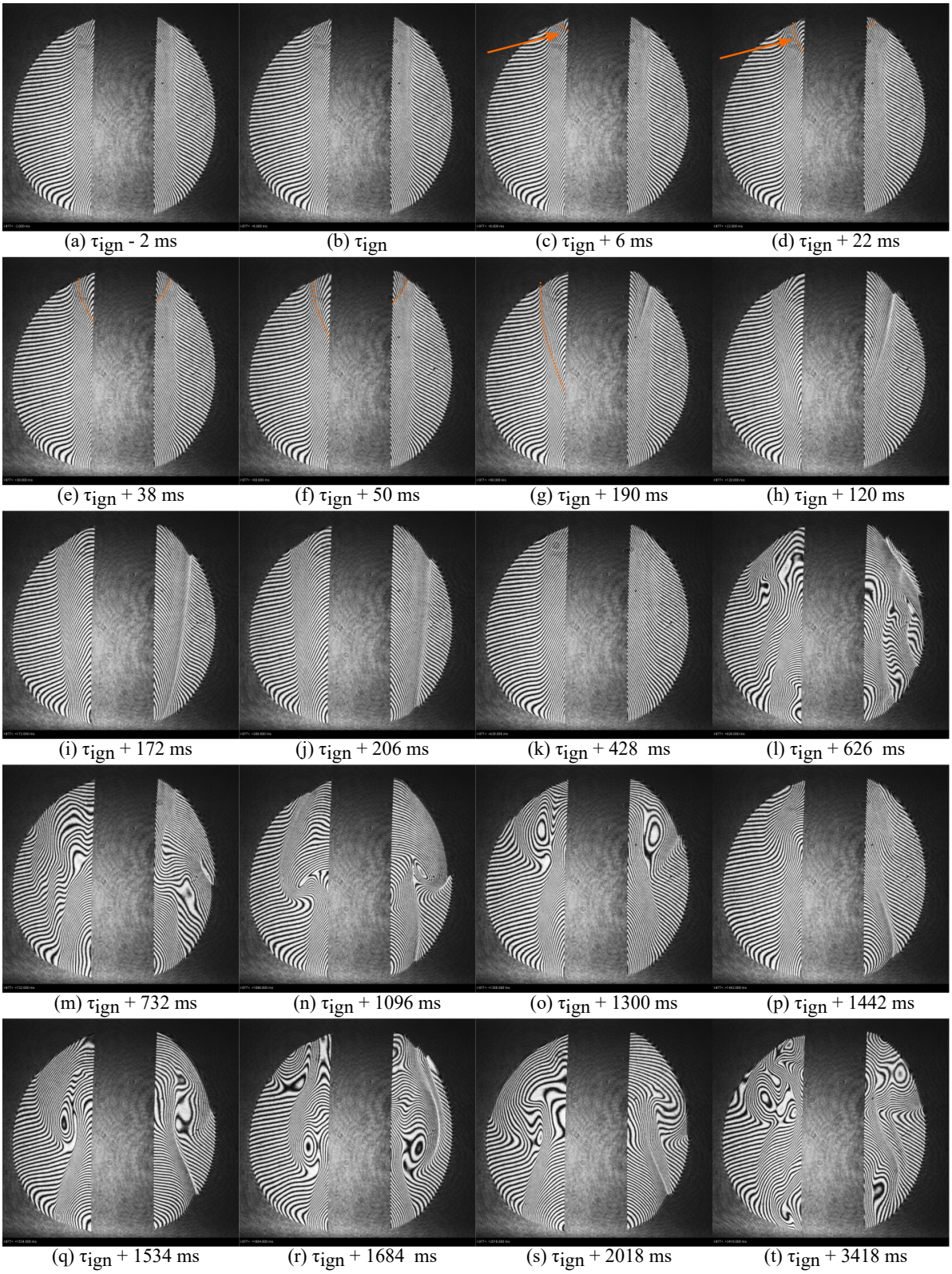

Figure E.16: Shot 492: Interferogram image sequence for P_0 = 1 atm, β = 8.45.

Appendix F

CAT DESIGN DRAWINGS

F.1 Component Drawings

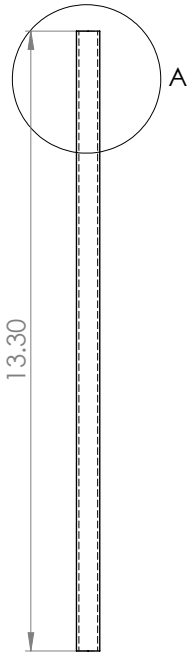

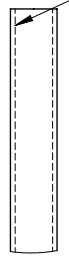

DETAIL A
SCALE 2 : 3

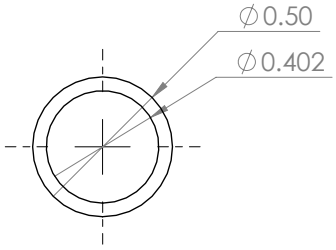

TOP VIEW 2:1 SCALE

NOTE: ENDS TOLERANCED FOR BRAZING
WITH COPPER TUBE END (P002)
SEE CYLINDER ASSEMBLY (DWG A01)

		NAME	DATE
UNLESS OTHERWISE SPECIFIED:			
DIMENSIONS ARE IN INCHES TOLERANCES: FRACTIONAL ± ANGULAR: MACH ± BEND ± TWO PLACE DECIMAL ±0.01 THREE PLACE DECIMAL ±0.005	DRAWN	Conor M.	12/15/21
	CHECKED		
	ENG APPR.		
	MFG APPR.		
	Q.A.		
INTERPRET GEOMETRIC TOLERANCING PER:	COMMENTS:		
MATERIAL: STAINLESS STEEL 304	QTY: 1		
FINISH			
DO NOT SCALE DRAWING			

TITLE:

Tube 133

SIZE	DWG. NO.	REV
A	P001	
SCALE: 1:3	WEIGHT:	SHEET 1 OF 1

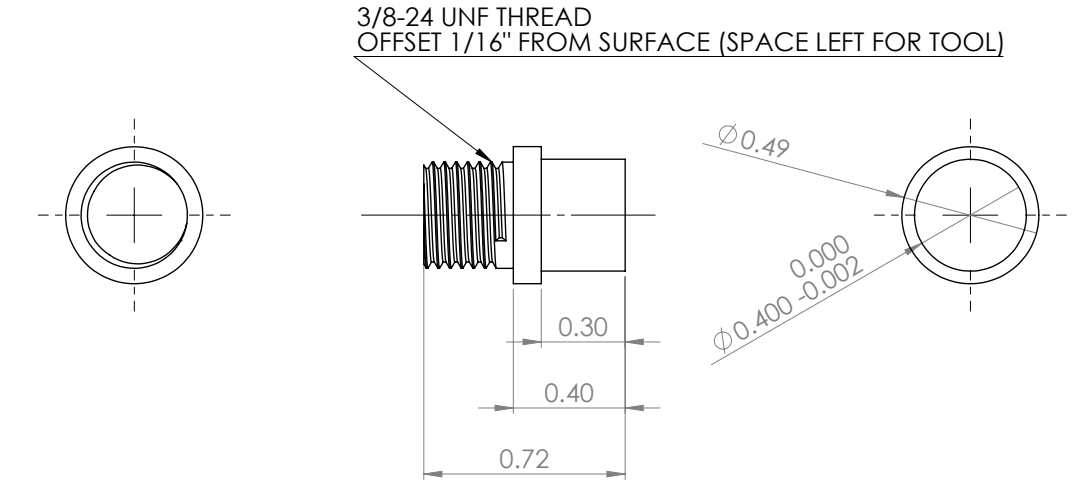

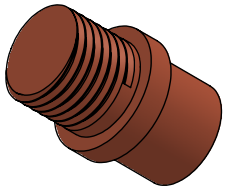

NOTE: END TOLERANCED TO BRAZE INTO TUBE 133 (PART 001), SEE CYLINDER ASSEMBLY (DWG A01)

		NAME	DATE
UNLESS OTHERWISE SPECIFIED:	DRAWN	Conor M.	12/15/21
DIMENSIONS ARE IN INCHES TOLERANCES: FRACTIONAL ± ANGULAR: MACH ± BEND ± TWO PLACE DECIMAL ±0.01 THREE PLACE DECIMAL ±0.005	CHECKED		
	ENG APPR.		
	MFG APPR.		
INTERPRET GEOMETRIC TOLERANCING PER:	Q.A.		
MATERIAL: COPPER 110	COMMENTS: QTY: 12		
FINISH			
DO NOT SCALE DRAWING			

TITLE: Copper Tube End

SIZE	DWG. NO.	REV
A	P002	

SCALE: 2:1	WEIGHT:	SHEET 1 OF 1

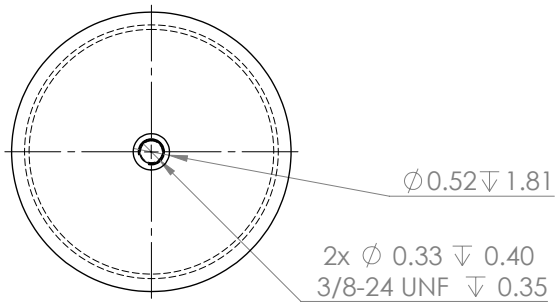

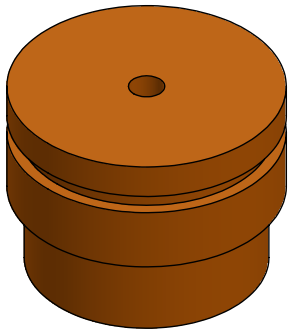

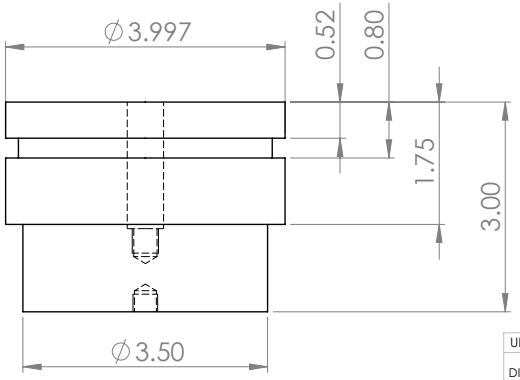

FOR O-RING DYNAMIC O.D.
GLAND SEAL: -342

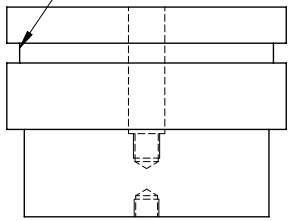

NOTE: MUST FIT INTO P004 TO
FORM DYNAMIC GLAND O.D. SEAL, SIZE -340
SEE ASSEMBLY (A02)

		NAME	DATE
UNLESS OTHERWISE SPECIFIED:	DRAWN	Conor M.	12/15/21
DIMENSIONS ARE IN INCHES TOLERANCES: FRACTIONAL ± ANGULAR: MACH ± BEND ± TWO PLACE DECIMAL ±0.01 THREE PLACE DECIMAL ±0.005	CHECKED		
	ENG APPR.		
	MFG APPR.		
INTERPRET GEOMETRIC TOLERANCING PER:	Q.A.		
MATERIAL: COPPER 110	COMMENTS:		
FINISH	QTY: 1		
DO NOT SCALE DRAWING			

TITLE:
Copper Bottom Block

SIZE	DWG. NO.	REV
A	P003	

SCALE: 1:2	WEIGHT:	SHEET 1 OF 1

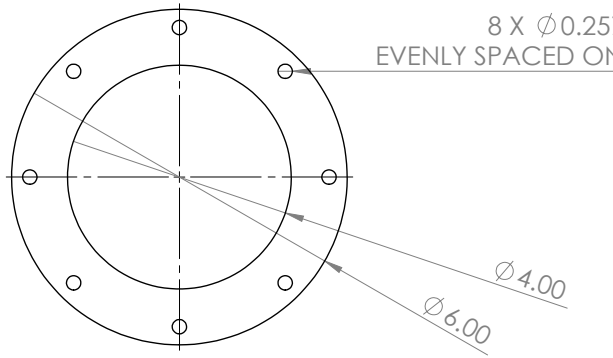

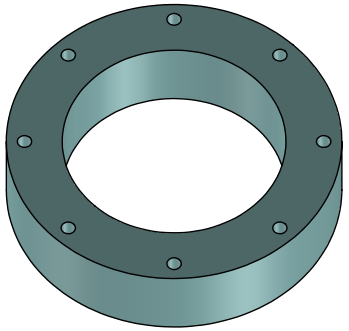

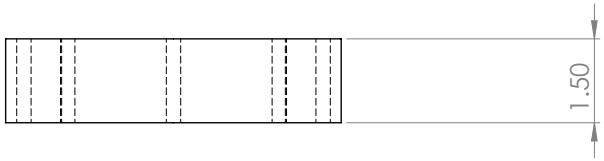

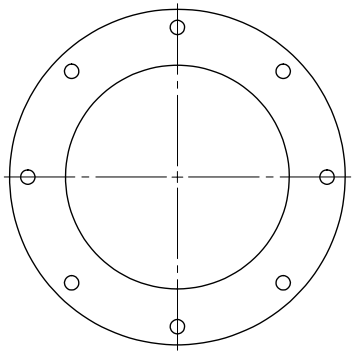

NOTE: MUST FIT WITH P003 TO
FORM DYNAMIC GLAND O.D. SEAL, SIZE -340
SEE ASSEMBLY (A02)

UNLESS OTHERWISE SPECIFIED:		NAME	DATE
DIMENSIONS ARE IN INCHES TOLERANCES: FRACTIONAL ± ANGULAR: MACH ± BEND ± TWO PLACE DECIMAL ±0.01 THREE PLACE DECIMAL ±0.005	DRAWN	Conor M.	12/15/21
	CHECKED		
	ENG APPR.		
	MFG APPR.		
	Q.A.		
INTERPRET GEOMETRIC TOLERANCING PER:	COMMENTS:		
MATERIAL 6061 ALUMINUM	QTY: 1		
FINISH			
DO NOT SCALE DRAWING			

TITLE:
Bottom Insulator Plate

SIZE	DWG. NO.	REV
A	P004	
SCALE: 1:2	WEIGHT:	SHEET 1 OF 1

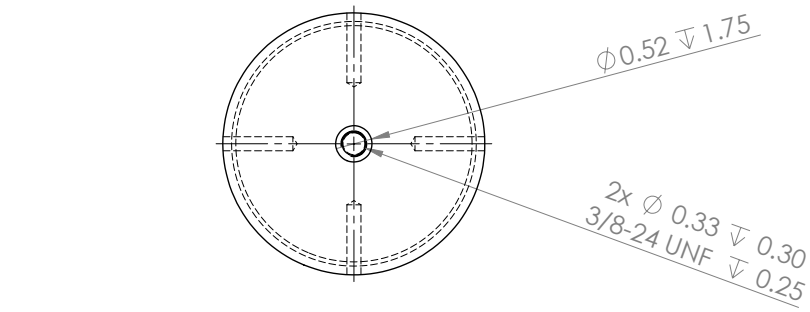

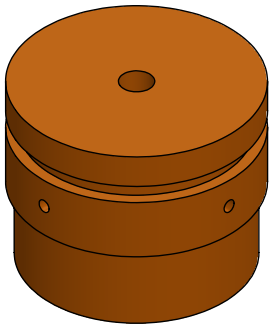

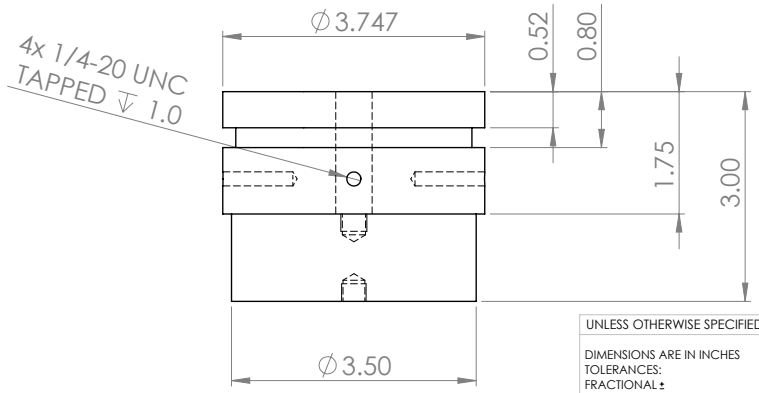

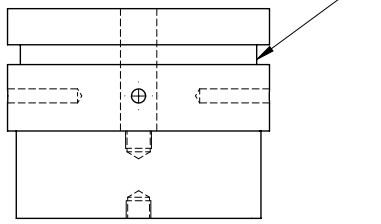

NOTE: MUST FIT INTO P004 TO
FORM DYNAMIC GLAND O.D. SEAL, SIZE -340
SEE ASSEMBLY (A02)

		NAME	DATE
UNLESS OTHERWISE SPECIFIED:			
DIMENSIONS ARE IN INCHES TOLERANCES: FRACTIONAL ± ANGULAR: MACH ± BEND ± TWO PLACE DECIMAL ±0.01 THREE PLACE DECIMAL ±0.005	DRAWN	Conor M.	12/15/21
	CHECKED		
	ENG APPR.		
	MFG APPR.		
	Q.A.		
INTERPRET GEOMETRIC TOLERANCING PER:	COMMENTS:		
MATERIAL: COPPER 110	QTY: 1		
FINISH			
DO NOT SCALE DRAWING			

TITLE: Copper Top Block

SIZE	DWG. NO.	REV
A	P005	
SCALE: 1:2	WEIGHT:	SHEET 1 OF 1

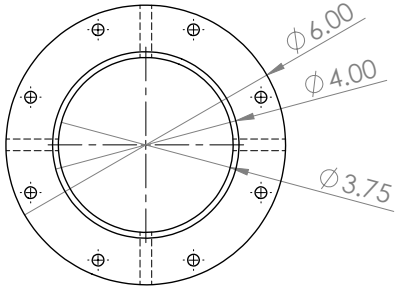

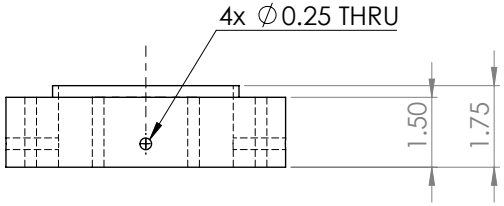

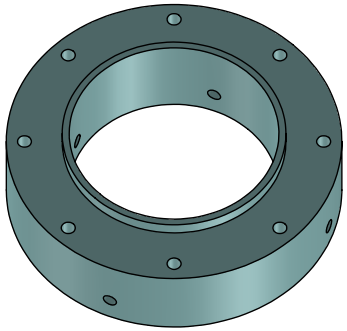

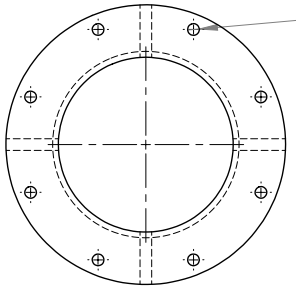

NOTE: MUST FIT WITH P005 TO
FORM DYNAMIC GLAND O.D. SEAL, SIZE -340
SEE ASSEMBLY (A03)

		NAME	DATE
UNLESS OTHERWISE SPECIFIED:			
DIMENSIONS ARE IN INCHES TOLERANCES: FRACTIONAL ± ANGULAR: MACH ± BEND ± TWO PLACE DECIMAL ±0.01 THREE PLACE DECIMAL ±0.005	DRAWN	Conor M.	12/15/21
	CHECKED		
	ENG APPR.		
	MFG APPR.		
INTERPRET GEOMETRIC TOLERANCING PER:	Q.A.		
MATERIAL DELRIN (ACETAL RESIN)	COMMENTS: QTY: 1		
FINISH			
DO NOT SCALE DRAWING			

TITLE: Top Insulator Plate

SIZE	DWG. NO.	REV
A	P006	

SCALE: 1:3	WEIGHT:	SHEET 1 OF 1

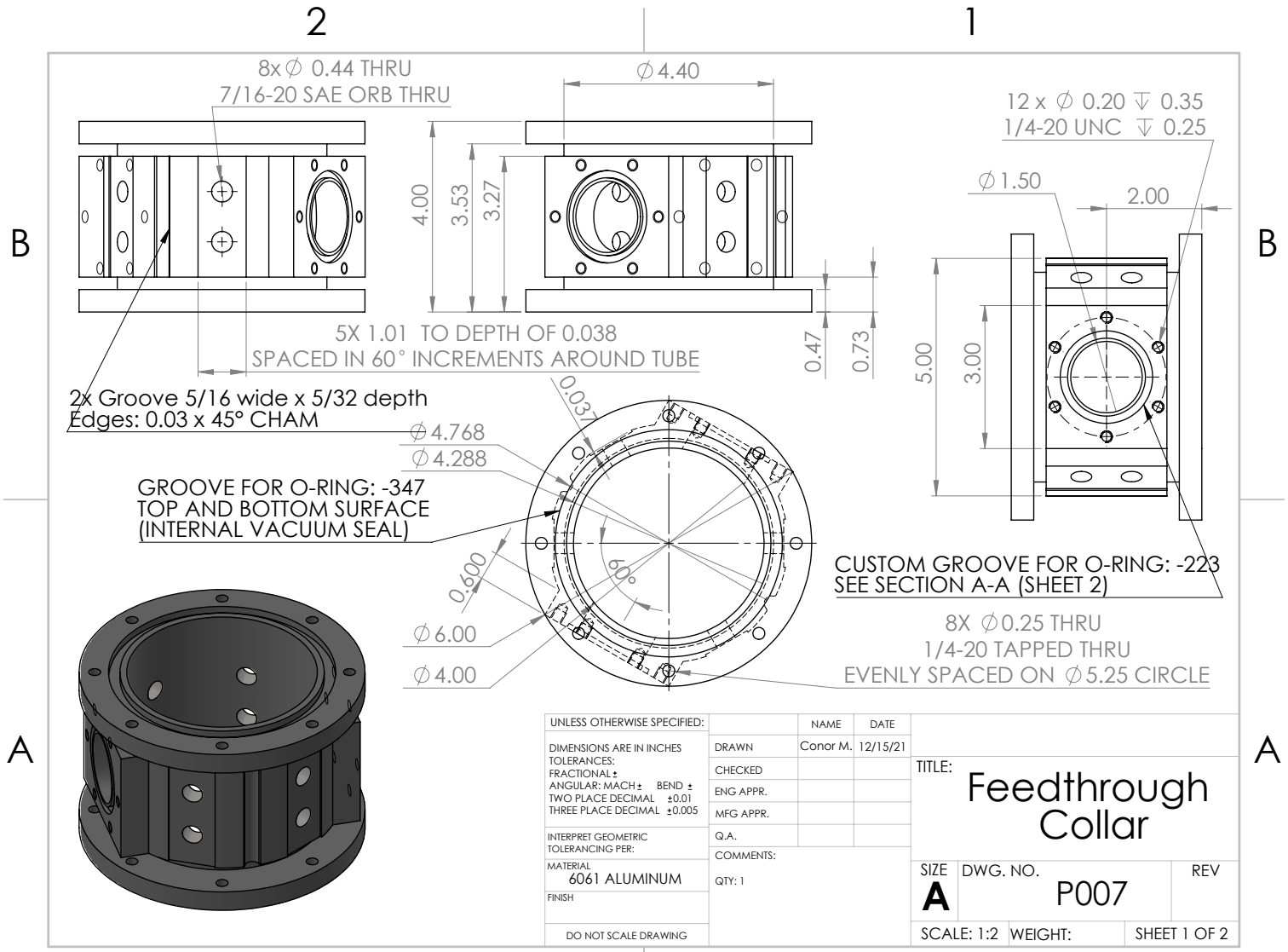
2
1
B
A
8x ∅ 0.44 THRU
7/16-20 SAE ORB THRU
∅ 4.40
4.00
3.53
3.27
0.47
0.73
5X 1.01 TO DEPTH OF 0.038
SPACED IN 60° INCREMENTS AROUND TUBE
12 x ∅ 0.20 ↧ 0.35
1/4-20 UNC ↧ 0.25
∅ 1.50
2.00
5.00
3.00
2x Groove 5/16 wide x 5/32 depth
Edges: 0.03 x 45° CHAM
0.03
∅ 4.768
∅ 4.288
GROOVE FOR O-RING: -347
TOP AND BOTTOM SURFACE
(INTERNAL VACUUM SEAL)
0.600
60°
∅ 6.00
∅ 4.00
CUSTOM GROOVE FOR O-RING: -223
SEE SECTION A-A (SHEET 2)
8X ∅0.25 THRU
1/4-20 TAPPED THRU
EVENLY SPACED ON ∅5.25 CIRCLE
UNLESS OTHERWISE SPECIFIED:
DIMENSIONS ARE IN INCHES
TOLERANCES:
FRACTIONAL ±
ANGULAR: MACH ± BEND ±
TWO PLACE DECIMAL ±0.01
THREE PLACE DECIMAL ±0.005
INTERPRET GEOMETRIC TOLERANCING PER:
MATERIAL
6061 ALUMINUM
FINISH
DO NOT SCALE DRAWING
NAME
DATE
DRAWN
Conor M.
12/15/21
CHECKED
ENG APPR.
MFG APPR.
Q.A.
COMMENTS:
QTY: 1
TITLE:
Feedthrough Collar
SIZE
A
DWG. NO.
P007
REV
SCALE: 1:2
WEIGHT:
SHEET 1 OF 2

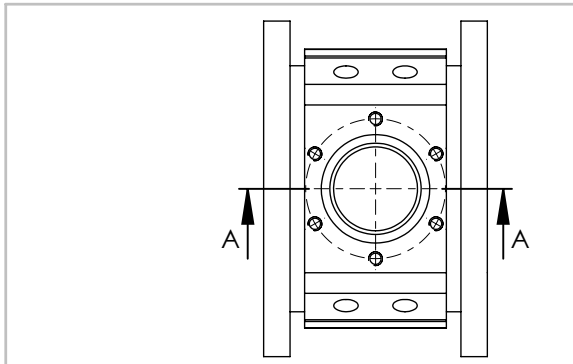

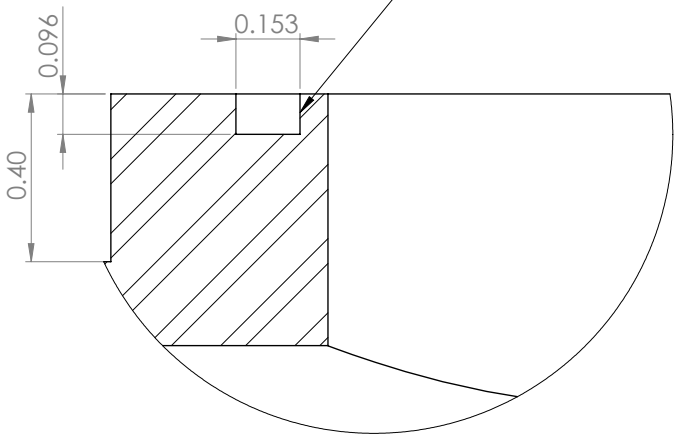

DETAIL B
SCALE 3 : 1

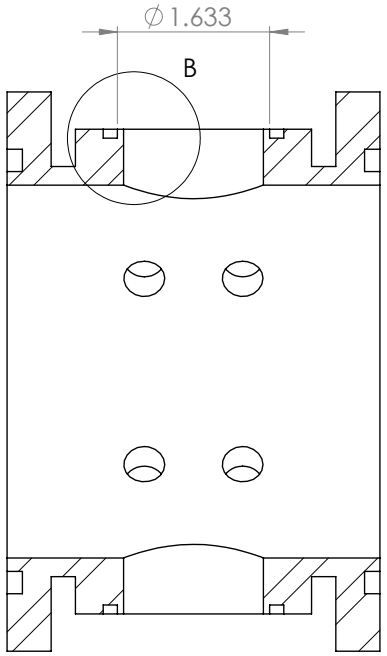

SECTION A-A
SCALE 1 : 1.5

		NAME	DATE
UNLESS OTHERWISE SPECIFIED:			
DIMENSIONS ARE IN INCHES TOLERANCES: FRACTIONAL ± ANGULAR: MACH ± BEND ± TWO PLACE DECIMAL ±0.01 THREE PLACE DECIMAL ±0.005	DRAWN	Conor M.	12/15/21
	CHECKED		
	ENG APPR.		
	MFG APPR.		
	Q.A.		
INTERPRET GEOMETRIC TOLERANCING PER:	COMMENTS:		
MATERIAL 6061 ALUMINUM	QTY: 1		
FINISH			
DO NOT SCALE DRAWING			

TITLE:
Feedthrough Collar

SIZE	DWG. NO.	REV
A	P007	
SCALE: 1:2	WEIGHT:	SHEET 2 OF 2

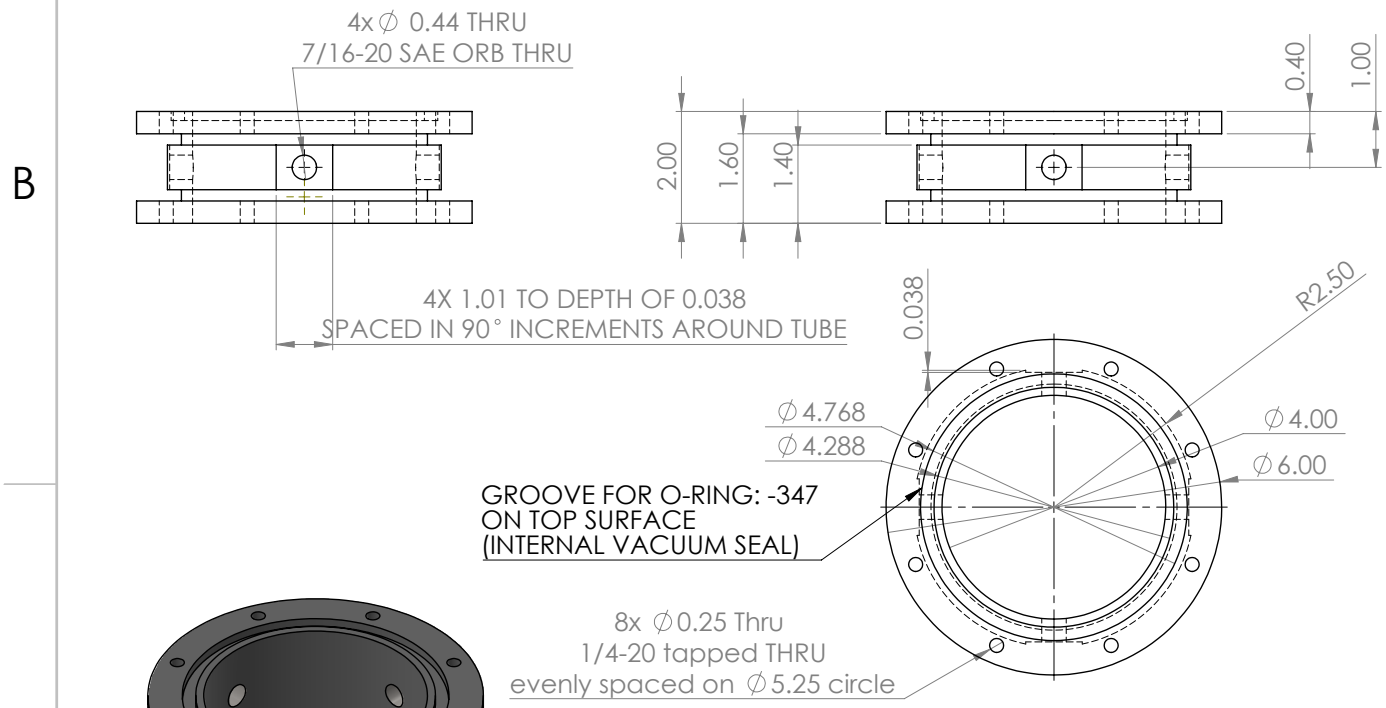

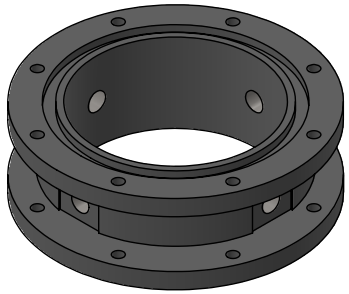

		NAME	DATE
UNLESS OTHERWISE SPECIFIED:			
DIMENSIONS ARE IN INCHES TOLERANCES: FRACTIONAL ± ANGULAR: MACH ± BEND ± TWO PLACE DECIMAL ±0.01 THREE PLACE DECIMAL ±0.005	DRAWN	Conor M.	12/15/21
	CHECKED		
	ENG APPR.		
	MFG APPR.		
	Q.A.		
INTERPRET GEOMETRIC TOLERANCING PER:	COMMENTS:		
MATERIAL 6061 ALUMINUM	QTY: 1		
FINISH			
DO NOT SCALE DRAWING			

TITLE:

Top Collar

SIZE	DWG. NO.	REV
A	P008	
SCALE: 1:2	WEIGHT:	SHEET 1 OF 1

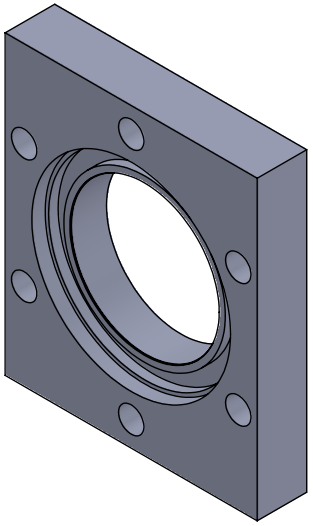

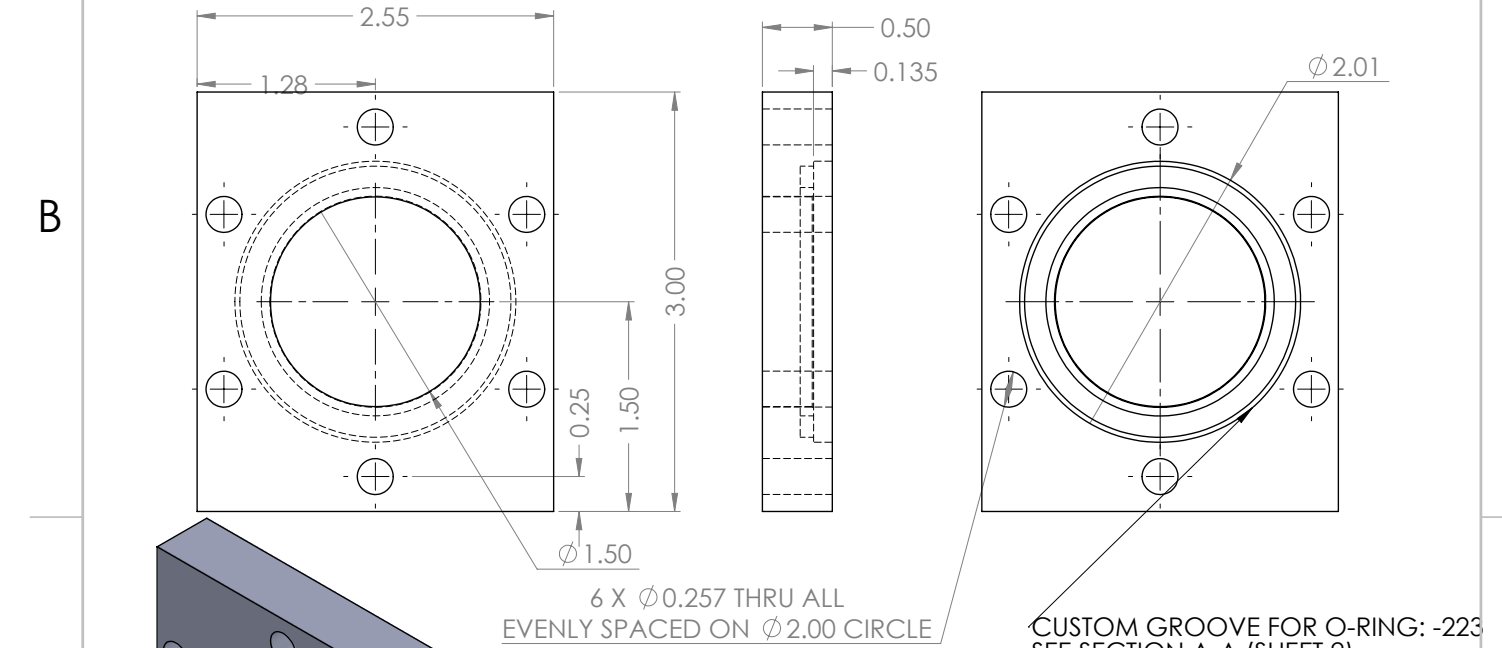

Note: Central ∅1.5 hole must be concentric with ∅1.5 hole on P007/P018 when assembled. (See assembly, A02)

UNLESS OTHERWISE SPECIFIED:		NAME	DATE
DIMENSIONS ARE IN INCHES TOLERANCES: FRACTIONAL ± ANGULAR: MACH ± BEND ± TWO PLACE DECIMAL ±0.01 THREE PLACE DECIMAL ±0.005	DRAWN	Conor M.	12/15/21
	CHECKED		
	ENG APPR.		
	MFG APPR.		
	Q.A.		
INTERPRET GEOMETRIC TOLERANCING PER:	COMMENTS:		
MATERIAL 6061 ALUMINUM	QTY: 4		
FINISH			
DO NOT SCALE DRAWING			

TITLE:

Window Holder

SIZE	DWG. NO.	REV
A	P009	
SCALE: 1:1	WEIGHT:	SHEET 1 OF 2

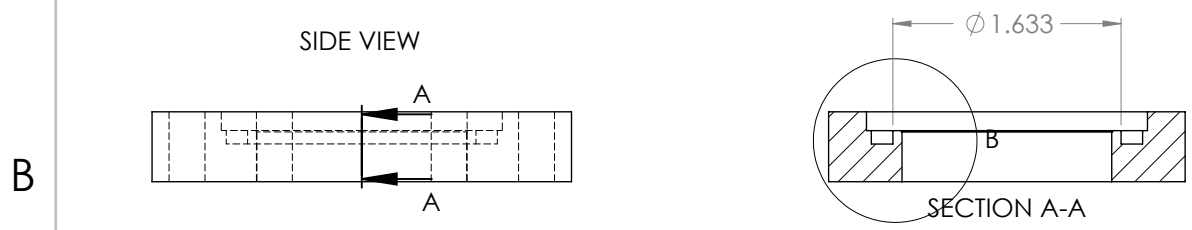

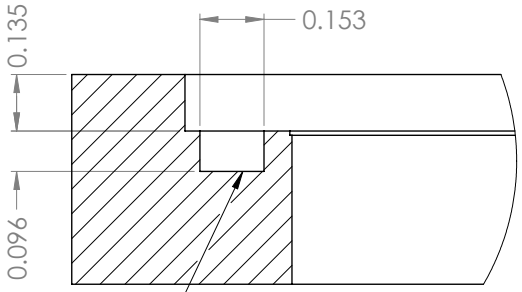

DETAIL B
SCALE 3 : 1

CUSTOM O-RING GROOVE FOR
-223 STATIC VACCUUM SEAL

UNLESS OTHERWISE SPECIFIED:		NAME	DATE
DIMENSIONS ARE IN INCHES TOLERANCES: FRACTIONAL ± ANGULAR: MACH ± BEND ± TWO PLACE DECIMAL ±0.01 THREE PLACE DECIMAL ±0.005	DRAWN	Conor M.	12/15/21
	CHECKED		
	ENG APPR.		
	MFG APPR.		
	Q.A.		
INTERPRET GEOMETRIC TOLERANCING PER:	COMMENTS:		
MATERIAL 6061 ALUMINUM	QTY: 1		
FINISH			
DO NOT SCALE DRAWING			

TITLE:

Window Holder

SIZE	DWG. NO.	REV
A	P009	
SCALE: 1:1	WEIGHT:	SHEET 2 OF 2

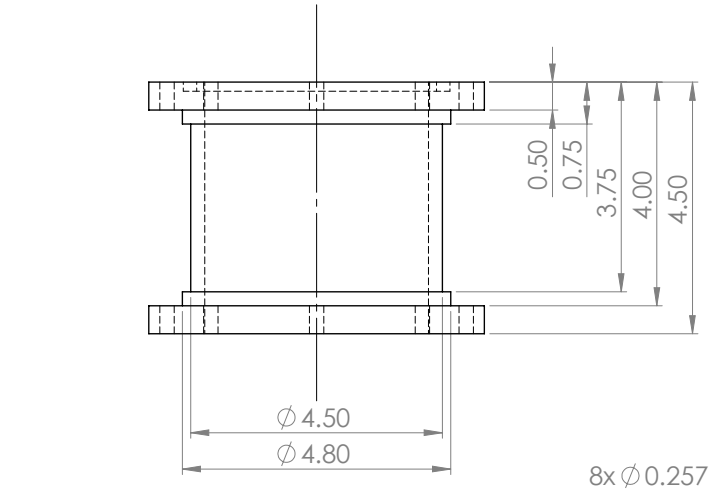

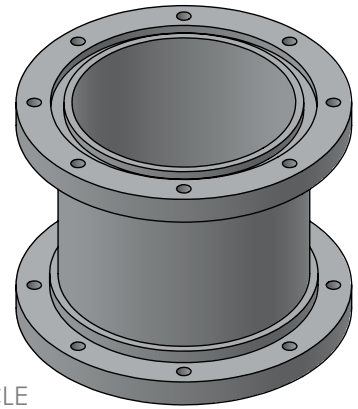

8x ∅0.257 THRU
EVENLY SPACED ON ∅5.25 CIRCLE

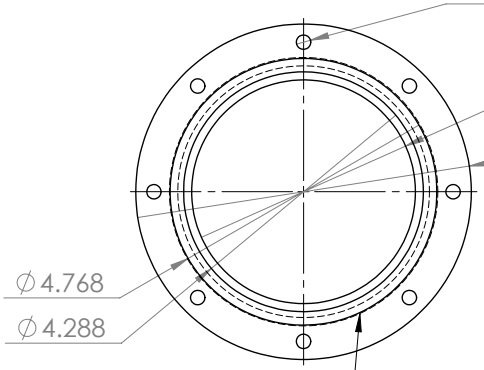

GROOVE FOR O-RING: -347
ON TOP SURFACE
(INTERNAL VACUUM SEAL)

		NAME	DATE
UNLESS OTHERWISE SPECIFIED:			
DIMENSIONS ARE IN INCHES TOLERANCES: FRACTIONAL ± ANGULAR: MACH ± BEND ± TWO PLACE DECIMAL ±0.01 THREE PLACE DECIMAL ±0.005	DRAWN	Conor M.	12/15/21
	CHECKED		
	ENG APPR.		
	MFG APPR.		
INTERPRET GEOMETRIC TOLERANCING PER:	Q.A.		
MATERIAL 6061 ALUMINUM	COMMENTS: QTY: 1		
FINISH			
DO NOT SCALE DRAWING			

TITLE:
Outer Tube 4.5

SIZE	DWG. NO.	REV
A	P010	
SCALE: 1:2	WEIGHT:	SHEET 1 OF 1

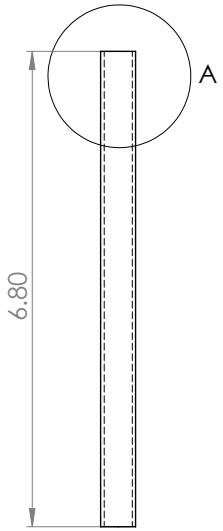

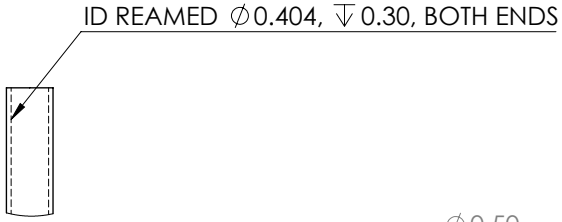

DETAIL A
SCALE 2 : 3

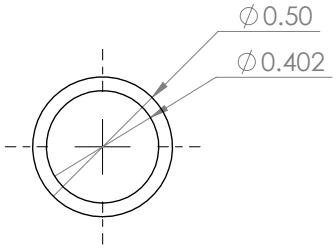

TOP VIEW 2:1 SCALE

NOTE: ENDS TOLERANCED FOR BRAZING
WITH COPPER TUBE END (P002)
SEE CYLINDER ASSEMBLY (DWG A01)

UNLESS OTHERWISE SPECIFIED:		NAME	DATE
DIMENSIONS ARE IN INCHES TOLERANCES: FRACTIONAL ± ANGULAR: MACH ± BEND ± TWO PLACE DECIMAL ±0.01 THREE PLACE DECIMAL ±0.005	DRAWN	Conor M.	12/15/21
	CHECKED		
	ENG APPR.		
	MFG APPR.		
	Q.A.		
INTERPRET GEOMETRIC TOLERANCING PER:	COMMENTS:		
MATERIAL STAINLESS STEEL 304	QTY: 1		
FINISH			
DO NOT SCALE DRAWING			

TITLE:

Tube 68

SIZE	DWG. NO.	REV
A	P011	
SCALE: 1:2	WEIGHT:	SHEET 1 OF 1

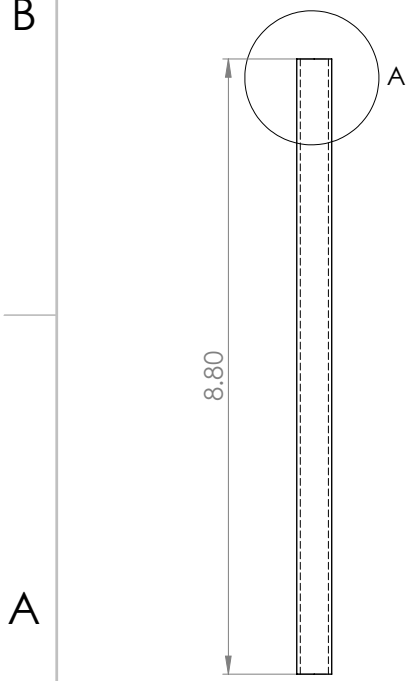

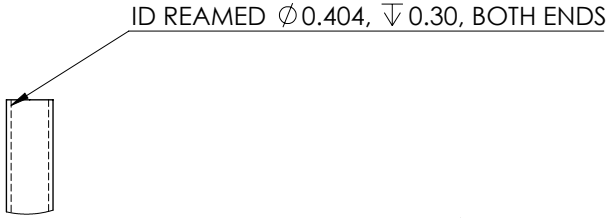

DETAIL A
SCALE 2 : 3

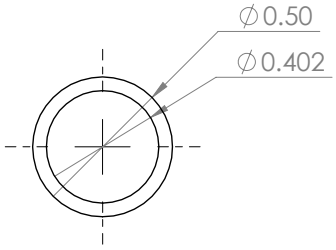

TOP VIEW 2:1 SCALE

NOTE: ENDS TOLERANCED FOR BRAZING
WITH COPPER TUBE END (P002)
SEE CYLINDER ASSEMBLY (DWG A01)

UNLESS OTHERWISE SPECIFIED:		NAME	DATE
DIMENSIONS ARE IN INCHES TOLERANCES: FRACTIONAL ± ANGULAR: MACH ± BEND ± TWO PLACE DECIMAL ±0.01 THREE PLACE DECIMAL ±0.005	DRAWN	Conor M.	12/15/21
	CHECKED		
	ENG APPR.		
	MFG APPR.		
	Q.A.		
INTERPRET GEOMETRIC TOLERANCING PER:	COMMENTS:		
MATERIAL STAINLESS STEEL 304	QTY: 1		
FINISH			
DO NOT SCALE DRAWING			

TITLE:

Tube 88

SIZE	DWG. NO.	REV
A	P012	
SCALE: 1:2	WEIGHT:	SHEET 1 OF 1

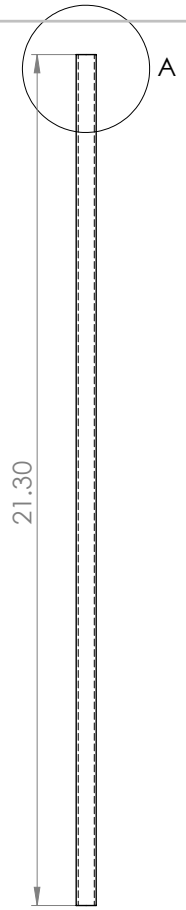

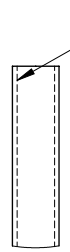

DETAIL A
SCALE 2 : 3

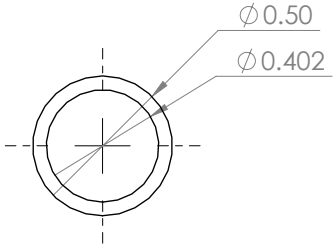

TOP VIEW 2:1 SCALE

NOTE: ENDS TOLERANCED FOR BRAZING
WITH COPPER TUBE END (P002)
SEE CYLINDER ASSEMBLY (DWG A01)

UNLESS OTHERWISE SPECIFIED:		NAME	DATE
DIMENSIONS ARE IN INCHES TOLERANCES: FRACTIONAL ± ANGULAR: MACH ± BEND ± TWO PLACE DECIMAL ±0.01 THREE PLACE DECIMAL ±0.005	DRAWN	Conor M.	12/15/21
	CHECKED		
	ENG APPR.		
	MFG APPR.		
	Q.A.		
INTERPRET GEOMETRIC TOLERANCING PER:	COMMENTS:		
MATERIAL STAINLESS STEEL 304	QTY: 1		
FINISH			
DO NOT SCALE DRAWING			

TITLE:

Tube 213

SIZE	DWG. NO.	REV
A	P013	
SCALE: 1:3.5	WEIGHT:	SHEET 1 OF 1

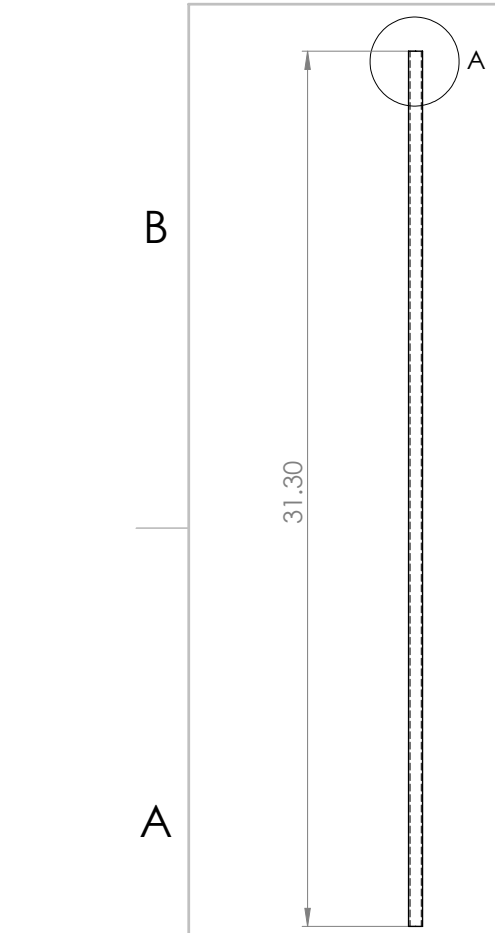

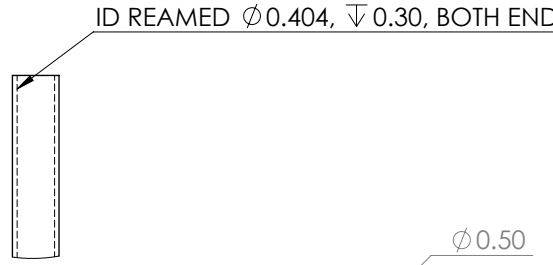

DETAIL A
SCALE 2 : 3

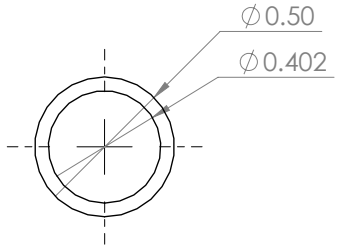

TOP VIEW 2:1 SCALE

NOTE: ENDS TOLERANCED FOR BRAZING
WITH COPPER TUBE END (P002)
SEE CYLINDER ASSEMBLY (DWG A01)

UNLESS OTHERWISE SPECIFIED:		NAME	DATE
DIMENSIONS ARE IN INCHES TOLERANCES: FRACTIONAL ± ANGULAR: MACH ± BEND ± TWO PLACE DECIMAL ±0.01 THREE PLACE DECIMAL ±0.005	DRAWN	Conor M.	12/15/21
	CHECKED		
	ENG APPR.		
	MFG APPR.		
	Q.A.		
INTERPRET GEOMETRIC TOLERANCING PER:	COMMENTS:		
MATERIAL STAINLESS STEEL 304	QTY: 1		
FINISH			
DO NOT SCALE DRAWING			

TITLE:

Tube 313

SIZE	DWG. NO.	REV
A	P014	
SCALE: 1:5	WEIGHT:	SHEET 1 OF 1

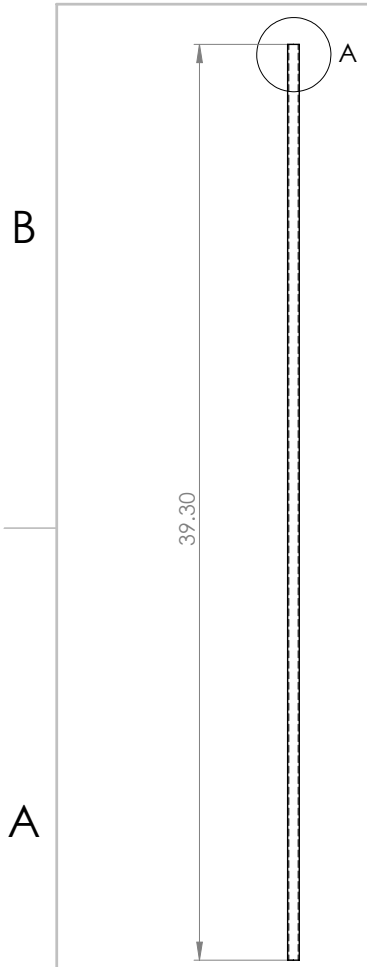

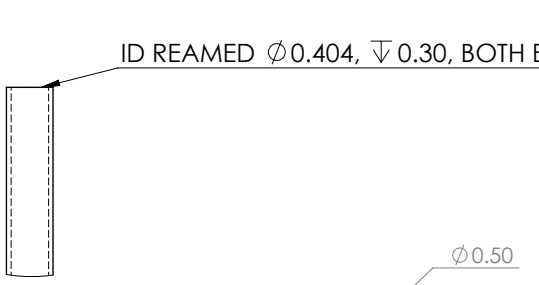

DETAIL A
SCALE 2 : 3

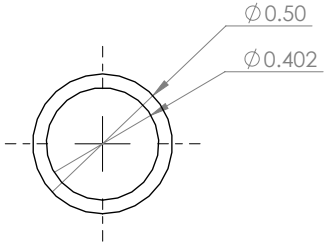

TOP VIEW 2:1 SCALE

NOTE: ENDS TOLERANCED FOR BRAZING
WITH COPPER TUBE END (P002)
SEE CYLINDER ASSEMBLY (DWG A01)

UNLESS OTHERWISE SPECIFIED:		NAME	DATE
DIMENSIONS ARE IN INCHES TOLERANCES: FRACTIONAL ± ANGULAR: MACH ± BEND ± TWO PLACE DECIMAL ±0.01 THREE PLACE DECIMAL ±0.005	DRAWN	Conor M.	12/15/21
	CHECKED		
	ENG APPR.		
	MFG APPR.		
	Q.A.		
INTERPRET GEOMETRIC TOLERANCING PER:	COMMENTS:		
MATERIAL STAINLESS STEEL 304	QTY: 1		
FINISH			
DO NOT SCALE DRAWING			

TITLE:

Tube 393

SIZE	DWG. NO.	REV
A	P015	
SCALE: 1:6	WEIGHT:	SHEET 1 OF 1

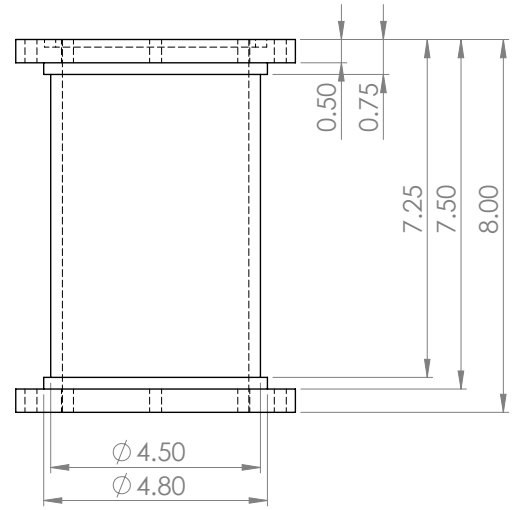

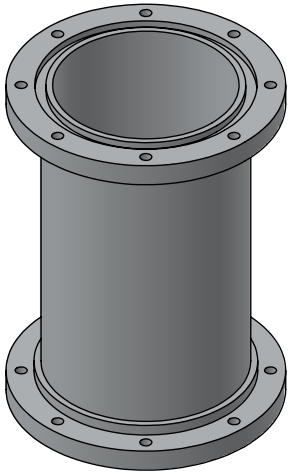

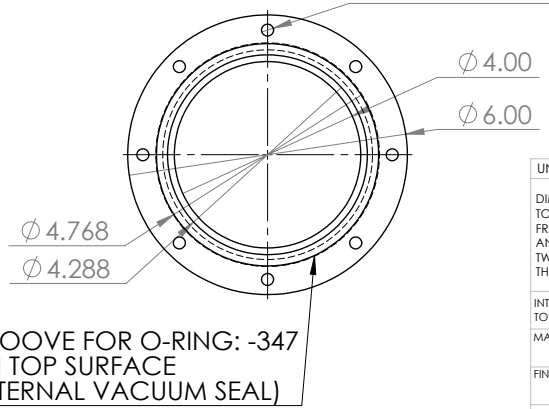

GROOVE FOR O-RING: -347
ON TOP SURFACE
(INTERNAL VACUUM SEAL)

UNLESS OTHERWISE SPECIFIED:		NAME	DATE
DIMENSIONS ARE IN INCHES TOLERANCES: FRACTIONAL ± ANGULAR: MACH ± BEND ± TWO PLACE DECIMAL ±0.01 THREE PLACE DECIMAL ±0.005	DRAWN	Conor M.	12/15/21
	CHECKED		
	ENG APPR.		
	MFG APPR.		
INTERPRET GEOMETRIC TOLERANCING PER:	Q.A.		
MATERIAL 6061 ALUMINUM	COMMENTS: QTY: 1		
FINISH			
DO NOT SCALE DRAWING			

TITLE:

Outer Tube 8

SIZE	DWG. NO.	REV
A	P016	
SCALE: 1:3	WEIGHT:	SHEET 1 OF 1

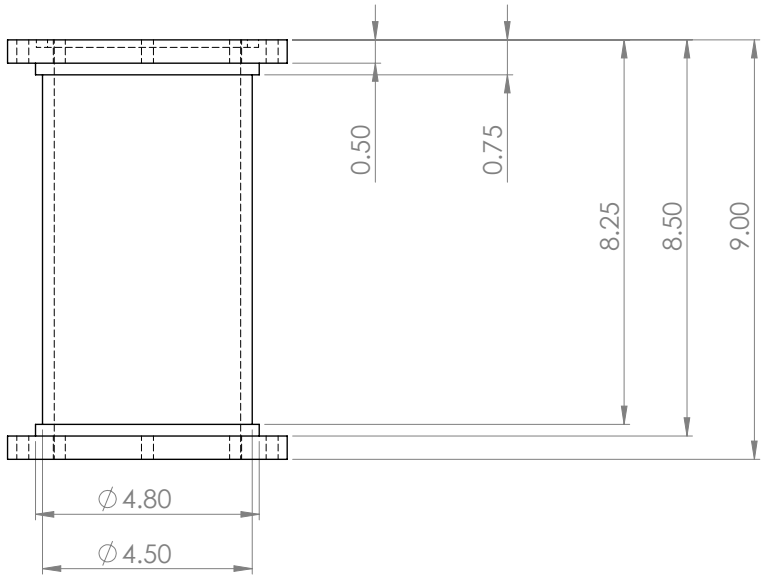

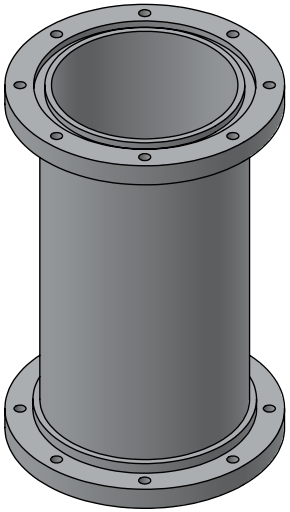

8x ∅0.257 THRU
EVENLY SPACED ON ∅5.25 CIRCLE

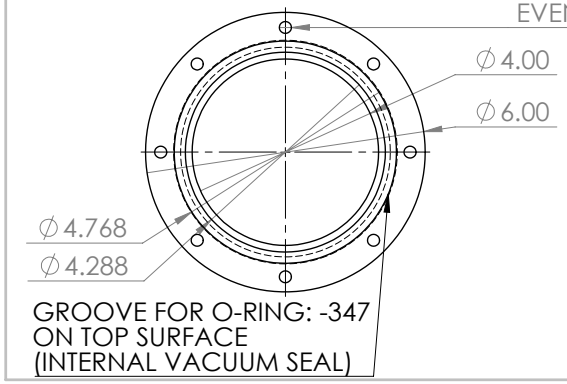

GROOVE FOR O-RING: -347
ON TOP SURFACE
(INTERNAL VACUUM SEAL)

UNLESS OTHERWISE SPECIFIED:		NAME	DATE
DIMENSIONS ARE IN INCHES TOLERANCES: FRACTIONAL ± ANGULAR: MACH ± BEND ± TWO PLACE DECIMAL ±0.01 THREE PLACE DECIMAL ±0.005	DRAWN	Conor M.	12/15/21
	CHECKED		
	ENG APPR.		
	MFG APPR.		
	Q.A.		
INTERPRET GEOMETRIC TOLERANCING PER:	COMMENTS:		
MATERIAL 6061 ALUMINUM	QTY: 2		
FINISH			
DO NOT SCALE DRAWING			

TITLE:

Outer Tube 9

SIZE	DWG. NO.	REV
A	P017	
SCALE: 1:3	WEIGHT:	SHEET 1 OF 1

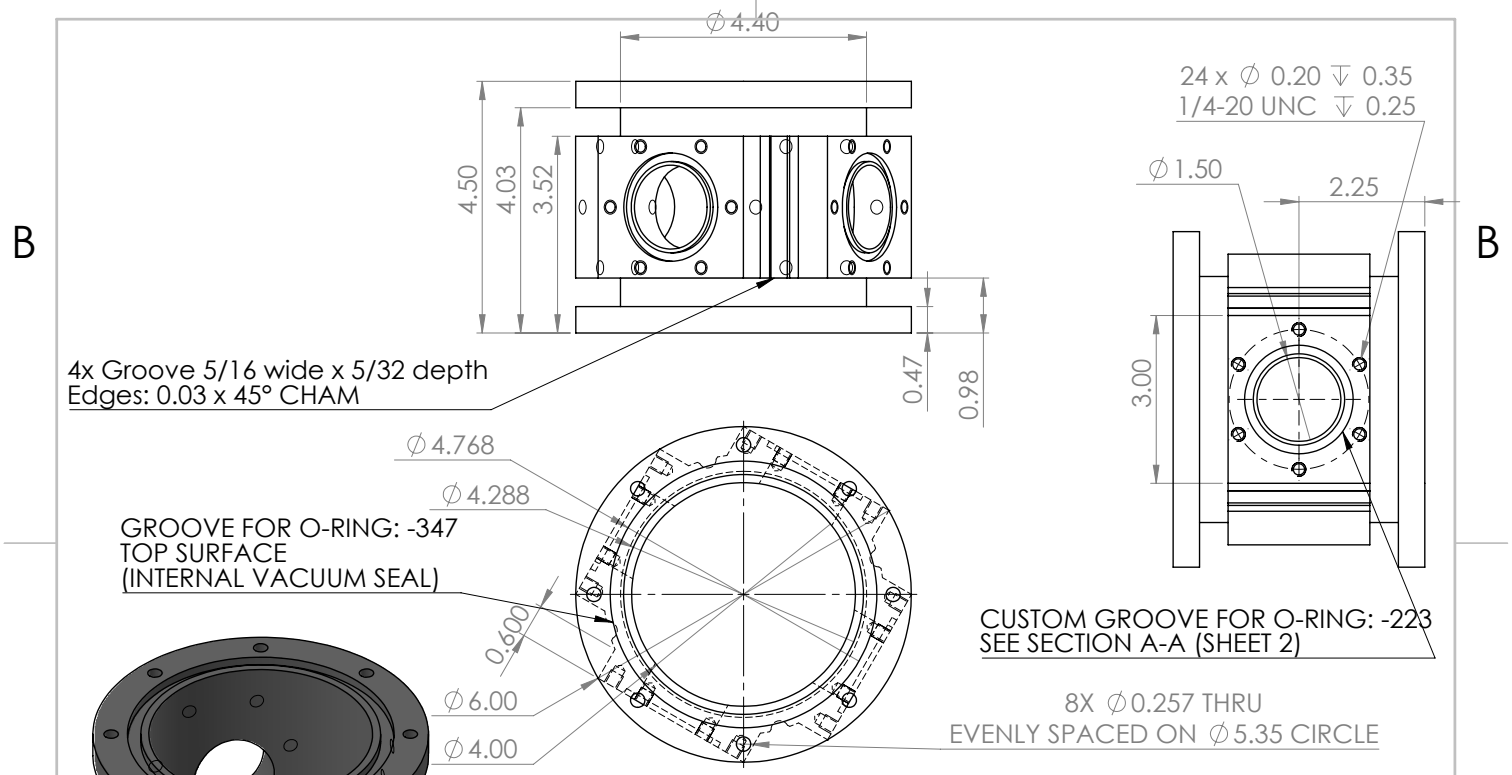

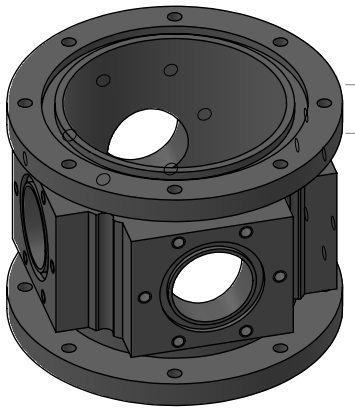

		NAME	DATE
UNLESS OTHERWISE SPECIFIED:			
DIMENSIONS ARE IN INCHES TOLERANCES: FRACTIONAL ± ANGULAR: MACH ± BEND ± TWO PLACE DECIMAL ±0.01 THREE PLACE DECIMAL ±0.005	DRAWN	Conor M.	9/13/22
	CHECKED		
	ENG APPR.		
	MFG APPR.		
	Q.A.		
INTERPRET GEOMETRIC TOLERANCING PER:	COMMENTS:		
MATERIAL 6061 ALUMINUM	QTY: 1		
FINISH			
DO NOT SCALE DRAWING			

TITLE:

Window Collar

SIZE	DWG. NO.	REV
A	P018	
SCALE: 1:2	WEIGHT:	SHEET 1 OF 2

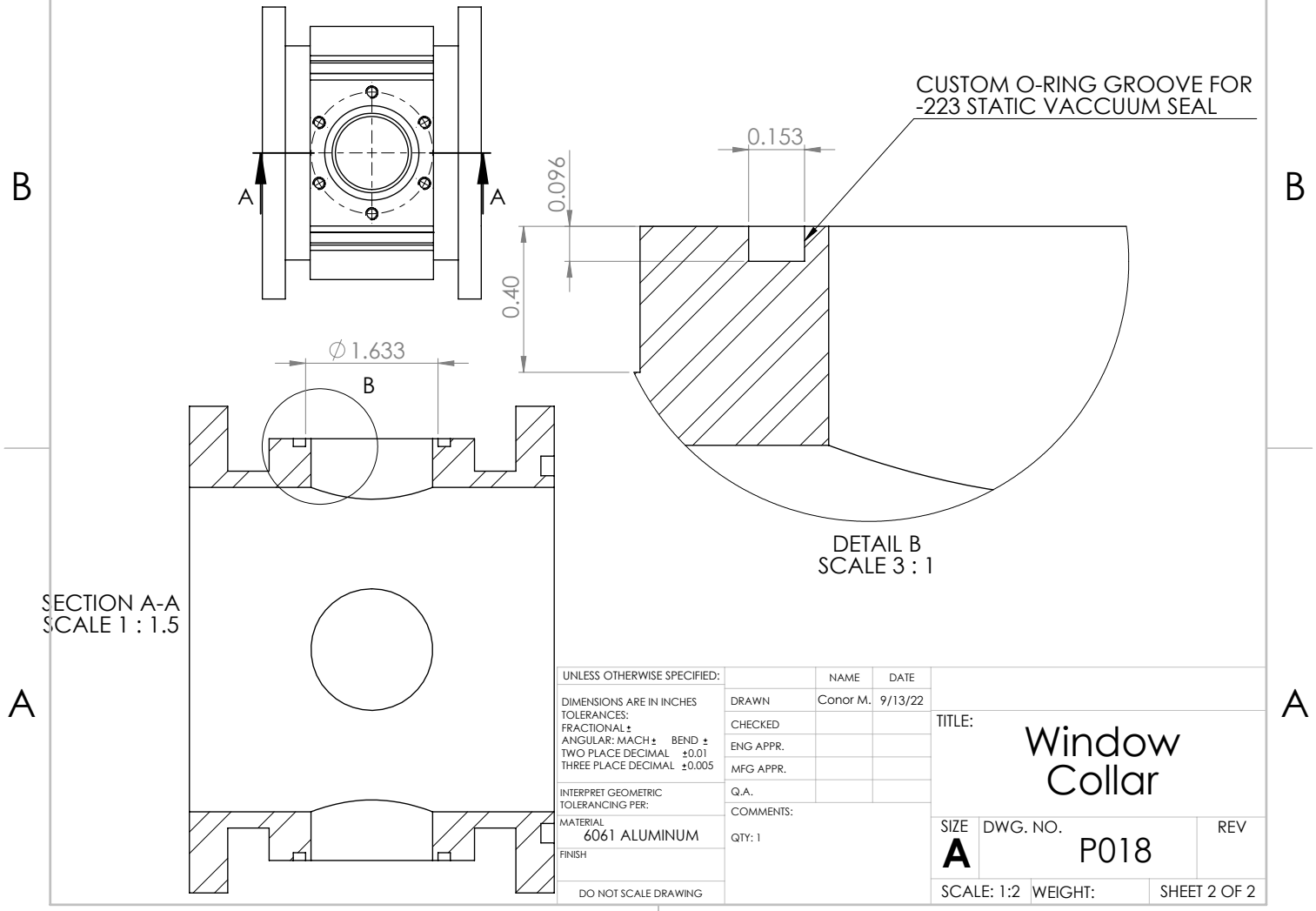
2
1
B
A
A
A
CUSTOM O-RING GROOVE FOR
-223 STATIC VACCUUM SEAL
0.153
0.096
0.40
∅1.633
B
SECTION A-A
SCALE 1 : 1.5
DETAIL B
SCALE 3 : 1
UNLESS OTHERWISE SPECIFIED:
DIMENSIONS ARE IN INCHES
TOLERANCES:
FRACTIONAL ±
ANGULAR: MACH ± BEND ±
TWO PLACE DECIMAL ±0.01
THREE PLACE DECIMAL ±0.005
INTERPRET GEOMETRIC TOLERANCING PER:
MATERIAL
6061 ALUMINUM
FINISH
DO NOT SCALE DRAWING
NAME
DATE
DRAWN
Conor M.
9/13/22
CHECKED
ENG APPR.
MFG APPR.
Q.A.
COMMENTS:
QTY: 1
TITLE:
Window Collar
SIZE
A
DWG. NO.
P018
REV
SCALE: 1:2
WEIGHT:
SHEET 2 OF 2

F.2 Assembly Drawings

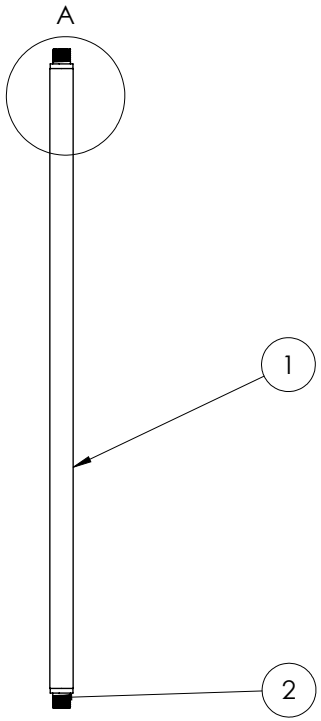

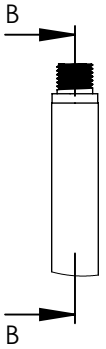

DETAIL A
SCALE 2 : 3

FIT P002 INTO P001 AND FURNACE BRAZE TO JOIN (BOTH TOP AND BOTTOM)

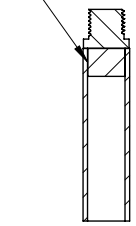

SECTION B-B
SCALE 2 : 3

UNLESS OTHERWISE SPECIFIED:		NAME	DATE
DIMENSIONS ARE IN INCHES TOLERANCES: FRACTIONAL ± ANGULAR: MACH ± BEND ± TWO PLACE DECIMAL ±0.01 THREE PLACE DECIMAL ±0.005	DRAWN	Conor M.	12/15/21
	CHECKED		
	ENG APPR.		
	MFG APPR.		
	Q.A.		
INTERPRET GEOMETRIC TOLERANCING PER:	COMMENTS:		
MATERIAL	QTY: 1		
FINISH			
DO NOT SCALE DRAWING			

TITLE:

Cylinder 133 Assembly

SIZE	DWG. NO.	REV
A	A01	
SCALE: 1:3	WEIGHT:	SHEET 1 OF 1

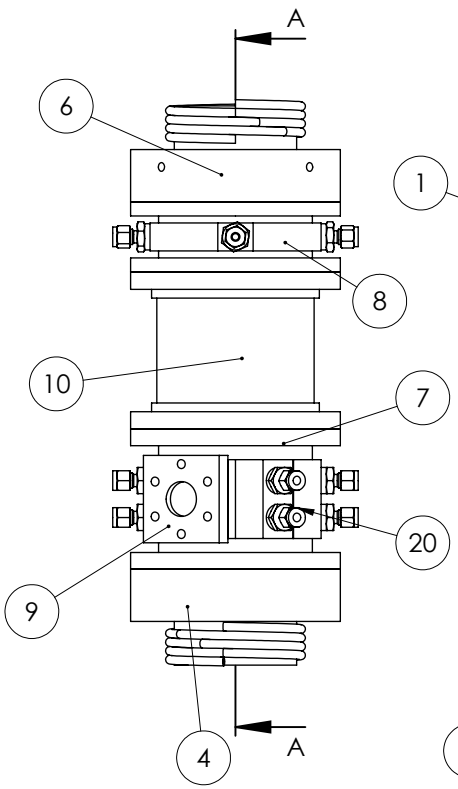

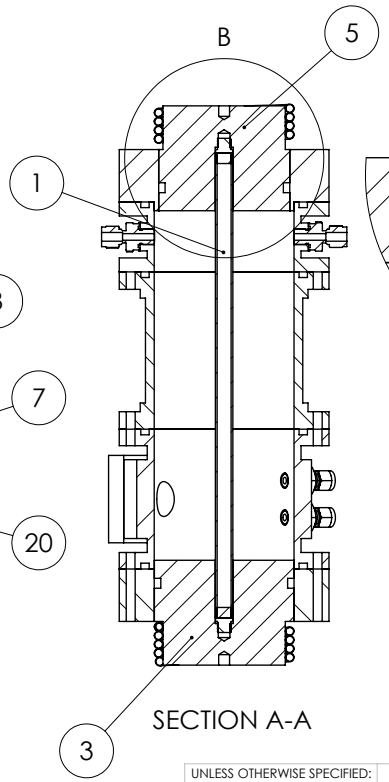

SECTION A-A

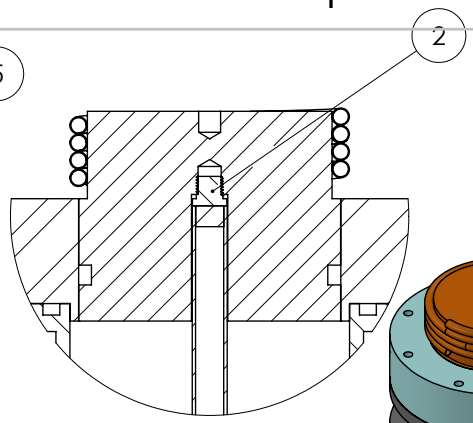

DETAIL B
SCALE 1 : 2

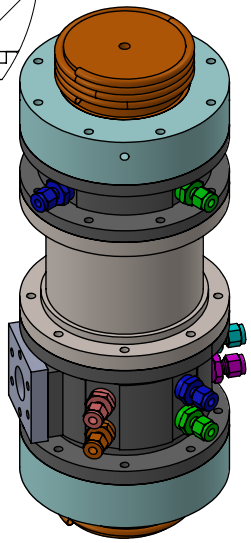

UNLESS OTHERWISE SPECIFIED:		NAME	DATE
DIMENSIONS ARE IN INCHES TOLERANCES: FRACTIONAL ± ANGULAR: MACH ± BEND ± TWO PLACE DECIMAL ±0.01 THREE PLACE DECIMAL ±0.005	DRAWN	Conor M.	12/15/21
	CHECKED		
	ENG APPR.		
	MFG APPR.		
	Q.A.		
INTERPRET GEOMETRIC TOLERANCING PER:	COMMENTS:		
MATERIAL	QTY: 1		
FINISH			
DO NOT SCALE DRAWING			

TITLE: Full Assembly 133

SIZE	DWG. NO.	REV
A	A02	
SCALE: 1:4	WEIGHT:	SHEET 1 OF 1

Appendix G

SHADOWGRAPH IMAGE SEQUENCES OF H28 AT ALL WALL TEMPERATURES

This appendix presents representative sequences of images for each of the steady state T_w values outlined in Section 6.4.2.1. The T_w = 555 K and T_w = 1015 K cases are included in Chapter 6 and not reproduced here. These are snapshots of much longer videos which were used for quantitative transition analysis using the intermittency approach introduced in Chapter 6. These instead provide a qualitative illustration of the flow features and degree of turbulence as a function of T_w. In Appendix G.2 a 12 gauge copper wire was wrapped around the cylinder at a height of 12 in to prematurely trip the flow for relatively low T_w conditions.

For all figures in this appendix Δt between frames is 1/30 s. All images were processed using POD for background removal, contrast stretched, and brightened for presentation.

G.1 H28 shadowgraph images for a range of wall temperatures

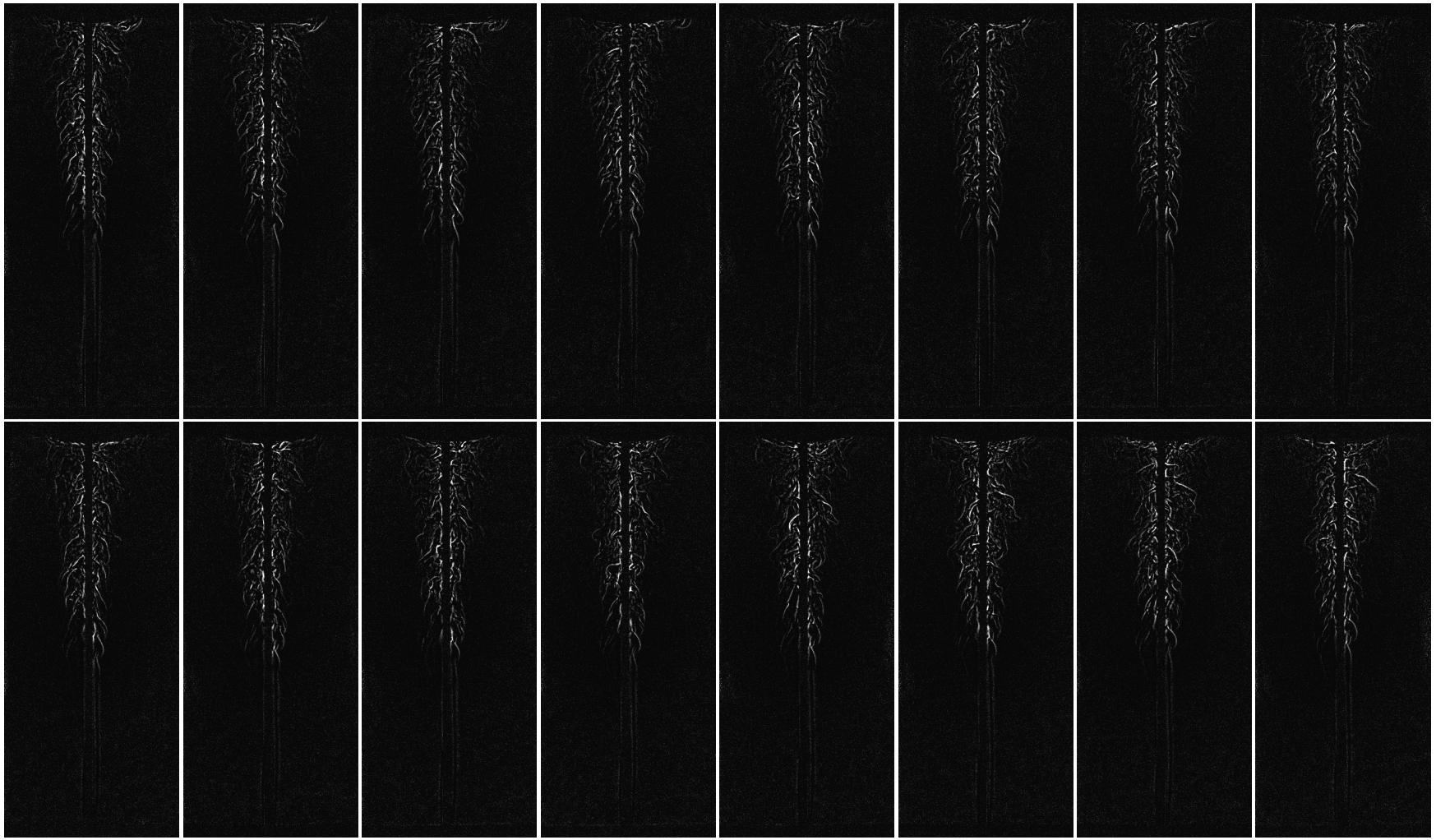

Figure G.1: Processed Shadowgraph image sequence for T_w = 625 K.

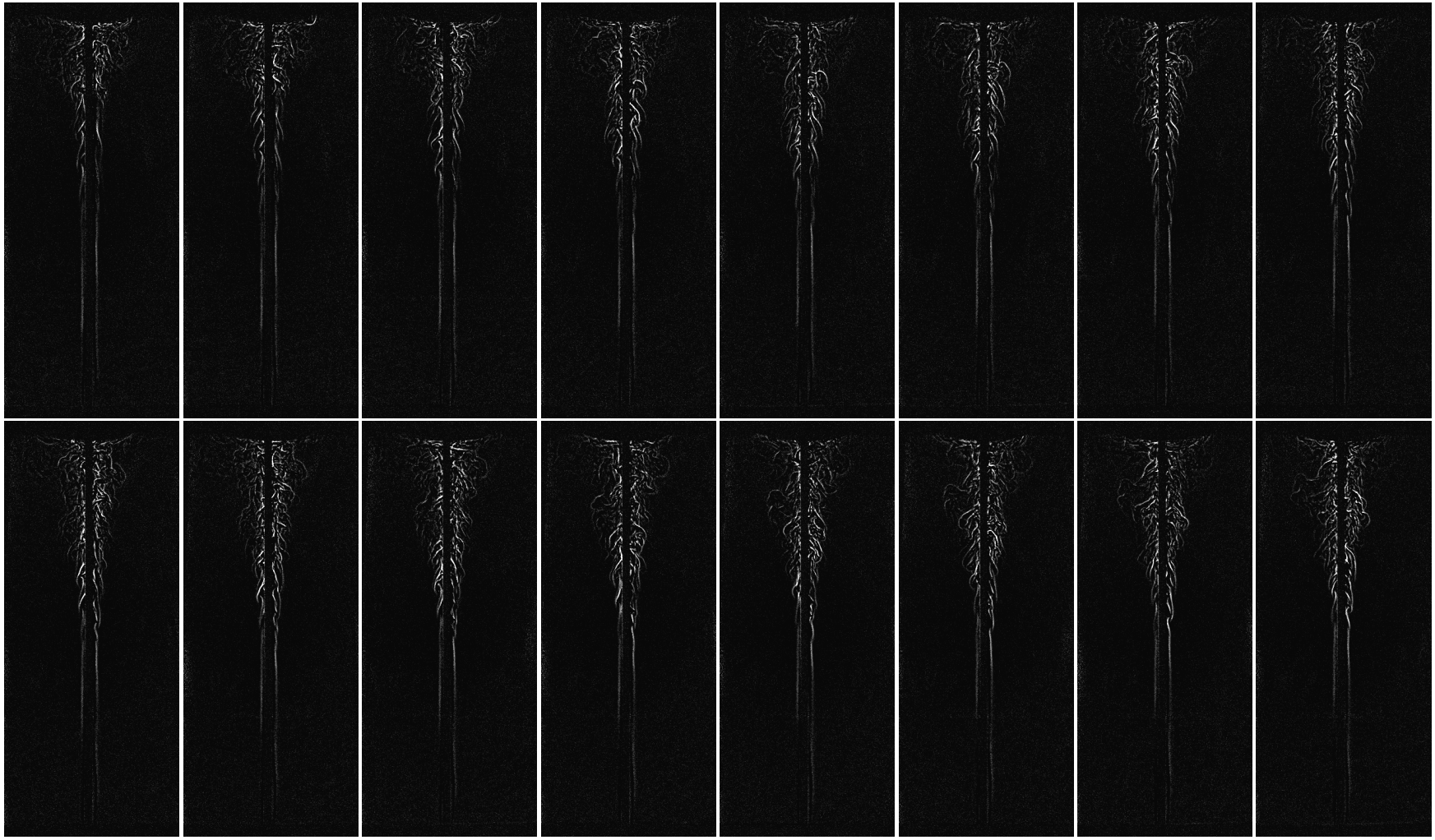

Figure G.2: Processed Shadowgraph image sequence for T_w = 745 K.

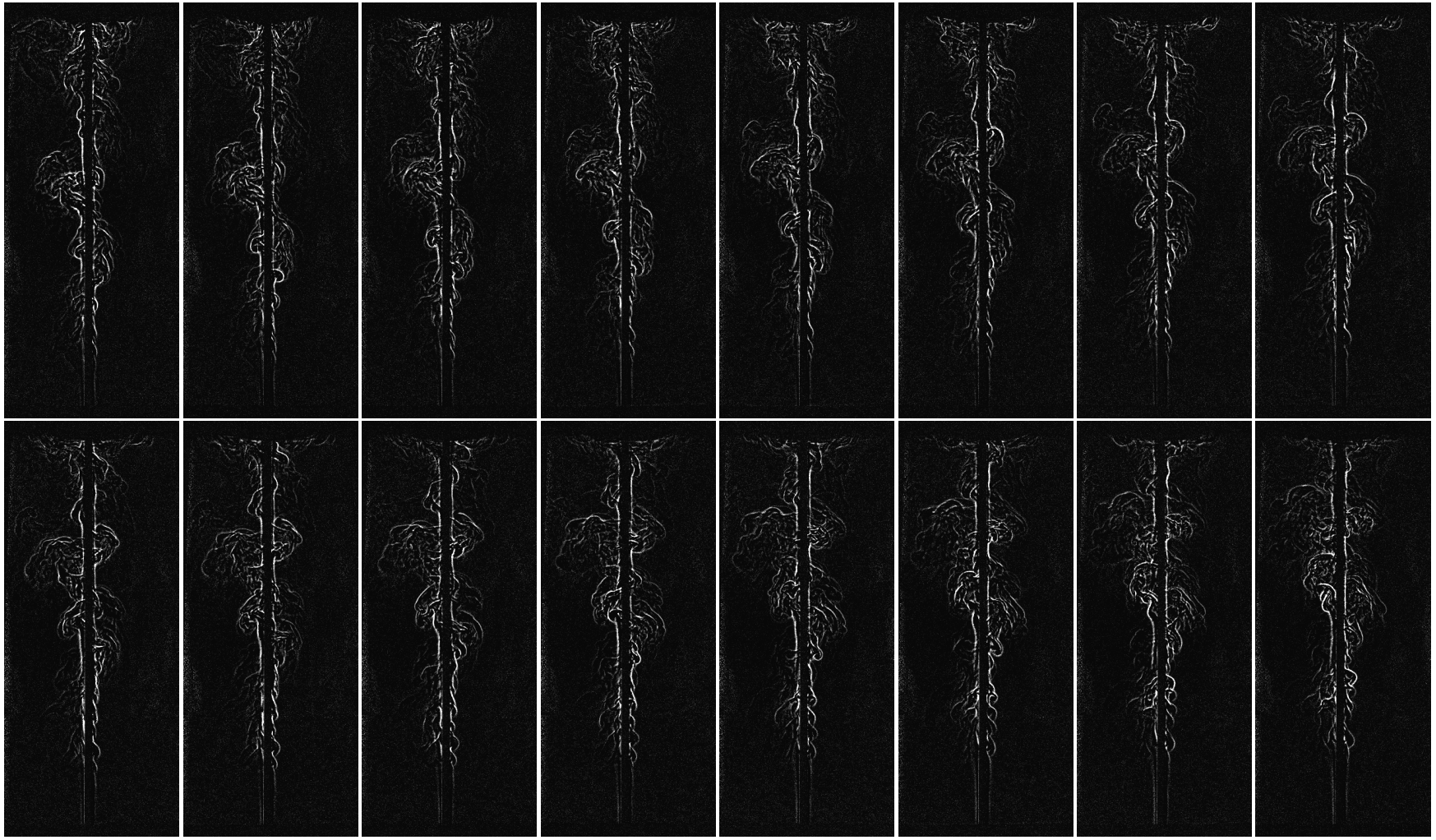

Figure G.3: Processed Shadowgraph image sequence for T_w = 850 K.

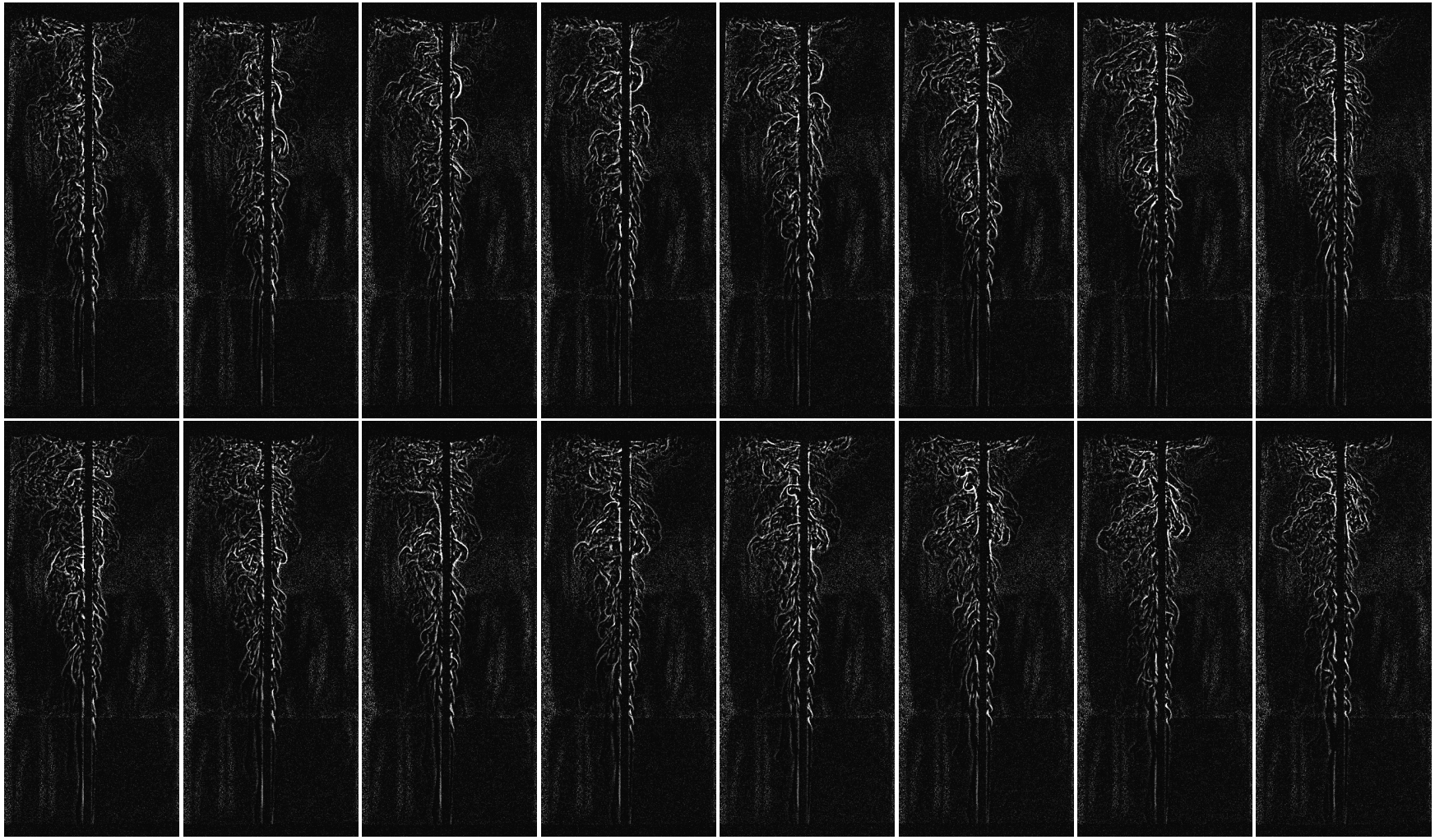

Figure G.4: Processed Shadowgraph image sequence for T_w = 950 K.

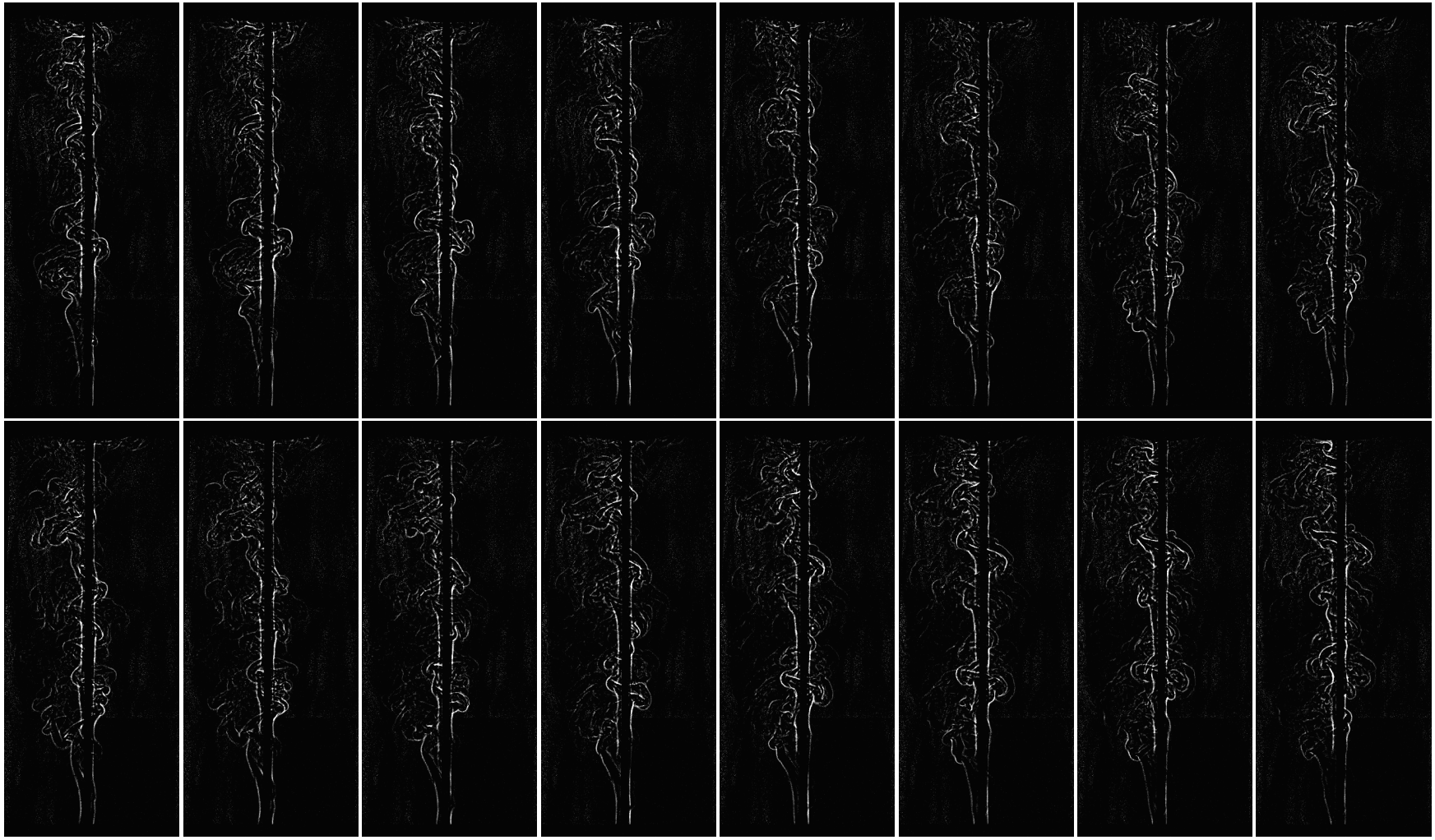

Figure G.5: Processed Shadowgraph image sequence for T_w = 1140 K.

G.2 H28 with Imposed Flow Disturbance (Trip Wire)

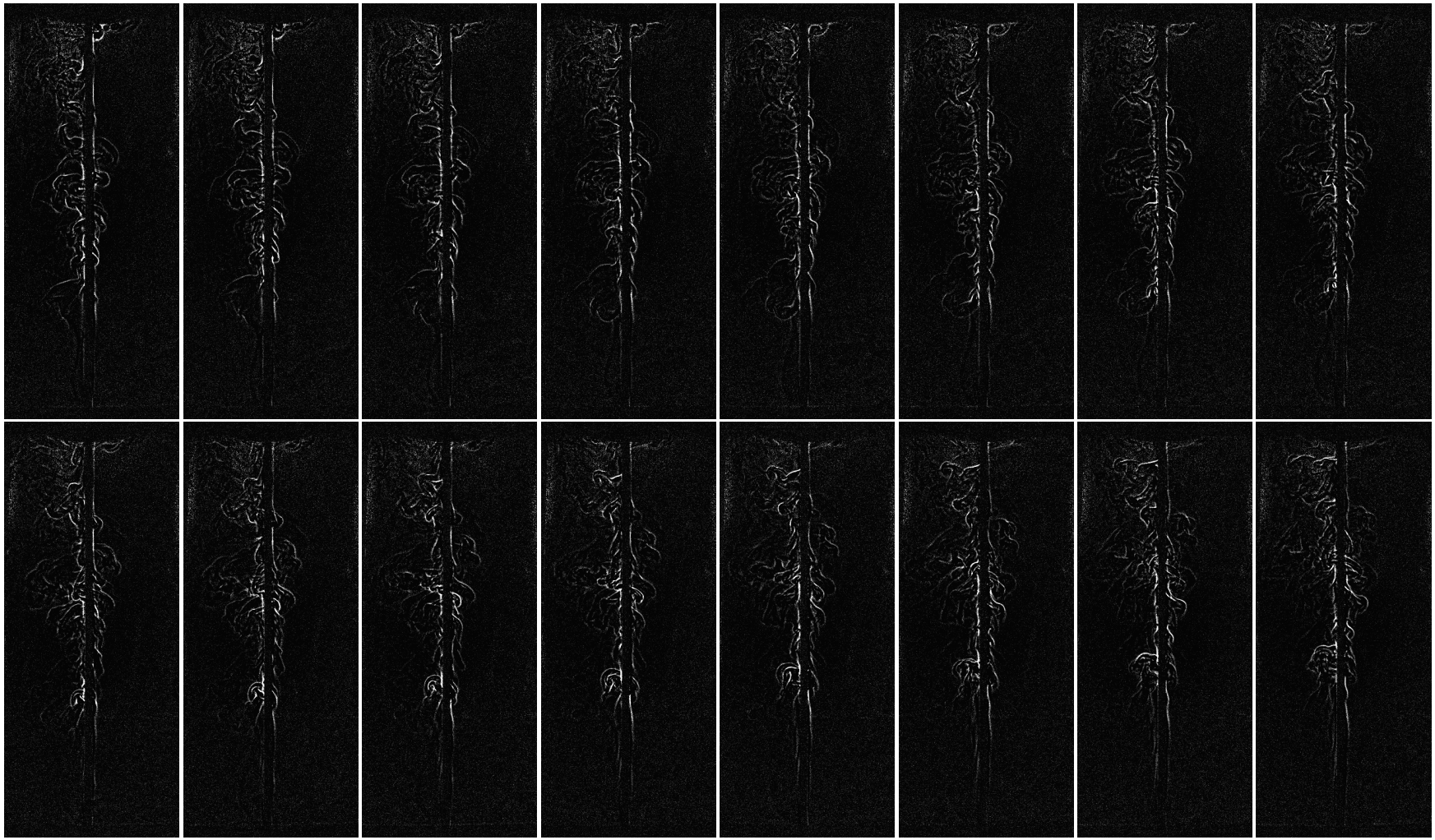

Figure G.6: Processed Shadowgraph image sequence for T_w = 555 K with an imposed flow disturbance (trip wire).

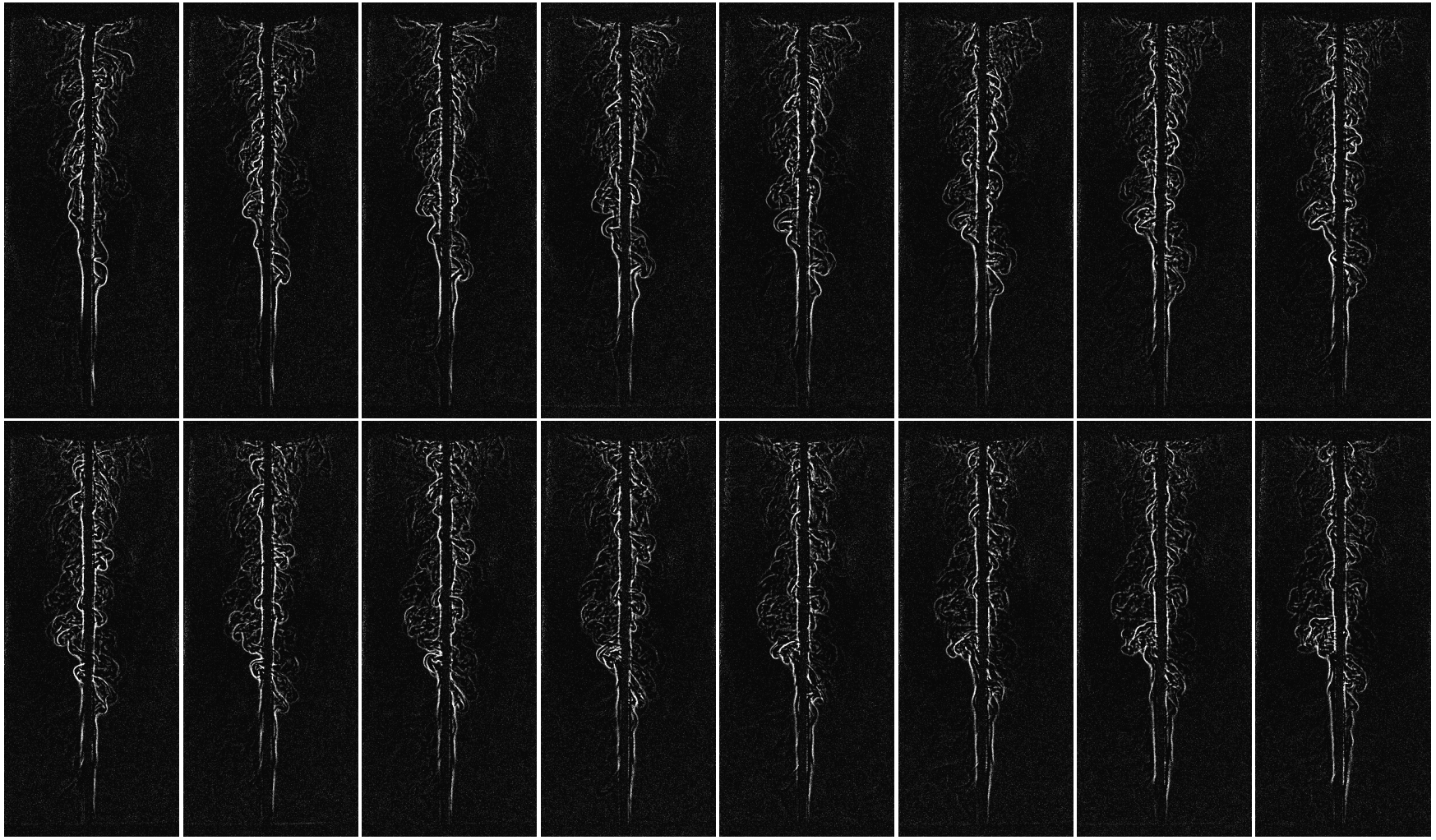

Figure G.7: Processed Shadowgraph image sequence for T_w = 745 K with an imposed flow disturbance (trip wire).

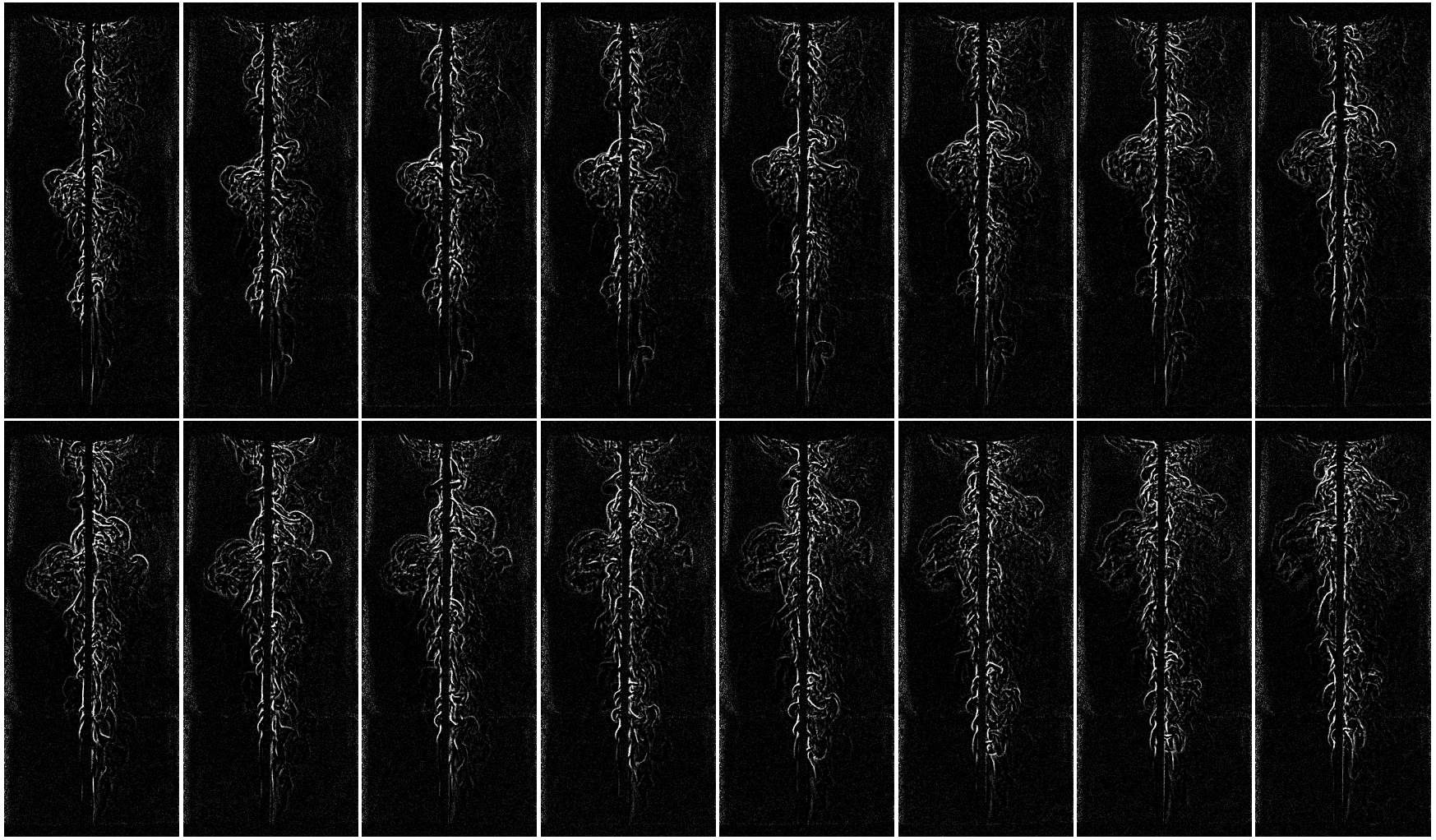

Figure G.8: Processed Shadowgraph image sequence for T_w = 850 K with an imposed flow disturbance (trip wire).

Appendix H

CAT SHOT DATA

This section summarizes the ignition data obtained using the Confined Autoginition Test (CAT) for stoichiometric n-hexane/air mixtures. In accordance with the discussion in Section 7.3, the data are organized into two groups:

1. Steady state: T_w =const. (Appendix H.1)
2. Transient: dT_w/dt =const. (Appendix H.2)

For steady state shots the I and Volt values given are the steady state values. For transient shots these are instead the values of the constant current (high heating rates) or initial heating current (low to moderate heating rate). The only steady state ignition conditions found were on the transient heating period at lower temperatures than the steady set point value $T_{ign} < T_{set}$. The reported dT_w/dt values were as mesured by the pyrometer.

H.1 CAT data: Steady State

Table H.1: CAT ignition data for Steady State shots.

Shot #	**Config.**	H **(in)**	T_0 **(°C)**	I **(A)**	**Volt (V)**	P_{tot} **(torr)**	$P_{C_6H_{14}}$ **(torr)**	P_{N_2} **(torr)**	P_{O_2} **(torr)**	T_{set} **(K)**	T_{ign} **(K)**	P_{max} **(atm)**	$\frac{dP}{dt}\|_{max}$ **(atm/s)**	t_{ign} **(s)**	**Ign (0/1)**
17	A5	10	20.2	255	3.0	101.2	2.22	78.36	20.62	1050					0
18	A5	10	20.1			101.5	2.24	78.51	20.75	1100	1038			35	1
19	A5	10	20.0			101.5	2.22	80.55	18.73	1100	1040			67	1
20	A5	10	20.2			101.5	2.26	78.33	20.91	1050	1050			84	1
21	A5	10	20.0	265	2.5	101.5	2.27	79.01	20.22	1050					0
22	A5	10	20.2			101.5	2.25	78.32	20.93	1100	1055			61	1
23	A5	10	20.1	255	2.3	101.4	2.19	78.39	20.82	1025					0
36	A5	10	20.5	265	2.5	101.5	2.26	78.39	20.85	1050					0
40	A5	10	20.5	210	1.9	101.4	2.14	78.82	20.44	900					0
41	A5	10	20.4	180	1.6	101.5	2.24	78.53	20.73	825					0
42	A5	10	20.5	250	2.3	101.3	2.21	78.33	20.76	1000					0
43	A5	10	20.0			101.5	2.21	78.51	20.78	1050	1045		38.30	55	1
44	A5	10	20.4	230	2.0	101.5	2.21	78.30	20.99	950					0
45	A5	10	20.4	265	2.5	101.4	2.34	78.41	20.65	1030					0
46	A5	10	20.4	255	2.3	101.5	2.26	79.49	19.75	1000					0
47	A5	10	20.4	265	2.4	101.5	2.23	78.51	20.76	1025					0
48	A5	10	20.4	190	1.7	101.5	2.27	78.46	20.77	850					0
49	A5	10	20.4	255	2.4	101.5	2.32	78.41	20.77	1000					0
50	A5	10	23.1	220	2.0	101.5	2.22	78.27	21.01	950					0
51	A5	10	23.2	270	2.5	101.5	2.28	78.65	20.57	1050					0
52	A5	10	23.2	270	2.5	101.3	2.27	78.57	20.46	1050					0

Table H.1: CAT ignition data for Steady State shots. (continued)

Shot #	**Con-fig.**	H **(in)**	T_0 **(°C)**	I **(A)**	**Volt (V)**	P_{tot} **(torr)**	$P_{C_6H_{14}}$ **(torr)**	P_{N_2} **(torr)**	P_{O_2} **(torr)**	T_{set} **(K)**	T_{ign} **(K)**	P_{max} **(atm)**	$\frac{dP}{dt}\|_{max}$ **(atm/s)**	t_{ign} **(s)**	**Ign (0/1)**
57	A20	36	26.2	200	5.1	101.3	2.21	77.89	21.20	925					0
60	A20	36	25.4			101.5	2.27	78.36	20.87	975	950.5	6.70	132.08	94	1
61	A20	36	26.0	200	5.0	101.5	2.26	78.24	21.00	900					0
74	A10	18	26.0	180	3.0	101.5	2.26	78.47	20.77	850					0
75	A10	18	25.7	210	3.5	101.5	2.25	78.32	20.93	925					0

H.2 CAT data: Transient

Table H.2: CAT ignition data for Transient shots.

Shot #	**Config.**	H **(in)**	T_0 **(°C)**	I **(A)**	**Volt (V)**	P_{tot} **(torr)**	$P_{C_6H_{14}}$ **(torr)**	P_{N_2} **(torr)**	P_{O_2} **(torr)**	$\frac{dT}{dt}$ **(K/s)**	T_{ign} **(K)**	P_{max} **(atm)**	$\frac{dP}{dt}\|_{max}$ **(atm/s)**	t_{ign} **(s)**	**Ign (0/1)**
24	A5	10	20.3	300	5	101.7	2.23	78.32	21.15	4.39	1084	2.43	13.43	133	1
25	A5	10	20.4	400	5	101.4	2.25	78.55	20.60	12.72	1036	5.85	22.00	55	1
26	A5	10	20.4	500	5	101.5	2.24	78.81	20.45	23.41	1054	6.14	27.04	35	1
27	A5	10	20.3	450	5	101.4	2.22	78.36	20.82	17.93	1059	5.98	20.63	42	1
28	A5	10	20.3	450	5	101.4	2.24	78.29	20.87	18.01	1058	6.01	24.98	42	1
29	A5	10	20.4	500	5	101.4	2.24	78.38	20.78	23.12	1055	6.24	23.51	34	1
30	A5	10	20.4	400	5	101.4	2.18	78.55	20.67	13.01	1071	5.24	14.15	55	1
31	A5	10	20.3	300	5	101.2	2.24	78.34	20.62						0
32	A5	10	20.3	600	5	101.5	2.25	78.89	20.36	29.18	1037	6.67	38.32	24	1
33	A5	10	20.3	450	5	104.8	2.26	78.69	23.85	19.36	1041	6.33	30.78	41	1
34	A5	10	20.4	300	5	101.5	2.19	78.35	20.96	3.03	1075	3.40	6.15	128	1
35	A5	10	20.4	400	5	101.5	2.23	78.72	20.55	12.43	1051	6.06	23.01	53	1
36	A5	10	20.5	600	5	101.5	2.26	78.39	20.85						0
37	A5	10	20.4	325	5	101.4	2.25	78.35	20.80	4.90	1082	3.06	10.06	101	1
38	A5	10	20.4	500	5	101.3	2.23	78.29	20.78	22.13	1029	5.18	51.10	32	1
39	A5	10	20.4	300	5	101.4	2.20	78.31	20.89						0
53	A5	10	23.2	600	5	101.3	2.26	78.36	20.68	27.59	1092	5.96	93.34	42	1
54	A5	10	23.1	600	5	101.3	2.23	78.58	20.49	26.98	1076	6.35	118.17	30	1
55	A20	36	26.4	375	10	101.9	2.26	79.58	20.06	12.30	895			52	1
56	A20	36	26.1	300	10	101.1	2.21	77.70	21.19	6.29	942	6.30	95.09	90	1
58	A20	36	25.8	375	10	101.3	2.21	77.91	21.18	11.04	927	7.37	152.59	55	1

Table H.2: CAT ignition data for Transient shots. (continued)

Shot #	**Config.**	H **(in)**	T_0 **(°C)**	I **(A)**	**Volt (V)**	P_{tot} **(torr)**	$P_{C_6H_{14}}$ **(torr)**	P_{N_2} **(torr)**	P_{O_2} **(torr)**	$\frac{dT}{dt}$ **(K/s)**	T_{ign} **(K)**	P_{max} **(atm)**	$\frac{dP}{dt}\|_{max}$ **(atm/s)**	t_{ign} **(s)**	**Ign (0/1)**
59	A20	36	25.9	250	10	101.3	2.21	78.04	21.05	1.97	980	5.30	58.83	159	1
62	A20	36	25.7	350	10	101.5	2.24	78.58	20.68	9.87	932			62	1
63	A20	36	25.8	300	10	101.3	2.27	78.37	20.66	6.19	956	6.23	107.85	93	1
64	A20	36	25.8	375	10	101.3	2.25	78.98	20.07	11.71	925	7.41	175.06	52	1
65	A20	36	26.1	215	10	101.3	2.25	78.01	21.04						0
66	A20	36	26.1	250	10	101.3	2.28	78.20	20.82	0.99	984	4.65	42.00	318	1
67	A20	36	26.2	250	10	102.2	2.22	78.28	21.70						0
68	A20	36	25.9	375	10	101.3	2.27	78.05	20.98	11.49	934	7.20	158.37	62	1
69	A20	36	25.9	250	10	101.5	2.28	78.29	20.93					582	1
70	A20	36	25.9	250	10	101.5	2.26	78.13	21.11						0
71	A20	36	24.2	250	10	101.5	2.27	78.43	20.80	0.25	972	2.78	6.56	977	1
72	A20	36	24.2	250	10	101.3	2.26	78.11	20.93	2.51	952	5.64	82.39	169	1
76	A10	18	25.6	250	10	101.3	2.20	78.51	20.59	1.01	985	4.23	23.84	326	1
77	A10	18	25.8	250	10	101.5	2.24	78.56	20.70	0.50	992	3.51	21.33	578	1
78	A10	18	25.9	250	10	101.5	2.28	79.25	19.97	2.04	988	5.54	54.62	211	1
79	A10	18	25.5	300	10	101.5	2.28	78.60	20.62	5.15	970	6.31	116.67	97	1
80	A10	18	25.8	375	10	101.3	2.22	78.43	20.65	12.76	930	7.08	127.13	52	1
81	A10	18	25.4	275	10	101.5	2.26	78.47	20.77	3.63	989	5.87	82.45	127	1
82	A10	18	25.4	325	10	101.3	2.25	78.29	20.76	7.82	973	6.49	113.95	78	1
83	A10	18	25.4	375	10	101.2	2.24	78.33	20.63	12.19	939	6.83	127.23	52	1
84	A10	18	25.3	350	10	101.1	2.24	78.32	20.54	10.48	947	6.70	115.95	63	1

Table H.2: CAT ignition data for Transient shots. (continued)

Shot #	**Config.**	H **(in)**	T_0 **(°C)**	I **(A)**	**Volt (V)**	P_{tot} **(torr)**	$P_{C_6H_{14}}$ **(torr)**	P_{N_2} **(torr)**	P_{O_2} **(torr)**	$\frac{dT}{dt}$ **(K/s)**	T_{ign} **(K)**	P_{max} **(atm)**	$\frac{dP}{dt}\|_{max}$ **(atm/s)**	t_{ign} **(s)**	**Ign (0/1)**
85	A10	18	25.4	300	10	101.3	2.26	78.29	20.75	5.96	984	6.08	92.31	96	1
86	A10	18	25.5	375	10	101.5	2.23	78.46	20.81	12.31	959	6.21	80.43	55	1
87	A10	18	25.7	250	10	101.3	2.25	78.50	20.55	1.01	1009	3.45	19.93	345	1
88	A10	18	20.0	250	10	101.5	2.25	78.36	20.89	3.34	979	6.25	116.56	109	1
89	A10	18	20.0	250	10	103.9	2.24	78.44	23.22	0.25	1015	2.50	4.48	1140	1
90	A10	18	20.0	375	10	101.4	2.24	78.61	20.55	12.67	942	7.37	41.48	53	1
91	A10	18	20.0	250	10	101.5	2.24	78.38	20.88	0.17	1028	1.70	4.11	1750	1
92	A10	18	20.0	375	10	101.3	2.19	78.35	20.76	12.67	947	7.50	36.86	53	1
93	A10	18	20.0	200	10	101.3	2.22	78.32	20.76	0.08					0
94	A10	18	20.0	375	10	102.2	2.23	78.26	21.71	12.40	945	6.79	34.11	53	1